SEDIMENTARY GEOLOGY AND GEOCHEMICAL STUDIES OF UPPER CRETACEOUS SANDSTONES, NORTHERN BIDA BASIN

By

ADEPOJU, S.A.

(05/55EA091)

B.Sc., M.Sc. (Ilorin)

A THESIS SUBMITTED TO THE POSTGRADUATE SCHOOL, UNIVERSITY OF ILORIN, ILORIN, NIGERIA

IN PARTIAL FULFILMENT OF THE REQUIREMENT FOR THE AWARD OF THE DEGREE OF DOCTOR OF PHILOSOPHY (Ph.D) DEGREE IN GEOLOGY

October, 2019

CERTIFICATION

This isto certify that Adepoju, Suraju Adesina (05/55EA091) carried out this research under my supervision and has been read and and approved as meeting the requirements for the award of a Doctor of Philosophy (Ph.D.) Degree in Geology.

Name	Signature	Date
External Examiner		
Dr. O.A. Omotoso		
Head of Department and Chief Examinar		
Prof. A.C. Tella		
Internal Examiner from a Related Department in the University (Name of the Dept.: Department of Chemistry)		
Prof. S.O. Akande		
Supervisor and Internal Examinar		
Dr. O.A. Adekeye		
Departmental Postgraduate Programme Coordinator and Internal Examiner		

DEDICATION

This project is dedicated;

- My late parents; Mr. Abdul-Wahab Ajibola Adepoju and Mrs. Waseelat Ajike Adepoju (Nee Ajirinnibi).
- All men of conscience who are dedicated to make the world a better place for the less privileged ones.

ACKNOWLEDGMENT

My first and most earnest, acknowledgment goes to my supervisor Professor Olusola Johnson Ojo who has provided many years of invaluable guidance, critical discussions, advice and support for this research. It has been an honor to be the Ph.D. student of a person who has been instrumental in ensuring my academic, professional and moral well being ever since we met. I appreciate all his contributions of time and ideas to make my Ph.D experience productive and I will forever remain grateful to you sir. My sincere appreciation also goes to my co-supervisor; Professor Samuel O. Akande for his invaluable contributions and encouragement towards the successful completion of this research.

Sincere thanks are extended to all the lecturers in the Department of Geology and Mineral Sciences, University of Ilorin for providing encouragement and valuable suggestions that improved the quality of this work. And to the member of non-academic staff of the department, I appreciate you too. Also, to Dr. (Mrs) Sola-Ojo, thanks for your advice and words of encouragement always, I'll be forever grateful to you as a God's sent for achieving this, thanks and God bless you and your children too.

This project is greatly benefited from grants; Tertiary Educational Trust Fund (TETFund through Kwara State University) and CV Raman Fellowship for African Researchers (2016) through the Department of Science and Technology, Government of India. My profound gratitude also goes to the Director, CSIR-National Geophysical Research Institute (NGRI), Hyderabad, India and member of the Isotope Geochemistry and Geochronology group, NGRI for the support received during my 6 months research visitation. To my guide at NGRI, Dr. Bulusu Sreenivas for his general guide, support and good hearth extended during my fellowship period, I say thank you sir. All your discussions and suggestions have contributed immensely to this research.

The completion of this research especially laboratory analysis witnessed the contributions from member of Isotope Geochemistry and Geochronology group at NGRI. I deeply appreciate the contributions of Dr. Vijaya Kumar, Ms. Manju and Mr. E.G.H.N. Santhos for teaching me how to use SEM, CL and EBSD scan and processing. Mr. Balu Gugulothu is appreciated for teaching on how to prepare, analyze and running samples while Dr. E.V.S.S.K. Babu guide and supervise the processing of samples for ICPMS analysis and also petrographic studies. I thank Adimah Nicholas Iraboh and Emmanuel Anthony for the hospitality accorded to me, their support and words of encouragement during my stay at NGRI hostel, I pray God continue bless you, Amen.

During the process of completing this research, it became clear to me that no knowledge is achieved in isolation and a researcher cannot complete a Ph.D thesis alone. Although the list of individuals I wish to thank extends beyond the limits of this format, however, I would like to thank the head of Department of Geology and Mineral Sciences, Dr. Olufemi Olaniyan and other member of staff of the Departmet. It is a pleasure to acknowledge the immense help and support I received from friends, Mr. Y. A. Jimoh, Haruna K. Abdul-Rasaq and Olawumi, Hakeem Bolaji, you are all well appreciated. Mr. Bamidele Oloruntoba and Mr. Hassan Abdul-Sobur Olanrewaju are well appreciated for their excellent support and good company during the several field works. Mr. Majeed Abiola of Midas Print is well appreciated for typesettings corrections, printings and binding.

I owe deepest gratitude to my late parents; Mr. Abdul-Wahab Ajibola Adepoju and Mrs. Waseelat Ajike Adepoju (Nee Ajirinnibi) with my aunt Mrs. Sidikat (Nee Ajirinnibi), I pray Almighty Allah (SWT) forgive all your shortcomings and make Al-Janah firdaus your last abode (Amin). To my siblings; Halimah, Monsuro, Quazeem and Khadijah, thank you for you prayers, supports and contributions. The moral and financial contributions of families of

Alhaji Tajudeen Apena and Alhaja Nusirat Folashade Apena, Mr. Ibrahim Olagoke (BODYUS) and wife Mrs. Risikat Olagoke with their children are well appreciated too.

Special and extremely grateful to my ever loving wife, Barrister (Mrs.) Surajudeen Kawthara Bukola (nee Hassan Abdur-Rahaman) for her unconditional love, caring, endurance and encouragement during the course of this study. To my children, Sumayyah Adebimpe Ajike, Suf'yan Adebayo Alabi and Sameer Akorede Akanbi, thanks for your endurance all these while, I love you all. The family of Dr. Yusuf Usman Oladimeji and Hajia Hafsat Morenikeji Yusuf and their children; Haneefat, Tasleemah, Jamaldeen, Jameelah and Tasleem have been source of support and encouragement too towards this achievement; all of you are very wonderful and dear to me. My father-in-law, Mr. Hassan Abdur-Rahaman is also appreciated for his support and prayers. May Allah reward you more than my wish to you all. And to some individuals, who were used by God to assist me during this program, I thank you all. Thanks and God bless you.

Lastly, all praises and adoration are due to Almighty Allah (SWT), the most Beneficent, the most Merciful, the Creator, Sustainer and Cherisher of the whole world for His immense mercy in concluding this research. May the peace and blessings of Allah be upon the noble soul of Prophet Muhammmad (PBUH), his household and companion till eternity (Amin).

Alhamdulillah Robil-Alamin……..

TABLE OF CONTENTS

Title Page	i
Certification	ii
Dedication	iii
Acknowledgement	iv
Table of Contents	vii
Lists of Figures	xv
Lists of Tables	xxx
Appendix	xxxv
Abstract	xlv

CHAPTER ONE: INTRODUCTION

1.1 Background Information	1
1.2 Location and Accessibility of the Study Area	4
1.3 Physiography	6
1.4 Previous Work	7
1.5 Statement of Problem	9
1.6 Justification	9
1.7 Aim and Objectives	10
1.8 Significance of the study	10

CHAPTER TWO: GEOLOGY OF THE STUDY AREA

2.1 General Statement	12
2.2 Tectonic Evolution	12

2.3 Structural Evolution 18

2.4 Stratigraphy 18

2.4.1 Stratigraphic Setting 18

2.4.1.1 Northern Bida Basin 19

2.4.1.2 Southern Bida Basin 22

CHAPTER THREE: METHODOLOGY

3.1 General Statement 27

3.2 Field Work 29

3.3 Facies Analysis 29

3.4 Laboratory Analysis 30

3.4.1 Pebble Morphometric Analysis 30

3.4.2 Grain Size Analysis 31

3.4.3 Thin Section Petrography 32

3.4.3.1 Detrital Mineral Composition 32

3.4.3.2 Heavy Mineral Analysis 33

3.4.4 Mineralogical Analysis (X-Ray Diffraction) 34

3.4.5 Bulk Geochemical Analysis 35

3.4.5.1 X-Ray Fluorescence Sample Preparation Procedure (Major Elements) 36

3.4.5.2 Trace and Rare Earth Elements Sample preparation procedure 38

3.4.6 Image Analysis (Zircon Typology) 41

3.5 Statistical Analysis (Factor Analysis and Principal Component Analysis) 44

3.6 Modal Analysis of employed Techniques 45

CHAPTER FOUR: RESULTS

4.1 Facies Analysis, Architectural Elements, Geometry and Paleocurrent 47

4.1.1 Lithofacies and Sub-facies description 47

4.1.1.1 Clast-supported, massive conglomerate (Gcm) sub-facies 50

4.1.1.2 Matrix-supported, massive conglomerate (Gmm) sub-facies 50

4.1.1.3 Crudely bedded conglomerate (Gh) sub-facies 53

4.1.1.4 Crudely stratified sandstone (Se) sub-facies 55

4.1.1.5 Planar cross-stratified sandstone (Sp) sub-facies 57

4.1.1.6 Horizontally stratified sandstone (Sh) sub-facies 58

4.1.1.7 Rippled cross-stratified sandstone (Sr) sub-facies 60

4.1.1.8 Massive sandstone (Sm) sub-facies 60

4.1.1.9 Finely laminated mudstone (Fl) sub-facies 63

4.1.1.10 Massive very fine sandstone and mudstone (Fm) sub-facies 63

4.1.2 Outcrop Facies Association Analysis and Characteristics 66

4.1.2.1 Outcrop Facies Association 1 (OFA1) 66

4.1.2.2 Outcrop Facies Association 2 (OFA2) 69

4.1.2.3 Outcrop Facies Association 3 (OFA3) 71

4.1.2.4 Outcrop Facies Association 4 (OFA4) 73

4.1.2.5 Outcrop Facies Association 5 (OFA5) 75

4.1.3 Architectural Elements and Sand Body Geometry 77

4.1.3.1 Gravel bars and bedforms (GB) 77

4.1.3.2 Sandy Bedforms (SB) Elements 79

4.1.3.3 Lateral Accretion Element (LA) 82

4.1.3.4 Laminated Sand Sheet Element (LS) 82

4.1.3.5 Overbank or Floodplain Element (OF) 84

4.1.3.6 Channels Elements (CH) 84

4.1.4 Paleocurrent 88

4.1.5 Gross Depositional Processes and facies models within the study area 94

4.2 Textural and Mineralogical Analyses 99

4.2.1 Grain Size Analysis (Mechanical Sieving) 99

4.2.1.1 Matrix-supported, massive conglomerate (Gmm) sub-facies 100

4.2.1.2 Crudely bedded conglomerate (Gh) sub-facies 100

4.2.1.3 Crudely stratified sandstone (Se) sub-facies 101

4.2.1.4 Planar cross-stratified sandstone (Sp) sub-facies 101

4.2.1.5 Horizontally stratified sandstone (Sh) sub-facies 101

4.2.1.6 Rippled cross-stratified sandstone (Sr) sub-facies 102

4.2.1.7 Massive sandstone (Sm) sub-facies 102

4.2.1.8 Finely laminated mudstone (Fl) sub-facies 102

4.2.1.9 Massive mudstone (Fm) sub-facies 103

4.2.2 Detrital Mineralogical Composition, Description and Modal Analysis 105

4.2.2.1 Crudely bedded Conglomerate (Gh) Sub-facies 105

4.2.2.2 Crudely stratified Sandstone (Se) sub-facies 109

4.2.2.3 Planar cross-stratified sandstone (Sp) sub-facies 112

4.2.2.4 Rippled Cross-stratified Sandstone (Sr) sub-facies 115

4.2.2.5 Horizontally stratified sandstone (Sh) sub-facies 117

4.2.2.6 Massive sandstone (Sm) sub-facies 120

4.2.2.7 Finely laminated, very-fine sandstone and mudstone (Fl) sub-facies 123

4.2.2.8 Massive, very-fine sandstone and mudstone (Fm) sub-facies 126

4.3 Heavy Minerals Description and Modal Composition 129

4.3.1 Massive, matrix-supported conglomerate (Gmm) sub-facies 129

4.3.2 Crudely bedded Conglomerate (Gh) sub-facies 132

4.3.3 Crudely stratified Sandstone (Se) sub-facies 135

4.3.4 Planar cross-stratified sandstone (Sp) sub-facies 138

4.3.5 Rippled cross-stratified sandstone (Sr) sub-facies 141

4.3.6 Horizontally stratified sandstone (Sh) sub-facies 143

4.3.7 Massive sandstone (Sm) sub-facies 146

4.3.8 Laminated, very-fine sandstone and mudstone (Fl) sub-facies 149

4.3.9 Massive, very-fine sandstone and mudstone (Fm) sub-facies 152

4.4 Mineralogical Composition (XRD) 155

4.5 Geochemical Data (XRF and ICPMS) 159

4.5.1 Major Elements (XRF) 159

4.5.1.1 Harker Variation Diagrams and Major Elemental Relationship 160

4.5.2 Trace Elements (ICPMS) 167

4.5.2.1 Transition metal trace elements (TTE - Cr, V, Co, Ni, Sc) 167

4.5.2.2 Large-ion lithophile elements (LILE; Rb, Cs, Ba, Sr, Th, U) 167

4.5.2.3 High field strength elements (HFSE; Zr, Hf, Y, Nb, Ta) 168

4.5.3 Rare Earth Elements (ICPMS) 176

4.5.4 Statistical Analysis 184

4.5.4.1 Correlation Matrix 184

4.5.4.1.1 Major Elements 184

4.5.4.1.2 Trace Elements 186
4.5.4.2 Factor and Principal Component Analysis 190
4.5.4.2.1 Major Elements 193
4.5.4.2.2 Trace Elements 197

CHAPTER FIVE: DISCUSSION

5.1 Paleo-Environments, Diagenetic History and Reservoir Potentials 201
5.1.1 Depositional Environments 202
5.1.1.1 Facies Analysis Evidence 202
5.1.1.2 Pebble Morphogenesis Evidence 204
5.1.1.3 Grain Size (Sieving) Data Evidence 214
5.1.2 Diagenesis and Reservoir Quality 220
5.1.2.1 Petrographic Evidence 221
5.1.2.2 Scanning Electron Microscope (SEM) and BackScattered Electron (BSE) Analysis 229
5.1.2.2.1 Types of Cement 229
5.1.2.2.2 Quartz Overgrowth 232
5.1.2.2.3 Feldspar Replacement and Dissolution 234
5.1.2.3 Paragenetic Sequence and Diagenetic History 236
5.1.2.4 Qualitative Porosity Evaluation and Reservoir Quality 238
5.2 Sandstone Classification 241
5.2.1 Petrographic Approach 242
5.2.2 Geochemical Approach 246
5.3 Provenance 249
5.3.1 Petrographic Evidence 249
5.3.2 Geochemical Evidence 250
5.3.2.1 Major Elements 250
5.3.2.2 Trace Elements 253
5.3.2.3 Rare Earth Elements 260

5.3.2.3.1 The Europium (Eu/Eu*) Anomaly variation 261
5.3.2.3.2 Rare earth elements normalized values and plots 265
5.3.2.3.2.1 The Upper Continental Crust normalized plot 266
5.3.2.3.2.2 The North American Shale Composite (NASC) normalized plot 268
5.3.2.3.2.3 The Post-Archean Average Shale (PAAS) normalized plot 270
5.3.3 Heavy Mineral Evidence 272
5.3.4 Mineralogical Composition Evidence 275
5.4 Paleotectonic Settings 276
5.4.1 Petrographic Evidence 276
5.4.1.1 Detrital Quartz 277
5.4.1.2 Feldspar 278
5.4.1.3 Rock Fragments 278
5.4.1.4 Petrographic Plots 279
5.4.2 Geochemical Evidence 283
5.4.2.1 Major Elements 284
5.4.2.2 Trace Elements 290
5.4.2.3 Rare Earth Elements 292
5.4.3 Heavy Mineral Evidence 294
5.5 Paleoweathering and Paleoclimate Conditions 295
5.5.1 Paleoweathering Conditions and Maturity 295
5.5.1.1 Petrographic Evidence 296
5.5.1.2 Geochemical Evidence 300
5.5.1.2.1 Major Elements Variations, Ratios and Plots 300
5.5.1.2.2 Trace and Rare Earth Elements 313
5.5.1.3 Heavy Minerals Evidence 318
5.5.2 Paleoclimatic Conditions 319
5.5.2.1 Petrographic Evidence 320

5.5.2.2 Geochemical Evidence 326

5.5.2.3 Mineralogical Composition Evidence 328

5.5.2.4 Zircon Morphology and Typology Evidence as Paleoclimate Indicator 328

CHAPTER SIX: CONCLUSIONS AND RECOMMENDATIONS

6.1 Conclusions 333

6.2 Recommendations 335

LISTS OF FIGURES

Figure 1.1: Geological map of Nigeria showing the position of the Bida Basin 3

Figure 1.2: Geological map of northern Bida Basin showing the Traverses covered in the present study. 5

Figure 2.1: Map showing Benue depression and associated basins and troughs. 14

Figure 2.2: Geological map of Bida Basin showing the locations of the gravity traverses. 15

Figure 2.3a: Model generated from gravity profile for Pategi-Zungeru Traverses. 16

Figure 2.3b: Model generated from gravity profile for Jebba-Keffi Traverse. 16

Figure 2.4: Total magnetic map of the Bida Basin. 17

Figure 2.5: Magnetic Residual Map of the Bida Basin. 17

Figure 3.1: Work flow showing the methodology adopted in this research 28

Figure 3.2: Sample preparation for Pellet prior to XRF analysis (a) Pellet preparation using the machine, (b) Some prepared pellets ready for analysis and (c) Powdered samples collected and spreading at the beginning of sample preparation to make pellets. 37

Figure 3.3a: Laboratory sample preparation for trace and rare earth elements prior to ICPMS analysis. 39

Figure 3.3b: Laboratory sample preparation for trace and rare earth elements prior to ICPMS analysis. 39

Figure 3.3c: Laser Ablation Microprobe Multi Collector Inductive Coupled Plasma Mass Spectrometer (LAM-MC-ICPMS) at NGRI (CSIR) for Trace and Rare Earth Elements analysis. 40

Figure 3.4: The TESCAN VEGA3 scanning electron microscope (SEM) machine equipped with backscatter electron (BSE) and cathodoluminescence (CL) for Image analysis. 43

Figure 3.5: Modality of the employed methodological techniques. 46

Figure 4.1: Field photograph showing typical clast-supported, massive conglomerate (Gcm) and matrix-supported, massive conglomerate (Gmm) sub-facies at: (a) Proposed Harmattan Patigi University, Patigi and (b) Baganko village, near Abiola farm (Lafiagi area). 52

Figure 4.2: Field photograph showing typical crudely bedded conglomerate (Gh) sub-facies at; (a) middle part of section at Shonga, along Tada road, (b) lower part of section at Wariku and (c) lower part of section at Baro, near railway line. 54

Figure 4.3: Field photograph showing typical crudely stratified sandstone (Se) sub-facies at; (a) middle part of section at Katcha (at the southern part and about 100m from the central motor park), (b) lower part of section at Wariku, along Lafiagi road, (c) middle part of section at Baro, near railway line and (d) lower part of section at Wushishi, near River Kaduna. 56

Figure 4.4: Field photograph showing typical planar cross-stratified sandstone (Sp) sub-facies at; (a) middle part of Agbonna ridge, Share, (b) an exposure at Rabba, near River Niger. Horizontally stratified sandstone (Sh) sub-facies at; (c) upper part of the exposure near railway at Baro, (d) middle part of Dokko ridge, behind police station, Dokko. 59

Figure 4.5: Field photograph showing typical example of a rippled cross-stratified sandstone (Sr) sub-facies at; (a) Rabba, near Mokwa (b) Dokko ridge, near Police Station and massive sandstone (Sm) sub-facies at; (c) Tanagi ridge, along Mokwa Kaduna road and (d) Patti-Chin along Baro. 62

Figure 4.6: Field photograph showing typical example of a massive mudstone (Fm) sub-facies at (a) Kutigi and (b) Rafingora, and typical example of finely laminated mudstone (Fl) sub-facies at (c) Tanagi and (d) Manigi. 65

Figure 4.7: Field photograph showing typical example of outcrop facies association 1 (OFA1) that are preserved fluvial Channel lags. 68

Figure 4.8: Field photograph showing typical example of outcrop facies association 2 (OFA2) that are preserved as braided fluvial channel at Shonga, Lafiagi, Lade, Patti-Wodata, Kajita, Rabba, Bida, Dokko, Jimma, Patti-Chin, Wushishi and Lemu. 70

Figure 4.9: Field photograph showing typical example of outcrop facies association 3 (OFA3) that are well preserved as a meandering channels sandstones and are well preserved at Shonga, Lafiagi, Lade, Patti Wodata, Kajita and Bida. 72

Figure 4.10: Field photograph showing typical example of outcrop facies association 4 (OFA4) that are well preserved as tidally influenced fluvial channel sandstone and are well preserved at Manigi, Rabba, Enagi, Kutigi, Lafiagi and Wushishi. 74

Figure 4.111: Field photograph showing typical example of outcrop facies association 5 (OFA5) that that are well preserved as a fluvial overbank/floodplain at Manigi, Tanagi, Rafingora, Enagi and Kutigi. 76

Figure 4.12: An outcrop showing a typical characteristic of a Gravel Bars and Bedform & Sandy Bedform Elements at Baganko and Ndeji respectively. 78

Figure 4.13a: An outcrop showing a typical example of Sandy Bedform (SB) and minor Overbank Fines (OF) Architectural Elements well preserved at Rabba. 80

Figure 4.13b: An outcrop showing a typical; (i) bi-directional wavy structure and burrowing of *Thallasanoides* (arrow in enlarged) and (ii) biotubation and clay drapes on medium-grained sandstone preserved at Rabba. 81

Figure 4.14: Panoramic View of an outcrop showing a typical example of; (a) Lateral Accretion Element (LA) preserved at Bida (ii) Laminated Sand Sheet Element (LS) preserved at Manigi, Tanagi and Rafingora. 83

Figure 4.15: An outcrop showing a typical example of; (a) a major and (b) minor CH architectural elements preserved at Maraba and Tanagi respectively. 85

Figure 4.15 contd.: An outcrop showing a typical example of a Channel Element (CH), Laminated Sand Sheet (LS) and Overbank Fines (OF) preserved at Rafingora. 86

Figure 4.16: Typical characteristics of Sandbody Geometry observed within the study area; (a) a Ribbon geometry common at the southeastern and southwestern parts, (b) a Wedge common at the southwestern and central parts, (c) a Lobate common at the central part and (d) a Sheet common at the northern part all within the study area. 87

Figure 4.17: The imbricated pebbles from the clast-supported, massive conglomerate (Gcm) and matrix-supported, massive conglomerate (Gmm) sub-facies preserved at Harmattan Patigi University, Patigi. 89

Figure 4.182: Rose diagrams summarizing paleocurrent data of planar-cross lamination/bedding and clast imbrications in some localities on the outcrops within study area. 92

Figure 4.19: Paleocurrent map of the study area. 93

Figure 4.20a: Lithostratigraphic correlations across the Northwest-Southeast direction, Northern Bida Basin. 95

Figure 4.20b: Lithostratigraphic correlations across the East-West direction, Northern Bida Basin. 96

Figure 4.21: Lithofacies map of the study area. 97

Figure 4.22: Depositional Environment Model of the Northern Bida Basin. 98

Figure 4.23: Particle size distribution classifications based on the percentages of Gravel, Sand and Mud (G-S-M). 104

Figure 4.24a: Photomicrographs of typical crudely bedded conglomerate (Gh) sub-facies (DOK-1G) at Dokko showing the mineral constituents; Qm (monocrystalline quartz), Qp (polycrystalline quartz) and C (Cement). 107

Figure 4.24b: Photomicrographs of typical crudely stratified sandstone (Se) sub-facies (DOK-1N) at Dokko showing the mineral constituents; Qm (monocrystalline quartz) and Qp (polycrystalline quartz). 110

Figure 4.24c: Photomicrographs of typical planar cross-stratified sandstone (Sp) sub-facies (PAT-1N) at PattiCChin showing the mineral constituents; Qm (monocrystalline quartz) and Mu (muscovite). 113

Figure 4.24d: Photomicrographs of typical horizontally stratified sandstone (Sh) sub-facies (RAB-1P) at Rabba showing the mineral constituents; Qm (monocrystalline quartz) and Qp (polycrystalline quartz). 118

Figure 4.24e: Photomicrographs of typical horizontally stratified sandstone (Sh) sub facies (PAT-1L) at PattiChin showing the mineral constituents; Qm (monocrystalline quartz), Mu (muscovite) and C (Cement). 121

Figure 4.24f: Photomicrographs of typical horizontally stratified sandstone (Sh) sub facies (BDA 1K) showing the mineral constituents; Qm (monocrystalline quartz), Qp (polycrystalline quartz) and MU (muscovite). 124

Figure 4.24g: Photomicrographs of typical finely laminated, very-fine sandstone and mudstone (Fl) sub-facies (LEM-1P) at Lemu showing the mineral constituents; Qm (monocrystalline quartz) and Zr (Zircon). 127

Figure 4.25a: Different heavy minerals types observed (under crossed nicol) in crudely bedded conglomerate (Gh) sub-facies; (a-i) Zircon (xenocrystic core, zoning, corroded, sillimanite inclusion and dark boundary), (j-l) Tourmaline (light brownish to bluish),

(m-o) Rutile (bluish, golden, deep red colored, conchoidal and knee-shaped), (p and s) Biotite (brownish), (q) garnet and (r) Staurolite. 133

Figure 4.25b: Different heavy minerals types observed (under crossed nicol) in crudely stratified sandstone (Se) sub-facies; (a-h) Zircon (zoning, weathered and corroded, xenocrystic core, inclusion and dark boundary), (j-l) Tourmaline (greenish, light brownish and yellowish), (m) Staurolite (yellowish), (n-p) Rutile (dark brownish and deep brownish knee-shaped). 136

Figure 4.25c: Different heavy minerals types observed (under crossed nicol) in the planar cross-stratified sandstone (Sp) sub-facies; (a-f) Zircon (weathered, pitted and etched, corroded, inclusion, xenocrystic core and zonning), (g-j) Tourmaline (dark, bluish and yellowish), (k & l), Rutile (brownish), (m-o) Staurolite (brownish and yellowish) and Biotite (brownish). 139

Figure 4.25d: Different heavy minerals types observed (under crossed nicol) in the horizontally stratified sandstone (Sh) sub-facies; (a-d) Zircon (weathered, pitted and etched, corroded, xenocrystic core and zonning), (e & i) Tourmaline (golden, light and red stained colored), (k), Rutile (brownish), (l & m) Staurolite (brownish and yellowish). 144

Figure 4.25e: Different heavy minerals types observed (under crossed nicol) in the massive sandstone (Sm) sub-facies; (a-d) Zircon (xenocrystic cored, corroded, weathered, pitted and etched dark boundary with inclusion), (e) Tourmaline (brownish and bluish), (f & g) Rutile (irregular brownish), (h) Staurolite (yellowish). 147

Figure 4.25f: Different heavy minerals types observed (under crossed nicol) in the laminated, very-fine sandstone and mudstone (Fl) sub-facies; (a-f) Zircon (weathered & corroded, zoned, xenocrystic core, pitted and etched with inclusion), (g-i) Tourmaline (golden and bluish), (j-m) Rutile (brownish, reddish and golden colored), (n & o) Staurolite (light colored) and garnet (bulbous). 150

Figure 4.25g: Different heavy minerals types observed (under crossed nicol) in the massive, very-fine sandstone and mudstone (Fm) sub-facies; (a-e) Zircon (weathered and corroded), (f-h) Tourmaline (dark, bluish and light reddish), (i & j), garnet (bluish and bulbous), (k & l) Rutile (brownish and reddish), (m-o) Sillimanite (needle-like, prismatic) and Staurolite (yellowish). 153

Figure 4.26: Harker's Variation plots showing the relationship of SiO_2 with other major elements for Northern Bida Basin sandstones. 161

Figure 4.27a: Scree plot of final dataset for Major Elements in Northern Bida Basin showing F1-F3 as significant and F4-F9 as minimal contributors respectively. 195

Figure 4.27b: Eigenvector plots from the Principal Component Analysis showing the grouping of certain elements of similar geological processes in Northern Bida Basin. Group of elements indicate process of maturity and provenance whereas SiO_2, Al_2O_3, Fe_2O_3 and MnO and TiO_2 group may indicate weathering and leaching. 195

Figure 4.28a: Scree plot of final dataset for Trace Elements in Northern Bida Basin showing F1-F2 as significant, F3-F6 as moderate and F7-F14 as minimal contributors. 199

Figure 4.28b: Eigenvector plots from the Principal Component Analysis showing the grouping of certain elements of similar geological processes; presence of Sc, Co, Zr, Nb, Hf, Th, U and Y in the group points to the significant elements for source rock and provenance whereas relationship of Rb, Sr and Ba indicate weathering and leaching process. 199

Figure 5.1: Some selected pebbles from; (a) clast-supported, massive conglomerate (Gcm) and matrix-supported and (b) massive conglomerate (Gmm) sub-facies for morphometric analysis. 206

Figure 5.2a: Bivariate plot of Roundness (%) against Elongation ratio. 211

Figure 5.2b: Bivariate plot of Coefficient of Flatness against Maximum Projection Sphericity Index. 212

Figure 5.2c: Bivariate plot of Maximum Projection Sphericity Index against Oblate Prolate Index. 213

Figure 5.3a: Graphic Mean Size against Graphic Standard Deviation. 215

Figure 5.3b: Bivariate plot of Graphic Standard Deviation against Graphic Mean Size. 216

Figure 5.3c: Bivariate plot of Graphic Skewness against Graphic Standard Deviation. 217

Figure 5.3d: Bivariate plot of Graphic Skewness against Graphic Standard Deviation. 218

Figure 5.3e: Bivariate plot of Graphic Standard Deviation against Graphic Mean Size showing clustering of the plotted samples near braided system as an evidence of fluvial depositional environment. 219

Figure 5.4: Photomicrograph of selected samples showing different Contact Index observed in the Northern Bida Basin sediments; (a) LEM-1P showing Point, Long and Floating contact as a result of Cementation; (b) PAT-1P showing Long and Point contact as a result of Cementation; (c). DOK-1N showing Point, Long and Suture contact as a result of Compaction and Cementation; (d) RAB-1P showing Point, Suture and Concavo-Convex contact as a result of Compaction and Cementation; (e) DOK-1G showing Point, Suture and Concavo-Convex contact as a result of Compaction and Cementation and (f) DOK-1K showing Suture and Concavo-Convex contact as a result of Compaction and Cementation. 225

Figure 5.5: Backscattered electron and Scanning electron micrographs showing Silica cement (Sc) in (a) AGB-1F and (b) RAB-1P; Clay cement (Cc) in (c) DOK-1N and Iron-oxide cement (Fec) in (d) AGB-1F. 231

Figure 5.6: Scanning electron micrograph showing Quartz overgrowth (Qo) forming at the edges of the host detrital quartz grains (Q) causing destruction of primary porosity in (a) PAT-1J, (b) DOK-1N, (c) AGB-1F and (d) RAB-1P. 233

Figure 5.7: Backscattered electron micrograph showing; (a) Feldspar replacement (FR) of the dissolved rock fragment (RF) in RAB-1P and (b) dissolution (D) of the detrital quartz (Q) in PAT-1J. 235

Figure 5.8: A diagenetic events pathway and paragenetic sequence in the Northern Bida Basin. 237

Figure 5.9: Scanning and Backscattered electron micrographs showing primary porosity occlusion and reduction; (a) with silica cement (Sc) in DOK-1N and (b) quartz overgrowth in DOK-1N; and porosity enhancement as a result of (c) feldspar dissolution and replacement causing microporosity (mp) and secondary porosity (sp) in RAB-1P and (d) rock fragment (RF) dissolution in PAT-1J causing secondary porosity. 240

Figure 5.10a: Standard Ternary petrographic classification of investigated sandstones using framework composition of Quartz-Feldspar-Rock Fragment (Q-F-R). 243

Figure 5.10b: Standard Ternary petrographic classification of investigated sandstones using framework composition of Quartz-Feldspar-Lithic Fragment (Q-F-L). 244

Figure 5.10c: Standard Ternary petrographic classification of investigated sandstones using framework composition of Quartz-Feldspar-Rock Fragment (Q-F-R). 245

Figure 5.11a: Bivariate geochemical classification of the investigated sandstones using log(SiO_2/Al_2O_3) versus log(Na_2O/K_2O). 247

Figure 5.11b: Bivariate geochemical classification of the investigated sandstones using log(SiO_2/Al_2O_3) versus log(Fe_2O_3/K_2O). 247

Figure 5.11c: Bivariate geochemical classification of the investigated sandstones using K_2O (%) versus Na_2O (%). 248

Figure 5.12a: Bivariate Al_2O_3/TiO_2 versus SiO_2 provenance discrimination plot showing Felsic field as source for the investigated sandstones. 252

Figure 5.12b: The standard SiO_2/10-CaO+MgO-Na_2O+K_2O ternary provenance discrimination plot showing granites fields as the source for the investigated sandstones. 252

Figure 5.13a: Bivariate TiO_2 versus Zr (ppm) provenance discrimination plot showing investigated sandstones sediments derivation from felsic Igneous Rocks. 256

Figure 5.13b: Bivariate TiO_2 (%) versus Ni (ppm) provenance discrimination plot showing acidic rocks for investigated sandstones. 256

Figure 5.13c: Bivariate Y/Ni versus Cr/V provenance discrimination plot showing investigated sandstones derivation from felsic Igneous Rocks. 257

Figure 5.13d: Bivariate Th/Sc versus Sc provenance discrimination plot for the investigated sandstone. 257

Figure 5.13e: Bivariate Th/Co versus La/Sc provenance discrimination plot for the investigated sandstone. 258

Figure 5.13f: Bivariate provenance discrimination plot using La/Th versus Hf showing felsic igneous rocks derivation for the investigated sandstone. 258

Figure 5.13g: Standard La-Th-Sc Ternary discrimination plot showing Felsic field for the investigated sandstones. 259

Figure 5.13h: The standard V-Ni-Th*10 ternary provenance discrimination plot showing Felsic fields as the source for the investigated sandstones. 259

Figure 5.14a: Bivariate Total REE versus Eu/Eu* provenance variation plot showing fractionation relationship for the investigated sandstone. 263

Figure 5.14b: Bivariate La_N/Yb_N versus Eu/Eu* provenance variation plot showing fractionation relationship for the investigated sandstones. 263

Figure 5.14c: Bivariate La_N/Sm_N versus Eu/Eu* provenance variation plot showing fractionation relationship for the investigated sandstone. 264

Figure 5.14d: Bivariate Gd_N/Yb_N versus Eu/Eu* provenance variation plot showing fractionation relationship for the investigated sandstone. 264

Figure 5.15a: Spider plot of rare earth element (REE) of investigated sandstone, normalized against average upper continent values (UCC) values. 267

Figure 5.15b: Spider plot of rare earth element (REE) of investigated sandstone, normalized against average North American Shale Composite (NASC) values. 269

Figure 5.15c: Spider plot of rare earth element (REE) of investigated sandstone, normalized against average Post Archean Australian Shale (PAAS) values. 271

Figure 5.16a: Different heavy minerals types observed (under crossed nicol) in the northern part of the study area; (a-i) Zircon (xenocrystic core, zoning, corroded, sillimanite inclusion and dark boundary), (j-l) Tourmaline (light brownish to bluish), (m-o) Rutile (bluish, golden, deep red colured, conchoidal and knee-shaped), (p and s) Biotite (brownish), (q) garnet and (r) Staurolite. 274

Figure 5.16b: Different heavy minerals types observed (under crossed nicol) in the central part of the study area; (a-h) Zircon (zoning, weathered and corroded, xenocrystic core, inclusion and dark boundary), (j-l) Tourmaline (greenish, light brownish and yellowish), (m) Staurolite (yellowish), (n-p) Rutile (dark brownish and deep brownish knee-shaped). 274

Figure 5.17a: Standard Qt-F-Lt Provenance Ternary plot showing Craton Interior and Recycled Orogeny fields for the investigated sandstone. 281

Figure 5.17b: Standard Qm-F-Lt Provenance Ternary plot showing Craton Interior and Recycled Orogeny field for the investigated sandstone. 281

Figure 5.17c: Standard Qm-F-Lt Provenance Ternary plot showing Continental Block Provenances filed for the investigated sandstone. 282

Figure 5.17d: Standard Qt-F-L Provenance Ternary plot showing Continental Block Provenances filed for the investigated sandstone. 282

Figure 5.18a: Bivariate K_2O/Na_2O versus SiO_2 paleotectonic discrimination plot showing Passive Margin for the investigated sandstone. 287

Figure 5.18b: Bivariate (K_2O/Na_2O) versus SiO_2 paleotectonic discrimination plot for the investigated sandstone. 287

Figure 5.18c: Bivariate TiO_2 versus (Fe_2O_3+MgO) paleotectonic discrimination plot showing paleotectonic settings for the investigated sandstone. 288

Figure 5.18d: Bivariate (Al_2O_3/SiO_2) versus (Fe_2O_3+MgO) paleotectonic discrimination plot showing Passive paleotectonic settings for the investigated sandstone. 288

Figure 5.18e: Bivariate SiO_2/Al_2O_3 versus K_2O/Na_2O paleotectonic discrimination plot after showing Passive Margin paleotectonic settings for the investigated sandstone. NB: A1 – Arc setting, basaltic and andesitic detritus; A2 – Evolved arc setting, Felsic-Plutonic detritus; ACM - Active Continental Margin; PM - Passive Margin. 289

Figure 5.18f: The standard paleotectonic discrimination ternary plot of $SiO_2/20$ (K_2O+Na_2O)-(TiO_2+Fe_2O_3+MgO) showing passive margin field for the investigated sandstone. 289

Figure 5.19a: The standard La-Th-Sc Ternary Tectonic discrimination diagram showing Passive Continental Margin fields for the investigated sandstones. 291

Figure 5.19b: The standard Th-Sc-Zr/10 Ternary Tectonic discrimination diagram showing Passive Continental Margin fields for the investigated sandstones. 291

Figure 5.20: Bivariate discrimination plot of Ba/La versus Eu/Eu* showing passive margin field for the investigated sandstones. 293

Figure 5.21: Standard Qm-P-K Ternary plot showing increase in maturity or stability field for the investigated sandstone. 299

Figure 5.22a: Bivariate chemical index plot using (Al_2O_3+K_2O+Na_2O) (%) versus SiO_2 (%) after Suttner and Dutta (1986) showing increasing in the chemical weathering and maturity trend for the Northern Bida Basin sandstone. 304

Figure 5.22b: Bivariate plot of ICV versus CIA showing the intense weathering for the investigated Northern Bida Basin sandstone. 305

Figure 5.23a: Bivariate plot of CIA versus SiO_2 showing the weathering trends and likely mineralogical composition of the investigated sandstone. 310

Figure 5.23b: The standard ternary A-CN-K {Al_2O_3-(Na_2O+CaO)-K_2O} plot showing weathering trends for the investigated sandstone compared with some typical source rocks. Note a general weathering trend (advanced weathering trend) in all plots towards the Al_2O_3 corner of the diagram. 311

Figure 5.23c: The standard ternary A-CNK-FM {Al_2O_3-(CaO+Na_2O+CaO) Fe_2O_3+MgO} plot showing weathering trends for the investigated sandstone compared with some typical source rocks. Note a general weathering trend (advanced weathering trend) in all plots towards the Al_2O_3 corner of the diagram. 312

Figure 5.24a: Bivariate chemical index plot using on Th/Sc versus Zr/Sc after McLennan *et al*. (1993) showing a trend to high Zr/Sc-ratios, indicating zircon addition to the sediment and therefore suggesting a recycling of an older sourced rock for the investigated Northern Bida Basin sandstone. 316

Figure 5.24b: Bivariate chemical index plot using on Th/U versus Th with an arrow showing a weathering trend for the investigated Northern Bida Basin sandstone. 316

Figure 5.24c: Bivariate chemical index plot using on La versus Th with an arrow showing a weathering trend for the investigated Northern Bida Basin sandstone. 317

Figure 5.25a: Bivariate log/log plot of the ratio of polycrystalline quartz to feldspar plus rock fragments versus ratio of total quartz to feldspar plus rock fragments (Qp/F+R vs. Qt/F+R) for the investigated Northern Bida Basin sandstone. 322

Figure 5.25b: Bivariate natural log/log plot of the ratio of total quartz to feldspar versus ratio of total quartz to total lithic fragments for the Northern Bida Basin sandstones. 323

Figure 5.25c: Ternary plots of Q-F-R modal values indicating humid to hot humid for the investigated Northern Bida Basin sandstones. 325

Figure 5.25d: Ternary plots of Q-F-L modal values indicating metamorphic provenance within humid palaeoclimate for Northern Bida Basin sandstone. 325

Figure 5.26: Bivariate Paleoclimate plot using SiO_2 (%) versus (Al_2O_3+K_2O+Na_2O) (%) for the studied Northern Bida Basin sandstone. 327

Figure 5.27a: Zircon typological classification and corresponding geothermometric scale. Index A reflects the Al/alkali ratio, controlling the development of zircon pyramids, whereas temperature affects the development of different zircon prisms. 331

Figure 5.27b: CL images showing representative, typology and assemblage of subhedral and euhedral detrital, microsteps reflecting successive overgrowth zones in zircon minerals of the Northern Bida Basin sandstone. 332

LISTS OF TABLES

Table 2.1: Regional stratigraphic successions in the Bida Basin. 26

Table 4.1: Lithofacies and sub-facies types in the study area. 49

Table 4.2: Paleocurrent data of planar- cross lamination/bedding and clast imbrication and their locations within the study area. 90

Table 4.3a: Mineralogical composition of crudely bedded conglomerate (Gh) sub-facies. 108

Table 4.3b: Mineralogical composition of crudely stratified sandstone (Se) sub-facies. 111

Table 4.3c: Mineralogical composition of planar cross-stratified sandstone (Sp) sub-facies. 114

Table 4.3d: Mineralogical composition of rippled cross-stratified sandstone (Sr) sub-facies. 116

Table 4.3e: Mineralogical composition of horizontally stratified sandstone (Sh) sub-facies. 119

Table 4.3f: Mineralogical composition of massive sandstone (Sm) sub-facies. 122

Table 4.3g: Mineralogical composition of laminated, very-fine sandstone and mudstone (Fl) sub-facies. 125

Table 4.3h: Mineralogical composition of very-fine, massive sandstone and mudstone (Fm) sub-facies. 128

Table 4.4a: Non-opaque heavy minerals composition (%) and calculated Heavy Mineral Index (HMI) values of massive, matrix supported conglomerates (Gmm) sub-facies. 131

Table 4.4b: Non-opaque heavy minerals composition (%) and calculated Heavy Mineral Index (HMI) of crudely bedded conglomerate (Gh) sub-facies. 134

Table 4.4c: Non-opaque heavy minerals composition (%) and calculated Heavy Mineral Index (HMI) of crudely stratified sandstone (Se) sub-facies. 137

Table 4.4d: Non-opaque heavy minerals composition (%) and calculated Heavy Mineral Index (HMI) of planar stratified sandstone (Sp) sub-facies. 140

Table 4.4e: Non-opaque heavy minerals composition (%) and calculated Heavy Mineral Index (HMI) of cross-stratified sandstone (Sr) sub-facies. 142

Table 4.4f: Non-opaque heavy minerals composition (%) and calculated Heavy Mineral Index (HMI) of horizontally stratified sandstone (Sh) sub-facies. 145

Table 4.4g: Non-opaque heavy minerals composition (%) and calculated Heavy Mineral Index (HMI) of massive sandstone (Sm) sub-facies. 148

Table 4.4h: Non-opaque heavy minerals composition (%) and calculated Heavy Mineral Index (HMI) of finely laminated sandstone and mudstone (Fl) sub-facies. 151

Table 4.4i: Non-opaque heavy minerals composition (%) and calculated index values of very fine, massive sandstone and mudstone (Fm) sub-facies. 154

Table 4.5a: Quantitative Mineralogical Composition results of the analyzed sediment samples within the southeastern part of the northern Bida Basin. 156

Table 4.5b: Quantitative Mineralogical Composition results of the analyzed sediment samples within the central part of the northern Bida Basin. 157

Table 4.5c: Quantitative Mineralogical Composition results of the analyzed sediment samples within the northern part of the study area. 158

Table 4.6a: Major Element Composition (%) of clast supported, massive conglomerate (Gcm) sub-facies in Northern Bida Basin. 162

Table 4.6b: Major Element Composition (%) of matrix supported, massive conglomerate (Gmm) sub-facies in Northern Bida Basin. 162

Table 4.6c: Major Element Composition (%) of crudely bedded conglomerate (Gh) sub-facies in Northern Bida Basin. 163

Table 4.6d: Major Element Composition (%) of crudely stratified sandstone (Se) sub-facies in Northern Bida Basin. 163

Table 4.6e: Major Element Cmposition (%) of planar cross-stratified sandstone (Sp) sub-facies in Northern Bida Basin. 164

Table 4.6f: Major Element Composition (%) of horizontally stratified sandstone (Sh) sub-facies in Northern Bida Basin. 164

Table 4.6g: Major Element Composition (%) of massive sandstone (Sm) sub-facies in Northern Bida Basin. 165

Table 4.6h: Major Element Composition (%) of laminated mudstone (Fl) sub-facies in Northern Bida Basin. 165

Table 4.6i: Major Element Composition (%) of massive mudstone (Fm) sub-facies in Northern Bida Basin. 166

Table 4.6j: Major Element Composition (%) of Published Data using for comparison with this study. 166

Table 4.7a: Trace Element Composition (ppm) of clast supported, massive conglomerate (Gcm) in the Northern Bida Basin. 169

Table 4.7b: Trace Element Composition (ppm) of matrix supported, massive conglomerate (Gmm) in Northern Bida Basin. 169

Table 4.7c: Trace Element Composition (ppm) of crudely bedded conglomerate (Gh) sub-facies in Northern Bida Basin. 170

Table 4.7d: Trace Element Composition (ppm) of crudely stratified sandstone (Se) sub-facies in Northern Bida Basin. 171

Table 4.7e: Trace Element Composition (ppm) of planar cross-stratified sandstone (Sp) sub-facies in Northern Bida Basin. 172

Table 4.7f: Trace Element Composition (ppm) of horizontally stratified sandstone (Sh) sub-facies in Northern Bida Basin. 173

Table 4.7g: Trace Element Composition (ppm) of massive sandstone (Sm) sub-facies in Northern Bida Basin. 174

Table 4.7h: Trace Element Composition (ppm) of laminated mudstone (Fl) sub-facies in Northern Bida Basin. 174

Table 4.7i: Trace Element Composition (ppm) of massive mudstone (Fm) sub-facies in Northern Bida Basin. 175

Table 4.7j: Trace Element Composition (ppm) of Published Data using for comparison with this study. 175

Table 4.8a: Rare earth element (REE) concentrations and normalized values of Gcm, Gmm and Gh sub-facies in the Northern Bida Basin. 177

Table 4.8b: Rare earth element (REE) concentrations and normalized values of crudely stratified sandstone (Se) sub-facies in the Northern Bida Basin. 178

Table 4.8c: Rare earth element (REE) concentrations and normalized values of Sp sub-facies in the Northern Bida Basin. 179

Table 4.8d: Rare earth element (REE) concentrations and normalized values of Sh sub-facies in the Northern Bida Basin. 180

Table 4.8e: Rare earth element (REE) concentrations and normalized values of Sm and Fl sub-facies in the Northern Bida Basin. 181

Table 4.8f: Rare earth element (REE) concentrations and normalized values of Fm sub-facies in the Northern Bida Basin. 182

Table 4.8g: Rare Earth Element values of Composition (ppm) of Published Data using for comparison with this study. 183

Table 4.9a: Summary Statistics (Quantitative Data) for Major Elements 185

Table 4.9b: Bivariate (Pearson) Correlation matrix for Major Elements 185

Table 4.10a: Summary statistics (Quantitative data) for Trace Elements 188

Table 4.10b: Bivariate (Pearson) Correlation matrix for Trace Elements 189

Table 4.11: Factor loadings and other corresponding values of the Principal Component Analysis for Major Elements. 196

Table 4.12: Factor loadings and other corresponding values of the Principal Component Analysis for Trace Elements. 200

Table 5.1a: Pebble morphometric data of clast-supported, massive conglomerate (Gcm) sub-facies. 207

Table 5.1b: Pebble morphometric data of matrix-supported, massive conglomerate (Gmm) sub-facies. 208

Table 5.1c: Pebble morphometric data of crudely bedded conglomerate (Gh) sub-facies. 209

Table 5.2: Pebble morphometric data ranges for the studied samples. 210

Table 5.3: Samples selected for Contact Index (CI) study. 226

Table 5.3 Contd.: Samples selected for Contact Index (CI) study. 227

Table 5.4a: Weathering index calculated values for fluvial sands. 324

Table 5.4b: The compiled data and interpretations for weathering trend, relation to parentage and weathering conditions. 324

APPENDICES

APPENDIX I

Table I: Samples selected for Pebble morphometric analysis. 360

Table II: Samples selected for grain Size Analysis. 361

Table II contd.: Samples selected for grain Size Analysis. 362

Table III: Samples selected for Petrographic (Thin Section) Analysis. 363

Table IV: Samples selected for Heavy Mineral Analysis. 364

Table V: Samples selected for X-Ray Diffraction (XRD) Analysis. 365

Table VI: Samples selected for X-Ray Fluorescence Analysis (Major Elements). 366

Table VII: Samples selected for Inductive Coupled Plasma Mass Spectrometry (ICPMS) for trace and rare earth elements (TE and REE). 367

Table VIII: Samples selected for diagenetic study using scanning electron microscope (SEM) and backscattered electron microscope (BSE). 368

Table IX: Samples selected for Zircon Typology using Cathodoluminescence (CL). 368

APPENDIX II – LITHOLOGICAL SECTIONS

Figure I: Legend used in this study. 369

Figure II: Lithological section of Enagi Formation exposed at Share Junction (SHJ-1); Longitude: 004°56'04.6"E; Latitude: 08°49'27.5"N. 370

Figure III: Lithological section of Enagi Formation exposed at Share Township (SHT-1); SHJ-1 - Longitude: 004°58'16.1"E; Latitude: 08°49'05.7"N. 371

Figure IV: Lithological section of Enagi Formation exposed at Zambufu (ZMB-1); Longitude: 08°46'505"N; Latitude: 005°11'792"E. 372

Figure V: Lithological section of Enagi Formation exposed at Gbale (GBL-1); Longitude: 08°45'23.7"N; Latitude: 005°11'16.7"E. 372

Figure VI: Lithological section of Enagi Formation exposed at Gbede-Woro (GDW-1); Longitude: 08°46'20.7"N; Latitude: 005°12'14.4"E. 373

Figure VII: Lithological section of Enagi Formation exposed at Ndeji (NDJ-1); Longitude: 08°45'42.7"N; Latitude: 005°14'26.2"E. 374

Figure VIII: Lithological section of Enagi Formation exposed at Gbugubu-1 (GBU-1); Longitude: 08°47'04.3"N; Latitude: 005°18'02.6"E. 375

Figure IX: Lithological section of Enagi Formation exposed at Gbugbu-2 (GBU-2); Longitude: 08°47'05.3"N; Latitude: 005°17'55.3"E. 376

Figure X: Lithological section of Enagi Formation exposed at Wariku Ridge (WAR-1); Longitude: 08°47'46.3"N; Latitude: 005°18'41.6"E. 377

Figure XI: Lithological section of Bida Formation exposed at Lafiagi (LAF-1); Longitude: 08°50'44.0"N; Latitude: 005°25'03.0"E. 378

Figure XII: Lithological section of Bida Formation exposed at Rugga-Naggi (RUG-1); Longitude: 08°50'35.0"N; Latitude: 005°27'36.0"E. 379

Figure XIII: Lithological section of Bida Formation exposed at Baganko (BGK-1); Longitude: 08°54'29.4"N; Latitude: 005°19'24.6"E. 379

Figure XIV: Lithological section of Bida Formation exposed at Lade (LAD-1); Longitude: 08°45'47.3"N; Latitude: 005°35'37.9"E. 380

Figure XV: Lithological section of Bida Formation exposed at Patigi (PTG-1); Longitude: 08°42'53.5"N; Latitude: 005°46'55.7"E. 381

Figure XVI: Lithological section of Bida Formation exposed at Kajita (KJT-1); Longitude: 08°42'45.2"N; Latitude: 006°02'51.9"E. 382

Figure XVII: Lithological section of Bida Formation exposed at Bida (BDA-1); Longitude: 005°59.98' E; Latitude: 09°05.98' N. 383

Figure XVIII: Lithological section of Bida Formation exposed at Mangotta (MGT-1); Longitude: 006°01.409'E; Latitude: 09°09.815'N. 384

Figure XIX: Lithological section of Bida Formation exposed at Wushishi Section (WUS-1); Longitude: 006°03.846'E; Latitude: 09°43.621'N. 385

Figure XX: Lithological section of Bida Formation exposed at Lemu (LEM-1); Longitude: 005°12'14.4"E; Latitude: 08°46'20.7"N. 386

Figure XXI: Lithological section of Bida Formation exposed at Kuchi (KCH-1); Longitude: 005°59.289'E; Latitude: 09°01.554'N. 387

Figure XXII: Lithological section of Bida Formation exposed at Jimma (JIM-1); Longitude: 005°56.090'E; Latitude: 08°58.994'N. 388

Figure XXIII: Lithological section of Bida Formation exposed at Dokko (DOK-1); Longitude: 005°37.545'E; Latitude: 08°56.744'N. 389

Figure XXIV: Lithological section of Bida Formation exposed at Agaei (AGE-1); Longitude: 006°19.119'E; Latitude: 09°02.197'N. 390

Figure XXV: Lithological section of Bida Formation exposed at Patti-Chin (PAT-1); Longitude: 09°04.449'N; Latitude: 006°14.018'E. 391

Figure XXVI: Lithological section of Bida Formation exposed at Katcha (KAC-1); Longitude: 006°18.910'E; Latitude: 08°45.127'N. 392

Figure XXVII: Lithological section of Bida Formation exposed at Baro (BAR-1); Longitude: 006°24.956'E; Latitude: 08°37.371'N. 393

Figure XXVIII: Lithological section of Enagi Formation at exposed Agbonna Ridge (AGB-1); Longitude: 004°58'36.3"E; Latitude: 08°49'32.3"N. 394

Figure XXIX: Lithological section of Enagi Formation exposed at Shonga (SHG-1); Longitude: 005°08'50.1"E; Latitude: 09°01'27.4"N. 395

Figure XXX: Lithological section of Enagi Formation exposed at Rabba (RAB-1); Longitude: 005°01.691'E; Latitude: 09°12.538N. 396

Figure XXXI: Lithological section of Enagi Formation exposed at Enagi (ENG-1); Longitude: 005°32.68' E; Latitude: 09°07.88' N. 397

Figure XXXII: Lithological section of Enagi Formation exposed at Kutigi (KUT-1); Longitude: 005°35.43' E; Latitude: 09°12.03' N. 398

Figure XXXIII: Lithological section of Enagi Formation exposed at Tanagi (TAN-1); Longitude: 005°43.798' E; Latitude: 09°55.342' N. 399

Figure XXXIV: Lithological section of Enagi Formation exposed at Rafingora-Tanagi (RAT-1); Longitude: 005°43.799' E; Latitude: 09°55.344' N. 400

Figure XXXV: Lithological section of Enagi Formation exposed at Manigi (MAN-1); Longitude: 005°32.277' E; Latitude: 09°46.599' N. 401

Figure XXXVI: Lithological section of Enagi Formation exposed at Maraba (MAR-1); Longitude: 005°08'50.1"E; Latitude: 09°01'27.4"N. 402

APPENDIX III – GRAIN SIZE ANALYSIS RESULT

Table Ia: Grain size distribution of clasts supported conglomerates (Gcm) sub-facies and interpretation. 403

Table Ib: Textural classification of clasts supported conglomerates (Gcm) sub-facies. 403

Table IIa: Grain size distribution of matrix supported conglomerate (Gmm) sub-facies and interpretation. 404

Table IIb: Textural classification of matrix supported conglomerate (Gmm) sub-facies. 405

Table IIIa: Grain size distribution of crudely bedded conglomerate (Gh) sub-facies and interpretation. 406

Table IIIb: Textural classification of crudely bedded conglomerates (Gh) sub-facies. 408

Table IVa: Grain size distribution of crudely stratified sandstone (Se) sub-facies and interpretation. 409

Table IVb: Textural classification of crudely stratified sandstone (Se) sub-facies. 412

Table Va: Grain size distribution of planar stratified sandstone (Sp) sub-facies and interpretation. 414

Table Vb: Textural classification of planar stratified sandstone (Sp) sub-facies. 416

Table VIa: Grain size distribution of rippled stratified sandstone (Sr) sub-facies and interpretation. 417

Table VIb: Textural classification of rippled stratified sandstone (Sr) sub-facies. 417

Table VIIa: Grain size distribution of horizontally stratified sandstone (Sh) sub-facies and interpretation. 418

Table VIIb: Textural classification of horizontally stratified sandstone (Sh) sub-facies. 421

Table VIIIa: Grain size distribution of massive sandstone (Sm) sub-facies and interpretation. 423

Table VIIIb: Textural classification of massive sandstone (Sm) sub-facies. 424

Table IXa: Grain size distribution of finely laminated mudstone (Fl) sub-facies and interpretation. 425

Table IXb: Textural classification of laminated, very-fine mudstone (Fl) sub-facies. 427

Table Xa: Grain size distribution of very fine, massive mudstone (Fm) sub-facies and interpretation. 428

Table Xb: Textural classification of very fine massive mudstone (Fm) sub-facies. 429

APPENDIX IV – RECALCULATED VALUES OF FRAMEWORK COMPOSITION

Table Ia: Recalculated framework composition (%) of crudely bedded conglomerate (Gh) sub-facies. 430

Table Ib: Mineralogical composition of crudely bedded conglomerate (Gh) sub-facies. 430

Table IIa: Recalculated framework composition (%) of crudely stratified sandstone (Se) sub-facies. 431

Table IIb: Mineralogical composition of crudely stratified sandstone (Se) sub-facies. 432

Table IIIa: Recalculated framework composition (%) of planar cross-stratified sandstone (Sp) sub-facies. 433

Table IIIb: Mineralogical composition of planar cross-stratified sandstone (Sp) sub-facies. 434

Table IVa: Recalculated framework composition (%) of rippled cross-stratified sandstone (Sr) sub-facies. 435

Table IVb: Mineralogical composition of rippled cross-stratified sandstone (Sr) sub-facies. 435

Table Va: Recalculated framework composition (%) of horizontally stratified sandstone (Sh) sub-facies. 436

Table Vb: Mineralogical composition of horizontally stratified sandstone (Sh) sub-facies. 437

Table VIa: Recalculated framework composition (%) of massive sandstone (Sm) sub-facies. 438

Table VIb: Mineralogical composition of massive sandstone (Sm) sub-facies. 438

Table VIIa: Recalculated framework composition (%) of laminated, very-fine sandstone and mudstone (Fl) sub-facies. 439

Table VIIb: Mineralogical composition of laminated, very-fine sandstone and mudstone (Fl) sub-facies. 410

Table VIIIa: Recalculated framework composition (%) of very-fine, massive sandstone and mudstone (Fm) sub-facies. 441

Table VIIIb: Mineralogical composition of very-fine, massive sandstone and mudstone (Fm) sub-facies. 441

Table IX: The Standard mineralogical maturity index (MMI) values. 442

APPENDIX V- RESULTS OF HEAVY MINERAL COMPOSITIONS

Table I: Heavy mineral composition of matrix supported, massive conglomerate (Gmm) sub-facies. 443

Table II: Heavy mineral composition of crudely bedded Conglomerate (Gh) sub-facies. 443

Table III: Heavy mineral composition of crudely stratified Sandstone (Se) sub-facies. 444

Table IV: Heavy mineral composition of planar cross-stratified sandstone (Sp) sub-facies. 445

Table V: Heavy mineral composition of horizontally stratified sandstone (Sh) sub-facies. 446

Table VI: Heavy mineral composition of rippled stratified sandstone (Sr) sub-facies. 447

Table VII: Heavy mineral composition of massive sandstone (Sm) sub-facies. 447

Table VIII: Heavy mineral composition of laminated mudstone (Fl) sub-facies. 448

Table IX: Heavy mineral composition of massive mudstone (Fm) sub-facies. 449

APPENDIX VI – RATIOS OF SOME MAJOR ELEMENTS VALUES AND GEOCHEMICAL LOGARITHM INDICATORS

Table Ia: Values of ratios of some major elements and geochemical logarithm indicators of Gcm, Gmm and Gh sub-facies in northern Bida Basin. 450

Table Ib: Values of ratios of some major elements and geochemical logarithm indicators of the Se and Sp sub-facies in the northern Bida Basin. 451

Table Ic: Values of ratios of some major elements and geochemical logarithm indicators of horizontally stratified sandstone (Sh) sub-facies in the northern Bida Basin. 452

Table Id: Values of ratios of some major elements and geochemical logarithm indicators of the Sm, Fl and Fm sub-facies in the northern Bida Basin. 453

Table Ie: Values of ratios of some major elements and geochemical logarithm indicators of Published Data using for comparison with this study. 454

Table IIa: Trace elements ratios values of clast supported, massive conglomerate (Gcm) in the northern Bida Basin. 455

Table IIb: Trace elements ratios values of the matrix supported, massive conglomerate (Gmm) in northern Bida Basin. 455

Table IIc: Trace elements ratios values of the crudely bedded conglomerate (Gh) sub-facies in northern Bida Basin. 456

Table IId: Trace elements ratios values of the crudely stratified sandstone (Se) sub-facies in northern Bida Basin. 457

Table IIe: Trace elements ratios values of the planar cross-stratified sandstone (sp) sub-facies in northern Bida Basin. 458

Table IIf: Trace elements ratios values of the horizontally stratified sandstone (Sh) sub-facies in northern Bida Basin. 459

Table IIg: Trace elements ratios values of the massive sandstone (Sm) sub-facies in northern Bida Basin. 460

Table IIh: Trace elements ratios values of the laminated mudstone (Fl) sub-facies in northern Bida Basin. 460

Table IIi: Trace elements ratios values of the massive mudstone (Fm) sub-facies in northern Bida Basin. 461

Table IIj: Trace Element ratios values of Composition (ppm) of Published Data using for comparison with this study. 462

APPENDIX VII

Figure I: X-Ray Diffractogram for sample KUD-1C. 463

Figure II: X-Ray Diffractogram for sample KUD-1G. 463

Figure III: X-Ray Diffractogram for sample KUT-1G. 464

Figure IV: X-Ray Diffractogram for sample KUD-1M. 464

Figure V: X-Ray Diffractogram for sample AGB-1A. 465

Figure VI: X-Ray Diffractogram for sample AGB-1C. 465

Figure VII: X-Ray Diffractogram for sample AGB-1K. 466

Figure VIII: X-Ray Diffractogram for sample ZMB-1A. 466

Figure IX: X-Ray Diffractogram for sample ZMB-1C. 467

Figure X: X-Ray Diffractogram for sample GBU-1C. 467

Figure XI: X-Ray Diffractogram for sample PTG-1C. 468

Figure XII: X-Ray Diffractogram for sample SHG-1R. 468

ABSTRACT

The sediments in the northern Bida Basin, northcentral Nigeria consisting of conglomerate, sandstone, siltstone and claystone lithofacies were studied using facies analyses (facies characterization, architectural elements, geometry, textural and compositional characteristics), X-Ray Fluorescence (XRF), Inductive Coupled Plasma Mass Spectrometry (ICPMS), Scanning electron microscope (SEM) equipped with backscattered electron microscope (BSE) and cathodoluminescence (CL) with the intention of determining the provenance, paleotectonics, paleoenvironment reconstruction and diagenetic history.

The facies analysis reveal five (5) outcrop Facies Association comprising of matrix-supported, massive conglomerate (Gmm), clast-supported, massive conglomerate (Gcm), clast-supported, crudely bedded conglomerate (Gh), crudely stratified to massive sandstone (Se), planar cross-bedded sandstone (Sp), rippled laminated sandstone (Sr), horizontally stratified sandstone (Sh), massive or slightly laminated sandstone (Sm), finely laminated sandstone, siltstone and claystone (Fl) and massive siltstone and claystone (Fsm). They were interpreted as alluvial intraformational conglomerate, braided fluvial channels, meandering channels, tidal channels and fluvial overbank/floodplain. Six identified architectural elements within the study area; channels (CH), gravel bars and bed forms (GB), lateral accretion (LA), laminated sand sheet (LS), sandy bedforms (SB) and overbank fines (OF) showed a river system ranging from floodplains to more high energy, braided fluvial systems of low sinuosity. Sheet and blanket sandbody geometry with typical vertical and lateral connectivity of sand bodies are common in the central and northern part while wedge and lobate types are common in the southern and eastern parts.

Sedimentary structures with paleocurrent importance include; planar lamination, planar and trough cross-bedding, compound cosets of strata with low-angle inclined bounding surfaces

and imbricated pebbles were mapped and measured. Dominant southwestern with minor south-eastern paleocurrent transport directions were obtained indicating a continuous influence of southwestern sediment source areas across the basin axis. Regionally, the proportion of overbank sediments increases to the central and western parts, with thick alluvial units occurring toward the south and southeast part of the basin.

The ternary plots based on petrographic data suggest that the sandstones petrofacies are mainly quartzarenite with minor sublitharenite while geochemical ternary plots classified the sandstones as mainly litharenite, sublitharenite and subarkose indicating multiple provenance of craton interior (in rifted continental margin basin setting) to orogenic sourced sediments. Petrographic characteristics and other variables with geochemical proxies indicate felsic igneous rocks as the dominant parent rock with minor contribution from metamorphic that has been intensely weathered physically, in tropical humid climatic conditions and low relief of the source area.

Application of statistical tools (Correlation matrix, Factor Analysis and Principal Component Analysis) show the main elemental distributions in the studied sediments and the geological processes which include source area composition, weathering process and diagenesis.

The geochemical proxies; Al_2O_3/TiO_2, SiO_2/Al_2O_3, K_2O/Al_2O_3, La/Th, La/Co, Th/Co, La/Sc, Cr/Th, Zr/Nb and Zr/Th revealed sediments' derivation mainly from felsic source rocks. Moreover, chondrite-normalized REE patterns, light REE enrichment, heavy REE flat pattern and negative Eu anomalies with discriminant diagrams also support felsic rock source derived from craton interior to orogenic recycled sources and deposition in a passive continental margin during the Cretaceous. Discrimination plots of $\log(K_2O/Na_2O)$ versus SiO_2, TiO_2 versus (Fe_2O_3+MgO), Al_2O_3/SiO_2 versus (Fe_2O_3+MgO) and $SiO_2/20-(K_2O+Na_2O)-(TiO_2+Fe_2O_3+MgO)$, La/Y versus Sc/Cr, La-Th-Sc, Th-Sc-Zr/10 indicate passive continental

margin paleotectonic settings. A higher Zr/Sc and Zr/Hf ratio with Th/Sc and Zr/Sc binary plot reflects considerable zircon enrichment in the source area.

The studied sandstones show relatively high chemical index of alteration (CIA= 71.73-95.4.68), plagioclase index of alteration (PIA= 92.33-95.4.76), chemical index of weathering (CIW= 93.90-95.4.76), chemical proxy for alteration (CPA= 97.74-95.4.90) with low weathering index of Parker (WIP= 0.16-27.34) which when compared with the UCC and PASC values imply that the source area was affected by intensive chemical weathering and therefore chemically mature. Similarity in the mineralogical constituents may be due to the heterogeneous resistance of minerals to the transport processes and represent two distinct tectonostratigraphic formations in the northern Bida Basin.

Diagenetic imprints identified in these sandstones include early cementation by silica and iron-oxide cement, compaction by development of quartz overgrowths, quartz fracture and replacement and dissolution of detrital feldspar. Generally, these diagenetic imprints have modified these sandstone through both porosity reduction and porosity enhancement.

In conclusion, this research shows that northern Bida Basin sediments were deposited by fluvial conditions during warm humid paleoclimatic settings. The sediments were sourced from felsic igneous rocks from the Basement Complex of southwestern Nigeria. Evidences of various degree of diagenetic phases including compaction, cementation, quartz overgrowth, feldspar and rock fragment dissolution leading to the formation of secondary (sp) and microporosity (mp) were revealed.

CHAPTER ONE

INTRODUCTION

1.1 Background Information

This thesis describes the aspects of the sedimentological, textural, mineralogical and geochemical and diagenetic characteristics to unravel paleoenvironment, provenance and porosity evaluation of the Campanian-Maastrichtian sediments in northern Bida Basin, north-central, Nigeria. There has been a call recently by the Federal Government of Nigeria to open up frontier inland basins for hydrocarbon prospectivity; therefore, this study was carried out to update the knowledge of sedimentological, geochemical and reservoir potential of the northern Bida Basin sediments for future research.

Bida Basin is one of the hinterland sedimentary basins in Nigeria with a sedimentary fill of about 4.0km Ojo (2012) and it is located between the northern Basement (Central Nigerian Shield) and southwestern Basement Complex of Nigeria (West African Shield). Generally, the Basin is northwest-southeast (NW-SE) trending intracratonic type (Figure 1.1) and contiguous with the Sokoto and Anambra Basins in the northwest and southeast to covering a territory of approximately 60,000 km^2 and delimited in the northeast and southwest by the Basement Complex according to Adeleye (1974) and Wright *et al.* (1985).

The structure of this thesis is stated below;

Chapter one gives a brief introduction of the study area and the rationale behind the research. The justification, aims and objectives and research significance is also stated.

Chapter two reviews the geology of the Bida Basin.

Chapter three presents and discusses the methodology employed to address the stated aim and objectives.

Chapter four presents the results of the field and laboratory works: facies analysis, architectural elements, geometry and paleocurrent analysis, textural and mineralogical analyses, geochemical data with statistical applications.

Chapter five presents the sedimentological and geochemical deductions on the paleoenvironments, diagenetic history and reservoir potential, petrofacies, provenance and paleotectonic settings. Deductions on the paleoweathering and paleoclimatic conditions were not left out in this chapter.

Chapter six presents general conclusions on this study and recommendation for further studies.

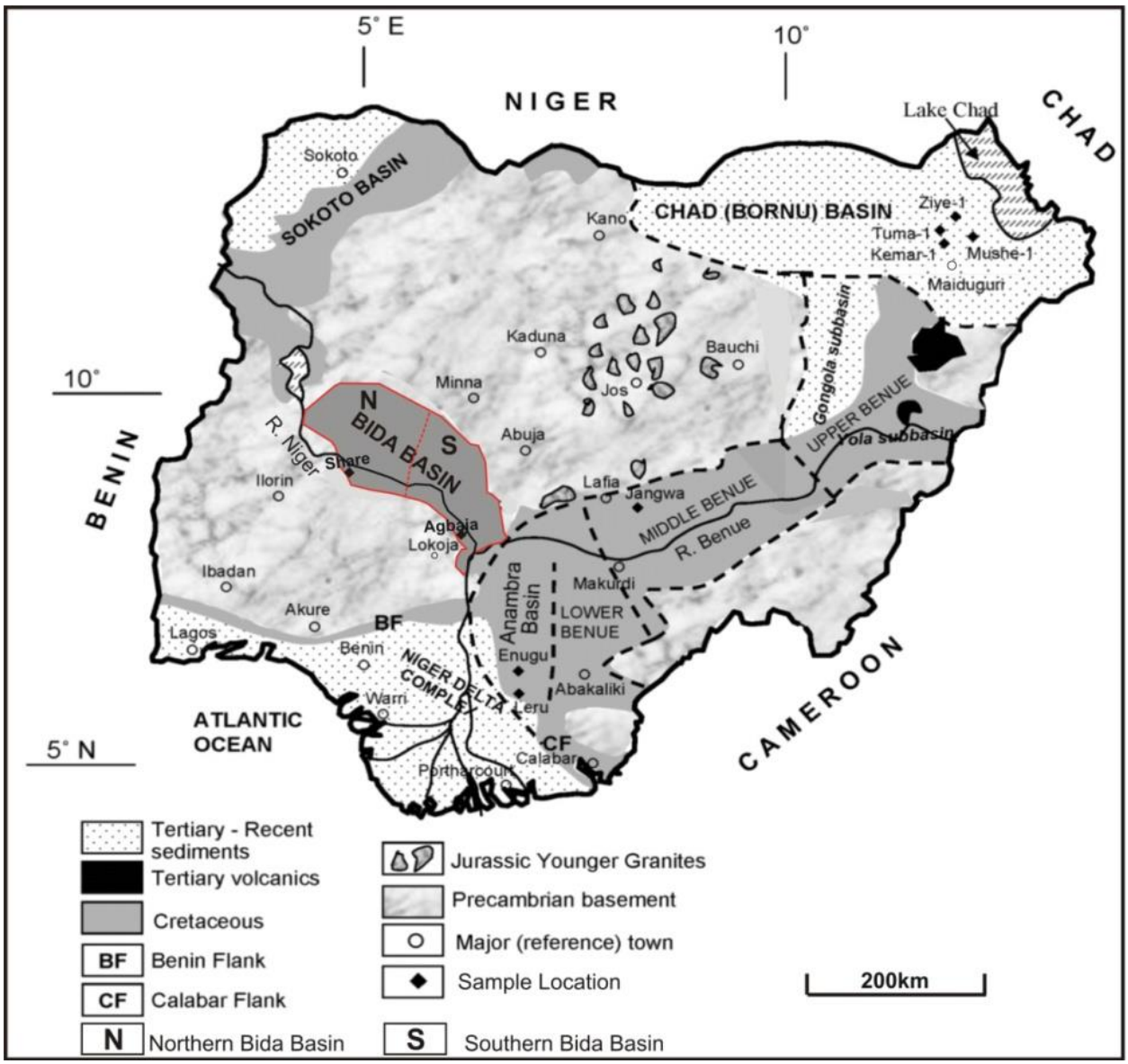


Figure 1.1: Geological map of Nigeria showing the position of the Bida Basin (modified after Obaje, 2012).

1.2 Location and Accessibility of the Study Area

The study area is located within the northern part of the Basin commonly reffered to as northern Bida Basin covering Sheets 182, 202, 203, 204 and 205 of Nigeria Geological Survey Agency (NGSA).

Eight (8) traverses were delineated for the field mapping (Figure 1.2) including; Share-Shonga (T1), Share-Lafiagi (T2), Gbugbu-Pategi-Kajita (T3), Mokwa-Enagi-Bida (T4), Mokwa-Manigi-Tanagi-Makera (T5), Bida-Wushishi-Lemu (T6), Bida-Jimma-Doko-Patti-Shabakollo (T7) and Bida-Agaie-Baro-Gulu Kandi (T8). The method of mapping using the traverse was adopted due to the accessibility to the study locations. Almost all the areas are connected with accessible road through the major towns and villages.

The Share-Shonga and Share-Lafiagi areas were accessible through Ilorin-Bode Saadu federal road that lead to the Gbugbu-Pategi-Kajita federal road linking the river Niger in the south. The Bida-Jimma-Doko-Patti-Shabakollo was accessible through the local Bida-Jimma road linking the river Niger in the north. The localities around Mokwa, Kudu, Enagi and Kutigi area were accessible through the newly constructed Abuja-Bida-Mokwa-Ilorin road while Wushishi-Lemu area were accessed through the old Zungeru-Bida federal road which links Minna. Other areas that were accessed through the federal roads include; Agaie-Gulu Kandi along Bida-Lapai-Gulu road and Manigi, Tanagi, Maraba along Mokwa-Makera. Meanwhile, Patti-Chin and Baro were accessed through non-motorable roads.

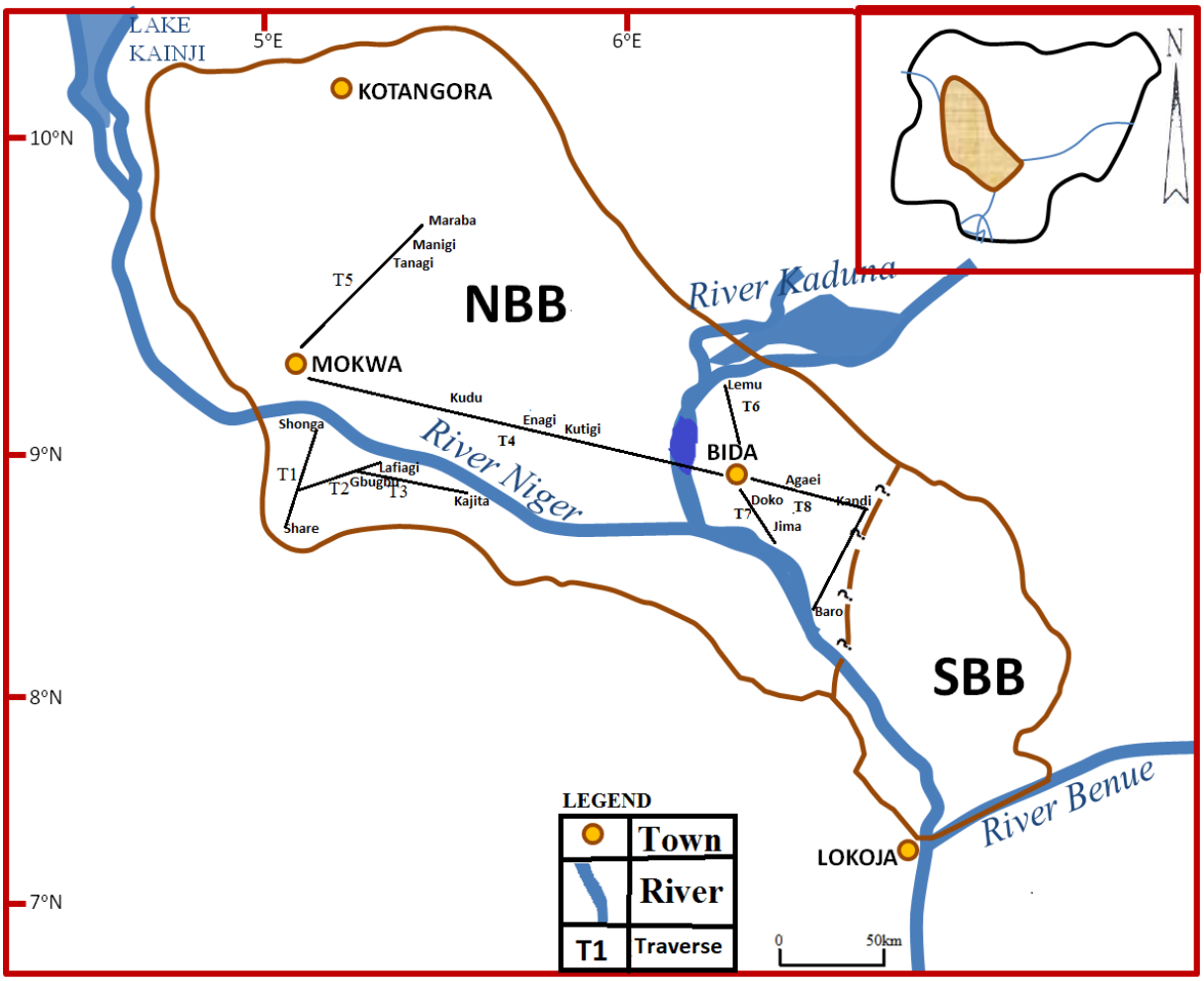


Figure 1.2: **Geological map of northern Bida Basin showing the Traverses covered in the present study.**

1.3 Physiography

The Basin transversed more or less axially by the river Niger with some of its major tributaries especially Benue and Kaduna Rivers dominates the physiography. The basin area has three physiographic units; the rolling plains, the Niger valley and the inselbergs (Adeleye, 1989). The inselberg topography occur along a belt stretching from east of Mokwa through south of Bida to Baro, Lokoja and southwest of Dekina.

About seventy percentage (70%) of the basin is covered by flat-lying to gently rolling plains. The monotony of the landscape is sometimes broken by mesas which are conical or flat-topped. Many of such hills are common along Mokwa-Bida and Bida-Zungeru roads. Around Lokogoma in the north, the plains lies between 120-360 meters above sea level; 120-240 meters around Kpaki; 150-135 meters around Bida and about 60-180 meters in the Agaie area to the south.

The River Niger runs NW - SE in the southern marginal areas of the Bida basin and forms the southern boundary of the study area. Its flood plain is broad and locally up to 20 kilometers wide. The flood plain is marked in most areas by a series of elongated ponds running parallel to the river channel. The most important tributaries are the River Kaduna, River Gbako and River Mariga which meander through the northern Nigeria basement complex, and display drainage dendritic drainage pattern.

The northern Bida Basin area lies within the Guinea Savannah region of Nigeria marked by dry season (November-March) and wet/raining season (April-October) with the highest amount of rain received in the month of July. The annual rainfall is between 1,000 and 1,250 millimeters and mean annual temperatures are between 18°C and 36°C with relative humidity of about 80% in the morning which drop to 70% during the dry season (Reuben, 1978). Two

air mass dominate the climate of the study area: the maritime air mass (moisture laden) influence by south-west trade wind and the tropical continental air mass (Harmattan) influence by north-east trade wind and responsible for low relative humidity, high day temperature of about 36°C, dry and dusty.

The vegetation is of typical Guinea Savannah belt of the West Africa are dominantly grasses of average height of 2.0-3.0 meters and also fire-resistant trees of about 18.0 meters high. The trees and grasses are interspersed and become gradually small in size and less luxuriant in appearance towards the north. Trees of between 3.0 and 6.0 meters high are found scattered on the plains. They have thick leaves and some (the acacias) grow thorns to minimize transpiration. Flood plains are characterized by tall grasses and scanty palm trees that stand at average height of 7.0 meters. The common trees are baobab, kapko, acacia, shear-butter and locust-beans plant.

1.4 Previous Work

The earliest work on the description of the geology of the Bida Basin is that of Falconer (1911) who described and named the exposures of ironstones (oolitic and pisolitic), sandstones and grits of the outliers, plateaux and sections in numerous locations around Kotangora, Lokoja and Patigi as “Lokoja Series”. The literature on the Northern Bida Basin is very scanty unlike the Southern Bida Basin and the other inland basins which have been widely documented. Contributions to the geology in the area include the works of Adeleye (1972, 1973 and 1974), Adeleye and Dessavaugie (1972). Their studies center on the stratigraphy and sedimentation of Upper Cretaceous succession of the Bida Basin where they defined and established the mappable litho-stratigraphic units that are currently being used for the Bida Basin.

Landsat imageries and borehole logs (with geophysical data) interpreted by Ojo and Ajakaye (1976) suggest a basin bounded by a system of linear faults trending NW-SE. Jan du Chene *et al*. (1979) documented the palynomorph-foraminifera associations for the interpretation of the paleoenvironments of the Lokoja and Patti formations. The gravity studies of Ojo (1984) point to a series of central positive anomalies flanked by negative anomalies, similar to the adjacent Benue Trough and typical of rift structures. Other related research works in the southern part of the basin include that Adeleye, 1973; Ladipo *et al*. (1994); Abimbola (1997); Braide (1992); Olugbemiro and Nwajide (1997). Akande *et al*. (2005) interpreted the paleoenvironments of the sedimentary successions in the southern Bida Basin as ranging from continental to marginal marine and marsh environments for the Cretaceous lithofacies. Ojo (2010) has also documented the palynomorphs assemblages and paleoenvironments of the Patti Formation and dated the shaly facies as Maastrichtian age. Also, efforts have been made on the hydrocarbon prospectivity of the basin including Obaje (2011, 2012) and Obaje *et al*. (2013).

Unlike Southern Bida Basin, few research works have been documented in the Northern Bida Basin. These include Olaniyan and Olobaniyi (1996) who attempted and studied aspects of sedimentology and stratigraphy of north of Niger River and suggested fluvial environments for the sandstones and the conglomerates. Recently, Ojo (2012) suggest fluvial processes of deposition for the Bida Formation sediments around Share-Patigi area and suggested an uplifted continental block provenance, warm humid paleoclimate, short transportation history and subarkose for the prevalent facies. All these previous works in the Northern Bida Basin did not provide the details of the possible source rocks that can lead to the discovery of working hydrocarbon system. This may be due to unavailability of data from detailed geological mapping, geochemical studies and petrophysical studies.

1.5 Statement of Problem

For all the above mentioned, it is clear that the geology of the Northern Bida Basin is less explored and have not been well studied and documented particularly when compared to the Southern Bida Basin. To date, the only available comprehensive sedimentological based studies in the Northern Bida Basin include those of Adeleye (1972, 1973) and recently few contribution of Ojo (2012), Ojo and Akande (2012). However, there are better exposures in several parts of the study area consequent to many recent highway contructions that provided excellent access for facies architecture and geometry analysis.

This study is designed to provide detailed information on sedimentology, and the facies architecture and associations and also to develop a stratigraphy and interprete the possible factors that controlled the sediment accumulation of the units. By this study, clear deductions will be made about the facies types and characteristics, provenance, tectonic setting, depositional environment and the resource potentials of the sediments in this part of the basin in the light of modern techniques such as X-Ray Fluorescence (XRF) and Inductive Coupled Plasma Mass Spectrometry (ICPMS), Scanning electron microscope (SEM) equipped with backscattered electron microscope (BSE) and cathodoluminescence (CL).

1.6 Justification

The geology of the northern Bida Basin has not been well described and documented particularly when compared with the Southern Bida Basin. The geochemical characterization and correlation of the clastic sediments within the study area has not been attempted and documented, therefore, this study will document and provide the depositional history and environments.

The present effort is significant because it plans to provide better understanding on aspects of the geology of the provenance and reservoir to help contribute to the necessary data base for future hydrocarbon prospecting in the inland Bida Basin, Nigeria.

1.7 Aim and Objectives

The main aim of this study is to outline the facies characteristics, diagenetic history, geochemical composition and relate these to paleogeographic evolution and economic resources of northern Bida Basin.

The key objectives of this research work include;

1. To produce a regional lithostratigraphic correlation, facies distribution map using field characteristics of the outcropping facies within the study area.
2. To determine the facies association, facies architecture and paleoenvironments.
3. To evaluate the petrographic characteristics and petrofacies of sandstones in the study area.
4. To determine geochemical characteristics of the sandstone facies.
5. To reconstruct the provenance, paleotectonics and weathering history of the studied sandstones using combined petrographic and geochemical data.
6. To determine the diagenetic history, cements and assess their effects on pores and reservoir quality of the sandstones facies in the study area.

1.8 Significance of the study

The present effort is significant because it plans to contribute to aspects of the geology of the reservoirs in parts of Bida Basin. The study will assist in providing a better understanding of lithofacies distribution and architecture elements, petrofacies and diagenetic history and their influence on the porosity. This research is therefore essential to contribute to the necessary

data base for future hydrocarbon prospecting in the basin as it aims at evaluating the geological, sedimentological and geochemical (inorganic) studies of the sediments which controls the reservoir properties of the rock.

CHAPTER TWO

GEOLOGY OF THE STUDY AREA

2.1 General Statement

This chapter discusses the geological settings of Bida basin using tectonic, structural and stratigraphic postulations. The purpose is to review the related past research on the tectonic, structural and stratigraphic postulations to the origin and evolution of the Basin.

2.2 Tectonic Evolution

The geological developments in the upper Cretaceous sediments of Bida Basin which are essentially clastic deposited had been postulated by King (1950) and Kennedy (1965) as associated with drifting apart of South American and African plates being produced by faulting and characterized with the break-up of the Gondwana. The opening of the Gulf of Guinea followed existing lines of weakness close to the edges of West African and Congo cratons (Figure 2.1) along which the major transform faults propagated.

Interpretation of Landsat images, borehole logs as well as geophysical data across the entire Bida Basin by Kogbe *et al*. (1983) suggest that the Basin is bounded by a system of linear faults trending NW-SE (Figure 2.2). The gravity studies by Ojo and Ajakaiye (1989) also confirm central positive anomalies flanked by negative anomalies as shown for the adjacent Benue Trough and typical of rift structures (Figure 2.3). Adeniyi (1985) outlined the basin configuration using the ground and aeromagnetic studies and suggested a wrench movement associated with transform fault systems that have resulted in the creation of the Basins and sub-Basins within and along the entire Benue Trough as well as the adjacent areas such as the Bida basin. It has also been most frequently regarded as the north-western extension of the Anambra Basin with both as the major depocenters during the Upper Cretaceous (Lang *et al*. (1986); Ladipo *et al*. (1994); Akande and Ojo (2002), and Ojo and Akande (2009).

The existence of a deep seated central positive anomaly flanked by negative anomalies typical of rift structure was indicated by geophysical study of Ojo and Ajakaiye (1989). Their acquired gravity data along several profiles perpendicular to the strike of the Bida Basin and interpretation estimated the sediment thickness to be between 3000-3500 m maximum (Figure 2.3). The gravity profile presented in figure 2.4 shows a regional trend of negative anomalies towards the southwestern suggesting the deepening of the basin. The densities were based on lithologies from outcrops and a Cretaceous age of the sedimentary infill. A central negative anomaly was observed and was flanked by positive anomalies in the areas around Mokwa and Bida region (Figure 2.4).

Recent interpretation of magnetic data by Udensi *et al*. (2003) and Udensi and Osazuwa (2004) suggests that up to 4700 m of sediment may have accumulated in parts of the basin. Meanwhile, Udensi and Osazuwa (2004) suggested an estimate of 4000 m as the maximum thickness of the sedimentary successions in the central part of the basin based on gravity and magnetic surveys. The positive anomalies extend as far as 60-80km to the east, suggesting that the Bida Basin is not a continuous half graben tectonic feature but separated into two rather distinct sub-Basins to the northwest and southeast. Udensi and Osazuwa (2004) carried out a magnetic study of the Bida area and average thickness of 3.39 km was estimated for depth to the basement within the study area (Figure 2.5).

Results of modeled values deduced from airborne residual magnetic anomalies data profiles of Udensi *et al.,* 2003 also show that the thickness of the basin varies from 0.80 km to 4.63 km (Figure 2.6) assuming that the residual magnetic variations were caused by basement topography. They concluded that based on the above that area with the largest thickness of sediments is located north of Pategi with a thickness of 4.63 km (Figure 2.6).

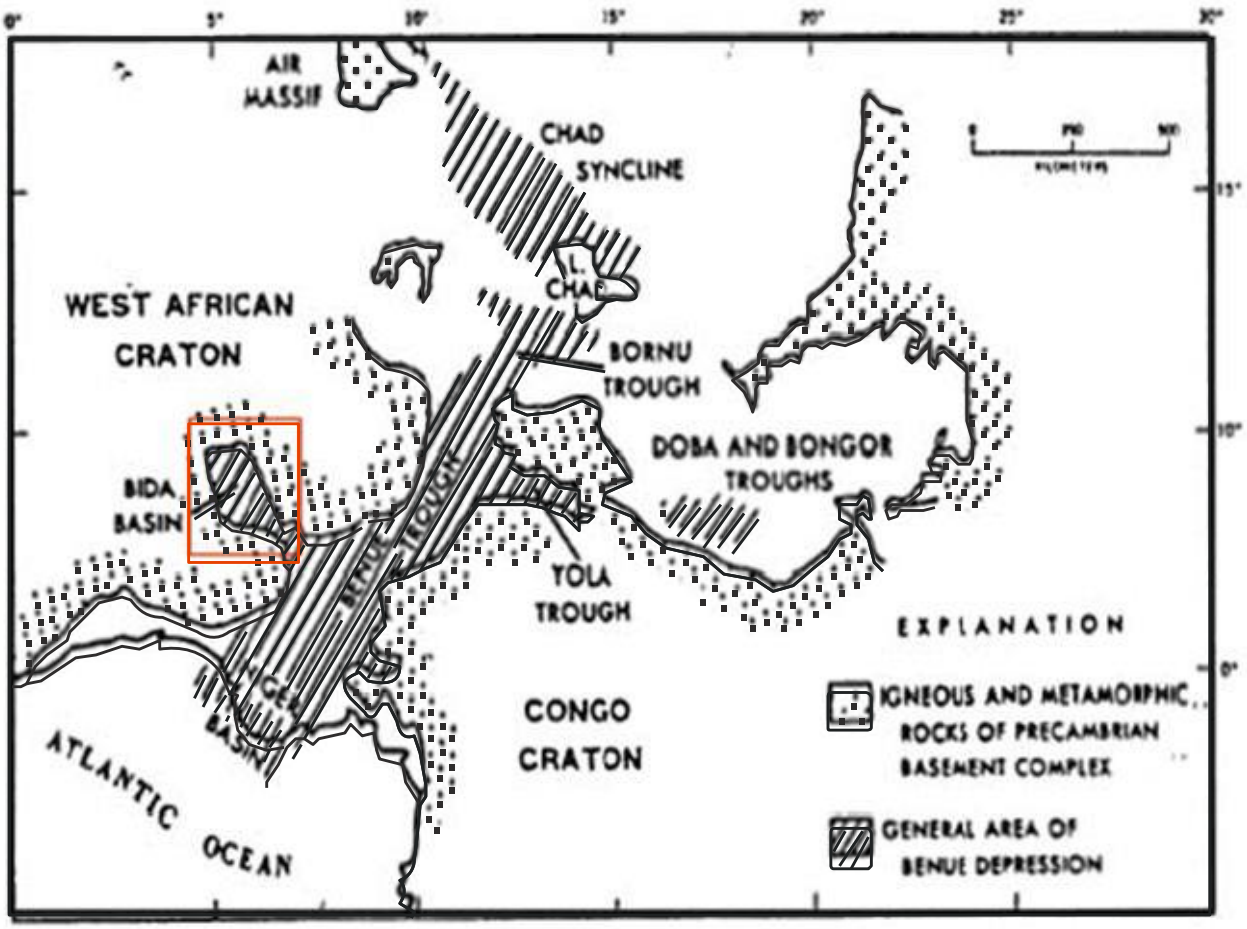


Figure 2.1: Map showing Benue depression and associated basins and troughs after Kogbe *et al*. (1983).

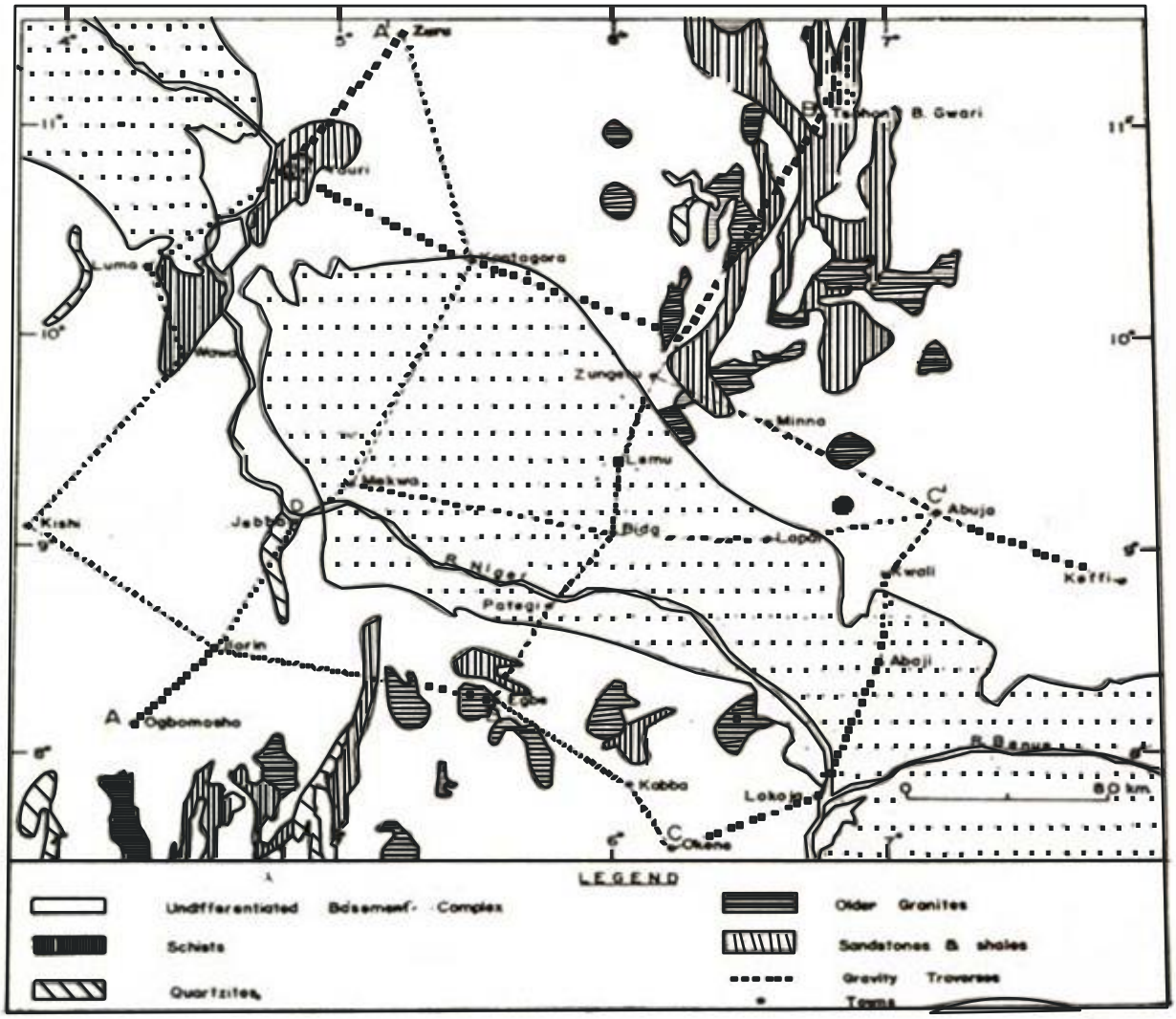


Figure 2.2: Geological map of Bida Basin showing the locations of the gravity traverses after Ojo and Ajakaiye (1989).

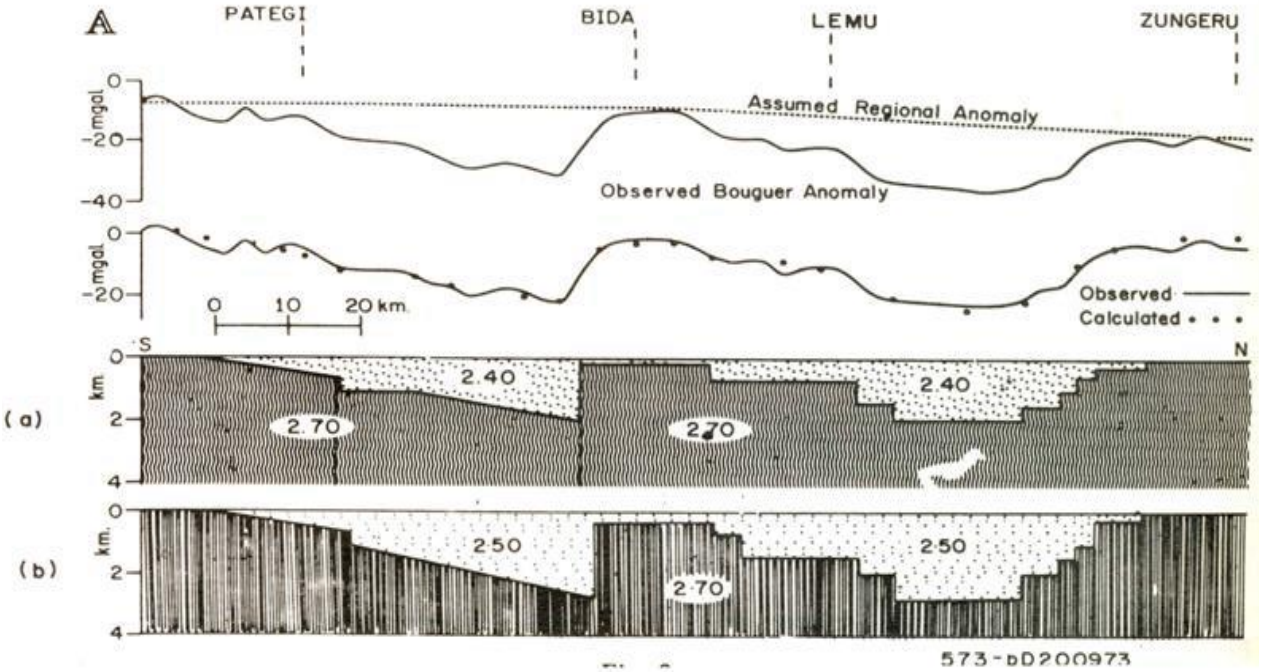


Figure 2.2a: Model generated from gravity profile for Pategi-Zungeru Traverses after Ojo and Ajakaiye (1989).

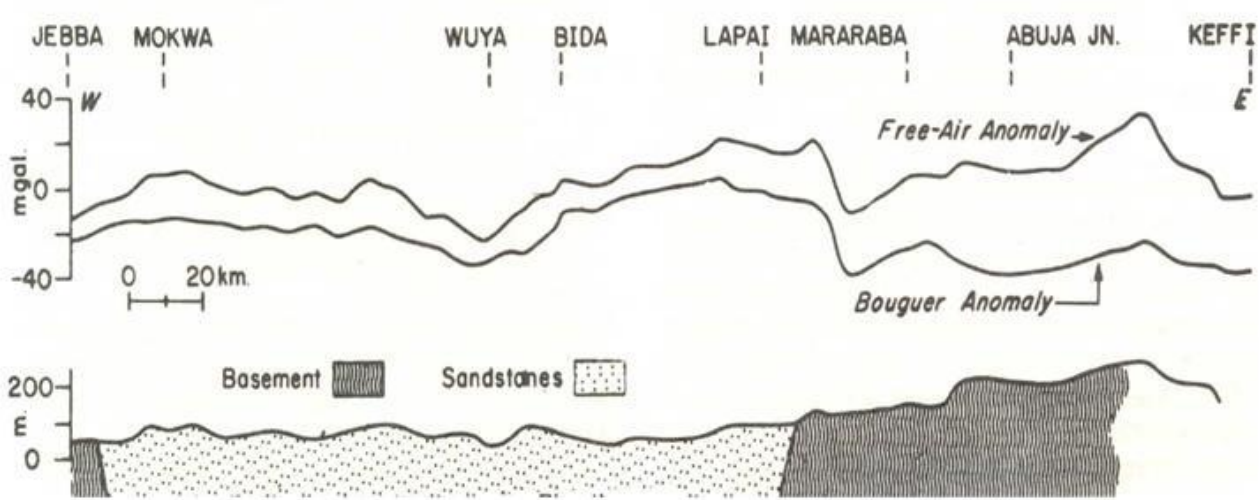


Figure 2.3b: Model generated from gravity profile for Jebba-Keffi Traverse after Ojo and Ajakaiye (1989).

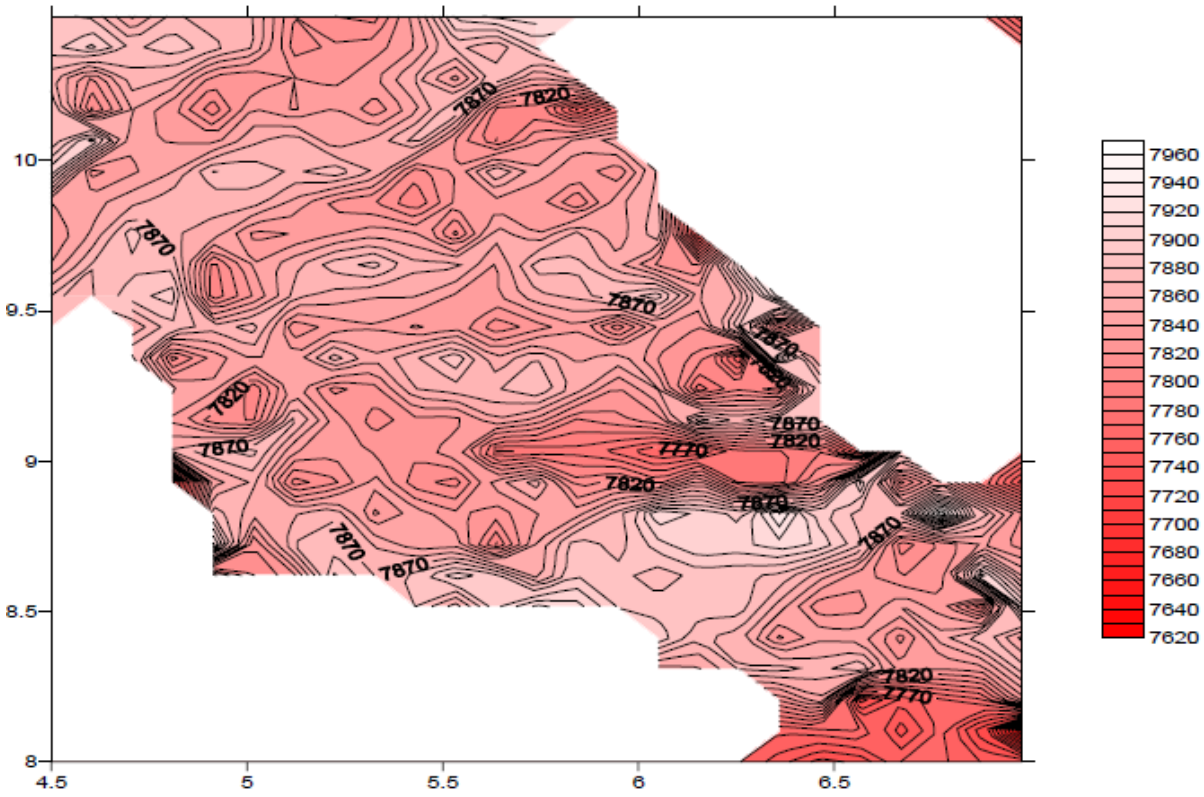


Figure 2.3: Total magnetic map of the Bida Basin after Udensi *et al*. (2003)

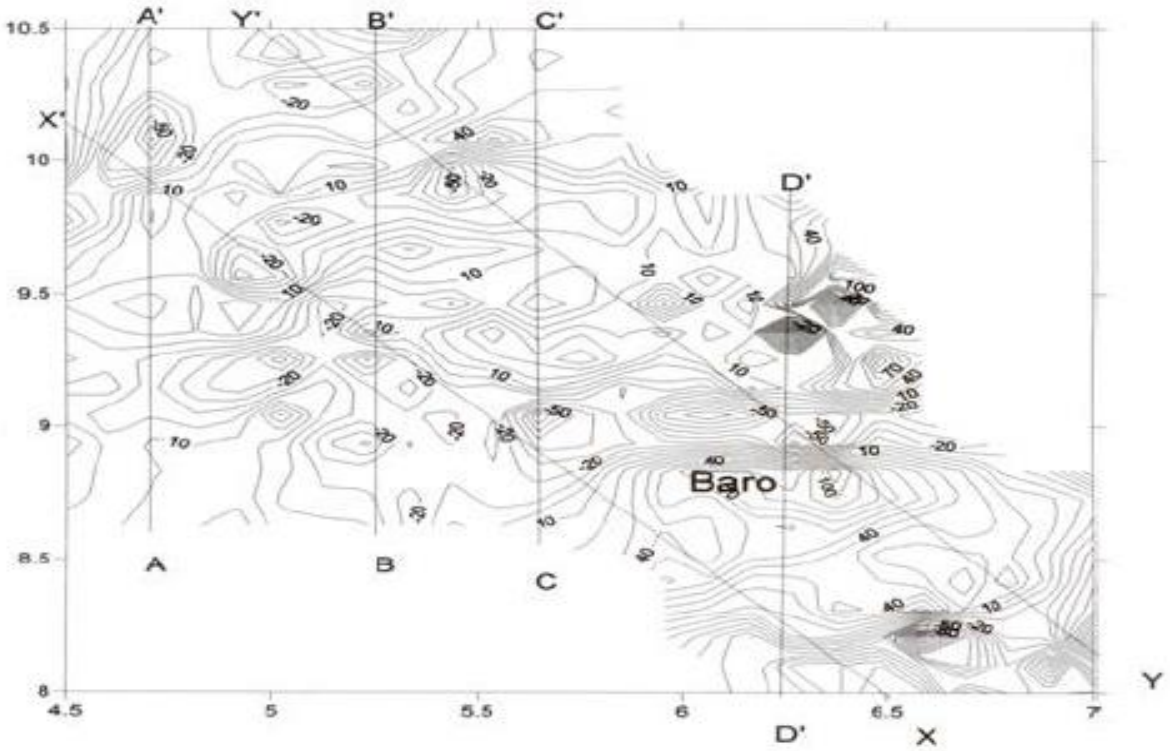


Figure 2.4: Magnetic Residual Map of the Bida Basin after Udensi *et al*. (2003).

2.3 Structural Evolution

Proposals of post-Santonian shallow cratonic sag and a pull-apart have been submitted by Whiteman (1982) and Braide (1992) respectively for the origin of Bida Basin. They believed that the Basin originated during the tectonic evolution of the Benue Trough which began in the late Jurassic-early Cretaceous with the opening of the Gulf of Guinea as a triple-junction rift (as the Benue arm failed to open fully, forming a failed-arm of the rift system), therefore, the opening of the Gulf of Guinea followed existing lines of weakness close to the edges of West African and Congo cratons along which the major transform faults propagated.

In a different model, the basin is thought to be associated with isostatic readjustments and gentle down-warping or subsidence of the granitic Basement Complex as a result of the removal of mantle material which led to the emplacement of the Younger Granite ring complexes during the Jurassic (Ojo and Ajakaiye, 1989; Whiteman, 1982). Braide (1992b) suggested a wrench fault tectonic model for the Bida Basin origin and by such it is considered as a graben resulting from the sinistral movements along the bounding Chain and Charcot fracture systems of the Benue Trough.

2.4 Stratigraphy

2.4.1 Stratigraphic Setting

The stratigraphy and sedimentation of the Upper Cretaceous (Campanian-Maastrichtian) successions of the Bida Basin have been documented by several workers including Adeleye (1973, 1974 and 1989), Agyingi (1991), Braide (1992), Ladipo *et al*. (1994) and Abimbola *et al*. (1999). The stratigraphic succession of the Bida Basin has been differentiated according to Adeleye (1973) into Northern Bida Basin and Southern Bida Basin.

Four mappable stratigraphic units and their lateral equivalents are recognizable within the Basin from north to south; the lower Bida Sandstone (comprising the Dokko and Jimma

members) in the northern part have Lokoja Sandstone as its lateral equivalent in the southern sub-Basin, this is overlain by the Sakpe Ironstone and the Enagi Siltstone which in turn is overlain by the Batati Ironstone in the Northern Bida Basin. The lateral equivalent of the Sakpe Formation and the Enagi Formation is the Patti Formation in the northern part of the Basin whereas the Agbaja Formation is the lateral equivalent of the Batati Formation. A correlation of the stratigraphic successions in the northern and southern parts of the Basin based on the lithologic and depositional characteristics is presented in table 2.1.

2.4.1.1 Northern Bida Basin

(a) Bida Formation

The Bida Formation Sandstone is the lateral correlation of the Lokoja Formation in the northern part of Bida Basin. It comprises of two members; the Dokko member is about 183 m thick while the Jimma member is about 90 m thick according to Adeleye (1972). The Dokko member is the basal unit and consists mainly of very poorly sorted pebbly arkose, sub-arkose and quartzose sandstones and thought to have been deposited in a braided alluvial fan setting based on the submission by Adeleye (1972). The Jimma sandstone member is dominated by cross-stratified quartzose sandstones, siltstones and claystones. Trace fossils comprising mainly of *Ophiomorpha*, *Thallasanoides* have been observed by Adeleye (1972).

Sedimentological evidence from the study by Whiteman (1982) indicates deposition in a braided stream environment for the Dokko sandstone member, while Jimma member is deposited under lower stream energy. Indication of channel margin deposit is taken to indicate deposition under tropical to subtropical conditions by Adeleye (1973) whereas Adeleye and Dessauvagie (1972) used evidence of leaf impression to proposed age of late Cretaceous (Campanian-Maastrichtian).

Ojo (2012) examined the depositional environments and petrographic characteristics of Bida Formation around Share-Pategi in the northern Bida Basin and suggest that the subarkosic sandstones within the area were derived from rifted and uplifted continental basement rocks in a warm humid paleoclimatic setting.

(b) Sakpe Ironstone Formation

The Sakpe Ironstone Formation comprises mainly of oolitic and pisolitic ironstones with sandy claystones locally at the base, followed by dominantly oolitic ironstone which exhibits rapid facies changes across the basin, at the top (Adeleye, 1972). According to Adeleye (1973), it comprises two members; Wuya and Baro ironstone. The Wuya Ironstone comprises mainly of oolitic and pisolitic ironstones with subsidiary sandy claystone locally present at the base with thickness of about 5meters at the type locality. The Baro ironstone member consists of oolitic ironstone and ferruginous sandstone which are locally pyritic and concretionary. Rapid facies change characterizes the unit and gradation exists between ferruginous and quartzose facies (Adeleye, 1973). The member caps the entire Baro plateau and the thickness varies, attaining a maximum of 3 meters. Whiteman (1982) considered Baro and Wuya members to be lateral equivalents.

Fossils like *Turritella* faunas and a bivalve indent characterizes Wuya member while Baro member yielded fossil wood and basal burrows which were identified as Skolithus by Adeleye (1973). Adeleye (1973) therefore uses fossil evidence to suggest a Maastrichtian age for the Sakpe ironstone Formation. He also holds the view that the Sakpe Ironstone Formation was deposited under marine condition in a Tethys sea connected with the Iullemmeden Basin. Meanwhile, Whiteman (1982) suggested late Cretaceous age using few fossils that were found in the formation and their limited variety.

(c) Enagi Siltstone Formation

This formation was proposed by Adeleye (1973) to consist of siltstone with subordinate amounts of sandstones, siltstone-sandstone admixtures and claystone and correlates with the Patti Formation in the southern Bida Basin. It occurs just below the tops of the major mesas such as the Dokko and Nupe plateau. The formation ranges in thickness between 30.0 and 60.0 m (Adeleye, 1972). Other lithofacies that can also be found include sandstone-siltstone intercalation and claystones. Maastrichtian age is assigned by Adeleye (1973) because of its stratigraphic position between the Sakpe ironstone and Batati ironstone. Adeleye (1973) suggested a fluviatile depositional environment which he stated it was as a result of the withdrawal of the Tethys northwards. The grain size, lithology, structures and flora, according to him indicate deposition under flood plain condition. However, Whiteman (1982) and Murat (1972) believed that the late Campanian deposits were laid down in the Bida basin which was a side basin adjacent to the Anambra Basin.

Recently, Ojo and Akande (2012) evaluated the facies relationships and depositional environments of the sedimentary Enagi Formation and concluded that the gross sedimentation pattern and characteristics in the Share area suggest predominance of trangressive shallow marine processes occasionally incised by fluvial channels.

(d) Batati Formation

This is the youngest Cretaceous unit in the northern Bida Basin and it is laterally correlated with the Agbaja Formation in the southern Bida Basin. It consists of argillaceous, oolitic and goethitic ironstones with ferruginous claystone and siltstone intercalations and shaly beds occurring in minor proportions, some of which have yielded nearshore shallow marine to fresh water fauna (Adeleye, 1973).

This Ironstone Formation is subdivided into the Edozhigi and the Kutigi ironstone members with Edozhigi member resting uncomformably on the Kutigi member according to Adeleye (1973). The Edozhigi member consists of goethitic and oolitic ironstone with a maximum thickness of 15 meters, whereas the Kutigi member consists of mixed goethitic and kaolinitic oolites with maximum thickness of 3 meters.

Braide (1992) interpreted the sedimentary paleoenvironment based on lithofacies suggested a meandering fluvial environment developed from alluvial fans and braided fluvial channels in poorly drained flood plains. Adeleye (1973) suggested that this formation might not be older than Maastrichtian due to the presence of fossil assemblages including *Ostrea, Lopha, Venericardia*, *Cardidea Faunus Beyenburgi Faunus*, *Miskalensis*, *Turritella* and burrows of *Alpheus sp*. He also concluded that the fossils indicate a marine transgression into the basin.

2.4.1.2 Southern Bida Basin

(a) Lokoja Formation

This is the basal unit overlying the Basement Complex uncomformably. It is the lateral equivalent of the Bida Foemation in the northern part of the Basin. It consists of sub-angular to sub-rounded quartz pebbles in a clay matrix. Lithologic units in this Formation range from conglomerates, coarse to fine grained sandstones with varying colour; milky to purple and sedimentary structures; massive to cross-stratified. Sub-angular to sub-rounded cobbles, pebbles and granule sized quartz grains are frequently distributed in a clay matrix. The conglomerates (grain- and matrix-supported) form recognizable beds at the base of distinct cycles at outcrops while sandstone units are frequently cross-stratified, generally poorly sorted and composed mainly of quartz and feldspar and are thus suggested by Ojo and Akande (2003) to be texturally and mineralogically immature.

The Lokoja Formation has been interpreted by Braide (1992) as continental (alluvial fan) deposit whereas Ladipo *et al*. (1994) suggested that the upper part have been inundated by marine conditions. The general characteristics of this sequence especially the fining upward character, compositional and textural immaturity and unidirectional paleocurrent trends, suggest a fluvial depositional environment dominated by braided streams with sands deposited as channel bars. Though, occurrence of some arenaceous foraminiferal microfossils diversity from clayey interval of the Lokoja Formation reported by Petters (1986) indicates shallow marine influence probably from Patti Formation.

(b) Patti Formation

The Patti Formation is about 70-100 meters thick and is well exposed along Abaji Kotonkarfi road cut consisting sandstone, siltstone, claystone and shale with lateral extension as Enagi in the northern part of the basin. The siltstones of this formation are commonly parallel stratified with occasional soft sedimentary structures (for example, slumps) and other structures such as wave ripples, convolute laminations and load structures. Trace fossils (especially *Thallasanoides*) are frequently preserved.

The subsidiary sandstone units of the Patti Formation are more texturally and mineralogically mature compared to the Lokoja Formation sandstone according to Ojo (1995). The predominance of argillaceous rocks, especially siltstones, claystones and shales in the formation requires suspension and settling of finer sediments in a quiet low energy environment probably in a restricted body of water (Braide, 1992).

The abundance of woody and plant materials comprising mostly land-derived organic matter, suggests prevailing fresh water conditions. However, biostratigraphic and paleoecologic studies by Petters (1986) have revealed the occurrence of arenaceous foraminifer in the shales

with an assemblage of *Ammobaculites*, *Milliamina*, *Trochamina* and *Textularia* which are essentially cosmopolitan marsh species similar to those reported by Gebhardt (1998) in the lower Maastrichtian marginal marine Mamu Formation (the lateral equivalent) in the adjacent Anambra Basin. Thus, similarity of Patti Formation lithofacies with the Mamu and Ajali formations in the Anambra Basin as indicated by Adeniran (1991), Nwajide and Reijers (1996) therefore supports marginal shallow marine to brackish water condition deposition.

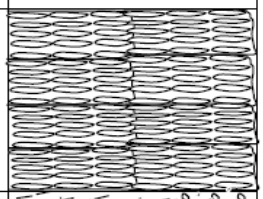
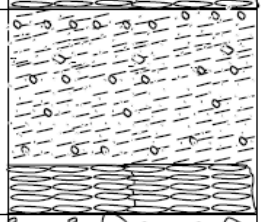
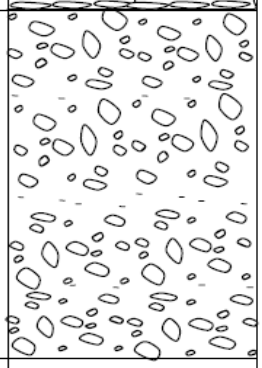
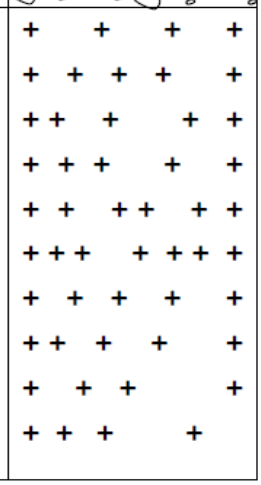
Akande *et al*. (2005) examined the source rock characteristics of the shale facies of the Patti Formation and noted its gas potential as a source rock. Ojo and Akande (2009) also studied the depositional characteristics of the sandstone facies of the Patti Formation and concluded it's an intracratonic Basin. Okunlola *et al*. (2012) examined the mineralogical composition of the Patti Formation claystone and shale at Ahoko and Abaji and concluded that they are composed of kaolinite and illite with non-clay minerals of microcline, quartz, zircon, pyrite and hematite.

(c) The Agbaja Ironstone Formation

This is the youngest Formation in the southern Bida Basin and it comprises of sandstones and claystones interbedded with oolitic, concretionary and massive ironstone beds in this region. It forms a persistent cap for the Campanian-Maastrichtian sediments in the southern part as a lateral equivalent of the Batati Ironstone Formation in the northern part of the Basin. Abimbola *et al*. (1994) identified and described three sub-facies; oolitic, concretional and massive ironstones with a thickness of ca. 20m at Agbaja plateau. He also reported marine influence by wave action which has caused a re-worked kaolin mud into concentric oolites often with nuclei of pyrite or siderite that have been replaced by iron oxides.

The intercalated sandstones and claystones within the ironstones were interpreted as abandoned channel sands and overbank deposits influenced by marine reworking to form the massive concretionary and oolitic ironstones according to Ladipo *et al*. (1994).

Table 2.1: Regional stratigraphic successions in the Bida Basin modified after Ojo and Akande (2012).

PERIOD	AGE	NORTHERN BIDA SUB-BASIN	SOUTHERN BIDA SUB-BASIN	LITHOLOGY
CRETACEOUS	MAASTRICHTIAN	Batati Formation	Agbaja Formation	
		Enagi Formation		
		Sakpe Formation	Patti Formation	
	CAMPANIAN	Bida Formation: Jima member / Doko member	Lokoja Formation	
PRECAMBRIAN	LOWER PROTEROZOIC	Basement Complex		

CHAPTER THREE

METHODOLOGY

3.1 General Statement

This chapter focuses on the methods employed in this research in other to achieve the aim and objectives of this research. The summary profile of the methodology employed in form of work flow is presented in the chart below.

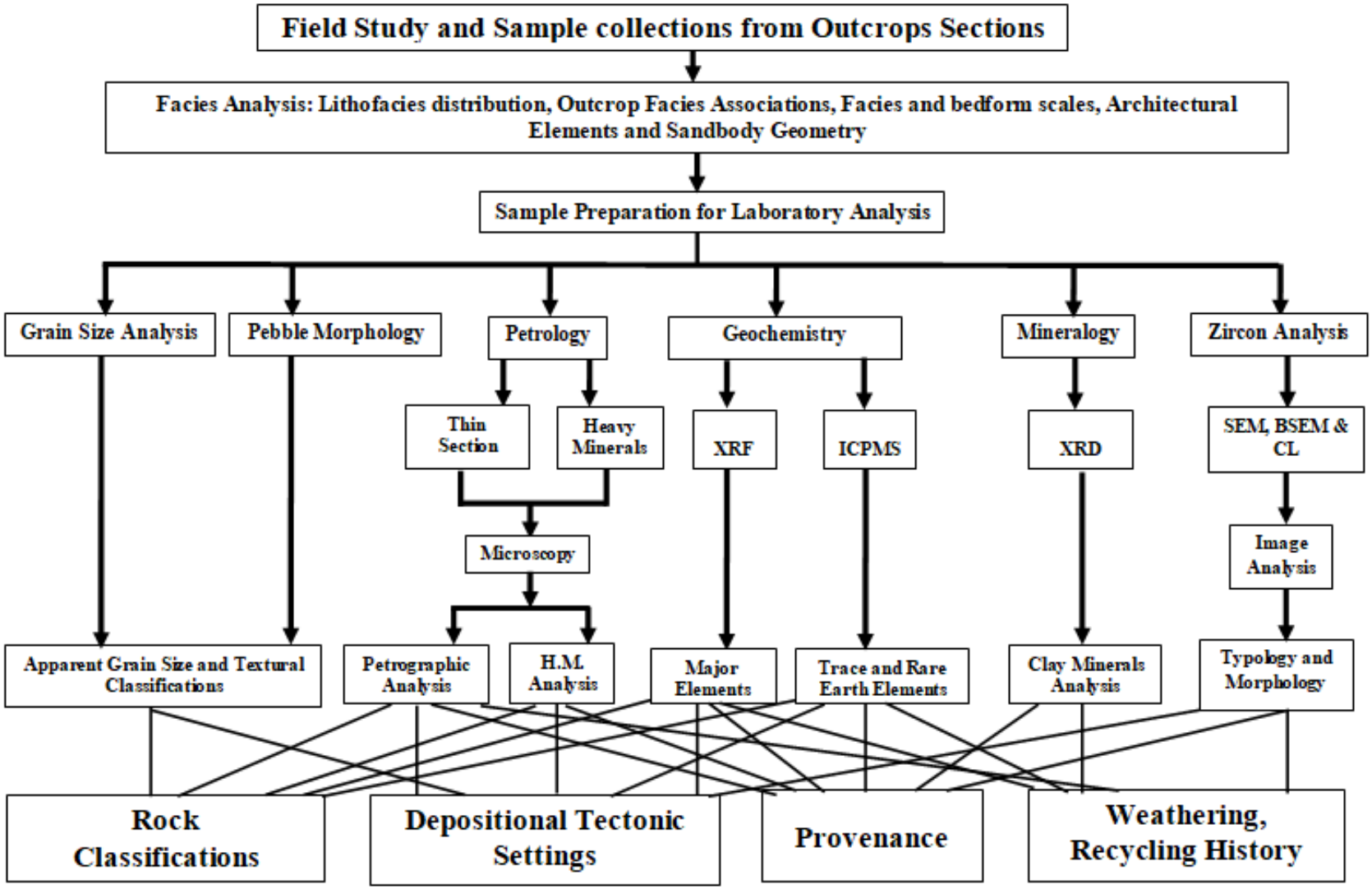


Figure 3.1 Flow chart showing the workflow of the analytical methods employed in this study

3.2 Field Work

The fieldwork for this research was conducted between 2014 and 2016 with mapping, logging and sampling done on the scale of 1:50,000 within Northern Bida Basin. The studied locations were accessible through major inter-state roads and minor roads as well as footpaths. Forty-six (46) surface outcrops sections were logged and beds were measured using measuring tapes and ruler (where applicable) for more precise measurements. Relevant information based on bed by bed measurements was thereby recorded in the field notebook.

Lithological sections representing each locations were constructed (Appedix II) at a 1cm = 1m scale showing detail description of the sedimentary successions, internal features of the beds such as colour, thickness, grain size, texture, mineralogy, physical and biogenic sedimentary structures together with data from measurement of attitude of the rocks and other. A composite stratigraphic profile of the strata was also constructed where necessary to allow selection of rock samples for further analysis.

Fresh representative samples were collected at different depth and horizon from the bottom to the top of each vertical profile of the exposed outcrops sections with horizontal and vertical spatial extents, and were properly stored in the sample bag and labeled for further laboratory analysis.

3.3 Facies Analysis

Field observation and lithofacies classification is a standard tool of facies-analysis (Miall, 1996). Facies analysis involves the detail measurement, description and record of vertical and lateral lithological sections within the study area Miall (1977). The approach of outcrop lithology is useful for interpreting beds in terms of depositional events. The established lithological variations were employed in interpreting the processes. Interpretations on the

environment of deposition of the sediments exposed in the area based on the sedimentological characteristics of facies analysis, architectural elements and the sand body geometry were carried out using this approach.

The facies analysis in this study is focused on the primary depositional attributes of a sediment succession from the developed graphic logs of the studied sections using the standard Miall (1977; 1985; 1996) scheme. The sedimentological information was transformed into detail graphical logs and this is presented in Appendix I. Three (3) lithofacies and ten (10) sub-facies were delineated from this study and detail id discussed in chapter four.

3.4 Laboratory Analysis

3.4.1 Pebble Morphometric Analysis

The pebble morphometry according to Stratten (1973) involves measuring the pebbles' diameter using venier caliper to measure the long (L), intermediate (I), and short (S) axes of pebbles to determine the independent and dependent morphometric parameters. Clast roundness estimation based on the percentage of convex parts of a pebble along its external circumference was estimated with the aid of the Sames (1966) charts.

Over 200 various sizes of clast samples were randomly collected from two locations; Patigi and Baganko, based on the sub-facies, screened to exclude the cracked or freshly broken ones prior to the morphometric analysis. The highly resistant cobbles and pebbles were then selected, numbered and subjected to the analysis to generate the statistical data. A total of one hundred and twenty-eight (128) pebbles and cobbles of quartz were finally measured and recorded (Appendix I, Table I).

3.4.2 Grain Size Analysis

Mechanical sieving is a traditional measurement technique, commonly employed for grain size determination in sand-dominated deposits because it is relatively simple (Hartmann, 2007; Cheetham *et al*., 2008). This analysis was performed using a particle-size analyzer to measure the size distribution of sediments ranging in size from <0.063 microns to 4.50 millimeters (mm) (clay to conglomerates) so as to determine the classes of the sandstones within the study area. The samples were disaggregated by using standard methods (Carver, 1971) and sieved at half phi interval, ASTM mesh while sample analysis were carried out by technique procedure given by Folk (1974). A total of three hundred and one (301) sandstone samples were analyzed for grain size analysis based on the sub-facies (Appendix I, Table II). Treatment with either 1% hydrogen peroxide or ultrasonic shaking in a solution of 0.1% sodium pyrophosphate was not required, since no organic matter were present.

In the laboratory, the samples (Appendix I, Table II) were disaggregated, coned, quartered and 100.0 gm of each samples were collected and processed. Sieving was done for each sample for 15 minutes on a Ro-tap sieve shaker, using a set of U.S. standard sieves. The sand size fractions were collected and weighed to an accuracy of 0.01 gm using single pan electronic balance. The data obtained were processed for determining the cumulative weight percentages and grain size parameters; mean size (Mz), standard deviation (σi), skewness (Ski) and kurtosis (KG) in determining the transportational mode, energy of the transportational medium and provenance following the formula after Inman (1952), Folk and Ward (1957) and Folk (1966). These parameters (Appendix II, Tables i-x) were also used in the preparation of various interrelationship scatter plots suggested by Folk and Ward (1957), Friedman (1961; 1967) and Moiola and Weiser (1968).

3.4.3 Thin Section Petrography

Well-consolidated sandstones samples with total number of seventy-five (75) were selected among the collected samples based on the sub-facies, gathered from distinct beds spanning the stratigraphic section for petrographic (thin section) analysis (Appendix I, Table III). Rock thin-section preparation and studies were taken in the thin section workshop and microscope laboratory respectively at the National Geophysical Research Institute (NGRI), Hyderabad, India using standard procedure for petrological studies. The detail result from this study is presented in chapter four.

In the laboratory, a rock saw was used to cut the sandstone samples into chips, suitable for standard 27 by 46 mm thin sections before study under the NIKKON polarizing microscope and standard petrological techniques were employed in description. Meanwhile heavy minerals analysis was carried out on the sand fractions of the selected samples and was subjected to a standard method of heavy mineral separation. The mineral separation was taken at the Geology workshop, Kwara State University, Malete, Kwara State and the extracted minerals were subjected to microscopic study at the NGRI, Hyderabad.

3.4.3.1 Detrital Mineral Composition

Petrographic study of the detrital minerals involves determination of framework composition, authigenic components, cement-grain relationship and diagenetic signatures. Detrital grain contacts were counted separately while nature and the contact relationships (contact index) were computed using Pettijohn *et al*. (1987) method. Mineralogical compositions of each sample was determined by compositional modal analysis following the traditional method and conventional point-count which minimizes the control of grain size on sand composition according to Gazzi (1966), Dickinson (1970) and Ingersoll *et al*. (1984). Pore spaces were

skipped and the number of point counts of interstitial material such as cement was recorded and included in the total framework grain counts per slide.

The categories of different identified grain types and their varieties include; quartz (monocrystalline and polycrystalline), feldspar (potassium and plagioclase), sedimentary lithics or rock fragments and opaque minerals (iron-rich minerals). The resulting grain composition data were compiled and the three end members (quartz, feldspar, and lithics/rock fragments) were re-calculated to percentage to form framework composition in order to determine the trends of compositional change over time (See appendix IV). The following compositional parameters were further determined; total quartz (Q or Qt), monocrystalline quartz (Qm), polycrystalline quartz (Qp), total feldspar grains (F), plagioclase feldspar (P), potassium feldspar (K), lithic fragments (L), total lithic fragments (Lt), sedimentary lithic fragments (Ls), volcanic lithic fragments (Lv), metamorphic lithic fragments (Lm).

The detail discussions on the applications of framework compositional data for conventional triangular (ternary) diagrams plotting; Q-F-L, Qm-F-Lt and Qt-F-L after McBride (1963), Pettijohn (1973), Folk (1974), Dickinson and Suczek (1979), Dickinson *et al*. (1983) models to better understand sediment classification and evolution history on the source areas and palaeogeographic reconstructions of the Bida Basin sediments will be provided in chapter five.

3.4.3.2 Heavy Mineral Analysis

Sixty-two (62) representative, unweathered, friable sandstone samples were selected and analyzed for their heavy mineral composition (Appendix I, Table IV). Disaggregated portions of the selected samples were used to obtain the heavy mineral fraction. Samples were prepared using the standard laboratory technique described by Mange and Maurer (1992),

separating out the heavy minerals from the 62.5-250μm disaggregated fine-sand fraction using bromoform (tribromo-ethane with density of 2.89g/dm^3) using separating funnel.

After separation, a portion of the heavy fraction was used for preparing slides, mounted in epoxy resin. For the statistical analysis and further discussions and interpretations, 200 transparent grains were counted applying the ribbon method of Mange and Maurer (1991). To obtain more information on the heavy mineral content, mineral varieties were divided into non-opaque and opaque (see Appendix IV, Tables xxviii).

3.4.4 Mineralogical Analysis (X-Ray Diffraction)

The mineralogical composition study of a rock samples inevitably requires X-ray powder diffractometer and provides the most efficient method for the determination of mineralogical composition of sedimentary rocks. Thirty-five (35) representative samples (Appendix I, Table V) were selected for the x-ray diffraction (XRD) analysis based on the facies variations. About 50.0g of each pulverized samples were analyzed using XRD facility at the Department of Geology, Faculty of Natural and Agricultural Sciences, University of Pretoria, South-Africa.

Sample preparation includes pulverizing of about 35.0 g in a thoroughly cleaned agate ring mill, preparation of glass discs and pressed into a steel sample holder. Glass discs were made from 0.4 g of the annealed sample powder and 4.0 g Li-tetra/metaborate while 1.0 g binder was added to 6.0 g sample material to prepare the pressed powder tablets. They were then analyzed using a PANalytical X'Pert Pro powder diffractometer in θ–θ configuration with an X'Celerator detector and variable divergence- and fixed receiving slits with Fe filtered Co-Kα radiation (λ=1.789Å). The diffractogram presents a permanent record of intensity against diffraction angles which is obtained directly by a strip chart recorder.

The analyzed samples were scanned from 0° to 70° at a scanning speed of 0.02^{o} 2θ/sec and the 2θ values of the peaks were converted into d-spacing in A^{o} for Cu Kα radiations. The identified minerals within the study area as obtained by PHILLIPS PW1840 model diffractometer using nickel filtered Cu Kα radiation are presented in tables while their peak values are shown in the charts presented in appendix D. The phases were identified using X'Pert Highscore plus software. The relative phase amounts (weight%) were estimated using the Rietveld method (Autoquan Program). Errors are on the 3 sigma level in the column to the right of the amount.

3.4.5 Bulk Geochemical Analysis (XRF and ICPMS)

Representative samples (sandstones, siltstones and claystones) were selected for the bulk geochemical analysis from the collected samples based on the facies variations following standard techniques by Tucker (1996). About 50-100g of the whole rock samples were reduced to chips of 2-4 mm and pulverized in a mortal agate mill to avoid contamination. Forty-six (46) samples (Appendix I, Table VI) were selected for major elemental compositions while one hundred and fifty-six (156) rock samples (Appendix I, Table VII) were selected for trace and rare earth elements and analyzed at the National Geophysical Research Institute (NGRI), Hyderabad, India. Replicate analyses of samples and standards indicate that errors for major elements vary between 1 and 2%.

The bulk inorganic geochemical analysis (whole-rock geochemical analysis) of sediment is a standard geochemical tool, performed by x-ray fluorescence (XRF) and inductive coupled plasma mass spectrometry (ICPMS) for the determination of major and trace with rare earth elements respectively. The geochemical character of a sediment is directly determined by its framework components and its authigenic mineral content, because it is controlled by various factors which includes; hydraulic sorting, composition of the source terrain, chemical

weathering, diagenesis, metamorphism and hydrothermal alteration (McLennan, 1989; Fralick and Kronberg, 1997).

Whole-rock geochemical analysis was performed to aid chemostratigraphic characterization in this study, because geochemical signature of the strata determined by the bulk elemental concentration of the elements can be affected by facies, weathering, diagenesis, provenance and basin redox conditions according to Ratcliffe *et al.* (2007). Analysis of geochemical changes throughout the succession, as well as between outcrop sections, enabled the development of a stratigraphic framework for the study interval. Therefore, the geochemical data were interpreted based on the relative abundances and variations within stratigraphic successions and with reference to the standard published referenced values. Collation of all these information along with the published data allowed interpreting the prevalent paleoclimatological and paleoenvironmental conditions, which in turn were contrasted in relation with regional and global climatic models.

3.4.5.1 X-Ray Fluorescence Sample Preparation Procedure (Major Elements)

The determination of major elemental composition; SiO_2, Al_2O_3, Fe_2O_3, MnO, MgO, CaO, Na_2O, K_2O, TiO_2 and P_2O_5 of the selected sediment samples were carried out using x-Ray Fluorescence (XRF) facility at the NGRI, Hyderabad, India. Prior to analysis, selected samples were made into pellet in the XRF laboratory (Figure 3.2).



Figure 3.2: Sample preparation for Pellet prior to XRF analysis (a) Pellet preparation using the machine, (b) Some prepared pellets ready for analysis and (c) Powdered samples collected and spreading at the beginning of sample preparation to make pellets.

3.4.5.2 Trace and Rare Earth Elements Sample Preparation Procedure

For the trace and rare elements analysis, 50.0mg of each samples was digested with mixture of 3.0 ml of concentrated hydrogen fluoride (HF), 1.0 ml of concentrated hydrogen nitrate (HNO_3) and 1.0 ml of concentrated hydrogen per chlorate ($HClO_4$) for 48 hours in a tightly closed Teflon vessel on a hot plate at temperature <150°C (Figure 3.3). Later, the solution was evaporated to dryness and extracted with 60.0 ml of 1% HNO_3. Analysis of these samples was also carried out using Laser ablation multicollector inductive coupled mass plasma spectrometer (LAM-MC-ICPMS) at the NGRI-CSRI, Hyderabad, India (Figure 3.3c). Each sample was run against an internationally recognized standard reference material (SRMs) viz., GSR 4, GSR 6, GXR-6 to correct long-term instrument drift.

The rare earth elements data were normalized relative to the Chondrite (Cl) after (Boynton, 1984), Post Archean Australian Shale (PAAS) after McLennan (2001), Upper Continental Crust (UCC) after McLennan (1989) and North American Shale Composite (NASC) after Gromet *et al.* (1984) values. Accuracy of the trace and REE element analyses is within 5%.



Figure 3.1a: Laboratory sample preparation for trace and rare earth elements prior to ICPMS analysis.



Figure 3.3b: Laboratory sample preparation for trace and rare earth elements prior to ICPMS analysis.



Figure 3.3c: Laser Ablation Microprobe Multi Collector Inductive Coupled Plasma Mass Spectrometer (LAM-MC-ICPMS) at NGRI (CSIR) for Trace and Rare Earth Elements analysis.

3.4.6 Image Analysis (Zircon Typology)

Five (5) samples (Appendix I, Table VIII) were selected from the studied petrographic samples for image analysis of scanning electron microscope (SEM) equipped with backscattered electron microscope (BSE) and cathodoluminescence (CL) acquired in a TESCAN VEGA3 which is capable of high spatial resolution (~1um) and relatively high analytical sensitivity (Figure 3.4). Six (6) samples were selected for zircon morphological and typological characteristics analysis; three (3) samples each from Bida and Enagi formations (Appendix I, Table IX).

Prior to the image acquiring, the samples were prepared as clean, flat, uncovered petrographic thin-sections and stable in a 10-5 torr vacuum environment and under electron bombardment. For best results, samples must be polished to within a 0.05 um flat surface. After preparation, samples were coated with an approximately 200 Angstrom (10 nm) layer of carbon using a carbon material in an evaporator.

The TESCAN VEGA3 is normally equipped with up to 5 wavelength-dispersive spectrometers. It also contains;

I. an electron gun (usually a heated tungsten filament) produces the electrons, which are then focused with 2 condenser lenses, filtered through several apertures and finely focused on the specimen (with the objective lens) on the area of interest, (essentially the image of the filament is “de-magnified” by the electron lens system in a manner analogous to the looking through the wrong end of a telescope),

II. a high vacuum (10-6 torr) is required, for the life of the filament and to minimize electron dispersion in the column,

III. Scanning coils, so the beam can raster across a specimen, producing a scanned image (a la SEM),

IV. secondary electron detectors (which in scanning mode yield SE images, showing surface features),

V. backscattered electron (BSE) detectors yielding images where different phases of differing mean atomic number stand out sharply,

VI. cathodoluminescence (CL) detectors, where the light emitted from the electron specimen interaction can be imaged, and can clearly show features in minerals and semi-conductors that would be difficult to see compositionally (these are features due to differences in specific trace element concentrations, or crystal lattice defects).

For zircon analysis, about 3-4 kg of freshly collected sediment samples were sieved for the fraction proportion smaller than 2 mm. Zircon grains were concentrated by a combination of Wilfley shaker table and then handpicked under binocular microscope. The zircon grains were mounted in vacuum-grade epoxy resin discs, diamond-polished and given conductive carbon coating. The zircons were imaged at a working distance of 17 mm and accelerating voltage of 15–20 kV. For each of the samples studied, the typologic distribution was based on examination of at least 300 unbroken zircon crystals from a single sample.



Figure 3.2: The TESCAN VEGA3 scanning electron microscope (SEM) machine equipped with backscatter electron (BSE) and cathodoluminescence (CL) for Image analysis.

3.5 Statistical Analysis (Factor Analysis and Principal Component Analysis)

The geochemical data were subjected to statistical analysis using Factor Analysis and Principal Component methods. Factor analysis was used to identify the structure underlying such variables and to estimate scores to measure latent factors themselves while principal components analysis is used to find optimal ways of combining variables into a small number of subsets.

Generally, principal component analysis (PCA) and factor analysis (FA) are used to identify underlying constructs or factors that explain the correlations among a set of items. They are often used to summarize a large number of items with a smaller number of derived items, called factors. The main applications of these techniques can be found in the analysis of multiple indicators, measurement and validation of complex constructs, index and scale construction, and data reduction. These approaches are particularly useful in situations where the dimensionality of data and its structural composition are not well known.

Key concepts of Factor Analysis and Factor Analysis and Principal Component Analysis

Factor: A linear combination of items (in a regression sense, where the total test score is the dependent variable and the items are the independent variables).

Eigenvalue: The standardized variance associated with a particular factor. The sum of the eigenvalues cannot exceed the number of items in the analysis, since each item contributes 1 to the sum of variances.

Factor loading: For a given item in a given factor, this is the correlation between the vectors of subjects' responses to that item, with the vector of (subjects) predicted scores, according to a regression equation treating the entire set of items as independent variables. The factor

loading expresses the correlation of the item with the factor. The square of this factor loading indicates the proportion of variance shared by the item with the factor.

Scree plot: A plot of the obtained eigenvalue for each factor.

3.6 Modal Analysis of employed Techniques

This aspect describes the modal description of the methods employed in this research. The distribution of the techniques and tools; field and laboratory are presented in form of pie chart in figure 3.4. The pie chart shows that field work constitute forty percent (40%) of the total research while the remaining sixty percent (60%) covers various employed laboratory analysis (Figure 3.5).

The laboratory analyses comprises of pebble morphology and mechanical sieving to determine the textural characteristics of the sediments and their depositional environment, the thin section petrography and modal analysis, whole rock geochemical analysis to quantify the sediments chemical composition and characteristics, the Scanning Electron Microscopy (SEM) and Backscattered Electron Microscopy (BSEM) for identification of some minerals and the Cathodoluminescence of the zircon to highlight the typology and provenance.

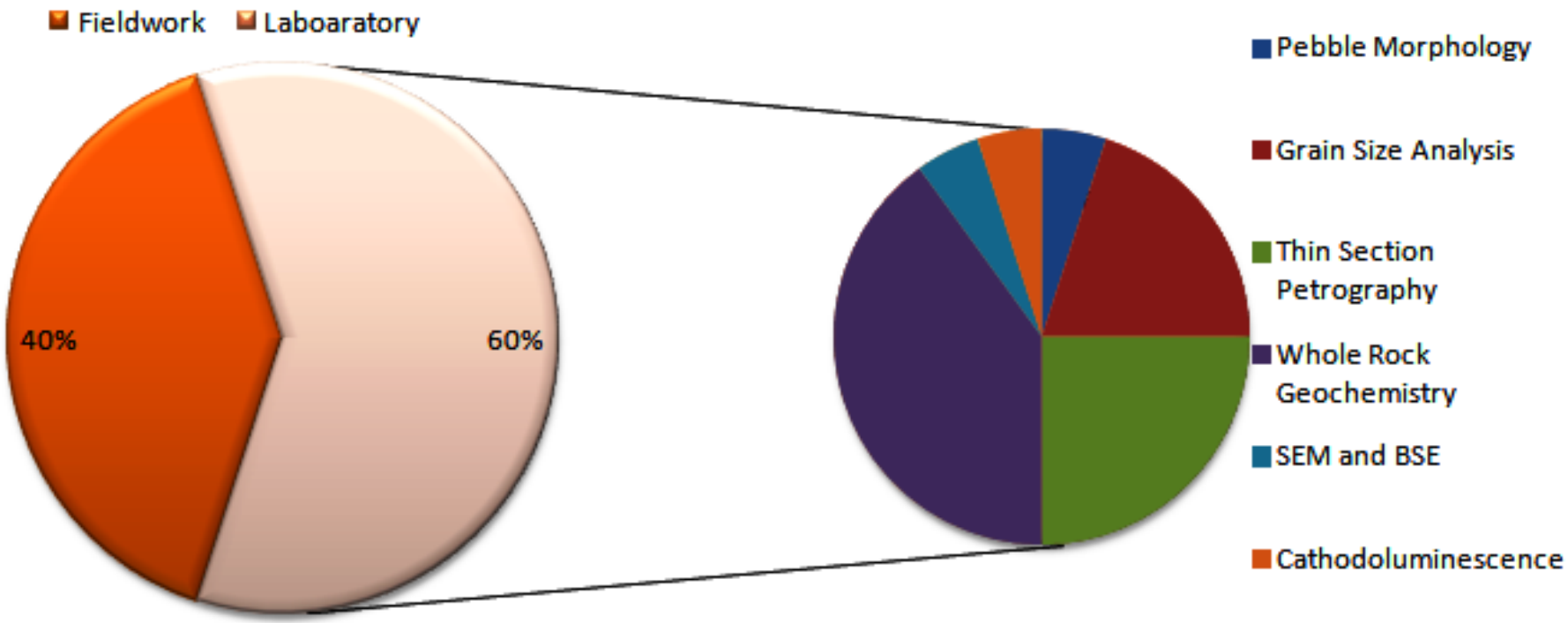


Figure 3.3: Modality of the employed methodological techniques.

CHAPTER FOUR

RESULTS

4.1 Facies Analysis, Architectural Elements, Geometry and Paleocurrent

This part describes the outcroping sedimentary strata within Northern Bida Basin with the purpose of deducing facies and associations to identify the depositional environment and palaeogeographic settings of the study area.

4.1.1 Lithofacies and Sub-facies description

The sedimentary facies refers to the sum of the characteristics; dimensions, sedimentary structures, grain sizes and types, colour and biogenic content of a sedimentary unit (Middleton, 1973). Reading and Levell (1996), and Walker (2006) defined facies as description of rocks and grouping sedimentary rocks seen in the field.

In this study, the facies description of forty-five (45) outcrop lithological sections is based on the observed physical and chemical processes of the sediments during and after deposition. Textural characteristics of the measured outcrops sections; grain size and sorting, sedimentary structures and degree of bioturbation were among the important features considered during lithostratigraphic description of the outcrop sections into vertical transition which reflects a marked change in the sedimentary architecture.

Three (3) basic lithofacies; conglomerate, sandstone and mudstone (siltstone and claystone) and ten (10) sub-facies were identified within the study area (Table 4.1) which will help in interpreting the depositional environments. The recognized sub-facies; clast-supported, massive conglomerate (Gcm), matrix-supported, massive conglomerate (Gmm), clast-supported, crudely bedded conglomerate (Gh), crudely stratified (Se), planar cross-stratified

sandstone (Sp), rippled stratified sandstone (Sr), horizontally stratified sandstone (Sh), massive sandstone (Sm), finely laminated mudstone (Fl) and massive mudstone (Fm) were arranged into distinctive cycles and associations. They are discussed in details below according to the Miall (1985, 1996) classification schemes.

Table 4.1: Lithofacies and sub-facies types in the study area

Lithofacies	Sub-facies Code (after Miall, 1985, 1988, 1992)	Description	Location
Conglomerate	Clast Supported Conglomerate (Gcm)	Massive, poorly sorted, clast-supported, imbricated conglomerate.	Patigi, Baganko, Ndeji, Shonga
	Matrix Supported Conglomerate (Gmm)	Massive, poorly sorted, subrounded to subangular conglomerate.	Patigi, Baganko, Lade, Share town, Shonga, Patti-Chin and Baro
	Crudely bedded Conglomerate (Gh)	Weakly laminated, poorly sorted, very coarse-pebbly sandstone.	Shonga, Zambufu, Gbugbu, Wariku, Lafiagi, Baganko, Baro
Sandstone	Crudely bedded Sandstone (Se)	Weakly bedded sandstone (fine to very coarse grained).	Share, Shonga, Rabba, Bida, Enagi, Wushishi, Baro, Lemu and Dokko
	Planar cross-bedded sandstone (Sp)	Planar cross bedded sandstone (fine to very coarse grained).	Kutigi, Jimma, Dokko, Kajita, Bida, Tanagi Rabba
	Rippled cross-bedded sandstone (Sr)	Rippled cross-bedded sandstone (fine to very coarse grained).	Share, Wariku, Rabba
	Horizontally stratified sandstone (Sh)	Planar laminated sandstone (fine to very coarse grained).	Rabba, Bida, Kutigi, Tanagi, Manigi, Maraba, Lemu, Dokko, Jimma
	Massive sandstone (Sm)	Massive sandstone (fine to very coarse grained).	Share, Shonga, Jimma, Dokko, PattiChin, Kajita, Enagi, Lemu, Lafiagi, Rabba
Mudstone	Finely laminated mudstone (siltstone and claystone) (Fl)	Planar laminated claystone to siltstone.	Share, Kutigi, Enagi, Rabba, Tanagi, Rafingora, Manigi
	Massive mudstone (siltstone and claystone) (Fm)	Massive claystone to siltstone.	Share, Gbugbu, Kutigi, Enagi, Rabba, Tanagi, Rafingora, Manigi

4.1.1.1 Clast-supported, massive conglomerate (Gcm) sub-facies

The clast-supported, massive conglomerate (Gcm) sub-facies is moderately well sorted, composed of sub-rounded to rounded pebble size clasts and granules (0.3 to 14.0cm in diameter), mainly quartz, commonly occurs within beds of 0.5 to 3.0 meters thick. This sub-facies is closely compared with Orthoconglomerate of Pettijohn (1957). The bed's thickness implies the operation of mass-flows of considerable magnitude with rolling bedload of the large clasts along a bed and it's suggested to be a deposit from traction by a unidirectional current.

Majority of the clasts with ordered imbricated fabric lie tangential to bedding (Figure 4.1a and b). The shape and size of the sandwiched clasts also reflect a high discharge and higher energy of the depositional current. An occasional gradation from Gcm to Gmm and Gh (coarse sub-facies) was observed (Figure 4.1a) which indicate diminish of flow energy strength and in support of deposition from a single current according to Walker (1978).

Gcm sub-facies comprise lowest component (2%) of total sub-facies present in the whole study area. It is usually observed in lower and upper parts of the lithological sections exposed at the proposed Harman-Patigi University, Patigi and behind Baganko village, near Abiola farm (Lafiagi area). This sub-facies were also observed in some places within Share town, also as a road cut section in Ndeji and along Share-Lafiagi road.

4.1.1.2 Matrix-supported, massive conglomerate (Gmm) sub-facies

The matrix-supported, massive conglomerate (Gmm) sub-facies is generally supported by poorly sorted, coarse-grained sandstone matrix for the clasts (Figure 4.1b). It is otherwise referred to as Paraconglomerate by Pettijohn (1957). Individual beds of Gmm ranges between

0.2 and 1.0m thick with sharp bases and the clasts present are usually of size range between 1.7 and 8.7cm in diameter (Adepoju *et al*., 2018a). The clasts sitting in a poorly sorted matrix are mostly sub-angular to rounded, non-imbricated granules to pebbles (mainly quartz and schist) which usually decrease upward in each cycle (Figure 4.1b).

Gmm sub-facies comprise about 5% of the total sub-facies present within the study area. Its generation may be connected with the result of catastrophic flooding events, during which channels formed and they were filled with poorly sorted or unsorted coarse materials as it display relatively high-hydraulic properties which is attributed to a gravel-dominated braided rivers in a fluvial system according to Smith (1974) and Miall (1977).

Typical Gmm sub-facies were observed at the following exposed lithological sections; middle part of the outcrop sections at proposed Harman-Patigi University, Patigi, Baganko village, near Abiola farm (Lafiagi area), at Lade along Gbugbu-Patigi road, Share town, Shonga town, Patti-Chin and Baro.



Figure 4.3: Field photograph showing typical clast-supported, massive conglomerate (Gcm) and matrix-supported, massive conglomerate (Gmm) sub-facies at: (a) Proposed Harmattan Patigi University site, Patigi (Longitude: 08°42'53.5"N; Latitude: 005°46'55.7"E); and (b) Baganko village, near Abiola farm, Lafiagi area (Longitude: 08°54'29.4"N; Latitude: 005°19'24.6"E.).

4.1.1.3 Crudely bedded conglomerate (Gh) sub-facies

The crudely bedded conglomerate (Gh) is composed of few sub-angular to sub-rounded, poorly sorted gravel lenses that floats within the sand matrix with grading exhibiting an abrupt upward transition into Gcm and Gmm sub-facies. The beds thickness ranges from 0.3 to 0.8m. In few occasions, Gh sub-facies consists of stratified gravels that commonly infill channelized erosive basal surfaces and the gradational top contact (Figure 4.2a and c). It has 15% proportions among the evaluated sub-facies. Occasionally, the pebbly clasts form irregular bands on the erosional surface defining a bounding surface between the lower and upper bed (Figure 4.2b).

Due to the crudely bedded nature of Gh sub-facies beds, it is interpreted to represent the accretion of gravel in longitudinal bars which usually begins with the largest clasts as diffuse gravel sheets according to Cant (1982), Adepoju *et al*. (2018a). This attributes like Gcm and Gmm sub-facies indicate gravel-dominated braided rivers in a fluvial system according to Smith (1974) and Miall (1990).

Gh sub-facies were observed in the middle and lower parts of the exposed outcrops at Shonga, Zambufu, Gbedeworo, Gbugbu, Wariku, Lafiagi, Baganko and Baro, all in the south-eastern part of the northern Bida Basin.



Figure 4.4: **Field photograph showing typical crudely bedded conglomerate (Gh) sub-facies at; (a) middle part of section at Shonga, along Tada road (Longitude: 005°08'50.1"E; Latitude: 09°01'27.4"N), (b) lower part of section at Wariku (Longitude: 08°47'46.3"N; Latitude: 005°18'41.6"E) and (c) lower part of section at Baro, near railway line (Longitude: 006°24.956'E; Latitude: 08°37.371'N).**

4.1.1.4 Crudely stratified sandstone (Se) sub-facies

The crudely stratified to massive sandstone (Se) sub-facies is composed of sands and minor silts, medium sorted and occur only at the lower and middle parts of the studied sections (Figure 4.3a and b). It consists of sub-angular to sub-rounded extraformational and isolated pebble clasts within the bodies of sandstones grains (Figure 4.3c and d).

The thickness of each bed varies between 0.5m to 2.0m and commonly passes upward into coarser bed (Figure 4.3d) with lower boundary usually gradational with facies Gh. The bottom contacts are erosional, causing undulatory, concave up bases while the tops of the beds are commonly gradational into facies Sp and Sh according to Adepoju *et al*. (2018a). Se sub-facies has 22% component of total sub-facies present.

Association of Se and Sm sub-facies in some locations (e.g. Rabba, Bida, Wushishi, Baro, Lemu, Dokko) is suggestive of development of low sinuosity channel bars arising from channel switching and lack of point bar sedimentation according to Allen (1982), Selley (1985) and Blair (1987) or suggests an upper flow regime during transportation as stated by Miall (1988). This sub-facies could be deposited by a moderately to high-energy environment from channels of the main fluvial channel system.

Se sub-facies were observed in the exposed outcrops within the central part of the study area including Share, Shonga, Rabba, Bida, Enagi, Wushishi, Baro, Lemu and Dokko.

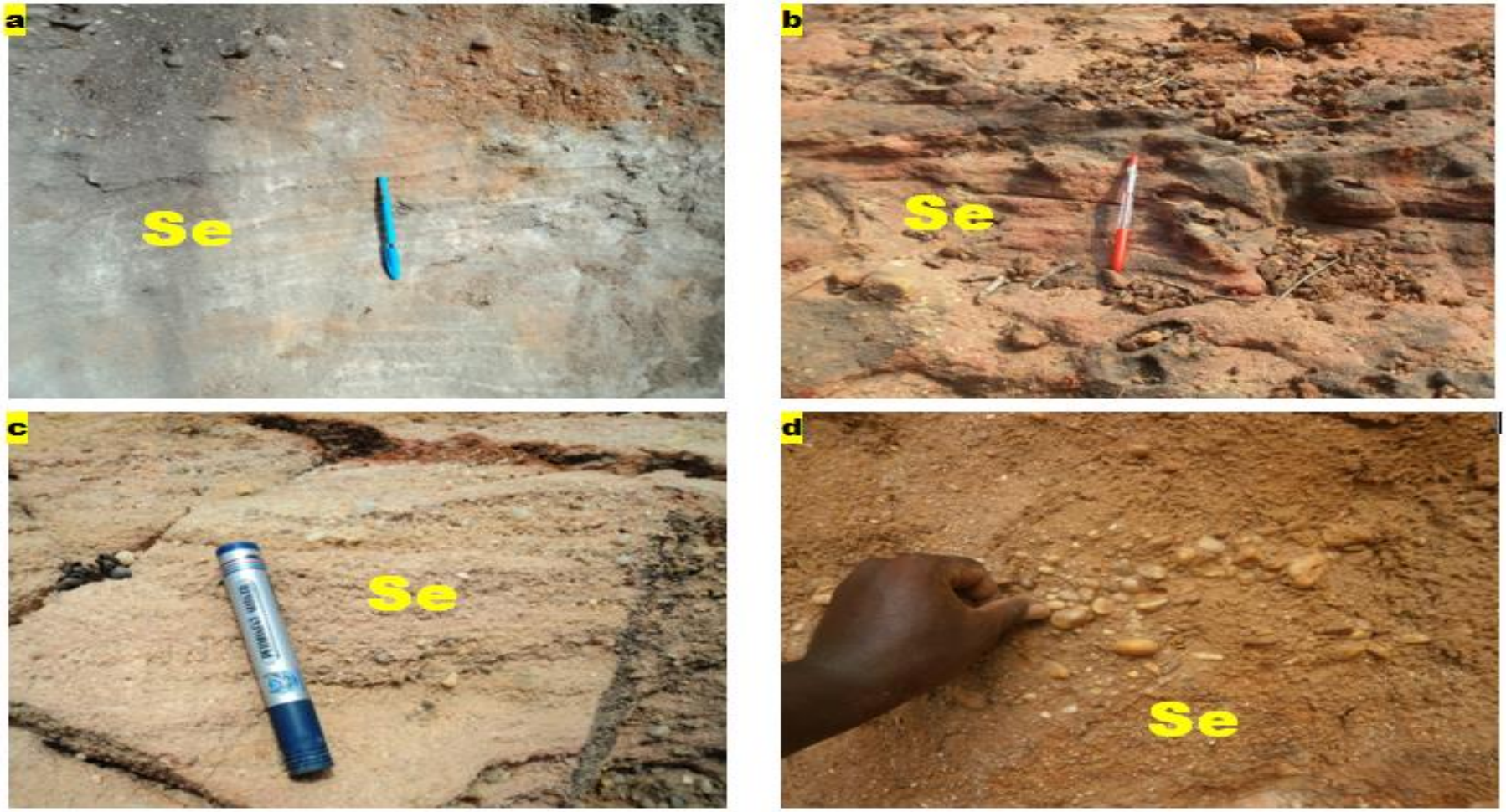


Figure 4.5: Field photograph showing typical crudely stratified sandstone (Se) sub-facies at; (a) middle part of section at Katcha, at the southern part and about 100m from the central motor park (Longitude: 006°18.910'E; Latitude: 08°45.127'N), (b) lower part of section at Wariku, along Lafiagi road (Longitude: 08°47'46.3"N; Latitude: 005°18'41.6"E), (c) middle part of section at Baro, near railway line and (d) lower part of section at Wushishi, near River Kaduna (Longitude: 006°24.956'E; Latitude: 08°37.371'N).

4.1.1.5 Planar cross-stratified sandstone (Sp) sub-facies

The planar cross-stratified sandstone (Sp) sub-facies comprises of very coarse- to fine-grained sandstone which are arranged into lenticular or tabular sets up to 12.0m thick and characterized internally by planar cross-stratification (Figure 4.4a and b). The beds which are usually tabular commonly occur laterally as far as thirty meters (30.0m) and each bed having thickness ranging from 2.0 to 15.0m. The upper and lower boundaries of Sp sub-facies are gradational and the bounding surfaces may be traced for tens of meters. The beds in few occasions appeared well lithified (e.g. Enagi, Mangota, Jimma, Dokko and Kajita). The component of Sp sub-facies is 11.30% of total sub-facies present within the study area.

Sp sub-facies are interpreted as the product of straight crested 2D dunes which are common in shallow sandbed braided rivers. The down-current dipping cross-strata are common with the cosets containing regularly spaced sets of cross-stratification 2-5 cm thick on low angle bounding surfaces (Figure 4.4a and b). The foresets dip often diverges strongly from the dip of bounding surfaces by 30°-60°. The occurrence of this facies commonly in the southeastern, southwestern and central parts is suggested to have formed by deposition from traction in a low-energy, unidirectional current or the deposition in small channel infills according to Miall (1996).

Sp sub-facies were observed in Agbonna ridge at Share, road-side exposures at Gbedeworo and Lafiagi and a ridge at Lemu. The sub-facies is also present at the ridge in Kutigi, Jimma, Dokko, Kajita, Bida, Tanagi and at the river cut exposure in Rabba, near Mokwa.

4.1.1.6 Horizontally stratified sandstone (Sh) sub-facies

The horizontally stratified sandstone (Sh) sub-facies is composed of coarse-, medium- and fine-grained sandstone, with fine laminae arranged into thin beds possessing a parting lineation defined mica (muscovite) intercalations (Figure 4.4d). Individual beds range from 0.2 to 8.0m in thickness with gradational tops and bases. The Sh sub-facies have been observed grading upwards into Sr sub-facies. Sh sub-facies are the second commonest sub-facies within the study area, comprising 22% of total sub-facies present.

The grain size profiles generally fine-upward, are rarely irregular due to apparently random interlamination and stacking of alternating lithologies, thus, record a rapid change in flood regime that recognizes a high energy situation followed by waning of the flow and fallout of finer particles. The horizontal cosets of approximately 2.0m thick within the Sh sub-facies with lenticular or irregularly wedge-shaped beds is well compared with the large 3D dunes (megaripples) and small dunes of shallow sandbed braided rivers suggested by Collinson (1970), Smith (1970, 1971, 1972).

Sh sub-facies could be deposited via high-energy that spilled into a lower energy environment from channels during flooding of the main fluvial channel system according to Miall (1996), Prothero and Schwab (2004). This sub-facies was observed at the lithological sections at Agbonna ridges at Share and Shonga. Other locations where the sub-facies were recorded includes; Wariku, Rabba, Bida, Enagi, Kutigi, Rafingora, Tanagi, Manigi, Maraba, Lemu, Dokko, Jimma and Wodata.

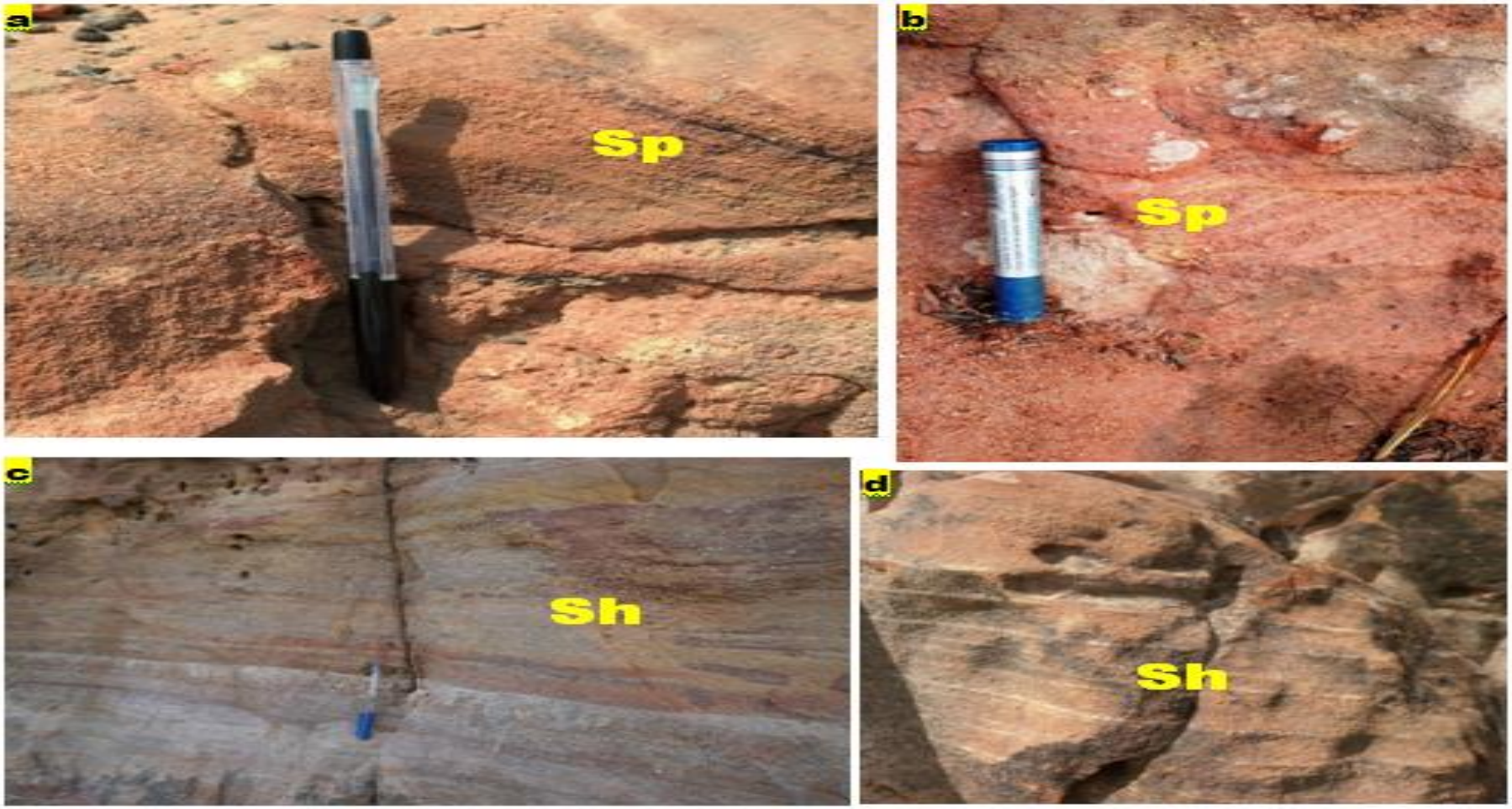


Figure 4.6: Field photograph showing typical planar cross-stratified sandstone (Sp) sub-facies at; (a) middle part of Agbonna ridge, Share (Longitude: 004°58'36.3"E (Latitude: 08°49'32.3"N); (b) an exposure at Rabba, near River Niger (Longitude: 005°01.691'E; Latitude: 09°12.538N). Horizontally stratified sandstone (Sh) sub-facies at; (c) upper part of the exposure near railway at Baro (Longitude: 006°24.956'E; Latitude: 08°37.371'N), (d) middle part of Dokko ridge, behind police station, Dokko (Longitude: 005°37.545'E; Latitude: 08°56.744'N).

4.1.1.7 Rippled cross-stratified sandstone (Sr) sub-facies

The rippled stratified sandstone (Sr) sub-facies comprise few centimeters to meters thick rippled cosets and bedsets of sandstone and commonly observed at the middle and upper parts of the studied outcrops (Figure 4.5a). The thickness of single beds of this sub-facies varies between 0.2m to 2.50m and may or may not show an erosive lower surface, but the upper contact is often irregular (Figure 4.5a). Sr sub-facies constitute relatively minor component comprising about 1.3% of the total sub-facies present.

The ripples represent lower flow regime unidirectional traction currents which can also be formed as a result of rapid deposition of grains from suspension in fluvial environments. The Sr sub-facies may also be deposited from presence of a subtle primary-current lineation and under lower flow velocities according to Prothero and Schwab (2004).

The lithological sections that show typical characteristics of the Sr sub-facies were observed in the lower part of Agbonna ridge at Share, the middle part of Shonga ridge, the middle part of road side exposure in Wariku along Lafiagi and at the river side exposure in Rabba near Mokwa.

4.1.1.8 Massive sandstone (Sm) sub-facies

The massive sandstone (Sm) sub-facies comprise beds of non-organize sandstone, usually of centimeters to meters thick (Figure 4.5b and c). The thickness of single beds varies between 2.0 and 5.0m and may contain sub-rounded to rounded, floating pebbles. Sm sub-facies make a total 4% component of the total sub-facies present. This grain size result is a characteristic of low to medium energy of deposition in a fluvial environment.

The Sm sub-facies is suggested to have formed by very rapid sedimentation, probably by high discharge events such as sheet-floods or as as a result of rapid deposition of grains from saltation in fluvial environments as suggested by Miall (1996).

Sm sub-facies are well exposed in the most of the outcrops found in the south-eastern, south-western and central parts of the study area. For example, at the upper part of the Share ridge, the middle and upper part of Shonga, Jimma, Dokko, PattiChin, Kajita, Enagi and Lemu ridges. The sub-facies were also observe at the middle and upper parts of the road cut exposures in Lafiagi and Wariku, and at the middle and upper parts of the river side exposure at Rabba near Mokwa.



Figure 4.7: Field photograph showing typical example of a rippled cross-stratified sandstone (Sr) sub-facies at; (a) Rabba, near Mokwa (Longitude: 005°01.691'E; Latitude: 09°12.538N) (b) Dokko ridge, near Police Station (Longitude: 005°37.545'E; Latitude: 08°56.744'N). Massive sandstone (Sm) sub-facies at; (c) Tanagi ridge, along Mokwa-Kaduna road (Longitude: 005°43.798' E; Latitude: 09°55.342' N) and (d) Patti-Chin along Baro (Longitude: 09°04.449'N; Latitude: 006°14.018'E).

4.1.1.9 Finely laminated mudstone (Fl) sub-facies

The finely laminated mudstone (Fl) sub-facies are composed mostly of laminated siltstone and claystone beds with erosional or sharp laminae boundaries (Figure 4.6c). The lower and upper boundaries are generally sharp and planar with each bed unit ranges in thickness from 2.0 to 4.0 m (Figure 4.6a). The sub-facies are composed mostly of whitish to light brown, occasionally interlaminated siltstone, clayey-siltstone and very fine-grained sandstone with thickness of each units varies from 0.5 to more than 1.0 meter (Figure 4.6c and d). Typically this sub-facies is sharply topped by Sm or Sh, sub-facies. Fl also has relatively higher component, comprising 11.40% of total sub-facies present.

Fl sub-facies contains little evidence of bedload deposition and is interpreted as deposition from suspension settling of fine to very fine-grained sandstone, silt- and clay-sized particles, which may have been flocculated and formed in overbank and floodplain environments. The alternating siltstone-claystone in some parts of the area may indicate widespread deposition from suspension across low relief, abandoned flood plains.

Finely laminated mudstone sub-facies are well exposed in the exposed outcrops within northern and central (as intebeddings) parts of the study area. The location where the typical characteristics were observed includes; the middle and upper parts of the Agbonna ridge at Share and other ridges at Kutigi, Enagi, Rabba, Tanagi, Rafingora and Manigi.

4.1.1.10 Massive very fine sandstone and mudstone (Fm) sub-facies

The massive mudstone (Fm) sub-facies mainly composed of massive siltstone, claystone and minor very fine grained sandstone. It is composed of varying colorations; whitish to brownish (Figures 4.6a and b). The lower boundary is commonly irregular due to the underlying

topography while the upper boundary usually flat and always lacks any observable sedimentary structure. Each bed unit ranges in thickness from 0.2m to 10.0m with the profiles ranges from 10 to 50.0m and like Fl sub-facies. It is typically overlain by Fl and underlain by Sm, Se and Sh sub-facies. Its component is about 5% of the total sub-facies present.

Fm sub-facies is generally massive and homogeneous which suggested to be formed because of rapid deposition from suspension in overbank settings or to lack of platy grains. Like Fl sub-facies, Fm also shows evidence of deposition from suspension settling of fine-grained sandstone, silt- and clay- sized particles, which may have been formed in overbank and floodplain environments. The alternating siltstone and claystone, indicates widespread deposition from suspension over the upper parts of sandy bedforms or across low relief, abandoned flood plains.

Fl sub-facies usually exposed in association with Fm sub-facies and commonly found in the most of the outcrops in the northern and central parts of the northern Bida Basin. They were studied at the middle and upper parts of the ridges in Share, Gbugbu, Kutigi, Enagi, Rabba, Tanagi, Rafingora and Manigi.

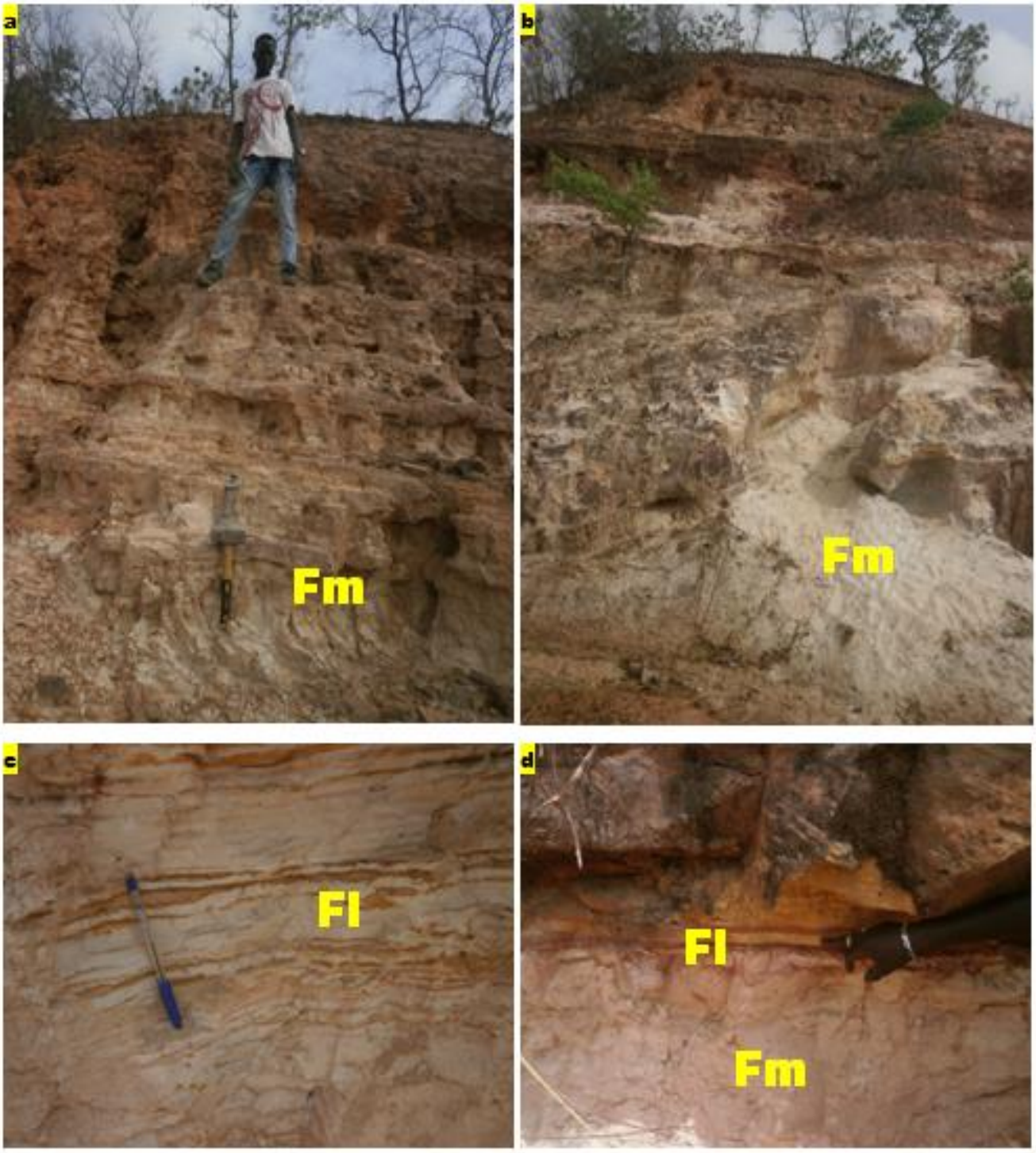


Figure 4.8: Field photograph showing typical example of a massive mudstone (Fm) sub-facies at (a) Kutigi (Longitude: 005°35.43' E; Latitude: 09°12.03' N) and (b) Rafingora (Longitude: 005°43.799' E; Latitude: 09°55.344' N); and typical example of finely laminated mudstone (Fl) sub-facies at (c) Tanagi (Longitude: 005°43.798' E; Latitude: 09°55.342' N) and (d) Manigi (Longitude: 005°32.277' E; Latitude: 09°46.599' N).

4.1.2 Outcrop Facies Association Analysis and Characteristics

Facies associations are assemblages of spatially and genetically related facies, distinguished as the principal "building blocks" of the sedimentary succession (Collinson, 1996). According to Miall (1977) and Collinson (1999), the grouping and interrelationship characteristic of adjacent facies is very important in depositional environment and succession interpretations because of ambiguity nature of facies.

The outcrop facies association (OFA) description and analysis are based on the combinations of facies (litho- and sub-facies) based on genetic variations and interrelationship and it will aid the understanding of depositional environments and processes that formed it. The interpreted outcrop facies associations (OFA) were grouped into five (5) categories and are further described in detail below. The description will be employed in providing a general facies scale across the study area for the recognition of deposition environments.

4.1.2.1 Outcrop Facies Association 1 (OFA1)

The outcrop facies association 1 (OFA1) comprises of major conglomerates sub-facies (Gcm, Gmm and Gh). Occasionally, subordinate sandstone (Se) sub-facies occur laterally as confined, lenticular bodies in an assocciation with OFA1. The typical lithological sections with OFA1 composed angular clast sized constituents which suggest a channel lags deposits. The basal contact is usually erosional and commonly displays a poorly sorted, conglomeratic base. The basal surfaces of this facies association were observed to have eroded down many meters into the underlying sediment. The individual bodies can form larger deposits with highly variable morphology ranging from small (~5 meters thick, ~10 meters wide) to a large (10 meters thick, ~20 meters wide) channelized body.

OFA1 is interpreted as fluvial deposit. The preserved conglomeratic bed suggests a migration of longitudinal and transverse bars during maximum discharge in the rivers according to Miall (1996). The discontinuous nature of OFA1 from southern to northern part of the northern Bida Basin is related to the key characteristic of lag deposits within ancient channels as submitted by Miall (1985), where the coarsest bedload components of a channel commonly collect. Therefore, the OFA1 is interpreted to represent channelized fluvial flow of gravel-dominated braided rivers (in proximal settings).

The OFA1 is predominant in the stratigraphic sections at the southeastern and southwestern part of the northern Bida Basin. Typical lithological sections where this facies association are well observed includes; an exposure at the northern part, behind Baganko village, near Abiola farm (after Lafiagi), the exposure at the western part proposed Harman Patigi University, Patigi, located at about 5.0km south of the River Niger (Figure 4.7). Also, minor OFA1 were aboserved at Gbugbu, Gbale, Gbedeworo, all along Share-Gbugbu road.

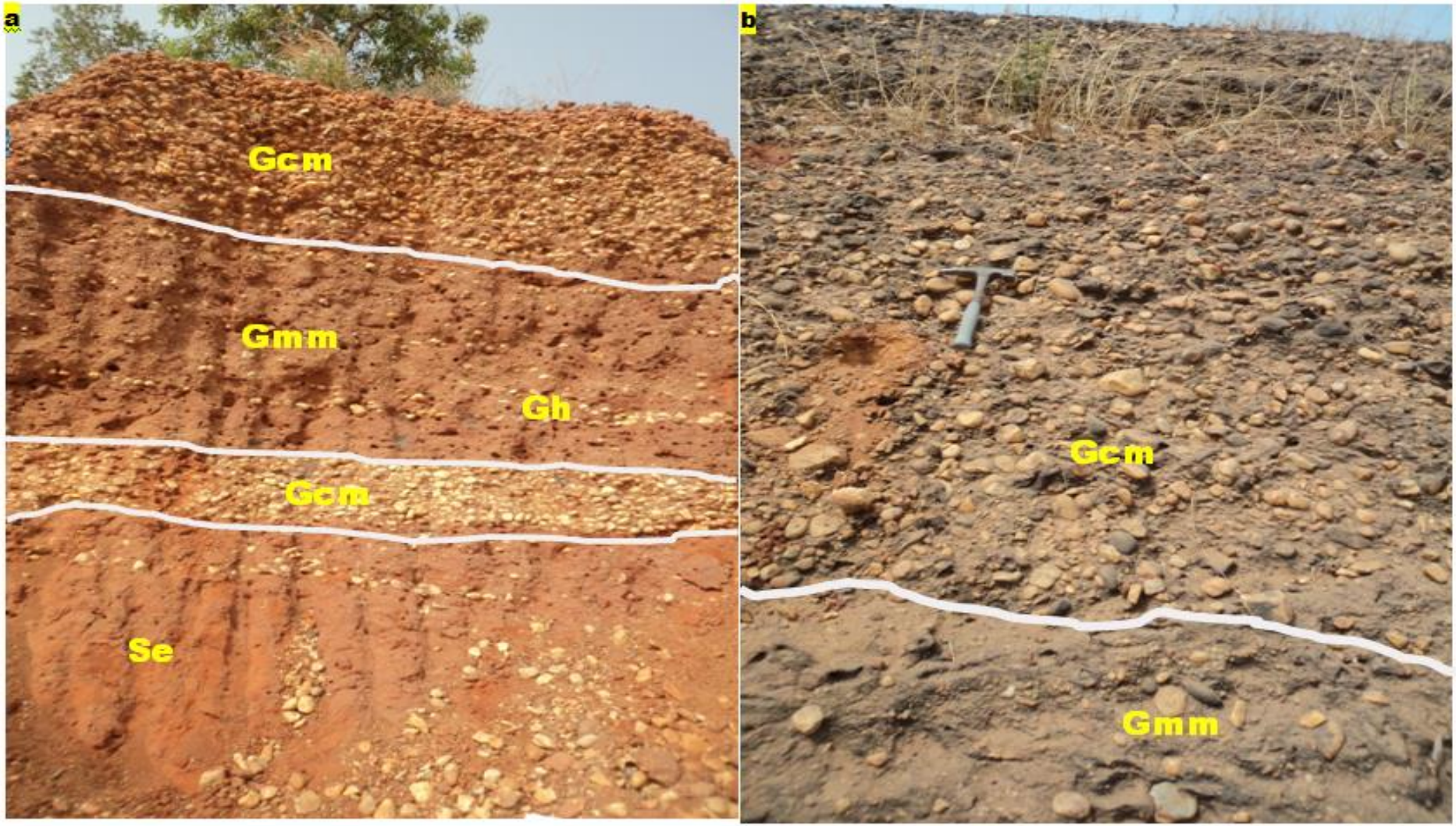


Figure 4.9: Field photograph showing typical example of outcrop facies association 1 (OFA1) that are preserved fluvial Channel lags (Longitude: 08°42'53.5"N, Latitude: 005°46'55.7"E; Longitude: 08°54'29.4"N, Latitude: 005°19'24.6"E).

4.1.2.2 Outcrop Facies Association (OFA2)

The outcrop facies association 2 (OFA2) composed of a major tabular sandstone beds that occur laterally as a confined bodies exceeding 2.0–15.0 m in thickness with minor coarse sub-facies (Figure 4.8). The composed sandbodies; crudely stratified sandstone sub-facies (Se), massive sandstone sub-facies (Sm) and minor planar cross-bedded sandstone sub-facies (Sp) and minor horizontally stratified sandstone sub-facies (Sh). They are interpreted in this study as thick and a braided fluvial channel. The morphology of the channel varies from ~20 to 50 meters thick with 100 meters wide bodies of tabular sandstone. The fining upward sequences dominate the OFA2 and it commonly overlies OFA1 as this is clearly represented at Shonga, Patti-Wodata and Rabba (Figure 4.8a and b). Minor to moderate bioturbation is typically observed near the top of major tabular sandstones (Figure 4.8b).

The general facies distribution, fining-upward character and large-scale bodies observed within the OFA2 are well compared with the braided fluvial channels as suggested by Miall (1996). OFA2 may also be interpreted to represent channelized fluvial flow changing from gravel-dominated braided rivers (in proximal settings) to sandy braided river further away. The presence of fining upwards sequences with mud rip-up clasts at the base of the channels is consistent with fluvial sedimentation (Miall, 1996; Blum and Aslan, 2006).

The typical OFA2 are well predominant in the stratigraphic sections in parts of southwestern and central part of the northern Bida Basin. Amongst the locations where the OFA2 are well preserved includes Shonga, Lafiagi, Lade, Patti Wodata, Kajita, Rabba, Bida, Dokko, Jimma, Patti-Chin, Wushishi and Lemu.

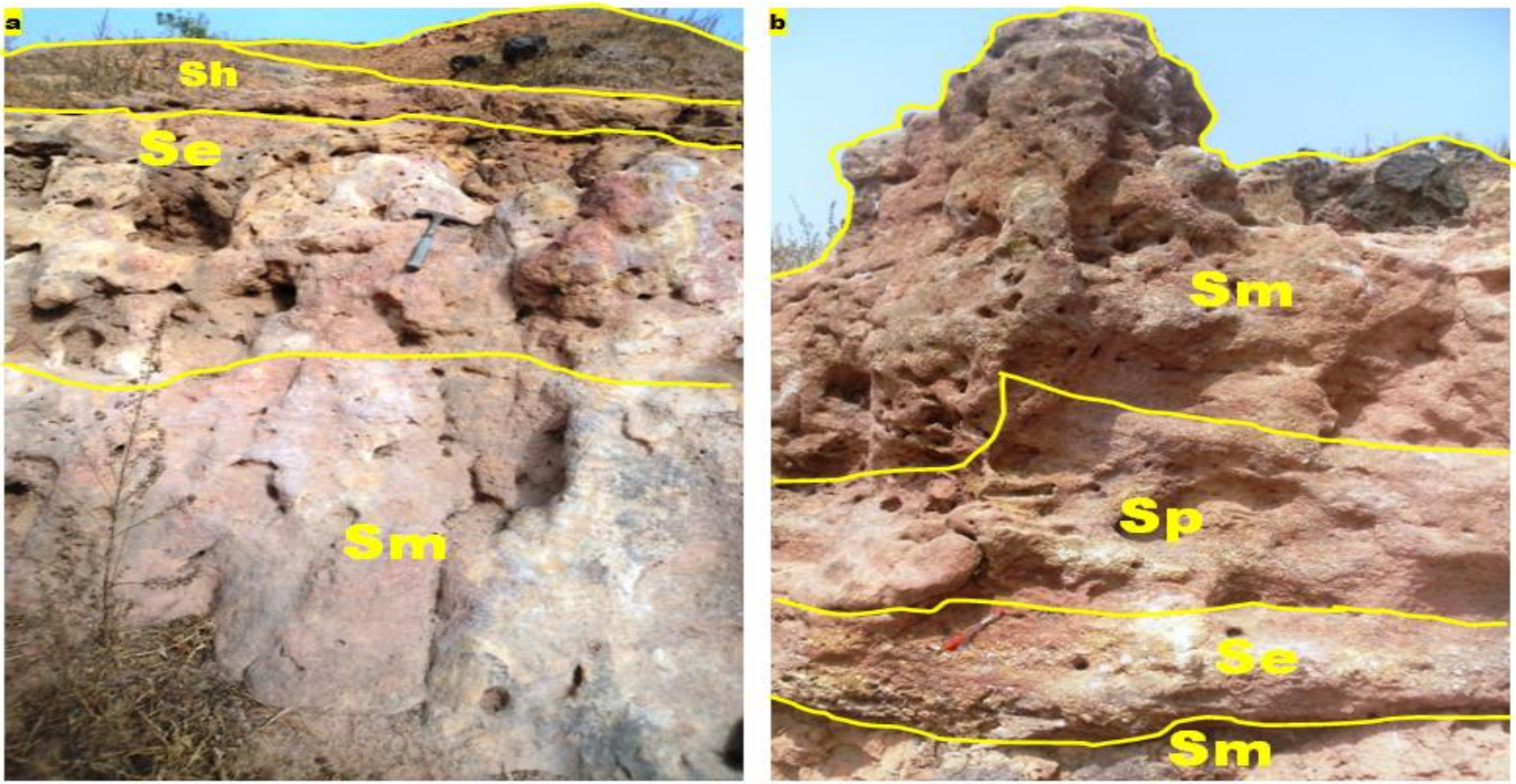


Figure 4.10: Field photograph showing typical example of outcrop facies association 2 (OFA2) that are preserved as braided fluvial channel at Shonga, Lafiagi, Lade, Patti-Wodata, Kajita, Rabba, Bida, Dokko, Jimma, Patti-Chin, Wushishi and Lemu (Longitude: 005°08'50.1"E, Latitude: 09°01'27.4"N; Longitude: 005°56.090'E, Latitude: 08°58.994'N; Longitude: 005°37.545'E, Latitude: 08°56.744'N; Longitude: 08°42'45.2"N; Latitude:006°02'51.9"E).

4.1.2.3 Outcrop Facies Association 3 (OFA-3)

The outcrop facies association 3 (OFA3) composed basically of horizontally stratified sandstone sub-facies (Sh), planar cross-bedded sandstone sub-facies (Sp), crudely stratified sandstone sub-facies (Se), massive sandstone sub-facies (Sm) with minor crudely bedded conglomerate (Gh) sub-facies. The interrelationships of the sub-facies that make this association usually form a lenticular sandbodies dominantly of meandering channels (Figure 4.9). The morphology of the channelized sandstone bodies is highly variable; 10 to 20 meters thick, ~10 meters wide.

The nature of the channels, common sedimentary structures (planar, horizontal and lamination) and the fining upwards sequences of the OFA3 are consistent with fluvial sedimentation especially in a meandering settings according to Miall (1996) and Blum and Aslan (2006). Also, the major lenticular sandstones bodies may be interpreted as suspended load fluvial channel deposits with stable banks within the ancient meandering rivers Miall (1996).

Lithological exposures of OFA3 are well represented in the central part of the northern Bida Basin, particularly at Shonga, Lafiagi, Lade, Patti Wodata, Kajita and Bida.

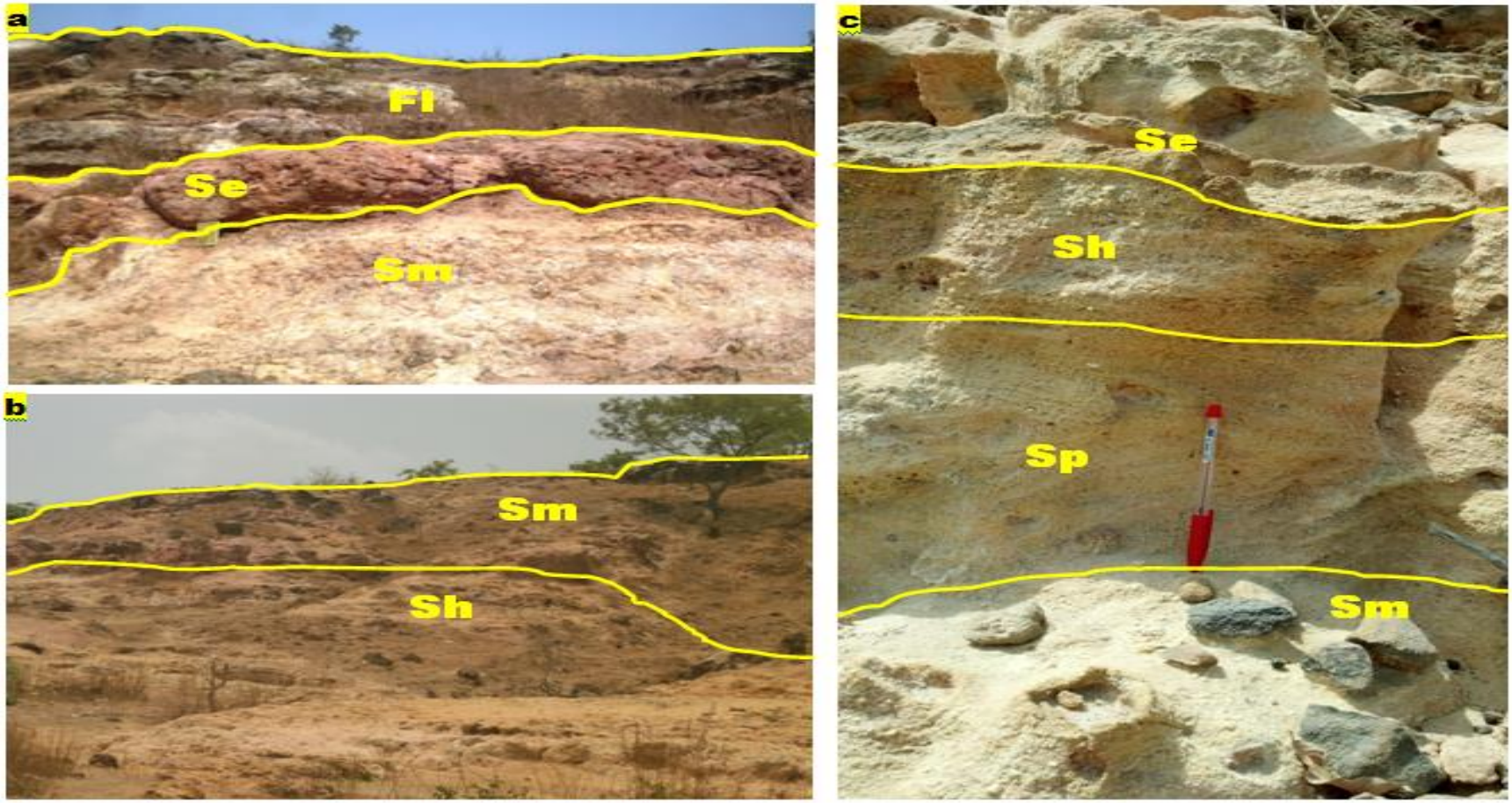


Figure 4.11: Field photograph showing typical example of outcrop facies association 3 (OFA3) that are well preserved as a meandering channels sandstones and are well preserved at Shonga, Lafiagi, Lade, Patti Wodata, Kajita and Bida (Longitude: 09°04.449'N, Latitude: 006°14.018'E; Longitude: 08°50'44.0"N, Latitude: 005°25'03.0"E; Longitude: 08°45'47.3"N, Latitude: 005°35'37.9"E; Longitude: 08°42'45.2"N, Latitude: 006°02'51.9"E; Longitude: 005°59.98' E, Latitude: 09°05.98' N).

4.1.2.4 Outcrop Facies Association 4 (OFA4)

The outcrop facies association 4 (OFA4) is a minor body that shows the interrelationships of planar cross-bedded sandstone sub-facies (Sp), rippled laminated sandstone sub-facies (Sr), finely laminated mudstone (Fl) sub-facies with minor crudely stratified sandstone sub-facies (Se) which occurs as a sheet-like sandstone bodies or as thin restricted channels (Figure 4.10). The morphology of these sandstone bodies ranges between 5 to 20 meters thick, ~30 meters wide.

Presence of reactivation surface, foreset of overtuned cross stratified, bi-directional wavy structure and burrowing of *Thallasanoides* (Figure 4.10a and b), biotubation and clay drapes in this facies association suggest a tidal influence. The deposit is interpreted to be formed from upper regime laminar flow with an unconfined sheet-flow. The observed planar-cross bedded within the sandbody may be interpreted as dune migration within small crevasse channels where sedimentation rates is at its peak and therefore crevasse splay and overbank deposits are rapidly deposited according to Bown and Kraus (1987), Davies-Vollum and Kraus (2001), Blum and Aslan (2006).

The typical lithostratigraphic sections that comprise OFA4 are dominated in the central part of the northern Bida Basin. Amongst the localities where this facies association were observed includes Manigi, Rabba, Enagi, Kutigi, Lafiagi and Wushishi.

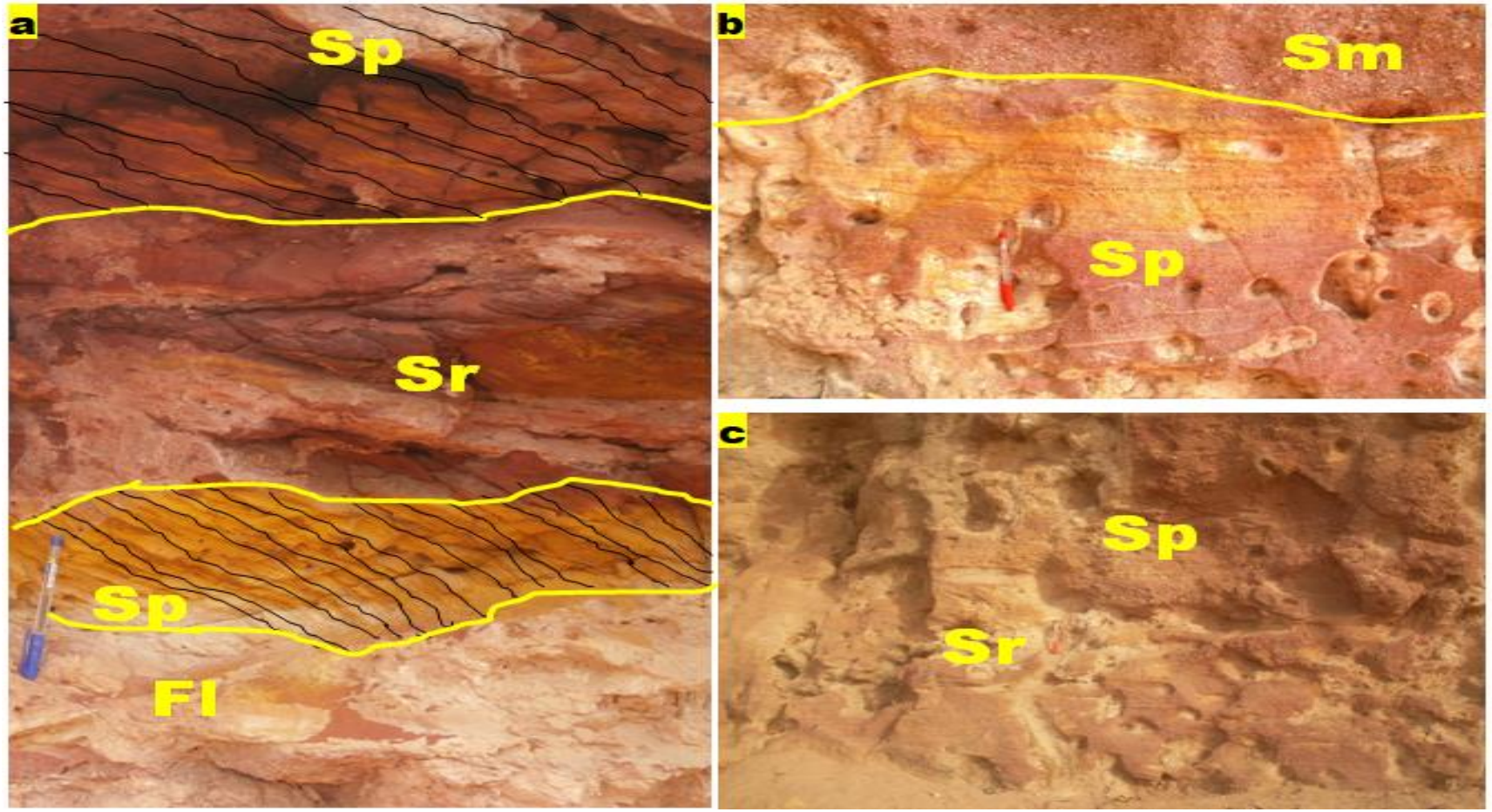


Figure 4.12: Field photograph showing typical example of outcrop facies association 4 (OFA4) that are well preserved as tidally influenced fluvial channel sandstone and are well preserved at Manigi, Rabba, Enagi, Kutigi, Lafiagi and Wushishi (Longitude: 005°32.277' E; Latitude: 09°46.599' N; Longitude: 005°35.43' E, Latitude: 09°12.03' N; Longitude: 08°50'44.0"N; Latitude: 005°25'03.0"E; Longitude: 006°03.846'E, Latitude: 09°43.621'N).

4.1.2.5 Outcrop Facies Association 5 (OFA5)

The outcrop facies association 5 (OFA5) composed basically the fine sub-facies; finely laminated mudstone (Fl) sub-facies and massive mudstone sub-facies (Fm) with minor horizontally stratified sandstone sub-facies (Sh). This facies association was shown as a preserved succession, especially in the northern part of the study area. In few locations like Enagi, Kutigi, Tanagi and Rafingora, OFA4 were observed occurred within OFA5 (Figure 4.11). The thickness of individual OFA5 bands can be tens of meters thick and 200m wide with erosional contact usually below or on top.

The OFA5 is interpreted to represent an overbank deposits with evidence of an extensive sheet like splays which may occur during large flood occurrences distributing water and sediment across the splay (Smith *et al*., 1989; Kraus and Aslan, 1993; Rhee and Chough, 1993), and whitish to brownish variegated band characteristics.

Lithological exposures of OFA5 which are typical of crevasse splay/floodplain overbank fines are commonly found at Enagi, Kutigi, Rafingora, Manigi, Tanagi and Maraba.

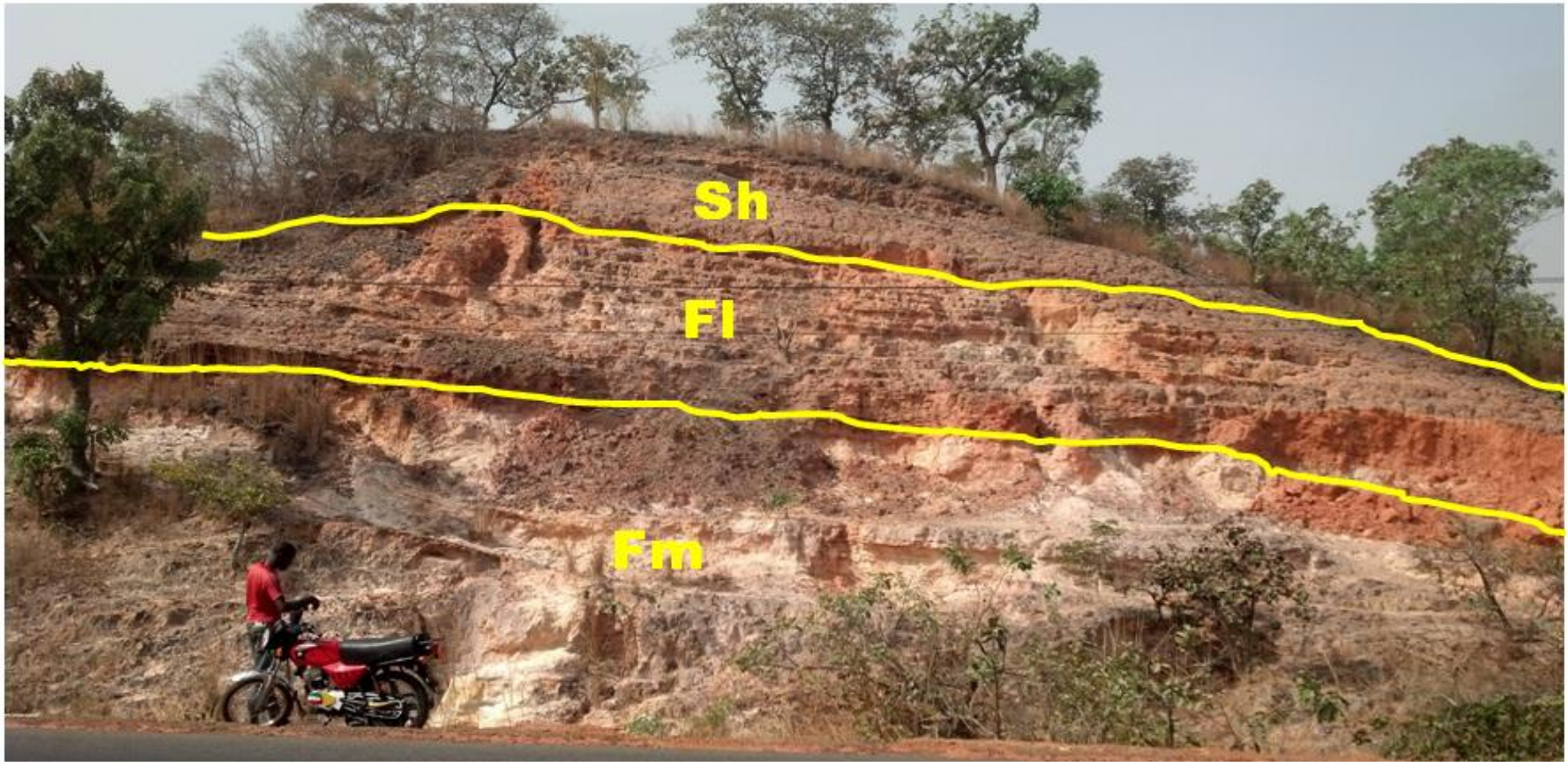


Figure 4.13: Field photograph showing typical example of outcrop facies association 5 (OFA5) that that are well preserved as a fluvial overbank/floodplain at Manigi, Tanagi, Rafingora, Enagi and Kutigi (Longitude: 005°32.277' E, Latitude: 09°46.599' N; Longitude: 005°43.798' E, Latitude: 09°55.342' N; Longitude: 005°43.799' E, Latitude: 09°55.344' N; Longitude: 005°32.68' E, Latitude: 09°07.88' N; Longitude: 005°35.43' E; Latitude: 09°12.03' N).

4.1.3 Architectural Elements and Sand Body Geometry

Architectural-element analysis is a descriptive method based on rock-body geometry, dimensions and nature of contacts in addition to the criteria used to define facies associations. The analysis is based on the uses of elements proposed by Miall (1985) as constants in the fluvial environment and defined by bedform composition, internal sequence and external geometry.

Discussions here centers on the architectural elements and body geometry of the sandstone body observed using the bedform composition, internal sequence and external geometry of grouped facies association. Following, general classification scheme of Miall (1978a, 1978b, 1988), the following six (6) architectural elements which are further discussed in detail were identified within the study area; gravel bar and bedforms (GB), sandy bedforms (SB), laminated sand sheet (LS), lateral accretion (LA), overbank or floodplain (OF) and channel (CH).

4.1.3.1 Gravel bars and bedforms (GB)

The Gravel bars and bed forms (GB) element is essentially made-up of vertically stacked layers of alluvial channels (intraformational conglomerates) and the braided fluvial channels (Tabular sandstone) elements. This architectural element occurs as isolated forms (Figure 4.12a and b). Element GB record either migrating channel bedloads comprising of coarse-grained or braided fluvial channels sediments basically of OFA1 and OFA2 that are interpreted to have been brought by higher river flow.

Where GB occurs, it usually has sharp erosional bases and often erodes sand bedforms and channels which indicate a sudden increase in the velocity of the depositional current. The thicknesses of the gravel bars and bedforms are up to 10.0 m with a flat based and top gravel bar and the geometry formed is a lobate type (Figure 4.16c).

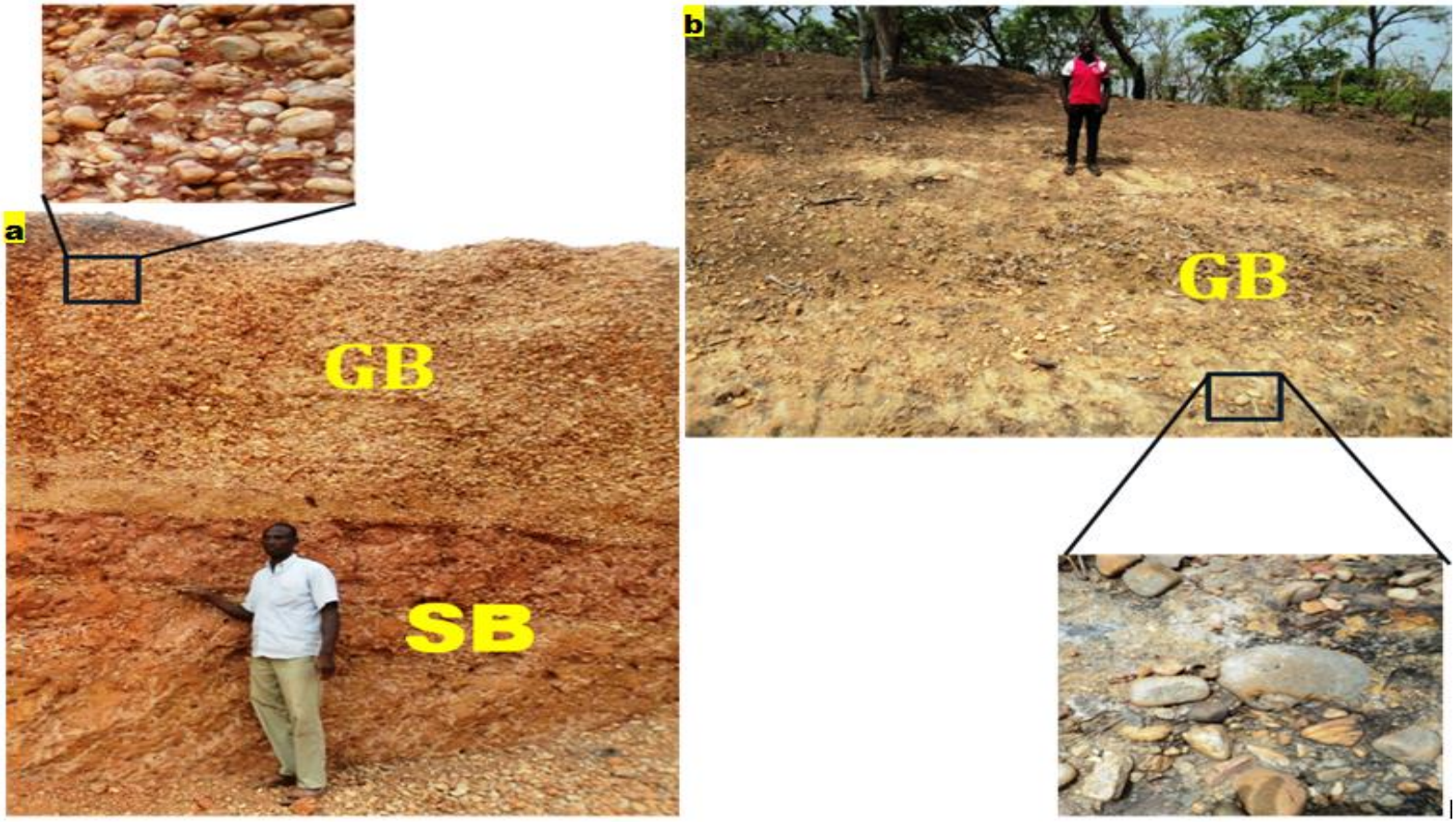


Figure 4.14: An outcrop showing a typical characteristic of a Gravel Bars and Bedform & Sandy Bedform Elements at (a) Baganko (Longitude: 08°54'29.4"N, Latitude: 005°19'24.6"E) and (b) Ndeji (Longitude: 08°54'29.4"N, Latitude: 005°19'24.6"E).

4.1.3.2 Sandy Bedforms (SB) Elements

Sandy Bedforms (SB) is a tabular and sheet-like body of sand bed deposits comprising basically of OFA2, OFA3 and OFA4. Thickness may range from 10.0 to 20.0 m thick and about 50.0 m wide. The SB architectural element characterizes a point bar and tidal channels deposit as it shows a fining-up section vertical relationship. The point bar and tidally influenced sediments in SB are suggested to be developed by the erosion of the bank and later accompanied by deposition on the opposite side of the channel where the flow is sluggish and the bedload can no longer be carried. It is also characterized by the bedload which is carried by the flow in the channel, with the coarsest material carried in the deepest parts of the channel.

A typical SB element observed at the lithostratigraphic section in Rabba (Figure 4.13a) show smaller sets of cross-stratification, bi-directional and oscillating waves structures, clay drapes, reactivation surfaces and *Thallasanoides* burrows which support occasional tidal marine influences (Figure 4.13b). They appear as sheet-like and occasionally ribbon type geometry and were dominated in the central and northern parts of the study area (Figure 4.16a and d).

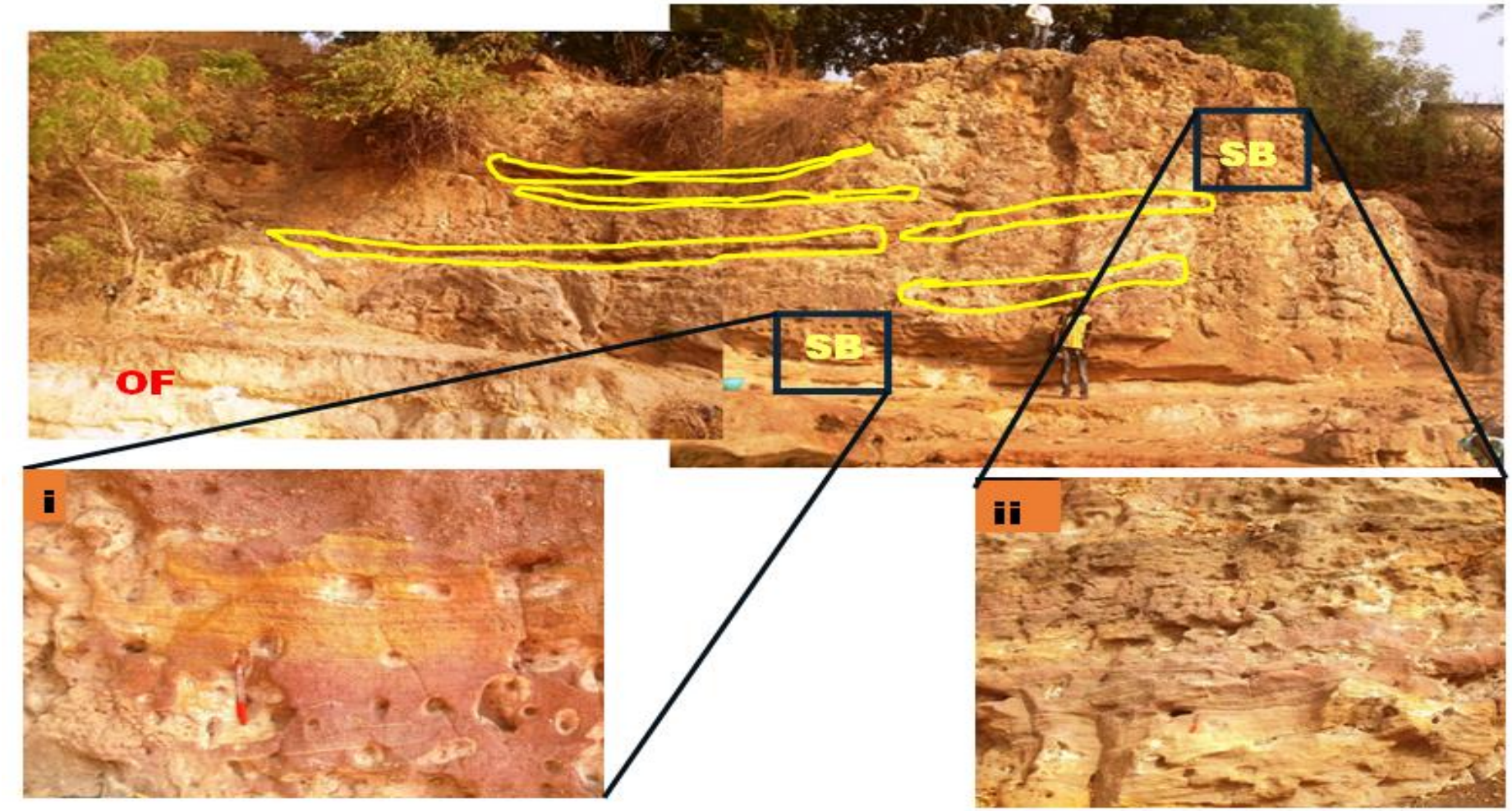


Figure 4.13a: An outcrop showing a typical example of Sandy Bedform (SB) and minor Overbank Fines (OF) Architectural Elements well preserved at Rabba (Longitude: 005°01.691'E; Latitude: 09°12.538N).

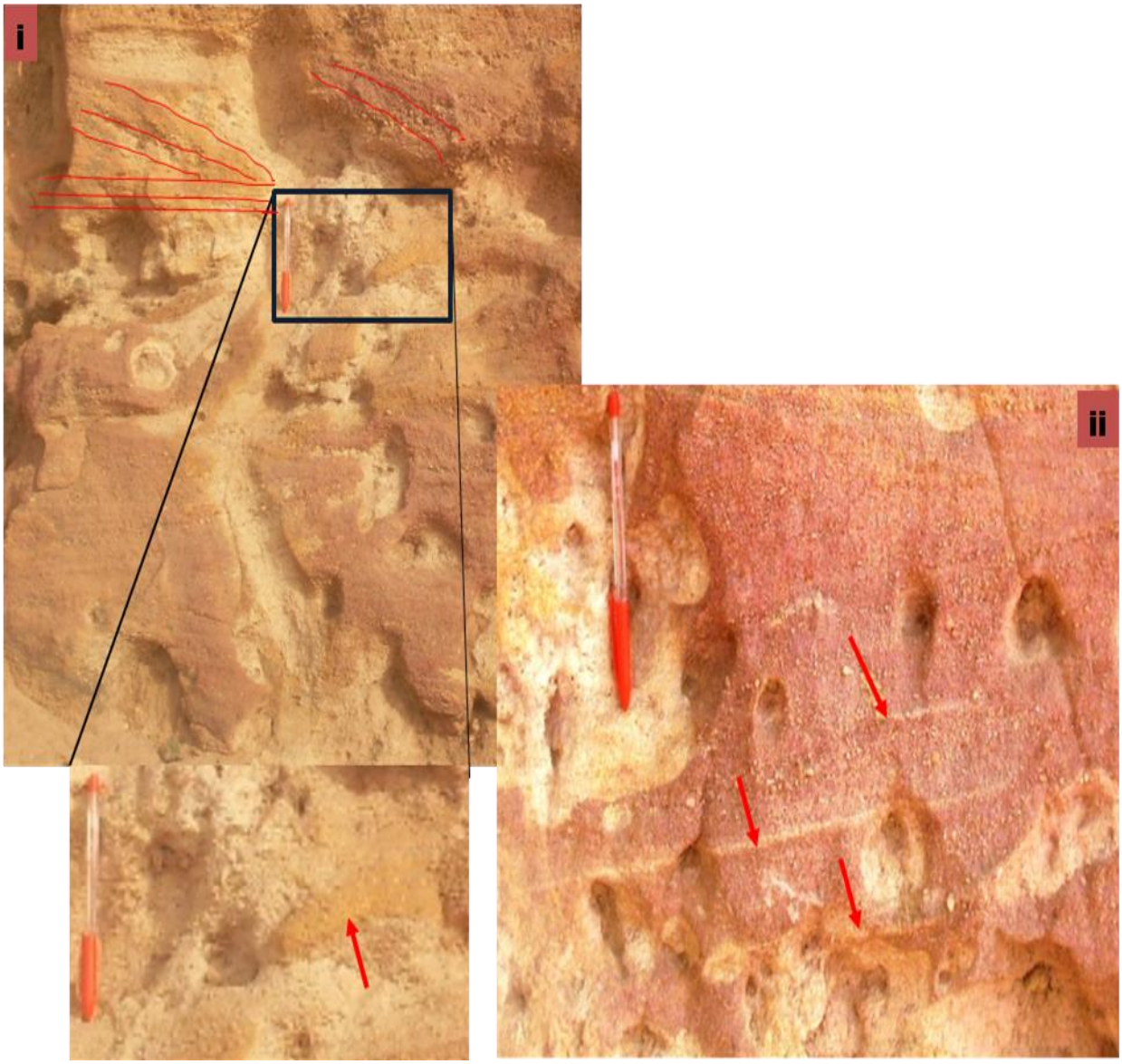


Figure 4.13b: An outcrop showing a typical; (i) bi-directional wavy structure and burrowing of *Thallasanoides* (arrow in enlarged) and (ii) biotubation and clay drapes on medium-grained sandstone preserved at Rabba (Longitude: 005°01.691'E; Latitude: 09°12.538N).

.

4.1.3.3 Lateral Accretion Element (LA)

The Lateral Accretion Element (LA) is characterized by 1.0 to 2.0 m thick and 10.0 m wide units of tabular and lenticular bodies and minor tidal channel sandstones which are dominated by packages of OFA2, OFA3 and OFA5 (Figure 4.14a). This succession is interpreted as the preserved of proximal overbank environments where sediment was supplied via overbank sheet flow and perhaps crevassing during floods according to Fielding and Webb (1996).

The LA element consists of different smaller-scale elements that characterizes a well exposed lithostratigraphic sections at Manigi, Tanagi and Rafingora and Bida that represent components of braided fluvial, meandering channels and minor fluvial overbank in which most of these sediments were suggested to have carried onto the floodplain by suspended load that was mainly clay- and silt sized debris but may include fine sand if the flow is rapid enough to carry sand in suspension.

The geometry of LA formed a wedge and ribbon type (Figure 4.16a and b) which typically contains a fining-upward trend and is commonly found in the central and northern parts of the study area.

4.1.3.4 Laminated Sand Sheet Element (LS)

The laminated sand sheet element (LS) occurred and usually comprises of association of major lenticular sandstone and fluvial overbank/floodplain with basically OFA4 and OFA5 (Figure 4.14a and b). This element with composition of laterally continuous sediments for up to 15.0 m thick occurred mainly as a sheet shaped geometry and fine-grained lithology suggests a bar-top to bar-flank sand sheet deposit. A typical example of LS dominates the lithostratigraphic sections in the northern part of the northern Bida Basin.

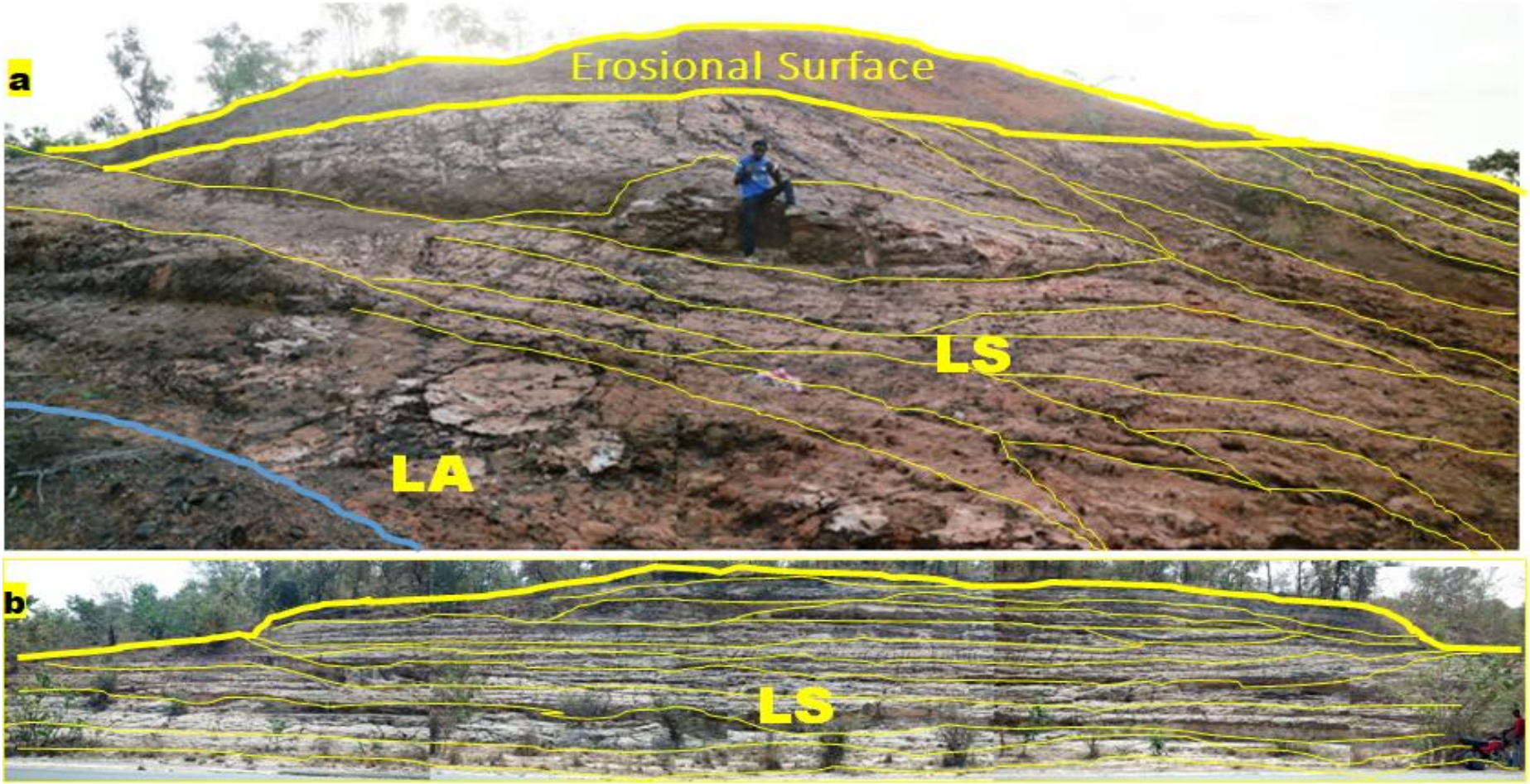


Figure 4.15: Panoramic View of an outcrop showing a typical example of; (a) Lateral Accretion Element (LA) preserved at Bida (ii) Laminated Sand Sheet Element (LS) preserved at Manigi, Tanagi and Rafingora (Longitude: 005°43.798' E, Latitude: 09°55.342' N; Longitude: 005°43.799' E, Latitude: 09°55.344' N; Longitude: 005°32.277' E; Latitude: 09°46.599' N).

4.1.3.5 Overbank or Floodplain Element (OF)

The overbank or floodplain architectural (OF) element composed predominantly vertical aggradations of outcrop facies association 5 (OFA5) showing thin lenses or laminae of finer sub-facies (Figure 4.15a and c). OF element can have lateral continuous composition of up to 30.0 m thick and usually occurred mainly as normal graded, well preserved beds with evidence of less energy but high sinuosity.

Generally, this element is characterized by interbeds and intercalations of finer sub-facies having basically a sheet-like shape, and in other few places as ribbon and wedge geometry (Figure 4.16a and b). OF elements were commonly observed in the northern part of the study area especially in Tanagi, Rafingora and Manigi.

4.1.3.6 Channels Elements (CH)

The channel elements (CH) are composed of major tabular sandstone bodies which are dominated in braided fluvial channels with minor intraformational conglomerates formed within the channel lags. The deposits of CH architectural element are usually characterized by mass flow and bedload that occur mainly at high flow stages when the bars are submerged in water. The CH elements often erode sand bedforms, frequently associated with other elements (Figure 4.14a, b and c) where the total sediments fill may show several episodes of erosion and refilling. Major CH elements often occur in the southeastern and southwestern parts of northern Bida Basin while minor CH body was observed in the northern parts of the study area (Figure 4.14b). The geometry form of CH is a Lobate and Sheet types and these were observed in the southeastern and northern parts of the study area (Figure 4.16c and d).

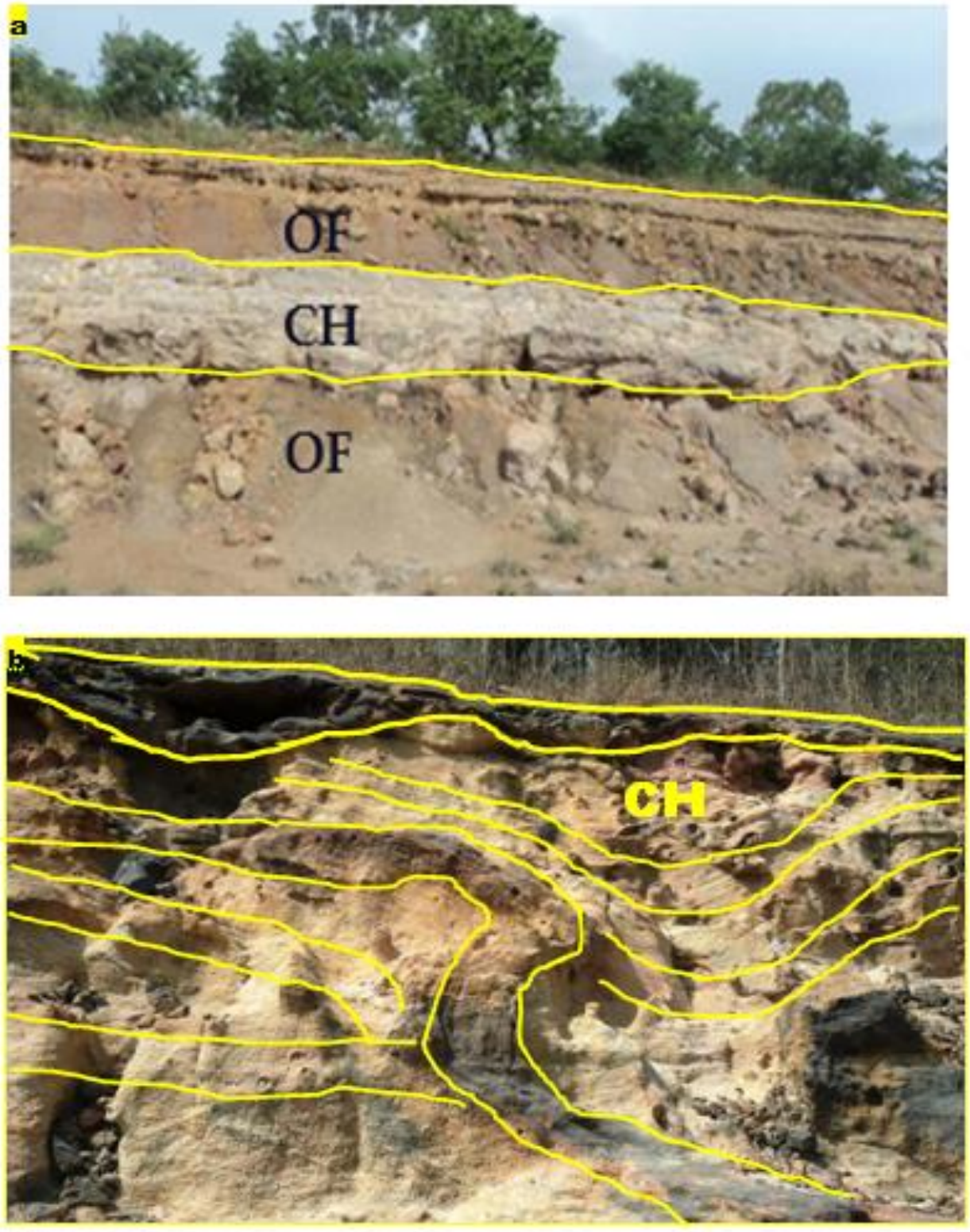


Figure 4.16: An outcrop showing a typical example of; (a) a major and (b) minor CH architectural elements preserved at Maraba and Tanagi respectively (Longitude: 005°43.798' E, Latitude: 09°55.342' N; Longitude: 005°08'50.1"E; Latitude: 09°01'27.4"N).

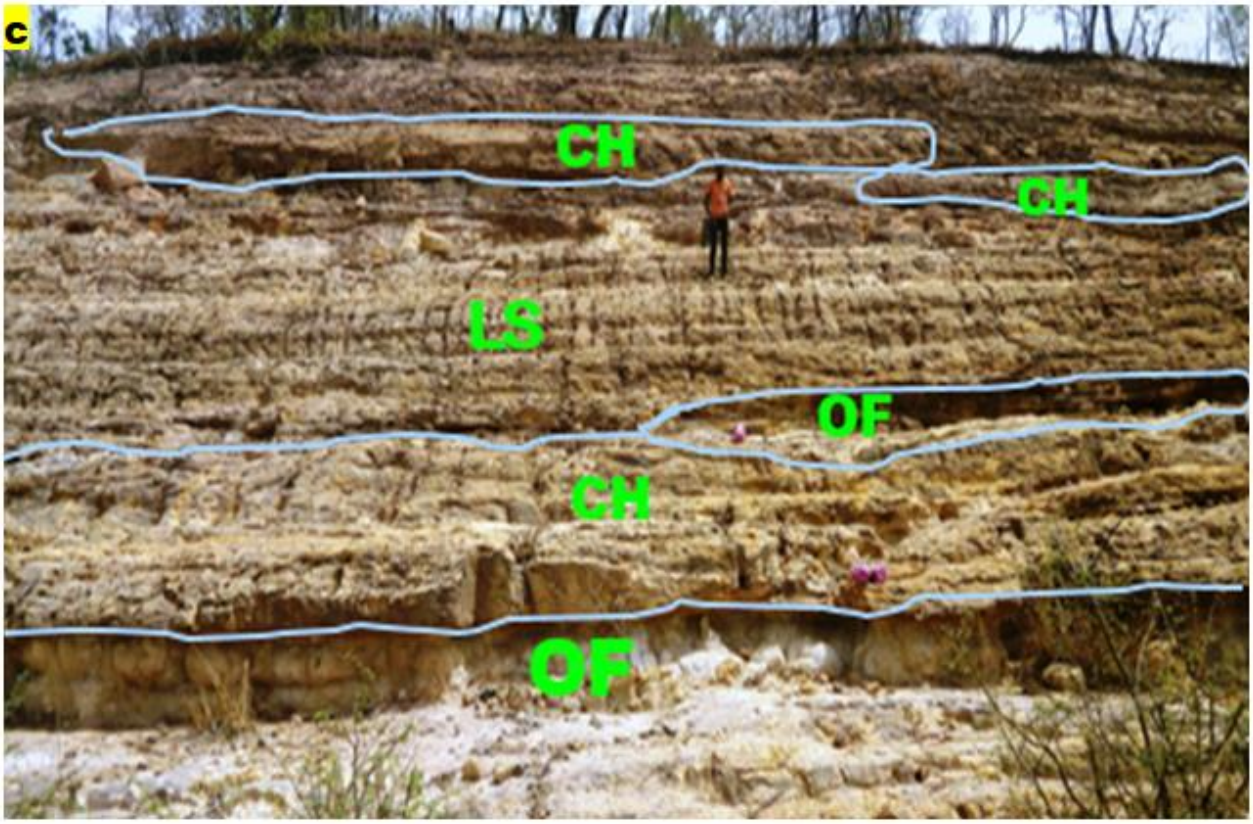


Figure 4.15c: An outcrop showing a typical example of a Channel Element (CH), Laminated Sand Sheet (LS) and Overbank Fines (OF) preserved at Rafingora (Longitude: 005°43.799' E; Latitude: 09°55.344').

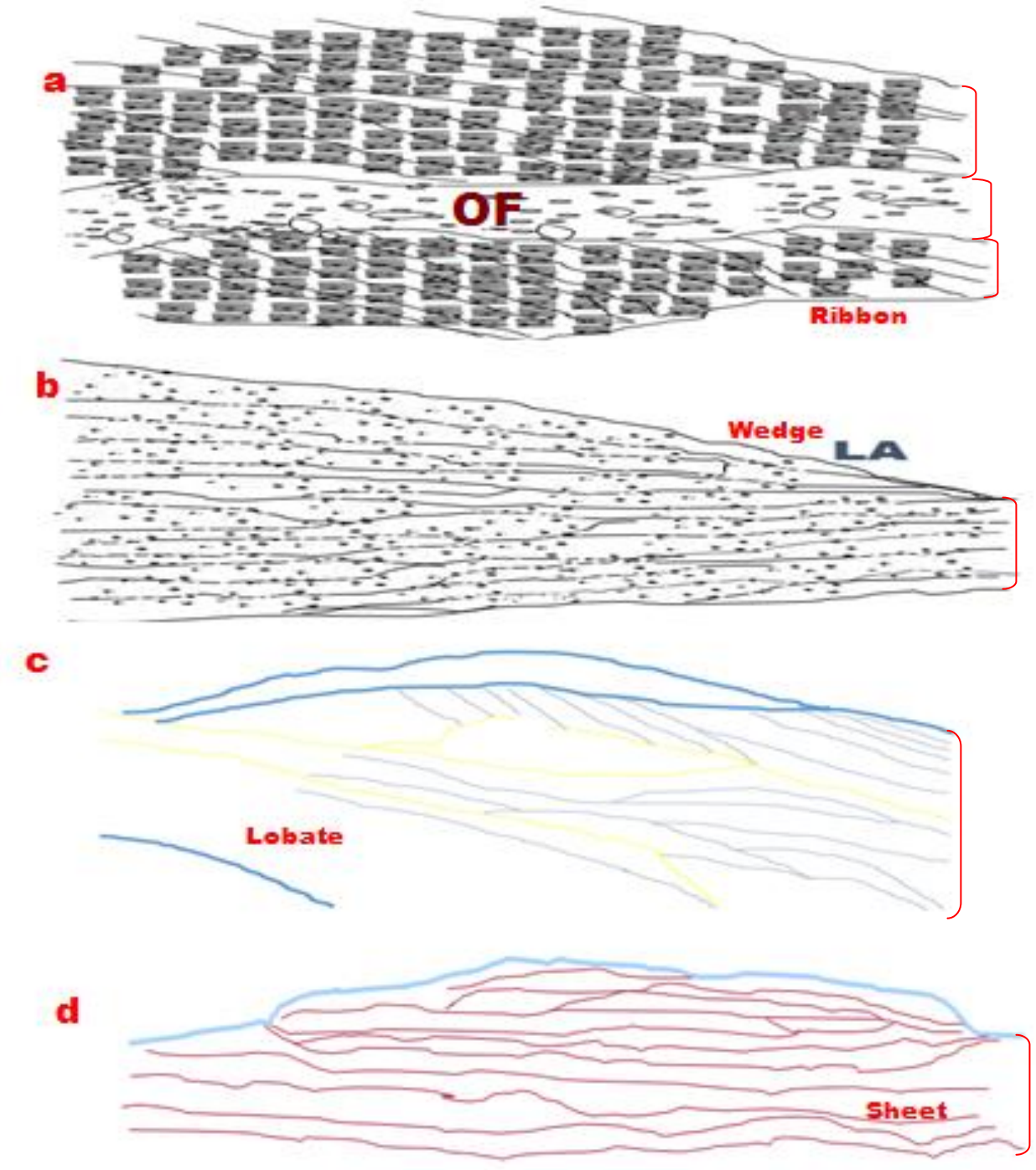


Figure 4.17: Typical characteristics of Sandbody Geometry observed within the study area; (a) a Ribbon geometry common at the southeastern and southwestern parts, (b) a Wedge common at the southwestern and central parts, (c) a Lobate common at the central part and (d) a Sheet common at the northern part all within the study area.

4.1.4 Paleocurrent

Palaeocurrent data were obtained across the study area for the determination of the source area from which the sediments were derived and the paleoflow direction. In all the exposed outcrops within the study area, paleocurrent measurements were taken at ten (10) different localities from measurements of planar lamination and cross-bedding and clast imbrications (Figure 4.17).

A Window based Rose program was used for the plotting of paleocurrent measurements (Table 4.2). The plots indicate mostly unidirectional with minor bi-directional paleocurrent pattern northeastern and northwestern paleocurrent directions (Figure 4.18). This indicates that the source areas were on the southwestern and southeastern directions respectively (Figure 4.19).

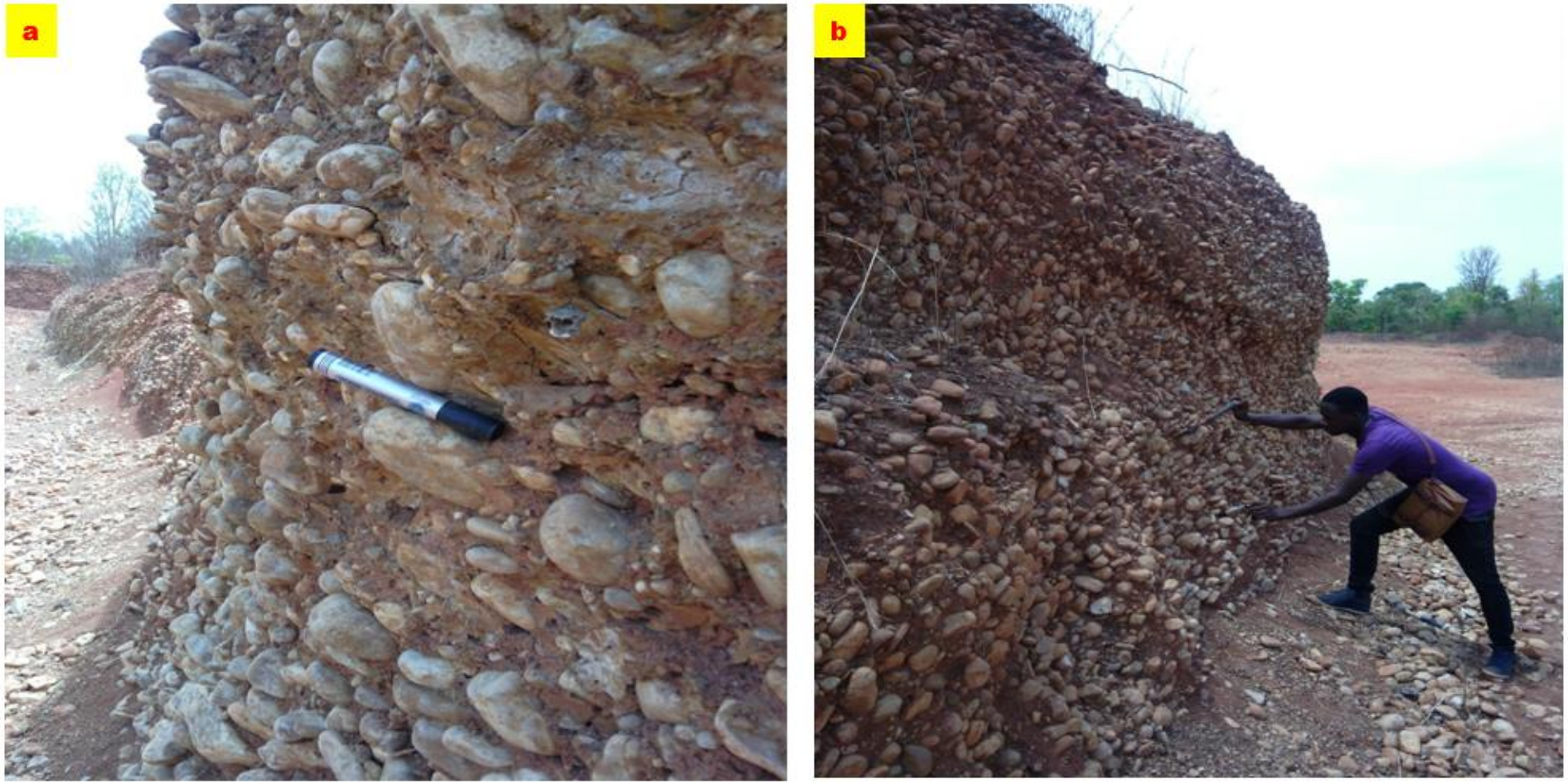


Figure 4.18: The imbricated pebbles from the clast-supported, massive conglomerate (Gcm) and matrix-supported, massive conglomerate (Gmm) sub-facies preserved at Harmattan Patigi University site, Patigi (Longitude: 08°42'53.5"N; Latitude: 005°46'55.7"E).

Table 4.2: Paleocurrent data of planar- cross lamination/bedding and clast imbrication and their locations within the study area

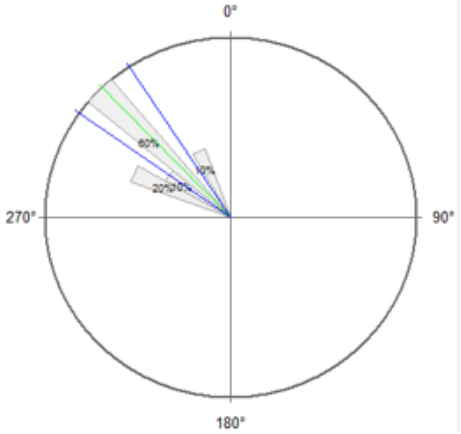
Locality	Maraba		Rafingora		Manigi		Rabba		Enagi		Doko		Jima		Patigi (Pebble)	
	Azimuth	Dip	Azimuth	Dip	Azimuth	Dip	Azimuth	Dip	Azimuth	Dip	Azimuth	Dip	Azimuth	Dip	Azimuth	Azimuth
1	060	40°E	029	48°E	040	40°E	086	20°E	080	20°E	270	10°W	220	18°E	020°	010°
2	058	60°E	032	50°E	044	50°E	090	18°E	080	26°E	280	8°W	200	20°E	005°	020°
3	061	40°E	030	50°E	040	54°E	090	20°E	080	18°E	270	12°W	320	10°E	002°	010°
4	060	46°E	032	52°E	040	52°E	090	22°E	082	22°E	280	12°W	210	18°E	009°	004°
5	062	44°E	031	46°E	039	48°E	090	18°E	079	20°E	270	8°W	220	16°E	020°	012°
6	060	44°E	033	48°E	041	48°E	040	40°E	078	18°E	280	14°W	220	18°E	002°	352°
7	062	44°E	032	50°E	040	50°E	080	16°E	080	20°E	270	12°W	200	18°E	020°	340°
8	060	40°E	032	48°E	040	48°E	089	20°E	080	22°E	320	10°W	220	20°E	003°	020°
9							090	18°E	080	18°E	270	8°W	218	22°E	006°	014°
10							089	28°E	080	22°E	280	12°W	216	22°E	007°	010°

Jima (JIM 1)



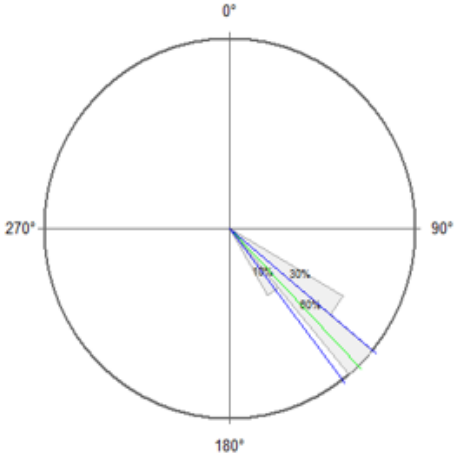
Type of Rose: Unidirectional
Number of Points: 10
Number of Classes (Size): 36 (10°)
Maximum Class: 60%
Vector Mean (Compass Direction): 220.15
Angular Deviation: ± 29.36
Vector Magnitude: 8.69
Consistency Ratio: 0.8688

Kuchi (KCH 1)



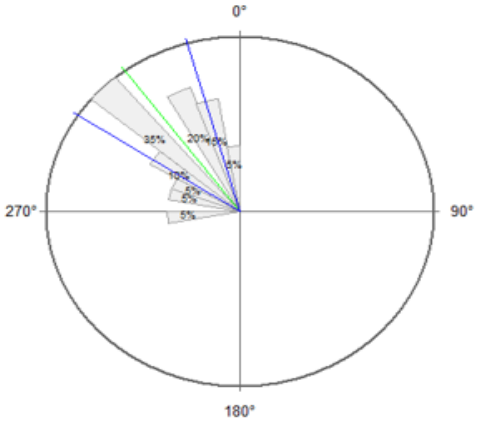
Type of Rose: Unidirectional
Number of Points: 10
Number of Classes (Size): 36 (10°)
Maximum Class: 60%
Vector Mean (Compass Direction): 316.18 (NW)
Angular Deviation: ± 10.81
Vector Magnitude: 9.82
Consistency Ratio: 0.9822

Share (AGB 1)



Type of Rose: Unidirectional
Number of Points: 10
Number of Classes (Size): 36 (10°)
Maximum Class: 60%
Vector Mean (Compass Direction): 136.31
Angular Deviation: ± 6.43
Vector Magnitude: 9.94
Consistency Ratio: 0.9937

Tsaragi (Pebbles)



Type of Rose: Unidirectional
Number of Points: 20
Number of Classes (Size): 36 (10°)
Maximum Class: 35%
Vector Mean (Compass Direction): 323.67 (NW)
Angular Deviation: ± 20.35
Vector Magnitude: 18.74
Consistency Ratio: 0.9369

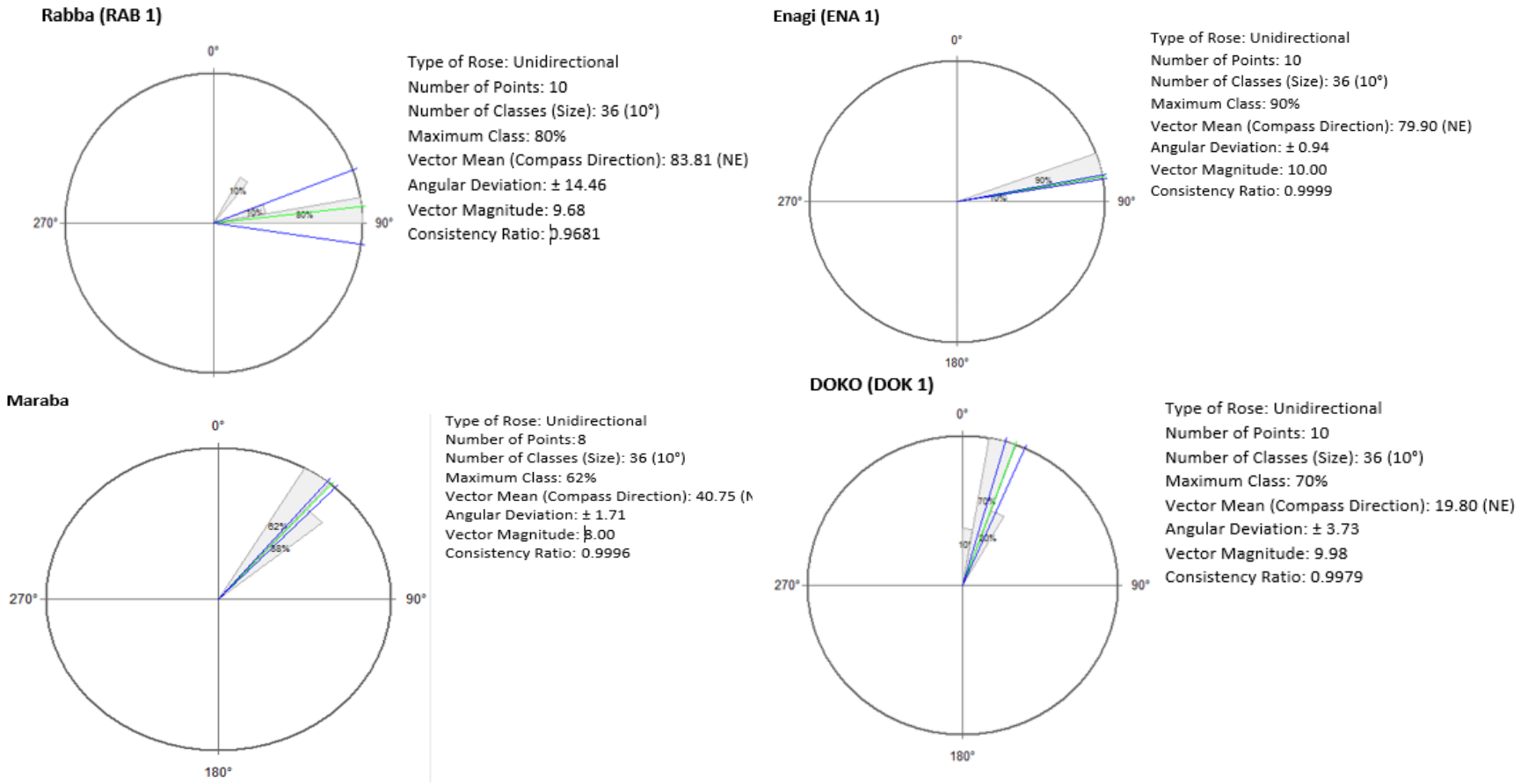


Figure 4.19: Rose diagrams summarizing paleocurrent data of planar- cross lamination/bedding and clast imbrications in some localities on the outcrops within study area.

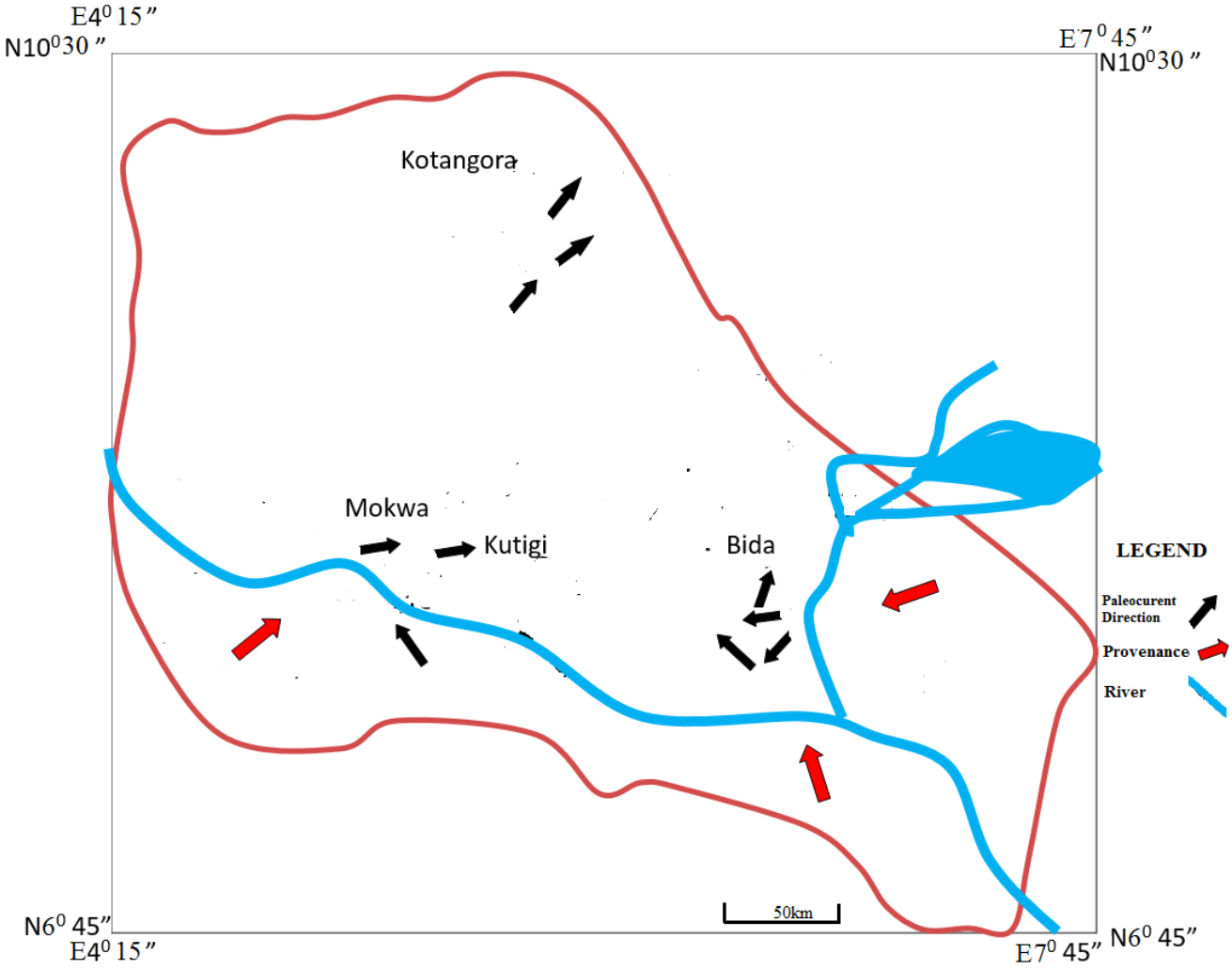


Figure 4.20: Paleocurrent map of the study area

4.1.5 Gross Depositional Processes and Facies Models

Discussions on fluvial styles and facies models within the Northern Bida Basin are presented here. Facies descriptions of the sedimentary exposures and the lithostratigraphic correlations across the study area (Figure 4.20a and b) have indicated a gross fluvial depositional processes and facies assemblage with occasional shallow marine tendency.

The facies analysis shows that coarser sub-facies that signify high velocity/energy deposit dominate the eastern, southeastern and southwestern parts of the study area. The architectural-element analysis shows that these parts comprise gravel bars and bedforms (GB) and channels (CH) with minor SB elements. According to Miall (1996), dominance of GB, CH and SB elements in sand dominated fluvial systems points to a low-sinuosity, high energy, braided river. This area therefore, represents a proximal depositional style within the source area that is probably tectonically controlled.

There was a record of lateral facies changes (Figure 4.21a and b) from the southeastern and southwestern towards the central and then to northern parts of the study area as the channel sandstones of higher energy, low sinuosity passes and changes to a braided river of less energy but higher sinuosity facies. The sandy bedforms (SB), lateral accretion (LA) and minor laminated sand sheet (LS) are the dominating elements within this part of the study area. At the northern part, the finer sub-facies characterized by laminated sand sheet (LS) and overbank fines (OF) with minor channel elements bodies predominates.

Generally, the preserved sedimentary record within the study area as shown in the lithofacies map (Figure 4.20) show gradual transition of depositional styles from low sinuosity, high energy, braided river (proximal) to the less energy, high sinuosity braided river (distal) also suggests likely combinations of autocyclic and allocyclic processes as the controlling mechanisms on the sediments architecture within northern Bida Basin (Figure 4.22).

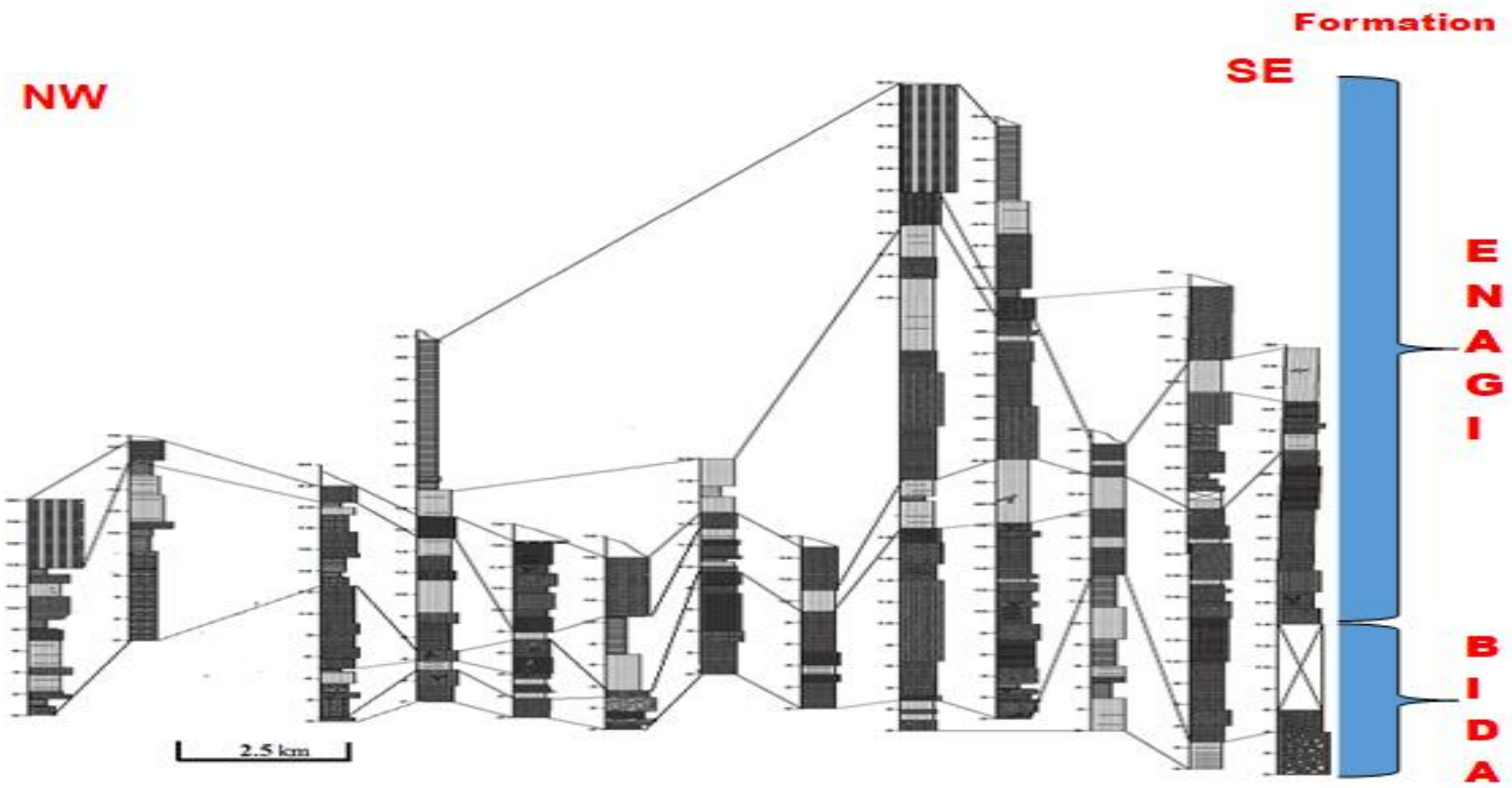


Figure 4.21a: Lithostratigraphic correlations across the Northwest-Southeast direction, Northern Bida Basin.

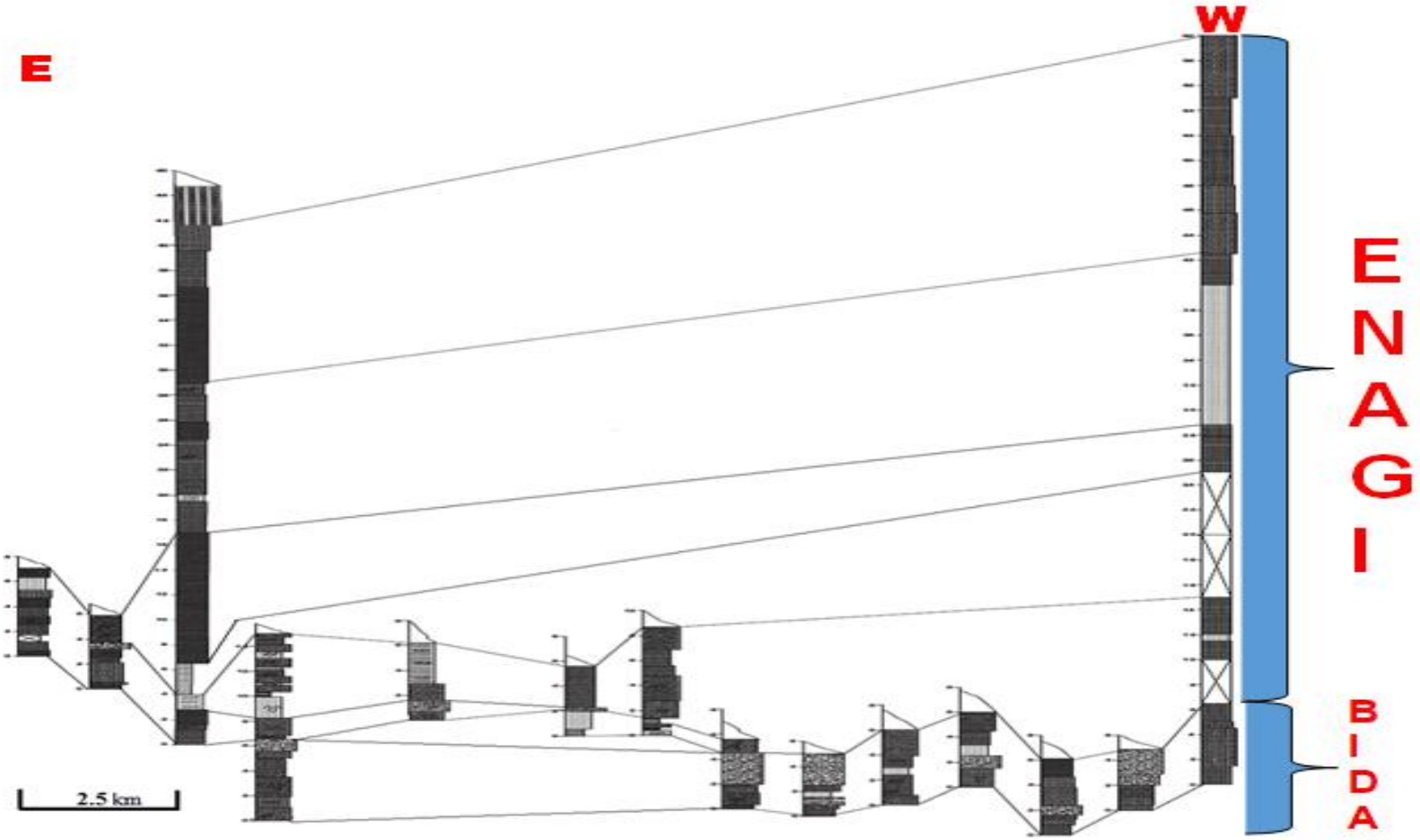


Figure 4.20b: Lithostratigraphic correlations across the East-West direction, Northern Bida Basin.

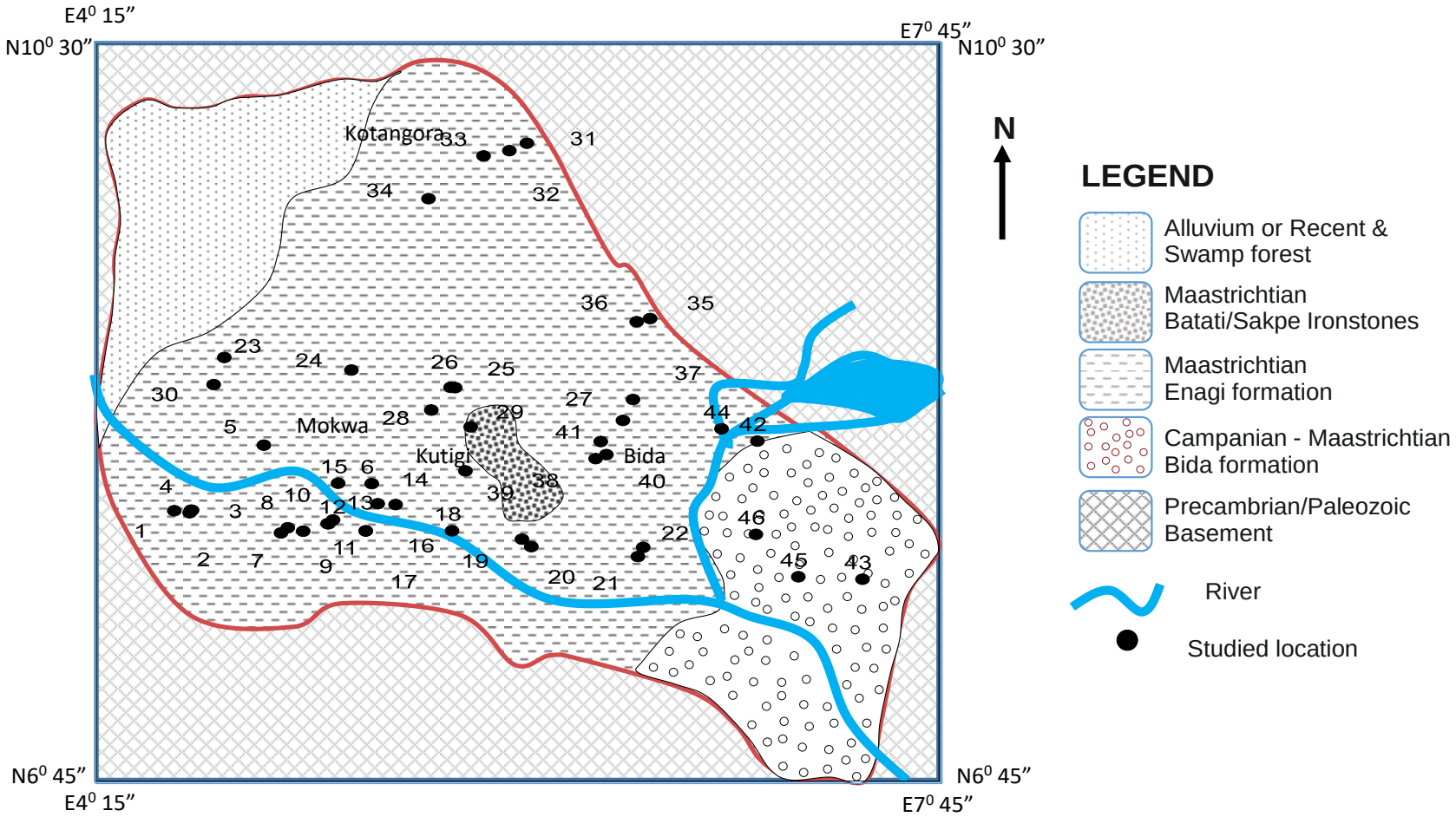


Figure 4.22: Lithofacies map of the study area.

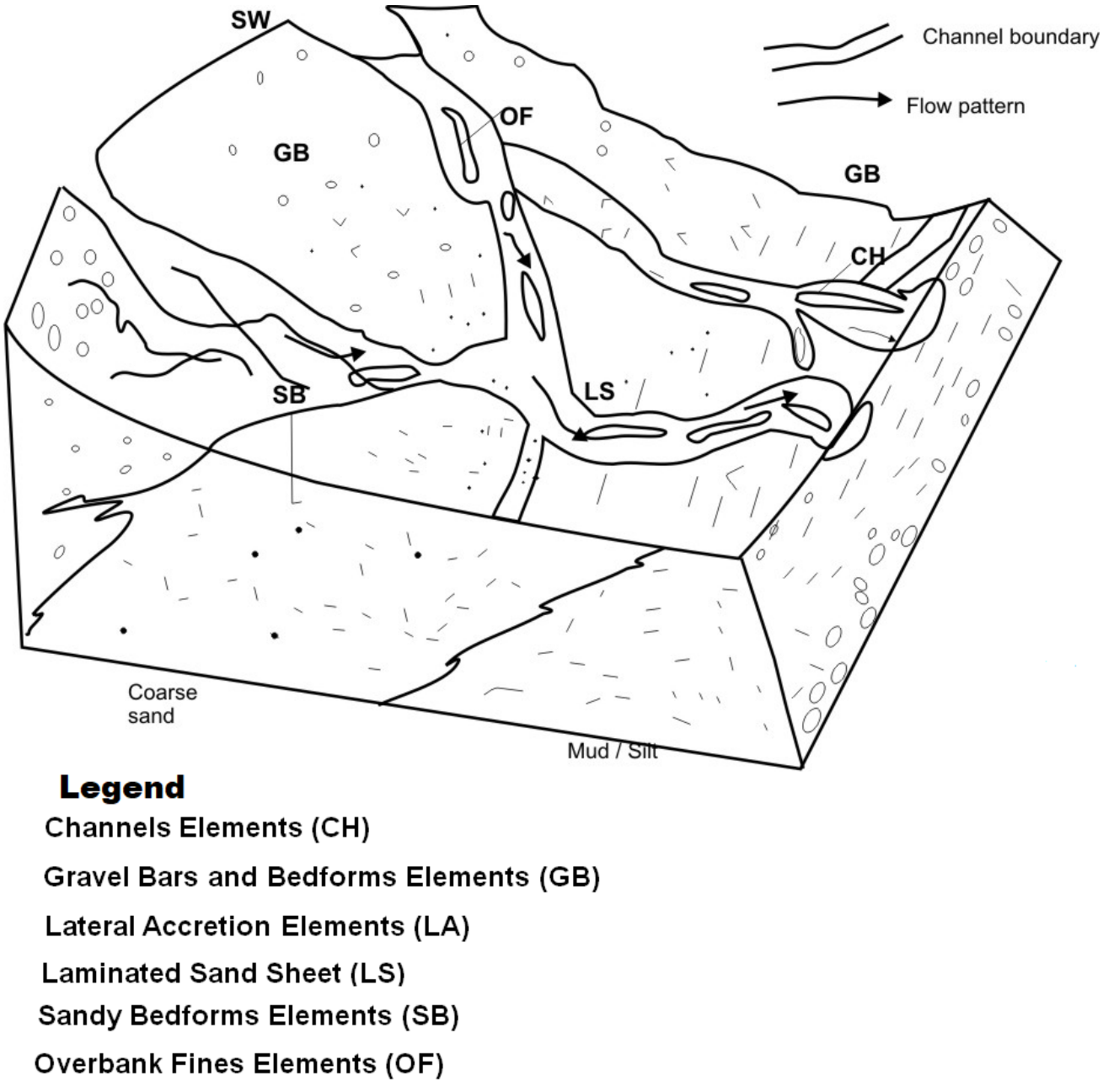


Figure 4.23: Depositional Environment Model of the Northern Bida Basin.

4.2 Textural and Mineralogical Analyses

This part presents and discusses the description of textural characteristics and mineralogical composition of detrital and heavy mineral constituents of the studied sandstones. The pebble morphometric (roundness, sphericity, surface features and overall fabric), grain-size and petrographic analyses can provide unequivocal identification of transporting agents and depositional setting.

The study of textural characteristics of sedimentary rocks refers to the application of pattern formed by the shape, size and three dimensional (3D) arrangements of the particles that make up sediment or a sedimentary rock for description, comparison and interpretation to allow identification of transporting agents and depositional setting (Krumbein and Pettijohn, 1938 and Otto, 1939). According to Suttner (1974), Friedman (1961, 1962) and Moss (1963) sedimentary textures reflect their provenance, depositional environment and diagenetic characteristics. The northern Bida Basin sandstones were studied for their textural attributes to estimate the influence of texture on detrital modes and petrofacies.

4.2.1 Grain Size Analysis (Mechanical Sieving)

Application of grain size (granulometric) analysis of terrigenous sediments has served as one of the effective tools in deciphering the depositional environment of sediments and in determining the depositional processes responsible for their formations. This has been emphasized by the pioneer workers; Krumbein (1937, 1938), Hjulstorm (1939), Inman (1949, 1952), Passega (1957, 1964), Folk and Ward (1957), Mason and Folk (1958), Stewart (1958), Moss (1962, 1963), Sahu (1964, 1983), Klovan (1966), Friedman (1961, 1967), Chappell (1967), Moiola and Weiser (1968), Visher (1969) and others. The above listed workers

underlined the importance of relationship between the grain size of clastic sediments and the environment in which they formed and the processes that formed them.

In this study, a total number of three hundred (300) sandstone samples were selected from those collected from the studied outcrop and processed following the standard dry sieving procedure after Müller (1967). The generated data were then processed using GRADISTAT software after Blott and Pye (2001) to determine the statistical parameters; graphic mean (Mz), inclusive graphic standard deviation (σi), inclusive graphic skewness (Ski) and graphic kurtosis (K_G) in phi units (φ). The generated statistical results were further interpreted using Folk and Ward (1957) formula and presented in Appendix III, Tables Ia-Xa. The detail description and interpretation of the results are presented below.

4.2.1.1 Matrix-supported, massive conglomerate (Gmm) sub-facies

The graphic mean values obtained from the matrix-supported, massive conglomerate (Gmm) sub-facies ranges from very coarse (-0.822) to coarse sands (0.826). Standard deviation (σi) ranges from 0.779 to 1.651 indicating moderately to poorly sorted sandstone. Skewness (Ski) value ranges from -0.441 to 1.370 belongs to very coarse to fine skewed class and the graphic kurtosis (KG) values from 0.445 to 1.318 characterize very platykurtic to leptokurtic class.

4.2.1.2 Crudely bedded conglomerate (Gh) sub-facies

The graphic mean of crudely bedded conglomerate (Gh) sub-facies ranges from -0.823 to 1.888 indicating very-coarse to medium sandstone. Standard deviation (σi) values range from 0.659 to 1.841 indicating few moderately well to higher poorly sorted sands. Skewness (Ski) value ranges from -0.545 to 2.742 indicating very-coarse to very-fine skewed (2.742) and graphic kurtosis (KG) values range from 0.435 to 2.118 suggesting platykurtic to very leptokurtic sandstone.

4.2.1.3 Crudely stratified sandstone (Se) sub-facies

The graphic mean values obtained from the crudely stratified sandstone (Se) sub-facies have graphic mean (Mz) value ranges from -1.039 to 1.271 indicating very coarse- to medium-grained sandstone. Most of the samples are medium grained followed by very few very-coarse grained. Standard deviation (σi) values range from 0.544 to 1.805 indicating moderately to poorly-sorted with most of the samples as poorly sorted and few moderately sorted. The Skewness (Ski) value ranges from 0.438 to 0.863 belonging to very coarse to very fine skewed class and the graphic kurtosis (KG) value ranges from -0.387 to 1.976 suggesting very platykurtic to very leptokurtic sandstone.

4.2.1.4 Planar cross-stratified sandstone (Sp) sub-facies

The graphic mean values obtained from the planar cross-stratified sandstone (Sp) sub-facies have calculated graphic mean (Mz) of Sp sub-facies ranges from -0.729 to 1.765 indicating few medium- and very coarse-grained sandstone (mostly coarse grained samples). The standard deviation (σi) values ranges from 0.868 to 1.834 indicating moderately to poorly sorted with most of the samples showing poorly sorted and few moderately sorted. The skewness (Ski) value ranges from -0.454 to 1.018 interpreting as very coarse to very fine skewed with majority very coarse and few very-finely skewed. The graphic kurtosis (KG) values range from 0.422 to 1.601 suggesting overall very platykurtic to very leptokurtic sandstone.

4.2.1.5 Horizontally stratified sandstone (Sh) sub-facies

The graphic mean values obtained from the horizontally stratified sandstone (Sh) sub-facies shows ranges from -0.754 to 2.643, therefore interpreted as very coarse to fine-grained sandstone (with higher very-coarse and few fine-grained). The standard deviation (σi) ranges

from 0.607 to 2.22 and it implies that sandstone are moderately well to poorly-sorted. Majority of the sediments are poorly sorted while few are moderately well sorted. Skewness (Ski) values vary between -0.531 and 1.98 which denotes very coarse to very fine skewed. Kurtosis (KG) value of the sandstone ranges from 0.451 to 1.944 implying very platykurtic to very leptokurtic.

4.2.1.6 Rippled cross-stratified sandstone (Sr) sub-facies

The mean size of the rippled cross-stratified sandstone (Sr) sub-facies ranges from -0.530 to 1.574, so, interpreted as very coarse to medium sands. The standard deviation (σi), ranges from 0.955-1.446 and implies that sandstone are moderately to poorly-sorted. The skewness (Ski) values vary between -0.063 and 0.155 characterizing symmetrical to fine sands and kurtosis (KG) value ranges from 0.866 to 1.130 implying platykurtic to leptokurtic for the sandstone.

4.2.1.7 Massive sandstone (Sm) sub-facies

The graphic mean values obtained from the massive sandstone (Sm) sub-facies have mean (Mz) values ranging from -2.00 to 1.318 interpreting as very coarse- to medium-grained sands. The standard deviation (σi) value ranges from 1.030 to 1.767 implying all poorly-sorted sandstone. The skewness (Ski) values vary between -0.455 and 0.886 and denotes very coarse to fine skewed while kurtosis (KG) value which ranges from 0.427 to 1.431 imply very platykurtic to leptokurtic.

4.2.1.8 Finely laminated mudstone (Fl) sub-facies

The finely laminated mudstone (Fl) sub-facies have mean (Mz) values with value ranges from 0.042 to 2.684 interpreting as coarse- to fine-grained sands. Standard deviation (σi) ranges from 0.535 to 1.866 and it implies that sandstone is moderately well to poorly sorted.

The skewness (Ski) values vary between -0.450 and 0.250 and interpret as very coarse to fine skewed sands and the graphic Kurtosis (KG) value of the sandstone ranges from 0.593 to 1.946 interpreting as very platykurtic to very leptokurtic.

4.2.1.9 Massive mudstone (Fm) sub-facies

The massive mudstone (Fm) sub-facies have graphic mean (Mz) sands ranges from -0.413 to 2.904 interpreting as very coarse- to fine-grained sandstone. The standard deviation (σi) ranges from 0.479-1.719 and it implies that sandstone are well to poorly-sorted. The skewness (Ski) values vary between -0.351 and 1.763 which denotes very coarse to very fine skewed while graphic Kurtosis (KG) value of the sandstone ranges from 0.370 to 1.509 implying very platykurtic to very leptokurtic.

Further textural classification were also attempted by plotting the three (3) sediment textural composition members; gravel (G), sand (S) and mud (M) on the ternary diagram proposed by Blott and Pye (2012) using the data presented in Appendix III, Tables Ib-Xb. The plot in figure 4.23 shows that the studied sediments generally belong; Sand (S), very slightly gravelly sand {(vg)S}, slightly gravelly sand ((g)S) and gravelly sand (gS); others are sandy gravel (sG) while the trace class is made up of very slightly muddy {(vm)(g)S- and very slightly muddy sand {(vg)(vm)S}.

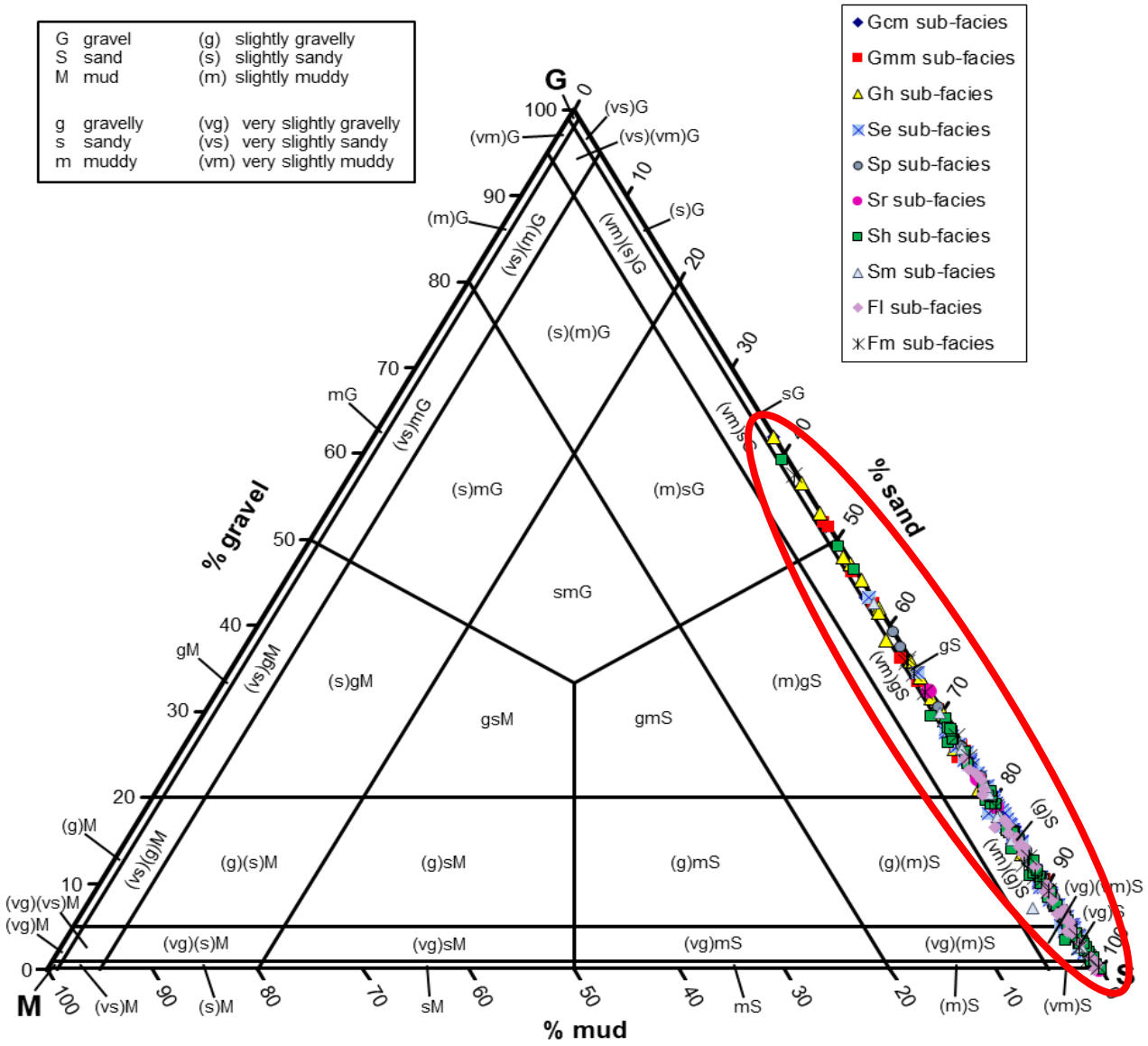


Figure 4.23: Particle size distribution classifications based on the percentages of Gravel, Sand and Mud (G-S-M) after Blott and Pye (2012).

4.2.2 Detrital Mineralogical Composition, Description and Modal Analyses

The description of petrographic components and modal composition of the light minerals is discussed here with the aim to identify the compositional variations across the study area. The various types of minerals recognized under polarizing microscope based on their optical characteristics; colour, form, relief, extinction angle, pleochroism, twining and bifringence are discussed below. The detrital mineral description of the components revealed the following minerals: quartz, feldspars, rock fragments, micas, cements (iron, clay and silica) and heavy minerals.

Framework composition of the mineral constituents from the petrographic study is presented in (Tables 4.3a-4.3h) while the recalculated framework constituents to 100 percentage of the three important detrital (quartz, feldspar and lithic fragments) and their varieties is presented in appendix IV, tables Ia-VIIIa. These values shall further be employed in chapter five for different diagram plottings; for example, sandstone classification after McBride (1963), Folk (1980) and Pettijohn *et al*. (1987), provenance and plate tectonic settings after Ingersoll and Suczek (1979), Dickinson *et al*. (1983), Dickinson (1985), paleo-climate after Suttner (1974), Basu (1985), Suttner and Dutta (1986) and diagenetic modification after McBride (1985).

4.2.2.1 Crudely bedded Conglomerate (Gh) Sub-facies

Generally, the crudely bedded conglomerate (Gh) sub-facies is composed mostly of moderately to poorly sorted, coarse to very coarse grained, very angular to sub-angular grains. Quartz is the dominant detrital mineral in the framework composition and made up of monocrystalline (Qm) and polycrystalline varieties and appears as relatively clear colorless. Both quartz varieties (Qm and Qp) are euhedral to subhedral, very angular to sub-angular and

exhibited by non-undulose and undulose types (Figure 4.24a). Fractured polycrystalline quartz grains (Qp) with mineral inclusions (zircon) are also present (Figure 4.2a-XPL).

Feldspars is the next in abundance in the framework composition (Table 4.3a) and like quartz, its grains are typically clear, colorless and show low bifringence, but can be distinguished from quartz by their twining and refractive indices. Microcline and plagioclase varieties are the common variety of feldspar grains and are usually unaltered. The lithic fragments observed are minor and includes; sedimentary (siltstone lithoclast), igneous (volcanic) and metamorphic lithoclasts.

The matrix is made up of clay and silt, and it therefore appears as extremely fine-grained material in the examined samples and appeared typically dark while the identified dominating cementing mineral is kaolinite often formed as a coatings and rims around the framework grains. Other cement identified, though in trace amount is a ferruginous minerals which were classified iron-oxide; limonite, goethite and hematite. Heavy mineral also observed in minor amounts in the framework.

The modal analysis of Gh sub-facies (Table 4.3a) show dominant of total quartz (Q: 77-80%), total feldspar (F: 0-2%) and total lithic or rock fragments (L/R: 2-6%). Other components includes; matrix and cements (20-25%) and accessory minerals (0%). The quartz varieties; monocrystalline (Qm) and polycrystalline (Qp) have their values ranges from 68.6 to 77.2% and 0.8 to 17.5% respectively, whereas the feldspar varieties constitute only alkali feldspar (K-feldspar) with value ranges from 0 to 2%. Also, the total lithic fragments (Lt) varieties includes; sedimentary lithic fragments (Ls- 0-2%), volcanic lithic fragments (Lv- 0-4%) and metamorphic lithic fragments (Lm- 0-5%).

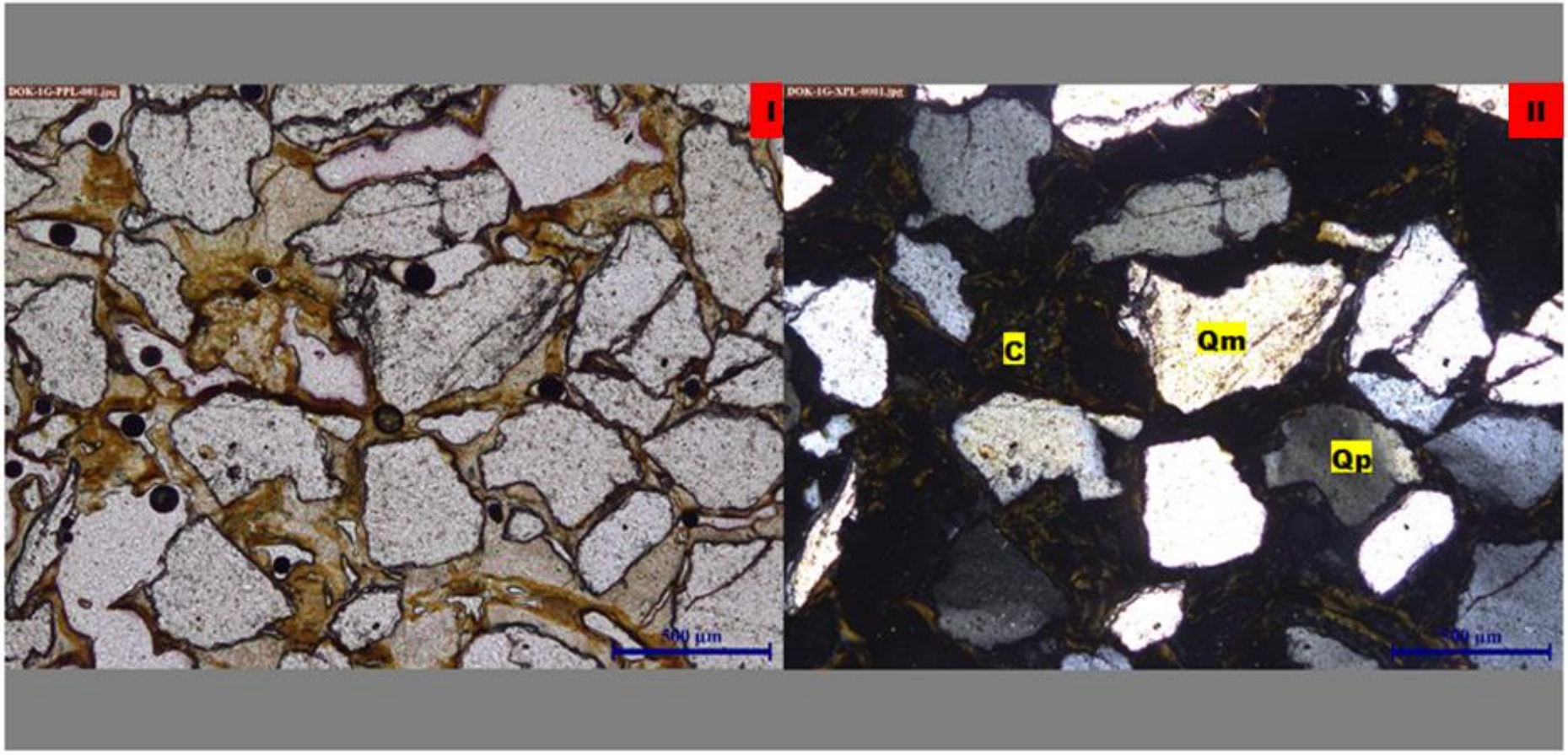


Figure 4.24a: Photomicrographs of typical crudely bedded conglomerate (Gh) sub-facies (DOK-1G) at Dokko showing the mineral constituents; Qm (monocrystalline quartz), Qp (polycrystalline quartz) and C (Cement). NB: (I) PPL and (II) XPL.

Table 4.3a: Mineralogical composition of crudely bedded conglomerate (Gh) sub-facies

Location	Sample Code	Quartz			Feldspar			Lithic/Rock Fragment				Matrix and Cement	Accessory Minerals	Total
		Qm	Qp	Qt	P	K	F	Ls	Lv	Lm	Lt			
Dokko	**DOK-1G**	77.2	0.8	78	0	0	0	1	0	1	2	20	0	**100**
Enagi	**ENG-1K**	67.9	2.1	70	0	1	1	1	2	1	4	25	0	**100**
Kajita	**KJT-1Q**	52.5	17.5	70	0	0	0	0	0	5	5	25	0	**100**
Maraba	**MAR-1G**	.68.6	1.4	70	0	2	2	2	4	0	6	22	0	**100**
Patti-Chin	**PAT-1M**	76.4	1.6	78	0	0	0	1	1	0	2	20	0	**100**

4.2.2.2 Crudely stratified Sandstone (Se) sub-facies

This sub-facies (Se) composed mostly of angular to sub-angular, poorly to moderately well sorted, coarse to very coarse grained, euhedral to subhedral, floating to point contact and minor suture contact. The dominating framework mineral is the quartz and appears as relatively colourless grains under microscope and consist of both monocrystalline (Qm) and polycrystalline (Qp) varieties with former higher in percentage than latter. Both varieties exhibited non-undulose and undulose and are mostly fresh (Figure 4.24b).

Feldspar grains observed has varieties of the potassic (common) and plagioclase (less). This could be attributed to the relatively shorter distance of transportation of the sediments. Lithic fragments examined only as very small amount, representing reworked material brought into the sediment by erosional processes during the sediment transport. Clay minerals are the main cement and appeared as clay rims around the grains, points to allochthonous materials. Muscovite (Mu) is identified as the major mica variety while heavy minerals are tourmaline and zircon which appeared as inclusions within the quartz grains.

The result of modal analysis (Table 4.3b) shows composition dominantly of quartz (Q: 68-82%), few feldspars (F: 0-3%) and total lithic/rock fragments (L/R: 2-6%) respectively. The other components have their respective compositions as follows; accessory minerals (0-1%) and matrix & cements (15-28%). Quartz varieties; monocrystalline (Qm) and polycrystalline (Qp) ranges from 64.6 to 81.2% and 0.7 to 3.9% respectively, whereas the feldspar varieties; potassic- and plagioclase feldspars values ranges from 0 to 1% and 0 to 2% respectively. The lithic/rock fragments varieties and their compositions includes; sedimentary lithic fragments (Ls- 0-2%), volcanic lithic fragments (Lv- 1-3%) and metamorphic lithic fragments (Lm- 0-3 %).

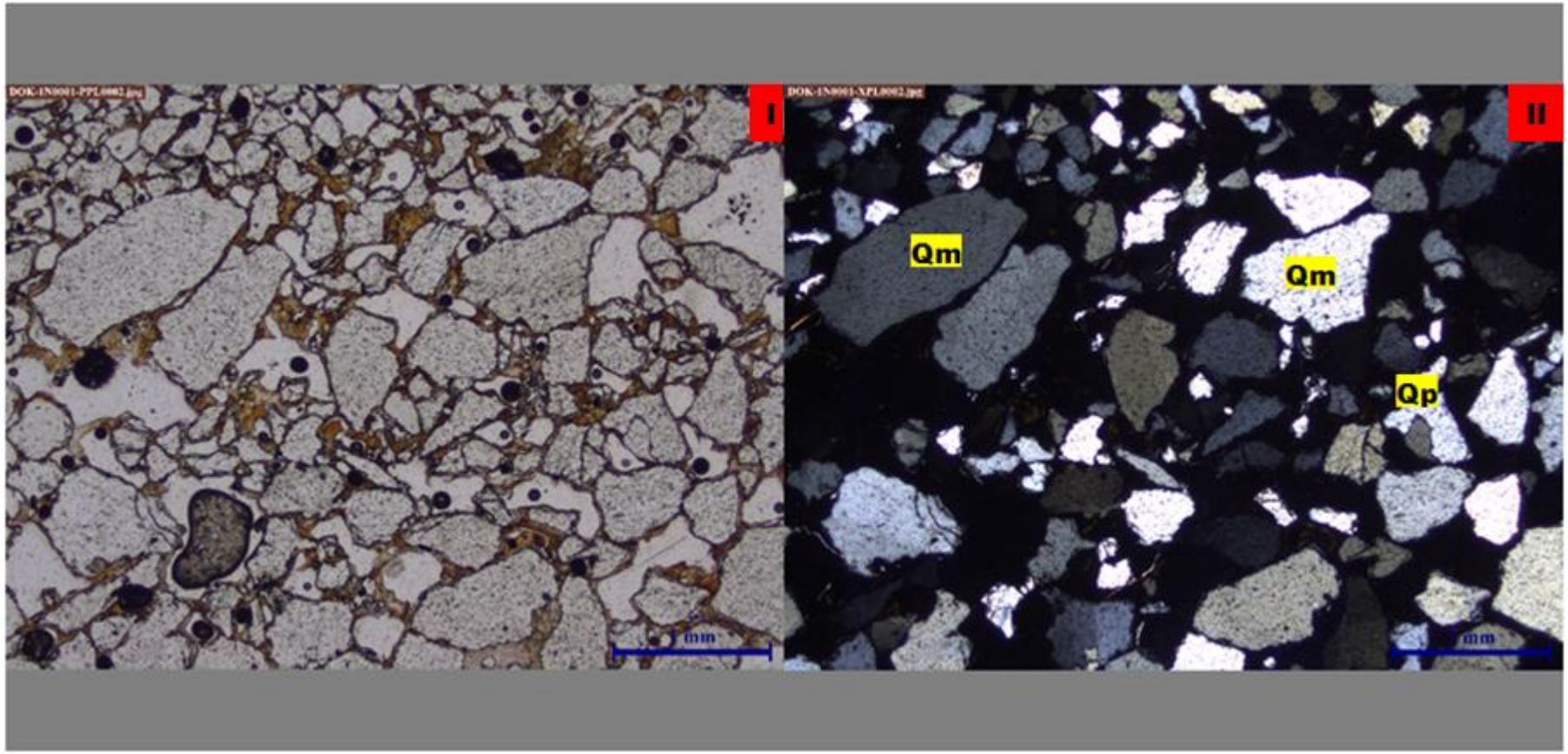


Figure 4.24b: Photomicrographs of typical crudely stratified sandstone (Se) sub-facies (DOK-1N) at Dokko showing the mineral constituents; Qm (monocrystalline quartz) and Qp (polycrystalline quartz). NB: (I) PPL and (II) XPL.

Table 4.3b: Mineralogical composition of crudely stratified sandstone (Se) sub-facies

Location	Sample Code	Quartz			Feldspar			Lithic/Rock Fragment				Matrix and Cement	Accessory Minerals	Total
		Qm	Qp	Qt	P	K	F	Ls	Lv	Lm	Lt			
Agbonna	**AGB-1F**	74.3	0.7	75	0	0	0	0	2	0	2	22	1	**100**
Dokko	**DOK-1N**	81.2	0.8	82	0	0	0	0	1	1	2	15	1	**100**
Jimma	**JIM-1E**	66.5	3.5	70	1	2	3	1	2	0	3	23	1	**100**
Katcha	**KAC-1E**	73.5	1.5	75	0	2	2	2	1	0	3	20	0	**100**
Kajita	**KJT-1A**	66.6	1.4	68	0	1	1	1	2	0	3	28	0	**100**
Kutigi	**KUT-2B**	67.9	2.1	70	0	0	0	0	1	3	4	25	1	**100**
Kutigi	**KUT-2L**	74.5	1.5	77	0	0	0	1	1	0	2	20	1	**100**
Lemu	**LEM-1E**	74.1	3.9	78	1	2	3	0	1	2	3	16	0	**100**
Patti-Chin	**PAT-1E**	78.4	1.6	80	0	1	1	1	2	0	3	15	1	**100**
Tanagi	**TAN-1C**	64.6	3.4	68	0	0	0	1	3	0	4	28	0	**100**

4.2.2.3 Planar cross-stratified sandstone (Sp) sub-facies

Petrographic study of the planar cross-stratified sandstone (Sp) sub-facies revealed that it is composed mostly of sub-angular with few sub-rounded, poorly to moderately well sorted, medium to coarse (with minor fine), euhedral to subhedral, straight, point contact, suture and few concavo-convex contact grains (Figure 4.24c).

The dominating grain among the framework composition is fresh quartz (few altered) with the major monocrystalline (Qm) variety and minor polycrystalline (Qp) with pronounce undulatory extinctions. Meanwhile, feldspars occur in small amounts and include both K-feldspar (K) and plagioclase (P) varieties. In most of the studied Sp sub-facies samples, alteration or replacement of plagioclase grains was observed. Matrix (ferruginous (Iron-oxide) and clay cements) are composed of clay and silt, and appears as extremely fine-grained material and appears as a rims and coatings around framework grains, fills the pore throats, encloses several framework grains causing the effect of floating grains in Se sub-facies. Mica observed is a muscovite (Mu) and was identified with rather low concentrations.

The modal analysis (Table 4.3c) shows that quartz dominates while others make lesser percentage in the total framework with the respective ranges of values as follows; quartz (Q-65-85%), feldspar (F- 0-3%), total lithic/rock fragments (L/R- 1-12%), accessory minerals (0-4%) and matrix and cements (12-25%). the quartz varieties; monocrystalline (Qm) and polycrystalline (Qp) ranges from 52 to 85% and 0 to 13% respectively, while for feldspar varieties (plagioclase and potassic) ranges from 0 to 1% and 0 to 2% for the former and later respectively. Also, composition of varieties of the total lithic fragments (Lt) which includes sedimentary lithic fragments (Ls), volcanic lithic fragments (Lv) and metamorphic lithic fragments (Lm) varies in the following proportions; 0-2%, 0-3% and 0-9% accordingly.

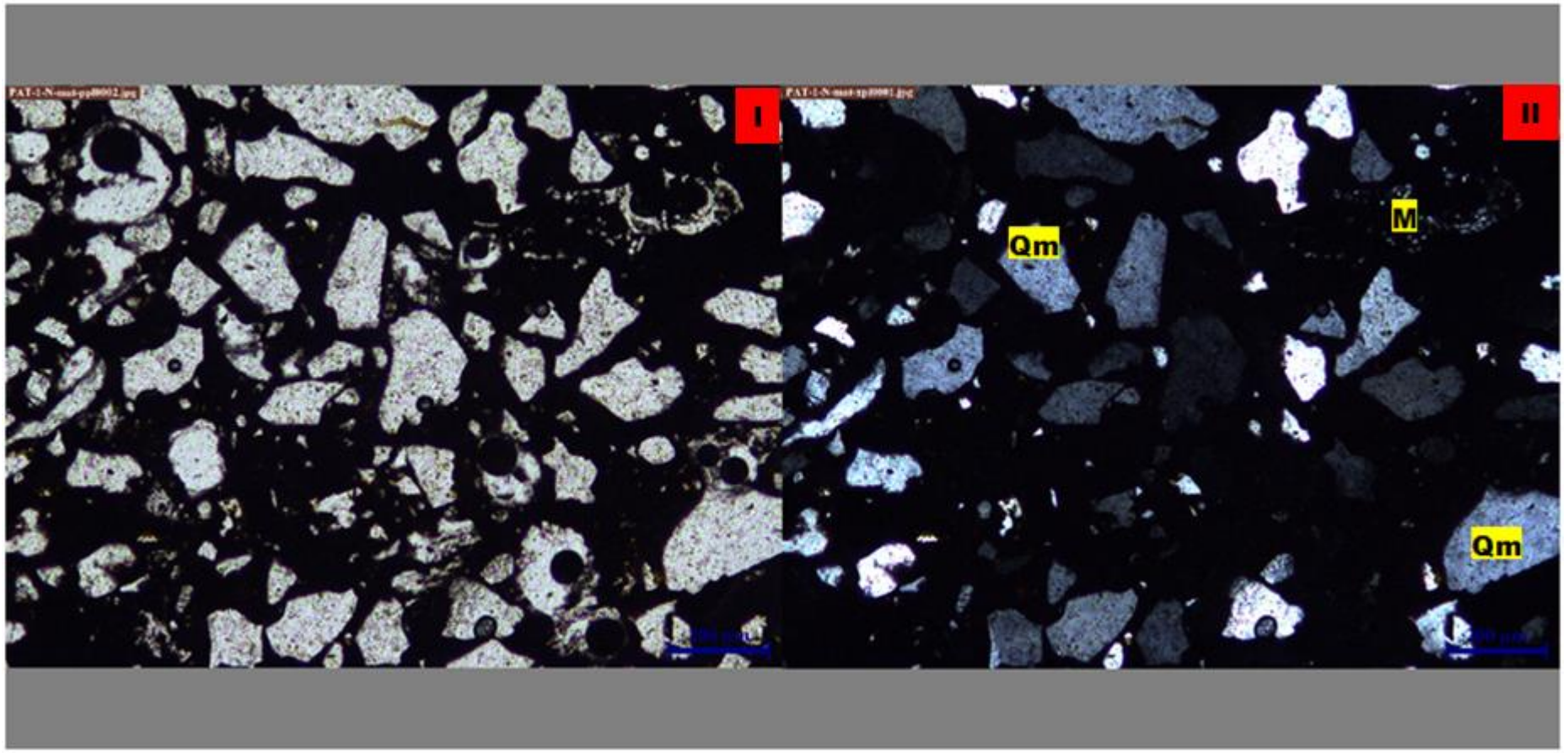


Figure 4.24c: Photomicrographs of typical planar cross-stratified sandstone (Sp) sub-facies (PAT-1N) at PattiCChin showing the mineral constituents; Qm (monocrystalline quartz) and Mu (muscovite). NB: (I) PPL and (II) XPL.

Table 4.1c: Mineralogical composition of planar cross-stratified sandstone (Sp) sub-facies

Location	Sample Code	Quartz			Feldspar			Lithic/Rock Fragment				Matrix and Cement	Accessory Minerals	Total
		Qm	Qp	Qt	P	K	F	Ls	Lv	Lm	Lt			
Bida	**BDA-1L**	71.5	1.5	73	0	0	0	1	1	0	2	25	0	**100**
Dokko	**DOK-1V**	79.2	0.8	80	0	0	0	0	1	0	1	18	1	**100**
Enagi	**ENG-1F**	69.3	0.7	70	0	0	0	0	1	0	1	25	4	**100**
Jimma	**JIM-1S**	70.6	1.4	72	0	2	2	1	2	0	3	23	0	**100**
Katcha	**KAC-1B**	81.2	0.8	82	0	0	0	0	2	0	2	16	0	**100**
Maraba	**MAR-1B**	68.6	1.4	70	0	0	0	2	3	0	5	25	0	**100**
Maraba	**MAR-1D**	71.3	3.7	75	1	2	3	0	0	2	2	20	0	**100**
Maraba	**MAR-1L**	66.5	3.5	70	0	2	2	1	2	0	3	24	1	**100**
Mangota	**MGT-1C**	74.7	2.3	78	0	1	1	1	0	0	1	20	0	**100**
Patti-Chin	**PAT-1J**	85.0	0	85	0	1	1	0	1	0	1	12	1	**100**
Patti-Chin	**PAT-1N**	84.2	0.8	85	0	0	0	0	1	0	1	14	0	**100**
Tanagi	**TAN-1A**	68.4	3.6	72	0	0	0	2	1	0	3	25	0	**100**
Tanagi	**TAN-1G**	52.0	13	65	0	0	0	0	3	9	12	22	1	**100**

4.2.2.4 Rippled Cross-stratified Sandstone (Sr) sub-facies

Generally, rippled cross-stratified sandstone (Sr) sub-facies composed mostly of poorly to moderately sorted, medium to coarse, angular to sub-rounded, euhedral to subhedral grains. Quartz grain is the most abundant (Table 4.3d) with both monocrystalline (Qm) and polycrystalline (Qp) quartz varieties exhibiting straight extinction undulose and angular to sub-rounded but Qm grain content is higher than Qp.

Feldspar (F) made the next abundance to quartz (Table 4.4) in the framework composition with pottasic (K) and plagioclase (P) observed as the feldspar variety with contents of former higher than later. Alteration or replacement of plagioclase grains is observed in few samples. The frequencies of both plagioclase and K-feldspar vary in the sandstone sediment samples. Sedimentary lithoclast and igneous rock fragments were identified as lithic fragments exhibiting point to long contacts with some floating grains. Matrix is very rare in all the studied samples and occurs as crushed lithic fragments, tiny quartz grains and pseudo-matrix. Iron and clay form the cement materials whereas muscovite (mica) forms the accessory minerals, though both occur in low proportions.

The detrital framework composition includes; quartz (Q) been the most dominant in the framework composition with its value ranges from 81 to 83% whereas other components are relatively less with their compositional values as follows; feldspar (1-2%), lithic/rock fragments (1%), accessory minerals (1%), matrix and cements (14-15%). The quartz varieties; monocrystalline (Qm) and polycrystalline (Qp) have compositions range from 78.8 to 81.2 % and 1.8-2.2% respectively, while the feldspar varieties (potassic and plagioclase) values range from 1-2% and 0% respectively (Table 4.3d). Other compositions includes; total lithic/rock fragments varieties; sedimentary lithic fragments (Ls-1%), volcanic lithic fragments (Lv- 0%) and metamorphic lithic fragments (Lm- 0%).

Table 4.3d: Mineralogical composition of rippled cross-stratified sandstone (Sr) sub-facies

Location	Sample Code	Quartz			Feldspar			Lithic/Rock Fragment				Matrix and Cement	Accessory Minerals	Total
		Qm	Qp	Qt	P	K	F	Ls	Lv	Lm	Lt			
Agbonna	**AGB-1J**	78.8	2.2	81	0	2	2	1	0	0	1	15	1	**100**
Manigi	**MAN-1F**	81.2	1.8	83	0	1	1	1	0	0	1	14	1	**100**

4.2.2.5 Horizontally stratified sandstone (Sh) sub-facies

The horizontally stratified sandstone (Sh) sub-facies revealed mostly angular (minor) to sub-rounded, poorly (few) to moderately well- and well sorted (minor), medium to very coarse (minor), euhedral to subhedral, floating, straight, point and concavo-convex contact (observed in minor samples) grain constituents (Figure 4.24d).

Like other sub-facies discussed above, quartz is also the dominating framework mineral in Sh. The grains are made up of higher monocrystalline (Qm) and minor polycrystalline (Qp) grains and exhibited both extinction and undulatory characteristics and few are altered. Feldspar grain is the next in abundance and is highly altered as observed and both K-feldspar (K) and plagioclase (P) were observed as the varieties. Whereas, lithic fragments observed are sedimentary and igneous lithic grains that occur in different sizes representing reworked material. The matrix which appears as extremely fine-grained material and high ferruginous and fair amount of clay minerals occurring as rims coatings that may be inherited from reworked framework grains which might be connected to the diagenetic effect. In some cases, the cements are visible next to grains, and may occupy entire pores than do grains. Muscovite (Mu), zircon, tourmaline where also occurred in few samples as both heavy minerals and inclusions in low concentrations.

The framework composition of this sub-facies comprises of quartz (Q- 58-87%), feldspar (0-2%), rock fragments (0-10%), accessory minerals (0-2%) and matrix & cements (2-3%). Quartz varieties; monocrystalline (Qm) and polycrystalline (Qp) values ranges from 52.2 to 87.0% and 0 to 4.8% respectively, feldspar variety compositions; potassic (0-2%) and plagioclase (0%) whereas, lithic/rock fragments varieties; sedimentary (Ls), volcanic (Lv) and metamorphic (Lm) have compositions as 0-8%, 0-2% and 0-2% respectively (Table 4.3e).

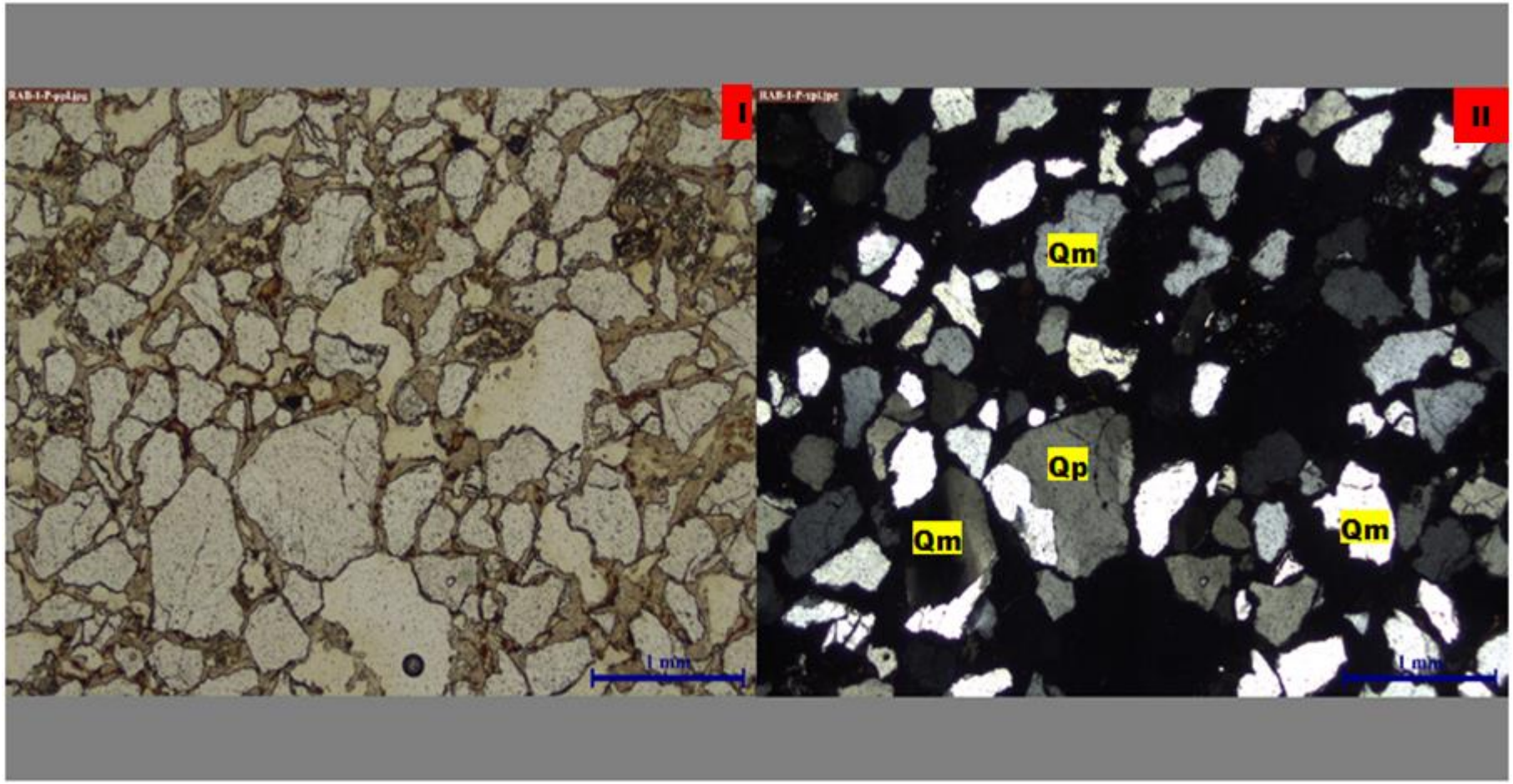


Figure 4.24d: Photomicrographs of typical horizontally stratified sandstone (Sh) sub-facies (RAB-1P) at Rabba showing the mineral constituents; Qm (monocrystalline quartz) and Qp (polycrystalline quartz). NB: (I) PPL and (II) XPL.

Table 4.3e: Mineralogical composition of horizontally stratified sandstone (Sh) sub-facies

Location	Sample Code	Quartz			Feldspar			Lithic/Rock Fragment				Matrix and Cement	Accessory Minerals	Total
		Qm	Qp	Qt	P	K	F	Ls	Lv	Lm	Lt			
Agbonna	**AGB-1C**	74.2	0.8	76	0	0	0	2	0	1	3	20	1	**100**
Bida	**BDA-1B**	69.3	0.7	70	0	0	0	0	2	0	2	28	0	**100**
Bida	**BDA-1F**	77.2	0.8	78	0	0	0	0	0	0	0	22	0	**100**
Bida	**BDA-1M**	74.3	0.7	75	0	0	0	0	2	0	2	22	1	**100**
Dokko	**DOK-1K**	69.3	0.7	70	0	0	0	1	1	0	2	26	2	**100**
Dokko	**DOK-1Y**	74.5	1.5	77	0	1	1	1	1	0	2	20	0	**100**
Dokko	**DOK-Z2**	76.4	1.6	78	0	0	0	1	0	1	2	18	2	**100**
Enagi	**ENG-1H**	77.6	0.4	80	0	0	0	1	2	0	3	16	1	**100**
Enagi	**ENG-1V**	74.3	0.7	75	0	0	0	0	1	0	1	22	2	**100**
Jimma	**JIM-1F**	52.2	4.8	58	0	0	0	8	2	0	10	30	2	**100**
Katcha	**KCH-1D**	66.5	3.5	70	0	0	0	0	1	1	2	28	0	**100**
Kutigi	**KUT-2A**	73.9	3.1	77	0	0	0	0	1	0	1	22	0	**100**
Kutigi	**KUT-2G**	87.0	0	87	0	0	0	0	0	0	0	12	1	**100**
Kutigi	**KUT-2J**	72.3	0.7	73	0	0	0	0	0	0	0	25	2	**100**
Kutigi	**KUT-2K**	72.5	1.5	74	0	0	0	1	2	0	3	22	1	**100**
Lemu	**LEM-1H**	74.5	1.5	76	0	2	2	2	0	0	2	18	2	**100**
Manigi	**MAN-1H**	74.3	0.7	75	0	1	1	1	1	0	2	22	0	**100**
Maraba	**MAR-1C**	74.5	1.5	77	0	1	1	0	0	2	2	20	0	**100**
Mangota	**MGT-1H**	79.2	0.8	80	0	0	0	0	0	0	0	20	0	**100**
Rabba	**RAB-1H**	70.3	3.7	74	0	0	0	2	0	1	3	22	1	**100**
Rabba	**RAB-1P**	74.7	2.3	77	0	1	1	2	2	0	4	18	0	**100**
Rafingora-Tanagi	**RAT-1P**	86.0	0	86	0	0	0	0	2	0	2	12	0	**100**
Wariku	**WAR-1H**	76.2	0.8	77	0	0	0	0	2	0	2	20	1	**100**

4.2.2.6 Massive sandstone (Sm) sub-facies

The massive sandstone (Sm) sub-facies composed mostly fine to medium, well sorted, angular to sub-rounded (minor), subhedral grains exhibiting point contact, suture and concavo-convex contact. Quartz is the most abundant component consisting of monocrystalline (Qm) and polycrystalline (Qp) varieties. Qm grains show markedly more abundant than the Qp while both shows straight extinction and undulose extinction features. There is comparatively less feldspar than the quartz and where observed, are usually altered (Figure 4.25e).

A sedimentary lithic fragment is predominant. Mica (muscovite) was observed as low concentrations. Matrix is present as a clay and silt while cement materials are composed of ferruginous mineral (limonite, goethite and hematite) and are seen often coatings around framework grains of form a rims encloses several framework grains.

The modal compositions of this sub-facies shows the ranges of values for; quartz (Q) from 78 to 85%, feldspar (F) 1 to 2%, total lithic/rock fragments (Lt) 0 to 2%, accessory minerals (1-2%) and matrix & cements (10-18%). The compositional values of the three end member varieties are; monocrystalline (Qm) and polycrystalline (Qp) ranges from 76.8 to 81.3% and 1.2 to 3.8%, potassic-feldspar (1-2%) and plagioclase-feldspar (0-1%), and sedimentary (Ls), volcanic (Lv) and metamorphic (Lm) with composition as 0-1%, 0-1% and 0-1% respectively (Table 4.3f).

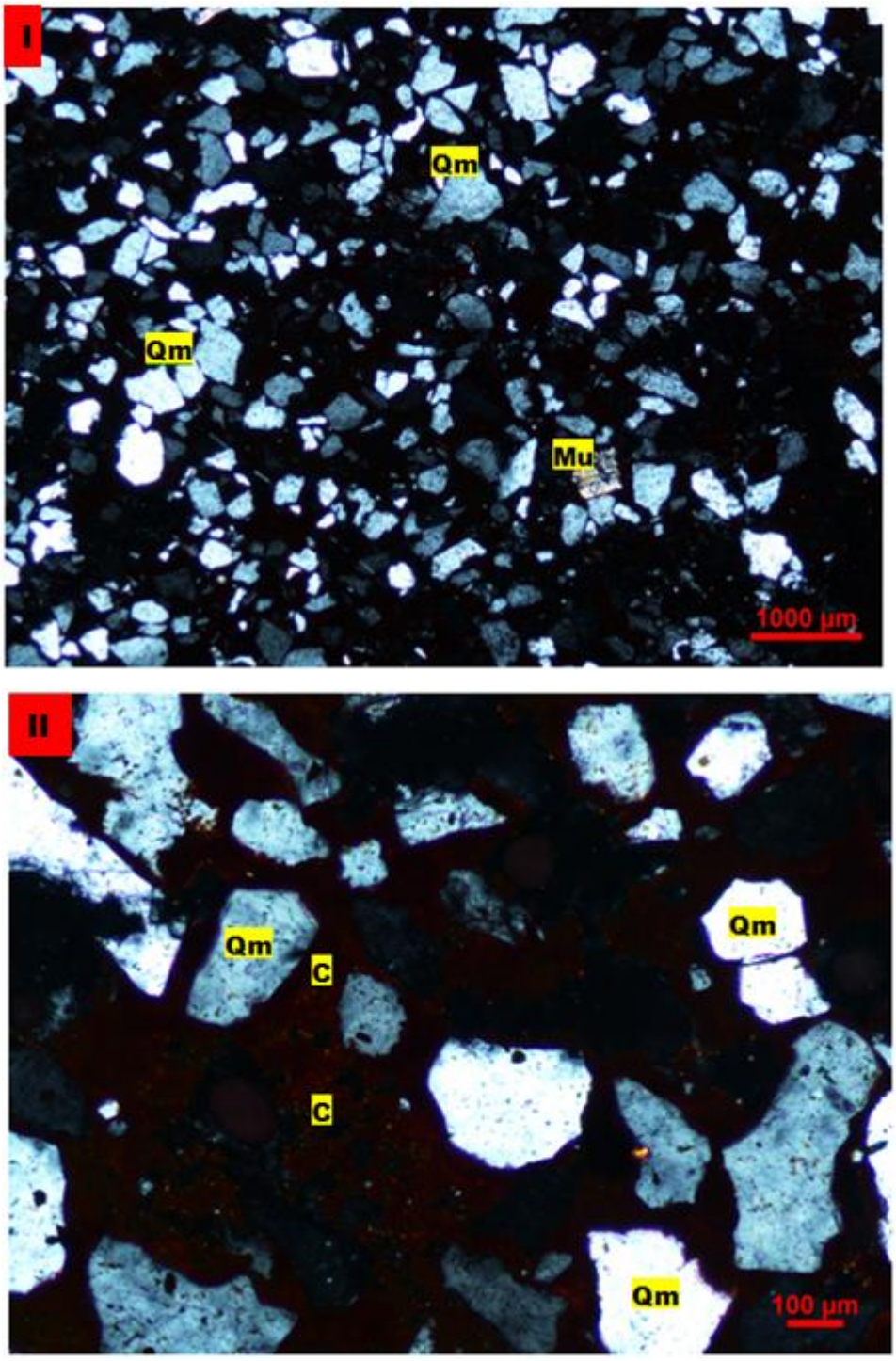


Figure 4.24e: Photomicrographs of typical horizontally stratified sandstone (Sh) sub-facies (PAT-1L) at PattiChin showing the mineral constituents; Qm (monocrystalline quartz), Mu (muscovite) and C (Cement). NB: (I) and (II) PPL.

Table 4.3f: Mineralogical composition of massive sandstone (Sm) sub-facies

Location	Sample Code	Quartz			Feldspar			Lithic/Rock Fragment				Matrix and Cement	Accessory Minerals	Total
		Qm	Qp	Qt	P	K	F	Ls	Lv	Lm	Lt			
Agaei	**AGE-1A**	78.4	1.6	80	0	1	1	0	1	1	2	16	1	**100**
Agaei	**AGE-1G**	79.1	2.9	82	0	2	2	0	0	0	0	14	2	**100**
Agaei	**AGE-1J**	81.3	1.7	83	1	1	2	0	0	0	0	14	1	**100**
Patti-Chin	**PAT-1L**	81.2	3.8	85	0	1	1	1	0	1	2	10	2	**100**
Rafingora-Tanagi	**RAT-1H**	76.8	1.2	78	0	1	1	1	1	0	2	18	1	**100**

4.2.2.7 Finely laminated, very-fine sandstone and mudstone (Fl) sub-facies

The finely laminated, very-fine sandstone and mudstone (Fl) sub-facies composed of mostly moderately well sorted, fine to medium (minor), angular to sub-rounded (dominant) grain compositions. The grains that made up the framework composition are mostly subhedral and appear as floating, straight and point contact.

Quartz grain with monocrystalline (Qm) and polycrystalline (Qp) varieties is the dominating mineral in the framework and it exhibits both straight and undulose characteristics (Figure 4.24f). Some quartz grains have inclusions of opaque and non-opaque minerals. The feldspars observed next in abundance after quartz and are typically colourless and are partly decomposed or altered whereas, lithic fragments are dominantly sedimentary lithoclasts, though observed in small amount. Mica (muscovite) appeared as platy and parallel extinction and has low concentrations compared to others. Ferruginous minerals (limonite, goethite and hematite) are the major identified cements and appears in some examined samples while clay cements observed in lesser amount, whereas, matrix present as a clay and silt.

The modal compositions of this sub-facies in table 4.3g shows the range of values as follows; quartz (Qt- 68-83%), total feldspar (F- 0-2%), lithic/rock fragments (Lt- 1-5%), accessory minerals (0-1%), and matrix & cements (12-26%). Also, the varieties of the three end member and their proportions are as follows; quartz: monocrystalline (Qm- 66.6-83%) and polycrystalline (Qp- 0-2.3%), feldspar: (potassic- 0-2%) and (Plagioclase- 0%) while total lithic/rock fragments (Lt) are sedimentary (Ls- 0-5%), volcanic (Lv- 0-3%) and metamorphic (Lm- 0-1%) varieties.

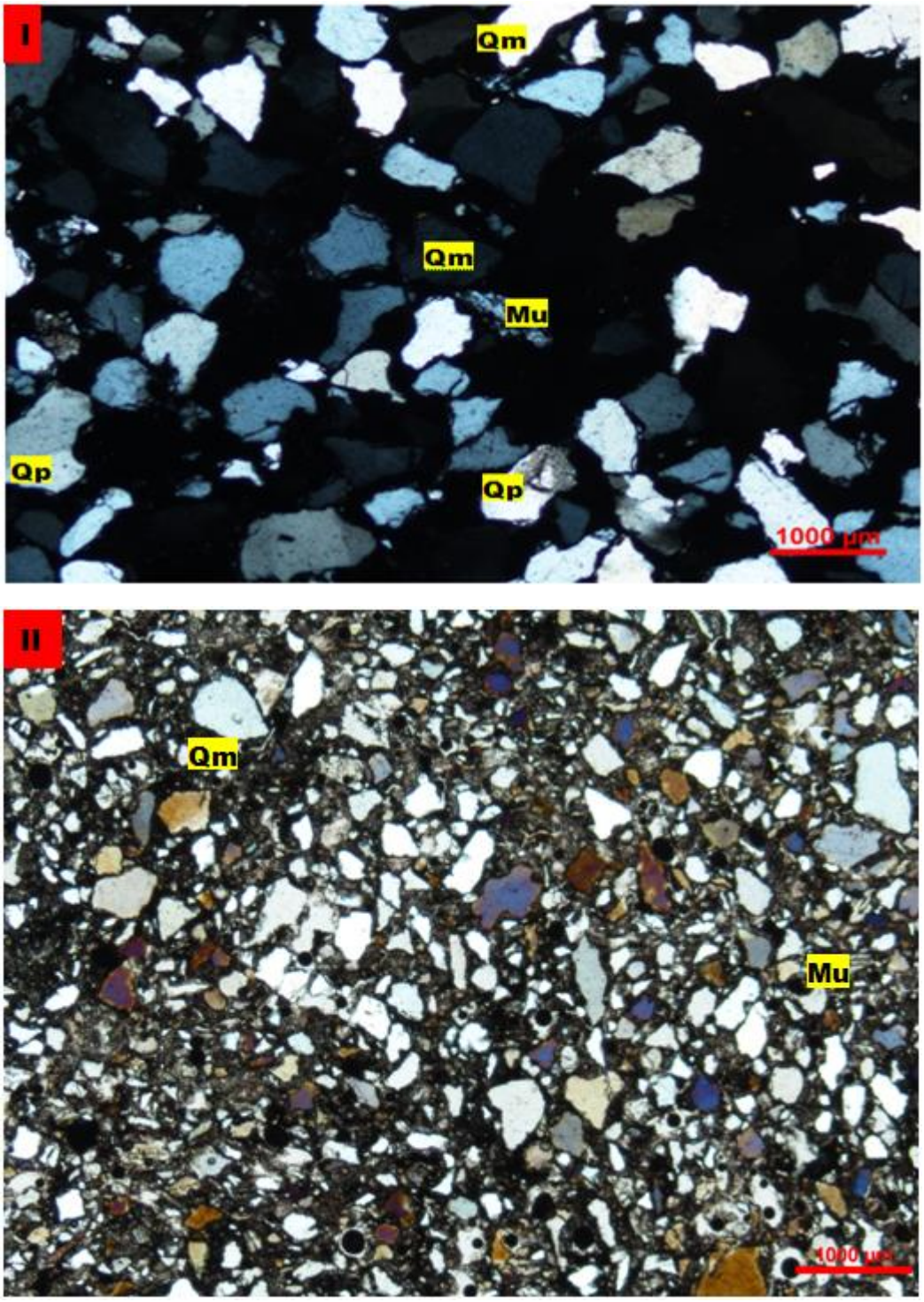


Figure 4.24f: Photomicrographs of typical horizontally stratified sandstone (Sh) sub-facies (BDA 1K) showing the mineral constituents; Qm (monocrystalline quartz), Qp (polycrystalline quartz) and MU (muscovite). NB: (I) and (II) XPL.

Table 4.3g: Mineralogical composition of laminated, very-fine sandstone and mudstone (Fl) sub-facies

Location	Sample Code	Quartz			Feldspar			Lithic/Rock Fragment				Matrix and Cement	Accessory Minerals	Total
		Qm	Qp	Qt	P	K	F	Ls	Lv	Lm	Lt			
Bida	**BDA-IK**	77.2	0.8	78	0	0	0	2	1	0	3	18	1	**100**
Jimma	**JIM-1B**	74.7	2.3	78	0	0	0	0	2	1	3	18	1	**100**
Katcha	**KAC-1V**	66.6	1.4	68	0	2	2	2	3	0	5	25	0	**100**
Katcha	**KAC-1X**	73.5	1.5	75	0	1	1	2	2	0	4	20	0	**100**
Katcha	**KAC-1Y**	80.0	0	80	0	2	2	0	1	0	1	16	1	**100**
Kuchi	**KCH-1F**	69.3	0	70	0	0	0	1	2	0	3	26	1	**100**
Manigi	**MAN-1D**	70.0	0	70	0	0	0	5	0	0	5	25	0	**100**
Patti-Chin	**PAT-1C**	82.0	0	82	0	2	2	0	2	2	4	12	0	**100**
Patti-Chin	**PAT-1H**	83.0	0	83	0	0	0	1	0	1	2	14	1	**100**
Rafingora-Tanagi	**RAT-1J**	72.3	0.7	73	0	1	1	2	1	0	3	22	1	**100**

4.2.2.8 Massive, very-fine sandstone and mudstone (Fm) sub-facies

The examined samples in this sub-facies shows characteristics of framework compositions of very fine-fine, sub-angular to sub-rounded, moderately well to well sorted grains. The framework grains contacts vary from floating (dominant) to straight and point with most of them showing alteration along the grain boundaries.

Like the previous sub-facies discussed above, quartz form the dominating framework mineral with both monocrystalline (higher) and polycrystalline (minor) grain varieties exhibited a colourless, straight and undulose characteristics (Figure 4.24g). Feldspars were observed in very low content and consisting of plagioclase grains that show various degrees of alteration. Lithic fragments are dominantly of sedimentary and volcanic clasts with minor metamorphic clast (Figure 4.2g). Mica occurs as detrital flakes and its concentration is low. The major observed mineral cements is iron-oxides while the minor is a clay minerals and matrix observed are in form of a clay which makes up more than the silt.

The framework composition (Table 4.3h) are as follows; quartz (Q) 68-85%), feldspar (F) 0-1%, lithic/rock fragments (L/R) 0-5%, mineral accessory (0-1%), matrix & cement (10-25%). The composition of monocrystalline (Qm) and polycrystalline (Qp) varieties ranges from 66.5 to 85% and 0 to 3.5% respectively, feldspar varieties also ranges in composition as; potassic (K) 0-1% and plagioclase (P) 0% whereas, lithic fragments (Lt) varieties have composition are as sedimentary (Ls- 0-3%), volcanic (Lv- 0-2%) and metamorphic (Lm- 0-2%).

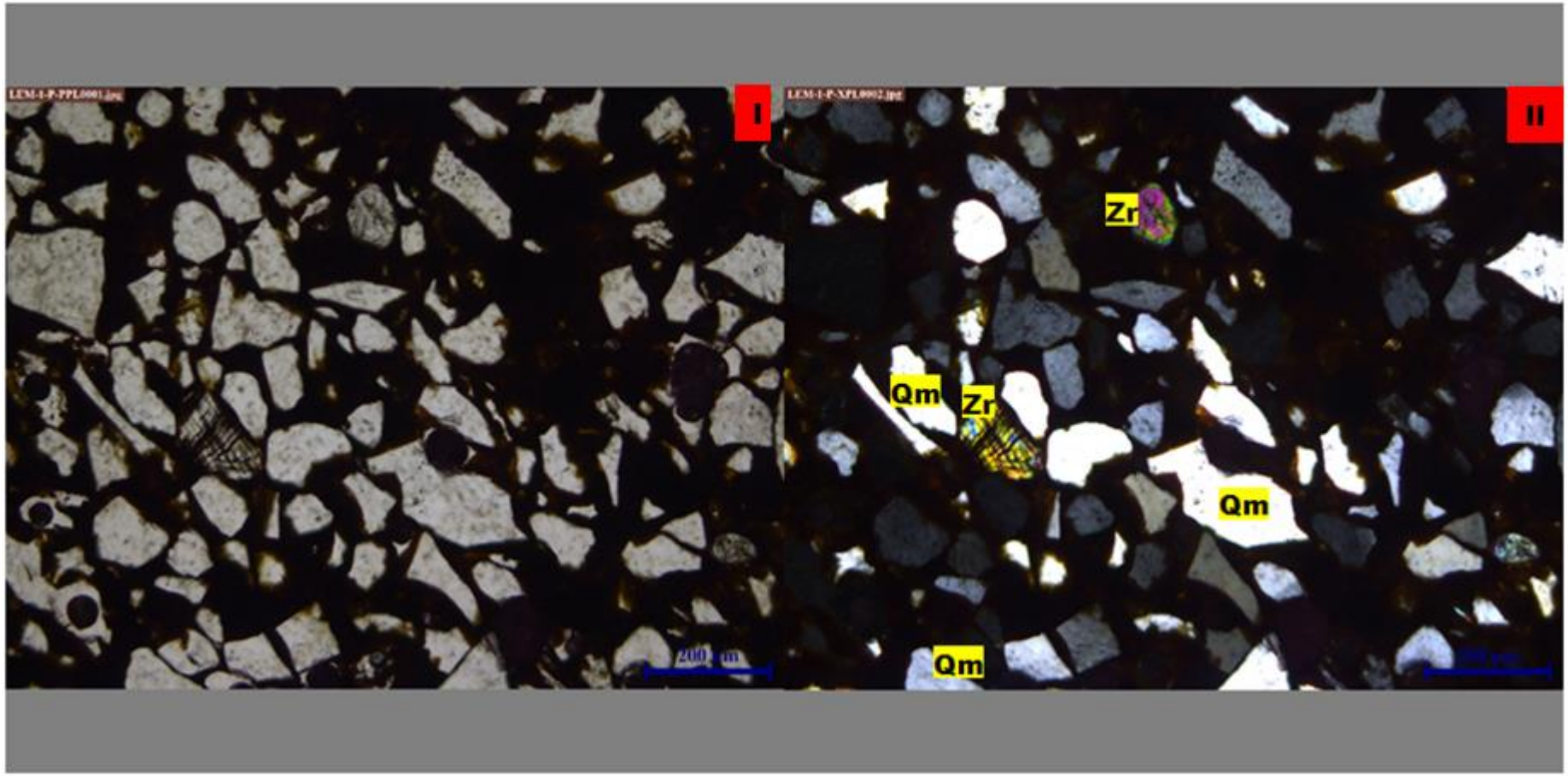


Figure 4.24g: Photomicrographs of typical finely laminated, very-fine sandstone and mudstone (Fl) sub-facies (LEM-1P) at Lemu showing the mineral constituents; Qm (monocrystalline quartz) and Zr (Zircon). NB: (I) PPL and (II) XPL.

Table 4.3h: Mineralogical composition of very-fine, massive sandstone and mudstone (Fm) sub-facies

Location	Sample Code	Quartz			Feldspar			Lithic/Rock Fragment				Matrix and Cement	Accessory Minerals	Total
		Qm	Qp	Qt	P	K	F	Ls	Lv	Lm	Lt			
Agbonna	**AGB-1E**	70.0	0	70	0	0	0	0	1	1	2	28	0	**100**
Dokko	**DOK-Z4**	73.5	1.5	75	0	0	0	0	2	0	2	22	1	**100**
Enagi	**ENG-1P**	84.2	0.8	85	0	0	0	1	0	2	3	11	1	**100**
Katcha	**KAC-1R**	84.2	0.8	85	0	0	0	0	0	0	0	15	0	**100**
Lemu	**LEM-1P**	85.0	0	85	0	0	0	1	1	2	4	10	1	**100**
Patti-Chin	**PAT-1K**	66.5	3.5	70	0	0	0	0	2	0	2	28	0	**100**
Rabba	**RAB-1D**	67.3	0.7	68	0	1	1	3	2	0	5	26	0	**100**

4.3 Heavy Minerals Description and Modal Composition

Heavy mineral analysis is one of the most sensitive and widely used technique in the determination of sandstone provenance (Morton and Hallsworth, 1994) because the composition of its fraction and its assemblages is chiefly controlled by the mineralogical composition of the source region (Morton, 1991; Amireh, 1991; Caironi *et al*., 1996; Dewey and Mange, 1999; Kutterolf, 2001; Wozazek, 2001; Diener, 2002).

Sixty-two (62) samples were selected based on the sub-facies for the study. Eight non-opaque types of heavy minerals were observed and focused on for description. Heavy mineral index (HMI) and ratio values of ultra-stable minerals; zircon, tourmaline and rutile were also determined for application in further interpretations. Summary of modal composition (mineral constituents) is presented in Appendix V, tables I-IX while percentages of individual minerals are presented in tables 4.4a-4.4i. These results will give the first insight into the heavy mineral spectrum and also provide basis for further data treatment. It is noted from the result that all the sub-facies share common mineral assemblages but there are distinct differences in their relative abundances.

4.3.1 Massive, matrix-supported conglomerate (Gmm) sub-facies

The matrix-supported, massive conglomerate (Gmm) sub-facies composed of more opaque than non-opaque constituents. The opaque varieties occur mostly as sub-rounded to sub-angular grains and were suggested to be iron-oxide varieties (goethite, hematite and limonite) due to the reddish and brownish coloration under polarizing microscope. The non-opaque varieties includes; zircon, tourmaline, rutile, sillimanite, staurolite, garnet, muscovite and biotite.

Zircon grain types ranges from colorless to brown, sub-hedral to anhedral (sub-angular to sub-rounded), equant to prismatic and generally exhibit crystal outline with dark boundaries. Inclusion and concentric type zoning are common features while few with xenocrystic cores were also observed. In some occasions, opaque minerals were also present as inclusions within the non-opaques. Some zircon grains were observed fractured. Tourmaline generally exhibit sub-angular grains with yellowish variety as the dominant while brownish types are few while rutile occurs as elongated, prismatic, sub-rounded grains having deep red and orange colour with dark boundaries. Staurolite is one of the important metamorphic minerals present having straw yellow colouration and occurs as angular to sub-angular grains with sub-conchoidal fractures. Garnet is characterized by its sub-rounded shape, conchoidal fracture and etches features. Muscovite, olivine and biotite were observed in lesser proportions.

Calculated modal analysis shows that total opaque is 53.0% while non-opaque minerals are 47.0% (Appendix V, table I). The modal compositions of non-opaque varieties were then recalculated to 100% to get the value of individual minerals (Table 4.4a). Also, the calculated HMI values; Zircon-Tourmaline-Rutile index (ZTR), Rutile-Zircon index (RZi), Staurolite-Tourmaline index (STi) and Density Index (Di) are also present on the same table.

Table 4.4a: Non-opaque heavy minerals composition (%) and calculated Heavy Mineral Index (HMI) values of massive, matrix supported conglomerates (Gmm) sub-facies.

Location	Sample Code	Non-Opaque								ZTR	RZi	STi	D*i*
		Zr	To	Ru	St	Bi	Mu	Si	Gr				
Dokko	**DOK-1C**	52.60	7.50	14.00	6.80	3.80	1.50	4.30	7.50	74.10	22.19	47.55	1.13

4.3.2 Crudely bedded Conglomerate (Gh) sub-facies

The crudely bedded conglomerate (Gh) sub-facies also contain more opaque and less non-opaque grain varieties. The opaque minerals constitute higher proportions and occur mostly as sub-rounded to sub-angular grains and were suggested to be iron-oxide varieties while the non-opaque varieties which constitutes the lesser proportions includes; zircon, tourmaline, rutile, sillimanite, staurolite, garnet, muscovite and biotite.

The zircon varieties ranges from euhdral to subhedral, sub-angular to sub-rounded, prismatic, colorless to brownish, clear to corroded and generally contains inclusions (zircon and sillimanite), dark boundaries and concentric zoning with few with xenocrystic cores (Figure 4.25a). Tourmaline grain varieties are mostly irregular, prismatic to needle-like, darkish to deep blue and golden to yellowish type. Rutile mineral grain types include; euhedral, conchoidal and pitting, sub-angular to sub-rounded, brownish to deep red types are common while few knee-shaped types are observed. There is a low occurrence of other opaque minerals compared to the ultra-stable minerals.

The modal composition and the recalculated (%) values of non-opaque grains with their heavy mineral index (HMI) values are presented in table 4.4b.

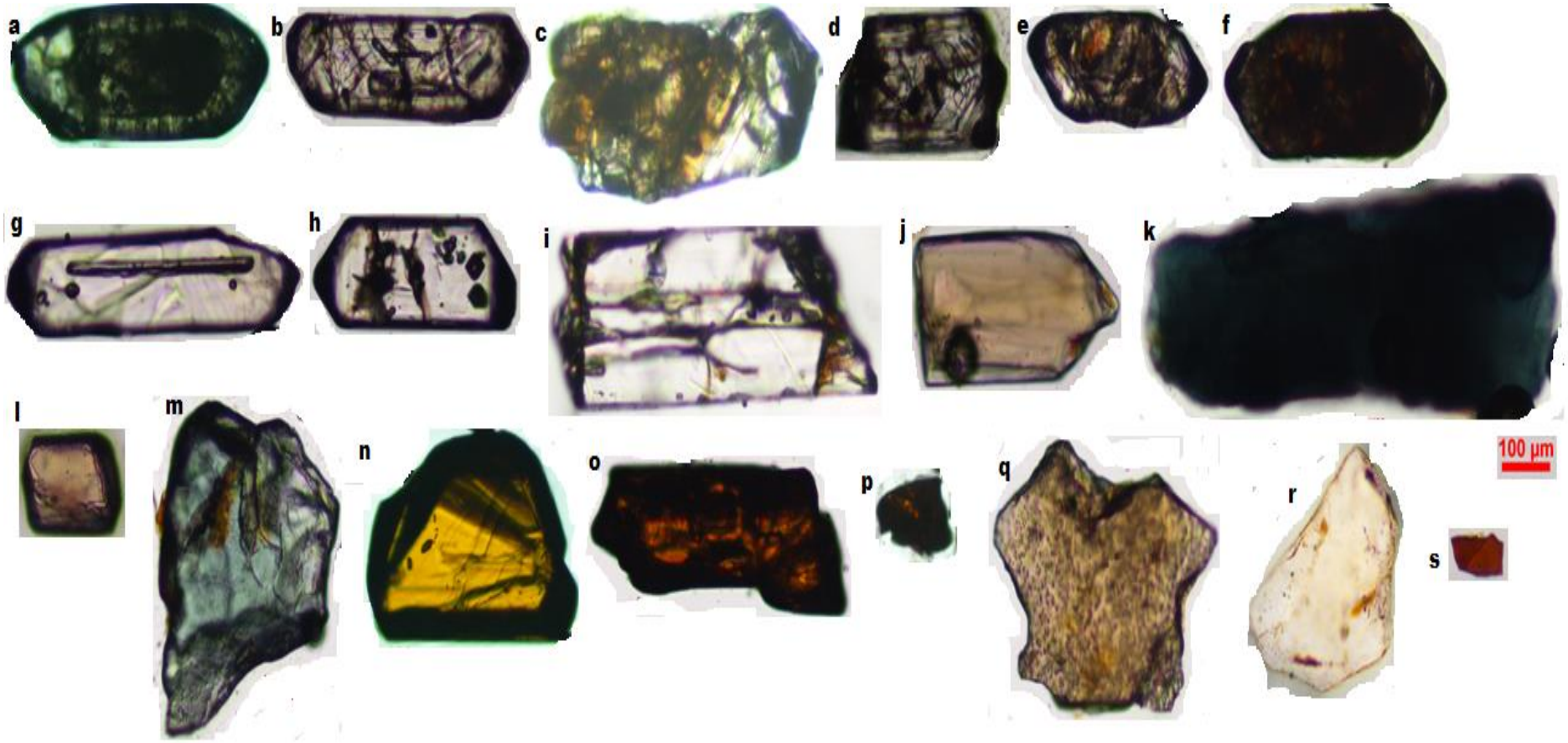


Figure 4.25a: Different heavy minerals types observed (under crossed nicol) in crudely bedded conglomerate (Gh) sub-facies; (a-i) Zircon (xenocrystic core, zoning, corroded, sillimanite inclusion and dark boundary), (j-l) Tourmaline (light brownish to bluish), (m-o) Rutile (bluish, golden, deep red colored, conchoidal and knee-shaped), (p and s) Biotite (brownish), (q) garnet and (r) Staurolite.

Table 4.4b: Non-opaque heavy minerals composition (%) and calculated Heavy Mineral Index (HMI) of crudely bedded conglomerate (Gh) sub-facies

Location	Sample Code	Non-Opaque								ZTR	RZ*i*	STi	D*i*
		Zr	To	Ru	St	Bi	Mu	Si	Gr				
Bida	**BDA-1J**	49.50	11.90	29.70	4.95	0.99	1.98	0.99	0.00	91.09	37.50	29.38	1.49
Dokko	**DOK-1G**	29.12	9.71	43.69	12.14	0.49	0.97	1.46	2.43	82.51	60.01	54.56	1.26
Dokko	**DOK-1S**	10.00	3.00	14.00	0.00	0.00	1.00	1.00	1.00	90.32	60.00	0.00	3.39
Lemu	**LEM -1K**	1.54	38.46	30.77	18.46	1.54	4.62	0.00	4.62	70.76	94.23	32.43	1.08
Lemu	**LEM-1B**	34.71	22.32	26.79	8.93	0.89	1.79	1.79	1.79	84.81	42.86	28.58	1.96
Rabba	**RAB-1C**	34.71	21.43	28.57	3.57	0.00	1.79	3.57	4.36	84.71	44.45	14.28	0.96

4.3.3 Crudely stratified Sandstone (Se) sub-facies

The crudely stratified sandstone (Se) sub-facies also composed of higher percentage of opaque than non-opaque varieties. Among opaque minerals, the commonly recognized includes; goethite, hematite and limonite based on their brownish, reddish and yellowish brown colouration respectively under polarizing microscope (Figure 4.25b). The non-opaque constitutes bulk zircon, tourmaline, and rutile while staurolite, biotite, muscovite sillimanite and garnet were found in lesser amount. Most of the heavy minerals are angular to sub-angular or rounded to sub-rounded.

Among the non-opaques; zircon grains are usually subhedral, prismatic, angular to sub-angular form with crystal outline and exhibit colorless and brownish coloration with few observed fractured and corroded with xenocrytic cores. Inclusion and concentric type zoning are also common features in some grains. Tourmaline occurs as prismatic, irregular, subhedral grains. The greenish yellow variety is dominant while other varieties are rare. Rutile occurs as equant, choncoidal, sub-rounded grains having deep red and orange color with dark boundaries. Other minerals; staurolite, biotite, muscovite, sillimanite and occurs as in few proportion as subordinate.

The values of recalculated percentage of the non-opaque with their heavy mineral index (HMI) values for further discussion in the later chapters are presented in table 4.4c.

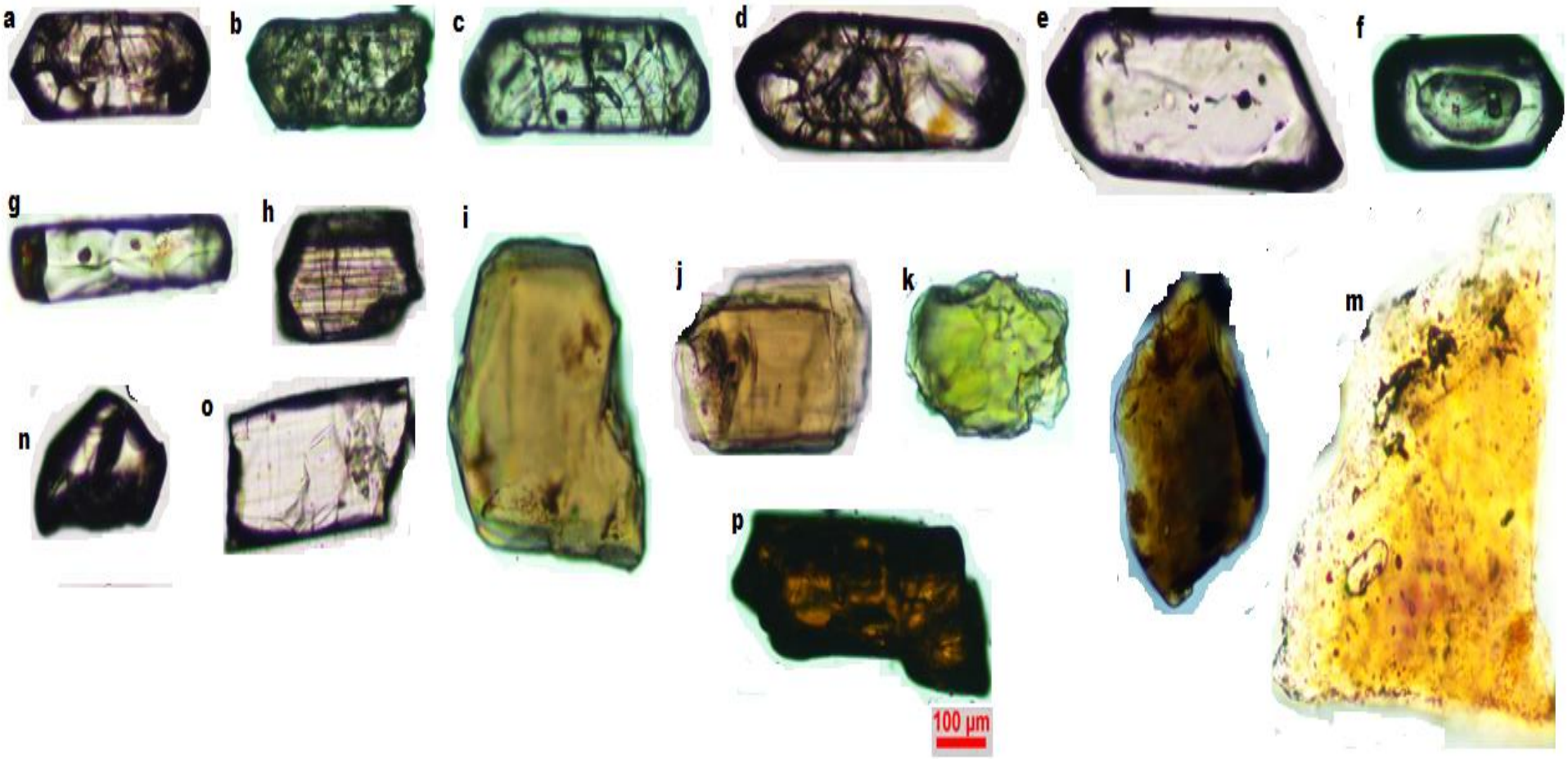


Figure 4.25b: Different heavy minerals types observed (under crossed nicol) in crudely stratified sandstone (Se) sub-facies; (a-h) Zircon (zoning, weathered and corroded, xenocrystic core, inclusion and dark boundary), (j-l) Tourmaline (greenish, light brownish and yellowish), (m) Staurolite (yellowish), (n-p) Rutile (dark brownish and deep brownish knee-shaped).

Table 4.4c: Non-opaque heavy minerals composition (%) and calculated Heavy Mineral Index (HMI) of crudely stratified sandstone (Se) sub-facies

Location	Sample Code	Non-Opaque								ZTR	RZi	STi	D*i*
		Zr	To	Ru	St	Bi	Mu	Si	Gr				
Baro	**BAR-1E**	2.00	6.00	10.00	1.00	2.00	0.00	0.00	0.00	84.71	83.33	14.29	6.67
Baro	**BAR-1L**	17.75	17.75	53.25	4.73	1.18	1.78	0.00	3.55	88.76	74.00	21.04	1.30
Bida	**BDA-1H**	4.55	9.09	4.55	44.45	4.55	22.73	0.00	9.09	18.19	50.00	83.33	4.55
Bida	**BDA-1Q**	11.11	29.63	18.52	14.81	11.11	14.81	0.00	0.00	59.27	62.50	33.33	2.22
Dokko	**DOK-1A**	22.73	27.27	36.36	4.54	1.81	2.73	0.91	3.64	86.37	61.53	14.27	2.36
Dokko	**DOK-1N**	4.66	30.19	37.74	13.21	3.77	4.66	0.00	3.77	73.59	86.96	30.44	3.02
Dokko	**DOK-1P**	16.00	20.00	14.00	0.00	8.00	0.00	6.00	2.00	76.12	48.39	0.00	2.84
Jimma	**JIM-1E**	24.25	14.15	24.25	14.15	10.10	7.07	0.00	2.02	64.66	50.00	50.00	2.22
Lemu	**LEM-1C**	27.40	23.97	34.25	6.85	1.37	3.42	1.37	1.37	84.62	54.56	22.23	1.37
Lemu	**LEM-1E**	23.81	38.10	28.57	4.76	0.00	2.86	0.95	0.95	90.48	54.54	11.11	1.71
Lemu	**LEM-1G**	30.49	24.39	28.05	3.66	2.44	2.44	2.44	6.10	82.92	47.92	13.05	2.26
Lemu	**LEM-1M**	9.52	47.62	23.81	9.52	4.76	4.76	0.00	0.00	80.96	71.44	16.66	1.90

4.3.4 Planar cross-stratified sandstone (Sp) sub-facies

The heavy mineral analysis of the planar cross-stratified sandstone (Sp) sub-facies like those sub-facies discussed above composed more opaque constitutes than non-opaque varieties. The constituted opaque minerals are suggested to be iron-oxide rich due to their colorations; dark, brownish and yellowish under microscope (Figure 4.25c). The non-opaque varieties includes; zircon, tourmaline, rutile, sillimanite, staurolite, garnet, muscovite and biotite with the ultra-stable constituents with more concentrations than others.

Zircon varieties exhibit euhedral to subhedral, equant to prismatic, colorless to brownish with dark boundaries. Fractured and corroded types and few with inclusions (zircon and sillimanite), and concentric zoning are also observed. Tourmaline grains are mostly irregular, angular, needle-like, dark with shades of blue and yellowish varieties while the rutile grain types exhibit subhedral, sub-rounded, choncoidal, brownish to deep coloration and sillimanite are generally colorless with prismatic to needle-like shape. Other observed opaque minerals occur in low concentration.

The recalculated (%) values of non-opaque grains with their calculated heavy mineral index (HMI) values are presented in table 4.4d.

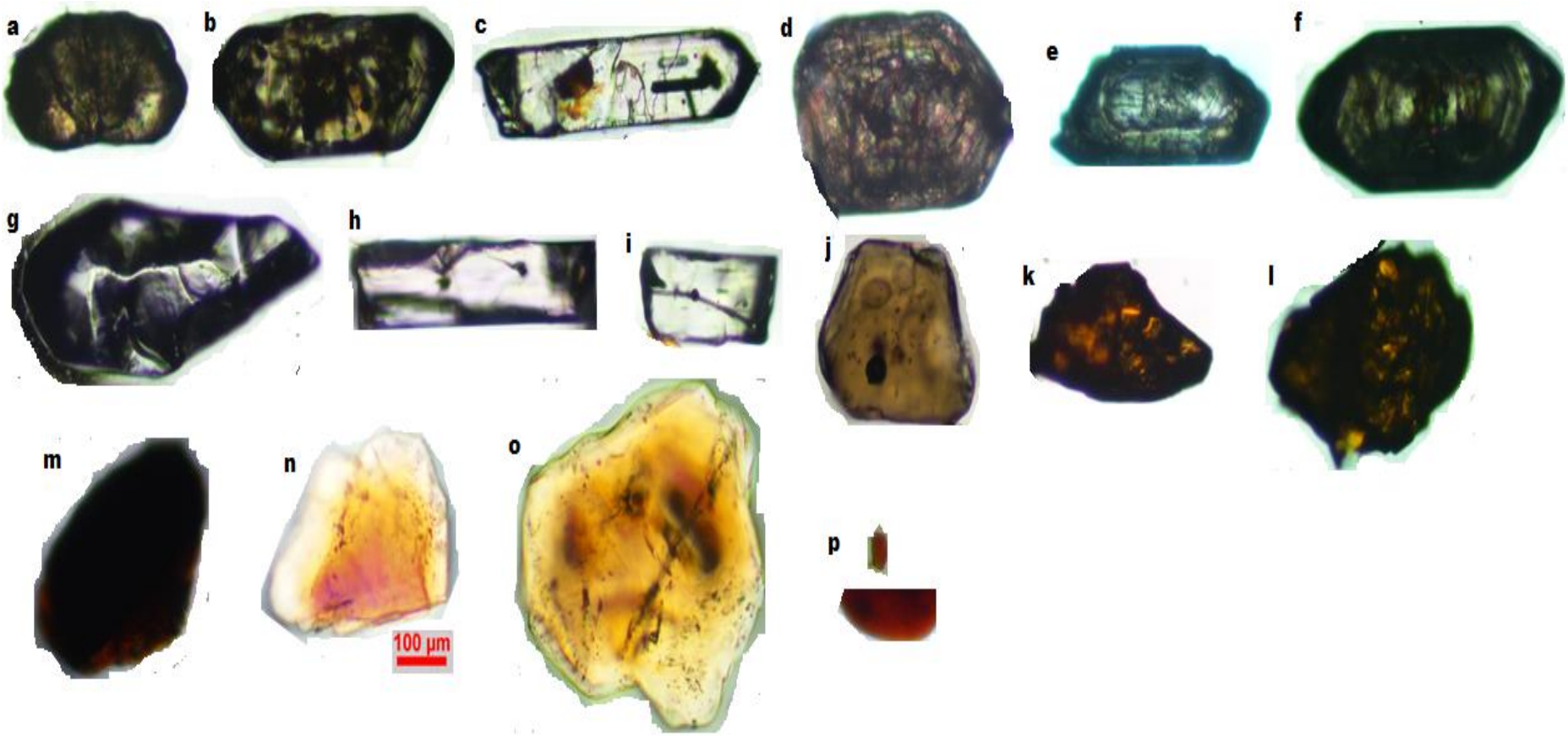


Figure 4.25c: Different heavy minerals types observed (under crossed nicol) in the planar cross-stratified sandstone (Sp) sub-facies; (a-f) Zircon (weathered, pitted and etched, corroded, inclusion, xenocrystic core and zonning), (g-j) Tourmaline (dark, bluish and yellowish), (k & l), Rutile (brownish), (m-o) Staurolite (brownish and yellowish) and Biotite (brownish).

Table 4.4d: Non-opaque heavy minerals composition (%) and calculated Heavy Mineral Index (HMI) of planar stratified sandstone (Sp) sub-facies

Location	Sample Code	Non-Opaque								ZTR	RZi	STi	D*i*
		Zr	To	Ru	St	Bi	Mu	Si	Gr				
Bida	**BDA-1C**	14.63	17.07	24.39	29.27	4.88	7.32	0.00	2.44	56.09	62.51	63.16	2.93
Bida	**BDA-1E**	28.46	12.20	40.65	9.76	3.25	2.44	1.63	1.63	81.29	58.82	44.44	0.89
Bida	**BDA-1P**	16.67	24.00	20.83	12.50	8.33	12.50	4.17	0.00	62.50	54.55	33.33	4.42
Dokko	**DOK-1R**	38.83	16.99	19.42	9.71	7.28	4.85	2.43	0.49	74.24	33.34	36.37	3.16
Dokko	**DOK-1V**	14.87	9.52	54.56	9.52	3.17	3.17	1.59	1.59	80.96	77.78	50.00	3.81
Jimma	**JIM-1Y**	14.00	10.00	24.00	30.00	0.00	10.00	0.00	10.00	50.00	62.50	74.00	4.50
Lemu	**LEM-1R**	11.11	47.62	23.81	4.76	3.17	3.17	1.59	4.76	82.55	68.18	9.09	2.54
Mangota	**MGT-1C**	50.00	20.00	84.00	0.00	2.00	1.00	4.00	3.00	93.37	62.96	0.00	3.92
Patti-Chin	**PAT-1J**	27.27	22.73	36.36	6.36	1.82	2.73	1.82	0.91	86.36	57.14	21.86	2.73
Rabba	**RAB-1E**	7.00	4.00	34.00	4.00	2.00	2.00	4.00	2.00	74.81	83.33	50.00	4.00
Tanagi	**TAN-1A**	30.17	17.24	38.79	3.45	1.72	4.31	4.31	0.00	86.21	56.25	16.67	0.95

4.3.5 Rippled cross-stratified sandstone (Sr) sub-facies

The rippled cross-stratified sandstone (Sr) sub-facies constitutes more opaque constitutes than non-opaque varieties like others. The opaque comprises of iron-oxide rich minerals; goethite, hematite and limonite based on their on their brownish, reddish and yellowish brown colouration respectively whereas non-opaque varieties comprises of zircon, tourmaline, rutile, sillimanite, staurolite, garnet, muscovite and biotite.

Varieties of zircon were observed; euhedral to subhedral in shape, equant to prismatic in form with varying coloration; colorless to brownish (with dark boundaries). Different types; fractured, corroded, concentric zoned and those with inclusions of other non-opaque minerals especially zircon and sillimanite were observed. Tourmaline grains were mostly irregular few angular, needle-like, darkish with shades of blue and yellowish colorations. The rutile grains are choncoidal, knee shaped, brownish to deep reddish colored while sillimanite are generally colorless with prismatic to needle-like shape. Other observed non-opaque minerals occur in low concentration.

The values of the non-opaque constituents were recalculated into percentage (%) and presented in table 4.4e. The calculated heavy mineral index (HMI); ZTR, RZ, ST and Di are presented together on the same table.

Table 4.4e: Non-opaque heavy minerals composition (%) and calculated Heavy Mineral Index (HMI) of cross-stratified sandstone (Sr) sub-facies

Location	Sample Code	Non-Opaque								ZTR	RZi	STi	D*i*
		Zr	To	Ru	St	Bi	Mu	Si	Gr				
Agbonna	**AGB-1J**	14.00	54.00	44.00	0.00	0.00	2.00	3.00	2.00	94.26	74.00	0.00	3.28
Lafiagi	**LAF-1B**	2.00	4.00	4.00	1.00	3.00	0.00	1.00	0.00	68.75	66.67	16.67	3.44
Manigi	**MAN-1F**	7.00	4.00	34.00	4.00	2.00	2.00	4.00	2.00	74.81	83.33	50.00	4.00
Rabba	**RAB-1P**	10.00	14.00	40.00	0.00	0.00	0.00	2.00	3.00	92.86	80.00	0.00	4.57

4.3.6 Horizontally stratified sandstone (Sh) sub-facies

Horizontally stratified sandstone (Sh) sub-facies have angular to sub-angular and sub-rounded forms of both non-opaque and opaque minerals as it constituents. The opaque minerals are also suggested to be iron-oxides rich varieties because of the coloration under the microscope while non-opaque varieties includes; zircon, tourmaline, rutile, staurolite, muscovite, biotite, sillimanite and garnet.

Varieties of zircon are observed as euhedral to subhedral, prismatic with dark boundaries and it is characterized by colorless, brownish, pale pink colors and zoning. Few grains with fracture and inclusion (with tourmaline) were also observed. Tourmaline types includes; prismatic, sub-angular grains showing color variations; colorless to brown and yellowish brown. Rutile varieties observed includes; conchoidal, etched, sub-rounded, and brownish to reddish brown color (Figure 4.25d). The sillimanite observed is prismatic and colorless.

The recalculated modal composition of the non-opaque constituents was recalculated to 100 percentages and presented in table 4.4f. Values of calculated heavy mineral index (HMI) are also presented.

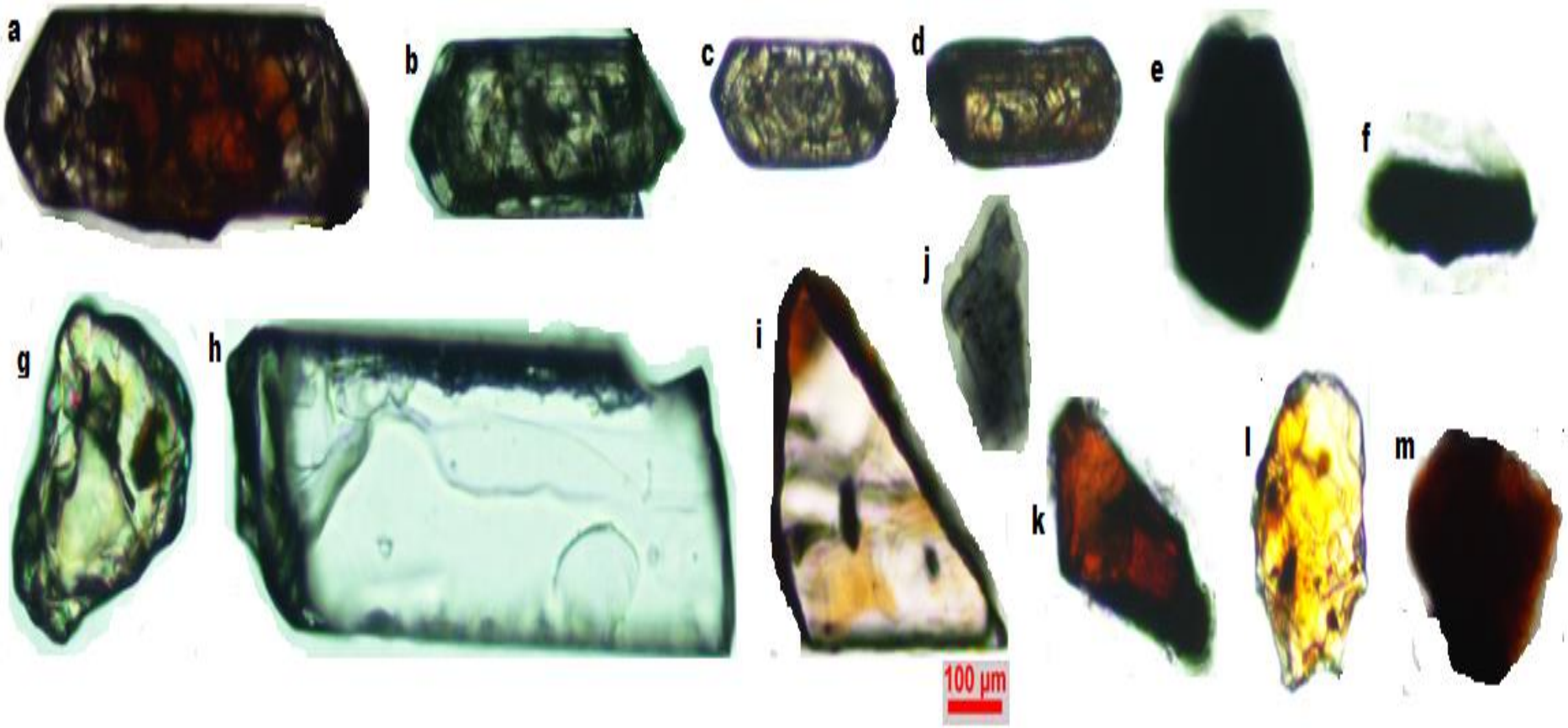


Figure 4.25d: Different heavy minerals types observed (under crossed nicol) in the horizontally stratified sandstone (Sh) sub-facies; (a-d) Zircon (weathered, pitted and etched, corroded, xenocrystic core and zonning), (e & i) Tourmaline (golden, light and red stained colored), (k), Rutile (brownish), (l & m) Staurolite (brownish and yellowish).

Table 4.4f: Non-opaque heavy minerals composition (%) and calculated Heavy Mineral Index (HMI) of horizontally stratified sandstone (Sh) sub-facies

Sample Code	Non-Opaque								ZTR	RZi	STi	D*i*
	Zr	To	Ru	St	Bi	Mu	Si	Gr				
BDA-1B	22.00	26.00	30.00	10.00	2.00	8.00	0.00	2.00	78.00	57.69	27.78	4.40
BDA-1F	32.14	10.71	24.00	17.86	3.57	7.14	0.00	3.57	67.86	43.75	62.51	1.79
BDA-1M	9.68	22.58	19.35	24.81	6.45	16.13	0.00	0.00	51.61	66.66	53.34	1.94
BDA-1S	4.26	13.16	39.47	18.42	10.53	13.16	0.00	0.00	57.89	88.24	58.33	3.68
DOK-1T	30.81	23.70	26.07	9.48	4.74	2.37	0.95	1.90	80.56	44.83	28.57	2.84
JIM-1A	24.59	19.67	24.59	24.59	3.28	3.28	0.00	0.00	68.85	50.00	54.56	3.11
JIM-1Q	28.17	28.17	34.21	4.23	0.00	2.82	1.41	0.00	91.54	54.55	13.06	7.75
JIM-1V	23.58	14.15	37.74	9.43	0.00	4.72	9.43	0.94	74.48	61.55	39.99	2.36
KUT-2A	2.75	32.11	54.05	4.59	0.00	1.83	1.83	1.83	89.92	94.24	12.51	3.67
KUT-2E	4.13	38.46	38.46	12.82	0.00	4.13	0.00	0.00	82.05	88.23	24.00	2.05
KUT-2J	0.00	9.09	44.45	18.18	0.00	9.09	9.09	9.09	54.55	100.00	66.67	3.64
LEM-1A	1.00	2.00	7.00	0.00	0.00	1.00	1.00	1.00	76.92	87.50	0.00	2.31
LEM-1H	22.73	19.70	37.88	10.61	1.52	3.03	3.03	1.52	80.29	62.50	34.00	2.12
LEM-1Q	12.99	32.47	38.96	6.49	1.30	2.60	2.60	2.60	84.41	74.00	16.66	1.30
PAT-1B	30.12	12.05	38.55	12.05	1.20	2.41	2.41	1.20	80.73	56.14	50.00	3.31
PAT-1G	0.00	20.00	20.00	40.00	0.00	20.00	0.00	0.00	40.00	100.00	66.67	18.00

4.3.7 Massive sandstone (Sm) sub-facies

The heavy minerals of the massive sandstone (Sm) sub-facies consist of more opaque with its constituent mainly as goethite, hematite and limonite as recognized by their brownish, reddish and yellowish colouration under light microscope. The non-opaque minerals; zircon, tourmaline, rutile, staurolite, sillimanite, biotite, muscovite and garnet are less in proportions than the opaque minerals.

Amongst the non-opaque minerals, zircon exhibit subhedral, elongate, angular to sub-angular with brownish to corroded colouration (Figure 4.25e). Few grains with inclusion were observed while zoning were less commonly observed. Tourmaline grains are anhedral, angular and occasionally wedge shaped and is light brown in color while rutile grains are brown and reddish in color mostly sub-rounded and exhibit conchoidal and etched form. Other non-opaque minerals occur in lesser proportions.

The results of recalculated modal analysis and the calculated heavy mineral index (HMI) values for this sub-facies; ZTR, RZi, STi and Di are presented in table 4.4g.

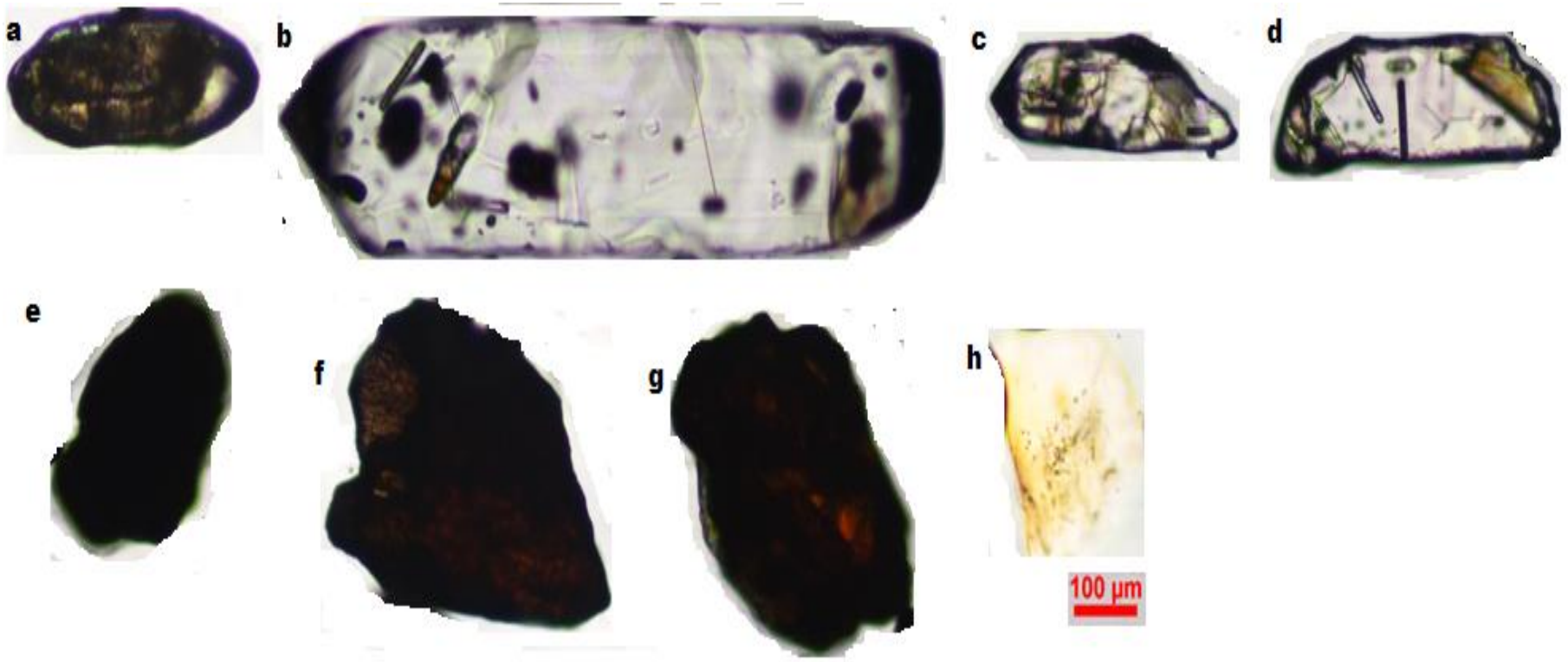


Figure 4.25e: Different heavy minerals types observed (under crossed nicol) in the massive sandstone (Sm) sub-facies; (a-d) Zircon (xenocrystic cored, corroded, weathered, pitted and etched dark boundary with inclusion), (e) Tourmaline (brownish and bluish), (f & g) Rutile (irregular brownish), (h) Staurolite (yellowish).

Table 4.4g: Non-opaque heavy minerals composition (%) and calculated Heavy Mineral Index (HMI) of massive sandstone (Sm) sub-facies

Location	Sample Code	Non-Opaque								ZTR	RZi	STi	D*i*
		Zr	To	Ru	St	Bi	Mu	Si	Gr				
Lemu	**LEM-1D**	24.32	28.48	34.81	4.43	1.27	1.90	1.90	1.90	88.60	57.89	13.46	1.61
Lemu	**LEM-1L**	26.65	31.35	37.62	0.94	0.63	0.63	1.57	0.63	94.60	58.53	2.91	0.95
Patti-Chin	**PAT-1D**	27.03	13.51	27.03	18.92	2.70	8.11	2.70	0.00	67.57	50.00	58.34	2.97

4.3.8 Laminated, very-fine sandstone and mudstone (Fl) sub-facies

The laminated, very-fine sandstone and mudstone (Fl) sub-facies composed higher proportion of the opaque minerals than non-opaque minerals. The opaque minerals are observed to be composed of iron-oxides minerals like goethite, hematite and limonite while zircon, tourmaline, rutile, staurolite, biotite, muscovite, sillimanite and garnet made up the non-opaque assemblage. Most of these heavy minerals are angular to sub-angular or rounded to sub-rounded (Figure 4.25f).

A zircon grain occurs mostly as subhedral, equant to elongated, prismatic, colorless to brownish colored with dark boundaries. Few grains show concentric zoning, corroded. Some also exhibit xenocrystic cores and are clouded with inclusions (zircon and sillimanite). Tourmaline varieties show pale green to yellowish brown pleochroism and they are characterized with cleavage. Occasionally, subhedral and rounded grains are also observed. The rutiles were observed as subhedral, sub-rounded grains and occasionally they are sub-rounded. The grains are reddish brown and darkish brown.

The recalculated modal analysis (%) of this sub-facies with its calculated heavy mineral index (HMI) is presented in table 4.4h.

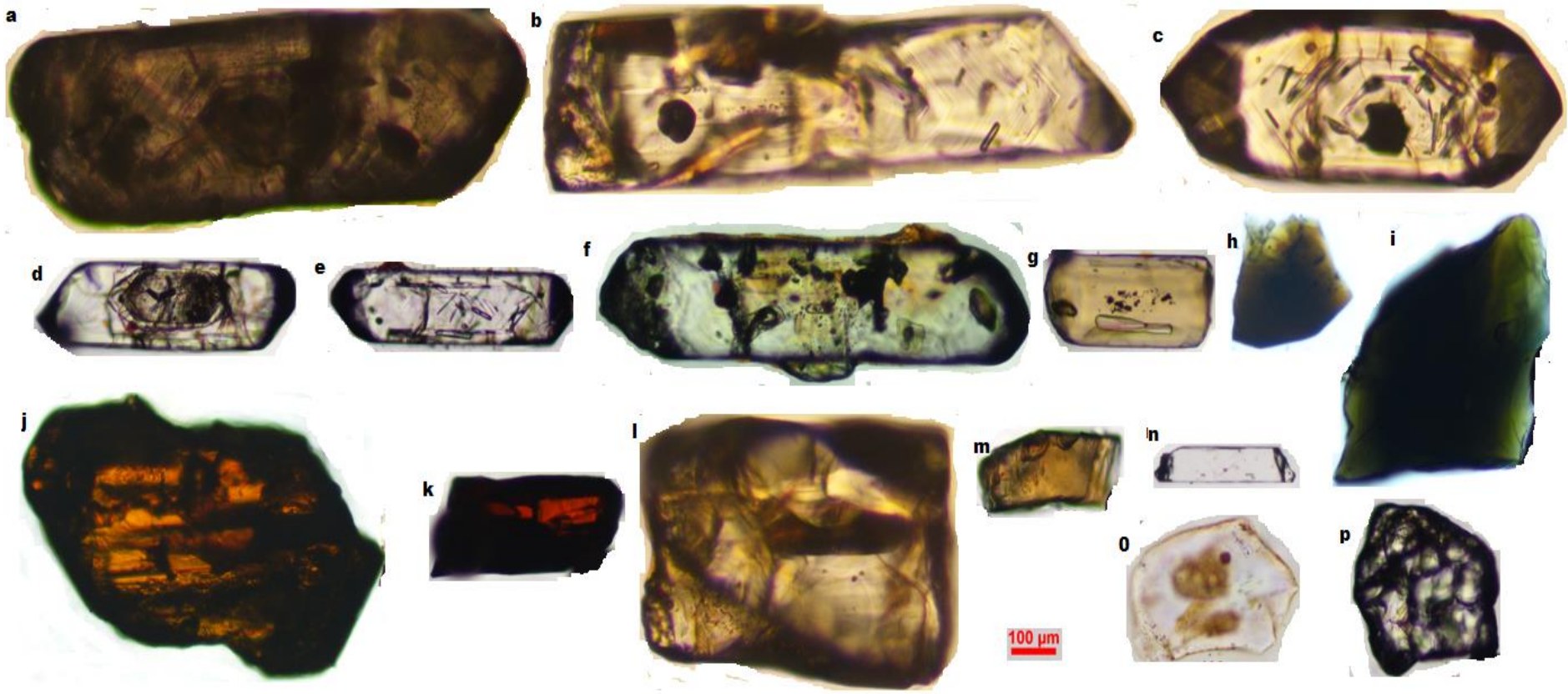


Figure 4.25f: Different heavy minerals types observed (under crossed nicol) in the laminated, very-fine sandstone and mudstone (Fl) sub-facies; (a-f) Zircon (weathered & corroded, zoned, xenocrystic core, pitted and etched with inclusion), (g-i) Tourmaline (golden and bluish), (j-m) Rutile (brownish, reddish and golden colored), (n & o) Staurolite (light colored) and garnet (bulbous).

Table 4.4h: Non-opaque heavy minerals composition (%) and calculated Heavy Mineral Index (HMI) of finely laminated sandstone and mudstone (Fl) sub-facies

Location	Sample Code	Non-Opaque								ZTR	RZi	STi	D*i*
		Zr	To	Ru	St	Bi	Mu	Si	Gr				
Bida	**BDA-1K**	14.38	23.08	23.08	14.38	14.38	0.00	7.69	0.00	61.55	60.01	39.99	7.69
Dokko	**DOK-1D**	24.00	10.00	30.00	0.00	0.00	2.00	2.00	0.00	94.20	54.55	0.00	4.35
Dokko	**DOK-1H**	1.00	7.00	8.00	2.00	10.00	0.00	2.00	0.00	53.33	88.89	22.22	1.67
Dokko	**DOK-1Z**	10.00	4.00	20.00	0.00	2.00	1.00	1.00	2.00	84.37	66.67	0.00	4.37
Jimma	**JIM-1D**	44.78	22.39	4.48	14.93	2.99	7.46	2.99	0.00	71.64	9.09	40.01	11.19
Jimma	**JIM-1M**	26.32	14.04	48.87	4.26	1.50	1.50	1.50	0.00	90.24	64.00	24.91	3.76
Kutigi	**KUT-2C**	3.23	48.39	22.58	12.90	0.00	9.68	3.23	0.00	74.19	87.49	21.05	3.87
Lemu	**LEM-1N**	21.40	24.29	42.80	3.89	0.78	1.95	2.72	1.17	89.49	66.67	13.33	1.95

4.3.9 Massive, very-fine sandstone and mudstone (Fm) sub-facies

The heavy mineral suite of the massive, very-fine sandstone and mudstone (Fm) sub-facies comprise of opaque varieties which were observed by the brownish, reddish and yellowish colouration under light microscope and were classified as iron-oxide minerals whereas the non-opaque assemblage consists of zircon, tourmaline, rutile, staurolite, biotite, muscovite, sillimanite and garnet opaque minerals. Most of the heavy minerals are angular to sub-angular and rounded to sub-rounded.

The zircon grains occur in a variety of forms from equant to prismatic, elongated, euhedral to subhedral types with well-defined crystal faces through sub-rounded forms to rounded forms (Figure 4.25g). The grain boundaries are characteristically dark with a xenocrystic core being present in certain cases. The grains are brownish, corroded and fractured. Few grains also contain opaque and non-opaque inclusions (zircon and tourmaline). The broken zircons are more predominating followed by sub-rounded and euhedral forms with perfectly developed crystal faces.

Tourmaline grains are euhedral to subhedral, needle-like to prismatic and angular to rounded. The varieties are dominantly brown followed by some yellowish and few cloudy as identified by their pleochroism characteristic. The rutile grains are identified by their peculiar ‘blood red’ coloured, conchoidal, etched and few elongated with irregular terminations. Staurolite are of light yellow to straw yellow colored and some show parallel extinction, low birefringence, faint pleochroism sometimes on the prismatic face. Some of the grains contain hackly fractures.

The recalculated modal composition (%) with the calculated heavy mineral index (HMI); ZTR, RZ, ST and Density are presented together in table 4.4i.

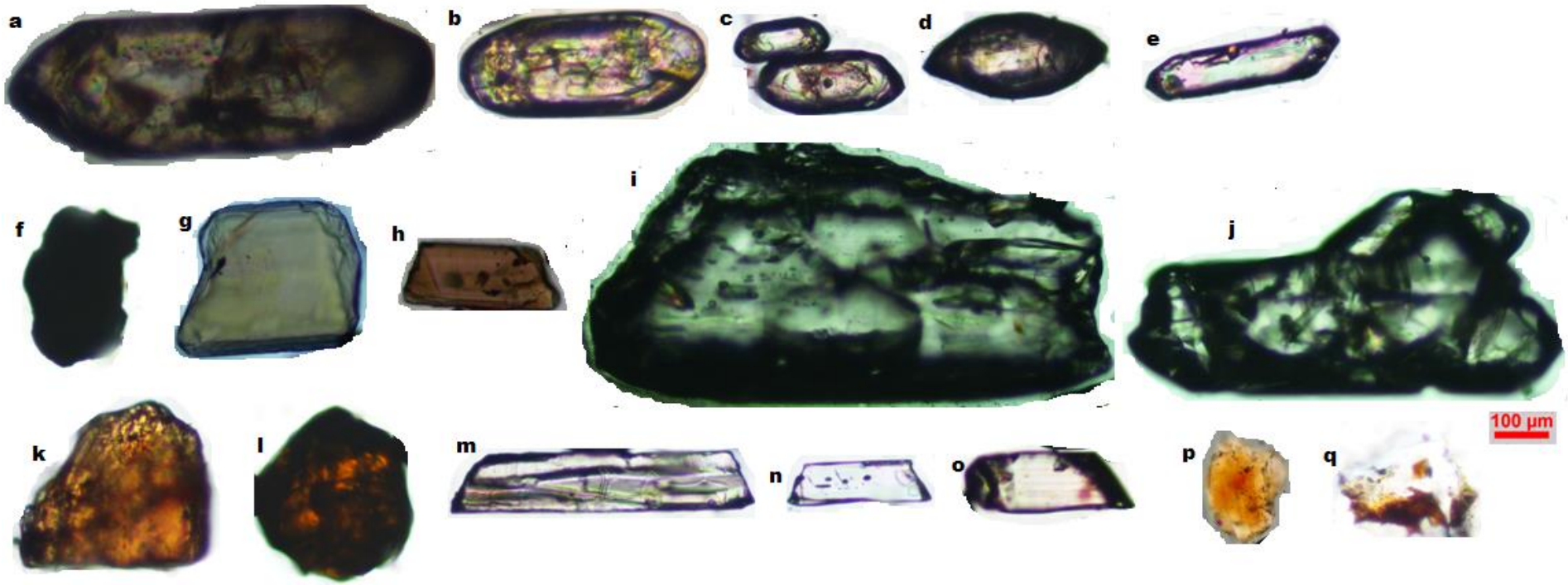


Figure 4.25g: Different heavy minerals types observed (under crossed nicol) in the massive, very-fine sandstone and mudstone (Fm) sub-facies; (a-e) Zircon (weathered and corroded), (f-h) Tourmaline (dark, bluish and light reddish), (i & j), garnet (bluish and bulbous), (k & l) Rutile (brownish and reddish), (m-o) Sillimanite (needle-like, prismatic) and Staurolite (yellowish).

Table 4.4i: Non-opaque heavy minerals composition (%) and calculated index values of very fine, massive sandstone and mudstone (Fm) sub-facies

Location	Sample Code	Non-Opaque								ZTR	RZi	STi	D*i*
		Zr	To	Ru	St	Bi	Mu	Si	Gr				
Dokko	**DOK-Z4**	28.17	39.91	18.78	7.04	0.94	2.35	1.88	0.94	86.85	40.00	14.99	1.69
Maraba	**MAR-1N**	18.52	24.69	40.12	6.17	2.47	3.09	3.09	1.85	83.33	68.42	19.99	1.98
Patti-Chin	**PAT-1K**	23.81	23.81	34.71	4.95	2.38	2.38	2.38	3.57	83.34	60.00	19.99	3.57

4.4 Mineralogical Composition (XRD)

The constituents, type and characteristics of the identified mineralogy in the studied sediments is discussed here to compliment the microscopic studies discussed earlier. Thirty-five (35) representative rock samples which form the important facies in the study area were selected for this analysis to provide the knowledge on the climatic and tectonic conditions operating during the Cretaceous sedimentation.

The detailed study of minerals (clay and associated non-clay minerals) has brought out some significant results. Generally, the quantitative (Tables 4.5a-4.5c) and qualitative (Appendix VII, figures I-XII) results shows major clay minerals as kaolinite and phyllosilicates while the dominant non-clay mineral impurities include quartz and mica (phlogophite, biotite and muscovite) which is characterized by its ubiquitous occurrence in all samples. The abundance of these minerals can be attributed to either source rock lithology or authigenesis as acidic igneous rocks (granite) can contribute substantial amount of detrital mica according to Dapples (1972).

Table 4.5a: Quantitative Mineralogical Composition results of the analyzed sediment samples within the southeastern part of the northern Bida Basin

LAF-1E	Weight%	**LAF-1L**	Weight%	**PAT-1B**	Weight%	**PAT-1J**	Weight%
Chrystotile	13.25	Chrystotile	12.06	Chrystotile	8.33	Chrystotile	2.27
Hematite	66.23	Phlogopite	70.92	Sepiolite	11.11	Hematite	7.95
Xonotlite	3.97	Hematite	5.4.93	Halloysite	13.89	Biotite	56.82
Quartz	4.64	Xonotlite	2.84	Dickite	8.33	Illmenite	3.98
Nacrite	3.97	Quartz	4.26	Muscovite	13.89	Muscovite	3.98
Albite	11.92			Quartz	16.67	Sepiolite	2.27
				Illmenite	16.67	Anhydrite	2.27
				Albite	11.11	Quartz	20.45
DOK-1D	Weight%	**DOK-1K**	Weight%	**DOK-1X**	Weight%	**PTG-1C**	weight%
Chrystotile	20.51	Chrystotile	6.77	Chrystotile	2.40	Goethite	6.46
Hematite	64.10	Kaolinite	5.4.02	Kaolinite	4.1.2.3	Kaolinite	66.05
Quartz	3.21	Ilmenite	74.19	Tobermorite	48.08	Muscovite	4.74
Anthophylii	12.18	Muscovite	3.01	Nacrite	1.44	Quartz	12.15
		Albite	3.01	Dickite	14.87	Trona	5.4.6
		Sepiolite	3.01	Xonotlite	7.69		
				Muscovite	1.44		
				Orthoclase	8.17		
				Ilmenite	2.40		
				Quartz	8.17		
LEM-1E	Weight%	**LEM-1T**	Weight%	**NDJ-1C**	Weight%	**NDJ-1H**	Weight%
Chrystotile	2.58	Illmenite	1.06	Hematite	2.88	Chrystotile	12.77
Xonotlite	7.74	Quartz	2.11	Illmenite	4.77	Anthophyllite	53.19
Anthophyllite	64.52	Dickite	34.21	Xonotlite	6.73	Hematite	4.26
Muscovite	3.23	Sepiolite	1.06	Muscovite	74.04	Kaolinite	3.19
Nacrite	4.52	Kaolinite	26.41	Nacrite	3.85	Quartz	4.26
Sepiolite	3.23	Orthoclase	13.38	Albite	2.88	Sepiolite	3.19
Antigorite	4.52	Antigorite	20.77	Orthoclase	3.85	Xonotlite	8.51
Albite	5.4.68					Anhydrite	3.19
						Monticellite	7.45
ZMB-1A	weight%	**ZMB-1C**	weight%	**GBU-1C**	weight%		
Kaolinite	15.4.68	Kaolinite	87.05	Kaolinite	37.52		
Muscovite	1.91	Muscovite	5.4.26	Muscovite	8.8		
Quartz	4.66	Quartz	2.35	Quartz	53.69		
Smectite	73.75	Rutile	1.34				

Table 4.5b: Quantitative Mineralogical Composition results of the analyzed sediment samples within the central part of the northern Bida Basin

AGB-1A	weight%	**AGB-1B**	**weight%**	**AGB-1C**	**weight%**
Anatase	3.83	Anatase	1.21	Anatase	1.54
Kaolinite	82.13	Kaolinite	90.93	Kaolinite	68.62
Muscovite	14.05	Muscovite	4.3	Muscovite	6.35
		Quartz	2.56	Quartz	23.49
AGB-1E	weight%	**AGB-1K**	weight%	**AGB-1S**	weight%
Anatase	3.97	Anatase	2.56	Goethite	31.84
Goethite	1.47	Goethite	8.62	Hematite	47.56
Kaolinite	75.4.09	Kaolinite	88.82	Kaolinite	18.72
Muscovite	14.28			Quartz	1.88
Quartz	1.19				
KUD-1A	**weight%**	**KUD-1C**	**weight%**	**KUD-1G**	**weight%**
Anatase	0.8	Kaolinite	16.19	Hematite	2.45
Kaolinite	17.78	Quartz	83.81	Kaolinite	22.77
Quartz	81.43			Quartz	74.78
KUT-1A	**weight%**	**KUT-1G**	**weight%**	**KUT-1M**	**weight%**
Anatase	3.2	Anatase	0.63	Anatase	1.87
Kaolinite	60	Kaolinite	32.96	Goethite	2.52
Muscovite	5.4.51	Muscovite	7.64	Kaolinite	35.4.5
Quartz	27.28	Quartz	57.47	Muscovite	4.21
		Rutile	1.3	Quartz	51.9
SHG-1B	Weight%	**SHG-1L**	Weight%	**SHG-1R**	weight%
Hematite	1.54	Xonotlite	2.33	Anatase	2.14
Chrystotile	2.05	Illmenite	2.91	Kaolinite	91.37
Witherite	2.05	Albite	2.91	Muscovite	6.49
Illmenite	27.18	Muscovite	58.14		
Albite	2.56	Kaolinite	2.33		
Xonotlite	6.67	Sepiolite	4.23		
Monticellite	6.67	Antigorite	2.91		
Anthophylii	51.28	Riebeckit	23.26		
ENG-1B	Weight%	**ENG-1L**	Weight%	**ENG-1V**	Weight%
Chrystotile	12.18	Chrystotile	5.4.23	Kaolinite	4.44
Kaolinite	64.10	Phlogopite	76.92	Phlogopite	74.07
Petalliite	4.49	Xonotlite	4.62	Xonotlite	3.70
Nacrite	3.21	Quartz	3.08	Quartz	2.96
Albite	3.85	Anthophylii	6.15	Muscovite	3.70
Xonotlite	3.21			Petalite	3.70
Riebeckit	2.56			Antigorite	7.41
Quartz	6.41				

Table 4.5c: Quantitative Mineralogical Composition results of the analyzed sediment samples within the northern part of the study area

RAB-1P	Weight%	**RAB-1B**	Weight%	**TAN-1A**	Weight%	**TAN-1D**	Weight%
Xonotlite	2.33	Chrystotile	3.18	Hematite	4.58	Quartz	7.87
Illmenite	2.91	Kaolinite	14.01	Quartz	6.11	Illmenite	4.49
Albite	2.91	Ilmenite	3.18	Xonotlite	3.05	Xonotlite	4.49
Muscovite	58.14	Hematite	10.83	Anthophylii	4.58	Chrystotile	4.49
Kaolinite	2.33	Muscovite	3.18	Witherite	4.34	Albite	4.49
Sepiolite	4.23	Sepiolite	63.69	Phlogopite	76.34	Sepiolite	6.74
Antigorite	2.91	Xonotlite	1.91			Monticellite	32.58
Riebeckite	23.26					Orthoclase	30.34
						Anhydrite	4.49

4.5 Geochemical Data (XRF and ICPMS)

The geochemical data; major, trace and rare earth elements of the investigated sediments and their statistical relationships is presents here with an attempts to further constrain their interpretations. In order to understand the geochemical characteristics of the studied sediments, some representative rock samples were selected and analyzed for bulk geochemical analysis (major, trace and rare earth elements). The result of bulk rock geochemical analysis will be employed later together with other results for further interpretations.

4.5.1 Major Elements

A total of forty-six (46) rock samples were selected for determination of major elemental composition using X-ray fluorescence methods and the results are presented in table 4.6a. Major elements are those elements that predominate in any rock analysis and their concentrations are expressed as a percentage (%) of their oxide (Rollinson, 1993). Result shows that SiO_2 is the dominating element while Al_2O_3, Na_2O, K_2O, Fe_2O_3 and MnO are generally comparably less except in few samples. Relative high content of Fe_2O_3 in some sediments may indicates part of the sediments was possibly precipitated as iron-rich minerals during sedimentation and/or diagenesis while general low TiO_2 concentration may indicate minor presence of phyllosilicates (Condie *et al*., 1992).

The result also shows that SiO_2 contents are comparatively higher than the values of average Upper Continental Crust (UCC) after McLennan (1989) and Post-Archean Australian Shale (PAAS) after McLennan (2001) sediments while other major elements; Al_2O_3, Na_2O, K_2O, FeO and MgO are relatively lower when compared with the standards (Table 4.6j).

Ratios of major oxides; SiO_2/Al_2O_3, Al_2O_3/SiO_2, Al_2O_3/TiO_2, K_2O/Na_2O, Na_2O/K_2O, Fe_2O_3+MgO have been used as an indicator of provenance (Bock *et al*., 1998; Gotze, 1998; Rahman and Suzuki, 2007) and evaluation tectonic setting of source rocks (Potter, 1978; Schwab, 1978; Holland, 1984; Condie and Wronkiewicz, 1990). The calculated ratio of major element presented in appendix VI, table Ia-Id show generally high SiO_2/Al_2O_3 values for all the sub-facies which reflects abundance of silica content as suggested by Potter (1978). Also, relatively high Al_2O_3/TiO_2 values may also indicate derivation of the detrital material from a continental source according to Fyffe and Pickerill (1993). General, slightly high K_2O/Na_2O value in some sub-facies may indicate presence of K-bearing minerals such as K-feldspar, muscovite and biotite according to McLennan *et al*. (1983) and Osae *et al*. (2000).

4.5.1.1 Harker Variation Diagrams and Major Elemental Relationship

The Harker diagrams are applied in this study because of its usefulness in providing quick comparison through construction of bi-variate plots in order to obtain their distribution patterns. These plots usually show relationship between SiO_2 contents and other oxides compositions e.g. Al_2O_3, Fe_2O_3, MnO, MgO, CaO Na_2O, K_2O, TiO_2 and P_2O_4. In this study, as expected, there is a decrease in the abundance of Al_2O_3, Fe_2O_3, CaO, MgO, Na_2O, MgO, MnO, K_2O, TiO_2 and P_2O_5 as SiO_2 increases (Figure 4.26).

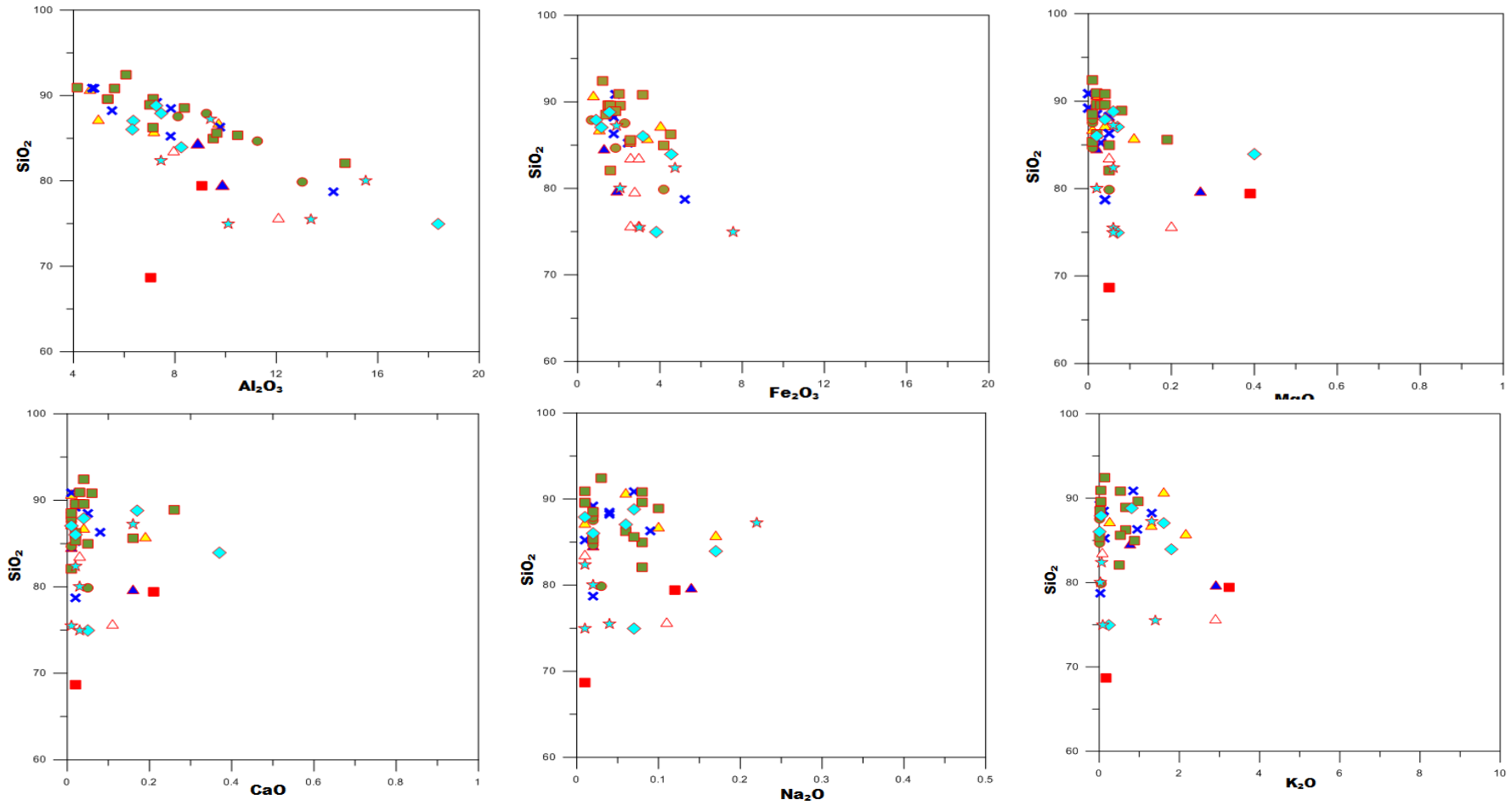


Figure 4.26: Harker's Variation plots showing the relationship of SiO_2 with other major elements for Northern Bida Basin sandstones.

Table 4.6a: Major Element Composition (%) of clast supported, massive conglomerate (Gcm) sub-facies in Northern Bida Basin

Location	Sample No	SiO_2	Al_2O_3	Fe_2O_3	MnO	MgO	CaO	Na_2O	K_2O	TiO_2	P_2O_5	CIA	PIA	CIW	CPA	WIP	ICV
Gbale	**GBL-1C**	84.44	8.90	1.28	0.01	0.02	0.01	0.02	0.77	0.25	0.01	91.75	99.63	99.66	99.78	6.31	0.27
Patigi	**PTG-1E**	79.57	9.87	1.90	0.01	0.27	0.16	0.14	2.91	0.37	0.01	74.46	94.87	97.05	98.60	24.61	0.58
Mean		82.01	9.39	1.59	0.01	0.15	0.09	0.08	1.84	0.31	0.01	83.61	97.75	98.36	99.19	14.46	0.42
Min.		79.57	8.90	1.28	0.01	0.02	0.01	0.02	0.77	0.25	0.01	74.46	94.87	97.05	98.60	6.31	0.27
Max.		84.44	9.87	1.90	0.01	0.27	0.16	0.14	2.91	0.37	0.01	91.75	99.63	99.66	99.78	24.61	0.58

Table 4.6b: Major Element Composition (%) of matrix supported, massive conglomerate (Gmm) sub-facies in Northern Bida Basin

Location	Sample No	SiO_2	Al_2O_3	Fe_2O_3	MnO	MgO	CaO	Na_2O	K_2O	TiO_2	P_2O_5	CIA	PIA	CIW	CPA	WIP	ICV
Gbale	**GBL-1E**	79.44	9.06	2.31	0.01	0.39	0.21	0.12	3.24	0.18	0.01	71.73	94.63	96.49	98.69	27.34	0.71
Patigi	**PTG-1D**	68.69	7.04	17.57	0.02	0.05	0.02	0.01	0.17	0.5	0.01	94.54	99.57	99.58	99.86	1.50	2.61
Mean		74.07	8.05	9.94	0.02	0.22	0.12	0.07	1.71	0.34	0.01	84.49	97.10	98.04	99.28	14.42	1.66
Min.		68.69	7.04	2.31	0.01	0.05	0.02	0.01	0.17	0.18	0.01	71.73	94.63	96.49	98.69	1.50	0.71
Max.		79.44	9.06	17.57	0.02	0.39	0.21	0.12	3.24	0.50	0.01	94.54	99.57	99.58	99.86	27.34	2.61

Table 4.6c: Major Element Composition (%) of crudely bedded conglomerate (Gh) sub-facies in Northern Bida Basin

Location	Sample No	SiO_2	Al_2O_3	Fe_2O_3	MnO	MgO	CaO	Na_2O	K_2O	TiO_2	P_2O_5	CIA	PIA	CIW	CPA	WIP	ICV
Gbugbu	**GBU-1D**	90.59	4.65	0.76	0.01	0.02	0.01	0.06	1.61	0.18	0.01	73.46	97.75	98.52	98.73	13.26	0.57
Kajita	**KJT-1C**	84.65	7.17	3.39	0.02	0.11	0.19	0.17	2.16	1.12	0.02	74.00	93.36	94.27	97.74	18.63	1.00
Kajita	**KJT-1Q**	86.65	9.72	1.05	0.00	0.01	0.04	0.10	1.30	0.37	0.01	87.12	98.41	98.62	98.97	11.05	0.30
Patigi	**PTG-1B**	87.08	4.98	4.03	0.01	0.04	0.01	0.01	0.26	0.27	0.01	94.68	99.58	99.60	99.80	2.20	0.93
Mean		87.49	6.63	2.31	0.01	0.05	0.06	0.09	1.33	0.49	0.01	82.32	94.58	98.00	98.81	11.29	0.70
Min.		84.65	4.65	0.76	0.00	0.01	0.01	0.01	0.26	0.18	0.01	73.46	93.36	94.27	97.74	2.20	0.30
Max.		90.59	9.72	4.03	0.02	0.11	0.19	0.17	2.16	1.12	0.02	94.68	99.58	99.60	99.80	18.63	1.00

Table 4.6d: Major Element Composition (%) of crudely stratified sandstone (Se) sub-facies in Northern Bida Basin

Location	Sample No	SiO_2	Al_2O_3	Fe_2O_3	MnO	MgO	CaO	Na_2O	K_2O	TiO_2	P_2O_5	CIA	PIA	CIW	CPA	WIP	ICV
Agbonna	**AGB-1B**	88.50	7.84	1.67	0.00	0.02	0.05	0.04	0.12	0.33	0.04	97.43	98.89	98.90	99.48	1.28	0.28
Bida	**BDA-1D**	89.22	4.59	1.52	0.01	0.00	0.02	0.02	0.01	0.28	0.01	99.43	99.55	99.55	99.77	0.19	0.26
Doko	**DOK-1D**	78.74	14.25	4.21	0.01	0.04	0.02	0.02	0.03	0.92	0.03	99.52	99.75	99.75	99.88	0.44	0.44
Enagi	**ENG-1J**	90.88	4.74	1.83	0.01	0.00	0.01	0.07	0.85	0.17	0.02	83.68	98.03	98.38	98.63	7.17	0.62
Gbale	**GBL-1D**	84.25	7.83	2.44	0.01	0.03	0.02	0.01	0.14	0.58	0.01	97.88	99.61	99.62	99.87	1.24	0.41
Kajita	**KJT-1A**	86.32	9.78	1.75	0.01	0.05	0.08	0.09	0.95	0.60	0.01	89.76	98.17	98.34	99.13	8.27	0.36
Kutigi	**KUT-2D**	90.86	4.82	1.03	0.01	0.01	0.01	0.01	0.04	0.23	0.02	98.77	99.58	99.59	99.79	0.40	0.28
Patigi	**PTG-1A**	88.25	4.52	1.75	0.01	0.05	0.01	0.04	1.31	0.19	0.01	80.23	98.83	99.10	99.28	10.78	0.61
Mean		84.55	7.76	2.15	0.01	0.03	0.03	0.04	0.43	0.41	0.02	93.34	99.05	99.15	99.48	3.72	0.41
Min.		78.74	4.74	1.03	0.00	0.00	0.01	0.01	0.01	0.17	0.01	80.23	98.03	98.34	98.63	0.19	0.26
Max.		90.88	14.25	4.21	0.01	0.05	0.08	0.09	1.31	0.92	0.04	99.52	99.75	99.75	99.88	10.78	0.62

Table 4.6e: Major Element Cmposition (%) of planar cross-stratified sandstone (Sp) sub-facies in Northern Bida Basin

Location	Sample No	SiO_2	Al_2O_3	Fe_2O_3	MnO	MgO	CaO	Na_2O	K_2O	TiO_2	P_2O_5	CIA	PIA	CIW	CPA	WIP	ICV
Agbonna	**AGB-1K**	79.89	13.02	4.18	0.02	0.05	0.05	0.03	0.05	1.00	0.12	99.10	99.46	99.46	99.81	0.63	0.41
Bida	**BDA-1A**	84.68	11.25	1.84	0.00	0.01	0.01	0.02	0.01	0.23	0.02	99.68	99.76	99.76	99.82	0.21	0.19
Bida	**BDA-1R**	87.55	8.12	2.28	0.01	0.01	0.01	0.02	0.01	0.40	0.02	99.57	99.67	99.67	99.82	0.18	0.34
Doko	**DOK-1X**	87.91	9.24	0.67	0.00	0.01	0.01	0.02	0.01	0.30	0.03	99.65	99.72	99.72	99.83	0.16	0.11
Mean		84.01	10.41	2.24	0.01	0.02	0.02	0.02	0.02	0.48	0.05	99.50	9.65	99.65	99.82	0.30	0.26
Min.		79.89	8.12	0.67	0.00	0.01	0.01	0.02	0.01	0.23	0.02	99.10	99.46	99.46	99.81	0.16	0.11
Max.		87.91	13.02	4.18	0.02	0.05	0.05	0.03	0.05	1.00	0.12	99.68	9.76	99.76	99.83	0.63	0.41

Table 4.6f: Major Element Composition (%) of horizontally stratified sandstone (Sh) sub-facies in Northern Bida Basin

Location	Sample No	SiO_2	Al_2O_3	Fe_2O_3	MnO	MgO	CaO	Na_2O	K_2O	TiO_2	P_2O_5	CIA	PIA	CIW	CPA	WIP	ICV
Agbonna	**AGB-1G**	82.09	14.71	1.59	0.01	0.05	0.01	0.08	0.50	1.41	0.06	96.14	99.36	99.38	99.44	4.53	0.25
Bida	**BDA-1B**	88.54	8.37	1.37	0.01	0.01	0.01	0.02	0.02	0.32	0.02	99.50	99.69	99.69	99.79	0.25	0.21
Doko	**DOK-1K**	84.36	10.47	2.56	0.01	0.01	0.02	0.02	0.01	0.30	0.03	99.59	99.70	99.70	99.86	0.22	0.28
Enagi	**ENG-1E**	89.63	7.14	1.48	0.00	0.02	0.03	0.08	0.97	0.25	0.02	86.91	98.31	98.54	98.96	8.25	0.40
Enagi	**ENG-1L**	84.98	9.51	4.18	0.01	0.05	0.05	0.08	0.88	0.40	0.02	90.45	98.55	98.68	99.17	7.60	0.59
Enagi	**ENG-1N**	86.26	7.13	4.52	0.01	0.02	0.02	0.06	0.66	0.47	0.02	90.67	98.81	98.92	99.23	4.61	0.81
Enagi	**ENG-1V**	92.44	6.07	1.21	0.01	0.01	0.04	0.03	0.14	0.75	0.02	96.60	98.74	98.76	99.48	1.36	0.36
Kutigi	**KUT-2A**	90.93	4.15	2.01	0.01	0.02	0.03	0.01	0.04	0.37	0.04	98.11	99.04	99.05	99.76	0.44	0.60
Kutigi	**KUT-2G**	89.59	4.35	2.06	0.01	0.03	0.02	0.01	0.04	0.35	0.02	98.71	99.44	99.44	99.81	0.44	0.47
Kutigi	**KUT-2K**	89.60	4.35	1.58	0.01	0.04	0.04	0.01	0.04	0.51	0.02	98.35	99.07	99.07	99.81	0.48	0.42
Rabba	**RAB-1F**	90.84	4.62	3.16	0.01	0.04	0.06	0.08	0.53	0.12	0.02	89.41	97.36	97.60	98.61	4.80	0.71
Rabba	**RAB-1H**	88.92	7.01	1.84	0.01	0.08	0.26	0.10	0.66	0.30	0.11	87.42	94.72	94.19	98.62	6.25	0.46
Rabba	**RAB-1P**	84.62	9.65	2.56	0.01	0.19	0.16	0.07	0.53	0.27	0.08	92.79	97.59	97.72	99.32	4.02	0.39
Mean		88.06	7.73	2.32	0.01	0.04	0.06	0.05	0.39	0.45	0.04	94.20	98.49	98.60	99.37	3.48	0.46
Min.		82.09	4.15	1.21	0.00	0.01	0.01	0.01	0.01	0.12	0.02	86.91	94.72	94.19	98.61	0.22	0.21
Max.		92.44	14.71	4.52	0.01	0.19	0.26	0.10	0.97	1.41	0.11	99.59	99.70	99.70	99.86	8.25	0.81

Table 4.6g: Major Element Composition (%) of massive sandstone (Sm) sub-facies in Northern Bida Basin

Location	Sample No	SiO_2	Al_2O_3	Fe_2O_3	MnO	MgO	CaO	Na_2O	K_2O	TiO_2	P_2O_5	CIA	PIA	CIW	CPA	WIP	ICV
Gbale	GBL-1A	74.56	12.08	2.97	0.01	0.2	0.11	0.11	2.9	0.27	0.01	79.47	97.66	98.21	99.10	24.21	0.54
Kudu	KUD-1A	83.41	7.95	2.57	0.01	0.05	0.03	0.01	0.08	1.34	0.02	98.51	99.49	99.5	99.87	0.80	0.51
Mean		79.49	10.02	2.77	0.01	0.13	0.07	0.06	1.49	0.81	0.02	88.99	98.58	98.86	99.49	12.51	0.53
Min.		74.56	7.95	2.57	0.01	0.05	0.03	0.01	0.08	0.27	0.01	79.47	97.66	98.21	99.10	0.80	0.51
Max.		83.41	12.08	2.97	0.01	0.20	0.11	0.11	2.90	1.34	0.02	98.51	99.49	99.50	99.87	24.21	0.54

Table 4.6h: Major Element Composition (%) of laminated mudstone (Fl) sub-facies in Northern Bida Basin

Location	Sample No	SiO_2	Al_2O_3	Fe_2O_3	MnO	MgO	CaO	Na_2O	K_2O	TiO_2	P_2O_5	CIA	PIA	CIW	CPA	WIP	ICV
Agbonna	AGB-1D	74.98	18.38	3.82	0.01	0.07	0.05	0.07	0.24	1.22	0.07	98.14	99.39	99.40	99.64	2.42	0.30
Bida	BDA-1K	86.04	6.32	3.17	0.04	0.02	0.02	0.02	0.01	4.89	0.04	99.11	99.29	99.29	99.67	0.28	1.13
Gbugbu	GBU-1B	87.07	6.36	1.15	0.01	0.07	0.01	0.06	1.61	0.28	0.01	79.10	98.55	98.91	99.07	13.31	0.50
Kajita	KJT-1F	83.96	8.25	4.55	0.01	0.40	0.37	0.17	1.80	0.32	0.02	77.97	92.33	93.90	97.99	16.29	0.92
Kajita	KJT-1J	88.83	4.56	1.54	0.00	0.06	0.17	0.07	0.81	0.20	0.02	87.36	96.38	96.77	99.07	7.17	0.39
Kudu	KUD-1C	87.93	7.46	0.89	0.01	0.04	0.04	0.01	0.05	1.00	0.02	98.68	99.33	99.33	99.87	0.56	0.27
Mean		84.80	9.01	2.52	0.01	0.11	0.11	0.07	0.75	1.32	0.03	90.06	97.55	97.93	99.22	6.67	0.59
Min.		74.98	6.32	0.89	0.00	0.02	0.01	0.01	0.01	0.20	0.01	77.97	92.33	93.90	97.99	0.28	0.27
Max.		88.83	18.38	4.55	0.04	0.40	0.37	0.17	1.80	4.89	0.07	99.11	99.39	99.40	99.87	16.29	1.13

Table 4.6i: Major Element Composition (%) of massive mudstone (Fm) sub-facies in Northern Bida Basin

Location	Sample No	SiO_2	Al_2O_3	Fe_2O_3	MnO	MgO	CaO	Na_2O	K_2O	TiO_2	P_2O_5	CIA	PIA	CIW	CPA	WIP	ICV
Doko	**DOK-1F**	80.04	14.52	2.06	0.01	0.02	0.03	0.02	0.03	0.28	0.03	99.53	99.70	99.70	99.86	0.39	0.16
Enagi	**ENG-1B**	84.56	9.40	1.89	0.01	0.06	0.16	0.22	1.31	0.57	0.02	84.75	94.50	96.10	97.68	12.06	0.45
Gbugbu	**GBU-1A**	74.51	13.36	2.99	0.01	0.06	0.01	0.04	1.40	0.32	0.01	90.21	99.58	99.63	99.70	11.51	0.36
Kudu	**KUD-1B**	74.98	10.10	7.56	0.01	0.06	0.03	0.01	0.09	1.35	0.07	98.73	99.60	99.61	99.90	0.89	0.90
Kudu	**KUD-1F**	82.39	7.45	4.73	0.01	0.06	0.02	0.01	0.06	1.53	0.03	98.81	99.60	99.60	99.87	0.63	0.86
Mean		80.04	11.17	3.85	0.01	0.05	0.05	0.06	0.58	0.81	0.03	94.41	98.80	98.93	99.40	4.10	0.55
Min.		74.98	7.45	1.89	0.01	0.02	0.01	0.01	0.03	0.28	0.01	84.75	94.50	96.10	97.68	0.39	0.16
Max.		84.56	14.52	7.56	0.01	0.06	0.16	0.22	1.40	1.53	0.07	99.53	99.70	99.70	99.90	12.06	0.90

Table 4.6j: Major Element Composition (%) of Published Data using for comparison with this study

Sample	SiO_2	Al_2O_3	Fe_2O_3	MnO	MgO	CaO	Na_2O	K_2O	TiO_2	P_2O_5	CIA	PIA	CIW	CPA	WIP	ICV
PAAS	62.80	18.90	4.52	0.11	2.20	1.30	1.20	3.70	1.00	0.16	70.36	84.88	88.32	94.03	40.76	0.89
UCC	66.60	14.40	4.04	0.10	2.48	3.59	3.27	2.80	0.64	0.15	52.74	64.75	69.18	82.49	48.97	1.16

- **The chemical index of alteration (CIA) = [Al_2O_3/(Al_2O_3 +CaO +Na_2O+K_2O)] ×100 (Nesbitt and Young 1982).**
- **The index of compositional variability (ICV) = (Fe_2O_3 +K_2O + Na_2O+ CaO + MgO + MnO + TiO_2)/Al_2O_3 (Cox *et al.* 1995).**
- **The Plagioclase Index of Alteration (PIA) = [(Al_2O_3− K_2O)/ (Al_2O_3 +CaO +Na_2O − K_2O)] ×100 (Fedo *et al*., 1995).**
- **The chemical index of weathering (CIW) = [Al_2O_3/(Al_2O_3 +CaO +Na_2O)] ×100 (Harnois, 1988).**
- **The weathering index of Parker WIP = 100×(2Na_2O/0.35+MgO/0.9+2K_2O/0.25+CaO/0.7) (first introduced by Parker in 1970 and developed by Hamdan and Burnham, 1996)**
- **The Chemical proxy for alteration (CPA) = [(Al_2O_3)/ (Al_2O_3 +Na_2O)] ×100 after Buggle *et al*. (2011)**

4.5.2 Trace Elements (ICPMS)

Trace element present in any rock analysis at less than 0.1% level with concentrations (ppm) of the element in sediments result from the competing influence of provenance, weathering, diagenesis, sediment sorting, and the aqueous geochemistry of the individual elements (Taylor and McLennan, 1985; Rollinson, 1993). Several studies have been carried out on trace elements present in sand-sized sediments (Willan, 2003; Osae *et al*., 2006; Rahman and Suzuki, 2007) and have shown that certain trace elements provide responsible good indicators of the overall composition of the source region (Taylor and McLennan, 1985 and McLennan, 1989).

The results of the important selected trace element concentrations; variations and ranges of seventy-eight (78) analyzed sediments are presented in table 4.7.

4.5.2.1 Transition metal trace elements (TTE - Cr, V, Co, Ni, Sc)

The transition metals in the first-row; Cr, V, Co, Ni, V and Sc generally behave similarly as highly compatible elements during magmatic fractionation processes, being enriched in mafic to ultramafic rocks because they can substitute for Fe and Mg during early stages of crystallization. However, during weathering, they might be mutually fractionated (Feng and Kerrich, 1990). Generally, transition trace elements (TTE) can substitute for Fe and Mg because they are enriched in mafic rocks, therefore, are compatible whereas the incompatible elements are enriched in felsic rocks. The concentrations of Cr, V, Co, Ni, V and Sc in the analyzed samples are presented in table 4.7.

4.5.2.2 Large-ion lithophile elements (LILE; Rb, Cs, Ba, Sr, Th, U)

The large-ion lithophile elements concentration (LILE) of the analyzed samples is also presented among those resented in table 4.7. From the result, generally, there is high content

of Ba and this may suggest sediments derivation from K/Ca feldspar rich source rocks (Cox and Lowe, 1995b; and Condie *et al*., 1995). In general, the sediments are enriched in both Uranium (U) and Thorium (Th) compared to an average UCC and NASC values.

4.5.2.3 High field strength elements (HFSE; Zr, Hf, Y, Nb, Ta)

High field strength elements (HFSE) are preferentially partitioned into melts during crystallization and anatexis (Feng and Kerrich, 1990), and as a result, these elements are enriched in felsic rather than mafic rocks. Because of their immobile characteristics, these elements are considered as a good provenance indicator, together with REE (Taylor and McLennan, 1985).

The high field strength elements concentration of the analyzed samples is also presented in table 4.7. Concentration of Zr, Hf, Y, Nb and Ta is presented in table 4.7. Zr and Hf are variably concentrated in the diverse stratigraphic units and are highly enriched in the sediments whereas Y and Nb concentrations are highly variable. Mean Zr/Hf values are relatively higher compared to UCC and NASC and it indicate possible result of recycling in the source areas.

Table 4.7a: Trace Element Composition (ppm) of clast supported, massive conglomerate (Gcm) in the Northern Bida Basin

Location	Sample No	Sc	Co	Rb	Sr	Zr	Nb	Ba	Hf	Th	U	Y	Cr	Ni	V
Gbugbu	GBL-1C	1.60	1.20	2.10	1.70	1.20	0.02	31.10	0.04	4.20	0.40	4.54	9.80	6.00	3.30
Patigi	PTG-1E	1.90	1.60	7.50	20.50	1.10	0.02	91.00	0.03	4.40	0.90	6.81	9.60	12.00	3.10
Mean		1.75	1.40	4.80	11.10	1.15	0.02	61.05	0.04	4.30	0.65	6.18	9.70	9.00	3.20
Min.		1.60	1.20	2.10	1.70	1.10	0.02	31.10	0.03	4.20	0.40	4.54	9.60	6.00	3.10
Max.		1.90	1.60	7.50	20.50	1.20	0.02	91.00	0.04	4.40	0.90	6.81	9.80	12.00	3.30

Table 4.7b: Trace Element Composition (ppm) of matrix supported, massive conglomerate (Gmm) in Northern Bida Basin

Location	Sample No	Sc	Co	Rb	Sr	Zr	Nb	Ba	Hf	Th	U	Y	Cr	Ni	V
Gbugbu	GBL-1E	1.50	4.50	7.80	30.70	0.40	0.02	129.00	0.02	4.00	0.30	14.46	4.90	3.00	4.10
Patigi	PTG-1D	2.90	3.30	6.10	2.70	9.80	0.15	18.90	0.26	14.50	4.10	1.23	88.20	176.00	4.80
Mean		2.20	3.90	6.95	16.70	4.10	0.085	73.95	0.14	10.60	2.70	7.85	47.05	89.50	4.45
Min.		1.50	3.30	6.10	2.70	0.40	0.02	18.90	0.02	4.00	0.30	1.23	4.90	3.00	4.10
Max.		2.90	4.50	7.80	30.70	9.80	0.15	129.00	0.26	14.50	4.10	14.46	88.20	176.00	4.80

Table 4.7c: Trace Element Composition (ppm) of crudely bedded conglomerate (Gh) sub-facies in Northern Bida Basin

Location	Sample No	Sc	Co	Rb	Sr	Zr	Nb	Ba	Hf	Th	U	Y	Cr	Ni	V
Gbugbu	**GBU-1D**	1.30	0.90	3.00	1.80	1.70	0.03	14.70	0.04	4.60	0.60	3.13	8.40	3.00	2.90
Kajita	**KJT-1C**	4.58	7.98	51.84	74.50	716.63	23.90	696.22	21.54	50.21	4.59	42.79	453.85	30.03	13.92
Patti-Chin	**PAT-1M**	3.08	3.89	1.31	0.91	48.65	1.81	22.99	2.02	3.34	1.26	2.45	698.40	13.59	14.02
Patigi	**PTG-1B**	1.60	1.10	4.20	1.40	4.90	0.03	24.10	0.13	14.20	1.70	4.54	14.80	33.00	2.70
Shonga	**SHG-1K**	2.54	3.03	4.16	6.92	139.59	4.62	43.83	4.73	4.39	1.08	7.10	397.77	22.31	14.60
Mean		2.62	3.38	13.10	17.65	182.29	6.28	160.57	4.69	14.55	2.05	12.00	314.84	20.39	9.83
Min.		1.30	0.90	1.31	0.91	1.70	0.03	14.70	0.04	3.34	0.60	2.45	8.40	3.00	2.70
Max.		4.58	7.98	51.84	74.5	716.63	23.9	696.22	21.54	50.21	4.59	42.79	698.40	33.00	14.02

Table 4.7d: Trace Element Composition (ppm) of crudely stratified sandstone (Se) sub-facies in Northern Bida Basin

Location	Sample No	Sc	Co	Rb	Sr	Zr	Nb	Ba	Hf	Th	U	Y	Cr	Ni	V
Agbonna	**AGB-1B**	3.91	3.67	4.91	27.83	137.00	8.33	52.80	4.36	7.33	0.83	9.45	382.13	26.77	13.87
Bida	**BDA-1D**	3.05	4.31	1.88	4.72	304.71	4.53	24.47	9.03	8.25	0.97	4.59	390.01	20.18	14.94
Dokko	**DOK-1D**	4.49	3.52	2.59	7.79	874.86	16.61	30.97	24.61	18.99	2.83	17.89	189.74	54.37	13.19
Enagi	**ENG-1J**	2.55	3.05	22.78	18.33	154.39	4.53	149.88	4.48	4.93	1.25	9.89	317.19	19.80	12.99
Gbale	**GBL-1D**	2.90	1.70	1.90	3.00	3.80	0.03	29.40	0.12	14.20	0.80	4.61	13.30	20.00	4.80
Jimma	**JIM-1L**	4.77	4.23	2.57	11.09	104.69	6.72	28.99	3.39	7.78	1.79	18.46	267.14	36.03	13.45
Jimma	**JIM-1R**	3.07	4.21	1.53	6.17	158.98	7.38	26.90	4.88	4.20	0.89	3.51	312.02	20.25	13.07
Jimma	**JIM-1X**	3.93	4.00	1.47	6.56	442.78	11.69	38.49	12.83	7.96	1.47	6.23	342.75	20.43	13.37
Kajita	**KJT-1A**	3.69	4.20	21.83	32.44	578.21	14.55	332.57	17.38	12.49	2.93	17.15	306.87	24.22	13.90
Kutigi	**KUT-2D**	1.40	1.50	1.30	1.10	3.50	0.08	4.50	0.09	3.60	0.92	0.95	8.00	5.4.00	4.10
Lemu	**LEM-1C**	4.97	3.32	6.98	29.76	559.09	14.79	121.21	16.86	20.60	2.62	31.71	174.34	51.34	12.36
Lemu	**LEM-1E**	2.25	3.53	14.84	4.80	199.70	4.68	118.30	6.10	4.48	1.90	6.57	1264.00	13.95	13.59
Lemu	**LEM-1G**	5.41	4.33	7.18	10.83	334.51	11.89	66.22	9.90	13.87	2.46	12.40	234.44	39.31	13.67
Patigi	**PTG-1A**	1.50	1.40	9.60	2.00	2.90	0.03	24.10	0.08	8.10	0.80	4.07	8.40	11.00	3.40
Shonga	**SHG-1B**	2.70	3.39	3.57	7.38	94.27	4.54	37.34	3.10	3.37	0.64	3.99	370.65	18.15	13.78
Shonga	**SHG-1X**	4.48	4.02	4.02	7.82	687.68	10.67	54.15	20.88	10.74	1.36	12.70	414.06	40.21	14.80
Mean		3.63	3.40	6.87	11.41	290.19	7.73	71.46	8.69	9.62	1.53	10.38	312.38	26.63	11.96
Min.		1.40	1.40	1.30	1.10	2.90	0.03	4.50	0.08	3.37	0.64	0.95	8.00	9.00	3.40
Max.		4.97	4.33	22.78	32.44	874.86	16.61	332.57	24.61	20.6	2.93	31.71	1264.00	54.37	14.80

Table 4.7e: Trace Element Composition (ppm) of planar cross-stratified sandstone (Sp) sub-facies in Northern Bida Basin

Location	Sample No	Sc	Co	Rb	Sr	Zr	Nb	Ba	Hf	Th	U	Y	Cr	Ni	V
Agbonna	**AGB-1K**	6.46	4.04	2.46	76.19	596.80	22.82	91.17	17.89	12.84	2.45	28.37	314.03	60.55	14.42
Baro	**BAR-1D**	2.13	1.70	14.92	6.53	186.40	4.21	140.90	7.39	6.84	1.38	11.08	14.25	11.11	4.03
Baro	**BAR-1H**	3.84	1.44	3.40	2.04	72.25	3.73	27.69	3.43	4.01	1.33	11.08	23.00	18.56	4.02
Bida	**BDA-1A**	3.30	3.37	1.88	6.63	166.29	6.37	29.59	4.26	4.88	0.82	4.74	258.88	24.55	13.38
Bida	**BDA-1R**	4.29	3.78	1.74	4.41	231.37	9.56	17.37	4.50	10.46	1.10	4.49	248.92	44.03	13.34
Doko	**DOK-1X**	2.94	2.80	1.20	11.16	247.84	6.51	34.66	7.72	7.60	1.17	4.71	223.67	14.75	11.28
Patti-Chin	**PAT-1J**	18.00	14.28	1.92	1.17	782.20	12.18	168.40	26.44	19.44	14.21	28.60	1056.00	12.15	2.53
Patti-Chin	**PAT-1N**	6.21	14.77	2.07	0.97	481.50	10.26	127.90	14.93	13.57	4.39	18.23	255.4.6	16.97	32.54
Tanagi	**TAN-1A**	3.10	3.47	1.31	3.13	101.94	2.84	26.51	3.52	2.88	1.41	4.70	247.03	12.55	12.58
Mean		4.59	4.85	3.43	12.47	318.51	8.72	73.91	10.53	9.28	3.14	13.22	293.93	24.14	12.12
Min.		2.13	1.44	1.20	0.97	72.25	2.84	17.37	3.43	2.88	0.82	4.70	14.25	11.11	2.53
Max.		18.00	14.77	14.92	76.19	782.20	22.82	168.40	26.44	19.44	14.21	28.60	1056.00	60.55	32.54

Table 4.7f: Trace Element Composition (ppm) of horizontally stratified sandstone (Sh) sub-facies in Northern Bida Basin

Location	Sample No	Sc	Co	Rb	Sr	Zr	Nb	Ba	Hf	Th	U	Y	Cr	Ni	V
Agbonna	**AGB-1G**	8.45	3.91	11.41	37.01	784.11	27.36	124.12	24.10	14.52	2.79	32.72	238.22	53.82	14.06
Baro	**BAR-1F**	2.64	1.48	2.62	3.27	121.80	4.01	30.34	4.39	4.57	1.29	10.17	14.07	14.99	3.22
Bida	**BDA-1B**	3.20	3.54	2.00	4.13	228.83	7.96	32.54	7.17	8.73	1.16	6.44	349.14	21.38	13.80
Dokko	**DOK-1K**	2.76	3.92	1.97	9.07	114.95	4.20	31.53	3.68	4.29	0.97	3.12	269.05	21.78	12.27
Dokko	**DOK-1T**	2.74	3.24	1.79	9.28	150.79	6.30	27.16	4.87	6.76	0.86	2.60	224.45	27.62	11.94
Enagi	**ENG-1E**	2.69	3.13	27.36	24.24	181.18	7.09	223.39	4.66	10.28	1.40	5.4.38	238.40	18.27	12.67
Enagi	**ENG-1H**	4.89	3.34	16.82	14.94	353.08	12.45	120.24	10.58	11.57	2.35	18.74	224.88	44.33	12.68
Enagi	**ENG-1L**	4.75	3.05	24.05	20.78	271.19	9.50	211.03	8.19	9.61	1.95	10.44	198.60	37.19	12.90
Enagi	**ENG-1N**	4.44	4.59	18.24	17.15	471.07	11.97	157.58	14.28	14.77	3.05	16.41	236.16	27.80	13.92
Enagi	**ENG-1V**	4.49	2.78	4.50	10.48	902.83	18.06	74.87	26.61	20.59	3.44	30.99	331.16	24.43	12.27
Kutigi	**KUT-2A**	2.00	2.00	1.30	2.20	4.50	0.15	18.20	0.13	7.50	1.14	4.38	13.20	14.00	4.40
Kutigi	**KUT-2G**	2.40	1.80	1.10	1.40	4.90	0.10	7.00	0.16	6.20	0.94	2.16	14.40	18.00	3.50
Kutigi	**KUT-2K**	2.30	1.20	1.20	2.30	4.20	0.05	9.40	0.16	8.00	0.87	4.17	14.20	16.00	2.90
Lemu	**LEM-1A**	4.25	4.11	17.69	18.14	444.01	12.89	162.19	13.57	13.08	2.28	17.67	332.39	29.21	13.63
Lemu	**LEM-1H**	3.36	13.62	11.68	4.77	124.50	4.60	172.20	4.54	6.73	3.28	13.26	418.30	14.18	39.56
Patigi	**PAT-1B**	3.72	2.89	10.53	13.93	214.51	8.23	100.10	6.82	8.85	1.61	7.54	254.68	30.82	11.76
Patigi	**PAT-1G**	4.30	3.62	2.60	4.02	256.82	9.68	36.05	8.48	14.78	2.98	11.17	184.29	34.68	11.15
Rabba	**RAB-1F**	3.34	3.07	14.94	17.82	60.21	2.98	152.94	2.08	3.06	1.06	4.02	314.40	23.41	14.88
Rabba	**RAB-1H**	3.21	3.10	16.93	26.58	146.83	7.02	179.50	4.71	3.82	1.17	6.33	301.67	24.84	13.27
Rabba	**RAB-1P**	3.35	3.31	16.40	22.00	110.60	6.95	159.62	3.23	3.87	0.78	4.54	299.05	29.14	13.10
Shonga	**SHG-1F**	2.63	2.26	2.63	6.82	102.79	4.03	34.63	3.13	4.55	0.62	4.04	273.56	19.93	12.76
Shonga	**SHG-1P**	3.41	2.91	2.75	4.99	339.87	11.87	31.48	10.38	6.75	0.88	7.17	329.03	23.57	13.54
Tanagi	**TAN-1C**	4.44	3.93	20.48	23.44	327.14	9.01	199.46	9.80	12.37	2.10	8.77	218.93	29.91	12.36
Tanagi	**TAN-1D**	3.21	2.27	22.32	20.35	140.24	6.40	174.82	4.57	4.31	2.33	3.93	230.78	18.98	11.76
Mean		3.71	3.57	10.60	13.38	244.49	8.20	102.97	7.55	9.08	1.72	10.09	230.33	24.93	12.43
Min.		2.00	1.20	1.10	1.40	4.20	0.05	7.00	0.13	3.06	0.62	2.16	13.20	14.99	2.90
Max.		8.45	13.62	27.36	37.01	902.83	27.36	223.39	26.61	20.59	3.44	32.72	418.30	53.82	39.56

Table 4.7g: Trace Element Composition (ppm) of massive sandstone (Sm) sub-facies in Northern Bida Basin

Location	Sample No	Sc	Co	Rb	Sr	Zr	Nb	Ba	Hf	Th	U	Y	Cr	Ni	V
Gbale	**GBL-1A**	2.30	2.40	11.20	14.70	1.70	0.03	72.70	0.04	4.60	0.50	6.44	12.20	18.00	3.70
Kudu	**KUD-1A**	3.50	1.00	1.90	3.60	14.40	0.09	19.70	0.36	10.10	0.89	4.67	22.60	30.00	3.10
Rabba	**RAB-1E**	3.64	4.71	19.22	28.21	154.30	4.14	237.12	6.75	2.72	2.09	8.09	309.76	14.78	13.22
Mean		3.15	2.70	10.77	14.50	57.13	1.42	109.84	2.38	4.81	1.16	6.73	114.85	21.26	6.67
Min.		2.30	1.00	1.90	3.60	1.70	0.03	19.70	0.04	2.72	0.50	4.67	12.20	14.78	3.10
Max.		3.64	4.71	19.22	28.21	154.30	4.14	237.12	6.75	10.10	2.09	8.09	309.76	30.00	13.22

Table 4.7h: Trace Element Composition (ppm) of laminated mudstone (Fl) sub-facies in Northern Bida Basin

Location	Sample No	Sc	Co	Rb	Sr	Zr	Nb	Ba	Hf	Th	U	Y	Cr	Ni	V
Agbonna	**AGB-1D**	9.92	4.37	10.33	53.01	499.64	26.89	106.39	14.77	17.86	2.72	26.95	341.34	66.23	17.12
Baro	**BAR-1J**	1.77	1.03	2.32	4.50	191.90	4.73	32.76	4.51	7.90	1.88	7.49	13.54	27.33	22.19
Bida	**BDA-1K**	14.79	4.78	2.27	6.82	2527.15	86.87	50.45	74.60	72.75	8.03	44.60	334.42	89.23	13.98
Gbugbu	**GBU-1B**	2.50	1.40	6.10	2.70	2.80	0.02	29.50	0.06	7.90	1.40	8.18	8.70	9.00	2.40
Jimma	**JIM-1B**	3.79	2.33	4.50	2.46	548.70	12.33	62.83	21.12	18.04	2.98	22.07	367.1	22.54	8.37
Kudu	**KUD 1C**	1.40	0.70	0.70	3.10	9.80	0.02	17.50	0.24	6.20	0.27	3.10	8.60	8.00	1.80
Rabba	**RAB-1L**	4.24	3.16	17.31	33.71	453.15	16.41	190.65	14.28	11.14	1.99	9.81	229.15	30.54	10.93
Mean		4.49	2.82	6.22	14.19	604.73	21.18	70.01	18.94	20.26	2.75	17.46	186.26	36.12	10.97
Min.		1.40	0.70	0.70	2.46	2.80	0.02	17.50	0.06	6.20	0.27	3.10	8.60	8.00	1.80
Max.		14.79	4.78	17.31	53.01	2527.15	86.87	190.65	74.60	72.75	8.03	44.60	367.10	89.23	22.19

Table 4.7i: Trace Element Composition (ppm) of massive mudstone (Fm) sub-facies in Northern Bida Basin

Location	Sample No	Sc	Co	Rb	Sr	Zr	Nb	Ba	Hf	Th	U	Y	Cr	Ni	V
Dokko	**DOK-1F**	3.26	3.52	1.70	11.48	130.60	4.93	37.38	4.03	6.28	1.04	4.46	341.42	19.17	13.61
Enagi	**ENG-1B**	4.21	4.60	37.42	39.59	421.01	14.39	334.07	12.33	14.32	1.95	14.95	321.70	24.54	13.74
Gbugbu	**GBU-1A**	3.30	1.20	6.90	2.00	3.60	0.02	28.80	0.12	7.00	0.40	2.50	12.50	23.00	3.90
Jimma	**JIM-1N**	8.92	4.07	4.58	9.83	1022.05	23.37	59.80	29.32	23.21	4.15	28.26	219.78	76.01	12.97
Kudu	**KUD-1B**	4.90	1.70	2.80	4.10	18.90	0.12	14.20	0.42	12.30	1.66	4.99	78.40	90.00	4.00
Kudu	**KUD-1F**	2.40	0.70	1.60	2.20	18.40	0.09	14.50	0.48	11.00	0.62	4.26	22.30	36.00	2.50
Kutigi	**KUT-2P**	4.80	1.50	1.30	2.90	9.70	0.02	10.70	0.24	14.70	1.59	8.57	42.10	44.00	3.50
Kutigi	**KUT-2Q**	3.50	0.60	1.90	3.20	4.40	0.02	11.80	0.15	9.70	1.91	13.54	22.00	30.00	1.60
Lemu	**LEM-1P**	3.75	12.99	9.95	3.74	512.00	11.89	91.84	18.15	26.78	7.77	21.10	254.2	24.58	24.20
Mean		4.37	3.16	6.94	8.37	214.03	4.59	61.73	6.55	14.63	2.34	10.76	132.61	40.81	9.11
Min.		2.40	0.60	1.20	2.00	3.60	0.02	10.70	0.12	6.28	0.40	2.50	10.70	19.17	1.60
Max.		8.92	12.99	37.42	39.59	1022.05	23.37	334.07	29.32	26.78	7.77	28.26	341.42	90.00	24.20

Table 4.7j: Trace Element Composition (ppm) of Published Data using for comparison with this study

Sample No	Sc	Co	Rb	Sr	Zr	Nb	Ba	Hf	Th	U	Y	Cr	Ni	V
PAAS	16.00	23.00	160.00	200.00	210.00	19.00	650.00	4.00	14.60	3.10	27.00	110.00	54.00	150.00
UCC	14.00	17.30	82.00	320.00	193.00	12.00	682.00	4.30	10.50	2.70	21.00	92.00	47.00	97.00

4.5.3 Rare Earth Elements (ICPMS)

Rare earth elements (REE) comprise the lanthanide elements (La to Lu) are grouped into; light rare earth elements (LREE; La to Sm) and heavy rare earth elements (HREE; Gd to Lu) Rollinson (1993). Rare earth elements (REE) content in the clastic sedimentary rocks can be affected by the size sorting and the content decreases steadily with increase in grain size (Cullers and Stone, 1991).

The result presented in Table 4.8 shows that the analyzed samples have high (LREE) than heavy rare earth elements (HREE) while Table 4.8g shows the standard published data compared with this study. The normalized REE patterns presented in are characterized by high LREE/HREE ratio with almost flat HREE pattern with low Eu anomaly which characterizes derivation from PAAS and NASC. The REE data were also normalized with mean chondrite data after Boynton (1985) and compared with average upper continental crust values (UCC) after McLennan (1989), Post Archean Australian Shale (PAAS) values after McLennan (2001) as presented as a spider diagrams in chapter five to show their relationship.

Table 4.8a: Rare earth element (REE) concentrations and normalized values of Gcm, Gmm and Gh sub-facies in the Northern Bida Basin

	Clast-supported, massive conglomerate (Gcm) sub-facies		Matrix supported, massive conglomerate (Gmm) sub-facies		Clast-supported, crudely bedded conglomerate (Gh) sub-facies			
Sample No	**Gbale**	**Patigi**	**Gbale**	**Patigi**	**Gbugbu**	**Patigi**	**Kajita**	**Patigi**
	GBL-1C	**PTG-1E**	**GBL-1E**	**PTG-1D**	**GBU-1D**	**PTG-1B**	**KJT-1C**	**PTG-1M**
La	13.00	14.10	24.90	4.10	26.10	17.70	104.19	4.96
Ce	28.70	23.60	36.8	11.30	129.20	36.80	208.90	4.50
Pr	2.86	3.45	4.82	0.96	6.51	3.31	24.20	0.79
Nd	10.09	11.50	20.65	3.28	21.58	10.85	83.84	2.60
Sm	1.52	1.95	3.56	0.60	3.77	1.82	14.19	0.54
Eu	0.33	0.39	0.88	0.10	0.85	0.20	1.08	0.09
Gd	1.31	1.53	2.77	0.36	2.10	1.42	12.95	0.51
Tb	0.18	0.25	0.44	0.07	0.28	0.18	1.74	0.08
Dy	0.94	1.29	2.59	0.26	1.09	0.85	8.24	0.47
Ho	0.20	0.24	0.49	0.06	0.14	0.18	1.71	0.09
Er	0.50	0.69	1.28	0.14	0.33	0.39	4.34	0.26
Tm	0.07	0.11	0.22	0.03	0.05	0.06	0.66	0.05
Yb	0.35	0.62	1.01	0.18	0.23	0.36	4.50	0.29
Lu	0.06	0.08	0.13	0.02	0.02	0.06	0.70	0.04
ΣREE	60.11	59.80	101.54	21.46	192.25	74.18	472.24	17.97
ΣLREE	56.17	54.60	91.73	20.24	187.16	70.48	436.32	16.09
ΣHREE	3.61	4.81	8.93	1.12	4.24	3.50	34.84	1.79
ΣLREE/ΣHREE	14.56	11.35	10.27	18.07	44.14	20.14	12.52	8.99
Eu/Eu*	0.23	0.18	0.12	0.64	0.15	0.11	0.01	0.45
Ce/Ce*	0.10	0.07	0.03	0.39	0.11	0.09	0.01	0.26
La/Yb	37.14	22.74	24.65	22.78	113.48	49.17	23.38	17.10
Y/Ho	27.7	28.38	29.51	20.50	22.36	24.22	24.02	24.54
Sm/Nd	0.15	0.17	0.17	0.18	0.17	0.17	0.17	0.21
La_N/Yb_N	24.11	14.31	16.63	14.38	76.54	33.2	14.76	11.51
La_N/Sm_N	4.38	4.55	4.40	4.30	4.36	6.12	4.66	4.78
Gd_N/Yb_N	3.03	1.99	2.21	1.62	7.37	3.19	2.32	1.42

Table 4.8b: Rare earth element (REE) concentrations and normalized values of crudely stratified sandstone (Se) sub-facies in the Northern Bida Basin

Sample No	Gbale	Patigi	Kajita	Bida	Lemu	Lemu	Lemu	Jimma	Jimma	Jimma	Dokko	Agbonna	Shonga	Shonga	Enagi	Kutigi
	GBL-1D	PTG-1A	KJT-1A	BDA-1D	LEM-1C	LEM-1E	LEM-1G	JIM-1L	JIM-1R	JIM-1X	DOK-1D	AGB-1B	SHG-1B	SHG-1X	ENG-1J	KUT-2D
La	16.50	24.40	26.16	14.65	74.95	12.21	40.98	34.04	12.23	18.66	24.10	24.91	14.03	18.09	22.27	4.70
Ce	51.1	52.10	49.86	42.68	154.84	22.84	86.19	54.51	24.17	34.93	36.99	50.74	24.06	49.90	39.93	19.10
Pr	3.69	4.61	4.56	2.82	17.06	2.52	7.79	4.66	2.49	3.53	4.06	6.14	2.20	3.58	4.11	0.73
Nd	12.77	19.02	19.09	8.84	54.53	8.42	24.91	17.83	8.08	11.09	12.78	21.74	6.69	12.04	13.18	3.06
Sm	2.16	2.87	3.25	1.37	9.80	1.45	3.81	2.51	1.21	1.78	2.03	3.98	1.04	1.96	2.24	0.50
Eu	0.33	0.63	0.51	0.17	1.88	0.20	0.65	0.55	0.22	0.26	0.33	0.75	0.17	0.27	0.37	0.05
Gd	1.74	2.24	3.16	1.08	7.80	1.39	2.91	2.27	0.83	1.33	1.87	3.07	0.95	1.89	2.23	0.27
Tb	0.23	0.27	0.51	0.15	1.21	0.18	0.43	0.38	0.13	0.19	0.37	0.45	0.14	0.33	0.36	0.04
Dy	1.15	1.23	2.85	0.84	6.26	1.11	2.16	2.28	0.65	1.06	2.55	2.24	0.77	2.04	1.89	0.17
Ho	0.21	0.22	0.63	0.18	1.26	0.23	0.45	0.53	0.14	0.24	0.61	0.43	0.16	0.47	0.40	0.02
Er	0.57	0.55	1.69	0.52	3.31	0.67	1.24	1.49	0.39	0.70	1.83	1.08	0.41	1.35	1.03	0.06
Tm	0.08	0.05	0.27	0.08	0.46	0.12	0.18	0.22	0.06	0.11	0.29	0.14	0.06	0.23	0.17	0.02
Yb	0.48	0.45	1.99	0.58	3.06	0.71	1.26	1.44	0.44	0.81	2.16	0.91	0.46	1.68	1.21	0.07
Lu	0.07	0.05	0.33	0.10	0.48	0.11	0.21	0.23	0.07	0.15	0.39	0.14	0.08	0.30	0.20	0.02
ΣREE	91.08	110.69	114.86	74.06	339.60	52.16	173.17	123.94	51.11	74.84	90.36	117.72	52.22	94.13	89.59	28.81
ΣLREE	86.22	104.00	103.92	71.36	313.88	47.44	163.68	114.55	48.18	69.99	79.96	108.51	49.02	84.57	81.73	28.09
ΣHREE	4.53	4.06	11.43	3.53	23.84	4.52	8.84	8.84	2.71	4.59	10.07	8.46	3.03	8.29	7.49	0.67
ΣLREE/ ΣHREE	19.03	20.75	5.4.09	20.22	13.17	10.50	18.52	12.96	17.78	14.25	7.94	12.83	16.18	10.32	10.91	41.93
Eu/Eu*	0.12	0.13	0.07	0.16	0.03	0.14	0.08	0.18	0.32	0.13	0.05	0.08	0.24	0.10	0.10	0.51
Ce/Ce*	0.11	0.05	0.05	0.14	0.02	0.10	0.04	0.07	0.07	0.05	0.04	0.04	0.11	0.11	0.06	0.61
La/Yb	34.38	56.44	13.15	26.98	24.49	14.5	32.52	23.64	27.8	23.04	11.16	28.47	32.67	10.77	18.40	67.14
Y/Ho	26.71	23.05	24.51	24.47	24.16	28.56	27.56	34.82	24.07	24.95	29.32	21.99	24.98	27.01	24.72	47.50
Sm/Nd	0.17	0.15	0.17	0.15	0.17	0.17	0.15	0.14	0.15	0.16	0.16	0.18	0.16	0.16	0.17	0.16
La_N/Yb_N	23.14	38.11	8.86	18.16	16.51	11.59	21.92	34.77	42.25	26.94	8.15	19.21	22.04	4.56	12.41	44.94
La_N/Sm_N	4.80	4.57	4.06	7.18	4.81	4.29	6.77	6.45	11.89	6.15	4.89	4.10	9.10	4.81	6.25	4.92
Gd_N/Yb_N	2.92	4.02	1.28	1.50	2.06	1.58	1.86	2.84	1.87	2.22	1.26	2.72	1.67	0.91	1.49	3.15

Table 4.8c: Rare earth element (REE) concentrations and normalized values of Sp sub-facies in the Northern Bida Basin

Sample No	Bida	Bida	Dokko	Baro	Baro	Patti-Chin	Patti-Chin	Agbonna	Tanagi
	BDA-1A	BDA-1R	DOK-1X	BAR-1D	BAR-1H	PAT-1J	PAT-1N	AGB-1K	TAN-1A
La	18.79	12.71	27.56	21.92	14.98	37.80	21.52	49.21	10.52
Ce	51.76	24.34	54.97	40.1	23.45	540.70	42.91	96.13	96.09
Pr	3.21	2.20	4.81	4.70	4.10	11.67	4.42	10.95	2.38
Nd	9.79	6.87	18.81	14.87	14.93	41.53	19.71	39.92	8.38
Sm	1.41	1.08	2.82	2.75	3.24	10.49	4.58	7.68	1.53
Eu	0.27	0.13	0.49	0.41	0.54	1.71	0.72	1.47	0.32
Gd	1.12	0.89	1.90	2.61	2.73	9.74	4.27	6.54	1.36
Tb	0.18	0.15	0.26	0.34	0.38	1.48	0.71	1.04	0.22
Dy	0.94	0.88	1.23	1.93	2.10	8.94	4.43	4.72	1.08
Ho	0.21	0.20	0.25	0.38	0.40	1.64	0.86	1.17	0.22
Er	0.57	0.61	0.67	1.08	1.07	4.53	16.86	3.06	0.53
Tm	0.09	0.10	0.10	0.19	0.18	0.87	0.45	0.43	0.08
Yb	0.59	0.72	0.69	1.09	1.05	4.62	2.71	2.83	0.57
Lu	0.10	0.12	0.12	0.16	0.16	0.82	0.40	0.42	0.09
ΣREE	89.03	52.00	116.68	93.53	71.31	677.54	124.55	226.57	123.37
ΣLREE	84.96	48.20	110.97	84.34	62.7	642.19	94.14	203.89	118.90
ΣHREE	3.80	3.67	4.22	7.78	8.07	33.64	30.69	21.21	4.15
ΣLREE/ΣHREE	22.36	13.13	21.26	10.97	7.77	19.09	3.07	9.61	28.65
Eu/Eu*	0.24	0.19	0.15	0.08	0.08	0.02	0.05	0.04	0.21
Ce/Ce*	0.13	0.13	0.08	0.05	0.04	0.16	0.05	0.02	0.50
La/Yb	31.85	17.65	39.94	20.11	14.22	6.73	7.94	17.39	18.46
Y/Ho	27.33	27.47	22.82	29.16	27.7	17.44	21.2	24.25	21.37
Sm/Nd	0.14	0.16	0.15	0.17	0.20	0.25	0.23	0.19	0.18
La_N/Yb_N	21.49	11.92	14.51	13.55	10.27	4.53	4.35	11.72	12.43
La_N/Sm_N	8.38	7.40	6.59	4.01	3.10	2.27	2.96	4.03	4.32
Gd_N/Yb_N	1.53	1.00	1.32	1.93	2.10	1.40	1.27	1.86	1.92

Table 4.8d: Rare earth element (REE) concentrations and normalized values of Sh sub-facies in the Northern Bida Basin

Sample No	Bida	Lemu			Dokko		Baro	Patti-Chin		Agbonna	Enagi					Kutigi			Rabba			Tanagi	
	BDA-1B	LEM-1A	LEM-1P	LEM-1H	DOK-1K	DOK-1T	BAR-1F	PAT-1B	PAT-1G	AGB-1G	ENG-1E	ENG-1H	ENG-1L	ENG-1N	ENG-1V	KUT 2A	KUT 2G	KUT 2K	RAB-1F	RAB-1H	RAB-1P	TAN-1C	TAN-1D
La	24.43	34.23	44.33	20.54	16.91	21.35	22.01	26.73	36.27	41.38	30.80	44.30	18.22	39.94	49.19	18.70	7.90	14.60	9.77	13.92	11.91	22.68	13.71
Ce	78.81	64.59	110.00	53.53	31.10	27.96	36.87	47.66	62.05	84.88	69.05	76.07	32.02	94.39	87.32	58.60	33.20	28.20	13.24	36.64	18.89	41.17	21.33
Pr	4.56	7.09	12.59	6.12	3.10	2.98	4.73	4.21	7.30	9.5	6.42	9.27	3.40	7.97	10.24	3.09	1.50	3.02	2.18	2.52	2.20	4.68	2.13
Nd	14.02	23.31	43.23	21.61	10.11	8.14	14.24	13.12	24.68	30.57	21.63	30.47	11.58	26.83	34.43	12.98	6.09	11.89	7.77	8.42	4.59	14.71	6.75
Sm	2.24	3.86	8.60	4.14	1.55	1.13	2.58	1.99	4.18	4.83	3.40	4.75	1.95	4.49	4.97	1.85	0.96	2.31	1.56	1.52	1.35	3.16	0.98
Eu	0.34	0.60	1.32	0.82	0.34	0.21	0.29	0.34	0.5	0.86	0.55	0.91	0.35	0.70	0.79	0.28	0.14	0.3	0.39	0.36	0.28	0.61	0.22
Gd	1.71	3.22	7.30	3.92	0.98	0.79	2.46	1.69	3.34	4.31	3.22	4.65	1.94	4.33	4.85	1.01	0.62	1.28	1.41	1.46	1.23	2.67	1.01
Tb	0.25	0.53	0.99	0.52	0.14	0.11	0.30	0.25	0.47	0.83	0.42	0.70	0.34	0.62	0.97	0.13	0.06	0.14	0.23	0.25	0.20	0.44	0.15
Dy	1.25	3.01	4.68	2.90	0.67	0.54	1.68	1.38	2.23	4.53	2.02	3.57	1.97	3.23	4.39	0.77	0.48	0.94	1.22	1.27	1.06	2.33	0.80
Ho	0.26	0.66	1.00	0.53	0.14	0.11	0.33	0.29	0.44	1.25	0.41	0.77	0.44	0.67	1.20	0.12	0.05	0.13	0.25	0.27	0.23	0.49	0.17
Er	0.70	1.87	2.72	1.41	0.37	0.32	0.92	0.81	1.12	3.60	0.99	2.04	1.20	1.72	3.29	0.35	0.22	0.32	0.64	0.69	0.62	1.23	0.46
Tm	0.10	0.28	0.48	0.24	0.05	0.05	0.15	0.12	0.15	0.55	0.16	0.33	0.20	0.27	0.53	0.04	0.02	0.04	0.10	0.11	0.10	0.21	0.07
Yb	0.73	2.02	2.86	1.30	0.37	0.34	0.82	0.84	1.01	3.96	1.11	2.33	1.52	1.86	3.82	0.34	0.18	0.37	0.70	0.82	0.67	1.54	0.50
Lu	0.12	0.33	0.41	0.20	0.06	0.05	0.13	0.14	0.16	0.65	0.17	0.37	0.26	0.31	0.60	0.02	0.02	0.04	0.10	0.13	0.10	0.24	0.09
ΣREE	130.52	146.60	241.51	117.78	64.89	64.08	88.51	99.57	143.9	192.70	140.35	181.53	74.39	187.33	209.59	98.28	51.44	63.58	39.56	68.38	46.13	97.16	48.37
ΣLREE	124.06	134.08	218.75	104.94	62.77	61.56	81.43	93.71	134.48	171.16	131.30	164.86	67.17	173.62	187.15	94.22	49.65	60.02	34.52	63.02	41.64	87.40	44.90
ΣHREE	4.12	11.92	21.44	11.02	2.78	2.31	6.79	4.52	8.92	20.68	8.50	14.76	7.87	13.01	21.65	2.78	1.65	3.26	4.65	4.00	4.21	94.15	3.25
ΣLREE/ΣHREE	24.43	11.25	10.20	9.61	22.58	26.65	11.99	16.98	14.08	8.28	14.45	11.24	8.53	13.35	8.64	34.25	30.09	18.41	7.42	12.60	9.89	9.55	13.82
Eu/Eu*	0.12	0.07	0.03	0.07	0.04	0.30	0.06	0.14	0.05	0.06	0.07	0.06	0.13	0.05	0.03	0.21	0.32	0.14	0.24	0.22	0.23	0.10	0.30
Ce/Ce*	0.10	0.04	0.03	0.06	0.02	0.11	0.05	0.06	0.03	0.03	0.05	0.03	0.07	0.04	0.02	0.11	0.32	0.07	0.08	0.14	0.10	0.05	0.11
La/Yb	34.84	17.44	14.50	14.8	44.70	62.79	26.84	31.82	34.91	10.45	27.75	19.44	11.99	21.47	12.88	54.00	43.89	39.46	13.96	16.98	17.78	14.73	27.42
Y/Ho	24.77	26.76	21.10	24.02	22.26	23.61	30.82	24.98	24.38	26.17	22.87	24.33	23.72	24.48	24.83	36.50	43.2	32.08	20.09	23.43	24.07	17.9	23.14
Sm/Nd	0.16	0.17	0.20	0.19	0.15	0.14	0.17	0.15	0.17	0.16	0.16	0.16	0.17	0.17	0.17	0.14	0.16	0.19	0.20	0.18	0.19	0.20	0.15
La_N/Yb_N	23.50	11.75	10.45	10.65	13.84	18.7	18.11	21.45	24.22	7.04	18.71	13.11	8.08	14.48	8.68	37.01	25.4.63	26.61	9.41	11.45	11.97	94.93	18.51
La_N/Sm_N	7.14	4.74	3.24	3.12	6.52	6.35	4.37	8.45	4.46	4.39	4.70	6.00	4.88	4.59	4.18	6.36	4.18	3.97	3.94	4.76	4.55	4.51	8.79
Gd_N/Yb_N	1.89	1.29	2.06	2.43	1.29	1.52	2.42	1.62	2.67	0.88	2.34	1.61	1.03	1.88	1.24	2.39	2.78	2.79	1.62	1.44	1.48	1.40	1.63

Table 4.8e: Rare earth element (REE) concentrations and normalized values of Sm and Fl sub-facies in the Northern Bida Basin

	Massive sandstone (Sm) sub-facies			Very fine, laminated mudstone (Fl) sub-facies						
Sample No	Gbale	Kudu	Rabba	Gbugbu	Bida	Jimma	Baro	Agbonna	Kudu	Rabba
	GBL-1A	KUD-1A	RAB-1E	GBU-1B	BDA-1K	JIM-1B	BAR-1J	AGB-1D	KUD-1C	RAB-1L
La	14.40	19.30	6.77	56.00	94.62	28.91	17.37	56.16	12.00	30.81
Ce	24.30	38.80	17.69	114.00	190.32	53.12	42.42	104.39	34.80	54.30
Pr	2.65	4.22	1.97	13.93	20.73	6.26	3.74	12.94	2.24	6.96
Nd	9.76	17.43	7.69	46.35	70.08	21.57	11.53	46.49	8.59	24.14
Sm	1.30	3.23	1.69	7.75	11.97	3.72	1.87	8.32	1.69	4.17
Eu	0.28	0.54	0.41	1.57	0.78	0.46	0.14	1.53	0.21	0.43
Gd	1.37	1.96	1.61	4.64	9.20	3.74	1.88	6.62	0.73	3.58
Tb	0.18	0.21	0.30	0.60	1.40	0.53	0.22	1.02	0.11	0.45
Dy	0.82	1.36	1.60	2.51	7.48	3.54	1.26	4.39	0.71	1.97
Ho	0.19	0.19	0.34	0.38	1.66	0.76	0.26	1.11	0.11	0.41
Er	0.54	0.56	0.88	0.83	4.89	2.21	0.76	2.98	0.29	1.04
Tm	0.08	0.07	0.14	0.12	0.77	0.42	0.13	0.42	0.03	0.17
Yb	0.47	0.53	1.07	0.74	4.80	2.39	0.79	2.88	0.30	1.26
Lu	0.07	0.07	0.16	0.08	0.99	0.37	0.12	0.45	0.04	0.21
ΣREE	57.41	88.47	42.32	249.50	420.69	128.00	82.49	251.70	62.85	130.90
ΣLREE	53.41	82.98	34.81	238.03	387.72	113.58	76.93	229.30	60.32	121.38
ΣHREE	3.72	4.95	6.10	5.4.90	32.19	13.96	4.42	20.87	2.32	9.09
ΣLREE/ΣHREE	14.36	16.76	4.87	24.04	12.04	8.14	14.19	10.99	26.00	13.35
Eu/Eu*	0.22	0.12	0.21	0.06	0.01	0.12	0.05	0.04	0.23	0.04
Ce/Ce*	0.08	0.05	0.16	0.02	0.01	0.06	0.10	0.02	0.16	0.03
La/Yb	30.64	36.42	6.33	74.68	16.31	12.1	21.99	19.50	40.00	24.45
Y/Ho	33.89	29.84	23.78	21.53	26.87	29.04	28.84	24.28	28.18	23.93
Sm/Nd	0.13	0.19	0.22	0.17	0.17	0.17	0.16	0.18	0.20	0.17
La_N/Yb_N	20.64	24.51	4.27	51.03	11.00	7.53	14.82	13.15	26.88	16.48
La_N/Sm_N	6.96	3.76	2.52	4.55	4.97	7.47	4.84	4.25	4.46	4.65
Gd_N/Yb_N	2.35	2.98	1.21	4.06	1.28	0.7	1.92	1.85	1.96	2.29

Table 4.8f: Rare earth element (REE) concentrations and normalized values of Fm sub-facies in the Northern Bida Basin

Sample No	Gbugbu	Lemu	Jimma	Dokko	Enagi	Kudu	Kudu	Kutigi	Kutigi	Kutigi
	GBU-1A	LEM-1P	JIM-1N	DOK-1F	ENG-1B	KUD-1B	KUD-1F	KUT-2P	KUT-2Q	KUT-2R
La	7.80	44.33	64.04	21.73	36.29	21.00	12.80	27.80	44.30	16.60
Ce	14.40	110.00	107.8	43.77	78.54	43.10	54.00	33.80	78.70	21.70
Pr	1.51	12.59	11.82	4.40	8.09	4.50	2.70	4.39	8.07	2.82
Nd	4.61	43.23	38.43	14.22	28.37	17.19	11.00	21.29	33.39	10.26
Sm	0.70	8.60	6.18	2.12	4.83	2.94	2.06	2.99	4.10	1.21
Eu	0.16	1.32	0.93	0.41	0.70	0.57	0.30	0.58	0.91	0.30
Gd	0.63	7.30	4.99	1.44	4.42	1.87	1.02	2.27	3.55	1.13
Tb	0.10	0.99	0.79	0.21	0.63	0.21	0.13	0.22	0.41	0.12
Dy	0.51	4.68	4.45	0.92	3.07	1.44	0.73	1.56	2.45	0.86
Ho	0.09	1.00	0.98	0.18	0.65	0.24	0.13	0.26	0.41	0.12
Er	0.25	2.72	2.82	0.45	1.68	0.66	0.40	0.72	1.17	0.36
Tm	0.04	0.48	0.43	0.06	0.27	0.07	0.05	0.08	0.15	0.04
Yb	0.24	2.86	3.12	0.41	1.94	0.64	0.35	0.57	0.99	0.31
Lu	0.03	0.41	0.53	0.07	0.32	0.08	0.05	0.08	0.12	0.03
ΣREE	31.07	241.51	247.31	90.39	169.80	94.51	84.72	97.61	179.72	54.86
ΣLREE	29.02	218.75	228.27	86.24	156.12	88.73	82.56	91.27	169.56	52.59
ΣHREE	1.89	21.44	18.11	3.74	12.98	4.21	2.86	4.76	9.25	2.97
ΣLREE/ΣHREE	14.35	10.20	12.60	23.06	12.03	17.03	28.87	14.85	18.33	17.71
Eu/Eu*	0.50	0.03	0.31	0.13	0.05	0.14	0.20	0.12	0.07	0.30
Ce/Ce*	0.18	0.03	0.08	0.04	0.04	0.05	0.18	0.03	0.02	0.06
La/Yb	32.50	14.5	20.53	53.00	18.71	32.81	36.57	48.77	44.75	53.55
Y/Ho	27.78	21.1	28.83	24.75	22.99	24.96	32.77	32.96	33.02	33.50
Sm/Nd	0.15	0.20	0.16	0.15	0.17	0.17	0.19	0.14	0.15	0.12
La_N/Yb_N	21.88	10.45	30.82	14.94	12.61	22.14	24.72	32.85	30.15	36.18
La_N/Sm_N	7.01	3.24	6.86	8.53	4.73	4.49	3.91	4.85	4.46	8.62
Gd_N/Yb_N	2.11	2.06	2.14	1.27	1.84	2.36	2.36	3.21	2.89	2.95

Table 4.8g: Rare Earth Element values of Composition (ppm) of Published Data using for comparison with this study

Sample No	Average Post Archean Australian Shale (PAAS) values after McLennan (2001)	Average upper continental crust values (UCC) after McLennan (1989)
La	38.20	31.00
Ce	79.60	63.00
Pr	8.83	7.10
Nd	33.90	27.00
Sm	4.55	4.70
Eu	1.08	1.00
Gd	4.66	4.00
Tb	0.77	0.70
Dy	4.68	3.90
Ho	0.99	0.83
Er	2.85	2.30
Tm	0.41	0.30
Yb	2.82	2.00
Lu	0.43	0.31
ΣREE	184.77	148.14
ΣLREE	166.08	132.80
ΣHREE	17.61	14.34
ΣLREE/ΣHREE	9.43	9.26
Eu/Eu*	0.71	0.66
La/Yb	13.55	14.50
Y/Ho	24.57	24.30
Sm/Nd	0.16	0.17
La_N/Yb_N	10.45	9.15
La_N/Sm_N	4.15	4.27
Gd_N/Yb_N	1.61	1.35

4.5.4 Statistical Analysis

4.5.4.1 Correlation Matrix

4.5.4.1.1 Major Elements

The generated summary and correlation matrix of variables and factors extracted are presented in table 4.9a. This quantitative result for major elements represents and mimics the bulk major elemental compositions of the study sediments. The forty-six (46) observations in the table represent the total number of the analyzed samples for the major elements while their individual minimum, maximum, mean and standard deviation values are also presented.

The correlation matrix (Pearson) table presented in table 4.9b is used to designate covariant groups of elements. This table shows nature of the groups of highly correlated elements and their relationship which can be used to deduce the important factors influencing the elements. From the table, it is shown that SiO_2 is negatively correlated with other major elements and this confirms presence of bulk of SiO_2 as quartz grains. Strong negative correlation of SiO_2 with Al_2O_3 (r = -0.668), Fe_2O_3 (r = -0.673) and weak negative correlation with MgO (r = -0.342) may point to the abundance distribution of quartz minerals which invariably indicate siliciclastic deposit. Strong correlations of MnO with TiO_2 (r = 0.732) may indicate contribution of phyllosilicates (rutile) while positive correlations of MgO with CaO (r = 0.791), K_2O (r = 0.717), Na_2O (r = 0.747) and CaO with Na_2O (r = 0.749), K_2O (0.550) and also Na_2O with K_2O (0.749) may suggest contributions of clay minerals.

Table 4.9a: Summary Statistics (Quantitative Data) for Major Elements

Variable	Observations	Minimum	Maximum	Mean	Std. deviation
SiO_2	46	68.69	92.44	84.063	4.233
Al_2O_3	46	4.15	18.38	8.598	3.129
Fe_2O_3	46	0.67	17.57	2.793	2.624
MnO	46	0.00	0.04	0.010	0.006
MgO	46	0.00	0.40	0.064	0.088
CaO	46	0.01	0.37	0.060	0.078
Na_2O	46	0.01	0.22	0.054	0.050
K_2O	46	0.01	3.24	0.682	0.852
TiO_2	46	0.12	4.89	0.606	0.750

Table 4.9b: Bivariate (Pearson) Correlation matrix for Major Elements

Variables	SiO_2	Al_2O_3	Fe_2O_3	MnO	MgO	CaO	Na_2O	K_2O	TiO_2
SiO_2	**1**								
Al_2O_3	*-0.668	**1**							
Fe_2O_3	*-0.673	0.085	**1**						
MnO	-0.227	-0.070	0.353	**1**					
MgO	*-0.342	0.135	0.095	0.056	**1**				
CaO	-0.059	0.022	0.000	0.005	*0.791	**1**			
Na_2O	-0.033	0.119	-0.110	-0.042	*0.588	*0.747	**1**		
K_2O	-0.200	0.031	-0.107	-0.033	*0.717	*0.550	*0.749	**1**	
TiO_2	-0.163	0.087	0.141	*0.732	-0.100	-0.115	-0.132	-0.228	**1**

* Very strong and strong correlations

** Moderate and weak correlations

4.5.4.1.2 Trace Elements

The data for quantitative trace elements results is presented in table 4.10a and this well represent the trace element composition results of the studied sediments. There are seventy-eight (78) observations with their individual minimum, maximum, mean and standard deviation values which are also presented in the table.

The summary and correlation matrix of variables is presented in table 4.10b. The results of correlation matrix is used to designate covariant groups of elements in the studied sediments by the using the relationship of the highly correlated elements to induce the function of different factors influencing the elements as shown by Pearson correlation matrix table in 4.10b. The result shows a very strong positive correlations of Sc with U (r = 0.809), strong Nb (r = 0.689), Y (r = 0.673), Zr (r = 0.663), Hf (r = 0.651), Th (r = 0.649), V (r = 0.634) and moderate correlation with Co (r = 0.450). Also, Co has strong positive correlation with U (r = 0.628), moderate correlation with Ba (r = 0.461), Y (r = 0.419) but weakly correlated with Th (r = 0.361), V (r = 0.343), Nb (r = 0.342) and Zr (r = 0.315). Nb has a strong positive correlation with Th (r = 0.714), Hf (r = 0.712), Y (r = 0.701), U (r = 0.616) and moderately correlated with V (r = 0.460). Also, Hf show very strongly correlated with Th (r = 0.839), strongly with Y (r = 0.739) and U (r = 0.680) but moderately correlated with V (r = 0.620).

There is also a very strong positive correlation of Zr with Hf (r = 0.990) and Th (r = 0.836), strongly correlated with Y (r = 0.751), Nb (r = 0.720) and moderate with U (r = 0.692). Th is strongly correlated with Y (r = 0.798) and U (r = 0.702) but moderately correlated with V (r = 0.508) but weakly correlated with (r = 0.460). Strong correlation of U with Y (r = 0.734) and moderate correlation with V (r = 0.493) are also recorded that probably indicate contributions of heavy mineral which is a good tool for provenance studies.

The strong positive correlation of Rb with Ba (r = 0.721), Sr (r = 0.652) and Sr with Ba (r = 0.800) and moderately with Y (r = 0.496) suggest that they are good tools for determining weathering, leaching and depositional environment. Also very strong positive correlation of Ba with Rb (r = 0.92) and Sr (0.72) may indicate contributions of clay mineral contentss and this can be supported by the positive correlation of Nb with Sc (r = 0.71), Zr (r = 0.95), Hf (r = 0.94), Th (0.83) and Y (r = 0.77).

Table 4.10a: Summary statistics (Quantitative data) for Trace Elements

Variable	Observations	Minimum	Maximum	Mean	Std. deviation
Sc	78	1.110	18.000	3.743	2.311
Co	78	0.600	30.520	3.522	3.636
Rb	78	0.150	124.400	8.429	12.854
Sr	78	0.910	85.4.010	11.732	14.987
Zr	78	0.400	1884.000	202.829	245.4.682
Nb	78	0.020	75.4.160	7.391	5.4.389
Ba	78	4.500	814.500	93.177	134.436
Hf	78	0.020	76.170	7.934	5.4.593
Th	78	1.440	74.520	10.476	5.4.591
U	78	0.270	14.210	2.251	2.177
Y	78	0.950	61.190	11.001	10.147
Cr	78	4.900	1296.000	383.807	227.479
Ni	78	3.000	176.000	13.396	16.326
V	78	1.600	92.870	15.4.725	14.525

Table 4.10b: Bivariate (Pearson) Correlation matrix for Trace Elements

Variables	Sc	Co	Rb	Sr	Zr	Nb	Ba	Hf	Th	U	Y	Cr	Ni	V
Sc	**1**													
Co	**0.450	**1**												
Rb	0.106	0.233	**1**											
Sr	0.208	0.226	*0.653	**1**										
Zr	*0.663	**0.315	0.052	0.104	**1**									
Nb	*0.689	**0.342	0.050	0.228	*0.720	**1**								
Ba	0.178	**0.461	*0.721	*0.800	0.175	0.145	**1**							
Hf	*0.651	0.295	0.064	0.110	*0.990	*0.712	0.185	**1**						
Th	*0.649	**0.361	0.191	0.214	*0.836	*0.714	0.299	*0.839	**1**					
U	*0.809	*0.628	0.197	0.187	*0.692	*0.616	**0.306	*0.680	*0.702	**1**				
Y	*0.673	**0.419	**0.290	**0.496	*0.751	*0.701	**0.464	*0.739	*0.798	*0.734	**1**			
Cr	0.203	0.168	0.123	0.092	0.194	0.080	0.188	0.205	0.040	0.186	0.079	**1**		
Ni	0.087	0.101	0.099	0.006	-0.066	-0.035	0.025	-0.079	0.154	0.180	-0.004	-0.205	**1**	
V	*0.634	**0.343	0.192	0.247	**0.460	*0.620	0.153	**0.470	*0.508	**0.493	**0.490	0.249	-0.079	**1**

* Very strong and strong correlations

** Moderate and weak correlations

4.5.4.2 Factor and Principal Component Analysis

The geochemical results presented in tables 4.6 and 4.7 (Major and trace elements) were subjected to Factor and Principal Component Analysis techniques to determine element associations and the geochemical processes during sediments deposition. In sediments the distribution of elements is determined to a large degree by non-equilibrium processes making prediction of the distribution of elements more difficult. Nevertheless the element distribution in sediments is characterized by the occurrence of geochemically coherent groups of elements, i.e. by groups of elements that under given conditions will behave in the same manner. The composition of these groups will be determined by certain underlying processes or fundamental Factors.

Factor analysis (FA) also called a multivariant analysis is a statistical technique that is used to reduce a large number of variables into fewer numbers of factors to explain variability among observed random variables in terms of fewer unobserved random variables called factors. Factor analysis extracts maximum common variance from all variables and puts them into a common score. The Factor Analysis techniques have been successfully employed and applied by various authors to the geochemistry of sediments. Spencer *et al*. (1968) and Hayashi *et al*. (1997) consider the distribution of elements in sediments to be largely governed by the following factors; source rock composition, the environmental conditions at the weathering site, the nature of transportation processes, the environmental conditions at the depositional site, tectonic events during the weathering, transportation and depositional cycle, and diagenetic processes.

The application of this tool usually begins with a learning set, a data subset used to establish correlations between observations and the factors being determined, and then proceeds to a

predicting set, where the relations are used for predicting the factors associated with additional observations. It is especially useful in geochemistry when one has a known target or some other way to understand the meaning of the obtained associations. Therefore, application of this technique in the present study is possible not only to locate groups of coherent elements in a complex data matrix but also to measure the extent of influence of the different groups. With the knowledge of the composition of the groups, it is then possible to infer the complex interacting causes that underlie element distributions in sediments. This is because, composition of siliciclastic rocks predominantly reflect the nature and proportion of their detrital components and hence their provenance according to Bhatia (1983), Roser and Korsch (1986 and 1988).

Principal component analysis (PCA), a classical multivariate statistical method, was introduced by Pearson (1901) using the matrix of correlations between variables to replace the original variables by components that preserve the original variance, but re-arrange it so that many fewer components account for the bulk of the variance in the data. Davis (1973) points out that "Factor analysis commonly is regarded as a deep and mysterious methodology of great complexity, because it essentially aims to reduce the observed relationships between many variables to simpler relationships among fewer variables. Given a data array, factor analytical techniques enable identification of any underlying pattern of relationships which would allow the data to be rearranged or reduced to a smaller set of underlying variables which can be taken as the factors accounting for the observed relationships in the dataset.

Several authours including Siegel *et al.* (1995), Reimann *et al*. (2002), Zhang *et al*. (2002), Pearce *et al*. (2005), Ali *et al*. (2006), Svendsen *et al*. (2007) and Pe-Piper *et al*. (2008) submitted that PCA is generally applied to reduce multidimensional datasets into lower

dimensions to determine element associations and to extract unobservable quantities hidden in the original measurements. It has been used in many disciplines, including engineering, geology and geophysics (Ka-mierczuk and Jarzyna, 2006) to indicate the relationships that exist among all studied variables and therefore improve and enables the creation of new variables referred to as the principal components (PCs) that represents the linear combinations of the original ones.

Each PC explains a percentage of the total variability of the original data and this percentage accounted for is interpreted as the portion "explained by" the process represented by the PC. The first PC is more highly correlated with the original variables than the second while the second is more correlated with them than the third, and so on. The individual transformed observations are called scores, and PCs interpreted as representing geological processes can be mapped by the scores. The final number of the principal components can be established by using the Kaiser criterion, or the scree test (Kaiser, 1960). The scree test is a graphical method that relies on finding a characteristic point on the plot of decreasing eigenvalues. According to this criterion, principal components with eigenvalues greater than 1.0 is the most important and thus will be extracted and employ for interpretations.

The geochemical results of the studied sediments were subjected to principal component analysis (PCA) to determine elemental assemblages associated with geochemical processes during sediments deposition. Reimann *et al*. (2002) concluded that application of PCA in study will not only explain the variance within a multivariate dataset using only a few underlying factors but also possibly find hidden structures in the dataset that would not have otherwise been recognized.

4.5.4.2.1 Major Elements

The Principal Component Analysis (PCA) as applied to the geochemical data in this study provides an insight into the processes prevalent in the study area. The result of the PCA for the major elements shows that each sample has case-wise scores for each principal component. A high case-wise score values that a sample correlates well with the component, while a low value indicates a poor correlation.

As can be seen in table 4.11, the first 3 factors out of nine (9) extracted factors outlined by the PCA results provides eigenvalues greater than 1.0 (>1) i.e. PC1-PC3, together they explain adequately the overall dimensionality of the data set and accounted for 77.175% % of the total variance in the data, while the remaining factors with eigenvalues lesser than 1.0 (<1.0) i.e. (PC4-PC9) accounted for only 22.875% of the total variance. The communalities, which give the fraction of the variance of each element that is explained by the factors extracted, varies and this implies that over 75% of the variance is explained by the 3 factors extracted from table 7.8 and therefore, no element is significantly loaded on all 3 factors. It is important to note at this explains that F1-F3 (PC1-PC3) indicates the contributions of main elements and therefore substantial geological processes that has prevailed within the study area while F4-F9 (P4-P9) suggests minimal contribution and therefore can be ignored.

Factor 1 (F1): The F1 explained 34.341% of the total variance and has high loadings of greater than 0.75 (>0.75) for MgO, CaO, Na_2O and K_2O which suggest contributions of the elements during weathering process and depositional environments.

Factor 2 (F2): This factor is characterized by very high loadings of 0.75–0.50 with 24.606% of the total variance on Fe_2O_3, MnO and Ti_2O (except for SiO_2 with higher but negative value) which may indicate prevalence of effect of clay mineral factors and diagenesis.

Factor 3 (F3): F3 explained 16.228% of the total variance and also with loadings between 0.75 and 0.50 on MnO and Ti_2O which may also indicate significant contribution of clay mineral factors. It is also suggested that clay minerals have principally formed in the source area rather than as a result of post-depositional diagenetic processes.

The graphical representation of these factors and the element loadings are presented in figures 4.26a (Scree plot) and b (F1 versus F2 plot) to give an indication of the extent of interrelation between the factors. The final datasets (Figure 4.27a) and Eigenvector plots showing the variance trends (Figure 4.27b) are graphical evidence that supports the above suggestions. In analyzing the graphs, three features are important;

(a) The relative distance of a variable from the two axes,
(b) The direction of a variable relative to the axes (both positive and negative loadings may be displayed) and
(c) The clustering of the variables.

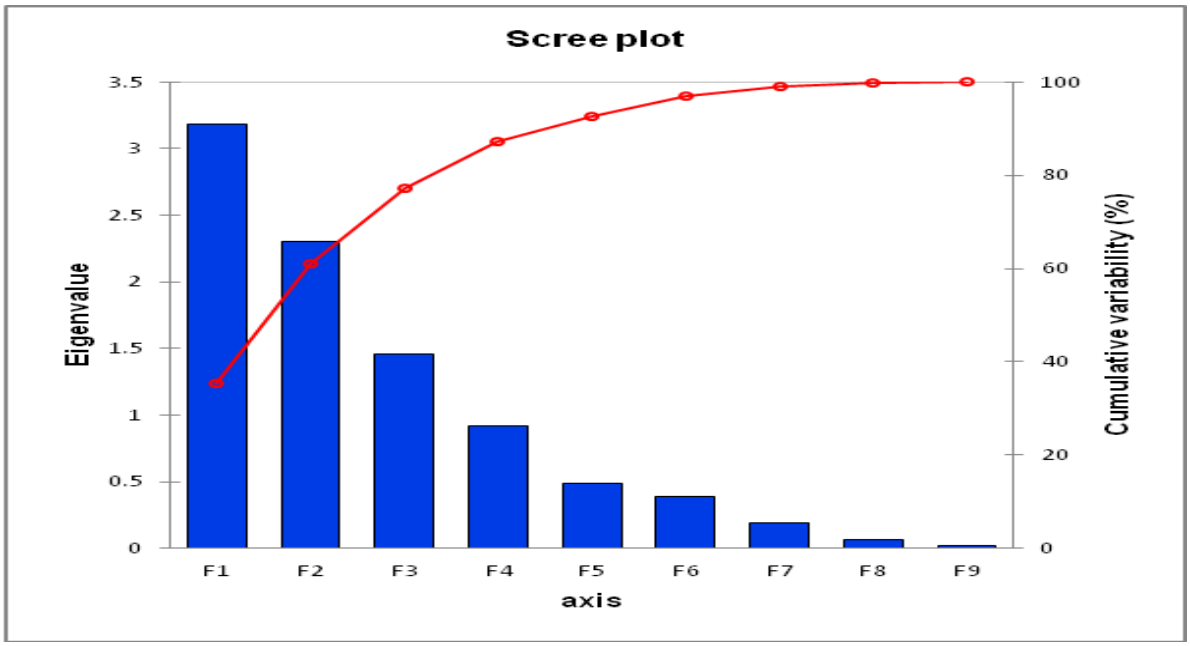


Figure 4.27a: Scree plot of final dataset for Major Elements in Northern Bida Basin showing F1-F3 as significant and F4-F9 as minimal contributors respectively.

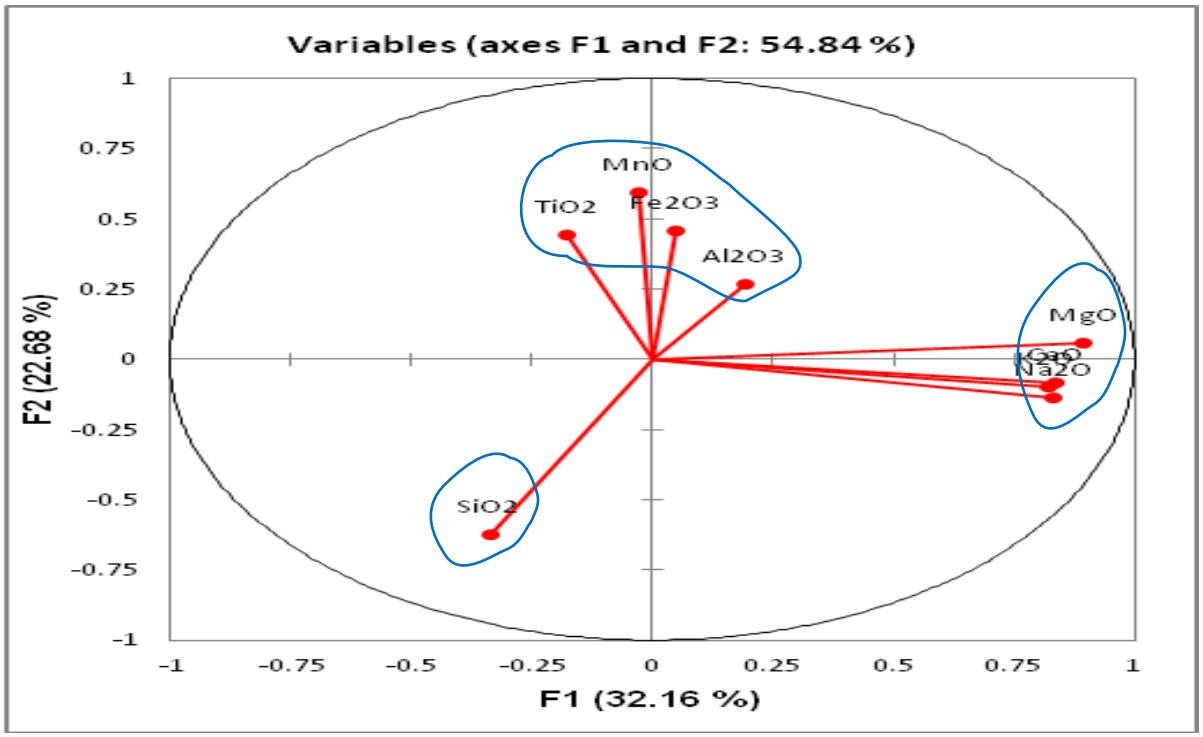


Figure 4.27b: Eigenvector plots from the Principal Component Analysis showing the grouping of certain elements of similar geological processes in Northern Bida Basin. Group of elements indicate process of maturity and provenance whereas SiO_2, Al_2O_3, Fe_2O_3 and MnO and TiO_2 group may indicate weathering and leaching.

Table 4.11: Factor loadings and other corresponding values of the Principal Component Analysis for Major Elements

Factor loadings	F1	F2	F3	F4	F5	F6	F7	F8	F9
SiO_2	-0.312	-0.808	0.463	-0.049	-0.114	0.065	0.046	0.083	0.079
Al_2O_3	0.213	0.458	-0.617	-0.580	-0.102	0.050	0.109	0.031	0.052
Fe_2O_3	0.038	0.729*	-0.147	0.626	-0.076	0.199	-0.064	0.043	0.052
MnO	-0.043	0.678*	0.659*	0.023	0.117	0.004	0.301	0.005	-0.006
MgO	0.894*	0.104	0.065	0.093	-0.085	-0.387	-0.022	0.142	-0.006
CaO	0.854*	-0.087	0.214	0.058	-0.438	-0.001	0.040	-0.140	0.013
Na_2O	0.855*	-0.157	0.154	-0.150	0.018	0.433	-0.029	0.085	-0.043
K_2O	0.855*	-0.121	0.066	-0.002	0.488	-0.031	-0.048	-0.074	0.053
TiO_2	-0.207	0.627*	0.576*	-0.387	-0.058	-0.021	-0.279	-0.007	0.013
Eigenvalue	3.181	2.305	1.460	0.914	0.484	0.385	0.192	0.062	0.017
Variability (%)	34.341	24.606	16.228	10.160	4.378	4.279	2.134	0.689	0.186
Cumulative %	34.341	60.947	77.175	87.334	92.712	96.991	99.124	99.814	100.000
Controlling Elements	**MgO, CaO, Na_2O & K_2O**	**Al_2O_3, MnO & TiO_2**	**MnO & TiO_2**	—	—	—	—	—	—
Controlling Processes	**Weathering Process and Depositional Environment**	**Clay mineral factors and Diagenesis**	**Clay mineral factors**	—	—	—	—	—	—

* Variables with >0.75 loadings; ** Variables with 0.75–0.50 loadings

4.5.4.2.2 Trace Elements

As shown in table 4.12, the first four PCs (PC1-PC4 on F1-F4) out (14) extracted PCs have eigenvalues of greater than 1.0; together they explain 78.942% of the total variance in the data and it implies that over 75% of the variance is explained by the 4 factors extracted. The elements; Sc, Co, Zr, Nb, Hf, Th, U, Y, V, Rb, Sr, Ba, Ni and Co present in the extracted PC are significantly loaded on all 4 factors. The remaining factors with eigenvalues lesser than 1.0 (<1.0) i.e. (PC5-PC14) accounted for 21.058% of the total variance (Table 4.12). It is important to note at this point that F1-F4 (PC1-PC4) indicates the contributions of main trace elements and therefore substantial and suggested to have contributed to the geological processes that has prevailed within the study area whereas F5-F14 (P5-P14) indicates minimal contribution and therefore can be ignored in interpretation.

Factor 1 (F1): The high loadings for Sc, Co, Zr, Nb, Hf, Th, U, Y and V and they account for 44.712% of total variance suggest that this factor should be designated a "heavy mineral factor". These elements in F1 also had higher loadings greater than 0.75 (>0.75) for all the elements in the category except for Co and V with loadings lesser than (<0.75). The recorded loading greater than 0.75 (>0.75) for majority of the elements but lesser (<0.75) for fewer elements might suggest contributions in more than one geological process but with one prevailing on the other. The elements with higher loadings were suggested to have contributed basically to the heavy mineral factors while the lower loadings suggest contributions to provenance process.

Factor 2 (F2): This factor is characterized by very high loadings on Ba, Rb and Sr with 16.644% of the total variance and strong loadings greater than 0.75 (>0.75). The pattern of loadings suggests that Factor 2 may indicate non-availability of a carbonate phase and the

occurrence of the elements in weathering and leaching processes. Presence of Rb could also possibly imply the presence of K-feldspar associated with the heavy mineral suite as a response to various physical sorting processes.

Factor 3 (F3): The F3 is characterized by very high loadings displayed by positive Ni and negative Cr strong loadings greater than 0.75 (>0.75) with 5.4.236% of the total variance and so designate as a heavy mineral factors.

Factor 4 (F4): This factor only explained 7.350% of the total variance with average strong positive loading lesser than 0.75 (<0.75) on Co and Cr which designate it heavy mineral factors.

The extent of interrelation between the factors (F1-F4) were graphically presented and the element loadings were presented on figures 4.28a (Scree plot) and b (F1 versus F2 plot). These figures also give an indication of the important three features including; the relative distance of a variable from the two axes, the direction of a variable relative to the axes and the clustering of the variables.

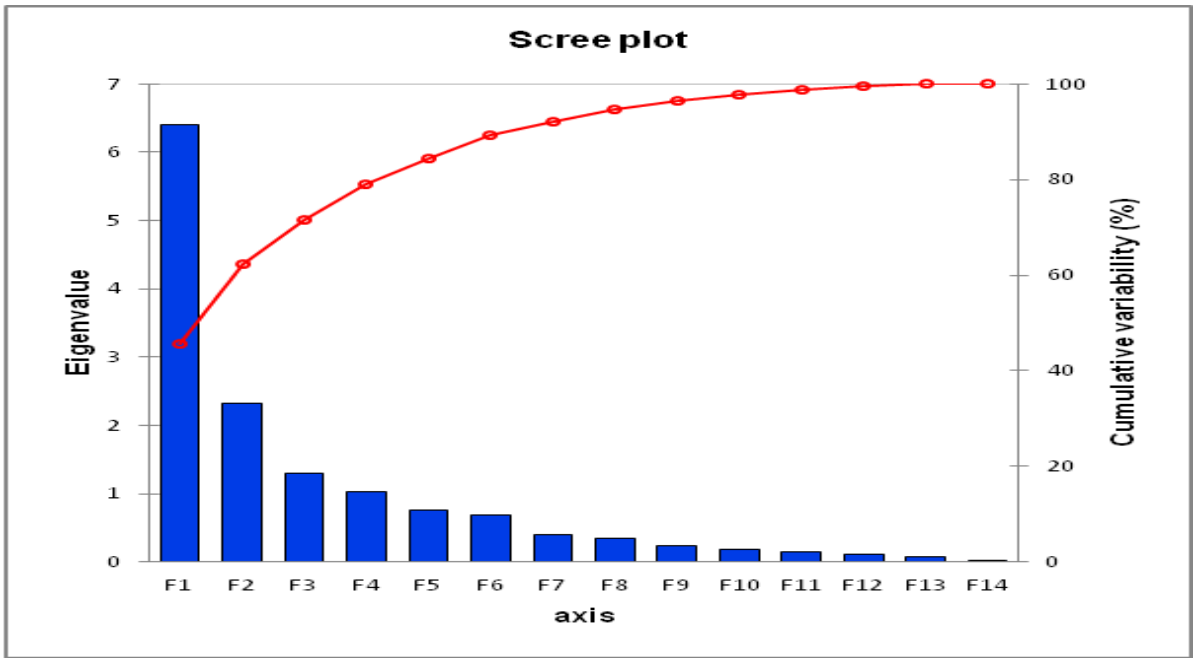


Figure 4.28a: Scree plot of final dataset for Trace Elements in Northern Bida Basin showing F1-F2 as significant, F3-F6 as moderate and F7-F14 as minimal contributors.

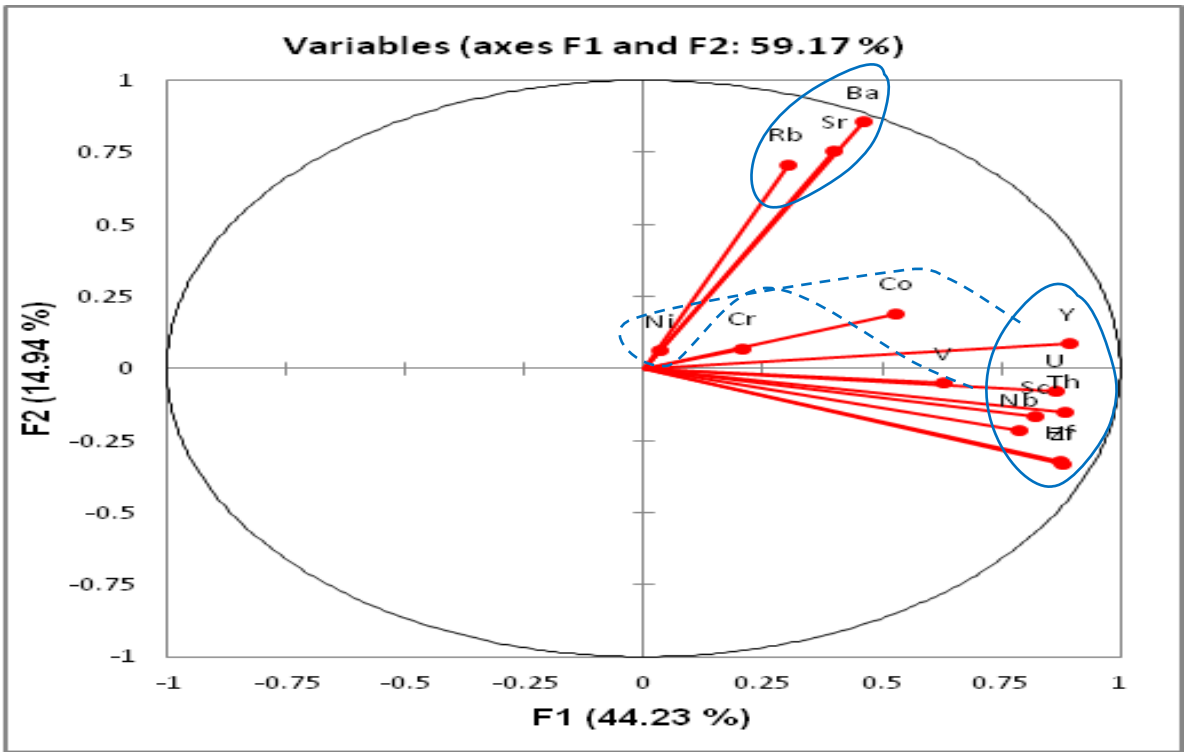


Figure 4.28b: Eigenvector plots from the Principal Component Analysis showing the grouping of certain elements of similar geological processes; presence of Sc, Co, Zr, Nb, Hf, Th, U and Y in the group points to the significant elements for source rock and provenance whereas relationship of Rb, Sr and Ba indicates weathering and leaching process.

Table 4.12: Factor loadings and other corresponding values of the Principal Component Analysis for Trace Elements

Factor Loadings	F1	F2	F3	F4	F5	F6	F7	F8	F9	F10	F11	F12	F13	F14
Sc	0.828*	-0.183	0.040	0.216	0.200	-0.063	-0.170	0.316	0.019	-0.171	0.124	-0.114	-0.035	-0.002
Co	0.565*	0.222	0.114	0.550*	-0.027	0.510*	0.101	-0.176	0.016	-0.026	-0.052	-0.105	0.023	-0.003
Rb	0.317	0.799*	0.015	-0.075	-0.011	-0.194	0.372	0.195	0.183	0.046	-0.043	-0.063	-0.002	-0.001
Sr	0.411	0.782*	-0.054	-0.245	0.160	-0.053	-0.295	-0.055	-0.054	-0.079	-0.100	-0.026	0.139	0.001
Zr	0.859*	-0.328	-0.071	-0.191	-0.268	-0.025	0.078	-0.027	-0.013	-0.132	-0.108	-0.007	-0.018	0.064
Nb	0.810*	-0.248	-0.019	-0.137	0.259	-0.002	-0.105	-0.213	0.368	0.033	0.033	0.047	-0.018	-0.001
Ba	0.458	0.818*	-0.034	-0.050	-0.161	0.114	-0.032	-0.093	-0.061	-0.095	0.157	0.133	-0.117	0.002
Hf	0.854*	-0.319	-0.091	-0.205	-0.268	-0.045	0.099	-0.034	-0.027	-0.141	-0.090	0.017	-0.003	-0.064
Th	0.872*	-0.159	0.187	-0.192	-0.128	-0.081	0.133	-0.112	-0.102	0.107	0.223	-0.060	0.120	0.003
U	0.857*	-0.084	0.174	0.287	-0.079	0.102	-0.041	0.255	0.011	0.108	-0.047	0.206	0.079	0.002
Y	0.892*	0.073	0.055	-0.228	-0.025	0.080	-0.175	0.050	-0.103	0.252	-0.082	-0.090	-0.121	-0.005
Cr	0.232	0.093	-0.673	0.484	-0.298	-0.362	-0.125	-0.084	0.032	0.075	0.014	-0.027	0.009	0.000
Ni	0.038	0.085	0.831*	0.288	-0.091	-0.423	-0.072	-0.143	-0.007	-0.028	-0.052	-0.003	-0.035	-0.001
V	0.668*	-0.070	-0.219	0.163	0.576*	-0.197	0.214	-0.112	-0.199	-0.003	-0.044	0.058	-0.028	0.002
Eigenvalue	6.400	2.330	1.293	1.029	0.755	0.692	0.409	0.347	0.239	0.179	0.139	0.107	0.073	0.008
Variability (%)	44.712	16.644	5.4.236	7.350	4.389	4.946	2.919	2.482	1.704	1.278	0.994	0.767	0.520	0.059
Cumulative %	44.712	62.356	71.592	78.942	84.331	89.277	92.196	94.678	96.382	97.659	98.654	99.421	99.941	100.000
Controlling Elements	**Sc, Co, Zr, Nb, Hf, Th, U, Y & V**	**Rb, Sr & Ba**	**Ni & Cr**	**Co & Cr**	**V**	**Co**	—	—	—	—	—	—	—	—
Controlling Process	**Heavy Minerals and Provenance**	**Weathering and Leaching**	**Heavy Minerals**		**Provenance**		—	—	—	—	—	—	—	—

* Variables with >0.75 loadings; ** Variables with 0.75–0.50 loadings

CHAPTER FIVE

DISCUSSION

5.1 Paleo-Environments, Diagenetic History and Reservoir Potentials

This section presents and discusses the depositional environments and diagenetic history and conditions of the studied sandstones. Depositional environments studies involving applications of statistical parameters or measures as a diagnostic using grain size analysis of sediments have long been oriented (McLaren, 1981). The depositional environments determination using graphic plots method have commonly been employed in many past studies (e.g. Folk and Ward, 1957; Mason and Folk, 1958; Moiala and Weiser, 1968). The graphic plot is a bivariate type that shows the combinations of two or more phi-graphic of grain size parameters' distributions; mean grain size, standard deviation, skewness and kurtosis as a measure in interpreting different aspects of depositional environments (Blatt, Mlddleton and Murray 1980). The application of textural characteristics and the derived statistical parameters of the studied sediments include parts of the discussions in this chapter with the intention of applying for interpreting the conditions and processes prevailed in the environments during sediments deposition.

Also applied in this study and discussed is the post-depositional effect (diagenesis) on some selected sandstone samples with main focus on its effects on porosity and reservoir quality. Applications of framework grain composition is considered and employed also for better understanding of potential controls on diagenesis using suggestions by Bloch (1994), De Ros *et al*. (1994), De Souza *et al*. (1995), Nentwich and Yole (1997), Ramm (2000). Therefore, basic data generated on textural characteristics of minerals, presented in chapter five will be discussed in detail here.

5.1.1 Depositional Environments and Depositional History

5.1.1.1 Facies Analysis Evidence

The interpretation of depositional environment and history in this study is discussed here based on the facies analysis; occurrence of lithofacies, sub-facies and architectural elements in several measured lithological sections and the lateral relationship observed. The study area is a strictly continental, sandstone-dominated fluvial succession. The sedimentary units in the southeastern part composed mainly coarse (conglomerates and sandstones) sub-facies which changes toward the northern part indicating provenance was from southwestern and southeastern parts of northern Bida Basin.

The coarse (conglomerates and sandstones) sub-facies units which were suggested to have deposited as channel lag and longitudinal bars indicate a relatively higher energy fluvial system with low sinuosity from the southeast toward the central part of the study area. Also, the absence of finer (mudstones) sub-facies in southern part probably signifies low sinuosity high energy conditions.

Presence of sandstone sedimentary successions with an increase in the proportion of fine-grained facies and a decrease in coarse sub-facies in the central part of the study area indicates a gradual decrease in energy regime over periods of decreased stream competency. This is also the relative paucity of gravel-grade extraformational clasts that suggests deposition was at a considerable distance from the principal source of sediment.

Also, presence of few lenses of sandstone within finer (mudstones) sub-facies in the northern part of the study area was suggested to have formed by braided river of less energy but higher sinuosity (overbank fines of claystone, siltstone and silty-claystone facies) during a lower stage of flooding in the upper flow regime.

The investigated outcrops are characterized by distinctive facies assemblage consisting recurring sequences of conglomerate, sandstones and mudstone that exhibit progressive decrease in thickness and grain size towards the top of each recurring sequence. Generally, the recognized facies associations (OFA1-OFA5), architectural elements (GB, SB, LS, LA, OF and CH), sandbody geometries (Ribbon, Wedge, Lobate and Sheet) were interpreted as mainly fluvial environments with occasional tidal marine influences.

The occurrence of thick layers of conglomerate with the sandwiched angular to sub-rounded pebbles may suggest periodic uplift of source rocks in the area with supply and deposition of sediments by strong turbulent currents. The coarse (conglomerates and sandstones) sub-facies that are most frequent in the southwestern and western part signify high energy, low sinuosity, braided river deposits which is typical of the Bida Formation. This sub-facies also indicate initial sediments deposition which serves as major sediment's provenance with more effect of physical erosion and subdued chemical weathering features which may also indicate the prevalence of continental periods.

The prevalence of finer (fine sandstone and mudstone) sub-facies of low energy, high sinuosity, meandering system in the central and northern part characterizes Enagi Formation. The Enagi Formation constitutes finer sub-facies with indications of bi-directional and oscillating waves structures, clay drapes, reactivation surfaces and *Thallasanoides* burrows that indicates fluvial environment with marine signatures. The sporadic occurrence of fine sandy/silty sub-facies as thin lenticular interbeds of claystone in the central and northern part of many fining upwards cyclical sequences imply restricted and localized deposition which further corroborates the nature of depositing sediments during Enagi sedimentation.

The paleocurrent data from parts of the northern Bida Basin presented in chapter four (4.5) indicate a major flow towards northeastern and northwestern directions (Figure 4.19) with low variation trend which may suggest low sinuosity stream. The changes in the fluvial flow system and corresponding lateral facies changes recorded from the Bida Formation to the Enagi Formation are probably tectonically controlled. The individual facies associations and sandbodies are commonly oriented in the direction of paleo-depositing streams and locally oriented transversely which is attributed to sand bars in the channel framework of low sinuosity braided streams.

5.1.1.2 Pebble Morphogenesis Evidence

The interrelationship between textural distribution and depositional environments and/or processes has been used successfully to identify the depositional environments and recognize operative processes of sedimentation of ancient terrigenous deposits (Friedman, 1967). Two important variables were determined from the pebble morphometric analysis; the independent variable which includes coefficient of flatness ratio (FR) and elongation ratio (ER) after Luttig (1962), maximum projection sphericity index (M.P.S.I) and oblate-prolate index (OPI) after Dobkins and Folk (1970), whereas the other one is the dependent variables; the scatter plots of maximum projection sphericity index (M.P.S.I) versus oblate-prolate index (OPI) and roundness (%) versus elongation ratio (ER). These statistical parameters have been employed by several past workers to evaluate and identify the depositional environment and are also employed in this study.

The results obtained from the analysis are presented in tables 5.1 and 5.2. The clast-supported, massive conglomerate (Gcm) sub-facies composed of clasts samples (Figure 5.1a) with flatness ratio (FR) ranging from 0.47 to 0.87, elongation ratio (ER) range from 0.77 to

1.20, maximum projection sphericity index (M.P.S.I) from 0.60 to 0.96, oblate-prolate index values from -8.17 to 5.67 and roundness from 20 to 80% (angular to rounded). Also matrix-supported, massive conglomerate (Gmm) sub-facies comprises of clast samples (Figure 5.1b) with flatness ratio (FR) ranging from 0.40 to 0.88, mean elongation ratio (ER) from 0.52 to 1.40, mean maximum projection sphericity index (M.P.S.I) ranges from 0.56 to 1.01, oblate-prolate index from -20.00 to 5.4.40, roundness from 20-90 % (angular to well rounded) while crudely bedded conglomerate (Gh) sub-facies is made up of flatness ratio (FR) ranging from 0.49 to 0.86, mean elongation ratio (ER) from 0.83 to 1.14, mean maximum projection sphericity index (M.P.S.I) from 0.49 to 0.90, oblate-prolate index range from -7.50 to 0.96, roundness from 20 to 70% (angular to sub-rounded). It also noted that all the studied clasts are dominantly of compact bladed and compact with few very platy, very bladed and very few elongate and bladed (Table 5.1).

Generally, the pebble assemblages result reveals sphericity (M.P.S.I) values higher than the sphericity line (>0.66), the oblate–prolate index ranges between -14.70 and 5.4.40, F.R. and E.R. from 0.33 to 0.86 and 0.33 to 0.88 respectively suggesting river deposition conditions. The bivariate plots of maximum projection sphericity against oblate–prolate index, coefficient of flatness against sphericity and roundness against maximum projection sphericity after Dobkins and Folk, (1970), Stratten (1973), Nwajide and Hoque (1982), indicate that the pebbles were deposited in a fluvial environment (Figures 5.2a-5.2c). Also, according to Sneed and Folk (1958), Dobkins and Folk (1970), dominant of compact (C) and compact bladed (CB) are most indicative of fluvial action, therefore, considering the mean geometric forms results; 40.3% compact bladed, 25.4.5% compact, 12.4% very platy, 11.6% very bladed, 4.4% elongate and 0.8% bladed (Table 5.2), it's clearly indicated that the studied pebbles were deposited in a fluvial environment according to Adepoju *et al*. (2018a).



Figure 5.1: Some selected pebbles from; (a) clast-supported, massive conglomerate (Gcm) and (b) matrix-supported, massive conglomerate (Gmm) sub-facies for morphometric analysis.

Table 5.1a: Pebble morphometric data of clast-supported, massive conglomerate (Gcm) sub-facies

Locations	S/N	L	I	S	F.R (S/L)	E.R (I/L)	M.P.S.I	O-P	Roundness	Form	R.F
PATIGI (PAT-1E)	1	5.4.50	5.4.00	4.00	0.53	0.95	0.66	-2.05	70	C	Quartz
	2	5.4.00	7.50	5.00	0.67	0.83	0.81	0.00	50	CB	Quartz
	3	7.00	5.00	4.50	0.64	0.86	0.78	-0.64	70	C	Quartz
	4	8.00	7.50	4.50	0.56	0.94	0.70	-2.01	70	C	Quartz
	5	5.50	5.20	4.00	0.62	0.95	0.73	-2.34	70	C	Quartz
	6	4.00	4.70	3.50	0.70	0.94	0.80	-2.10	70	C	Quartz
	7	8.50	8.60	4.00	0.47	1.01	0.60	-2.46	50	VB	Quartz
	8	4.00	4.80	3.50	0.70	0.96	0.80	-2.57	70	C	Quartz
	9	7.00	5.00	4.00	0.57	0.86	0.72	-0.95	50	CB	Quartz
	10	7.50	5.00	4.00	0.53	0.80	0.71	-0.38	50	CB	Quartz
	11	5.50	4.00	3.20	0.49	0.77	0.68	-0.22	50	CB	Quartz
	12	4.00	4.00	4.00	0.80	1.00	0.86	-4.00	50	C	Quartz
	13	5.00	4.50	4.00	0.67	0.92	0.79	-1.67	70	C	Quartz
	14	7.00	5.00	4.00	0.71	0.86	0.84	0.00	50	VP	Quartz
	15	4.50	4.00	3.00	0.55	0.91	0.69	-1.64	50	CB	Quartz
	16	4.50	4.20	4.50	0.82	0.95	0.89	-1.64	70	C	Quartz
	17	4.00	4.00	3.00	0.60	1.00	0.71	-3.00	50	VP	Quartz
	18	5.00	4.50	3.00	0.50	0.92	0.65	-1.67	50	CB	Quartz
	19	5.00	4.30	4.50	0.75	0.88	0.86	-0.25	70	C	Quartz
	20	7.00	5.50	4.00	0.57	0.93	0.71	-1.90	50	CB	Quartz
	21	4.50	4.00	3.30	0.60	0.91	0.73	-1.64	50	VP	Quartz
	22	4.50	4.00	3.00	0.55	0.91	0.69	-1.64	40	VB	Quartz
BAGANKO (BAK-1C)	1	4.00	5.00	3.50	0.70	1.20	0.74	-8.17	70	C	Quartz
	2	14.00	14.00	8.40	0.60	1.07	0.70	-4.07	80	VB	Quartz
	3	10.00	8.50	4.00	0.50	0.85	0.67	-1.00	80	CB	Quartz
	4	10.00	5.4.00	5.00	0.60	0.90	0.74	-1.50	80	VP	Quartz
	5	7.00	5.80	4.00	0.57	0.97	0.70	-2.48	70	C	Quartzite
	6	7.00	5.70	4.00	0.71	0.96	0.81	-2.50	60	CB	Quartz
	7	4.50	4.20	4.00	0.73	0.95	0.82	-2.18	60	CB	Quartz
	8	5.00	5.00	4.00	0.67	1.00	0.76	-3.33	70	C	Quartz
	9	5.00	4.70	4.00	0.83	0.78	0.96	5.67	70	CB	Quartz
	10	5.00	4.20	4.00	0.67	0.87	0.80	-0.67	40	VB	Quartz
	11	7.00	5.00	4.00	0.57	0.86	0.72	-0.95	70	C	Quartz
	12	5.4.00	7.00	5.00	0.67	0.78	0.83	1.11	80	VP	Quartz
	13	8.00	7.00	4.80	0.73	0.88	0.84	-0.33	60	VP	Quartz
	14	5.00	5.00	4.20	0.87	1.00	0.91	-4.1.2.3	50	VP	Quartz
	15	4.00	4.00	2.50	0.50	1.00	0.63	-2.50	60	CB	Quartz
	16	4.00	4.50	3.50	0.70	0.90	0.82	-1.17	80	C	Quartz
	17	4.00	4.80	3.50	0.70	0.96	0.80	-2.57	40	CB	Quartz
	18	4.00	4.50	3.40	0.68	1.10	0.75	-4.53	40	CB	Quartz
	19	4.00	4.10	4.00	0.80	0.82	0.92	3.20	50	VP	Quartz
	20	5.00	4.00	3.20	0.53	0.83	0.70	-0.76	40	CB	Quartz
	21	4.00	4.00	3.20	0.64	1.00	0.74	-3.20	40	CB	Quartz
	22	3.00	2.80	2.00	0.67	0.93	0.78	-2.00	20	CB	Quartz
	23	4.20	4.1.2.0	3.20	0.76	1.02	0.83	-4.57	30	CB	Quartz

Table 5.1b: Pebble morphometric data of matrix-supported, massive conglomerate (Gmm) sub-facies

Locations	S/N	L	I	S	F.R (S/L)	E.R (I/L)	M.P.S.I	O-P	Roundness	Form	R.F
PATIGI (PAT-1D)	1	1.70	1.60	1.30	0.76	0.94	0.85	-1.91	90	C	Quartz
	2	2.30	2.00	1.50	0.65	0.87	0.79	-0.82	90	C	Quartz
	3	2.40	2.00	1.70	0.71	0.83	0.84	0.51	90	CB	Quartz
	4	2.00	2.20	1.60	0.80	1.10	0.83	-8.00	60	CB	Quartz
	5	5.00	5.00	4.20	0.70	1.00	0.79	-3.50	60	C	Quartz
	6	5.50	7.00	4.00	0.62	1.08	0.71	-4.1.2.1	70	C	Quartz
	7	4.80	7.00	3.70	0.64	1.21	0.70	-5.83	40	VB	Quartz
	8	3.20	2.70	2.30	0.72	0.84	0.85	0.40	70	C	Quartz
	9	4.50	3.70	3.00	0.67	0.82	0.81	0.22	70	CB	Quartz
	10	4.20	2.70	3.80	0.73	0.52	1.01	5.4.40	50	CB	Quartz
	11	4.00	4.60	3.80	0.76	0.92	0.86	-1.27	70	C	Quartz
	12	4.50	5.80	4.70	0.65	0.94	0.77	-2.22	70	CB	Quartz
	13	4.00	4.50	4.20	0.84	1.10	0.86	-5.4.45	50	CB	Quartz
	14	5.50	5.40	4.10	0.63	0.98	0.74	-2.89	60	C	Quartz
	15	5.00	4.80	3.50	0.58	0.97	0.71	-2.45	70	C	Quartz
	16	4.00	4.20	2.30	0.46	0.84	0.63	-0.94	40	CB	Quartz
	17	4.80	4.00	3.40	0.71	1.04	0.78	-4.55	80	C	Quartz
	18	4.00	4.00	3.20	0.80	1.00	0.86	-4.00	90	C	Quartz
	19	3.40	3.20	3.00	0.88	0.94	0.94	0.00	50	CB	Quartz
	20	4.00	5.00	4.20	0.84	1.20	0.84	-14.70	40	VB	Quartz
	21	2.50	2.30	1.60	0.64	0.92	0.76	-1.78	70	C	Quartz
	22	8.00	8.00	4.20	0.53	1.00	0.65	-2.63	50	E	Quartz
	23	4.00	4.00	3.00	0.60	0.80	0.77	0.00	60	CB	Quartz
	24	4.00	4.1.2.0	3.50	0.88	1.08	0.89	-5.4.63	50	VB	Quartz
	25	4.50	4.50	3.50	0.64	1.00	0.74	-3.18	50	E	Quartz
	26	4.50	4.00	3.20	0.71	0.89	0.83	-0.82	50	VP	Quartz
	27	4.00	4.70	3.00	0.60	0.94	0.73	-2.10	80	C	Quartz
	28	4.00	3.80	2.00	0.50	0.95	0.64	-2.00	50	VP	Quartz
BAGANKO (BAK-1E)	1	8.00	7.00	4.50	0.69	0.88	0.81	-0.69	70	C	Quartz
	2	5.50	4.00	4.1.2.0	0.66	0.77	0.83	1.20	80	CB	Quartz
	3	4.50	4.00	3.50	0.64	0.91	0.76	-1.59	60	C	Quartz
	4	5.50	5.00	4.90	0.75	0.92	0.85	-1.41	70	CB	Quartz
	5	8.70	8.00	3.50	0.40	0.92	0.56	-1.47	60	E	Quartz
	6	4.50	4.00	3.90	0.71	0.91	0.82	-1.33	70	CB	Quartz
	7	4.00	4.50	3.80	0.76	0.90	0.86	-0.63	70	C	Quartz
	8	4.00	4.50	3.40	0.68	0.90	0.80	-1.28	50	C	Quartz
	9	4.00	3.50	2.40	0.60	0.88	0.74	-1.13	50	E	Quartz
	10	4.50	4.00	3.50	0.78	0.89	0.88	0.00	30	CB	Quartz
	11	4.50	4.00	3.50	0.78	0.89	0.88	0.00	30	B	Quartz
	12	4.00	4.50	2.50	0.50	0.90	0.65	-1.50	20	CB	Quartz
	13	3.00	2.50	2.00	0.67	0.83	0.81	0.00	30	CB	Quartz
	14	2.50	3.50	2.00	0.80	1.40	0.77	-20.00	30	CB	Quartz
	15	4.00	4.1.2.0	2.00	0.50	1.08	0.61	-3.25	30	VP	Quartz
	16	1.50	1.20	0.70	0.47	0.80	0.65	-0.58	20	VP	Quartz
	17	1.50	1.60	1.00	0.67	1.07	0.75	-4.67	50	CB	Quartz
	18	1.70	1.50	1.50	0.88	0.88	0.96	4.41	30	VP	Quartz
	19	1.00	1.00	0.70	0.70	1.00	0.79	-3.50	20	CB	Quartz
	20	1.70	1.50	1.00	0.59	0.88	0.73	-1.26	60	VB	Quartz
	21	1.50	1.60	0.90	0.60	1.07	0.70	-4.00	30	VP	Quartz

Table 5.1c: Pebble morphometric data of crudely bedded conglomerate (Gh) sub-facies

Location	S/N	L	I	S	F.R (S/L)	E.R (I/L)	M.P.S.I	O-P	Roundness	Form	R.F
Baganko (BAK-1B)	1	2.30	2.00	1.40	0.61	0.87	0.75	-1.01	50	E	Quartz
	2	4.00	3.50	2.90	0.73	0.88	0.84	-0.33	30	CB	Quartz
	3	3.50	3.50	3.00	0.86	1.00	0.90	-4.29	40	C	Quartz
	4	2.00	2.00	1.40	0.70	1.00	0.79	-3.50	40	VB	Quartz
	5	2.00	2.00	1.30	0.65	1.00	0.75	-3.25	40	VB	Quartz
	6	4.00	3.50	3.00	0.75	0.88	0.86	0.00	40	C	Quartz
	7	2.70	2.60	2.00	0.74	0.96	0.83	-2.65	30	CB	Quartzite
	8	1.70	1.50	1.20	0.71	0.88	0.83	-0.71	30	C	Quartz
	9	4.10	4.20	2.30	0.56	1.02	0.67	-3.12	40	VB	Quartz
	10	4.00	4.00	2.50	0.63	1.00	0.73	-3.13	30	VB	Quartz
	11	4.00	4.50	3.00	0.75	1.13	0.79	-7.50	40	CB	Quartz
	12	4.00	4.00	2.00	0.40	1.00	0.54	-2.00	40	E	Quartz
	13	3.00	3.00	2.30	0.77	1.00	0.84	-3.83	30	VB	Quartz
	14	4.00	4.50	2.20	0.55	1.13	0.65	-4.28	50	C	Quartz
	15	3.00	3.00	2.40	0.80	1.00	0.86	-4.00	30	CB	Quartz
	16	1.50	1.40	0.50	0.33	0.93	0.49	-1.33	40	CB	Quartz
	17	1.40	1.30	0.70	0.50	0.93	0.65	-1.79	30	CB	Quartz
	18	1.20	1.10	0.70	0.58	0.92	0.72	-1.75	20	C	Quartz
Baganko (BAK-1G)	1	4.50	4.60	2.50	0.56	1.02	0.67	-3.06	60	CB	Quartz
	2	4.70	4.00	2.50	0.53	1.06	0.64	-3.38	40	CB	Quartz
	3	4.50	4.50	3.50	0.78	1.00	0.85	-3.89	50	VP	Quartz
	4	2.00	2.00	1.50	0.75	1.00	0.83	-3.75	20	C	Quartz
	5	3.50	3.50	1.70	0.49	1.00	0.62	-2.43	50	E	Quartz
	6	4.00	4.80	3.00	0.60	0.96	0.72	-2.40	60	CB	Quartz
	7	3.50	3.20	2.40	0.69	0.91	0.80	-1.56	60	CB	Quartz
	8	4.00	4.00	2.50	0.63	1.00	0.73	-3.13	40	VB	Quartz
	9	5.00	4.00	3.50	0.58	0.83	0.74	-0.58	40	VB	Quartz
	10	7.00	5.00	3.50	0.50	0.86	0.66	-1.07	70	CB	Quartz
	11	3.50	4.00	2.00	0.57	1.14	0.66	-4.76	50	CB	Quartz
	12	2.90	2.70	1.80	0.62	0.93	0.75	-1.97	50	CB	Quartz
	13	4.50	3.80	3.00	0.67	0.84	0.81	-0.22	50	CB	Quartz
	14	2.00	2.00	1.50	0.75	1.00	0.83	-3.75	50	VP	Quartz
	15	3.50	3.00	2.70	0.77	0.86	0.89	0.96	40	C	Quartzite
	16	2.70	2.30	2.00	0.74	0.85	0.86	0.53	20	CB	Quartz

Table 5.2: Pebble morphometric data ranges for the studied samples

S/N	Sub-facies	No of Samples	F.R (S/L)	E.R (I/L)	M.P.S.I	O-P	Roundness
1	**Gcm**	45	0.47-0.87	0.77-1.20	0.60-0.96	(-8.17) – (+5.67)	20-80
2	**Gmm**	49	0.40-0.88	0.52-1.40	0.56-1.01	(-20.00)- (+5.4.40)	20-90
3	**Gh**	34	0.49-0.86	0.83-1.14	0.49-0.90	(-7.50)-(+0.96)	20-70

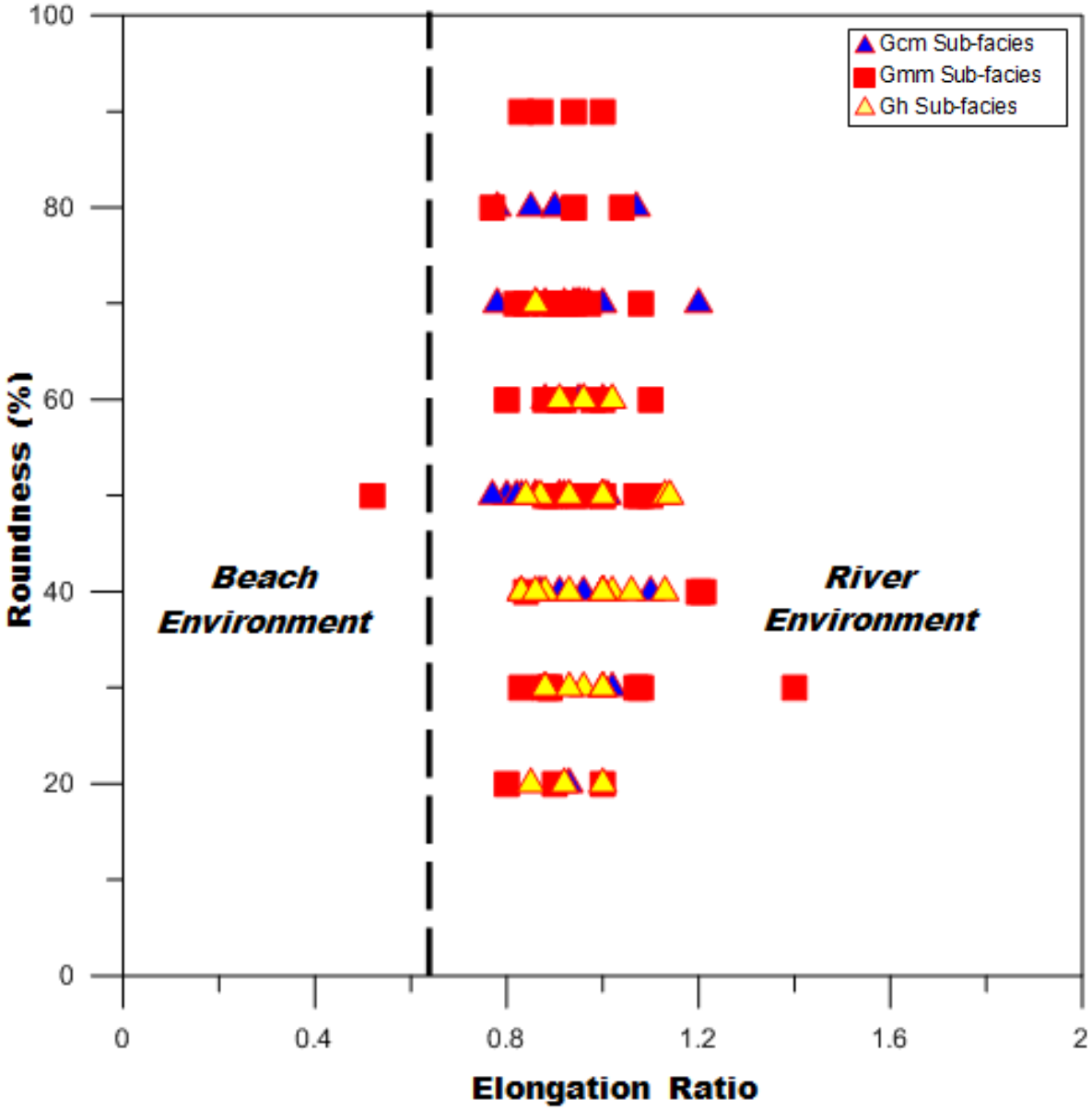


Figure 5.2a: Bivariate plot of Roundness (%) against Elongation ratio after Dobkins and Folk (1970).

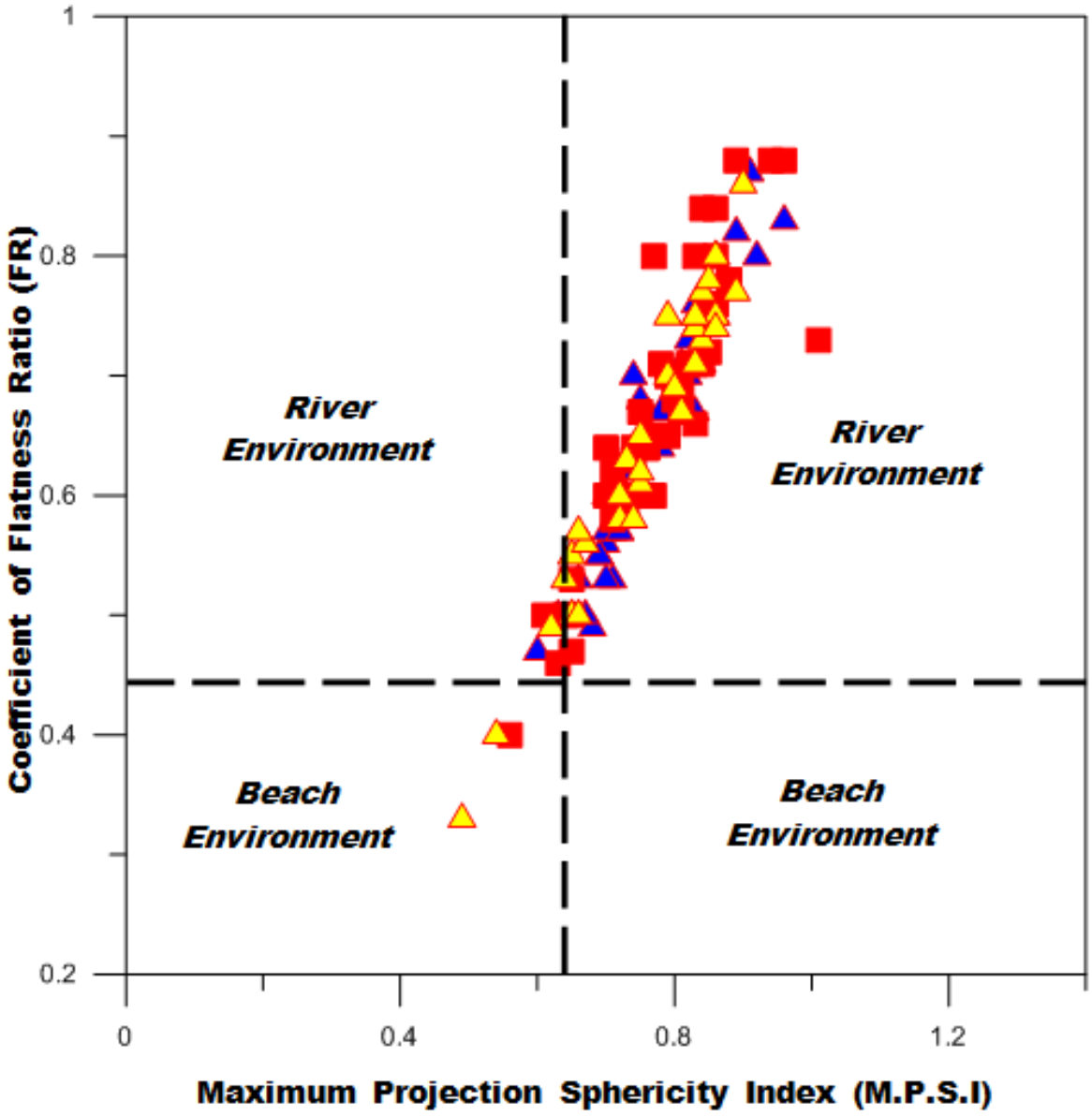


Figure 5.2b: Bivariate plot of Coefficient of Flatness against Maximum Projection Sphericity Index after Stratten (1973).

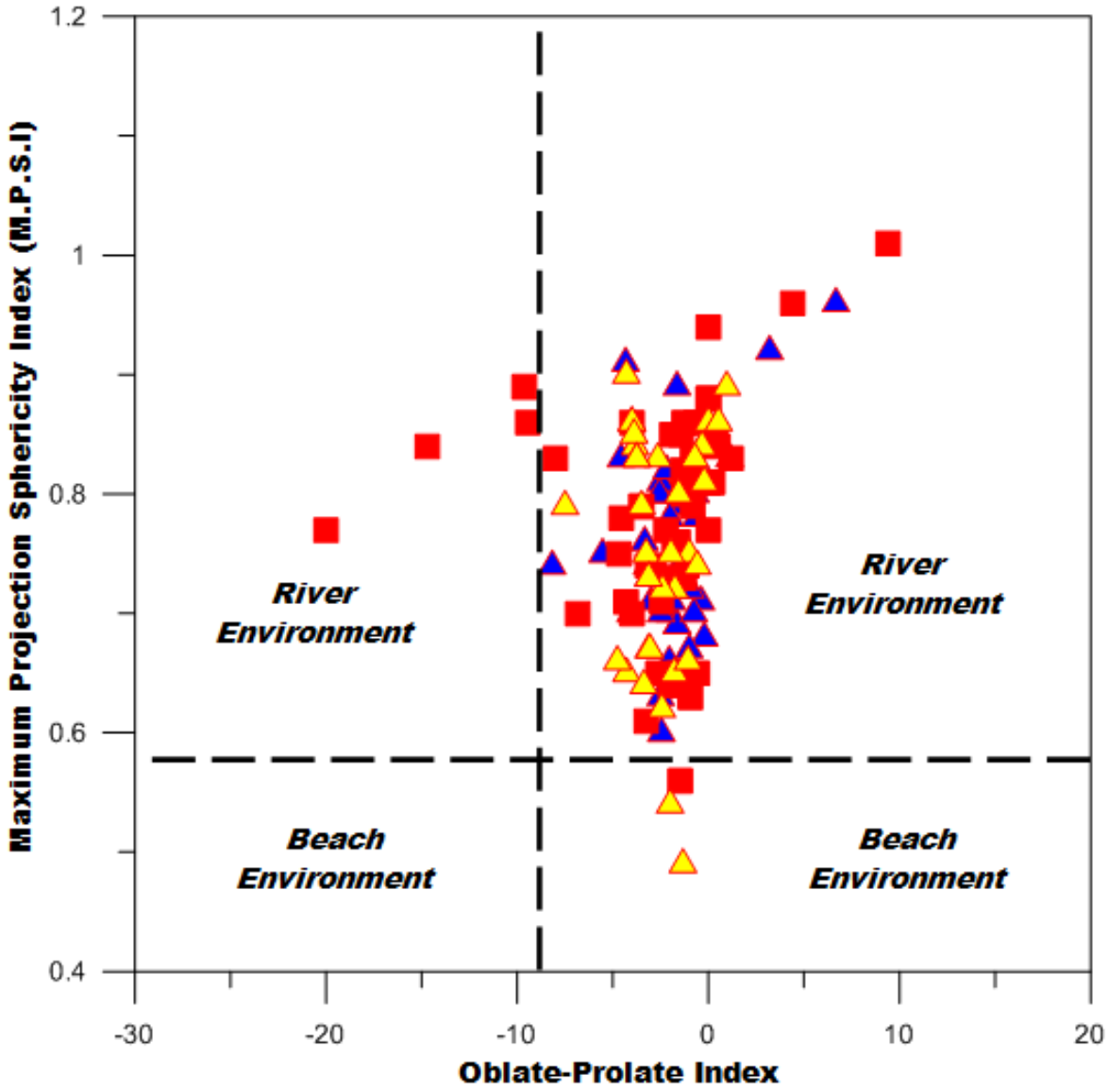


Figure 5.2c: Bivariate plot of Maximum Projection Sphericity Index against Oblate-Prolate Index after Dobkins and Folk (1970).

5.1.1.3 Grain Size (Sieving) Data Evidence

Result of grain size analysis is also employed in addition with the pebble morphogenesis in order to understand the environment of deposition of the studied sediments. The grain size parameters used includes; mean size, median, standard deviation, skewness and kurtosis, it is necessary to employ the discriminatory plots to show interrelationship between grain sizes. Past studies by many workers have shown that representative fields of a particular modern environment can be separated by bi-variate discriminant plots of one sediment size descriptor against another to discriminate depositional environments.

In this part of the reserach, the depositional environments was elucidate based on the discriminating bi-variate plots; graphic mean size (Mz) versus standard deviation (σi) after Friedman (1967), Moiola and Weiser (1968), graphic standard deviation (σi) versus graphic skewness (Ski) after Moiola and Weiser (1968) and standard deviation (σi) versus graphic skewness (Ski) after Friedman (1967). These plots presented in figure 5.3a, b, c and d show that all the sediments within the study area imprinted with river environments as concluded by Adepoju *et al*. (2018a). The bi-variate plot after Gleister and Nelson's (1971) also confirm the above statements as the analyzed samples clustered around the field of braided bar region (Figure 5.3e).

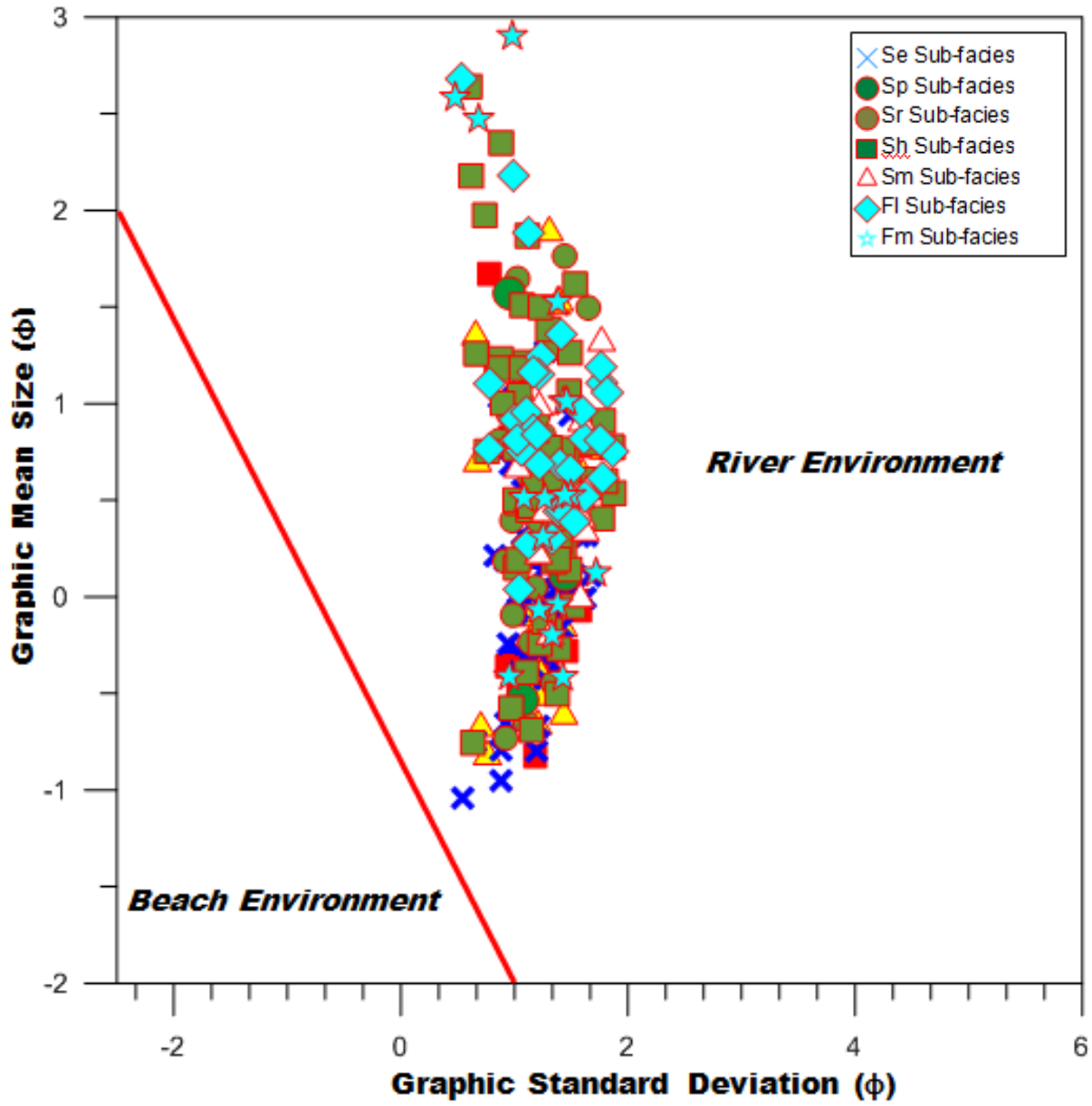


Figure 5.3a: Graphic Mean Size against Graphic Standard Deviation after Moiola and Weiser (1968).

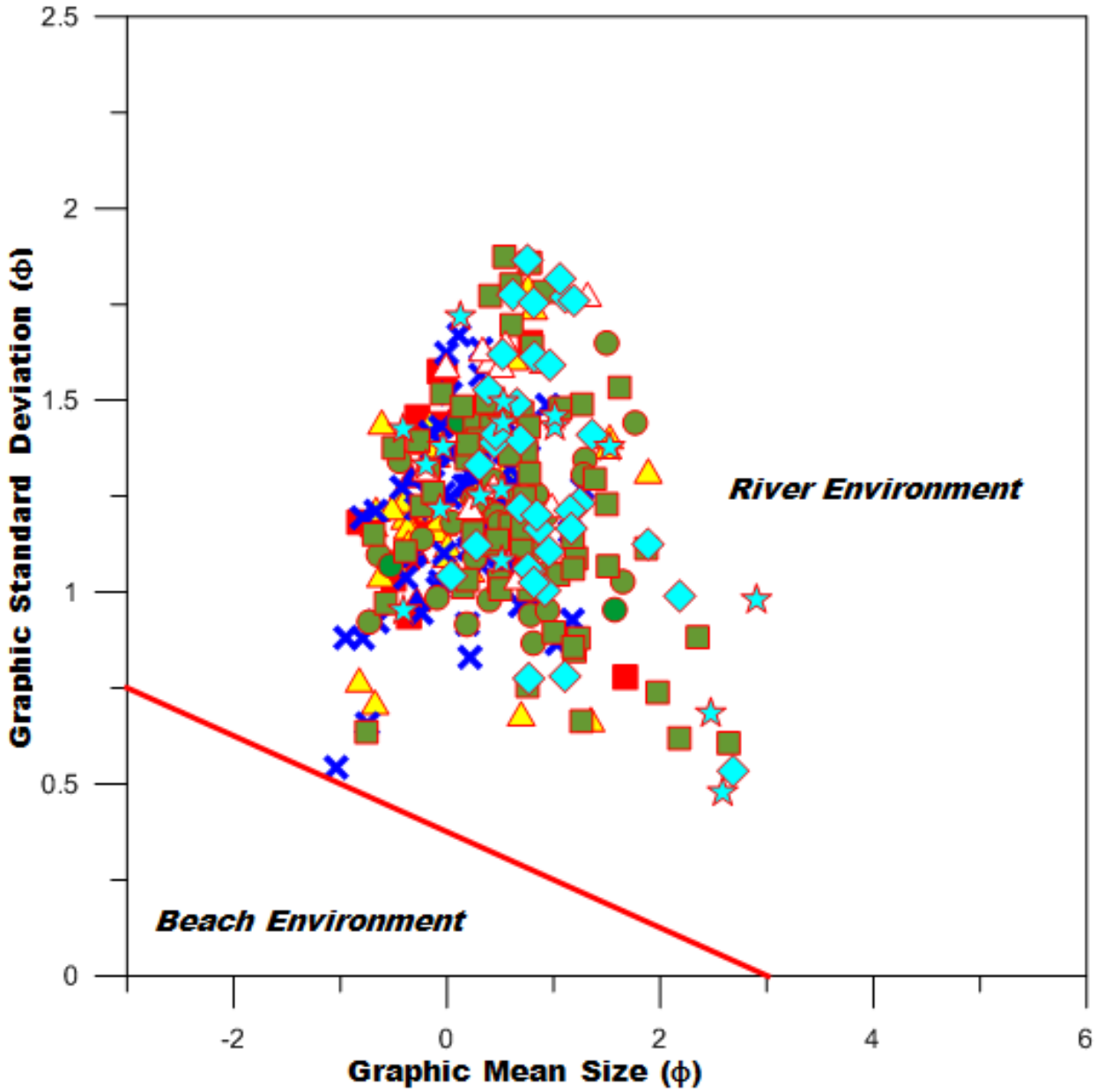


Figure 5.3b: Bivariate plot of Graphic Standard Deviation against Graphic Mean Size after Friedman (1967).

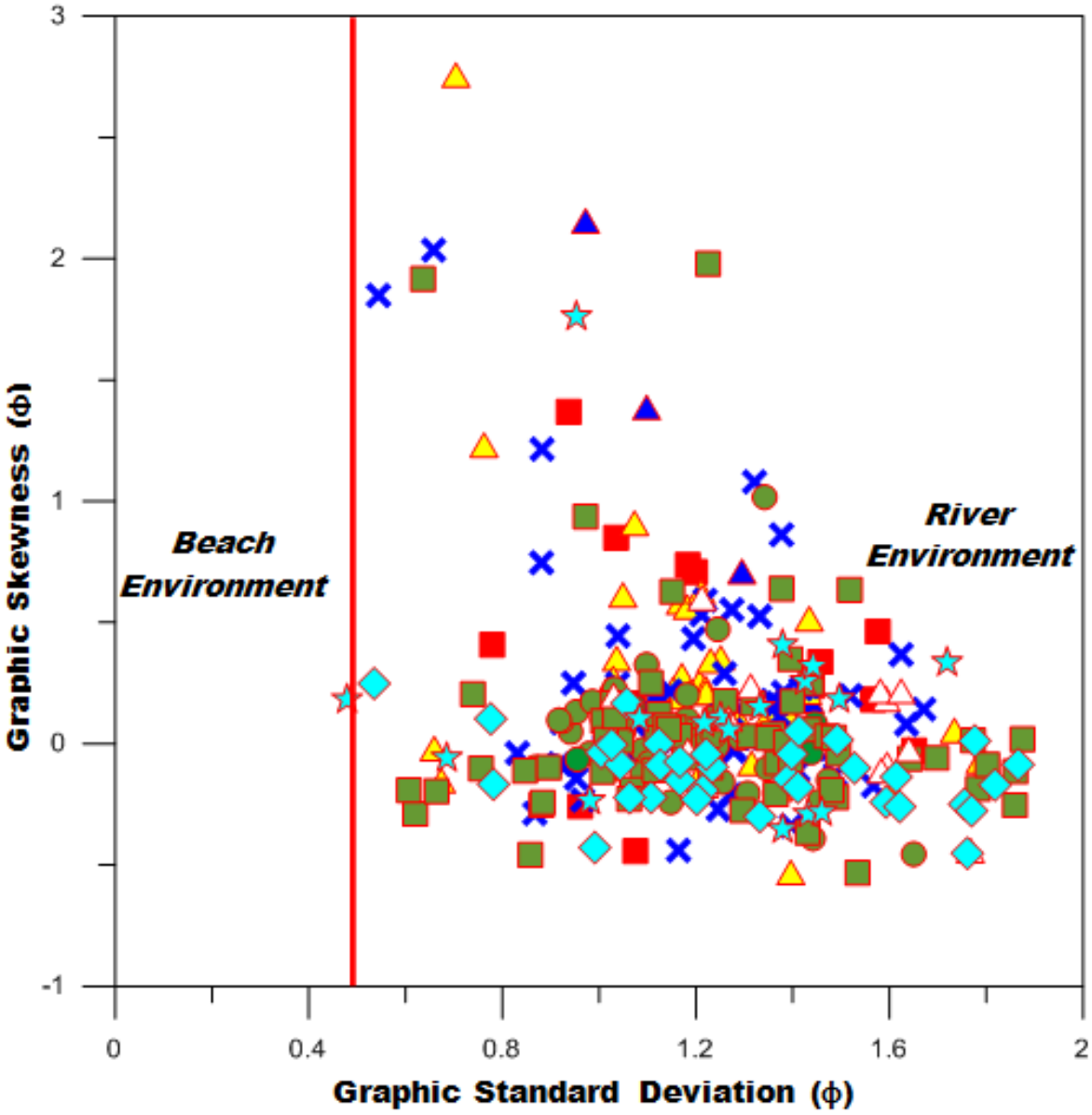


Figure 5.3c: Bivariate plot of Graphic Skewness against Graphic Standard Deviation after Moiola and Weiser (1968).

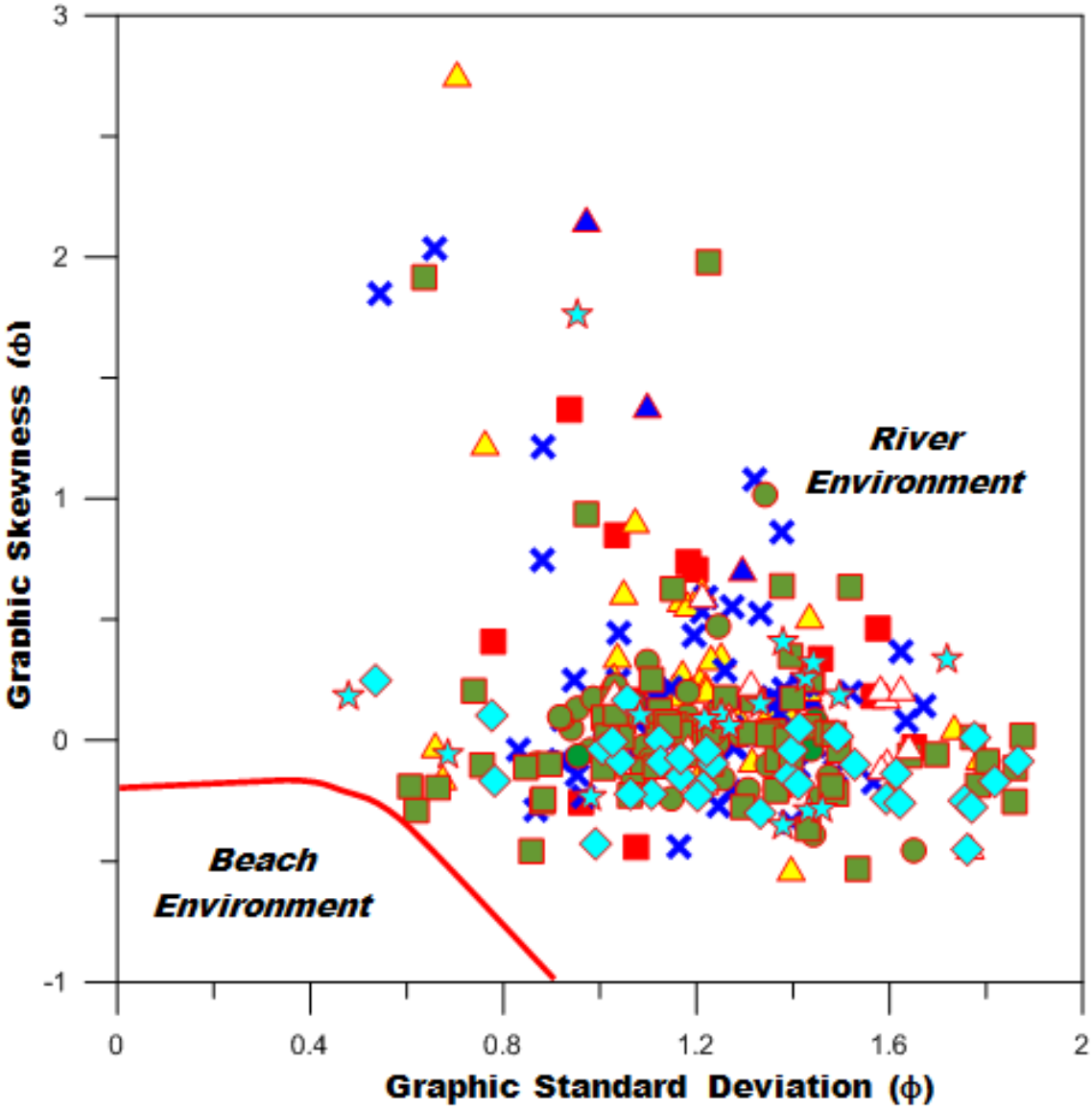


Figure 5.3d: Bivariate plot of Graphic Skewness against Graphic Standard Deviation after Friedman (1967).

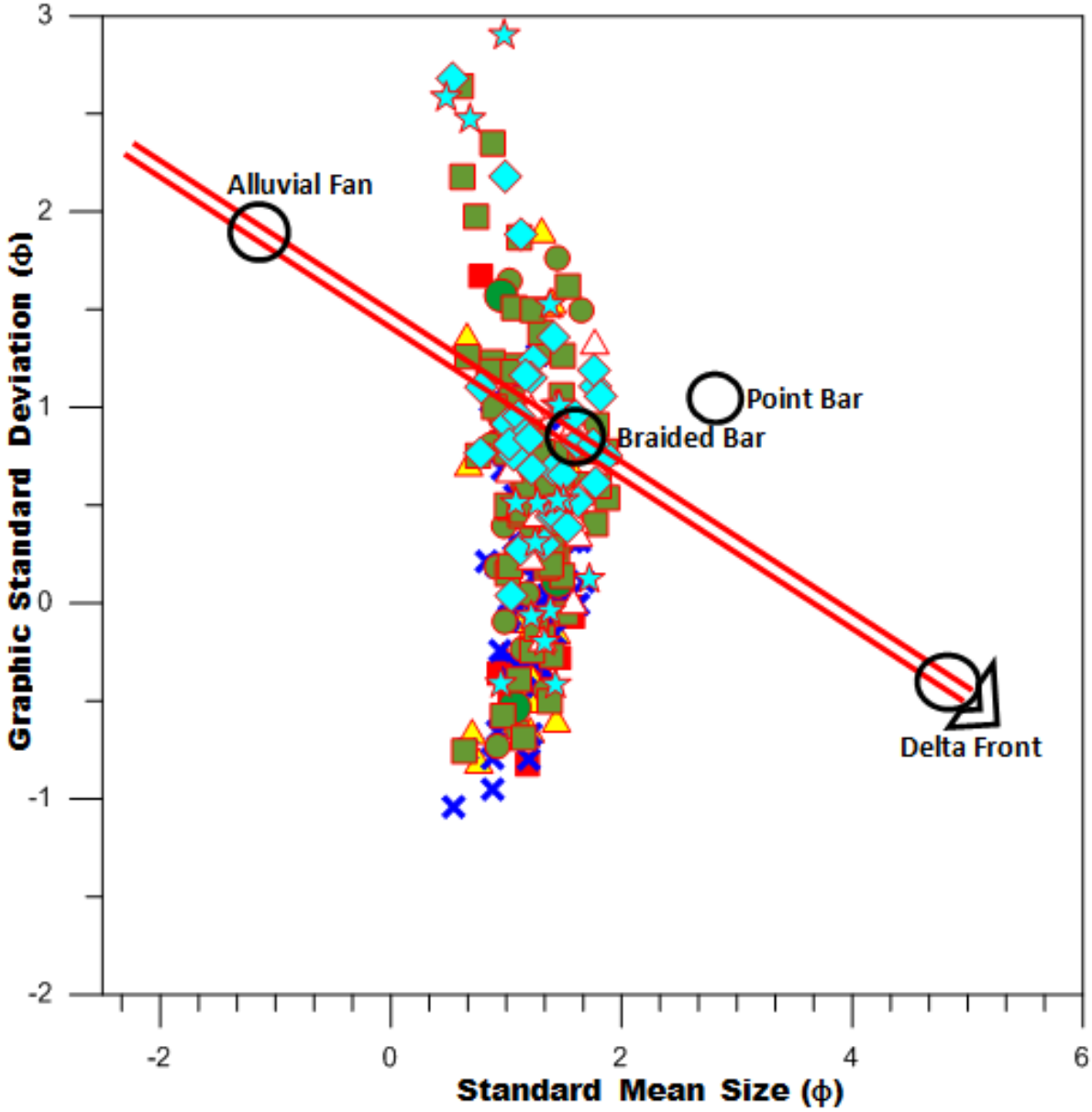


Figure 5.3e: Bivariate plot of Graphic Standard Deviation against Graphic Mean Size after Glaister and Nelson (1974) showing clustering of the plotted samples near braided system as an evidence of fluvial depositional environment.

5.1.2 Diagenesis and Reservoir Quality

Diagenesis has been described by Chilingarian *et al*. (1967) as a process which includes "all physicochemical, biochemical and physical processes modifying sediments between deposition and lithification at low temperatures and pressures characteristic of surface and near-surface environments". Morad *et al*. (2000) concluded that freshly deposited sand is a porous, non-equilibrium mixture of detrital minerals, therefore, diagenetic processes tend to bring them towards equilibrium with the prevailing physio-chemical conditions and this is achieved by reduction of porosity through compaction and precipitation of stable authigenic cements. Diagenesis in clastic rocks is controlled by factors such as texture, detrital composition, environment of deposition and associated lithology according to Burley *et al*. (1985) and Morad *et al*. (2000).

Stonecipher *et al*. (1984) concluded that diagenesis may enhance, preserve or destroy porosity and permeability, depending on a range of parameters such as detrital supply, lithofacies and tectonics as well as diagenetic processes. Gluyas and Cade (1997), Evans *et al*. (1997) and McKinley *et al*. (2011) predicted the porosity and permeability in sandstone reservoirs to be related to burial depth, grain size, authigenic cements and clay contents. Nevertheless, an understanding of the diagenetic minerals within sandstones, which is dependent on diagenetic processes, is crucial for the assessment of porosity and permeability of reservoirs.

This aspect of the present investigations focuses on the sandstone diagenesis with main aim of determining and describing the diagenetic minerals, their imprints and assessing their effects on the reservoir quality of the sandstones. Five (5) selected sandstone samples were further selected among those evaluated using thin section petrography for scanning electron

microscope (SEM) equipped with backscattered electron (BSE) for reservoir quality description and determination. Seven thin section samples were selected and subjected to image analysis (BSE and CL) based on their typical diagenetic features observed on them. Prior to the image analysis, the samples were studied for detailed petrographic examinations and photomicrographic documentations which were presented in chapter five. This study is essential to gain as much understanding of reservoir quality for a petroleum discovery to help focus further exploration and appraisal efforts in the Bida Basin, Nigeria.

5.1.2.1 Petrographic Evidence

The discussions on the mineralogical characteristics and grain relationships i.e. types and percentages of grain to grain contacts for this study is aimed to further help in understanding the aggregate packing of the rocks with a view to interprete their post-depositional history especially compaction as pore reduction process. Diagenesis in sandstones is characterized by alteration in matrix and framework mineral composition. The high resolution petrographic study shows that the studied sandstone had undergone diagenesis evidenced from different stages of feldspar alteration, lithic rock dissolution, quartz fracture and cements (silica, iron-oxide and clay) observed under microscope (Figure 5.5). The dissolution and loss of feldspar with absence of illitization in some samples may suggest that the feldspar were destroyed in the shallow burial zone where weathering was effective.

On the grain to grain relationships, the contact type is counted along linear traverse grid points in a line so as to determine the contact index (CI). The CI according to Taylor (1950) is the average number of grain contacts a grain has in its surroundings. He concluded that four grain-to-grain contact types can be encountered at the point spacing in the plane of thin sections; Tangential or point (P) contact, long (L) contact as a line, concavo-convex (C)

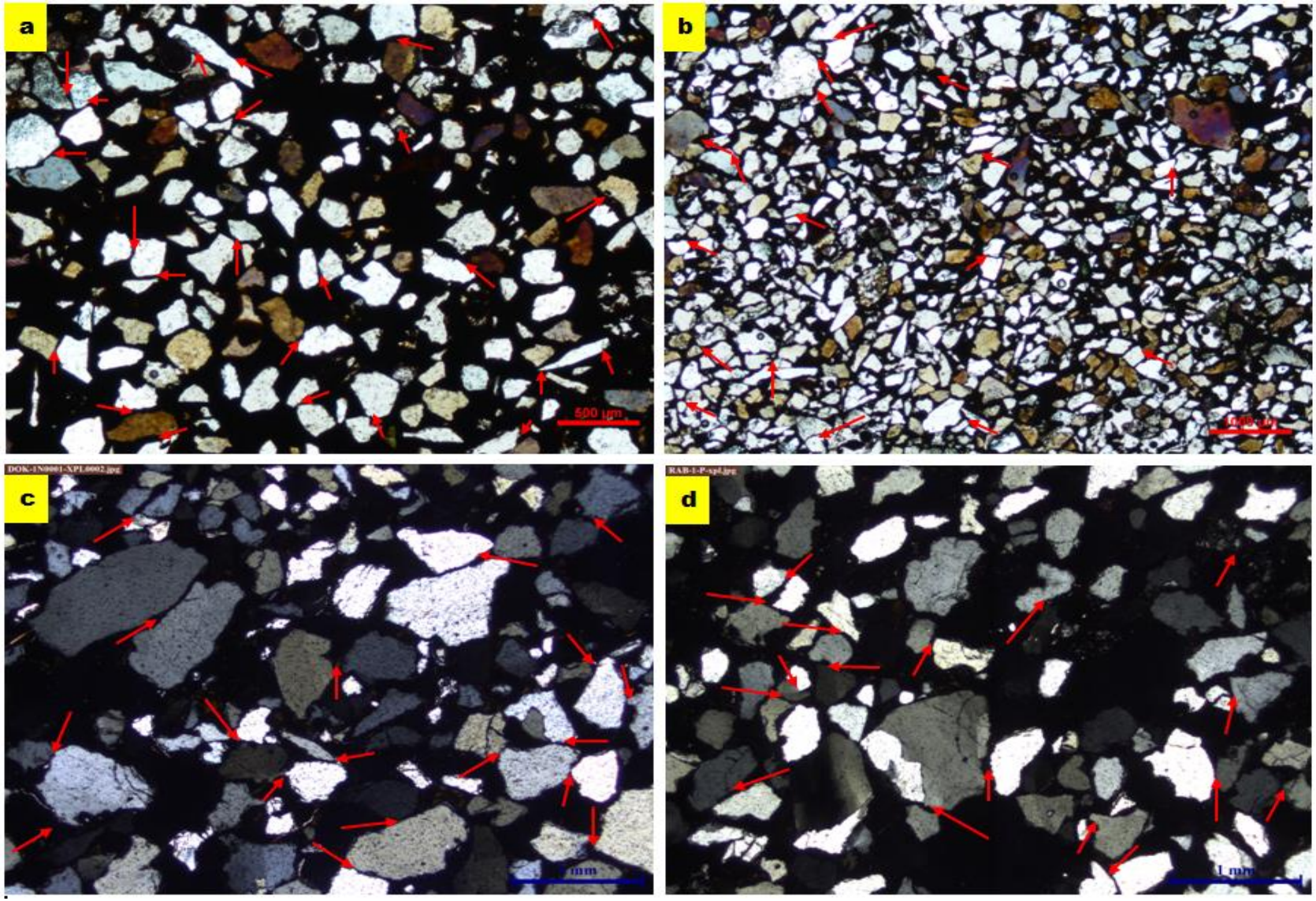
contact as curve line and sutured (S) contact as serrated interfingering contact whereas a floating grains (F) may be observed in a loosely packed sandstone. The contact index (CI) gives an indication about the degree of compaction of sediments because compaction changes the nature of grain contact and increased numbers of long and interpretative contacts appear at the expense of floating grains and point contacts.

The result of grain contacts observed during petrographic study is presented in table 5.3. The framework constituents of the sandstones as whole exhibits different types of contacts; floating, point, long, suture and concavo-convex (Figure 5.4). Majority of the sub-facies possess point, suture with few concavo-convex index therefore compaction process dominates, whereas, few sub-facies exhibit floating and long contacts and fewer portions of point contacts in the framework constituents which are intensely cemented as a result of development of iron and silica cements which probably precipitate at a later stage as suggested by Adepoju *et al*. (2018b).

Taylor (1950) considered floating and point contacts grains always representing original packing whereas the long contacts result from little pressure and precipitated cement while high degree of compaction results in pressure solution giving rise to concavo-convex and sutured contacts. Long contacts develop in the early stages of compaction of sand, when grains rotate and adjust themselves to the boundary of adjacent grains as a response to overburden pressure. With increasing pressure, when solid flow begins long contacts are made where yielding grains are pressed against adjacent rigid grains having relatively straight edges. Thus, long contacts represent an intermediate evolutionary stage between original point contacts and final sutured contacts. So, in this study, floating grains in some samples may point to corrosion of detrital grains and modification of texture by iron cement whereas

point and long contacts indicates that the sandstones were not subjected to high pressure solution, as a result of either shallow burial or early cementation according to Adepoju *et al*. (2018b). Presence of small numbers of concavo-convex as well as sutured contacts may also signify low role of chemical compaction but more cementation because boundaries of sutured contact might result in quartz overgrowths.

In general, the principal diagenetic processes that have modified the texture of the studied sediments are mechanical compaction and cementation which may points to minor burial and only little overburden which are indicative of compaction due to shallow burial and early cementation as suggested by Adepoju *et al*. (2018b). The observed evidence of compaction which may have resulted in volume reduction is less common to observed evidence of cementation which had resulted in porosity loss by the occlusion of pore spaces.



Please Turn Over to the next page for the Caption.

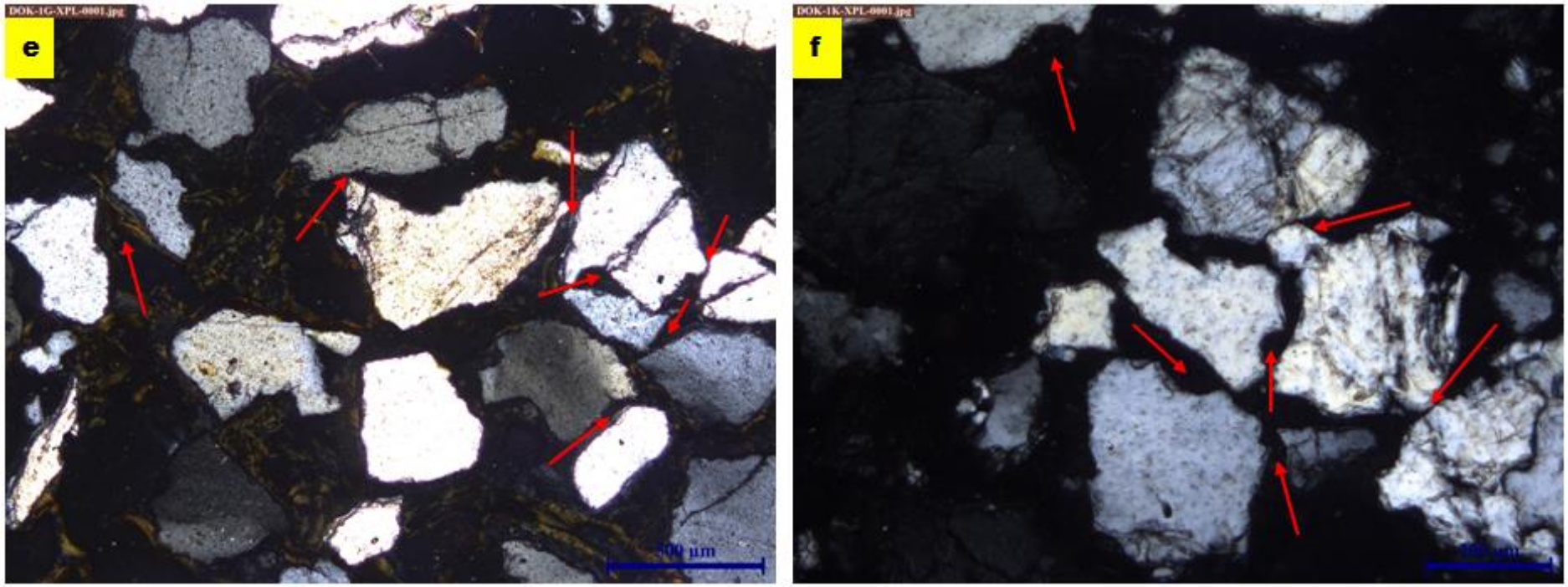


Figure 5.4: Photomicrograph of selected samples showing different Contact Index observed in the Northern Bida Basin sediments; (a) LEM-1P showing Point, Long and Floating contact as a result of Cementation; (b) PAT-1P showing Long and Point contact as a result of Cementation; (c). DOK-1N showing Point, Long and Suture contact as a result of Compaction and Cementation; (d) RAB-1P showing Point, Suture and Concavo-Convex contact as a result of Compaction and Cementation; (e) DOK-1G showing Point, Suture and Concavo-Convex contact as a result of Compaction and Cementation and (f) DOK-1K showing Suture and Concavo-Convex contact as a result of Compaction and Cementation.

Table 5.3: Samples selected for Contact Index (CI) study.

Sub-facies	Location	Sample Codes	Contact Index	Diagenetic Stage
Gh	**Patti-Chin**	**PAT-1M**	Point, Long and Suture	Compaction and Cementation
	Kajita	**KJT-1Q**	Long and Floating	Cementation
	Dokko	**DOK-1G**	Point, Suture and Concavo-Convex	Compaction and Cementation
Se	**Agbonna ridge**	**AGB-1F**	Long, Point and Suture	Compaction and Cementation
	Kutigi	**KUT-2B**	Long and Straight	Cementation
	Kutigi	**KUT-2L**	Point, Concavo-Convex & Suture	Compaction and Cementation
	Kajita	**KJT-1A**	Long and Floating	Cementation
	Patti-Chin	**PAT-1E**	Point and Suture	Compaction and Cementation
	Katcha	**KAC-1E**	Long and Floating	Cementation
	Lemu	**LEM-1E**	Point, Suture and Concavo-Convex	Compaction and Cementation
	Dokko	**DOK-1N**	Point, Long and Suture	Compaction and Cementation
Sp		**MGT-1C**	Point, Long and Suture	Compaction and Cementation
	Katcha	**KAC-1B**	Point, Suture and Concavo-Convex	Compaction and Cementation
	Patti-Chin	**PAT-1N**	Point and Long	Cementation
	Dokko	**DOK-1V**	Point, Suture and Concavo-Convex	Compaction and Cementation
	Enagi	**ENG-1F**	Point, Long and Suture	Compaction and Cementation
	Tanagi	**TAN-1G**	Long and Point	Cementation
	Tanagi	**TAN-1A**	Long and Point	Cementation
	Maraba	**MAR 1D**	Long and Point	Compaction
	Bida	**BDA-1L**	Point, Long and Suture	Compaction and Cementation
	Maraba	**MAR-1L**	Long and Point	Cementation
	Maraba	**MAR-1B**	Long and Point	Cementation
Sr	**Agbonna ridge**	**AGB-1J**	Point, Long and Suture	Compaction and Cementation
	Manigi	**MAN-1F**	Point, Long and Suture	Compaction and Cementation

Table 5.3 Contd.: Samples selected for Contact Index (CI) study

Sub-facies	Location	Sample Codes	Contact Index	Diagenetic Stage
Sh	**Agbonna ridge**	**AGB-1C**	Long and Point	Cementation
	Kutigi	**KUT-2A**	Long, Point and Suture	Compaction and Cementation
	Kutigi	**KUT-2G**	Point and Suture	Compaction
	Kutigi	**KUT-2J**	Long, Point and Suture	Compaction and Cementation
	Kutigi	**KUT-2K**	Long, Point and Suture	Compaction and Cementation
	Wariku	**WAR-1H**	Long and Floating	Cementation
	Maraba	**MAR-1C**	Point and Floating	Cementation
	Rabba	**RAB-1H**	Long, Point and Floating	Compaction and Cementation
	Manigi	**MAN-1H**	Point and Floating	Cementation
	Rabba	**RAB-1P**	Point, Suture and Concavo-Convex	Compaction and Cementation
	Bida	**BDA-1F**	Point and Suture	Compaction
	Bida	**BDA-1M**	Long, Point and Suture	Compaction and Cementation
	Lemu	**LEM-1H**	Point and Floating	Cementation
	Dokko	**DOK-Z2**	Point, Suture and Concavo-Convex	Compaction and Cementation
	Enagi	**ENG-1H**	Long and Floating	Cementation
	Enagi	**ENG-1V**	Long and Floating	Cementation
	Dokko	**DOK-1K**	Suture and Concavo-Convex	Compaction and Cementation
	Rafingora-Tanagi	**RAT-1P**	Long and Suture	Compaction

	Mangotta	**MGT-1H**	Long and Point	Cementation
	Dokko	**DOK-1Y**	Suture and Concavo-Convex	Compaction and Cementation
	Bida	**BDA-1S**	Long, Point and Suture	Compaction and Cementation
	Kuchi	**KCH-1D**	Long and Point	Cementation
Sm	**Agaei**	**AGE-IJ**	Point, Suture and Concavo-Convex	Compaction and Cementation
	Patti-Chin	**PAT-1L**	Pont and Suture	Compaction and Cementation
	Rafingora-Tanagi	**RAT1H**	Long, Point and Suture	Compaction and Cementation
Fl	**Bida**	**BDA-IK**	Point and Suture	Compaction
	Katcha	**KAC-IY**	Point and Floating	Cementation
	Patti-Chin	**PAT-1H**	Point and Suture	Compaction
	Patti-Chin	**PAT-1C**	Point, Suture and Concavo-Convex	Compaction and Cementation
	Rafingora-Tanagi	**RAT-1J**	Long and Suture	Compaction
	Kuchi	**KCH-1F**	Long and Point	Cementation
	Katcha	**KAC-1X**	Long and Point	Cementation
Fm	**Agbonna ridge**	**AGB-1E**	Long, Point and Suture	Compaction and Cementation
	Lemu	**LEM-1P**	Long and Point	Cementation
	Enagi	**ENG-1P**	Long, Point and Suture	Compaction and Cementation
	Dokko	**DOK-Z4**	Point, Suture and Concavo-Convex	Compaction and Cementation
	Patti-Chin	**PAT-1K**	Point and Suture	Compaction

5.1.2.2 Scanning Electron Microscope (SEM) and BackScattered Electron (BSE) Analysis

A scanning electron microscope (SEM) allows identification of minerals at much larger magnification and can differentiate among different minerals on a basis of BSE image gray-level scale. The abundance of minerals is quantified with different backscattered electron response, providing a simple, low-cost method of modal analysis. The method overcomes the problems with traditional point-counting method in mineral identification especially for diagenetic minerals. The image showed the size, shape, and continuity of pores, including micropores especially those that are much too small to be seen using petrographic microscope.

The description of the identified diagenetic minerals (silica, iron-oxide and clay cement) in the studied sandstones by image analysis is present here. Detrital and authigenic minerals were identified using a combination of thin sections and scanning electron microscopy analysis. The following diagenetic processes; cementation by silica and iron-oxide cement, compaction by development of quartz overgrowths, quartz fracture and replacement and dissolution of detrital feldspar were observed. Generally, silica cement dominates followed by iron-oxide (Goethite and Hematite).

5.1.2.2.1 Types of Cement

Silica Cement

Among the observed cements, silica was the first to have precipitated and form rims around the grains and nucleated in the centre of pore spaces and partially fills the interparticle or intergranular pore spaces (Figure 5.6a and b). Most quartz grains are partly covered by patchy smooth overgrowths of euhedral crystals around detrital quartz grains and usually in the boundaries between the detrital quartz grains. It is observed to be scattered throughout the

samples and suggested to have been sourced from pressure solution of detrital quartz and other silicates at grain contacts, conversion of clay minerals during diagenesis or decomposition or alternation of feldspars, may also release silica saturated solutions. The only potential sources of silica for quartz cement within the sandstones are from dissolved and replaced feldspars and the dissolution of detrital quartz grains (Adepoju *et al*., 2018b).

Iron-Oxide Cement

The iron-oxide cement occurs as interstitial pore-filling, pore-lining on the surface of both detrital quartz grains and quartz overgrowths. In few cases, empty voids are lined with a thin coating of iron oxide while some quartz grains are corroded and enveloped by iron oxide cement (Figure 5.6c). Hematite with co-existing goethite was suggested to constitute the iron-oxide mineral phase due to their reddish-brown and yellowish appearance under microscope and forms ball-like crystal clusters (Figure 5.6d). Some iron may have been derived from ferrous minerals within the sandstones, but most of the iron must have sourced by percolation from the overlain iron-rich sediment (Adepoju *et al*., 2018b).

Clay Cement

Clay mineral observed is basically a kaolinite (Figure 5.6d) occuring inform of feldspar replacement by kaolinitization process. Where observed, they appear as individual cleavage plates, aligned and form rims around the grains (Figure 5.6b and d). Kaolinization of detrital K-feldspars is common and ranges from partial to complete replacement by kaolinite due to weathering and breakdown of the detrital feldspar grains in a wet and humid climate as suugested by Adepoju *et al*. (2018b).

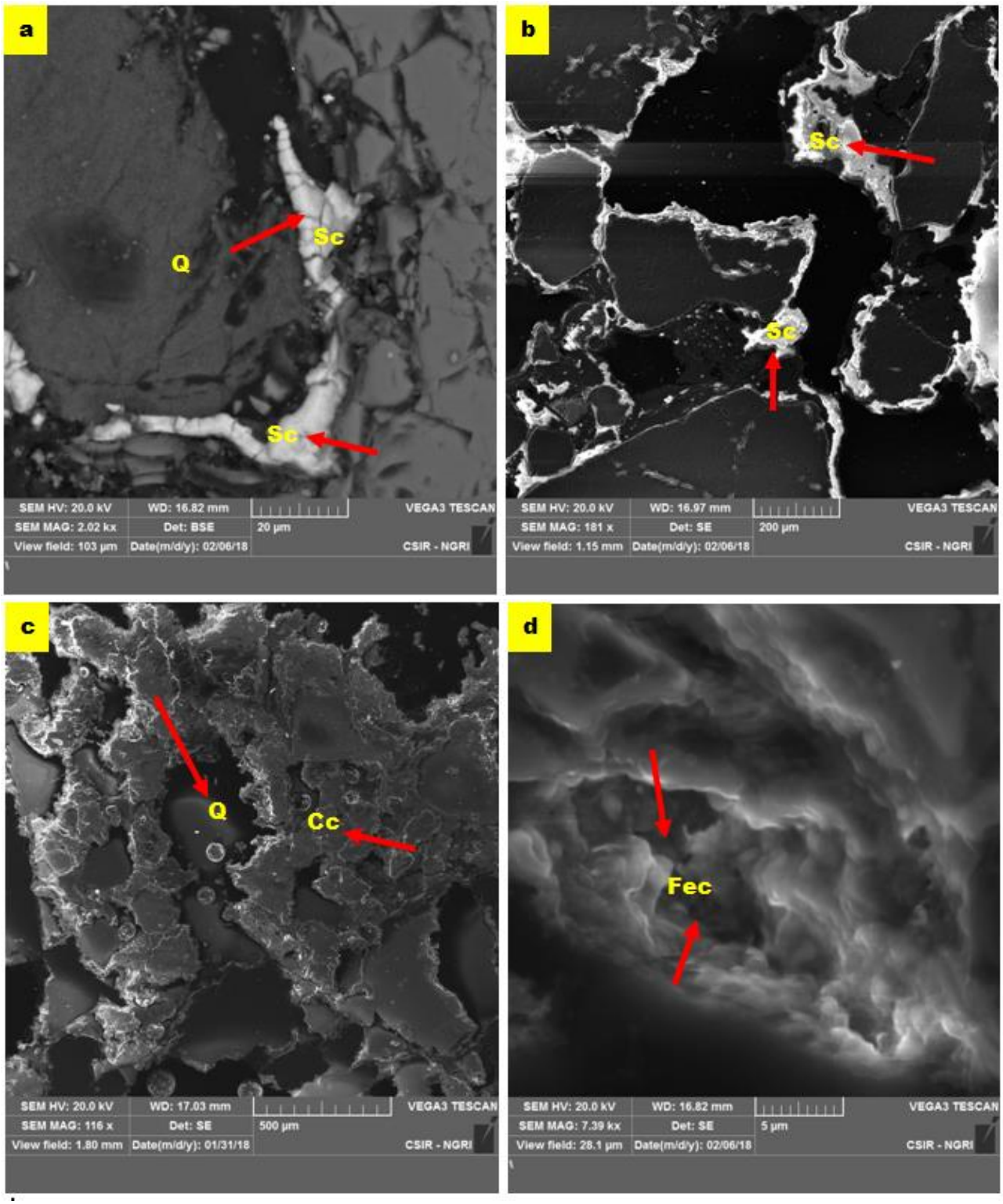


Figure 5.5: Backscattered electron and Scanning electron micrographs showing Silica cement (Sc) in (a) AGB-1F and (b) RAB-1P; Clay cement (Cc) in (c) DOK-1N and Iron-oxide cement (Fec) in (d) AGB-1F.

5.1.2.2.2 Quartz Overgrowth

The quartz overgrowth occurs as syntaxial overgrowths around framework quartz grains and, less commonly, as discrete euhedral crystals and may cover extensively to completely quartz grains that have clean surfaces (Figure 5.6a). The overgrowths, where observed commonly occur as several small crystals with detrital quartz grains partially rimmed with authigenic quartz that forms discontinuous rims of small rhombic quartz crystals around the detrital quartz grains (Figure 5.6a and b).

In few cases, the growth was inhibited by the formation of clay cement which covered many of the quartz nucleation sites reducing quartz development (Figure 5.6c), however, at gaps in the clay coatings, some quartz continued to develop, forming large euhedral overgrowths (Figure 5.6d). The quartz forming overgrowth was probably derived from dissolution of quartz grains and/or from compaction water and feature is indicative of compaction and pressure solution due to shallow burial or early cementation (Adepoju *et al*., 2018b).

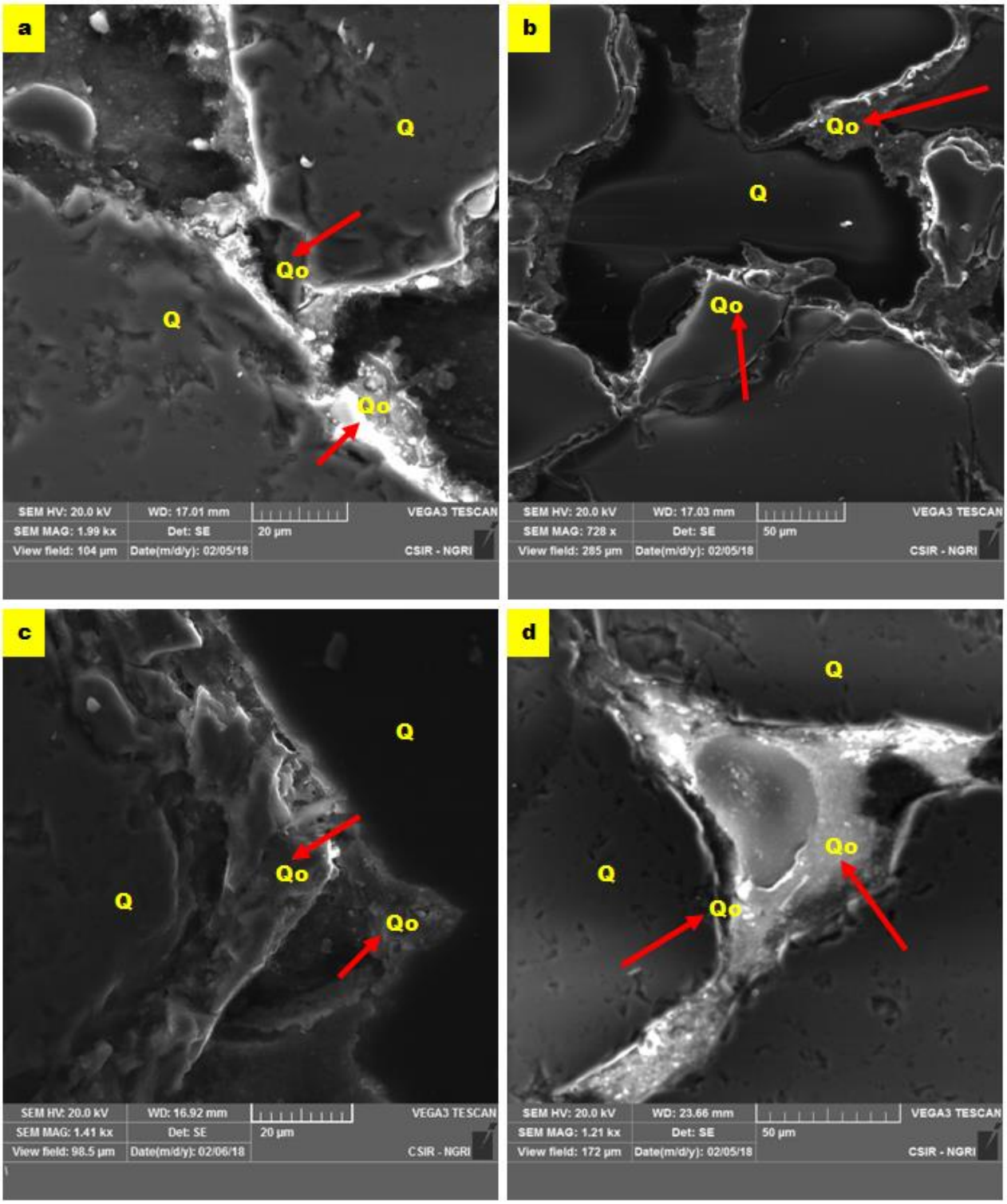


Figure 5.6: Scanning electron micrograph showing Quartz overgrowth (Qo) forming at the edges of the host detrital quartz grains (Q) causing destruction of primary porosity in (a) PAT-1J, (b) DOK-1N, (c) AGB-1F and (d) RAB-1P.

5.1.2.2.3 Feldspar Replacement and Dissolution

Feldspar replacement which probably has altered the composition of some of the studied sandstone was observed in this study. They occurred due to dissolution of detrital feldspar and replacement by the kaolinite. In few cases, former internal fabric of the feldspar grains often is still recognizable by intricate structures consisting of inherited minerals and newly formed minerals within the dissolved feldspars that form ghost structures after the former cleavage or twinning structures (Figure 5.7a and b).

In other cases, authigenic kaolinite as booklets or vermicular occurs with original feldspar texture surviving and remnants of detrital K-feldspar and served as nucleation sites for authigenic feldspar with the outlines of secondary pores. The presence of partially dissolved and replaced feldspars (Figure 5.7) indicates that grain alteration has progressed to the point that minerals more stable than ferromagnesian silicates have been altered (Adepoju *et al*., 2018b).

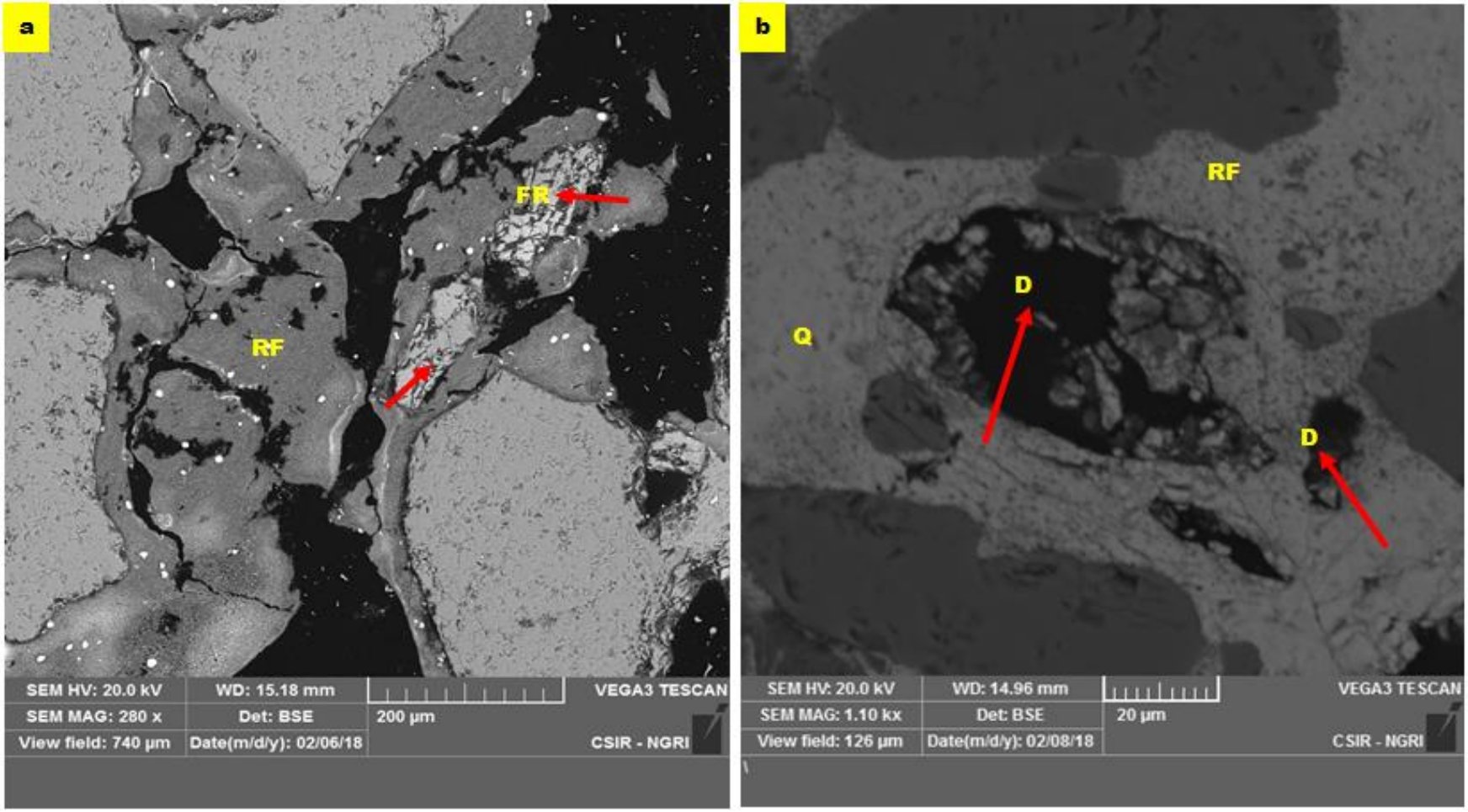


Figure 5.7: Backscattered electron micrograph showing; (a) Feldspar replacement (FR) of the dissolved rock fragment (RF) in RAB-1P and (b) dissolution (D) of the detrital quartz (Q) in PAT-1J.

5.1.2.3 Paragenetic Sequence and Diagenetic History

The diagenetic processes that occurred are; cementation, physical and chemical compaction, dissolution and replacement of minerals, grain-deformation and fracturing. The effects of compaction is evidenced in the sandstones; point and straight contacts and due to further compaction, the initial point and line contacts changed to convex–concave grain contacts and finally to suture contacts as observed more in the central part of the northern Bida Basin.

Compaction of the sediments continues during burial diagenesis due to the increase in overburden pressure which will increase tightness of grain packing and partial loss of pore spaces. Subsequently, quartz and feldspar overgrowths, as well as mineral replacement and clay mineral alteration (i.e., alteration of feldspar to kaolinite) dominate the burial diagenetic changes. Observations by scanning electron microscope (SEM) show that the kaolinite is pore filling and often fill the voids found in the dissolved feldspars. The booklet structure differed in size, and there were evidence of light cracking (Figure 5.7a) which implies that the kaolinite has been affected by a low degree of compaction probably at mechanical regime.

High pressure is suggested to result in the dissolution of feldspar where partial to complete replacement of some detrital grains and clay matrix by new minerals is a common phenomenon in this stage. The mineral replacement was confined to the K-feldspar only as it undergone partial to complete replacement by kaolinite in this stage or even dissolution to form secondary porosity. Or in some cases as progressive increase in burial depth, detrital grains started to pack more tightly resulting in grain fracture.

A diagenetic pathway and sequence constituted series of associated diagenetic changes in the studied sandstone is thus established and presented in figure 5.8.

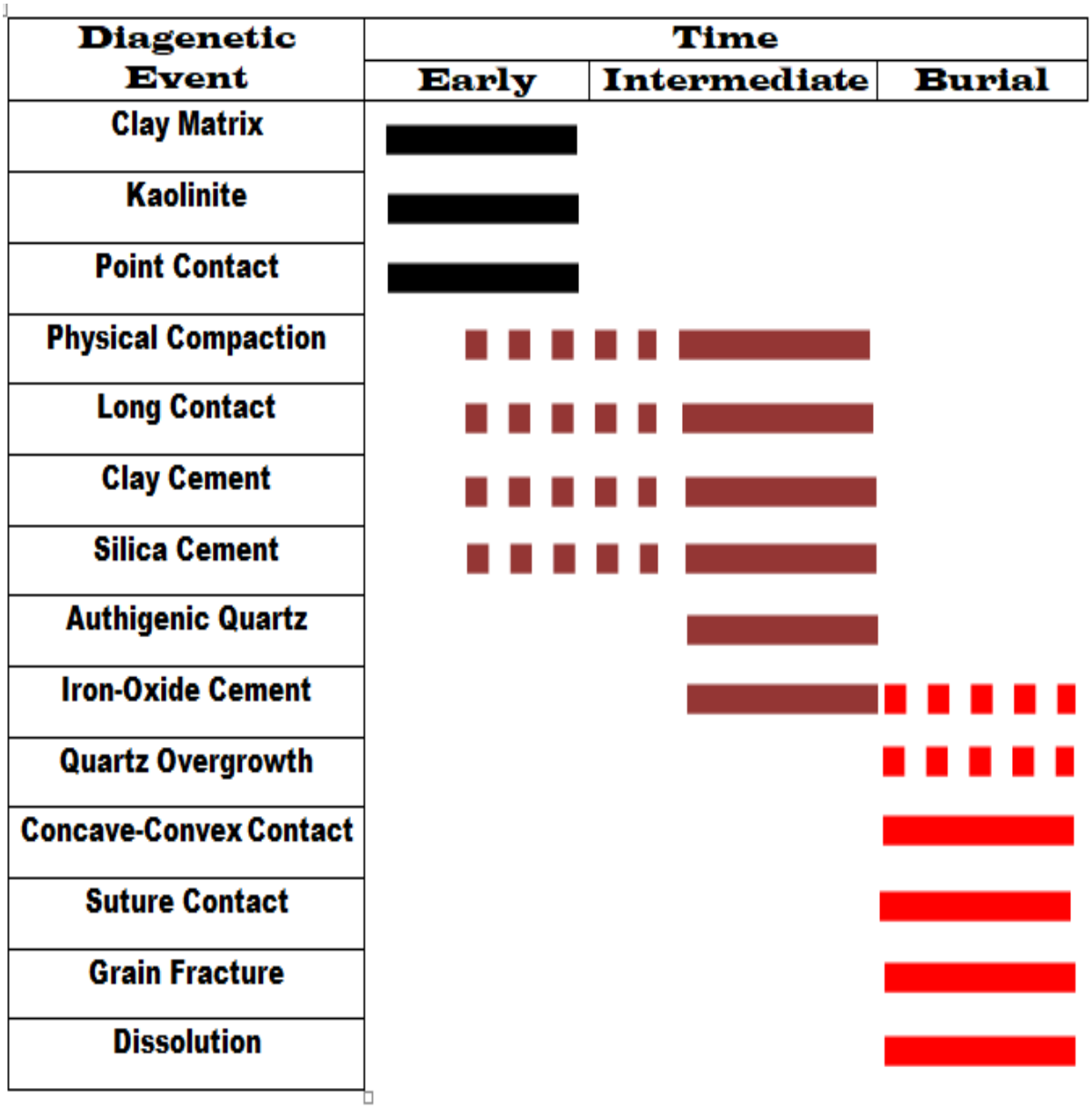


Figure 5.8: A diagenetic events pathway and paragenetic sequence in the Northern Bida Basin.

5.1.2.4 Qualitative Porosity Evaluation and Reservoir Quality

In this study, two porosity qualitative examinations were made; grain contact relationship (for diagenetic phases) and SEM measurements with BSE image analysis. Porosities from both methods show a good correlation for most of the samples. Petrographic and SEM examination of the studied sandstones revealed both primary and secondary porosity which were largely determined by diagenetic processes that either reduce or enhance porosity. The most important diagenetic processes occurred are compaction, cementation by silica, iron oxide and clay cements, fracturing, replacement and dissolution according to Adepoju *et al*. (2019a).

The observed primary porosities are primary intergranular and matrix micro pores which reduced more as sediments became more compacted due to overburden as evidenced by point and straight contacts. The quartz overgrowth coats the detrital quartz grains resulting in the decrease of pore radii and consequently reducing porosity (Figure 5.9b). The progressive burial was also responsible for primary porosity reduction due to compaction as indicated by long and sutured contact between neighboring clastic grains. Also, since quartz cements are known to be destructive on primary porosity, the existence of quartz cements could also possibly limit the preservation of primary porosity in the rocks as well as quartz grain fracture due to over-compaction which in some cases resulted in porosity reduction. Therefore, primary intergranular pores are reduced as a result of intense compaction and cementation (Figure 5.9a and b).

During burial diagenesis, preferential destruction of less stable mineral (Feldspar) or clastic grains by pore fluids produced pore spaces for secondary cementation. The observed secondary porosities in the rocks are secondary intragranular, dissolution and fractured pores which are resulted from the dissolution of unstable feldspar grains, from dissolution of clay

mineral formed by alteration of the feldspar and dissolution of earlier formed clay cements (Figure 5.9c and d).

Generally, the porosity types in the sandstones can be generalized as secondary porosity (sp) as a result of feldspar dissolution and microporosity (mp) found within leached feldspars and rock fragments with little contribution to reservoir quality due to very smaller pore size. This indicates that initial porosity was decreased by compaction and cementation and then increased by dissolution of unstable mineral. Most of the secondary pores are very small, isolated but more efficient, so can serve as reservoir of most of the studied sandstone.

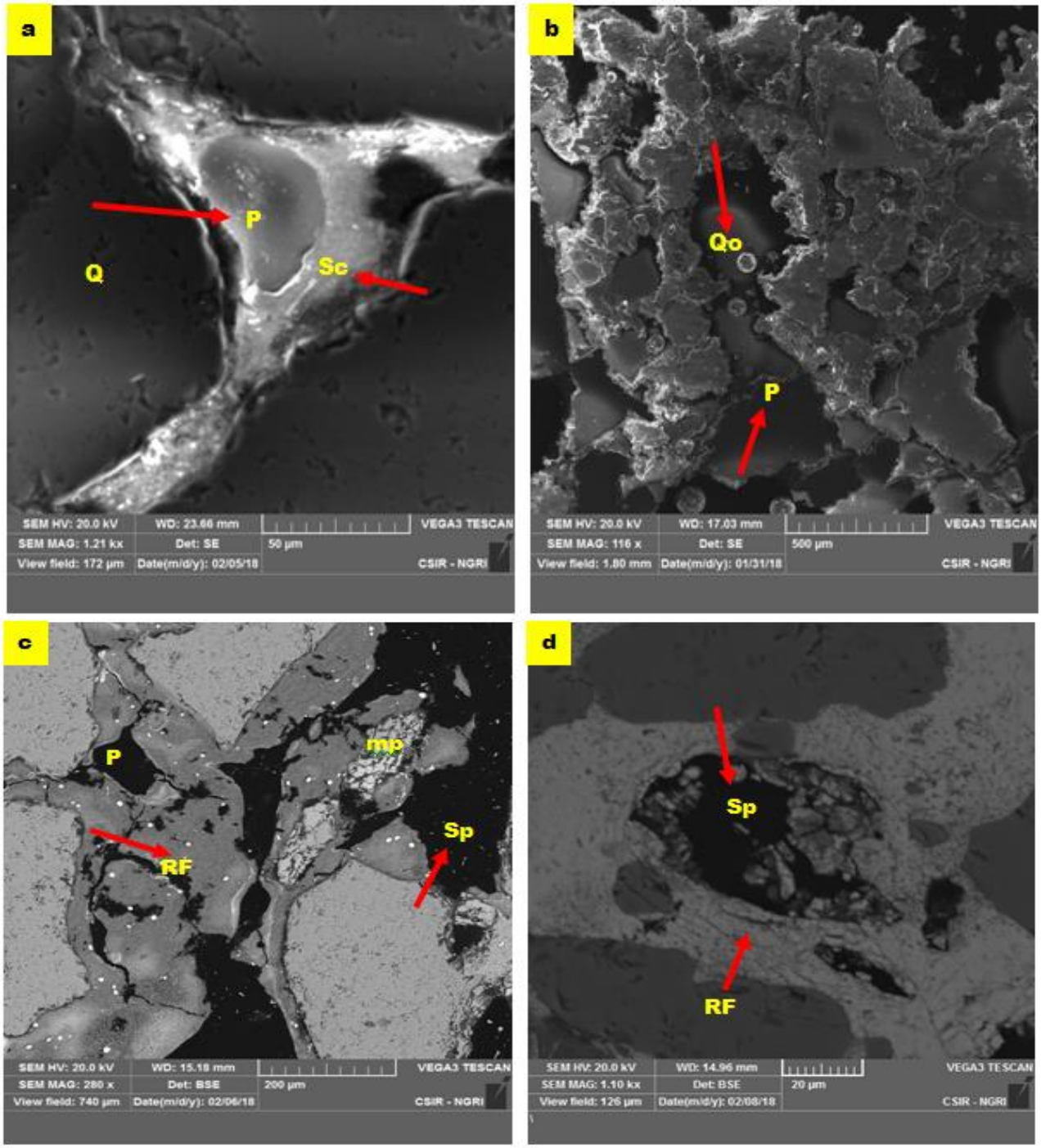


Figure 5.9: Scanning and Backscattered electron micrographs showing primary porosity occlusion and reduction; (a) with silica cement (Sc) in DOK-1N and (b) quartz overgrowth in DOK-1N; and porosity enhancement as a result of (c) feldspar dissolution and replacement causing microporosity (mp) and secondary porosity (sp) in RAB-1P and (d) rock fragment (RF) dissolution in PAT-1J causing secondary porosity.

5.2 Sediment Classification

This chapter describes textural characteristics, classification, petrology, petrofacies and provenance of the studied sandstones. Sandstone types and compositions are useful indicators for the source rock origin, depositional environments, diagenesis and tectonic setting (Pettijohn *et al*., 1972). An integrated petrographic (detrital and heavy minerals) and geochemical (major, trace and rare element) data and are presented in this section. An integrated approach is relevant to examination of the protolith from which the sandstones were derived. Therefore, the petrographic characteristics of various sediments in the study area supplemented with the geochemical evidences to determine the source area. Because the detrital mineralogy of sandstone is the inheritance from the source area, so, its study is one of the most pragmatic approaches which are used to reconstruct the provenance.

The sediment classifications using petrographic compositional data and bulk geochemical data is discussed in this part. Sediment classification also known as petrofacies, as defined by Dickinson and Rich (1972), implies detrital composition of sandstone and it can furnish vital clues regarding the provenance and its tectonic setup, source rock composition, role of climate, relief, transport and diagenesis (Dorsey, 1988; Critelli and Ingersoll, 1994; Pandita, 1996). Hence, it is necessary to synthesize the petrofacies for a logical identification of provenance.

Modal compositional data has been employed by many researchers for petrofacies studies of the clastic sedimentary rocks in order to understand their provenance and interprete the tectonic settings. The proportions of detrital framework grains plotted on triangular diagram provides effective discrimination of a variety of paleo-tectonic settings and have been used as a powerful tool for determining the origin and tectonic reconstruction of terrigenous deposits (Graham *et al*., 1976; Dickinson, 1985).

Some of the past workers from whom this research has benefitted include Crook (1974), Ingersoll (1978), Potter (1978), Dickinson and Suczek (1979), Ingersoll and Suczek (1979), Dickinson and Valloni (1980), Schwab (1981), Valloni and Mezzardi (1984), Bhatia (1985), Dickinson (1985), Bhatia and Crook (1986), Schwab (1986), Garzanti (1986), Stefani (1987), De Celles and Hertel (1989), Akhtar and Ahmad (1992), Akhtar *et al*. (1994), Cox and Lowe (1995), Critelli (1999) and Arribas *et al*. (2003).

5.2.1 Petrographic Approach

For the purpose of classification, compositions of the three-end members; quartz (Q), feldspar (F) and lithic or rock fragment (L/R) were re-calculated into percentage (100%) to determine the framework components of sub-facies. The result is thus presented as follows; crudely bedded conglomerate (Gh) - $Q_{91.89\text{-}100}F_{0\text{-}1.35}L/R_{0\text{-}5.76}$, crudely stratified sandstone (Se) - $Q_{92.11\text{-}97.62}F_{0\text{-}3.95}L/R_{2.38\text{-}4.56}$, planar cross-stratified sandstone (Sp) - $Q_{84.42\text{-}98.84}F_{0\text{-}3.75}L/R_{1.15\text{-}14.58}$, rippled cross-stratified sandstone (Sr) - $Q_{97.59\text{-}97.65}F_{1.18\text{-}1.20}L/R_{1.18\text{-}1.20}$, horizontally stratified sandstone (Sh) - $Q_{84.29\text{-}100}F_{0\text{-}2.5}L/R_{0}\text{-}_{14.71}$, massive sandstone (Sm) - $Q_{95.3\text{-}95.65}F_{1.14\text{-}2.38}L/R_{0\text{-}2}$, finely laminated, very-fine sandstone and mudstone (Fl) - $Q_{90.67\text{-}97.65}F_{0\text{-}2.67}L/R_{1.20\text{-}5.67}$ and massive very-fine sandstone and mudstone (Fm) - $Q_{91.89\text{-}100}F_{0\text{-}1.35}L/R_{0\text{-}5.75.}$

The modal composition above was then plotted on the Quartz-Feldspar-Lithic/Rock fragment ternary diagrams; Q-F-R after McBride (1963), Q-F-L after Pettijohn (1978) and Q-F-R diagram after Folk (1980) for classification determination. Based on the schemes mentioned above, the studied sediments are classified as quartzarenite to sublitharenite (Figure 5.10a and b) and with minor sub-arkoses (Figure 5.10c).

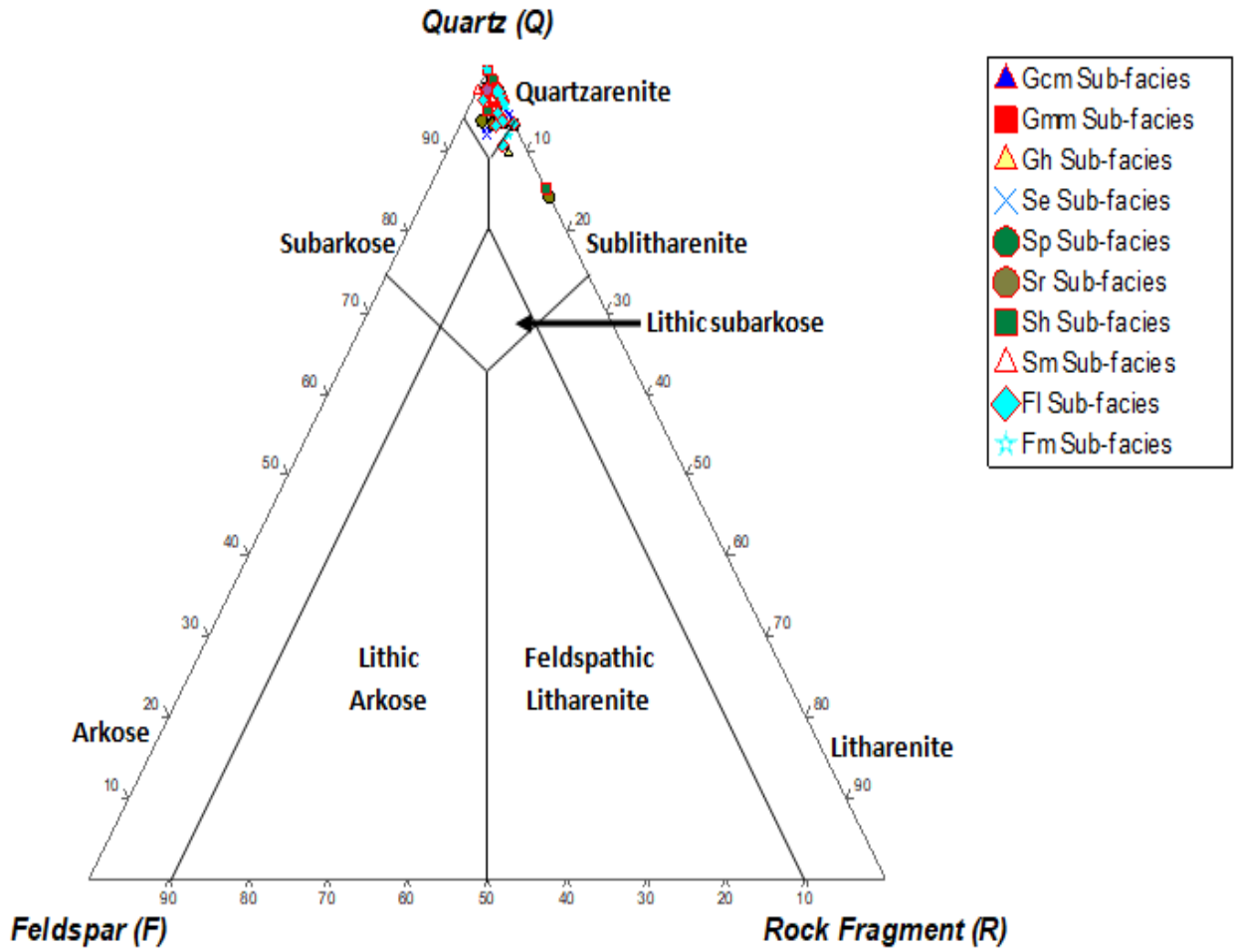


Figure 5.10a: Standard Ternary petrographic classification of investigated sandstones using framework composition of Quartz-Feldspar-Rock Fragment (Q-F-R) after McBride (1963).

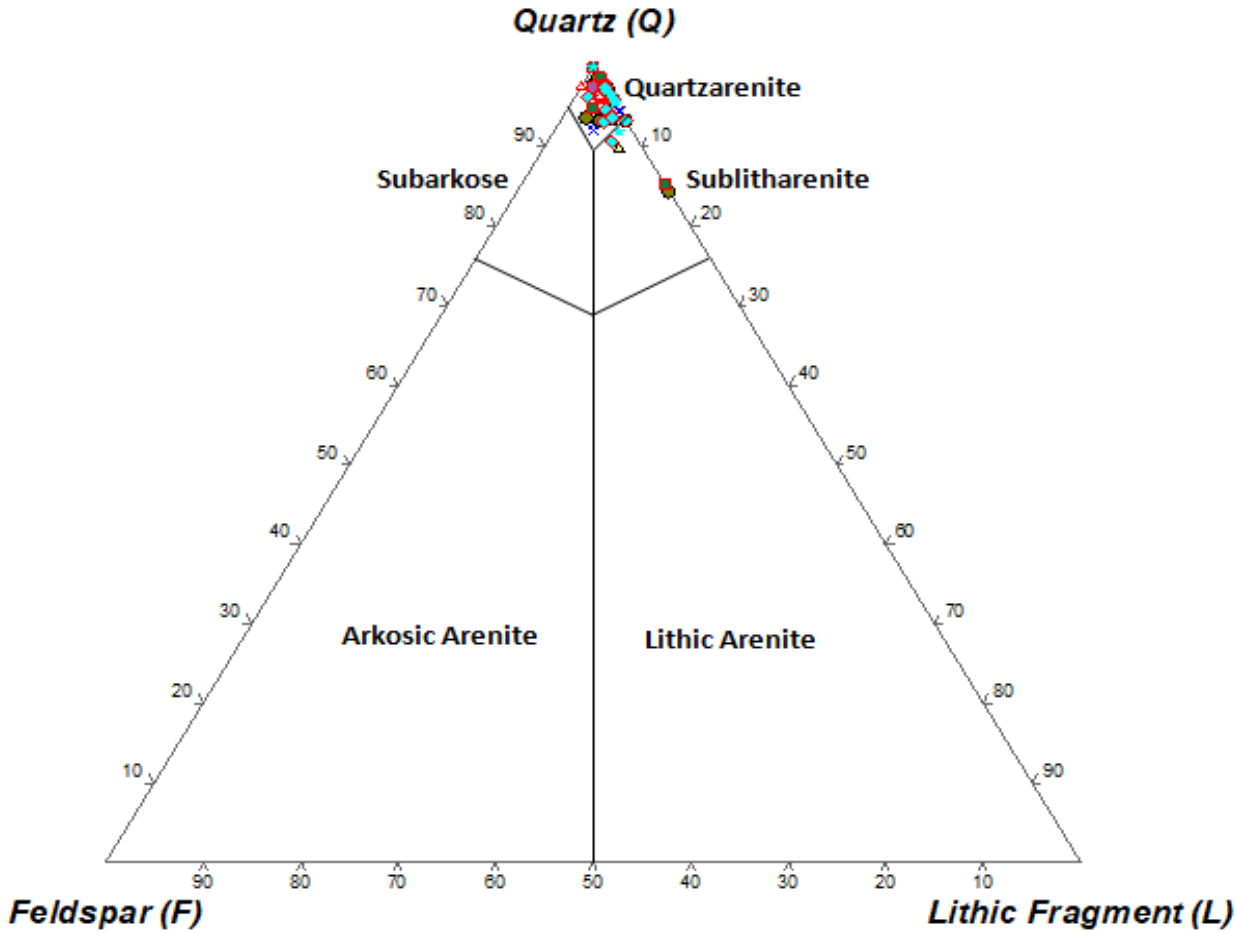


Figure 5.10b: Standard Ternary petrographic classification of investigated sandstones using framework composition of Quartz-Feldspar-Lithic Fragment (Q-F-L) after Pettijohn (1975).

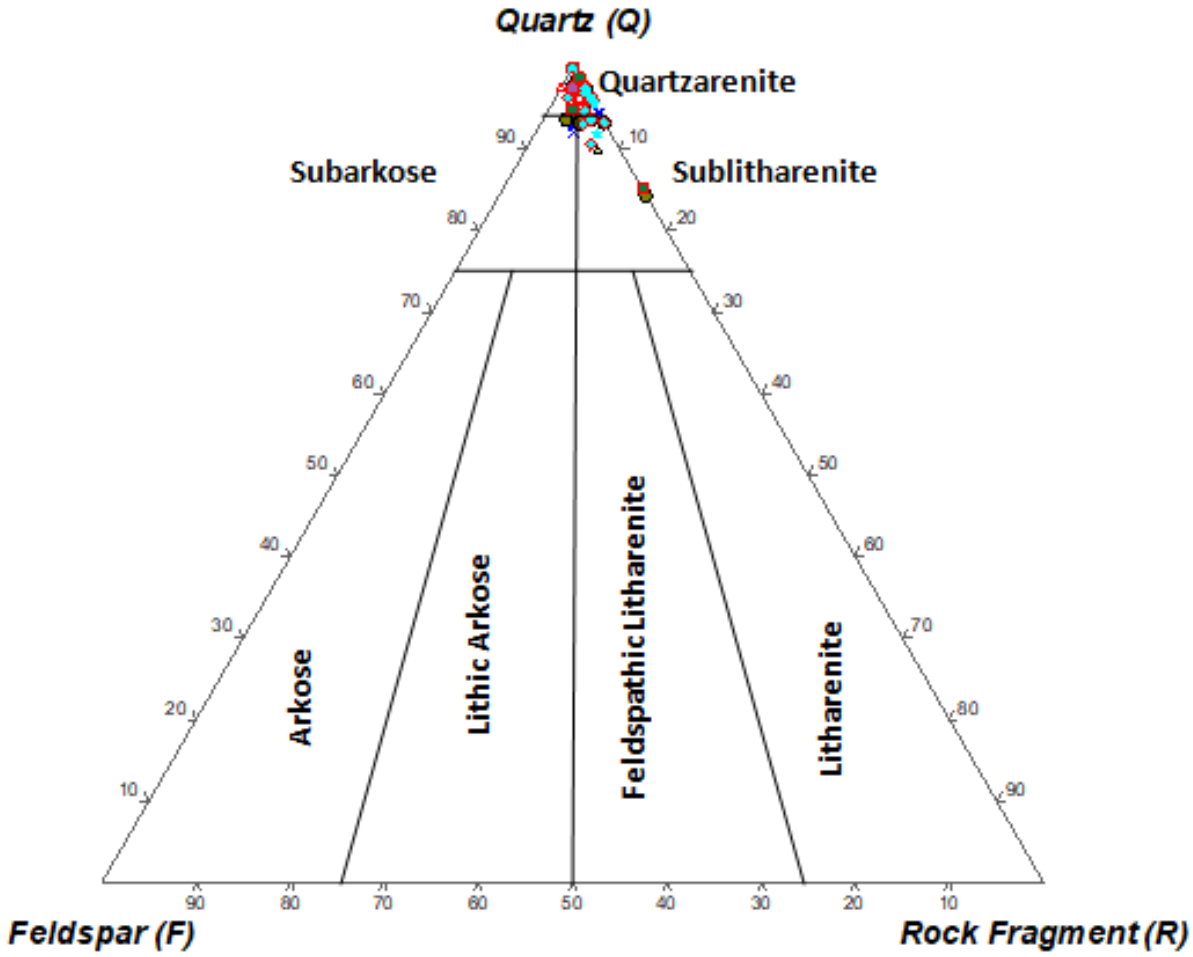


Figure 5.10c: Standard Ternary petrographic classification of investigated sandstones using framework composition of Quartz-Feldspar-Rock Fragment (Q-F-R) after Folk (1980).

5.2.2 Geochemical Approach

The chemical compositions of clastic sedimentary rocks, according to Hayashi *et al*. (1997) are controlled by various factors including composition of their source rocks, environmental parameters influencing the weathering of source rocks, duration of weathering, transportation mechanisms of clastic material from source region to depocenter, depositional environment, and post-depositional processes.

Many authors; Crook (1974), Pettijohn *et al*. (1972), Blatt *et al*. (1980), Herron (1988) have classified sandstones based on their chemical composition. But it is believed that geochemical classification of sandstones does not mimic conventional mineralogical of sandstones based upon quartz-feldspar-lithic fragment; rather differentiate between mature and immature sedimentary rocks. Rollinson (1993) concluded that geochemical classification of sedimentary rocks is not as developed as for igneous rocks. He also stated that most systems of sedimentary rock classification utilizes features which can be observed in thin section, so it is difficult to find a simple relationship between the mineralogical and chemical compositions of sandstones unlike igneous rocks.

In this research, the bulk rock geochemistry, like petrographic compositional data can be used to classify siliciclastic sediments based on standard "SandClass" geochemical classification scheme using ratios of $\log(Na_2O/K_2O)$ versus $\log(SiO_2/Al_2O_3)$ after Pettijohn *et al*. (1972), $\log(Fe_2O_3/K_2O)$ versus $\log(SiO_2/Al_2O_3)$ after Herron (1988) and K_2O (%) versus Na_2O (%) after Crook (1974). These geochemical plots of $\log(Na_2O/K_2O)$ versus $\log(SiO_2/Al_2O_3)$, $\log(Fe_2O_3/K_2O)$ versus $\log(SiO_2/Al_2O_3)$ and K_2O (%) versus Na_2O (%) were prepared and presented in figures 5.11a, b and c. The plots revealed that the quartz rich sandstones were geochemically classified as Fe-sand, litharenite, sublitharenite, arkose and subarkose and sub-facies wacke sub-facies.

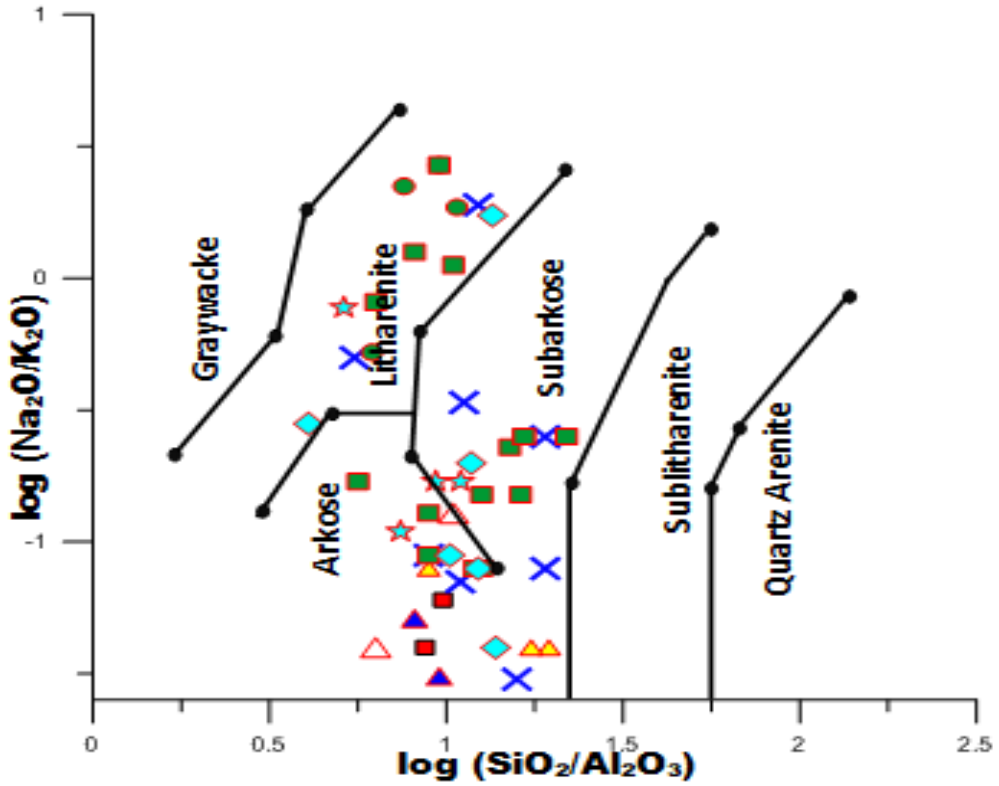


Figure 5.11a: Bivariate geochemical classification of the investigated sandstones using log(SiO_2/Al_2O_3) versus log(Na_2O/K_2O) after Pettijohn *et al*. (1972).

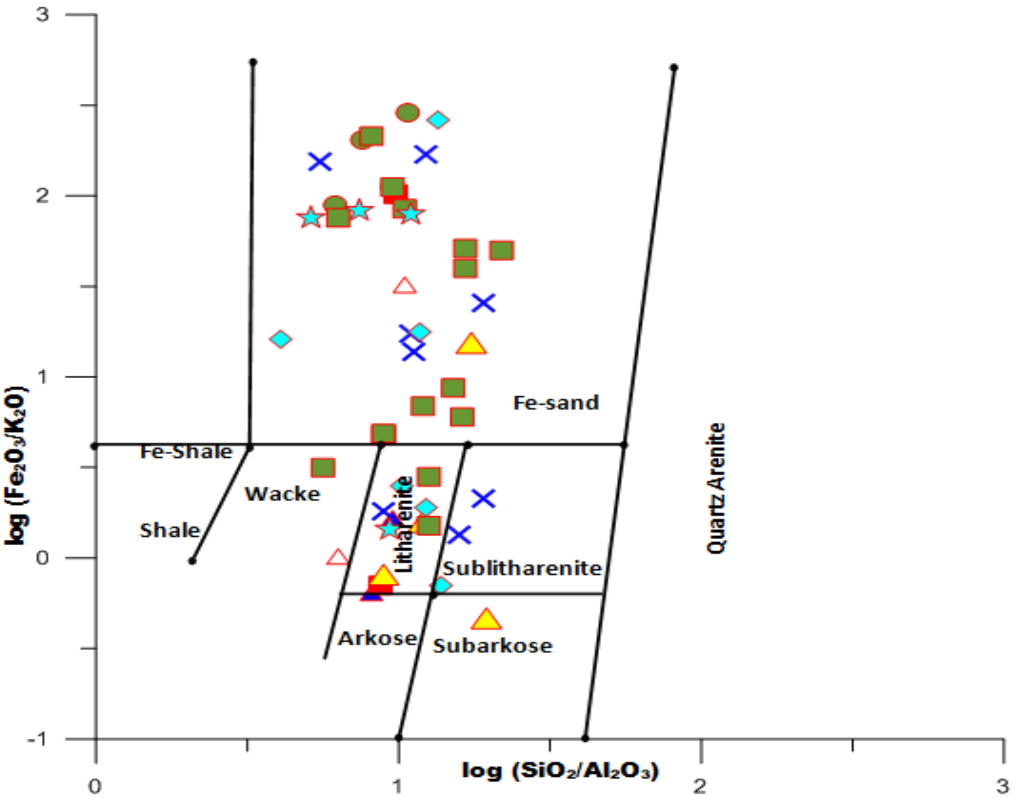


Figure 5.11b: Bivariate geochemical classification of the investigated sandstones using log(SiO_2/Al_2O_3) versus log(Fe_2O_3/K_2O) after Herron (1988).

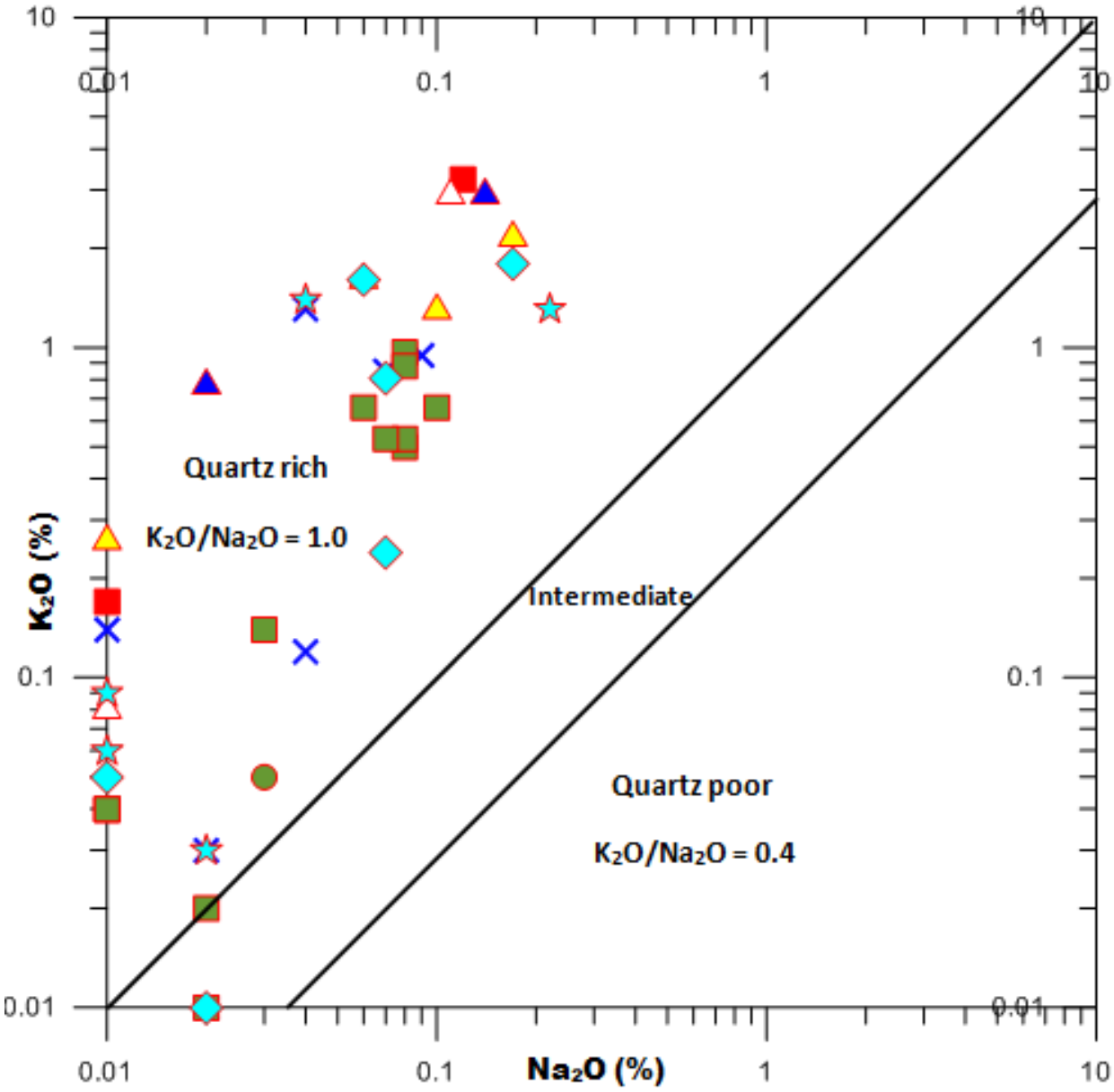


Figure 5.11c: Bivariate geochemical classification of the investigated sandstones using K_2O (%) versus Na_2O (%) after Crook (1974).

5.3 Provenance

Provenance studies using mineralogical compositions and abundances is based on the assumption that detrital grain compositions have not been altered significantly by sedimentary processes and the intention is to reconstruct and interprete the history of sediment from the initial erosion of parent rocks to the final burial of their detritus (Weltje and Eynatten, 2004). Conclusions from independent studies by Ingersoll *et al*. (1984) and Carozzi (1993) have shown that sandstone's petrographic analysis is one of the most commonly used techniques in studying provenance history of sediments, because the mineralogical composition of sandstone grains is key in the study of provenance.

5.3.1 Petrographic Evidence

The petrographic studies discussed in chapter four revealed the dominance of quartz in all the studied sandstone with less percentage of feldspar and rock fragments within the framework constituent. Based on the composition and detrital modal compositions, the sandstones are classified as quartzarenite and sublitharenite with minor sub-arkoses. The detrital composition modes shows that quartzarenite facies are characterized by abundant monocrystalline quartz and generally lack plagioclase, while sublitharenite composed more monocrystalline with few polycrystalline quartz. Change in sandstone petrofacies shown by compositional change over the area also reveals shifts and change in the rate of contributions from the source.

Generally, the occurrence of higher monocrystalline quartz grains with strong undulatory extinction and low polycrystalline quartz (Appendix IV, Tables I-IX) are suggestive of igneous source origin according to Blatt *et al*., (1980). Also, high ratio of monocrystalline to polycrystalline quartz grains (Qm/Qp) in this study supports sediments' derivation from a granitic source as suggested by Basu *et al*. (1975). Minor amount of sedimentary lithic fragments also suggests minimize reworking and rapid localized deposition. Conversely

evidence of igneous lithic fragment shown in figure 4.24f may indicate some reworking from a Basement Complex provenance. The muscovite grains (Figure 4.24e) indicate a low chemical weathering influence and that the detritus was derived from either a nearby granitic source area or muscovite rich metamorphic rocks.

5.3.2 Geochemical Evidence

5.3.2.1 Major Elements

The whole rock geochemistry of a sedimentary rock provides an understanding of provenance of sediments and subsequent sedimentary and weathering processes that impacted the sediments and also post-depositional diagenetic processes (Nesbitt and Young, 1982). Geochemistry of siliciclastic rocks may retain the chemical signature of source rocks, although sedimentary processes such as chemical weathering, physical sorting and diagenesis could influence the chemical compositions (Nesbitt *et al*., 1996; McLennan, 1993; Fedo *et al*., 1995).

The geochemical characteristics of clastic sedimentary rocks have been used to decipher the provenance of the source region (Taylor and McLennan, 1985; Condie *et al*., 1992). Particularly, ratios of SiO_2/Al_2O_3 after Potter (1978), Condie and Wronkiewicz (1990), K_2O/Na_2O after Schwab (1978) and Al_2O_3 and TiO_2 after Holland (1984) have been estimated to infer evolutionary changes in the continental crust compositions and the provenance.

The Al_2O_3 and TiO_2 contents of the siliciclastic sedimentary rocks are considered as significant indicators of their provenance, because during weathering of source rocks, Al and Ti remain essentially immobile, owing to low solubility of their oxides and hydroxides in low temperature aqueous solutions (Yamamoto *et al*., 1986; Sugitani *et al*., 1996). Hayashi *et al*. (1997) suggested that the ratio of Al_2O_3/TiO_2 can be used to determine sediments source area because its derived sedimentary ratio from fluvially transported detrital siliciclastic material

should be practically similar to those of the source, a suggestion was therefore made for ratio values as follows; mafic igneous rocks is suggested to have Al_2O_3/TiO_2 ratio ranging from 3 to 8, intermediate source rocks ratio range from 8 to 21 and the ratio for felsic igneous rocks range from 21 to 70.

In this study, the calculated Al_2O_3/TiO_2 for all the sandstone sub-facies (Appendix VI, Tables Ia-Id) indicates an intermediate to felsic source rocks. It is important to also note that mean value of Al_2O_3/TiO_2 for this study have relatively same values with the standard published values of the Post Archean Australian Shale (PAAS) after Taylor and McLennan (1985) and Upper Continental Crust sediments (UCC) after Rudnick and Gao (2003), also supported the major felsic source rock signature (Appendix VI, Table Ie).

The ratio of SiO_2 to Al_2O_3 (SiO_2/Al_2O_3) of the studied sandstones are relatively higher compared to typical PAAS and UCC sediments (See appendix V, Tables xxix-xxxii), therefore, points to sediments' derivation from felsic source. According to Cox *et al.* (1995), ratio of potassic to alumina (K_2O/Al_2O_3) can indicate relative abundance of alkali feldspar over plagioclase and clay minerals. He stated that ratio greater than 0.5 suggest a significant quantity of alkali feldspar relative to other aluminosilicates, in contrast, K_2O/Al_2O_3ratios lesser than 0.4 suggests lack of alkali feldspar in the rocks. The calculated mean values of K_2O/Al_2O_3 in this study (Appendix VI, Tables Ia-Id) are consistent with low amounts of feldspar as observed from the thin section petrography, so, implying quartz-rich source rocks.

By employing the major elements-based provenance discriminant plots, the investigated samples were plotted within the felsic field as source on the bivariate Al_2O_3/TiO_2 versus SiO_2 discrimination plot (Figure 5.12a) after Le Bas *et al*. (1986). This is supported by the $SiO_2/10$-$CaO+MgO$-Na_2O+K_2O ternary discrimination plot (Figure 5.12b) after Taylor and McLennan (1985) which shows sediment plotting within granites fields.

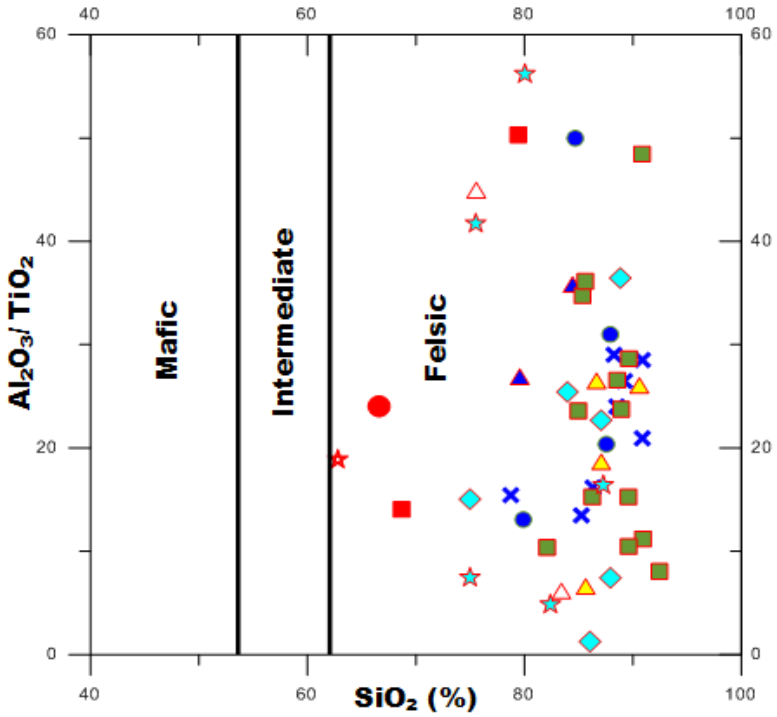


Figure 5.12a: Bivariate Al_2O_3/TiO_2 versus SiO_2 provenance discrimination plot after Le Bas *et al.* (1986) showing Felsic field as source for the investigated sandstones.

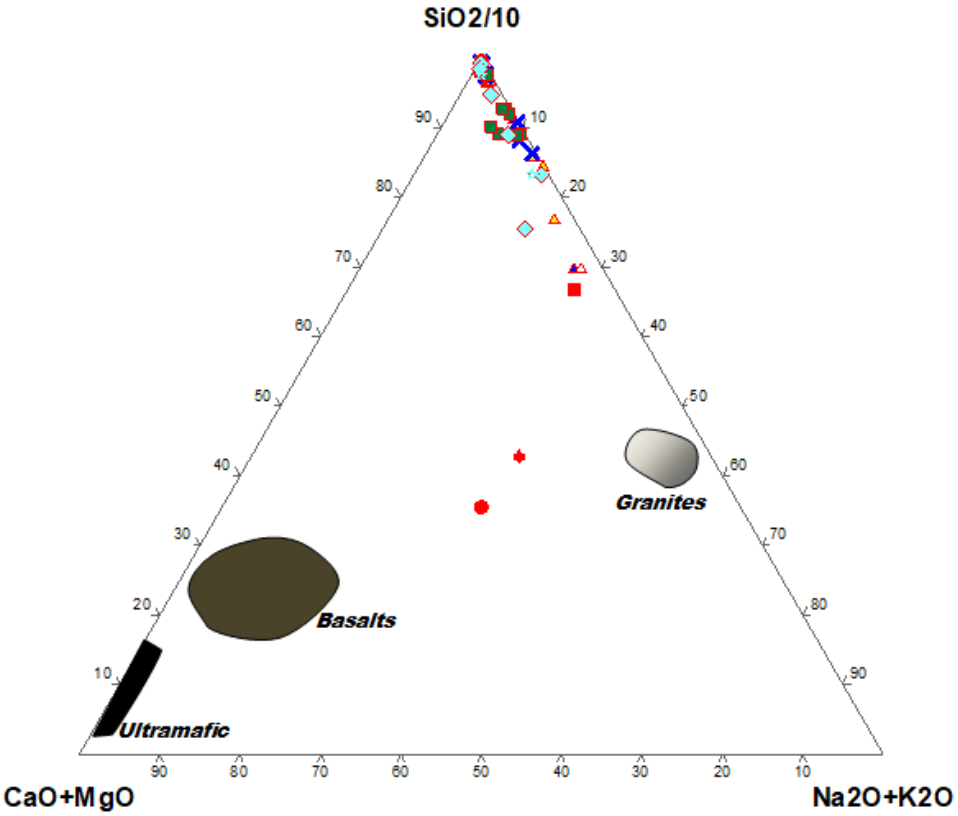


Figure 5.12b: The standard SiO_2/10-CaO+MgO-Na_2O+K_2O ternary provenancediscrimination plot after Taylor and McLennan (1985) showing granites fields as the source for the investigated sandstones.

5.3.2.2 Trace Elements

Trace elements are quantitatively transported into the clastic sedimentary rocks during weathering and deposition (McLennan, 1982). The effects of weathering under variable climatic conditions, on trace element distribution in clastic sedimentary rocks, were reported in previous geochemical studies (Suttner *et al*., 1981; Cullers *et al*., 1987; Cullers, 1988). For example immobile trace elements, like Y, Th, Zr, Hf, Nb and Sc are found to be suitable for determining the provenance and tectonic settings of a basin due to their low residence time in the seawater (Bhatia, 1983; Bhatia and Crook, 1986). Thus, in this study, some selected trace elements and value of their ratio from the analyzed are presented in tables for inferring the provenance.

The ferromagnesian trace elements such as Cr and Ni and the concentration of Cr and Zr in clastic rocks are useful indicators for provenance study (Bhatia and Crook, 1986; Condie, 1993). Also, Cullers *et al*. (1988), Taylor and McLennan (1985) and, Wronkiewicz and Condie (1990) concluded independently that silt fraction of sediment most closely reflects the provenance of the sediments whereby felsic source rocks usually contain lower concentrations of some trace elements like Cr, Co, Ni and V with higher concentrations of Ba, Sr, Y and Zr than mafic and intermediate source rocks because Cr and Zr are controlled by the chromite and zircon contents respectively. In this study, I observed depletion in Ni, Co and V, however, the sediments are enriched in Zr (Tables 4.7a-4.7i), and thus indicate that they were principally derived from felsic source rocks. Also, the mean relatively well compared values of the above listed elements in the studied sediments with the published

UCC and PAAS values (Table 4.7j) may be as a result of selective sorting of heavy minerals which may also indicate a felsic igneous in the source.

The Immobile elements; Zr, Nb and Y are preferentially enriched in felsic phases during crystallization and anatexis process; thus, make them a good provenance indicator according to Taylor and McLennan (1985) and Feng and Kerrich (1990). The mean values for Nb and Y in this study for all the sub-facies have lower values than the published UCC and PAAS whereas Zr have high mean values in all the sub-facies except Gcm, Gmm and Sm and this may thus indicate the presence of felsic phases in the source areas for these sediments (Table 4.7j).

The variations in compostions of Th and La (indicative of felsic) and, Sc and Co (indicative of mafic) contents have been used to differentiate the provenance of felsic and mafic rocks by various authors including McLennan *et al*. (1980), Taylor and Mclennan (1985), McLennan and Taylor (1991). Cullers (2002) also concluded that variations in contents of Th and La are useful as indicative of the felsic source rocks while Sc and Co is an indicative of the mafic source rocks. The geochemical values of Th, La, Sc and Co of the studied sediments show similar concentrations than the published UCC and PAAS values, so, support felsic source rocks.

The ratios of immobile trace elements such as La/Th, La/Co, Th/Co, La/Sc, Th/Sc, Cr/Th, Th/Co Ba/Rb, Zr/Nb, Zr/Hf and Zr/Th are considered as good indicators of source rocks as they yield different values in felsic and basic rocks, and are considered suitable indicators of source rock provenance (Taylor and McLennan 1985; Cullers, 1994 and 2000; Cullers *et al*., 1988; Wronkiewicz and Condie, 1990; Rollinson, 1993; Cullers, 1994, 2000, 2002; Cox et al., 1995; Cullers and Podkovyrov, 2000; Rahman and Suzuki, 2007). Also, Armstrong-Altrin

et al. (2004) further stated that La/Sc and Th/Sc ratios of sediments derived from felsic rocks are always higher than those of sediments derived from mafic rocks. The calculated geochemical mean ratio for the investigated samples (Appendix VI, Tables IIa-IIi) show that the sediments in all the sub-facies are similar to the mean values of the UCC and PAAS data (Appendix VI, Table IIj) thus supportive of felsic igneous source.

The obtained provenance bi-variate discrimination diagrams of the investigated samples includes; TiO_2 versus Zr (ppm) after Hayashi *et al*. (1997) (Figure 5.13a), TiO_2 versus Ni (ppm) after Floyd *et al*. (1989) (Figure 5.13b), Cr/V versus Y/Ni (Figure 5.13c) after Floyd *et al*. (1990) and Hayashi *et al*. (1997), Th/Sc versus Sc (Figure 5.13d) after McLennan *et al*. (1993), Th/Co versus La/Sc (Figure 5.13e) after McLennan *et al*. (1980), McLennan and Taylor (1991) and Cullers (2002), La/Th versus Hf (Figure 5.13f) after Floyd *et al*. (1990) and Hayashi *et al*. (1997) with ternary plots of La-Th-Sc (Figure 5.13g) after Roser and Korsch (1986) and V-Ni-Th*10 after Bracciali *et al*. (2007) confirmed that the sediments within the northern Bida Basin were sourced from an acidic igneous felsic provenance field.

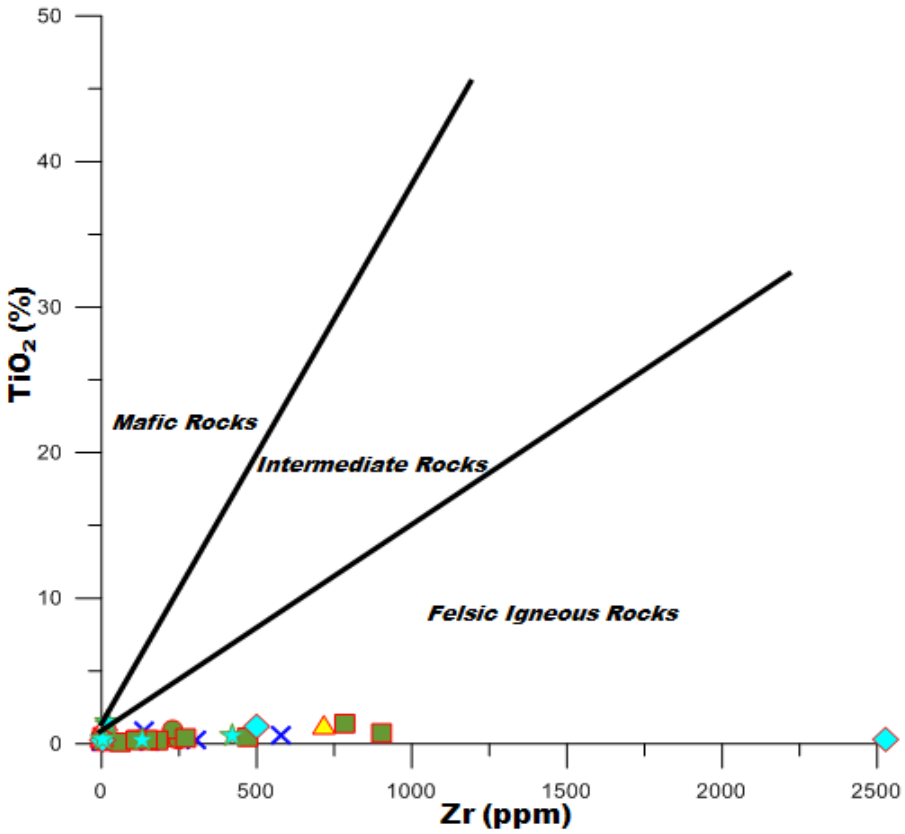


Figure 5.13a: Bivariate TiO_2 versus Zr (ppm) provenance discrimination plot after Hayashi *et al.* (1997) showing investigated sandstones sediments derivation from felsic Igneous Rocks.

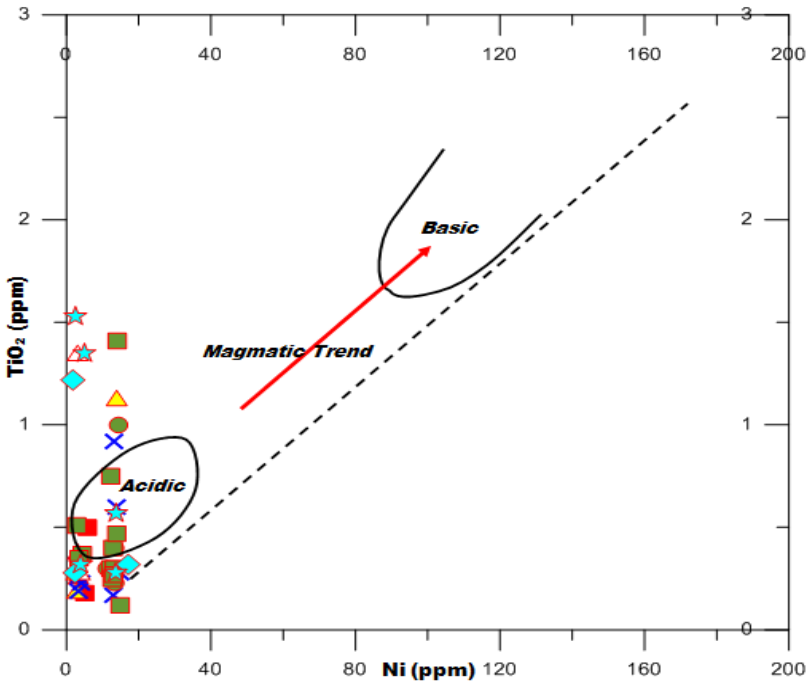


Figure 5.13b: Bivariate TiO_2 (%) versus Ni (ppm) provenance discrimination plot showing acidic rocks for investigated sandstones after Floyd *et al*. (1989).

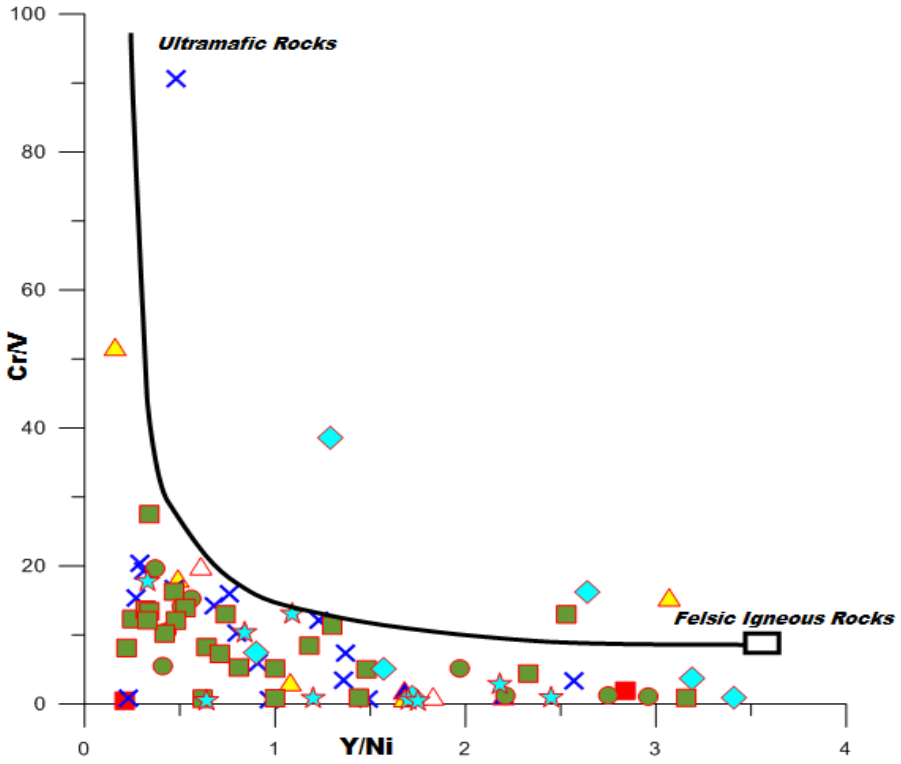


Figure 5.13c: Bivariate Y/Ni versus Cr/V provenance discrimination plot after Floyd *et al*. (1990) and Hayashi *et al*. (1997) showing felsic Igneous Rocks derivation for the investigated sandstones.

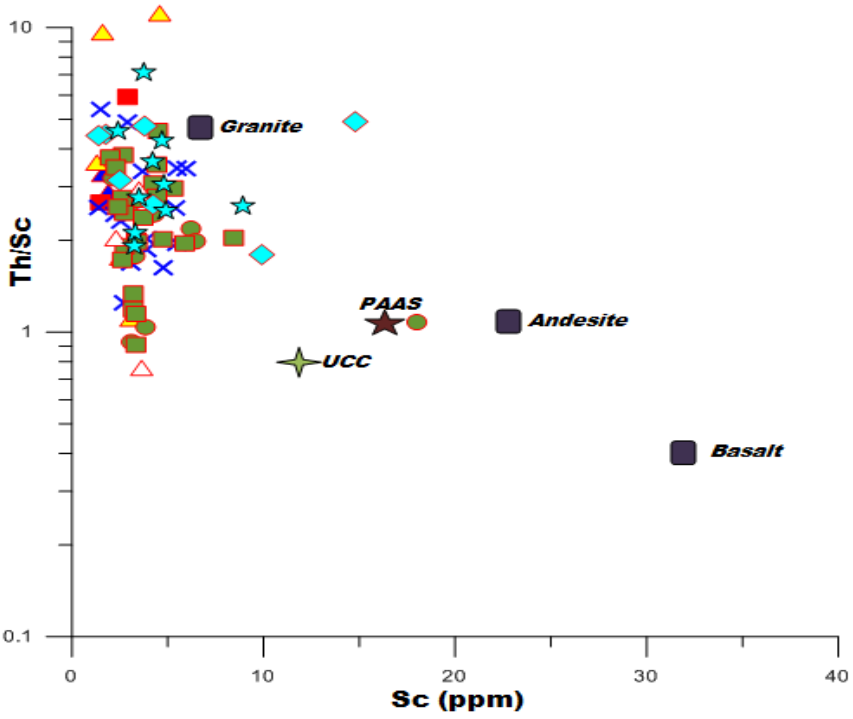


Figure 5.13d: Bivariate Th/Sc versus Sc provenance discrimination plot for the investigated sandstone; PAAS (Taylor and McLennan, 1985), UCC (McLennan, 2001) and granite, andesite, and basalt (Condie, 1993).

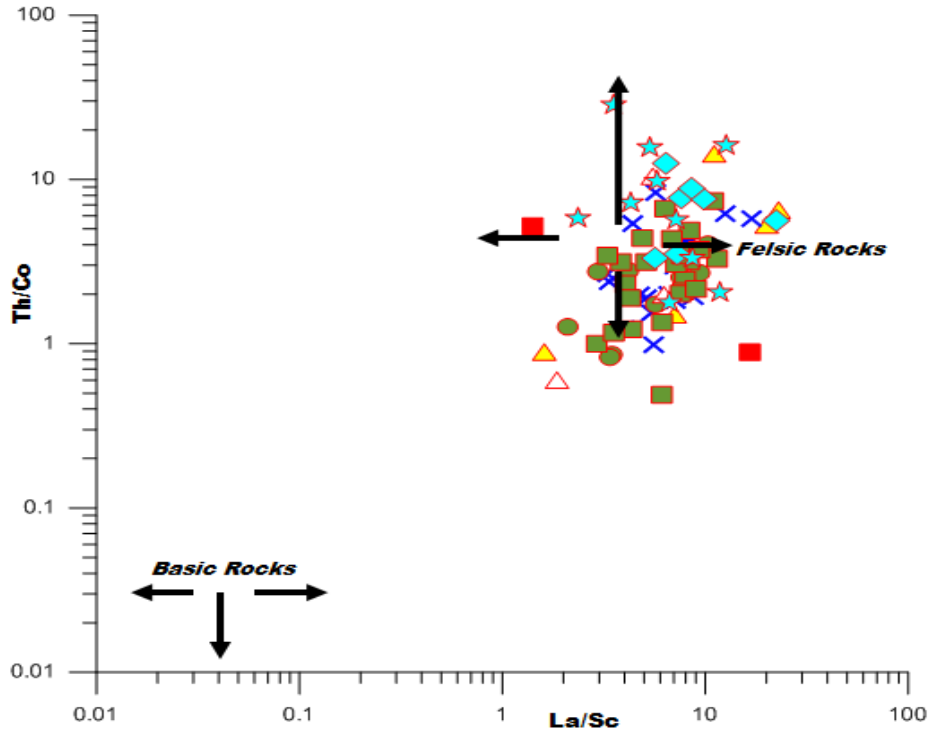


Figure 5.13e: Bivariate Th/Co versus La/Sc provenance discrimination plot for the investigated sandstone after McLennan *et al.* (1980), McLennan and Taylor (1991) and Cullers (2002).

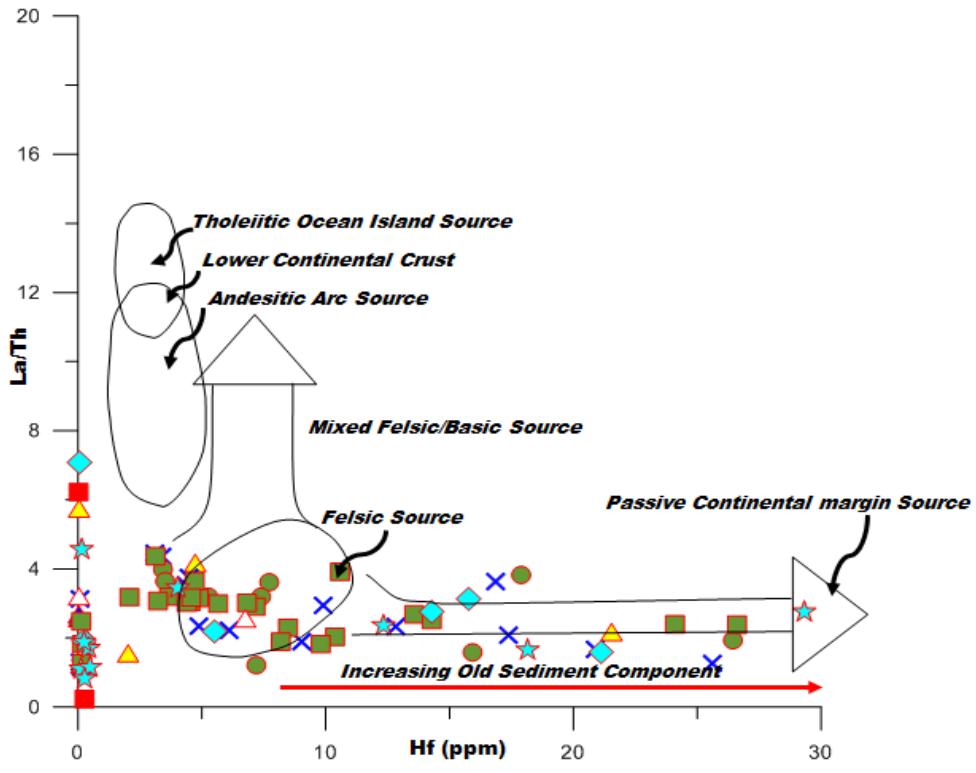
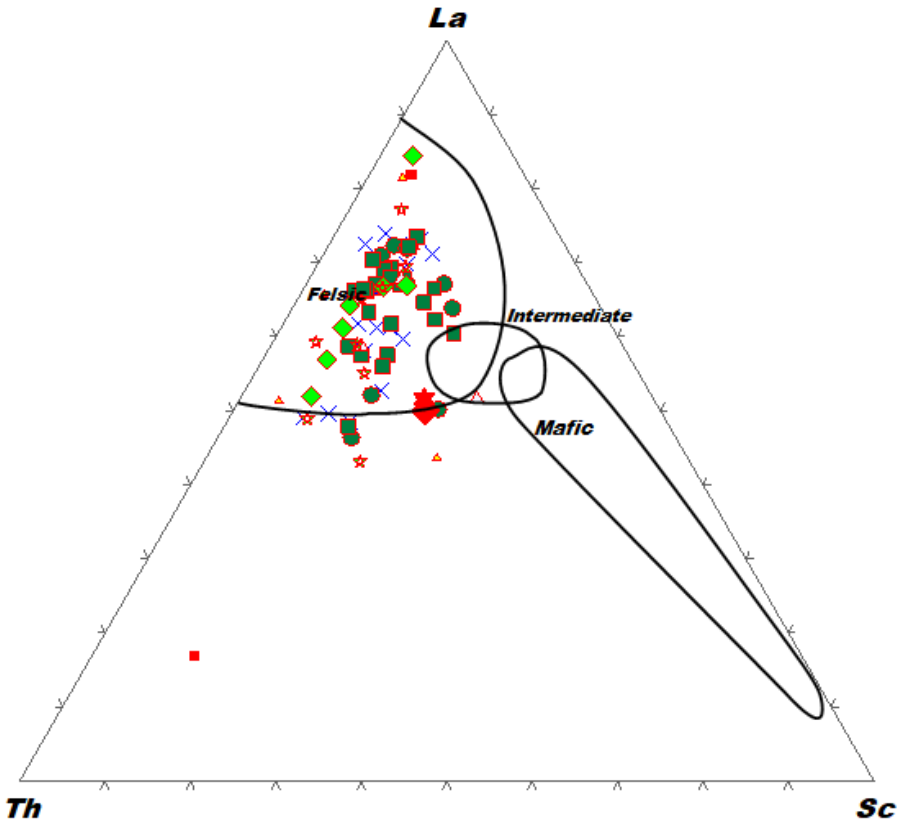


Figure 5.13f: Bivariate provenance discrimination plot using La/Th versus Hf after Floyd *et al.* (1990) and Hayashi *et al.* (1997) showing felsic igneous rocks



derivation for the investigated sandstone.

Figure 5.13g: Standard La-Th-Sc Ternary discrimination plot showing Felsic field for the investigated sandstones after Cullers (2002).

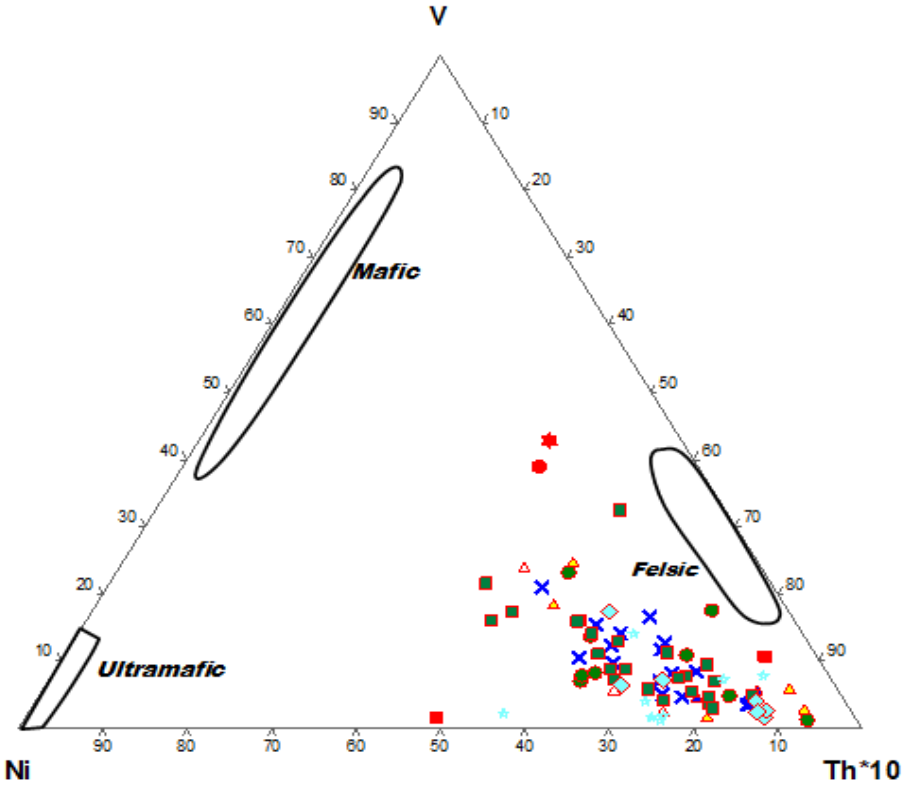


Figure 5.13h: The standard V-Ni-Th*10 ternary provenance discrimination plot after Bracciali *et al.* (2007) showing Felsic fields as the source for the investigated sandstones.

5.3.2.3 Rare Earth Elements

The rare earth elements (REE) are relatively insoluble and immobile elements, with short residence times in the ocean and accordingly are transferred almost quantitatively from upper crustal sources to terrigenous sedimentary rocks (Taylor *et al*., 1986; Cox and Lowe, 1995), therefore, their mode of distribution in clastic sedimentary rocks has fundamental importance in understanding the compositions and evolution of the continental crust sediments (Taylor and McLennan, 1985). They also provide information about the nature of weathering, erosion, sedimentary sorting, diagenesis, element mobility in crustal environment,

provenance of specific sedimentary sequences (Nathan, 1976; Bhatia and Taylor, 1981; Bhatia, 1985; Taylor and McLennan, 1985; McLennan, 1989).

Rare earth elements (REE) can be broadly classified into; light rare earth elements (LREE) and heavy rare earth elements (HREE) based on their atomic numbers according to Taylor and McLennan (1985). The LREE include low atomic number elements from lanthanum (La) to samarium (Sm) while the HREE are elements with higher atomic number from Gadolinium (Gd) to Lutetium (Lu). The source rock characteristics of sedimentary rocks; silicic and basic can be determined by the uses of rare earth element (REE) concentration values, ratio and pattern (diagrams) according to Roaldset (1973), Ronov *et al*. (1974), Cullers *et al*. (1975, 1979), Bavinton and Taylor (1980), Cullers and Graf (1983), McLennan *et al*. (1983, 1990), Bhatia (1985), Taylor and McLennan (1985), Bhatia and Crook (1986), Wronkiewicz and Condie (1990), Eriksson *et al*. (1992), McLennan and Hemming (1992), and Cullers (1994, 1995). It is inferred that felsic rocks are characterized by enriched LREE and LREE/HREE ratios whereas the mafic rocks exhibit low LREE/HREE ratio (Bhatia and Crook, 1986; Wronkiewicz and Condie, 1990; McLennan and Hemming, 1992; Cullers, 1994 and 1995).

In the present study, the REE results of analyzed samples; the calculated sums (ΣREE), light rare earth elements (LREE), heavy rare earth elements (HREE) and ratios of the light rare earth elements to heavy rare earth elements (ΣLREE/ΣHREE) are presented in tables 4.8a-4.8f. The results show that all the sub-facies are composed of LREE enrichment than HREE. High LREE/HREE ratios indicate felsic igneous rock origin. It is also interesting to note that the mean values of LREE/HREE for the studied sediments are similar to PAAS and UCC (Table 4.8g) which support sediment derivation from felsic source.

5.3.2.3.1 The Europium (Eu/Eu*) Anomaly variation

During magma crystallization, europium (Eu) usually incorporate into plagioclase, causing a higher concentration than unexpected of Eu than the other rare earth elements (REEs), so, resulting in a positive Eu anomaly. This according to Cullers and Graf (1983) cause a relatively depletion of Eu in magma and if separates from plagioclase crystals and solidifies, and the resulting chemical composition will show a negative Eu anomaly but in contrast, a relatively positive Eu anomaly would occur if magma accumulates plagioclase crystals before solidification. In summary, siliciclastic sediments characterized by a positive Eu anomaly is usually caused by a relatively high proportion of plagioclase feldspar, but this is a huge generalization as positive anomalies may result from post depositional diagenesis, with Eu enrichment in cements such a calcite.

Generally, the REE pattern and Europium anomaly (Eu/Eu*) in the sedimentary rocks provide clues for the source rock characteristics (Cullers and Graf, 1983; Dickinson, 1985, 1988; Taylor and McLennan, 1985; McLennan *et al*., 1993; Cullers, 1994, 1995) because felsic rocks are characterized by negative Eu/Eu* (<1.0) whereas the mafic rocks exhibit positive but low Eu/Eu* (>1.0). In this study, the calculated Eu/Eu* as presented in tables 4.8a-4.8f indicate that all the sediments are derived from a felsic source. The studied sediments also display very low values of Eu/Eu* compared with UCC (0.66) and PAAS (0.71), so confirm felsic origin for the studied sediments.

The common large negative Eu anomaly is also an indication of mechanical fractionation of plagioclase out of the system during weathering and transport (McLennan *et al*., 1993). The degree of light REE (LREE: La–Sm) versus heavy REE (HREE: Gd–Lu) enrichment is assessed through the ratio of chondrite-normalized La and Yb values (La_N/Yb_N). Fractionation within the LREE and the HREE is illustrated in figures 5.14a-5.14d. All the

plots revealed significant LREE enrichment with nearly flat chondrite-normalized HREE patterns La_N/Yb_N for the studied sediments.

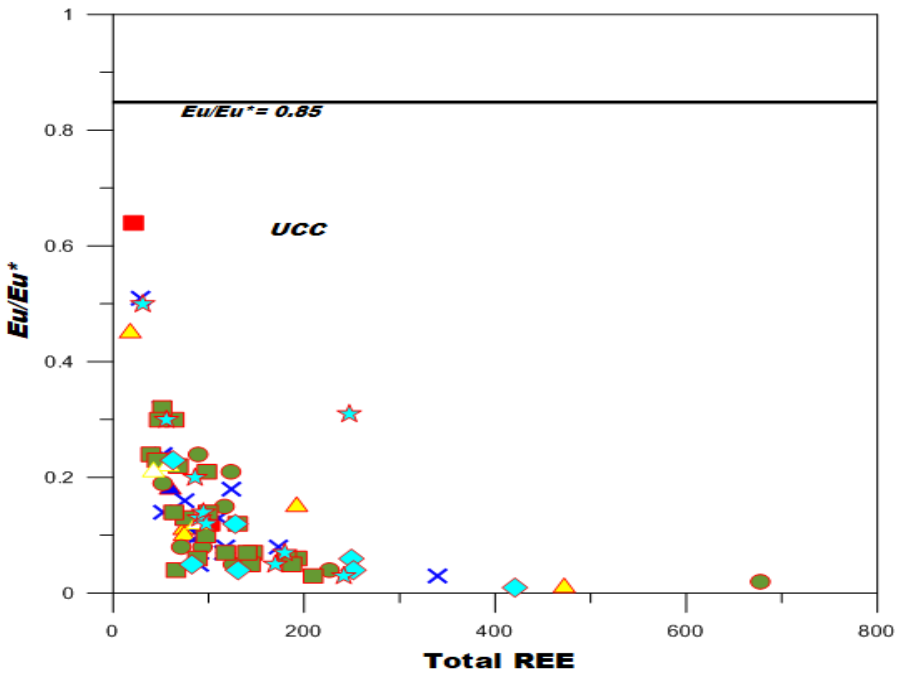


Figure 5.14a: Bivariate Total REE versus Eu/Eu* provenance variation plot showing fractionation relationship for the investigated sandstone after McLennan (1989).

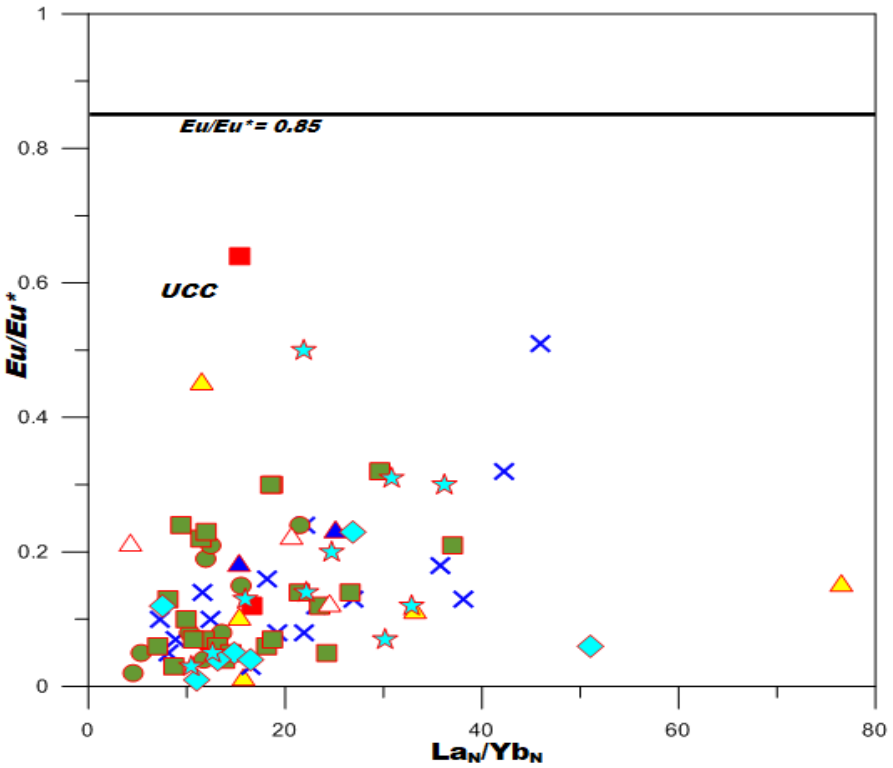


Figure 5.14b: Bivariate La_N/Yb_N versus Eu/Eu* provenance variation plot showing fractionation relationship for the investigated sandstones after McLennan (1989).

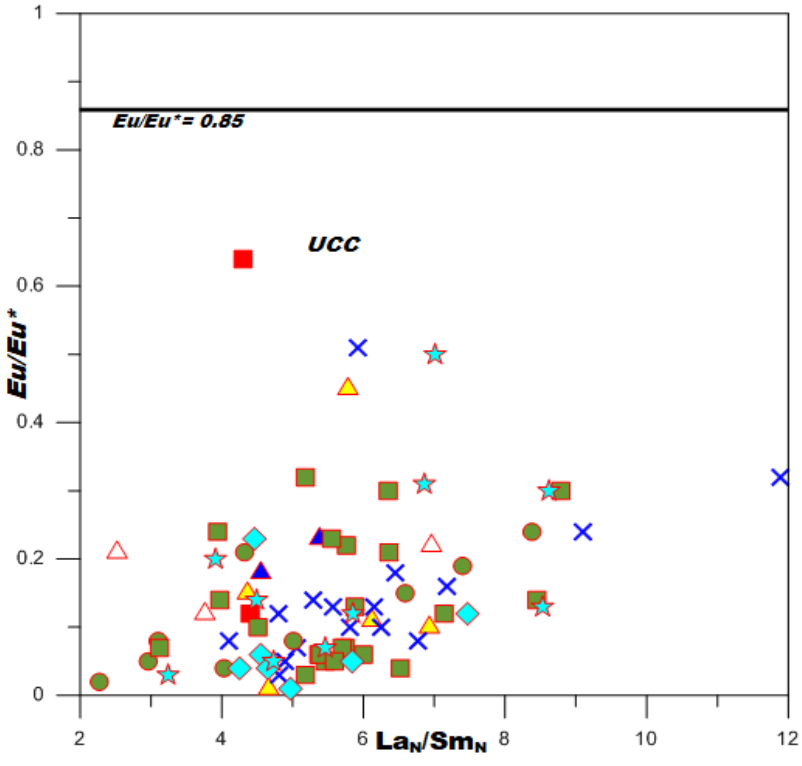


Figure 5.14c: Bivariate La_N/Sm_N versus Eu/Eu* provenance variation plot showing fractionation relationship for the investigated sandstone after McLennan (1989).

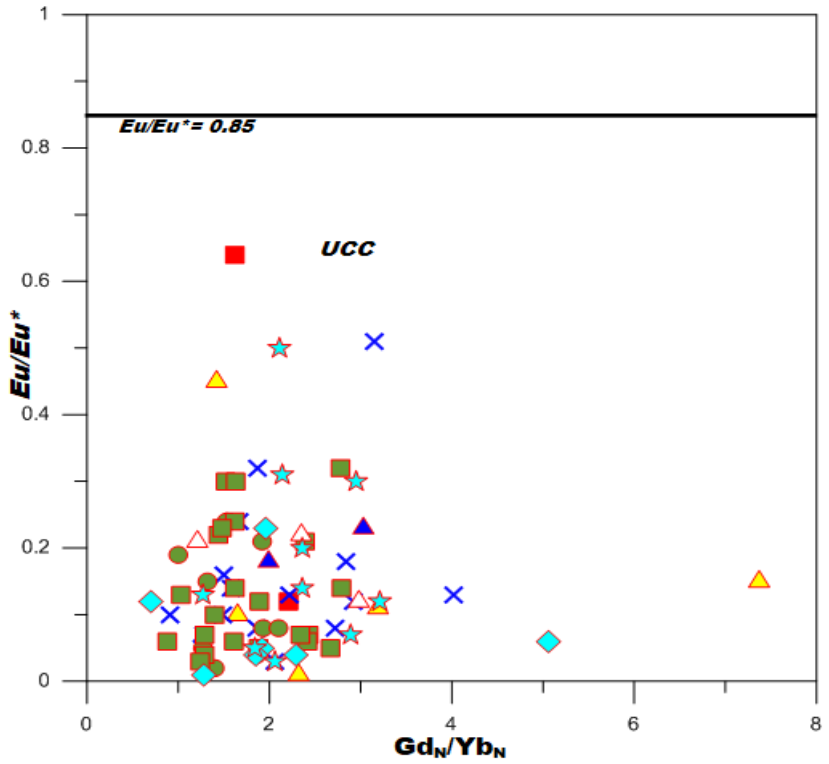


Figure 5.14d: Bivariate Gd_N/Yb_N versus Eu/Eu* provenance variation plot showing fractionation relationship for the investigated sandstone after McLennan (1989).

5.3.2.3.2 Normalized rare earth elements values and plots

According to McLennan (1989) and McLennan and Taylor (1991), the ratio of normalized Gd to Yb (Gd_N/Yb_N) can be employed to document the nature and composition of source rocks in the sedimentary rocks. They stated that UCC sediment generally have higher value of GdN/YbN ratios, typically above 2.0, whereas the PAAS value commonly ranges between 1.0 and 2.0. In this study, the calculated mean values of Gd_N/Yb_N for the all the sub-facies (Table) generally fall and fit within the UCC and PAAS sediment classification values. Also,

like GdN/YbN ratios, the possible change in the Sm/Nd ratios over the geological time had been examined by several workers (Goldstein *et al*., 1984; Miller and O'Nions, 1985; Depaolo, 1988; Dia *et al*., 1990), because of its sensitive to changes in sediment composition (McLennan and Hemming, 1992). The Sm/Nd ratios for all the sub-facies show low mean values which also support the above suggestions.

Normalization of REE in rocks is important because it functions to eliminate abundant variation between odd and even atomic number element so that fractionation of the REE group be identified (Rollinson, 1993; McLennan, 1989). The REE patterns also help distinguish felsic from mafic source of clastic sedimentary rocks (McLennan, 1989). The concentrations of the rare earth elements of the investigated samples have been normalized with the concentrations of the Chondrite after Boynton (1984), Upper Continental Crust (UCC) after Taylor and McLennan (1985), North Archean Australian Shale after (Gromet *et al*., 1984) and Post Archean Australian Average Shale (PAAS) after Taylor and McLennan (1985). In this research, the chondrite normalized values of the studied sediments were used basically for the calculations of normalized variations and anomalies, whereas UCC, NASC and PAAS normalized values were employed for plotting of normalized diagrams.

5.3.2.3.2.1 The Upper Continental Crust normalized plot

The upper continental crust normalized plot is a spider diagram that compares the normalized concentrations of REE of samples from this study to the average upper continental crust of McLennan (1989) and McLennan *et al*. (1993). In this study, the normalized REE distribution diagram (Figure 5.15a) revealed a relatively flattened HREE pattern and relatively steep LREE which is a characteristic of sediments recycled from the upper continental crust

(Taylor and McLennan 1985). Also, the plot pattern show characteristics of sediments derivation from continental interiors and deposited in passive margin settings according to McLennan (1981).

This normalized pattern for the studied samples can be differentiated into three classes showing abnormal variations in some normalized REE values. The first consists of high Ce for Sp sub-facies which may suggest the content of this element in the source rock did not change during weathering, second class comprises the elements Gcm, Gmm and Sm sub-facies showing enrichment in Eu in the studied samples relative to the UCC composition and this may be related to inheritance from the source rocks rich in felsic minerals while, in the third class, concentrations of elements Er is relatively high for Sp sub-facies and this may also related to non-change nature of the elements during weathering.

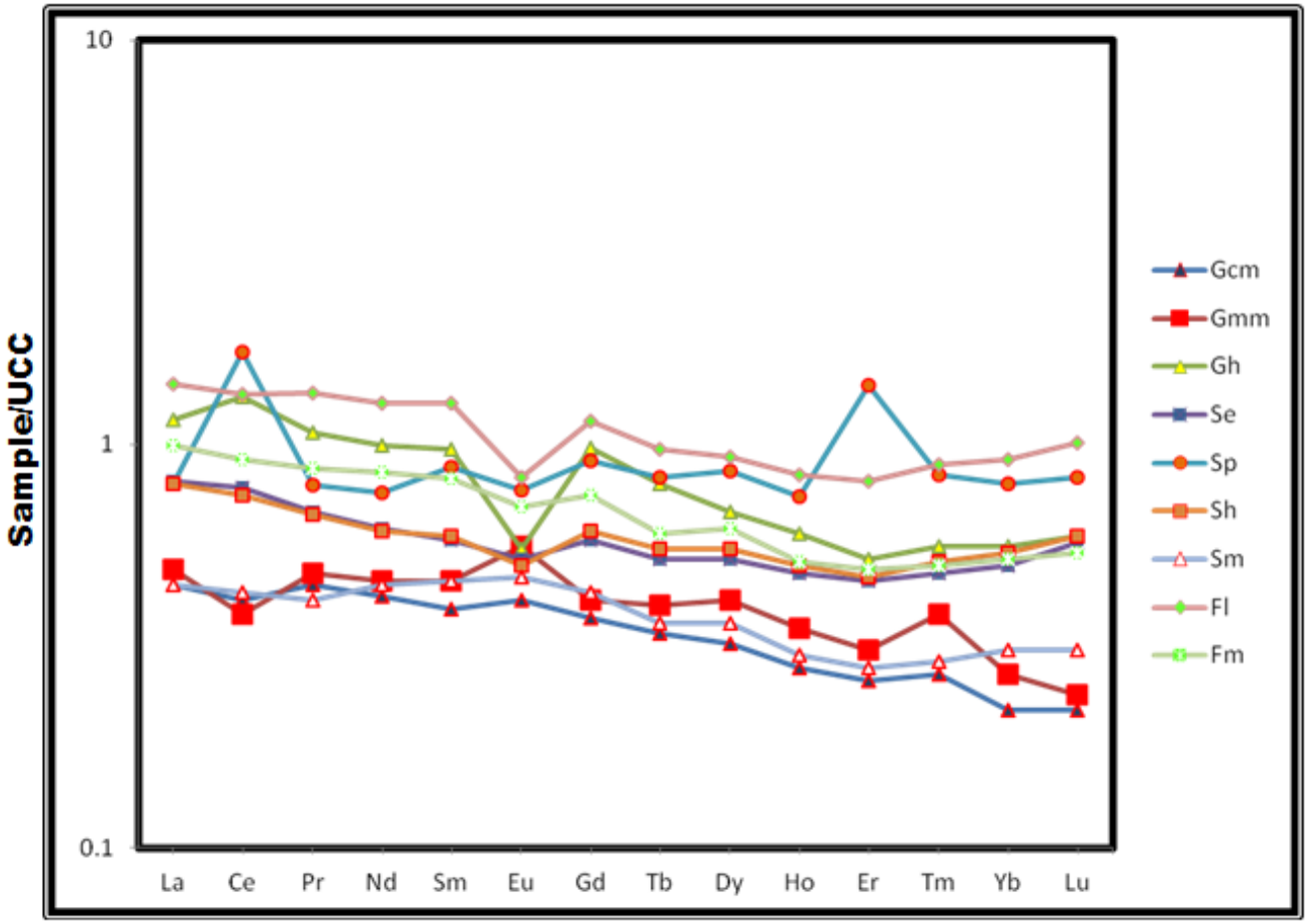


Figure 5.15a: Spider plot of rare earth element (REE) of investigated sandstone, normalized against average upper continent values (UCC) after McLennan (1989).

5.3.2.3.2.2 The North American Shale Composite (NASC) normalized plot

The North American Shale Composite (NASC) represents large volumes of very fine grained sediment that are thought to reflect the "average composition" of upper continental crust; it is almost identical to the Post-Archean Average Shale (PAAS) of Taylor and McLennan (1985).

The plot of the studied sediments normalized with North American Shale Composite (NASC) values (Figure 5.15b) like UCC normalized plot also show a relatively flattened HREE pattern and relatively steep depletion of LREE which also indicates a substantial contribution from felsic provenance. It is noted that there is similarity in the UCC plot (See figure 8.6a) with the NASC plot as the three classes; high Ce for Sp sub-facies, enrichment in Eu for Gcm, Gmm and Sm sub-facies and relatively high Er for Sp sub-facies were also noted. This similar characteristic confirms inheritance of the study sediments from the source rocks rich in felsic minerals.

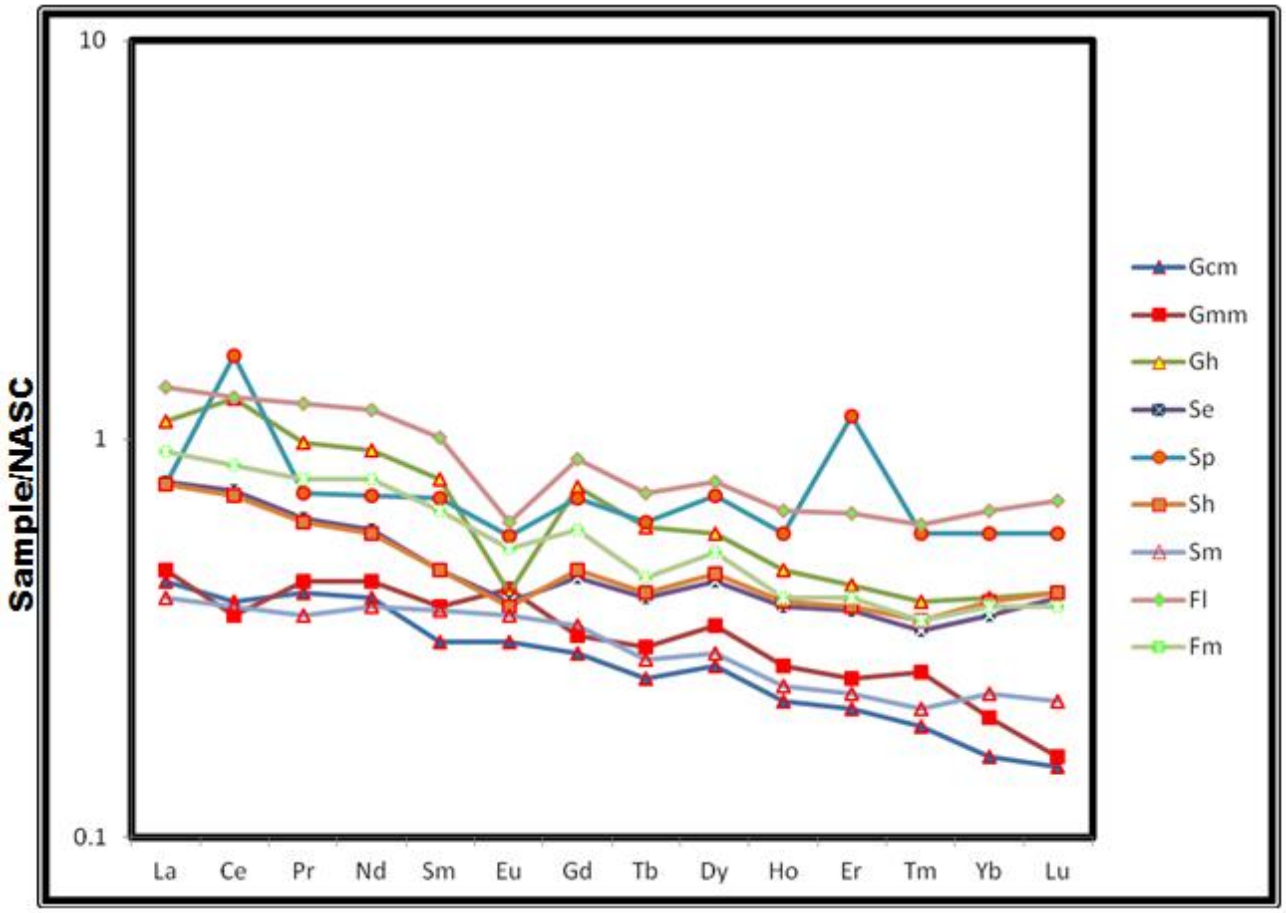


Figure 5.15b: Spider plot of rare earth element (REE) of investigated sandstone, normalized against average North American Shale Composite (NASC) after Gromet *et al*. (1985).

5.3.2.3.2.3 The Post-Archean Average Shale (PAAS) normalized plot

The Post-Archean Average Shale (PAAS) REE normalized plot after McLennan (2001) for this studied sandstone (Figure 5.15c) shows relatively flattened HREE pattern and steep depletion of LREE which also characterized sediments derived from cratonic interiors (McLennan *et al*., 1993).

The normalized NASC plot also revealed the same characteristics of the three groups as noted for the previous two plots (Figures 5.15a and 5.15b) but show highly steep pattern of LREE for Gcm, Fl and Fm sub-facies which might be an indication of mechanical fractionation of plagioclase out of the system during weathering and transport according to McLennan *et al*. (1993).

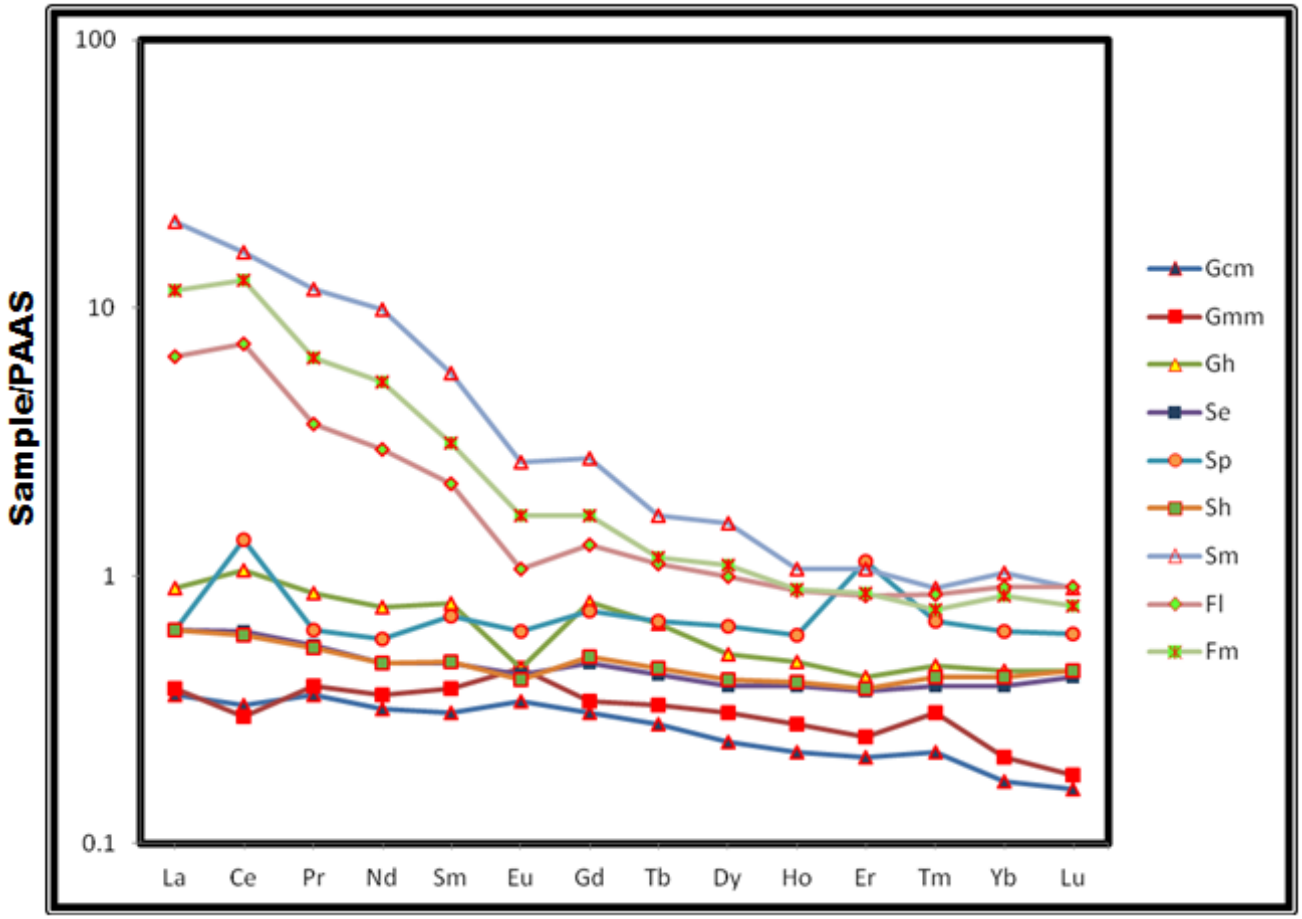


Figure 5.15c: Spider plot of rare earth element (REE) of investigated sandstone, normalized against average Post Archean Australian Shale (PAAS) values after McLennan (2001).

5.3.3 Heavy Mineral Evidence

Heavy mineral (HM) analysis is one of the most sensitive and widely used techniques in the determination of sandstone provenance (Morton and Hallsworth, 1994) because the composition of its fraction and its assemblages is chiefly controlled by the mineralogical composition of the source region (Morton, 1991; Amireh, 1991; Dewey and Mange, 1999). This approach was considered to infer probable provenance as these are good indicators according to Morton *et al*. (1992). HM occur in very small amounts in the sandstones and include opaques and non-opaques (Morton, 1991; Dewey and Mange, 1999).

Results of heavy mineral contents for this study are presented in appendix V, tables I-IX and show basic heavy mineral suites. The non-opaques occur mostly as reddish-brownish coloration and were suggested to be iron-oxide varieties (e.g. goethite, hematite and limonite), while non-opaque varieties is characterized by more zircon, tourmaline and rutile population but few garnet, biotite, sillimanite, and staurolite which are signatures that provide exceptionally useful clue to the nature of source rocks.

The studied sediments are composed of zircon, tourmaline, rutile, staurolite and garnet are predominantly angular to sub-angular, indicating derivation from primary source of igneous granitic and metamorphic origin Adepoju *et al*. (2018a). According to Milner (1962), detrital zircons normally originate from acidic and intermediate igneous rocks whereas garnet and tourmaline are well known metamorphic rock accessory minerals and present in few less amount. Also, the varieties of the observed zircon; euhedral to sub-hedral, prismatic with dark boundaries, xenocrystic cores, corroded, zoning (concentric type) and those with inclusions (sillimanite) while few are fractured. The angular, euhedral zircon and greenish to bluish tourmaline characterize acid to intermediate granitic source rocks according to Krynine (1946).

Tourmaline grain varieties are mostly irregular, darkish to deep blue, golden to yellowish (dominant) while rutile mineral grain occurs as irregular, knee-shaped having brownish to deep red and orange coloration. The blue-green variety of tourmaline indicates granite source but rounded nature of the grains suggests derivation from reworked sediments while rutile might have been derived from acid metamorphic rocks or even reworked sedimentary rocks.

The knee-shaped rutile might have been derived from acid metamorphic rocks. These varying types of zircon, tourmaline is concluded to have derived from a mixed composition of provenance comprising granitic igneous rocks and low metamorphic grade rocks through "first cycle", non-sedimentary source. Staurolite also presents in the studied sediments. It is characterized with straw yellow colouration, angular to sub-angular and sub-conchoidal fracture grains. Garnet is characterized by its sub-rounded and conchoidal shape with etches features (Figure 5.16a and b).

According to Milner (1962), detrital zircons normally originate from acidic and intermediate igneous rocks whereas garnet and tourmaline are well known metamorphic rock accessory minerals and present in few less amount. The angular, euhedral zircon and greenish to bluish tourmaline characterize acid to intermediate granitic source rocks according to Krynine (1946). The knee-shaped rutile might have been derived from acid metamorphic rocks.

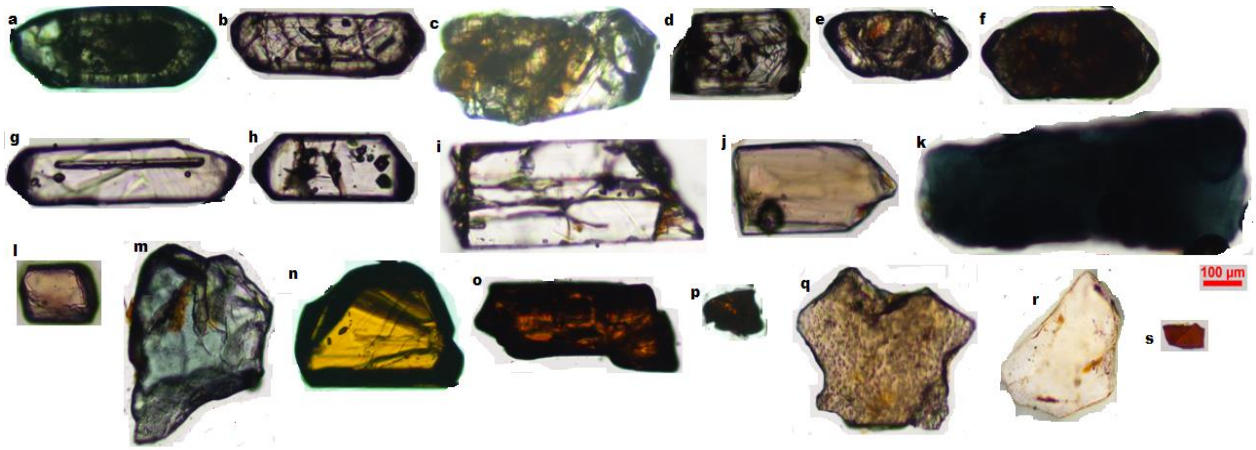


Figure 5.16a: Different heavy minerals types observed (under crossed nicol) in the northern part of the study area; (a-i) Zircon (xenocrystic core, zoning, corroded, sillimanite inclusion and dark boundary), (j-l) Tourmaline (light brownish to bluish), (m-o) Rutile (bluish, golden, deep red colured, conchoidal and knee-shaped), (p and s) Biotite (brownish), (q) garnet, and (r) Staurolite.

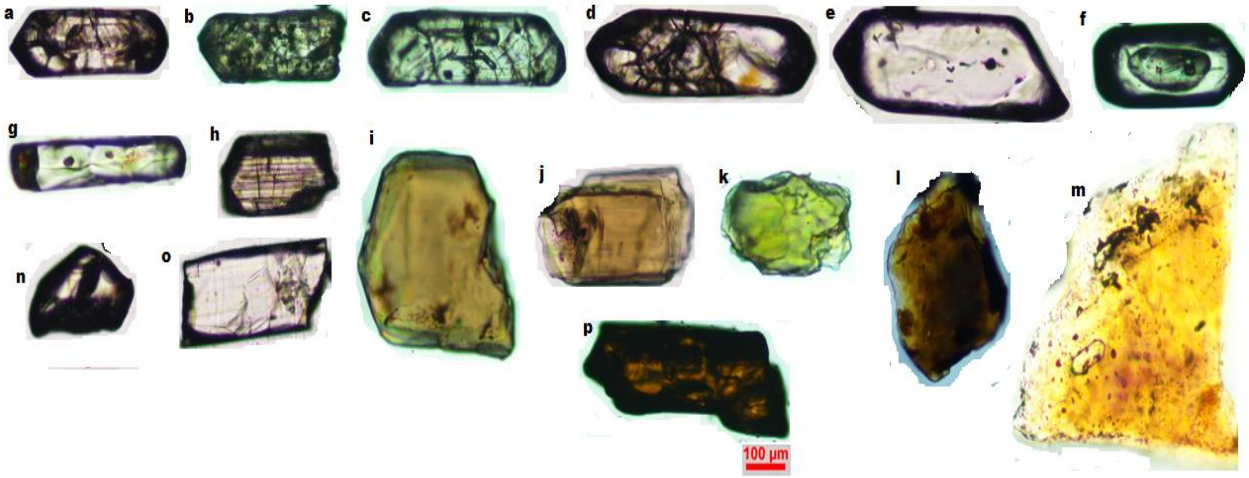


Figure 5.16b: Different heavy minerals types observed (under crossed nicol) in the central part of the study area; (a-h) Zircon (zoning, weathered and corroded, xenocrystic core, inclusion and dark boundary), (j-l) Tourmaline (greenish, light brownish and yellowish), (m) Staurolite (yellowish), (n-p) Rutile (dark brownish and deep brownish knee-shaped).

5.3.4 Mineralogical Composition Evidence

Mineralogical composition study is considered one of the most important tools for provenance analysis and it also provides information regarding the burial history of the sedimentary formation (Hardy and Tucker, 1988). This study has been applied by several past workers as an aid to study the environment of formation of clay (Lonnie, 1982; Hardy and Tucker, 1988).

The result of analyzed samples from the southwestern part of the study area including Lafiagi (LAF-1E and LAF-1L), Patti-Chin (PAT-1B and PAT-1J), Dokko (DOK-1D, DOK-1K and DOK-1X), Lemu (LEM-1E and LEM-1T), Ndeji (NDJ-1C and NDJ-1H), Patigi (PTG-1C), Zambufu (ZMB-1A and ZMB-1C) and Gbugbu (GBU-1C) is presented in table 4.5a. These mineral distributions show major contents from felsic igneous rocks and minor contributions from metamorphic rocks.

In the central part of the study area, the result of the analyzed samples from Agbonna (AGB-1A, AGB-1B, AGB-1C, AGB-1E, AGB-1K and AGB-1S), Shonga (SHG-1B and SHG-1L), Enagi (ENG-1B, ENG-1L and ENG-1V), Kudu (KUD-1A, KUD-1C, KUD-1G) and Kutigi (KUT-1A, KUT-1G and KUT-1M) presented in table 4.5b also show mineralogical compositions that resemble contributions from basically felsic igneous rock with minor metamorphic in the source. Resuls of samples analyzed from the northern part of the study area including Rabba (RAB-1B and RAB-1P) and Tannagi (TAN-1A and TAN-1D) presented in table 4.5c also show same mineralogical signatures in the sources as those from the southwestern and central parts of the study area.

Higher kaolinite composition amongst the mineralogical conctituents is an evidence of sediments' possible derivation from the pre-existing igneous rocks as a product of feldspar

decomposition either by weathering or by hydrothermal activity in acidic environment where drainage system was good. Hallam *et al*. (1991) stated and concluded that kaolinite formation is usually favored under tropical to sub-tropical (low pH and warm temperature) climatic conditions and abundant in regions of intense weathering. Potter *et al*. (1980) with Galán and Ferrell (2013) also described the favourable condition for the precipitation of kaolinite as indicated by periods with an increase in the humidity and may be linked to a rainy season.

Generally, it is a common geological belief that a depositional basin surrounded by felsic rock types such as granite and gneisses should favor the deposition of kaolinite clays, therefore, the mineralogical compositions show that the sediments were sourced from the Basement Complex of Southwestern Nigeria, eroded and deposition in different parts of the present Basin.

5.4 Paleotectonic Settings

The mineralogical and geochemical compositions of clastic sedimentary rocks as a proxy have been employed in several related studies in the past (Condie *et al*., 2001) because they provide an insight to their provenance and tectonic settings. Therefore, compositional studies of clastic rocks, particularly of sandstone have been established as the principal sources of information in deciphering nature of the source terranes and plate tectonic evolution (Ingersoll and Suczek, 1979).

5.4.1 Petrographic Evidence

Petrographic data provides important information on the sediments'nature in the source area (Johnsson, 1993), and it's one of the means to analyze the character of the provenance of clastic rocks which in turn is controlled by tectonic setting. Many studies have pointed to intimate relationship between detrital sand composition and tectonic setting (Crook, 1974;

Ingersoll, 1978; Potter, 1978; Ingersoll and Suczek, 1979; Dickinson and Valloni, 1980; Bhatia, 1985; Dickinson, 1985, Bhatia and Crook, 1986; Cox and Lowe, 1995; Critelli, 1999).

5.4.1.1 Detrital Quartz

The detrital quartz is a chemically and physically durable and most abundant mineralogical constituent of framework and has been used as a useful guide to composition of provenance (Folk, 1980). Many types of quartz grains have been distinguished based on criteria such as the shape and number of sub-crystals present in the grain and their extinction behavior when the microscope stage is rotated under crossed polars; some of these quartz grains are associated with specific types of source rocks (Scholle, 1979; Blatt *et al*., 1980).

In this study, varieties of quartz have been well identified and will be employed and related to source rocks studies. The result of mineralogical composition presented in appendix IV, tables I-IX shows that monocrystalline quartz with non-undulose and straight extinction is the predominant compare to the polycrystalline varieties in all the sandstone sub-facies. Scholle (1979) concluded that monocrystalline grains with straight extinction are common in quartz of igneous origin while polycrystalline quartz with crystal boundaries is characteristic of quartz from a metamorphic source. Conclusions from Basu *et al*. (1975) and Blatt et al. (1980) also confirmed that predominance of non-undulose monocrystalline quartz indicates a granitic provenance which is consistent with the provenance definition of Basu (1976), therefore this imply that the studied sediments were sourced from the granitic crystalline basement provenance.

Crook (1974) proposed the use of quartz content to infer tectonic setting, and linked quartz rich (>65% quartz) sandstones to passive continental margins (Atlantic type); intermediate

quartz (15–65% quartz) sandstones to active continental margins (Andean type), and quartz poor (<15% quartz) sandstones to magmatic island arcs. Evidence of quartz rich (>65% quartz) in the studied samples thus correspond to passive continental margins sandstones.

5.4.1.2 Feldspar

Feldspar is the next in abundance among mineralogical compositions of the detrital frameworks in the sub-facies. These feldspar clasts were partly altered where present or even absence (in some cases). However, where present, potassic varieties (K-feldspar) occur as the dominant over the plagioclase types. Presence or absence of feldspars in clastic sedimentary rocks depends on the process of erosion and decomposition operating, therefore, detrital feldspar is an index of both climatic vigor and tectonism.

In this study, dominant of detrital K-feldspar grains in the sub-facies suggest mainly derivation from granitic provenance according to Basu (1976) and Datta (2005). Basu (1976) submitted that feldspars have a lesser chance of survival in humid climate due to their instability, so may be selectively modified or removed from the detritus during weathering, transportation and diagenesis, resulting in decrease of their effectiveness as provenance indicator (Pettijohn *et al*., 1972; Datta, 2005). The result of this study also indicates intensive weathering in source area and/or greater abrasion of sediments during transport.

5.4.1.3 Rock Fragments

The rock fragment in sandstone framework is among the most informative of all detrital components in diagnosing and determining the provenance composition (Pettijohn *et al*., 1972). The low percentages of lithic fragments and matrix compared to the rest framework composition in the studied sediments signify features of compositionally mature sandstones.

5.4.1.4 Petrographic Plots

Sediment composition is obviously controlled by the source rocks from which the sediment is derived, as such, the composition of sediment correlates well with the source rocks under many conditions (Pettijohn *et al*., 1972). Since tectonic setting in turn controls source rock composition, the conjunction of plate tectonics and sandstones composition has shown that sandstones from a variety of tectonic settings exhibit considerable diversity that is related to tectonic association (Dickinson *et al*., 1979, 1980, 1983, 1985, 1988; Ingersoll *et al*., 1979, 1984; Yerino and Maynard, 1984; Valloni and Maynard, 1981). Accordingly, it is possible to reconstruct the paleo-tectonic settings of source areas by analyzing the detrital modes of siliciclastic strata in diverse depositional basins (Ingersoll *et al*., 1995).

Detrital mode-based ternary diagrams proposed by Graham *et al*. (1976), Ingersoll (1978), Dickinson and Suckzek (1979), Dickinson *et al*. (1983) and Dickinson (1985) are widely used to discriminate various tectonic settings and to interpret plate interactions in the geologic past. Thus, sandstone petrofacies analysis can furnish vital clues regarding the provenance and its tectonic setup and source rock composition. The ternary plots after Dickinson and Suczek (1979) and Dickinson *et al*. (1983) use the modal framework compositions were employed in this study for tectonic settings discrimination of the Bida Basin.

Dickinson (1985) had stated that the continental blocks include stable cratons and basement uplifts, which are tectonically consolidated regions of amalgamated ancient orogenic belts that have been eroded to deep levels while the magmatic arcs include the volcanic chain, granite plutons and metamorphosed sediments in arc-trench systems and the recycled orogens containing uplifted and deformed sedimentary and volcanic rocks, which are exposed to

erosion by orogenic uplift of fold-and-thrust belts, and mostly consist of sediments, but include volcanic rocks and metasediments.

Applications of the ternary plots; Qt-F-Lt plot (Figure 5.17a) after Dickinson and Suczek (1979), Qm-F-Lt plot (Figures 5.17b and 5.17c) after Dickinson (1985) and Qt-F-L plot (Figure 5.17d) after Dickinson *et al*. (1983) using the framework composition data in appendix IV, tables Ia-VIIIa and Ib to VIIIb shows that all the studied sediments in all the sandstone sub-facies plotted within the craton interior and minor recycled orogeny provenance representing material from a continental block provenance (Adepoju *et al*., 2018a). This may indicate possible mixing of sediment from an eroded, mature continental island arc, passive margin and from quartzose recycled sources (Adepoju *et al*., 2018a). Therefore, the source rocks may be of two types: a continental source (responsible for the quartz fragments and the high resistant lithic grains) and a plutonic-arc source (responsible for the amounts of quartz, feldspar and plutonic accessory-mineral fragments). The near absence or negligible proportion of polycrystalline quartz grains and metamorphic lithic fragments in figure 5.17d suggests that the source region may have been uplifted in an extensional or transform setting according to Dickinson (1985).

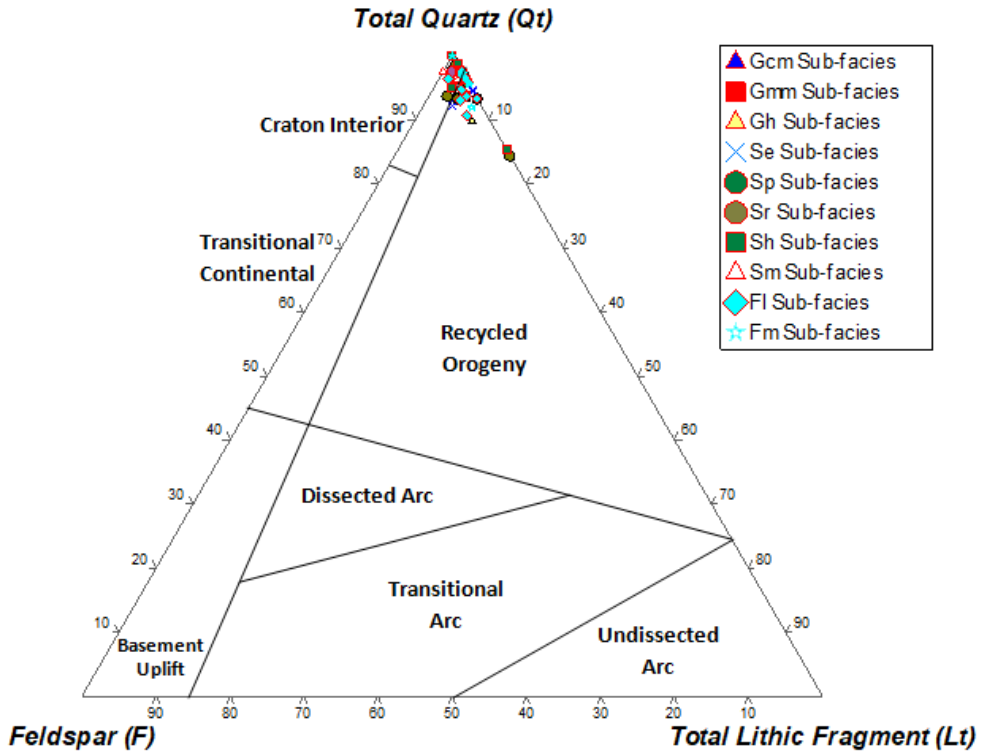


Figure 5.17a: Standard Qt-F-Lt Provenance Ternary plot after Dickinson (1985) showing Craton Interior and Recycled Orogeny fields for the investigated sandstone.

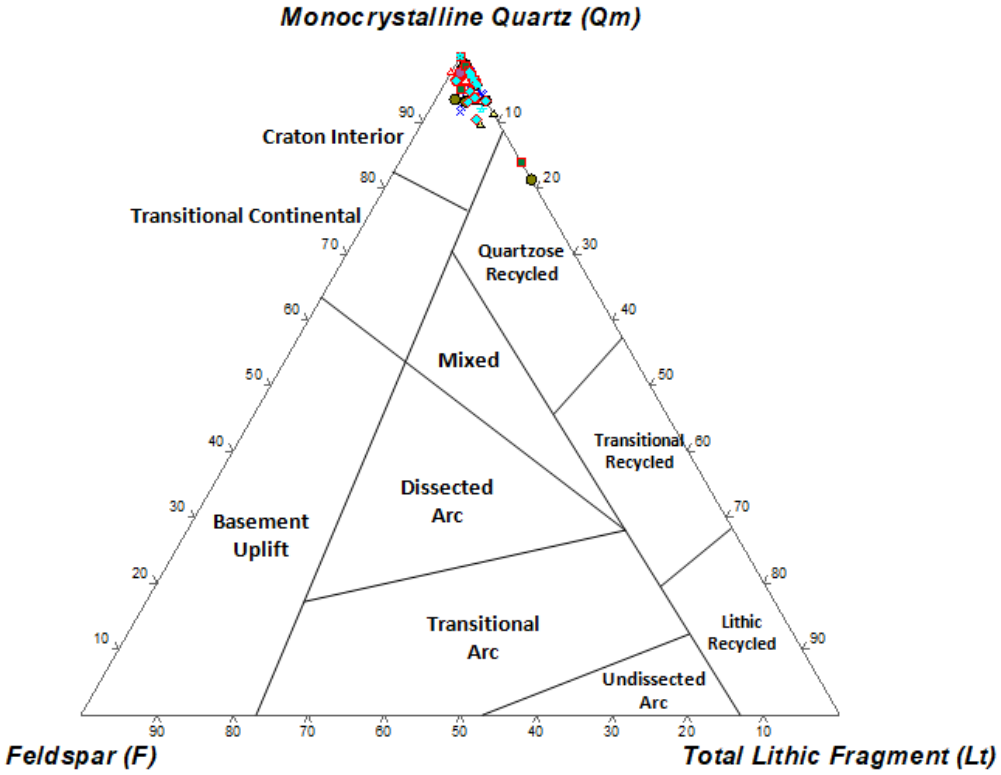


Figure 5.17b: Standard Qm-F-Lt Provenance Ternary plot after Dickinson *et al.* (1983) showing Craton Interior and Recycled Orogeny field for the investigated sandstone.

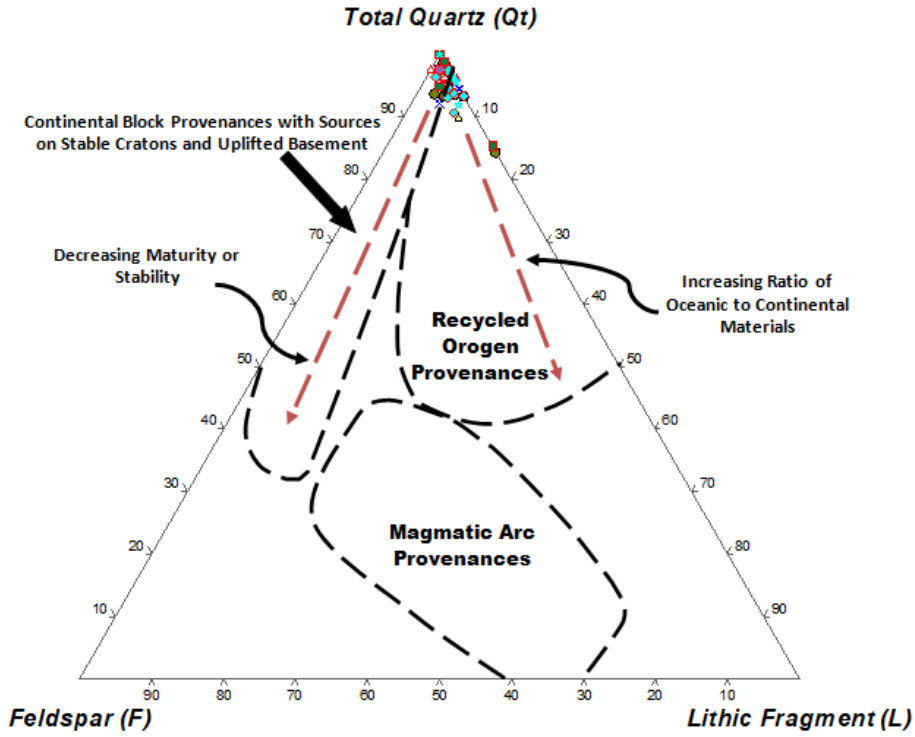


Figure 5.17c: Standard Qm-F-Lt Provenance Ternary plot after Dickinson *et al.* (1982) showing Continental Block Provenances filed for the investigated sandstone.

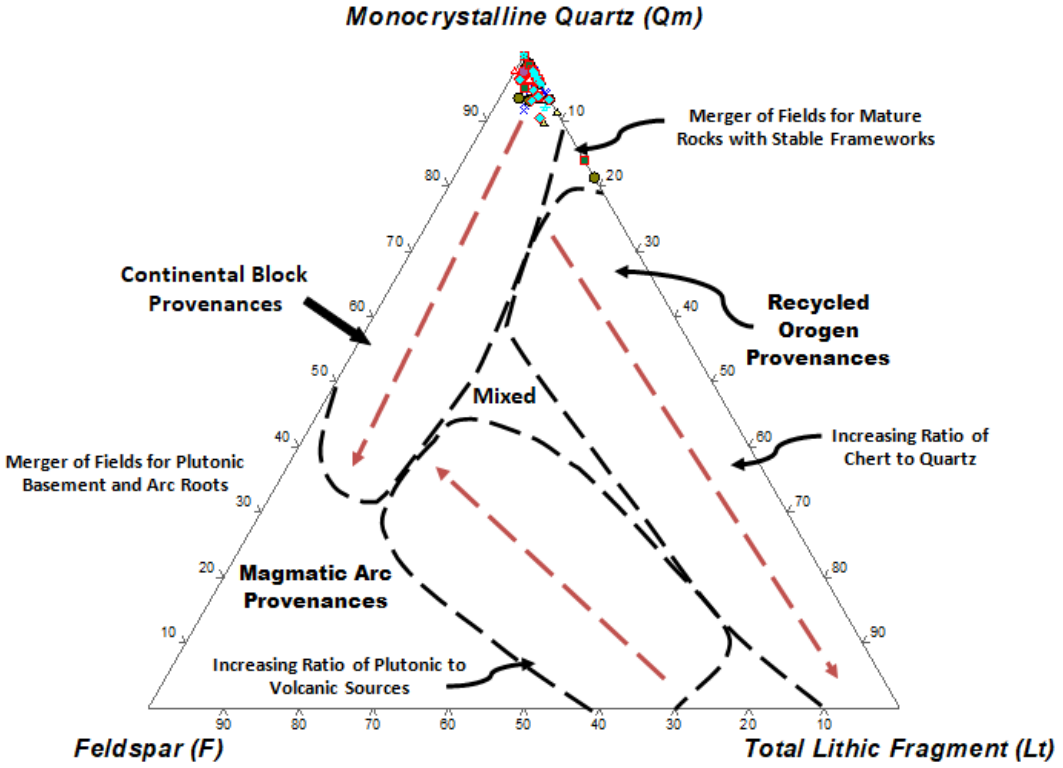


Figure 5.17d: Standard Qt-F-L Provenance Ternary plot after Dickinson *et al.* (1982) showing Continental Block Provenances filed for the investigated sandstone.

5.4.2 Geochemical Evidence

Geochemical approaches to provenance and paleotectonic settings study are important, not only to support but also to identify features not readily recognized by petrography. The main purpose is to compare and correlate the existing geochemical discrimination techniques of known clastic sedimentary rocks provenance and paleotectonic settings with the unknown hence provide a basis for using geochemical elements as provenance discriminators.

Several past studies including Bhatia and Crook (1986), Roser and Korsch (1986, 1988) have shown that chemical compositions of siliciclastic sedimentary rocks are significantly controlled by tectonic settings of their provenances and depositional basins, and as a result, the rocks from different tectonic settings possess terrain-specific geochemical signatures. For example, several geochemical discrimination diagrams have been proposed by several workers to infer paleotectonic settings of ancient siliciclastic sedimentary rocks. Few amongst the rest including Maynard *et al*. (1982), Bhatia (1983), Bhatia and Crook (1986), Roser and Korsch (1986, 1988), McLennan *et al*. (1990), McLennan and Taylor (1991), Floyd *et al*. (1991, Girty *et al*. (1993), Kroonenberg (1994) and Murphy (2000) focused their discussion to reflect provenance, transport, weathering, and depositional settings because geochemical characteristics give insights to the tectonic conditions.

The tectonics discrimination diagrams proposed by Bhatia (1983), Bhatia and Crook (1986), and Roser and Korsch (1986) and widely used in sedimentary geochemical studies to identify the tectonic settings of unknown basins is also employed in this resaerch. Verma and Armstrong-Altrin (2016) had also employed and recommended them for consideration as an important and useful tool for discriminating the tectonic settings of older sedimentary basins.

5.4.2.1 Major Elements

The major elements compositions of sedimentary rocks have been used to decipher the ancient tectonic settings of the sediments' depositional environment (Maynard *et al*., 1982). Several authors including Blatt *et al*. (1980), Bhatia (1983), Bhatia and Crook (1986), Roser and Korsch (1986, 1988) have related sandstone geochemistry to specific tectonic environment using the major elements and ratios to distinguish the tectonic settings. Also, Armstrong-Altrin *et al*. (2004), Bhatia (1983), Roser and Korsch (1986) have independently employed the major element geochemistry of the sandstones for drawing inferences related to the provenance type and the paleo-tectonic settings of ancient sedimentary basins.

Major oxides especially those with relative abundance of immobile oxides (SiO_2 and TiO_2) and depletion of the mobile phases (Al_2O_3, K_2O, CaO and Na_2O) and their ratios; Al_2O_3/SiO_2, K_2O/Na_2O, and $Al_2O_3/(CaO+Na_2O)$ are very useful geochemical tools for paleotectonic settings deduction of clastic sedimentary rocks according to Crook (1974), Bhatia (1983), Roser and Korsch (1986) and McLennan *et al*. (1990). The authors demonstrated that SiO_2 contents and K_2O/Na_2O ratios of sandstone appear to be particularly sensitive indicators of geotectonic setting, so, they suggested that the quartz-poor greywackes (quartz<15%, mean SiO_2-58%, K_2O/Na_2O<1 are indicative of magmatic island arcs which is an approximate average composition of the tholeiitic andesite, the quartz intermediate greywackes (quartz=15-65%, mean SiO_2-68-74%, K_2O/Na_2O <1) are indicative of Andean-type continental margins and have approximately the same composition as the upper level of continental crust while quartz-rich greywackes (quartz>65%, mean SiO_2=89%, K_2O/Na_2O >1) are characteristic of Atlantic-type continental margins and are similar in composition to the sand fraction of the continental platform cover. The parameters obtained from this study

(Tables 4.6a-4.6i; Appendix VI, Tables Ia-Id) fall in the quartz-rich greywackes (Atlantic-type continental margins) class.

Also, the discrimination diagram of log(K_2O/Na_2O) versus SiO2 after Roser and Korsch (1986) defined three main tectonic provenance on the basis of chemical composition of sandstones as follows; passive continental margin (PM) that composed of mineralogically mature (quartz-rich) sediments deposited in plate interiors at stable continental margins or intracratonic basins (mainly sourced from recycled sedimentary and metamorphic source rocks), active continental margin (ACM) with sediments composed of intermediate quartz content derived from tectonically active continental margins and deposited on or adjacent to active plate boundaries (e.g. trench, forearc and backarc settings) (mainly sourced from granites, gneisses, siliceous volcanic) and oceanic island arc (OIA) composed of quartz poor volcanogenic sediments derived from oceanic island arcs and deposited in a variety of settings including forearc, intra-arc and backarc basins etc (mainly sourced from calcalkaline or tholeiitic rocks). The plots presented in this study shows quartz-rich sediments (mineralogically mature), therefore, supports passive continental margin (PM) in the study area.

Dickinson and Suzek (1979), and Bhatia (1983) suggested a progressive decrease in Fe_2O_3+MgO, TiO_2, Al_2O_3/SiO_2 and an increase in K_2O/Na_2O and $Al_2O_3/(CaO+Na_2O)$ trends in major elemental geochemical compositions of clastic suites that implies maturity in different tectonic settings; oceanic island arc, continental island arc, active continental margins and passive margins. They concluded that sandstones of sedimentary basins adjacent to oceanic island arcs are characterized by high abundances of Fe_2O_3+MgO (8-14%) with TiO_2 (0.8-1.4%) and high mean ratios of Al_2O_3/SiO_2 (0.24-0.33) with lower K_2O/Na_2O (0.2-0.4) ratio. Also, sandstones of basins adjacent to continental island arcs from oceanic island-

arc types have lower Fe_2O_3+MgO (5-8%), TiO_2 (0.5-0.75) with Al_2O_3/SiO_2 (0.15-0.22) and higher K_2O/Na_2O (0.4-0.8) ratios while sandstones from active continental margins basins have very low Fe_2O_3+MgO (2-5%) and TiO_2 (0.25-0.45%) with K_2O/Na_2O ratio of approximately 1. The above geochemical standards favorably compare with the data in this study (Tables 4.6a-4.6i and Appendix VI, Tables Ia-Id), so, fit more into passive margin fields as it is generally enriched in SiO_2 and depleted in Al_2O_3, TiO_2, Na_2O, CaO with K_2O/Na_2O ratio greater than 1.

Several classifications attempt to discriminate various origins and tectonic settings (Maynard *et al*., 1982; Bhatia, 1983; Bhatia and Crook, 1986; Roser and Korsch, 1986, 1988). The tectonic setting geochemical Discriminant plots in sandstone suites includes; bivariate plots based on; the log(K_2O/Na_2O) versus SiO_2 after Roser and Korsch (1986) and Murphy (2000), the TiO_2 versus (Fe_2O_3+MgO), Al_2O_3/SiO_2 versus (Fe_2O_3+MgO) and the ternary plot of $SiO_2/20$-(K_2O+Na_2O)-($TiO_2+Fe_2O_3$+MgO) after Kroonenberg (1994) are very useful in separating data into broad tectonic discrimination groups; passive margin (PM), oceanic island arc (OIA), continental island arc (CIA), active continental margin (ACM) and passive margin (PM) because they are sensitive indicators of paleotectonic settings of the sediments' provenance.

In this study, the same pattern of paleotectonic field were observed in all bivariate and ternary discrimination plots; log(K_2O/Na_2O) versus SiO_2 after Roser and Korsch (1986) and Murphy (2000) (Figures 5.18a and 5.18b), TiO_2 versus (Fe_2O_3+MgO) after Bhatia (1983) (Figure 5.18c), Al_2O_3/SiO_2 versus (Fe_2O_3+MgO) after Bhatia (1983) (Figure 5.18d), SiO_2/Al_2O_3 versus K_2O/Na_2O (Figure 5.18e) after Roser and Korsch (1988) and $SiO_2/20$-(K_2O+Na_2O)-($TiO_2+Fe_2O_3$+MgO) after Kroonenberg (1994) (Figure 5.18f) as all the investigated samples fall within and near passive margin field.

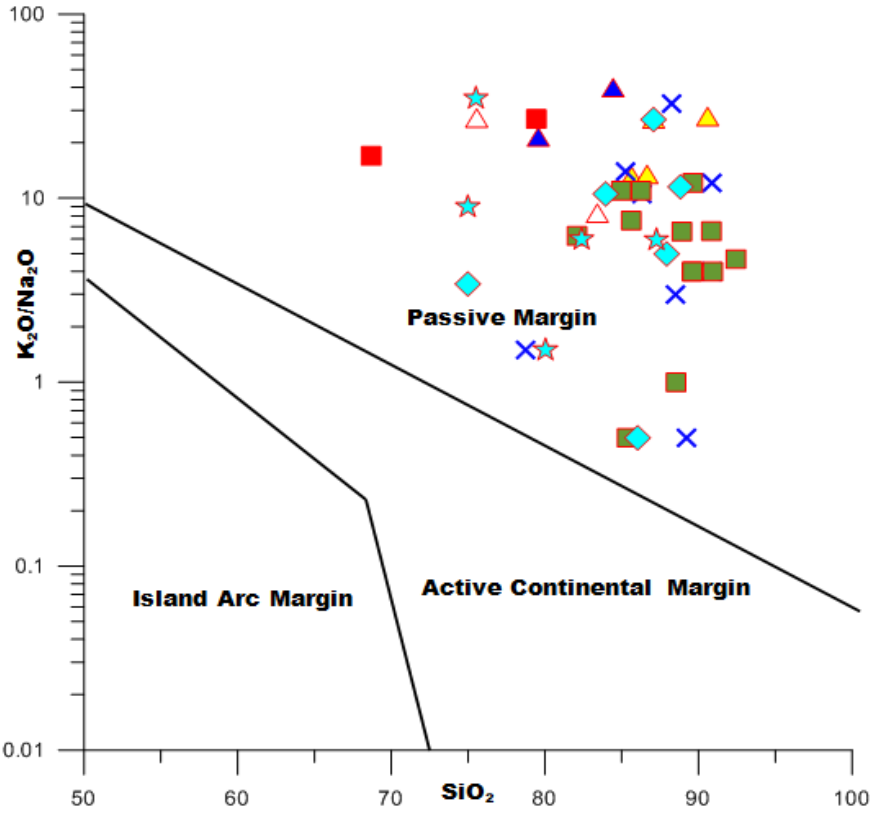


Figure 5.18a: Bivariate log(K_2O/Na_2O) versus SiO_2 paleotectonic discrimination plot after Roser and Korsch (1986) showing Passive Margin for the investigated sandstone.

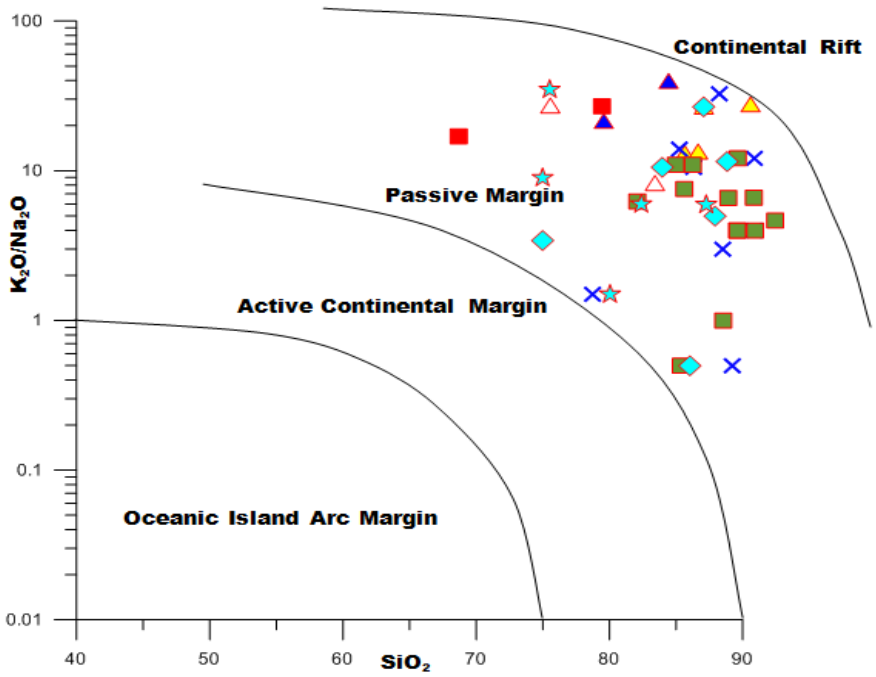


Figure 5.18b: Bivariate log(K_2O/Na_2O) versus SiO_2 paleotectonic discrimination plot after Murphy (2000) for the investigated sandstone.

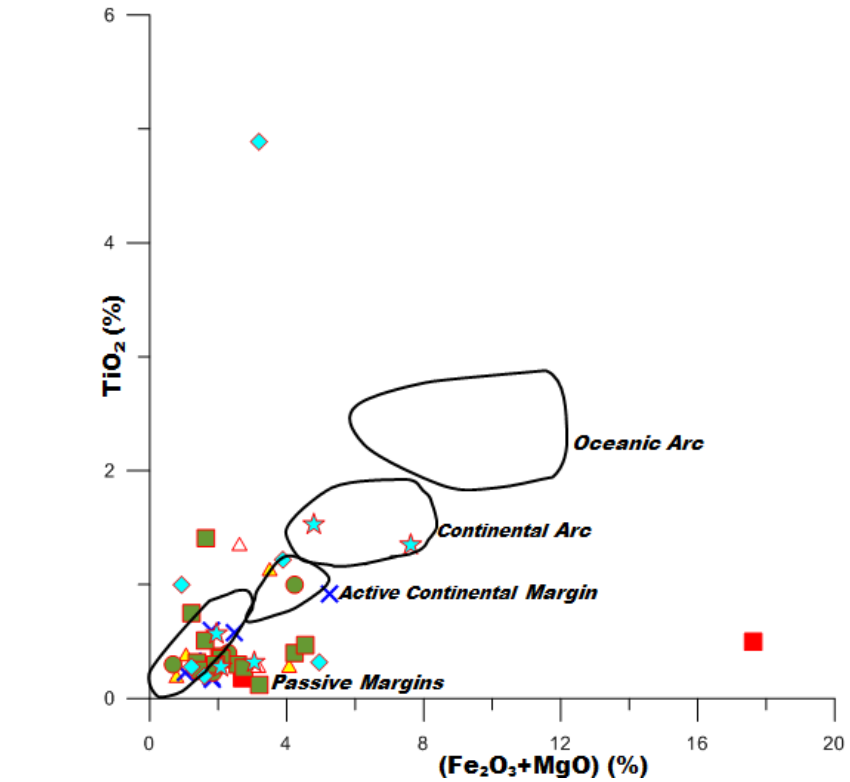


Figure 5.18c: Bivariate TiO_2 versus (Fe_2O_3+MgO) paleotectonic discrimination plot after Bhatia (1983) showing paleotectonic settings for the investigated sandstone.

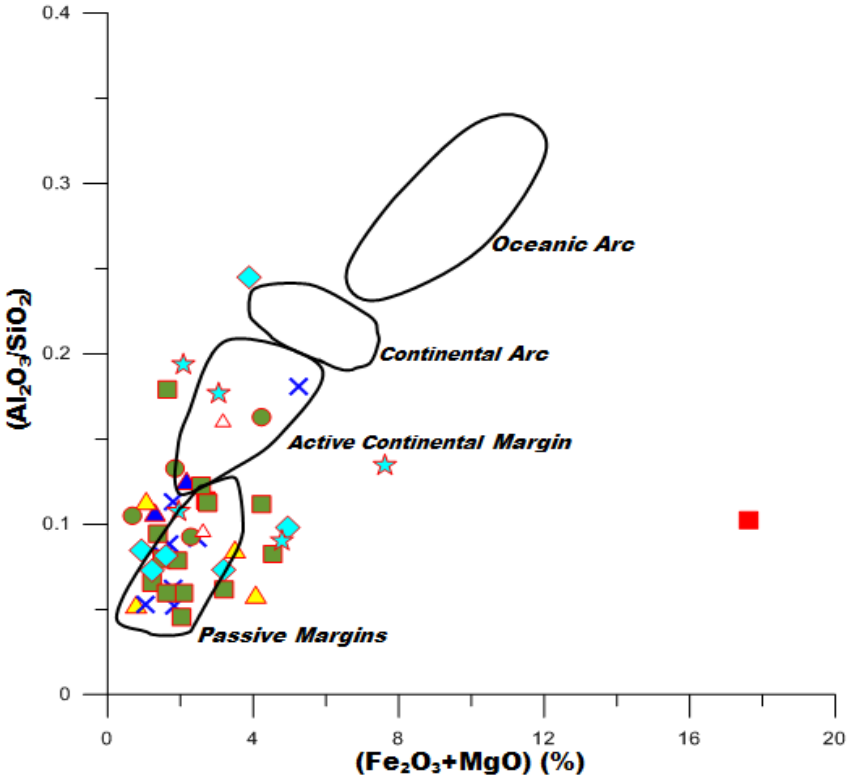


Figure 5.18d: Bivariate (Al_2O_3/SiO_2) versus (Fe_2O_3+MgO) paleotectonic discrimination plot after Bhatia (1983) showing Passive paleotectonic settings for the investigated sandstone.

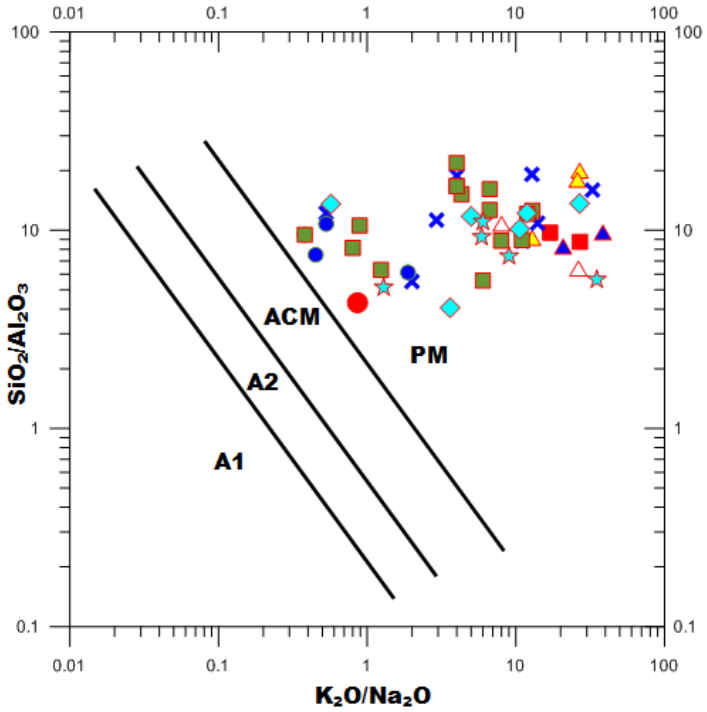


Figure 5.18e: Bivariate SiO_2/Al_2O_3 versus K_2O/Na_2O paleotectonic discrimination plot after Roser and Korsch (1988) showing Passive Margin paleotectonic settings for the investigated sandstone. NB: A1 – Arc setting, basaltic and andesitic detritus; A2 – Evolved arc setting, Felsic-Plutonic detritus; ACM - Active Continental Margin; PM - Passive Margin.

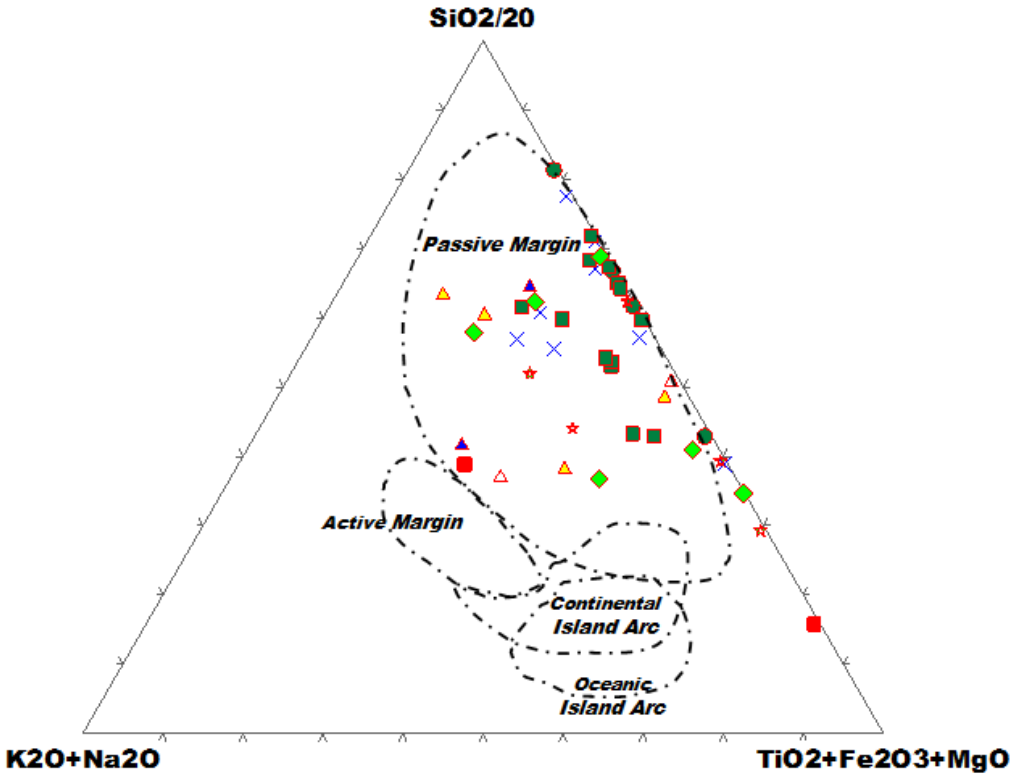


Figure 5.18f: The standard paleotectonic discrimination ternary plot of $SiO_2/20$-(K_2O+Na_2O)-(TiO_2+Fe_2O_3+MgO) after Kroonenberg (1994) showing passive margin field for the investigated sandstone.

5.4.2.2 Trace Elements

Trace elements (e.g., Ti, Co, La, Th, Sc, and Zr) in the clastic sedimentary rocks are considered to be immobile under conditions of weathering, diagenesis, and moderate levels of metamorphism, and are commonly preserved in sedimentary rocks; therefore, represent well-established provenance and tectonic setting indicators (Bhatia and Crook, 1986; Roser and Korsch, 1986; McLennan and Taylor, 1991; Spalletti *et al*., 2008). According to Bhatia and Crook (1986), trace elements are more useful for discriminating tectonic settings of siliclastics as compared to major elements because of concentration in accessory phases that may be subjected to hydraulic concentration. The abundance and plots of chromium (Cr), nickel (Ni), rubidium (Rb), Niobium (Nb), Thallium (Ta), vanadium (V), scandium (Sc), lanthanum (La), barium (Ba) in siliclastic sediments could be useful in separating the provenance because each field (passive margin, continental recycled, dissected arc and undissected arcs) are well separated and plotted in definable groups.

The application of the discriminant bivariate plots; La/Y versus Sc/Cr after Bhatia and Crook (1986), the ternary plots of Lanthanum-Thorium-Scandium (La-Th-Sc) after McLennan *et al*. (1993) and Thorium-Scandium-Zirconium/10 (Th-Sc-Zr/10) after Bhatia and Crook (1986) confirm that all the studied samples were plotted and clusters within the passive continental margin field (Figures 5.19a and 5.19b). The clear explanation of the passive margin tectonic settings is such that it comprises rifted continental margins; sedimentary basins on trailing continental margins supplied from collision orogeny and inactive or extinct convergent plate margins.

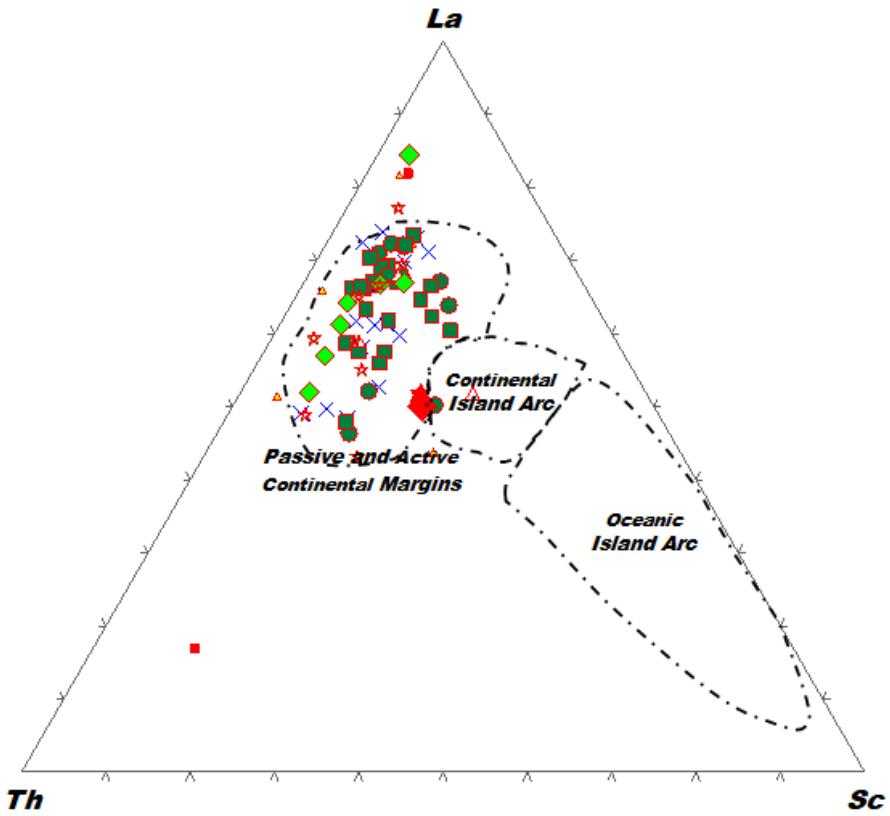


Figure 5.19a: The standard La-Th-Sc Ternary Tectonic discrimination diagram after Bhatia and Crook (1986) showing Passive Continental Margin fields for the investigated sandstones.

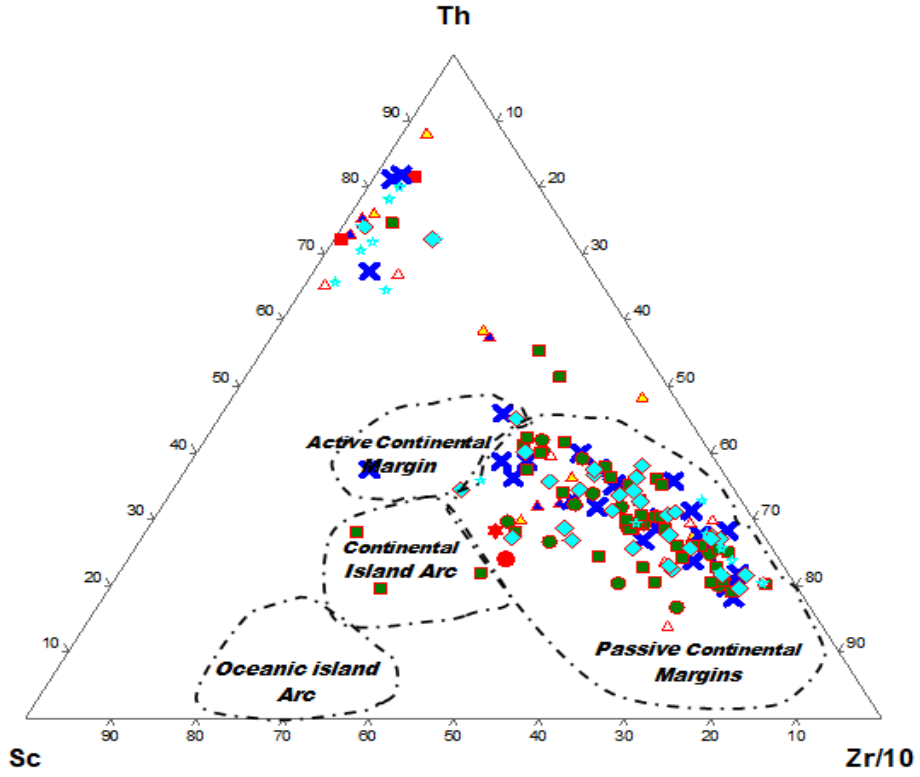


Figure 5.19b: The standard Th-Sc-Zr/10 Ternary Tectonic discrimination diagram after Bhatia and Crook (1986) showing Passive Continental Margin fields for the investigated sandstones.

5.4.2.3 Rare Earth Elements

The Rare Earth Element (REE) geochemical distribution in sandstones and mudstones provides evidence of tectonic province as indicated in the McLennan *et al*. (1990) and McLennan and Taylor (1991). Also, the previous work of Bhatia (1985), Bhatia and Crook (1986) has showed than an increase in REE abundance, a high low light rare earth element (LREE) to high rare earth element (HREE) ratio and a decrease in the Eu anomaly as the sandstones became more mature. They suggested that the sediments deposited in the continental margin are enriched in ΣREE and LREE with negative Europium anomaly (Eu/Eu*), whereas sediments deposited in an oceanic arcs are depleted in ΣREE and LREE and lack negative Eu/Eu*. Meanwhile, passive margin provenance is typically characterized with uniform REE pattern similar to PAAS, whereas sediments from active continental margin display intermediate ΣREE abundances with variable negative Eu/Eu* in the range of 0.6-1.0 according to Bhatia (1985) and McLennan (1989). In this study, the mean Eu/Eu* values of all the sub-facies (Tables 4.8a-4.8f) suggest the sediments are deposited within the passive margin setting.

The Ba/La versus Eu/Eu* is a plot that shows the relationships between the Ba/La ratio and Eu anomaly derived from the normalization of Chondrite values with the study sediments. Bhatia (1985) suggested that Arc rocks should typically have ratios of Ba/La and Eu/Eu* that are greater than 1 while passive margin sediments usually have Ba/La ratios less than 1 and Eu/Eu* less than or equal to one (1.0). The plot of Ba/La versus Eu/Eu* presented in figure 8.20 identified sediments source from passive margin sediments group. The plot also showed a distinct negative Eu anomaly and low Ba/La ratios.

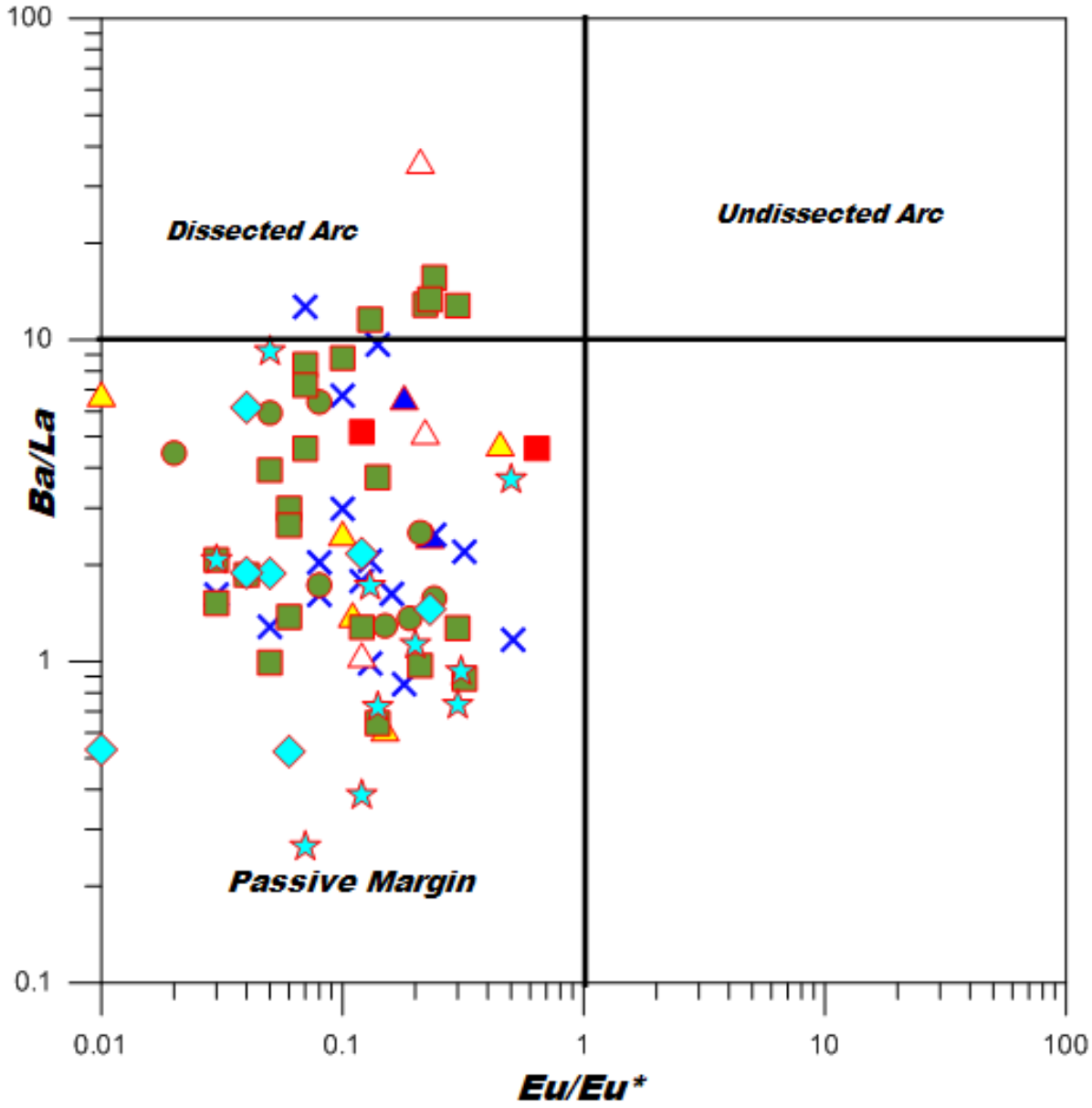


Figure 5.20: Bivariate discrimination plot of Ba/La versus Eu/Eu* after Bhatia (1985) showing passive margin field for the investigated sandstones.

5.4.3 Heavy Mineral Evidence

The parent rocks provide the initial control on the development of heavy-mineral suites in sandstones, and the aim of provenance studies is to isolate this factor by stripping off the other influences that modify the suite during the sedimentation and post-sedimentation processes Morton *et al*. (1992). Heavy minerals have long been used as a guide to the source rock compositions (Pettijohn, 1975) because heavy mineral suit of the sediments contains in particular tourmaline, zircon, rutile and opaques. This approach of heavy mineral analysis was considered to infer probable provenance as they are good indicators according to Morton and Hallsworth (1994), Morton *et al*. (2004).

The opaque heavy minerals are dominant in the coarser sub-facies while the transparent heavy minerals are quite appreciable in the finer sub-facies. The coarser sub-facies are incorporated with fresh and unweathered heavy mineral grains; zircon, tourmaline, staurolite and garnet grains that are predominantly angular in shape suggesting lower mobility and also indicating sediment derivation from primary sources. In contrast, heavy minerals present in fine sub-facies are predominantly rounded to sub-rounded forms, thus, suggest reworking of sediments from an older sedimentary provenance or a granitic provenance according to Morton and Hurst (1995).

The varieties of zircon observed within coarser sub-facies includes; angular, euhedral to subhedral, prismatic with dark boundaries, xenocrystic cores, corroded, zoning (concentric type) and those with inclusions (sillimanite) while few are fractured meanwhile euhedral to subhedral, greenish to bluish tourmaline suggests low abrasion. Meanwhile, within fine sub-facies, the sub-rounded to well-rounded, corroded zircon (due to weathering) with irregular, golden to straw yellowish tourmaline may suggests greater abrasion and (or) long transportation.

The geological significance of primary and secondary growths in zircons has been worked upon by Jocelyn and Pidgeon (1974) and Precambrian origin was assigned for the rocks due to the growths. The tourmaline varieties; mostly irregular, greenish to bluish and golden to straw yellow (dominant) characterize acid to intermediate granitic source rocks according to Krynine (1946). This evidence is supported with lesser occurrence of irregular and knee-shaped, orange to brownish and deep red coloration rutile.

Also, presence of angular to sub-angular straw yellow staurolite fractures and garnet characterized by sub-rounded shape, with sub-conchoidal fractures and etches features also signify granitic source rocks. Therefore, these minerals were suggested to have been derived from a mixed composition of provenance source probably from the Precambrian rocks. As stated earlier, angular and even euhedral variants appearance of zircon and tourmaline suggests derivation from a granitic terrain sourced within a craton interior and recycled orogenic provenance as suggested by Chaodong *et al*. (2005) and Ruiz *et al*. (2007).

5.5 Paleoweathering and Paleoclimate Conditions

The discussion here focuses on the application of sediments mineralogical and geochemical compositions and to unravel the paleoweathering history and its effect on the sediments maturity and paloeclimate conditions of the investigated sediments.

5.5.1 Paleoweathering Conditions and Maturity

The mineralogical and geochemical compositions of terrigenous sedimentary rocks are resultant of the cumulative interplay of several variables such as weathering conditions among others, Bhatia and Crook (1986), Roser and Korsch (1986), Cullers and Podkovyrov (2000), Taylor and Mclennan (1985), Mclennan and Taylor (1991), Fedo *et al*. (1996), Cox *et al*. (1995) and Nesbitt *et al*. (1996). Thus, clastic geochemistry can be effectively used to

interpret source rocks, tectonic setting, paleoweathering condition and paleoclimate (Bhatia, 1983; Condie, 1993; Mclennan *et al*., 1993). The systematic use of combined mineralogical and chemical datasets represents a potentially formidable tool to investigate compositional variability of sediments. Several attempts have been made to develop similar procedures for terrigenous sediments (Cox and Lowe, 1996; Rosen *et al.*, 2004).

The intensity and duration of weathering in the siliclastics sediments is associated with the relationships between alkali and alkaline earth elements (Nesbitt and Young, 1982). The upper crust contains a considerable amount of feldspar that degrades during soil formation to form clay minerals by chemical weathering according to Nesbitt and Young (1982, 1984 and 1989), Taylor and McLennan (1985) and Fedo *et al*. (1995). These chemical signatures are ultimately transferred to sedimentary records and supply a useful means for monitoring the intensity of chemical weathering controlled mainly by source rock composition, climatic conditions and rates of tectonic uplift of source region (Wronkiewicz and Codie, 1990).

5.5.1.1 Petrographic Evidence

Weathering causes the depletion of unstable minerals like feldspars and mafic minerals, whereas comparatively stable minerals like quartz and zircon, as well as clay minerals, are enriched in the detrital spectrum. Compositional and textural characteristics of the initial detritus are modified by abrasion and sorting during transport, when sediments are carried away from their source area. While sediment is in transit, chemical alteration acts as important sediment modifier during temporary storage of the sediment in alluvial systems (Johnsson and Meade, 1990), thereby further obscuring the original detrital spectrum.

The textural and mineralogical maturity of sandstone are two different descriptive and interpretive concepts used by Folk (1951, 1980) and Pettijohn (1975). Folk (1980) defined

textural maturity as the degree to which sandstone is free of interstitial clay, so that, the mature end-members will be a sandstone composed entirely of quartz and chert, therefore provides most important clue to the physical nature of the depositional environment.

Petrographic data obtained in this study (Appendix IV, tables Ia-IXa and Ib-IXb) demonstrate that K-feldspar dominates over plagioclase, which may result from intense weathering and/or recycling during the Cretaceous (Armstrong-Altrin *et al*., 2004). Absence of feldspar in some studied petrographic thin sections samples (see chapter four, figure 4.24a-g) suggest that the source area was exposed to long-term weathering and that the sediments were at least partly polycyclic which is the result of intensive chemical weathering, reworking and/or sedimentary recycling (Armstrong-Altrin *et al*., 2004). It is also suggested that high temperature and moisture content, could have aide intense weathering causing destruction of feldspars and other labiles, thereby increasing the compositional maturity by enrichment of more stable quartz. This is because combination of low relief, hot humid climate and ample vegetation provides prolonged residence time of sediments, thereby increasing the duration of chemical weathering and thus enriching the sediments in stable quartz (Franzinelli and Potter, 1983).

Sequential stages of abrasion and weathering through which the sediments passed can be determined by the maturity index of minerals as suggested by Nwajide and Hoque (1985). Roser and Korsch (1986) concluded that quartz survives preferentially to feldspars, mafic minerals and lithics with increasing sediments' mineralogical maturity. Also, Roser *et al*. (1996) concluded that evidence of maturity can also be deduced from the mineralogical attributes and the mineralogical maturity index (MMI) which is expressed as;

$$\text{Mineralogical Maturity Index (MMI)} = \frac{\text{Quartz}}{\text{Feldspar} + \text{Rock Fragment}} \%$$

The MMI shows the relationship of ratio of the stable grain (quartz) to unstable grains (feldspar and lithic fragments) which is an indication of compositional immaturity. The calculated MMI values in this study (Appendix IV, Tables Ib-IXb) when compared with the standard values suggested by Roser *et al*. (1996) shows that most analyzed sediments in the study area are classified as mineralogically and compositionally mature to super-mature and this may be due to a prolonged weathering, sorting and abrasion.

In the Qm-P-K ternary plot after Dickinson *et al*. (1982), only monocrystalline quartz grains (Qm) are plotted against variable proportions of plagioclase (P) and K-feldspar grains (K) with points cluster in the Qm field, which clearly shows that they are sourced from a highly mature and stable continental block provenance (Figure 5.21), presumably a largely quartz-rich passive margin setting with sands derived from plate interior, or stable continental margins.

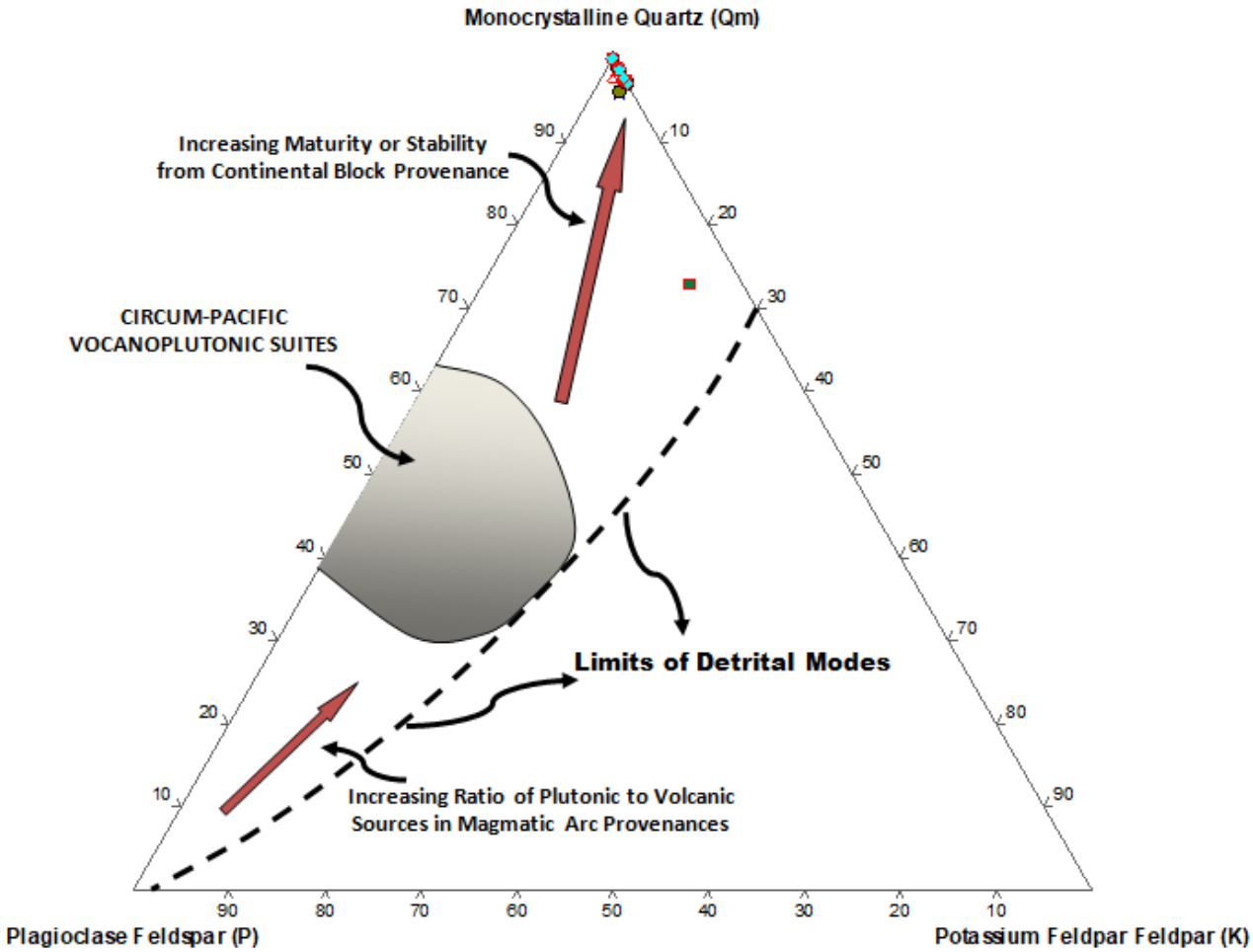


Figure 5.21: Standard Qm-P-K Ternary plot after Dickinson *et al*. (1982) showing increase in maturity or stability field for the investigated sandstone.

5.5.1.2 Geochemical Evidence

5.5.1.2.1 Major Elements Variations, Ratios and Plots

The geochemical composition of clastic sediments has been widely to evaluate the weathering history of the source area (Kermani *et al*., 2016). During transport and deposition, sediments undergo changes in their mineralogical and consequently in their major element composition, compared to their source rocks. For example, quartz (SiO_2) tends to become enriched while feldspars on the other hand break down, leading to the removal of Na_2O, K_2O and CaO (Fedo *et al*. 1995).

Conclusions has been drawn from the studies by Nesbitt and Young (1989), and Nesbitt *et al*. (1996) that chemical weathering conditions of clastic sedimentary rocks depends mainly on the weathering conditions at the source rock area. Nesbitt and Young (1982) also proposed that weathering history of ancient sedimentary rocks can be evaluated by examining depletion in alkalis (Na_2O, K_2O) and preferential enrichment of Al_2O_3 in sediments as a result of alteration of igneous rocks during weathering.

The chemical composition of weathering products in a sedimentary basin is expected to reveal concepts on mobility of various elements during weathering as concluded by Singh *et al*. (2005), so, effect of weathering processes on sedimentary rocks can be measured quantitatively in terms of the relative amount of certain major oxides in the rocks (Nesbitt and Young, 1982). The studied sediments are characterized by high silica (SiO_2) and low alumina (Al_2O_3). Mean concentrations (Tables 4.6a-4.6i) are greater than PAAS and UCC values (Table 4.6j). The high mean values of SiO_2 obtained for the studied sediments indicate relatively high quartz enrichment and high compositional maturity of the sandstone.

The silica-alumina ratios (SiO_2/Al_2O_3) of clastic rocks can be used as an indicator of sediment maturity because they are sensitive to sediment recycling and weathering processes, such that, as sediment maturity increases, quartz survives preferentially to feldspars, mafic minerals and lithics, therefore leading to increasing sediment maturity (Potter, 1978; Roser and Korsch, 1986; Roser *et al*., 1996). Roser *et al*. (1996) further stated that mean ratios of SiO_2/Al_2O_3 of an unaltered igneous rocks is always approximately to 3.0 for basic rocks while value ranges from 3.0 to 4.0 indicates acidic rocks, whereas values greater than 4.0 in sandstones are an indication of progressive maturity. In this study, calculated mean ratio of SiO_2/Al_2O_3 for all the studied samples are greater than 4.0 (See appendix VI, table Ia-Id), thus, confirming compositional maturity. The mean values are also greater than PAAS and UCC values (Appendix VI, table Ie), thereby further supporting the chemical maturity.

The alkali contents; sodic (Na_2O) and potassic (K_2O) is a measure of the feldspar content and can be used as chemical maturity index according to Roser and Korsch (1986), and Rollinson, 1992). Roser and Korsch (1986) submitted that sodic-potassic (Na_2O/K_2O) ratio can be employed to determine the maturity of the sandstone; since alkali abundance characterizes immature sandstones whereas low concentration show mature sandstone. Rollinson (1993) also employed alkali contents (Na_2O+K_2O) as an important index of chemical maturity, he concluded that values less than 2.0 indicates little or no feldspars which signify high chemical maturity whereas values greater than 2.0 indicate presence of feldspar and low chemical maturity. The higher SiO_2 with low K_2O/Na_2O and Al_2O_3/SiO_2 may be linked to high quartz-rich nature and low or absent of phyllosilicate content with (potassium) feldspar particles which may indicate a high sedimentary maturation according to (Bhatia, 1983; Roser and Korsch, 1988).

In this study, the mean values of Na_2O+K_2O and Na_2O/K_2O for all the studied samples indicate high sediment chemical maturity (See appendix VI, table Ia-Id). The Al_2O_3/Na_2O and TiO_2/Na_2O ratios can be used directly as markers for intensity of chemical weathering; higher ratios of Al_2O_3/Na_2O and TiO_2/Na_2O are found associated with the increase in kaolinite content and kaolinite/illite ratio (Roy *et al*., 2008). There is a variation in the mean values of Al_2O_3/Na_2O and TiO_2/Na_2O from the southwestern through the central to the northern parts of the studiy area and this may be due to the differential intensity and intense of weathering according to McLennan *et al*. (1980), Faundez *et al*. (2002) and Conception *et al*. (2012).

A compositional variability measure known as the index of compositional variability (ICV) was proposed by Cox *et al*. (1995) and is given in the equation below. The ICV is used to evaluate samples maturity, because increase in the degree of weathering, results in enhanced alumina content with a decrease in the ferromagnesian. Values of ICV greater than 1.0 signify compositionally immature sediments deposited in tectonically active settings whereas values less than 1.0 are compositionally mature sediments and are deposited in the tectonically quiescent or cratonic environment, where sediment recycling is active according to Cox *et al*. (1995). Table 4.6a-4.6i show the calculated ICV values for the studied study as generally less than 1.0 which is another strong indication of an intense weathering in the source environments. This also coincides with quartz abundance and in turn reflects the compositional maturity of the sediments in the study area.

Weathering indices of sedimentary rocks can provide useful information of tectonic activity and climatic conditions in the source region as increase of degree of chemical weathering may reflect the decrease in tectonic activity and/or change of climate towards warm and humid conditions which are more favorable for chemical weathering in source region

(Jacobson *et al*., 2003). The bivariate SiO_2 (%) versus (Al_2O_3+K_2O+Na_2O) (%) plot proposed by Suttner and Dutta (1986) for paleo-weathering reconstruction processes in sediments as a function of climate was employed in this study and shows that the studied samples fall within an increasing chemical weathering zone (Figure 5.22a).

Long *et al*. (2012) also suggested that combination of the Index of Compositional Variability (ICV) of Cox *et al*. (1995) and the Chemical Index of Alteration (Nesbitt and Young, 1982, 1984) can also be used to evaluate weathering trend and intensity. Cox *et al*. (1995) stated that ICV values of >0.84 are typical of major rock-forming minerals such as feldspars, amphiboles and pyroxenes, whereas values <0.84 are typical of alteration products such as kaolinite, illite and muscovite. In this study application of ICV versus CIA plot on the investigated samples show plotting within intense zone of CIA greter than 70 (Figure 5.22b) which confirms that the Northern Bida Basin sediments are chemically mature. It is also noted that most of the sediments are have lower ICV values of <0.84, though few samples have high ICV ratios of >0.84 but CIA >70, hence would regarded as mature and therefore confirm the chemical maturity of the studied sediments. This interpretation also support the the relationship between SiO_2 versus (Al_2O_3+K_2O+Na_2O) in figure 5.22a.

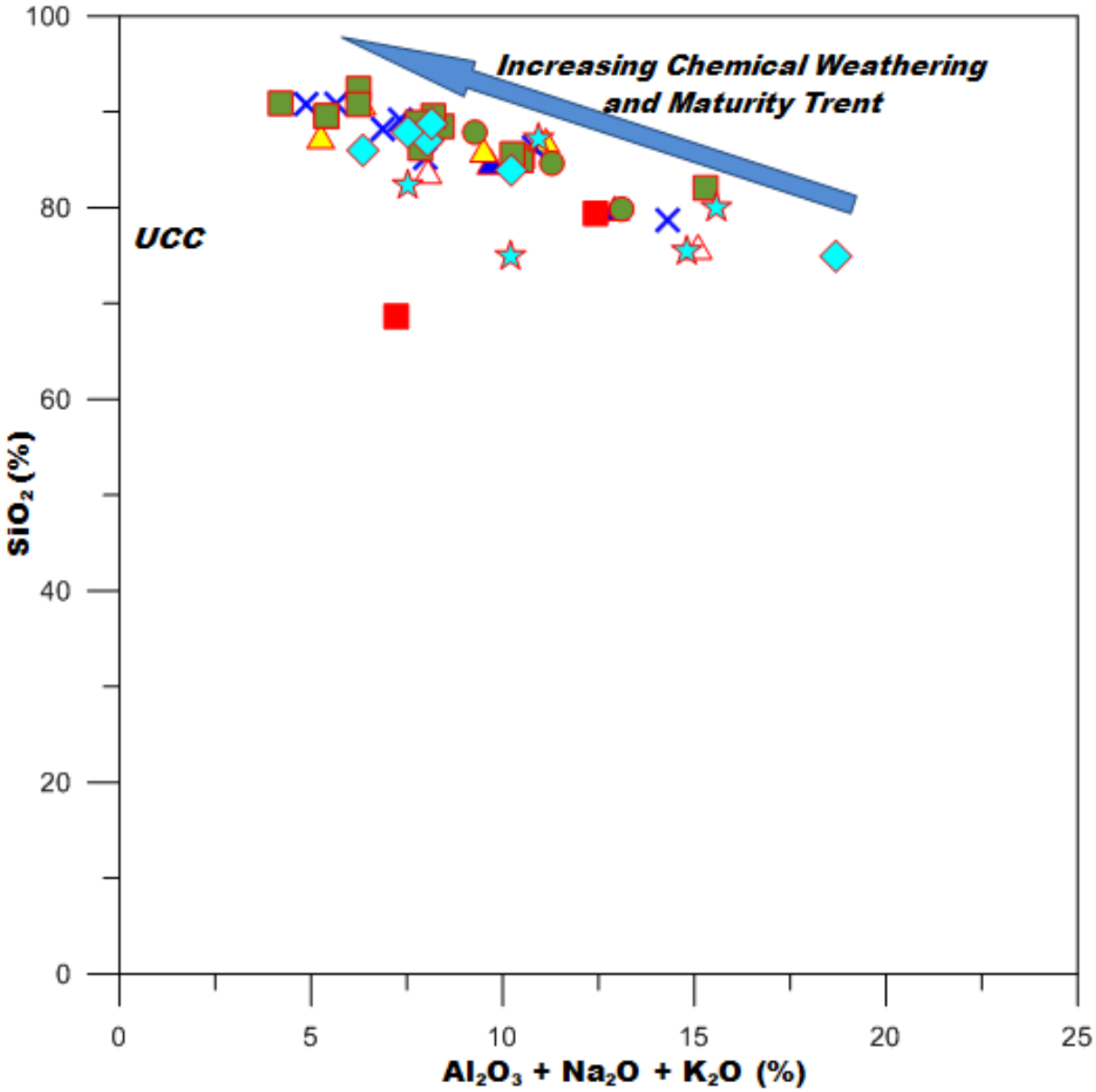


Figure 5.22a: Bivariate chemical index plot using (Al_2O_3+K_2O+Na_2O) (%) versus SiO_2 (%) after Suttner and Dutta (1986) showing increasing in the chemical weathering and maturity trend for the Northern Bida Basin sandstone.

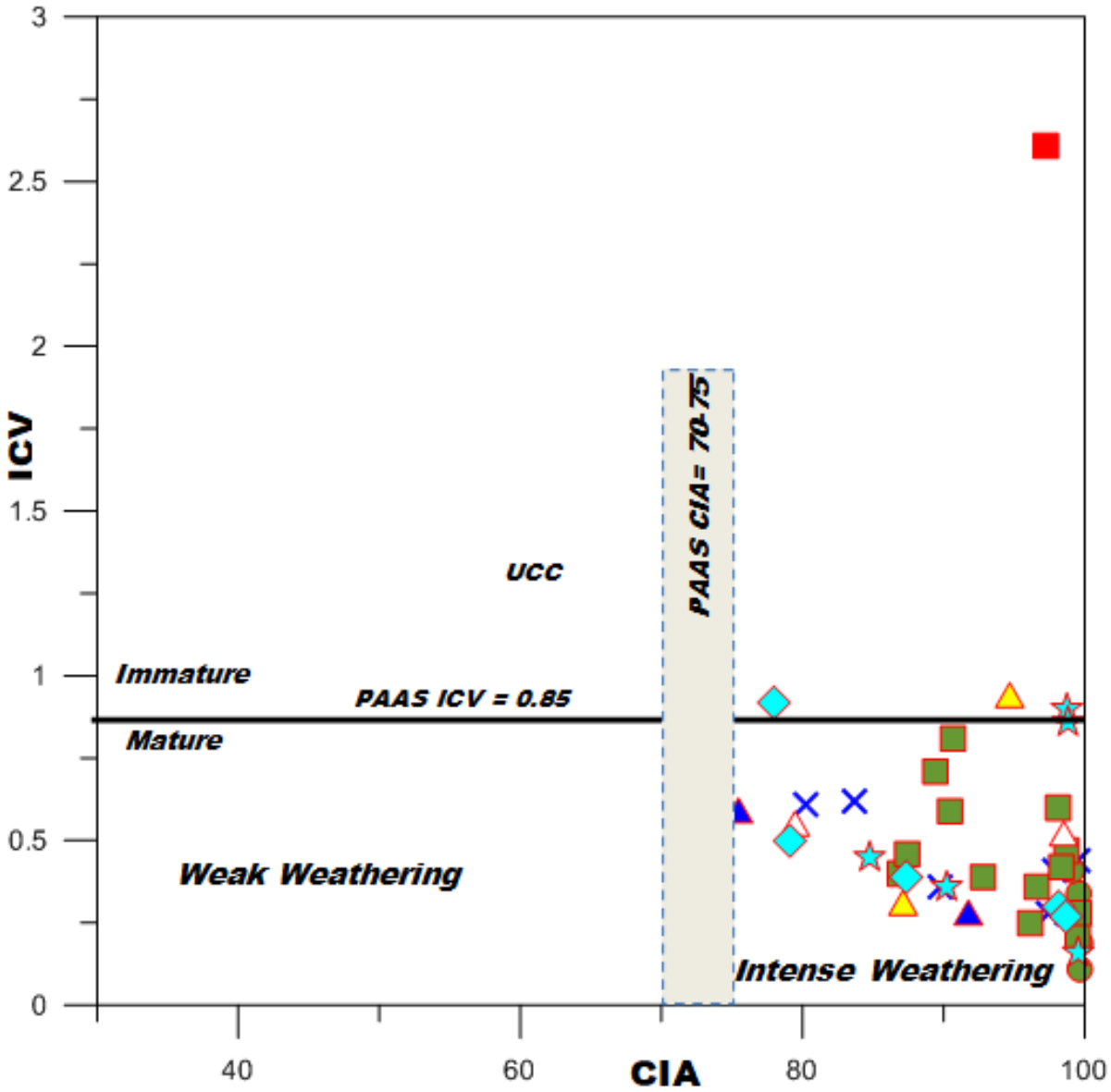


Figure 5.22b: Bivariate plot of ICV versus CIA after Long *et al*. (2012) showing the intense weathering for the investigated Northern Bida Basin sandstone.

The Weathering Index Values

The chemical composition of weathering products in a sedimentary basin is expected to reveal concepts on mobility of various elements during weathering (Singh *et al*., 2005). The degree of source rock weathering is quantified variously by a few indices of weathering have been proposed based on molecular proportions of mobile and immobile element oxides (Na_2O, CaO, K_2O and Al_2O_3) and has been employed in this study. Nesbitt *et al*. (1997) stated that during chemical weathering Ca, Na and K are largely removed from source rocks. The amount of these elements surviving in soil profiles and in sediments derived from them is a sensitive index of intensity of chemical weathering. The intensity and duration of weathering in the siliciclastic sediments is associated with the relationships between alkali and alkaline earth elements according to Nesbitt and Young (1982).

In reflecting sediments' chemical weathering, the chemical index of weathering (CIW) after Nesbitt and Young (1982, 1984, 1996), the chemical index of alteration (CIA) after Nesbitt and Young (1982) and the plagioclase index of alteration (PIA) after Fedo *et al*. (1995) may be sensitive to subtle geochemical changes and hence are widely being utilized for demonstrating the impact of climate on bedrock, neotectonic characteristics, and earth's surface environment over geologic time (Price and Velbel, 2003). The standard procedures were followed in calculating the weathering indices and the results are discussed in relation with the objective of the present study. In the studied samples, CaO is very low (Tables 4.6a-4.6i), hence there is no objective system to distinguish between CaO in carbonates and that in silicates, therefore CaO in studied clay samples is used in the calculation of weathering indices.

The most widely used chemical index to ascertain the degree of source area weathering is the Chemical Index of Alteration (CIA) proposed by Nesbitt and Young (1982) based on the

calculation in terms of molecular proportion in order to estimate the intensity of chemical weathering in the source area of siliciclastic sedimentary rocks. The basic understanding on this, is that chemical weathering strongly influences the mineralogy and major element composition of the sediments by removing labile cations (Ca^{2+}, Na^{+} and K^{+}) relative to residual constituents (Al^{3+} and Ti^{4+}) through the conversion of feldspar to clay minerals (Nesbitt and Young, 1982; Selvaraj *et al*., 2016). Since in feldspar, Al is the least mobile element, Nesbitt and Young (1982) proposed a chemical index of alteration (CIA) which enables determination of the intensity of weathering in source areas.

The CIA has been extensively used in various studies (Nesbitt and Young, 1984; Nagarajan *et al*., 2007; Armstrong-Altrin, 2009; Bandopadhyay and Ghosh, 2015; Ramos-Vázquez *et al et al*., 2017). Nesbitt and Young (1984) suggested that CIA value of the main rock-forming minerals (quartz, plagioclase, alkali-feldspars, pyroxene and olivine) is ~55 whereas clay minerals yield higher CIA values (usually ~75) with the highest value of approximately 100 that recorded kaolinite. He stated further that, high values of the index (> 90) indicate extensive conversion of feldspar to clay and hence intense alteration/weathering. Fedo *et al*. (1995) and Descourvieres *et al*. (2011) also concluded that CIA is a dimensionless parameter from 0.00 to 100 corresponding to increasing weathering and sediment maturity, its values between 50.0 and 60.0 indicate a low degree of chemical weathering, between 60.0 and 80.0 moderate weathering while values greater than 80.0 indicate intense chemical weathering. In general, the calculated CIA values in this study for all the sandstones (Tables 4.6a-4.6i) indicate that the sediments are highly weathered, which in turn suggests that the sediments have been derived from the source rocks that were subjected to both physical and chemical breakdown.

Chemical index of weathering (CIW) values for the source rocks and sediments reflect the amount of chemical weathering experienced by weathering materials (Nesbitt and Young, 1982). This index strongly affects the major element geochemical variability of sedimentary rocks and soils (Nesbitt *et al*., 1996) and can be evaluated in terms calculated molecular proportions after Nesbitt and Young (1982, 1984, 1996). Nesbitt and Young (1982) submitted that high CIW values (between 76 and 100) indicate intensive chemical weathering in the source areas whereas values less than or equal to 50 indicates fresh source areas. The higher mean values of CIW for the studied sediments (Tables 4.6a-4.6i) are higher, so, indicate very strong source weathering which is a characteristic for recycled sediments according to McLennan *et al*. (1993). It is also interesting to know that the mean values for the studied sediments is higher than published PAAS and UCC data (Tables 4.6j) and therefore confirm the intense source area weathering.

The role of source rock weathering and elemental redistribution during diagenesis which quantifies the degree of destruction of plagioclase and identifies albitization can also be assessed using the plagioclase index of alteration (PIA) according to Alvarez and Roser (2007). Source weathering and elemental redistribution during diagenesis also can be assessed using PIA according to Fedo *et al*. (1995). During the initial stages of weathering, Ca is leached rapidly than Na and K so lead to increase in weathering, and this is due to destruction of feldspars among which plagioclase is more preferentially removed than K-feldspars according to Nesbitt and Young (1984) and Nesbitt *et al*. (1996). The PIA is very useful for quantitative estimation of the degree of chemical weathering undergone by the rocks in the source area of clastic sediments (McLennan *et al*., 1993; Fedo *et al*., 1995). Fedo *et al*. (1995) stated that maximum value of PIA is 100 for completely altered materials (kaolinite and gibbsite) and weathered plagioclase has a PIA value of 50. Osae *et al*. (2006)

also concluded that low values of PIA below or equals 60 (~60) indicates low weathering whereas values between 75 and 100 indicate intensive weathering in the source areas. In this study, the calculated mean PIA values for all the investigated sediments (Tables 4.6a-4.6i) indicates a high weathering which is a characteristic of an intense destruction of feldspathic material of the sandstones during different stages of evolution of the sandstones. The results also show that the period of Maastrichtian is marked with very high PIA values and a peak value during Campanian.

Mobility of elements during the progress of chemical weathering of source material and post-depositional chemical modifications of the sandstones can be evaluated by bivariate plot of CIA versus SiO_2 after Nesbitt and Young (1982) and ternary plot of the molar proportions of Al_2O_3, Na_2O and CaO i.e. (A = Al_2O_3; CN = CaO+Na_2O; K = K_2O) in A-CN-K ternary diagram which is a valuable tool to evaluate the degree of weathering and diagenetic processes (Nesbitt and Young, 1982 and 1984). The A-CN-K plot define a narrow linear trend and the trend line runs slightly at an angle to the edges that shows that removal rates of Na and Ca from plagioclase or volcanic glass are generally greater than the removal rates of K from microcline or volcanic glass (Nesbitt and young, 1984). The bivariate CIA versus SiO_2 plot (Figure 5.23a) and ternary A-CN-K (Figure 5.23b) plots show prodeminance of kaolinite which signify intense chemical weathering. The A-CNK-FM {Al_2O_3-(CaO+Na_2O+ K_2O)-(Fe_2O_3+MgO)} ternary plot after Nesbitt and Young (1989, 1996) and Nesbitt *et al*. (1996) presented in figure 5.23c also display high intensity of weathering history as the sediments were plotted closer to high Al_2O_3 contents. This position illustrates the leakage of Ca, Na and K during intensive weathering, especially from feldspars in preference to Al_2O_3 or predominance of kaolinite and/or gibbsite in the materials, which suggests low or no mafic mineral input.

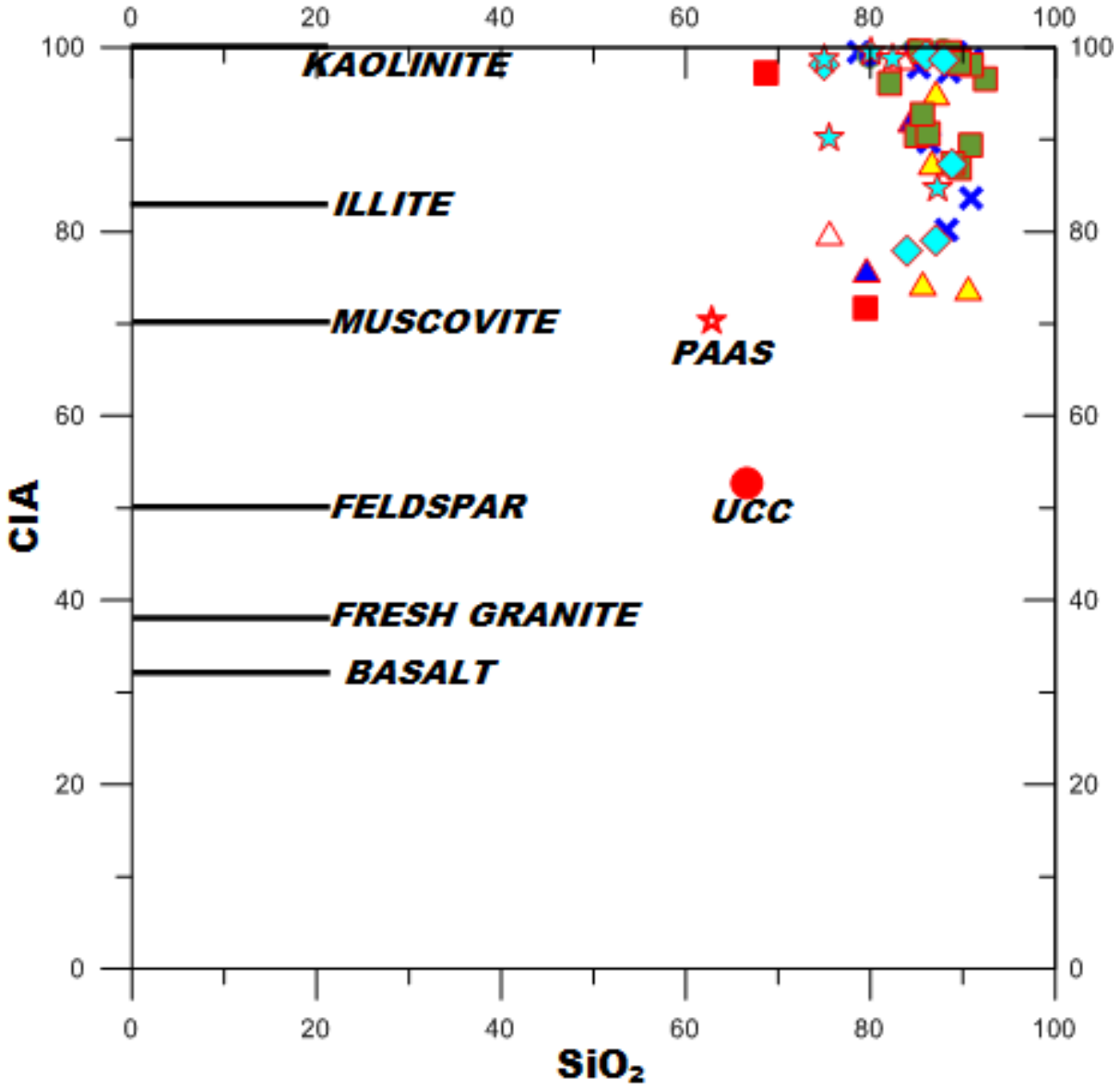


Figure 5.23a: Bivariate plot of CIA versus SiO_2 after Nesbitt and Young (1982) showing the weathering trends and likely mineralogical composition of the investigated sandstone.

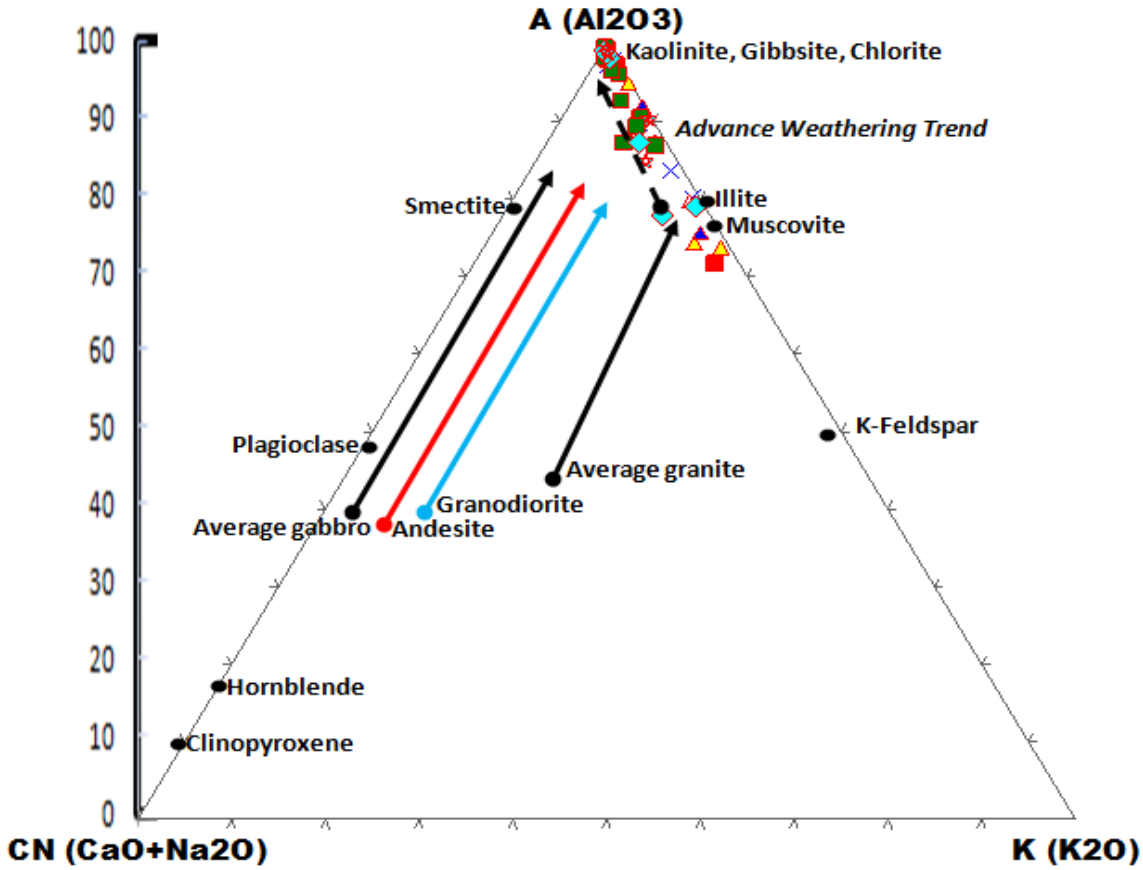


Figure 5.23b: The standard ternary A-CN-K {Al_2O_3-(Na_2O+CaO)-K_2O} plot after (Nesbitt and Young, 1984 & 1989) showing weathering trends for the investigated sandstone compared with some typical source rocks. Note a general weathering trend (advanced weathering trend) in all plots towards the Al_2O_3 corner of the diagram.

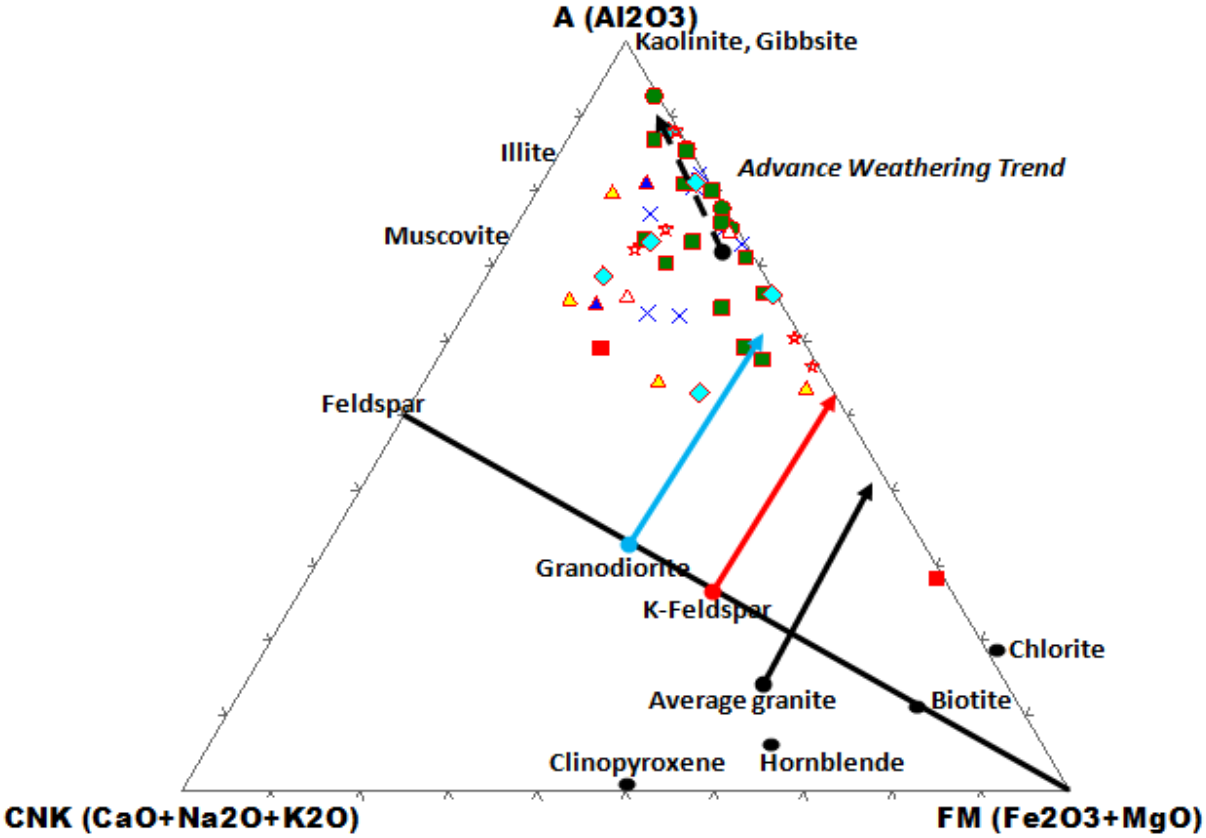


Figure 5.23c: The standard ternary A-CNK-FM {Al_2O_3-($CaO+Na_2O+CaO$)-Fe_2O_3+MgO} plot after (Nesbitt and Young, 1984; 1989) showing weathering trends for the investigated sandstone compared with some typical source rocks. Note a general weathering trend (advanced weathering trend) in all plots towards the Al_2O_3 corner of the diagram.

5.5.1.2.2 Trace and Rare Earth Elements

Relative concentration of resistant major oxides and trace elements present in sedimentary rocks are valuable indicators of source rocks (McLennan *et al*., 1985). Some trace elements; Zr, Th, Sc, Nb, Ga and rare earth elements (REE) are generally remaining constant from source rocks to the sediment because of their low solubility in water during weathering (Bhatia and Crook, 1986). The large ion lithophile elements such as Rb, Sr, Ba, Th, U and Cs behave similarly to related major elements during weathering processes, therefore, K_2O, Rb and Cs generally incorporate into clays, while CaO, Na_2O and Sr tends to leach during chemical weathering (Nesbitt *et al*., 1980). Some trace elements (especially HFSE) are principally resistant to weathering effects (Nesbitt and Young, 1982; Bhatia and Crook, 1986; McLennan *et al*., 1993). This is because these HFSE; Th, Sc, Hf and Co are least mobile during weathering, transportation, diagenesis and metamorphism (Taylor and McLennan 1985; Wronkiewicz and Condie, 1990). In this study, the mean concentration of Rb, Ba and Th (Tables 4.7a-4.7.3i and tables 4.8a-4.8f) are lower than PAAS and UCC and PAAS while uranium (U) is generally low (Tables 4.7j and 4.8g).

Uranium (U) and thorium (Th) in sedimentary rocks occur in association with several host elements, such as clay minerals, feldspars, heavy minerals, phosphates and organic matter (Ruffell and Worden, 2000), therefore, sedimentary recycling in oxidizing conditions results in a distinct fractionation of Th and U during rock weathering. Ruffell and Worden (2000) submitted that Th/U ratio increases as a result of successive cycles of weathering and redeposition and thus becomes a good marker of these processes. McLennan *et al*. (1993) concluded that Th/U ratio in weathering products are usually higher than UCC values of 3.5 to 4.0. The calculated mean values of Th/U ratio for the sediments in all the sub-facies in this study (Appendix VI, tables IIa-IIi) is higher than PAAS and UCC values (Appendix VI,

tables IIj) indicating chemically weathered sediments which also suggests more than a single cycle.

The ratio of rubidium to strontium (Rb/Sr) ratio of siliciclastic sediments is also useful for assessing the degree of source rock weathering according to Kimberley and Grandstaff (1986), McLennan *et al*. (1993), because, chemical weathering of source area produces higher Rb/Sr ratios in sedimentary rocks (Kimberley and Grandstaff, 1986). The mean Rb/Sr ratio of the studied sediments in all the sub-facies is relatively higher than average UCC and PAAS values and this suggests significant weathering in the source area, so, support the above deductions.

Other evidence for measuring the degree of sedimentary recycling can be envisaged from Zr/Sc ratio which leads to the enrichment of the stable mineral zircon in the deposits according to Nesbitt and Young (1982). The mean values of Zr/Sc of the studied sediments varied with are relatively higher compare to the published UCC and PAAS except for Gcm and Gmm sub-facies. This evidence also support that a recycled sedimentary source was an intense component (Roddaz *et al*., 2005). Similar mean values of La/Th for the studied sandstones as compared to UCC and PAAS also suggest significant weathering condition from the source. In addition, the Zr/Hf ratios can also be used to confirm compositional maturity for the studied sediments. The results show similar mean Zr/Hf ratios in the studied samples with PAAS and UCC indicating high sediment recycling with high maturity in the source area.

The recycling influence as an indicator of chemical differentiation can be recognized on the Th/Sc versus Zr/Sc bivariate plot according to McLennan *et al*. (1993), Cox *et al*. (1995). The bivariate plot for the studied samples demonstrates a linearly increasing compositional trend

toward a higher ratio of Zr/Sc (Figure 5.24a). This result suggests that the increase in the zircon concentration in the source area has undergone recycling before the transport of sediments to the Northern Bida Basin. Weathering trends can also be evaluated using bivariate plots of Th/U versus Th and La versus Th. In general, increase in Th/U ratio to more than 4.0 is an indication of chemical weathering and/or recycling owing to more loss of U in this process (McLennan *et al*., 1983).

High chemical weathering and chemical maturity can also be determined by the some trace elements plots. These plots Th/Sc versus Zr/Sc plot (Figure 5.24a), Th/U versus Th plot (Figure 5.24b) and La versus Th plot (Figure 5.24c) supported the discussions above.

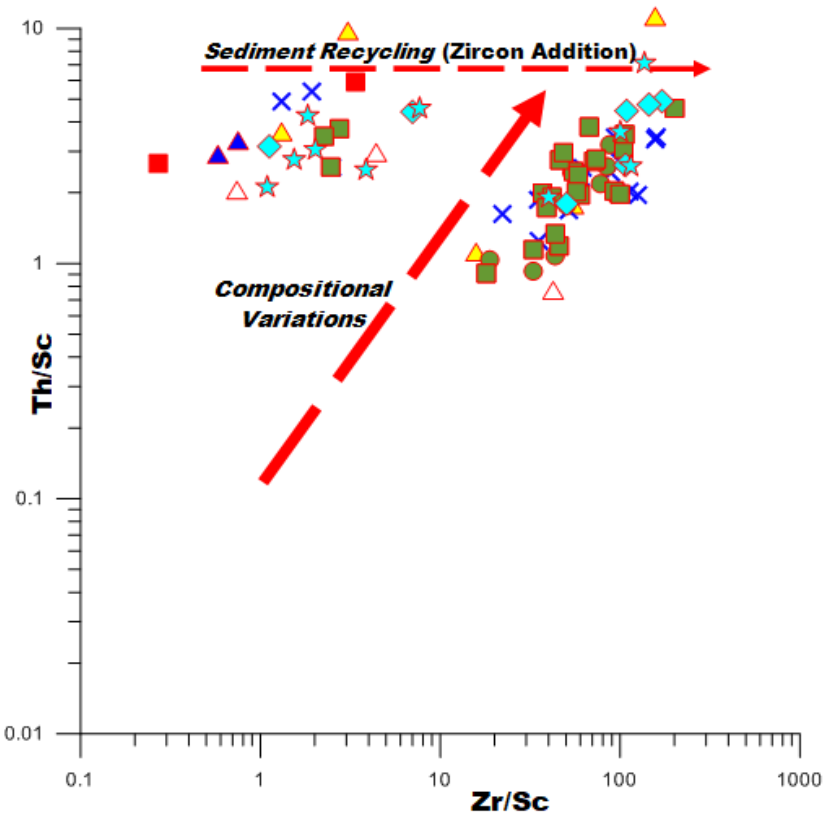


Figure 5.24a: Bivariate chemical index plot using on Th/Sc versus Zr/Sc after McLennan *et al.* (1993) showing a trend to high Zr/Sc-ratios, indicating zircon addition to the sediment and therefore suggesting a recycling of an older sourced rock for the investigated Northern Bida Basin sandstone.

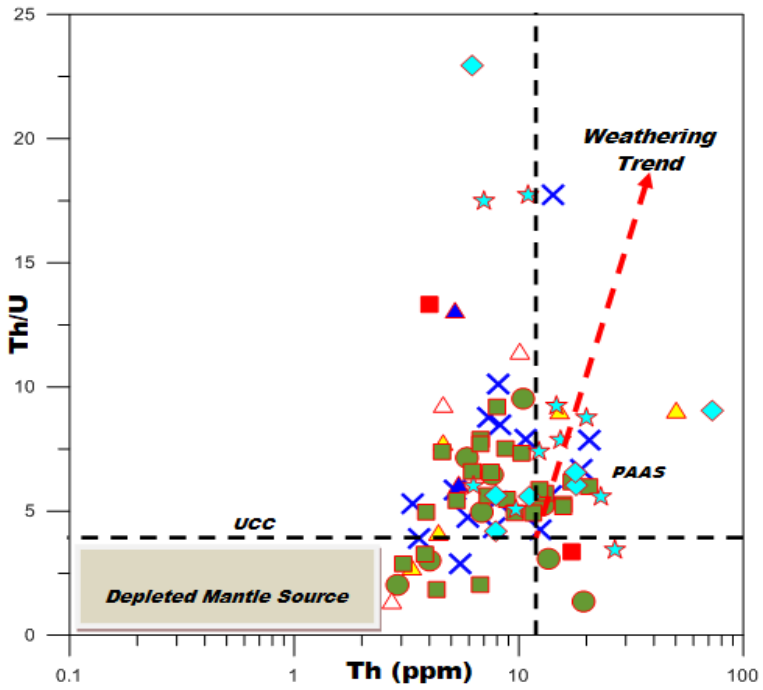


Figure 5.24b: Bivariate chemical index plot using on Th/U versus Th after McLennan *et al.* (1993) with an arrow showing a weathering trend for the investigated Northern Bida Basin sandstone.

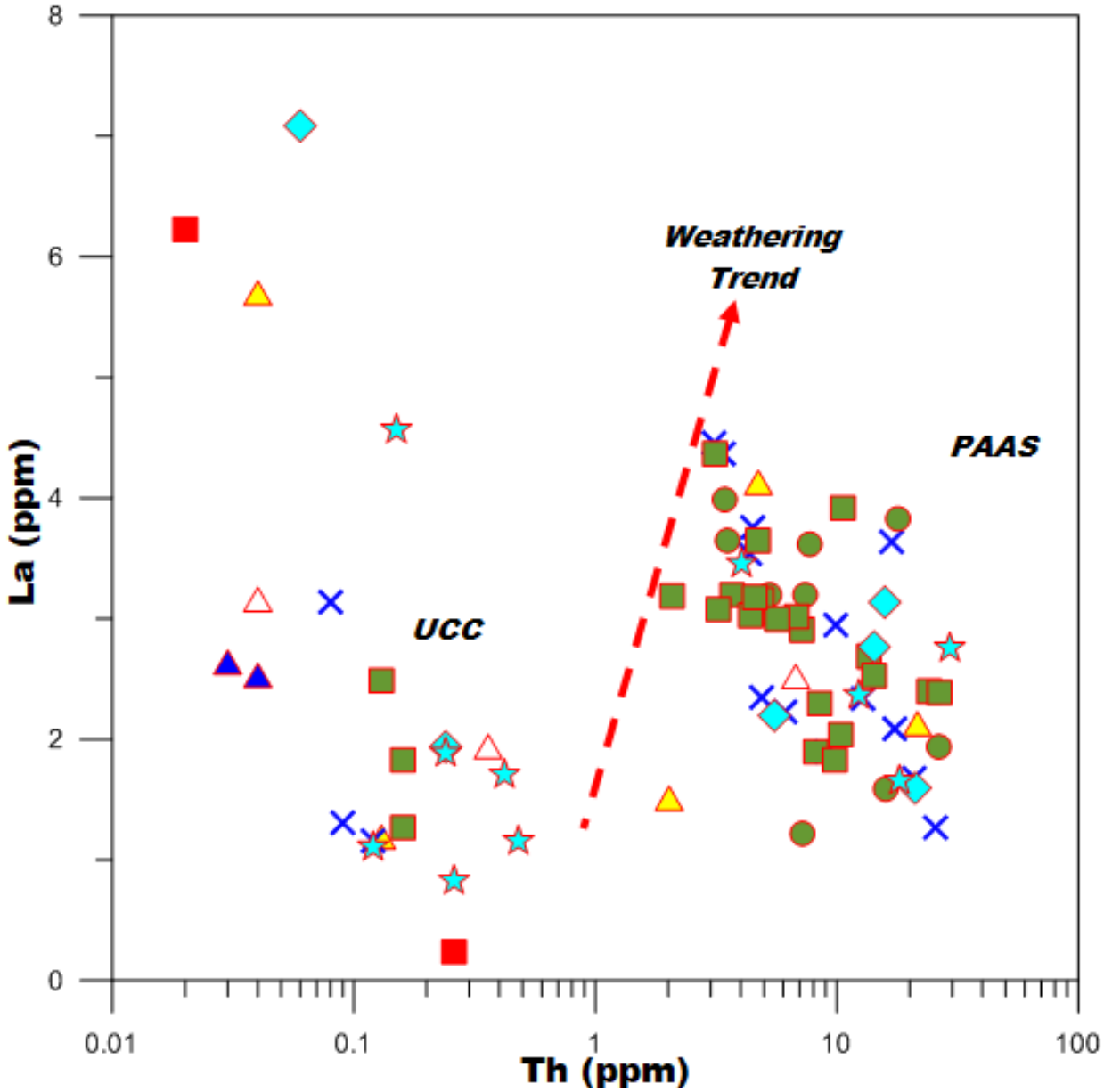


Figure 5.24c: Bivariate chemical index plot using on La versus Th after McLennan *et al.* (1993) with an arrow showing a weathering trend for the investigated Northern Bida Basin sandstone.

5.5.1.3 Heavy Minerals Evidence

The original composition of heavy mineral assemblages can be modified by weathering of parent rocks that prior to incorporation into transport system (Morton and Hallsworth, 1999). The degree to which heavy mineral assemblages are modified by weathering in the source area depends on three main factors: the original composition of the heavy mineral suite (controlled by the parent rock lithology), the physiographic setting, and the climate (Suttner *et al*., 1981). If the transport processes removing weathered material are potentially more rapid than the weathering processes generating the material, erosion is said to be weathering-limited (Johnsson *et al*., 1991). Under such conditions, detritus is quickly removed without significant modification by chemical weathering, and thus the provenance signature of the parent rocks is likely to be largely transferred into the transport system.

In contrast, when the weathering rate exceeds the capacity of transport processes to remove material, then erosion is transport-limited (Johnsson *et al*., 1991). Under transport-limited conditions, weathering products have a longer time to react with soil and groundwater, strongly affecting the composition of detritus. In this situation, extensive modification of the heavy mineral suites can occur before the sediment reaches the transport system. Also, it is earlier submitted that generation of acidic groundwater in humid environments under tropical or temperate climates causes strong evidence of corrosion, with etched grain surfaces and extensive dissolution of unstable heavy minerals (Friis and Johannesen, 1974).

In this study, a comparison of the relative order of stability of some selected heavy minerals like zircon, rutile, tourmaline and sillimanite shows, reasonably, a general increase in weathering from southern-southeastern (least weathered) to northern-northwestern (most weathered). There is no doubt that during the weathering processes, the mineralogy of the sandstones may be greatly altered and the degree to which this occurs in a sediment source

area essentially depends on the climate and the rate of erosion. Higher weathering effects in the central and northern part may be as a result of kaolinitic weathering under warm humid conditions during the late Cretaceous, the sands derived therefore is characterized by a high ZTR index (Tables 4.4a – 4.4i).

5.5.2 Paleoclimatic Conditions

The influence of climate on sandstone composition has been studied by many researchers; Darnell (1974), Young *et al*. (1975), Young (1976), Basu (1976, 1985), Potter (1978), Suttner *et al*. (1981), Franzinelli and Potter (1983), Mack (1984), Suttner and Dutta (1986), Grantham and Velbel (1988), Akhtar and Ahmad (1991) and Girty (1991). They had independent evidence for climate change through time, and their study showed that sandstone composition changed as climate changed.

Weathering indices of sedimentary rocks can provide useful information of tectonic activity and climatic conditions in the source region because increase of degree of chemical weathering may reflect change of climate towards warm and humid conditions which are more favorable for chemical weathering in source region (Jacobson *et al*., 2003). He emphasized that the increase in degree of chemical weathering may signify a decrease in tectonic activity and/or change towards more warm and humid conditions. The stronger chemical weathering is generally associated with warm and humid climates, while more arid climate is generally associated with relatively weak chemical weathering (Yan *et al*., 2007). Suttner and Dutta (1986) proposed a bivariate plot using SiO_2 versus (Al_2O_3+K_2O+Na_2O) to constrain the climatic condition during sedimentation of siliciclastic sedimentary rocks.

In this study, applications of combined petrographic and elemental composition data were employed to constrain the paleoclimatic conditions during deposition of sediments.

5.5.2.1 Petrographic Evidence

Texturally, a significant enrichment in quartz (Q) and depletion in plagioclase (P) grains in the studied sediments indicate humid and warm climatic conditions according to Folk (1980). Also, minor quantities of feldspars (mostly altered) among the studied sediments also supports this observation.

The study on climatic-physiographic control on sandstone composition has been presented by Ruxton (1970), Franzinelli and Potter (1983), Johnsson *et al*. (1988) and (Girty, 1991). Also Van de Kamp and Helmhold (1991) studied Holocene sandstones derived from granitic basement rocks in glacial, arid desert, temperate, subtropical and humid tropical climates and he proposed that arkoses sandstone with low ratio of quartz to sum of quartz and feldspar (Q/Q+F) with value ranges from 0.3 to 0.7 may form in humid to temperate climates, and this may unlikely to form in humid subtropical and tropical climates as the sandstones are tend to be more mature, therefore, will have higher values.

Application of the Van de Kamp and Helmhold (1991) assumption in this study confirmed its usefulness because for paleoclimate indicator. The studied sediments have higher Q/Q+F values ranges from 0.93 to 1.00 (Appendix IV, tables Ia-VIIIa), therefore, points towards sediments formation in the humid subtropical and tropical climates. Bivariant log/log plot of the ratio of polycrystalline quartz to feldspar plus rock fragments against the ratio of total quartz to feldspar plus rock fragments after Suttner and Dutta (1986) has been used for interpreting the paleoclimate of studied sediments. The plot indicates humid climatic conditions for the studied sediments in the northern Bida Basin (Figure 5.25a). Thus, climate and relief might have played an important factor in the formation and production of compositionally mature, quartz-rich sandstones.

The weathering index plot, proposed by Weltje *et al*. (1998) using natural log-ratios; ln(Q/L) versus ln(Q/F) permits the distinction of parent rock type, weathering history and paleotopography. He suggested that for many types of sandstone, values of both log-ratios are expected to correlate with weathering intensity, because quartz is more resistant to weathering than feldspar and lithic fragments.

The validity of this concept is checked in this study and the analyzed samples mainly fall within weathering index 2 and minor 4 boundaries (Figure 5.25b). These indices indicate that the sediments were mainly derived from moderate hills to low plains and the influence of climate on the sediment compositions was very high i.e. the sedimentation points towards a tropical humid condition (Tables 5.4a and 5.4b).

The ternary (Q-F-R) and (Qt-F-L) plot after Suttner *et al*. (1981) which use the compositional framework grain were employed in this study to determine climatic conditions during the sediments formation. This plot mimics the provenance field boundaries taken from Dickinson and Suczek (1979) to show the relationship of provenance and the climatic conditions during sediment deposition. The ternary plots of (Q-F-R) and (Qt-F-L) presented in figures 5.25c and 5.25d shows that Northern Bida Basin sediments were formed in a humid climatic setting during the time of deposition.

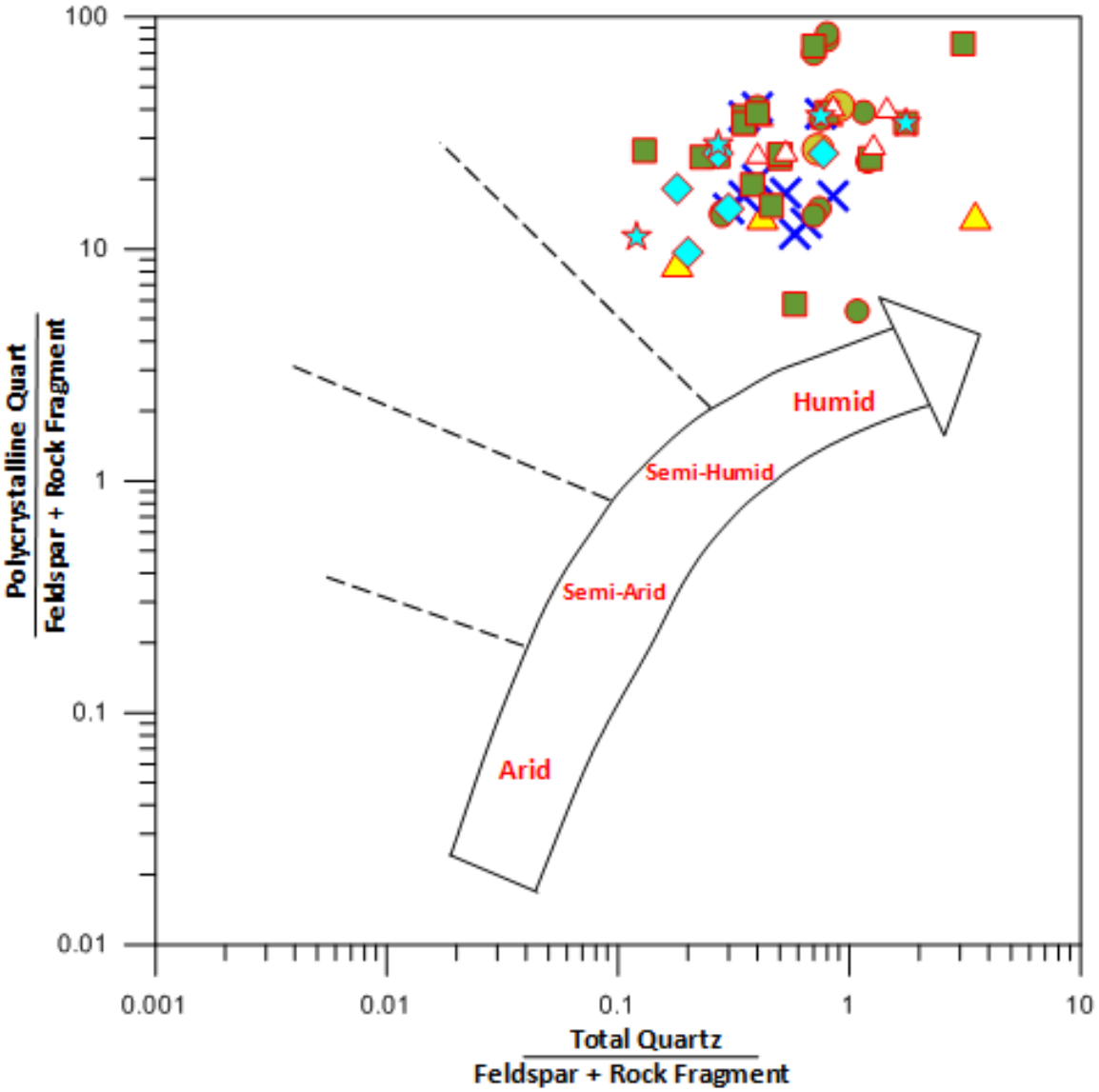


Figure 5.25a: Bivariate log/log plot of the ratio of polycrystalline quartz to feldspar plus rock fragments versus ratio of total quartz to feldspar plus rock fragments (Qp/F+R vs. Qt/F+R) after Suttner and Dutta, 1986) for the investigated Northern Bida Basin sandstone.

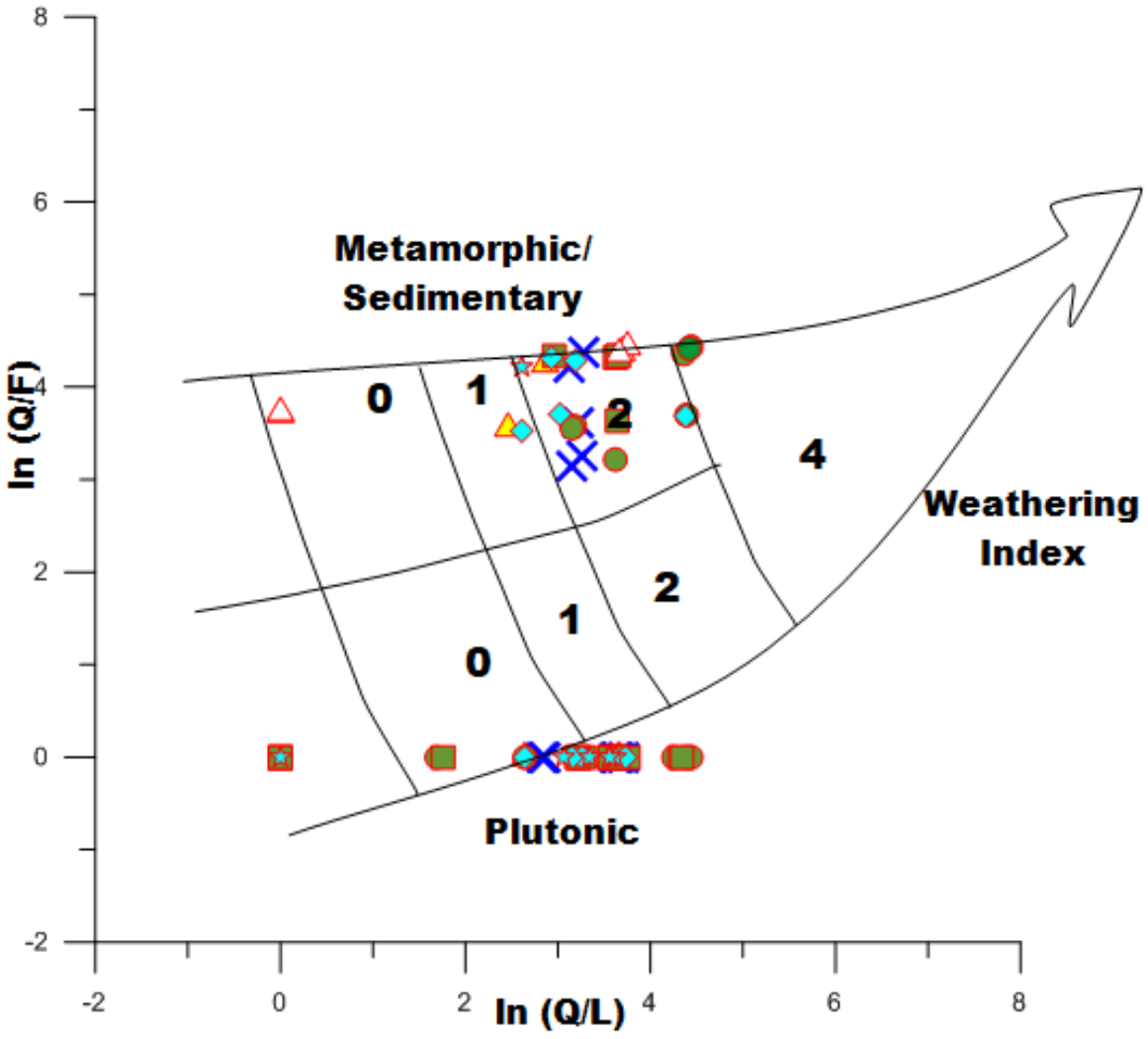


Figure 5.25b: Bivariate natural log/log plot of the ratio of total quartz to feldspar versus ratio of total quartz to total lithic fragments for the Northern Bida Basin sandstones after Weltje *et al*. (1998).

NB: Fields 0-4 refer to the semi-quantitative weathering indices defined on the basis of relief and climate, as indicated in the tables 5.4a and 5.4b.

Table 5.4a: Weathering index calculated values for fluvial sands after Weltje (2006).

SEMI-QUANTITATIVE WEATHERING INDEX			PHYSIOGRAPHY (Relief)		
			high (mountains) 0	moderate (hills) 1	low (plains) 2
Climate (Precipitation)	(semi-) arid & Mediterranean	0	0	0	0
	Temperate, Sub-humid	1	0	1	2
	Tropical, Humid	2	0	2	4

Table 5.4b: The compiled data and interpretations for weathering trend, relation to parentage and weathering conditions after Weltje (2006)

PL	PARENT LITHOLOGY	WI=(C*R)	WEATHERING INDEX
	P Plutonic and high-grade metamorphic M low- high-grade metamorphic S sedimentary (2nd cycle mixed P-M)		0 unweathered 1 slightly weathered 2 moderately weathered 4 intensely weathered
C	CLIMATE	R	RELIEF
	0 (semi-)arid and mediterranean 1 temperate sub-humid 2 tropical humid		0 high (mountains) 1 moderate (hills) 2 low (plains)

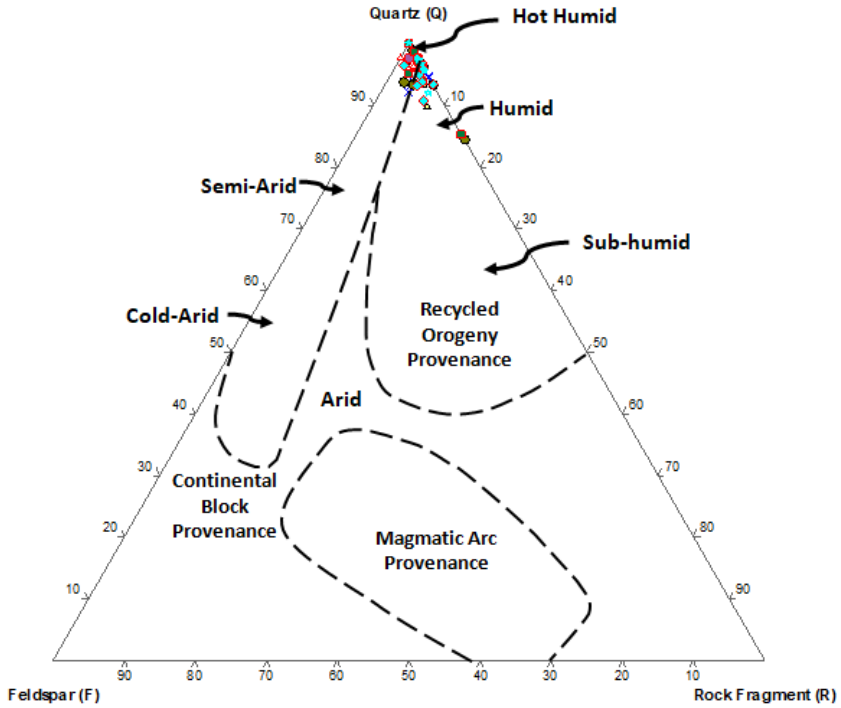


Figure 5.25c: Ternary plots of Q-F-R modal values after Suttner *et al*. (1981), indicating humid to hot humid for the investigated Northern Bida Basin sandstones. NB: Provenance field boundaries are taken from Dickinson and Suczek (1979).

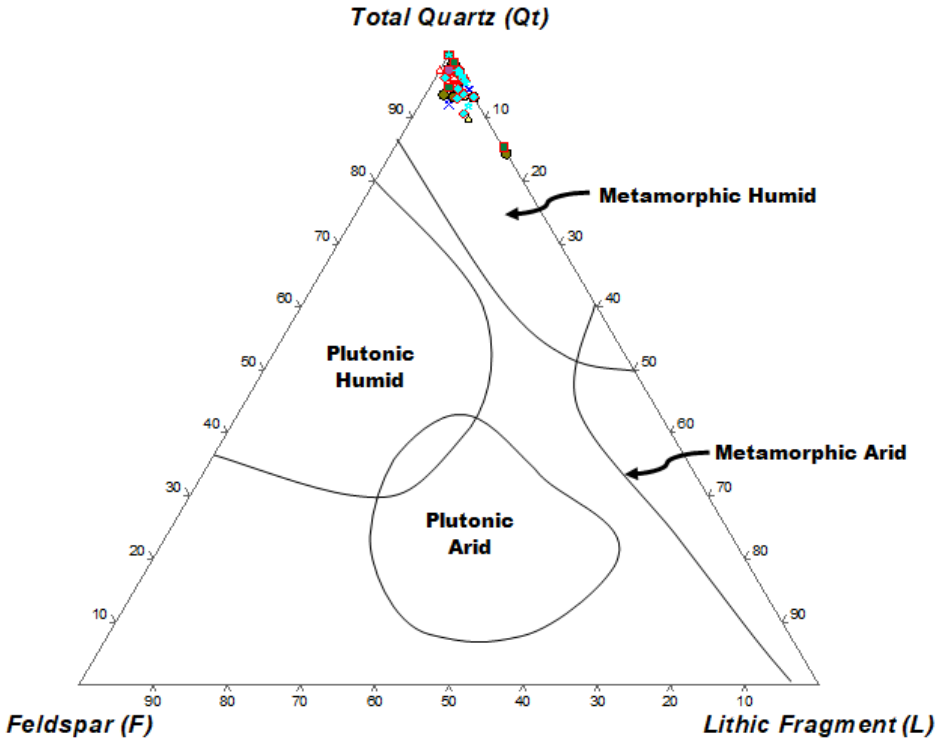


Figure 5.25d: Ternary plots of Q-F-L modal values after Suttner *et al*. (1981) indicating metamorphic provenance within humid palaeoclimate for Northern Bida Basin sandstone.

5.5.2.2 Geochemical Evidence

The sedimentary stratigraphic record is the outcome of an exogenic system consisting of geologic setting, changes in geochemical reactions between the sea and the earth, climate, and processes of sediment formation (Srinivasan, 1989) and diagenesis (Ramkumar, 1999). Therefore, the ensuing sedimentary records show differences in bulk chemistry as a result of changes in different combinations of minerals and neo-formed during post-depositional times, all of which were influenced by the climatic conditions. Wortmann *et al*. (2004) concluded that Maastrichtian deposits are predominantly continental in nature and may indicate humid climatic conditions accompanied by chemical weathering.

The paleoclimatic setting of the studied sediments is also deducted from the bivariate plot of major elements; SiO_2 (%) against total (Al_2O_3+K_2O+Na_2O) proposed by Cox *et al*. (1995). This reveals increasing chemical maturity in predominantly humid conditions for the Northern Bida Basin (Figure 5.26).

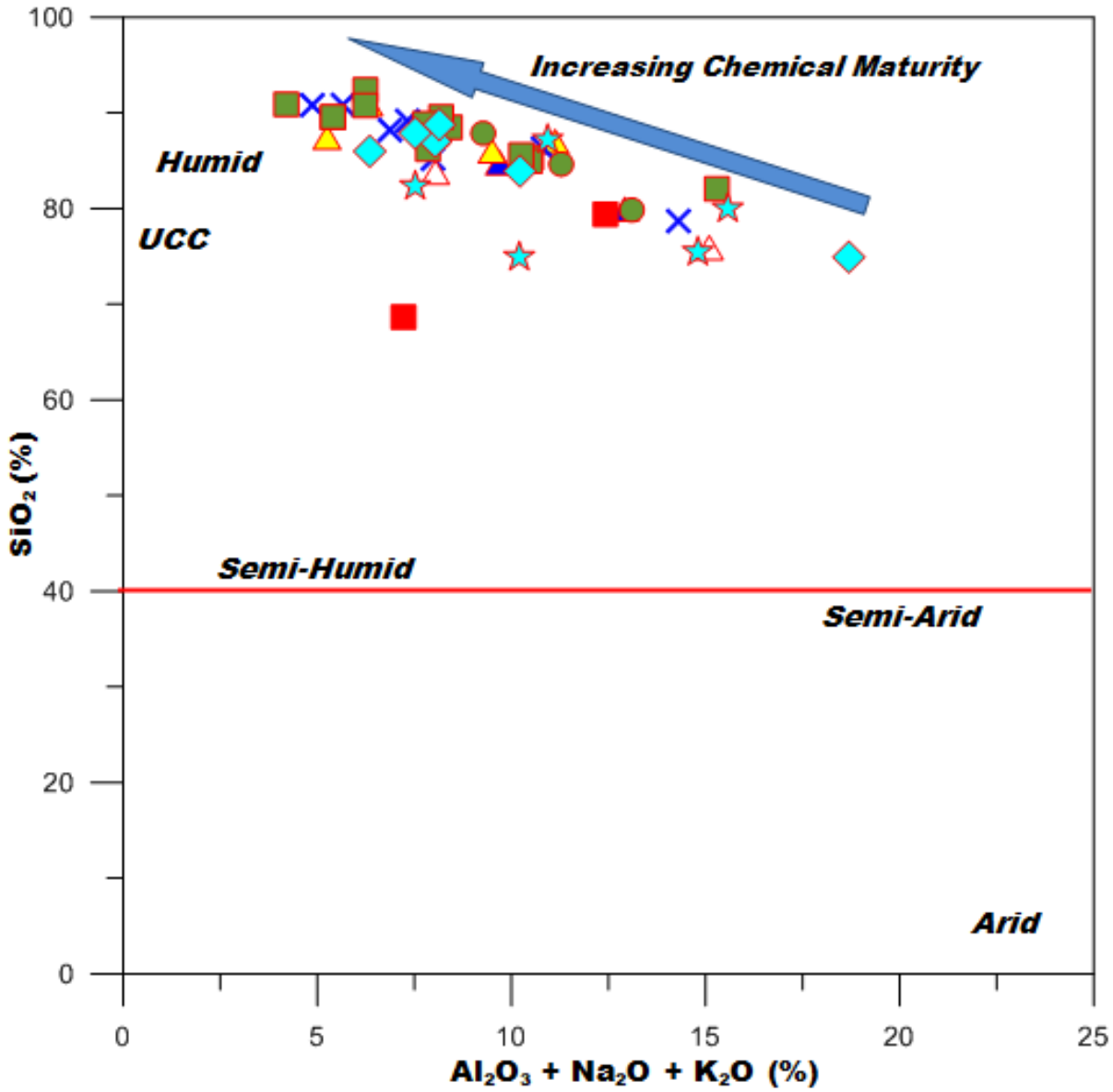


Figure 5.26: Bivariate Paleoclimate plot using SiO_2 (%) versus (Al_2O_3+K_2O+Na_2O) (%) after Cox *et al.* (1995) for the studied Northern Bida Basin sandstone.

5.5.2.3 Mineralogical Composition Evidence

Mineralogical characteristics of the analyzed sediments from the south-eastern, central and northern parts indicate a continental environment during deposition of sedimentary rocks. The results presented in tables 4.5a-4.5c and figures I-XII (Appendix VII) reveals nearly similar mineralogical compositions for the studied sediments. Generally, all the studied samples are dominated by kaolinite, mica varieties and quartz which suggest derivation of the sediments from granitic and gneissic terrain. High kaolinite content indicates that the sediments were derived from acidic igneous rocks (granite) that have been subjected to chemical weathering under warm, humid and wet climate at the source area during deposition (Dapples, 1972). The prevalence of kaolinite indicates continental weathering conditions in non-marine environment (Lonnie, 1982). Chamley (1989) suggested that dominance of kaolinite may suggest diagenetic impact on evidence of sufficient indurations. Therefore, presence of the kaolinite throughout the stratigraphic sequences is due to a stable environment within the prevalence of warm, humid and wet climate.

5.5.2.4 Zircon Morphology and Typology Evidence as Paleoclimate Indicator

Heavy mineral assemblages in sandstones retain fundamental provenance information despite the complex overprinting processes that affect their distribution (Morton and Hallsworth, 1999). Analysis of such high density accessory detrital minerals of sandstones offers a high-resolution approach to determination of sandstone provenance (Morton and Hallsworth, 1999; Pettijohn *et al*., 1972). Zircon is a common accessory mineral in igneous rocks (Heaman *et al*., 1990; Deer *et al.*, 1991; Hoskin and Schaltegger, 2003) and due to its chemical and physical durability, therefore, very useful to unravel the formation history of magmatic rocks (Corfu *et al*., 2003).

Zircon typology is based upon the relative abundance of prisms and pyramids (Pupin, 1980). Crystal forms have been divided into 64 main subtypes, corresponding to a unique combination of these crystal faces. The typology study of zircon populations is an extremely valuable tool, because zircons that have been reworked in a sedimentary deposit display typologies that make it possible to identify the different igneous rock-types present in the source region (Dabard *et al*., 1996). Early systematic investigations of zircon habits and their relation to petrogenesis were carried out by Poldervaart (1956), Frasl (1963) and Hoppe (1963). These studies have shown that the morphology of zircon varies and obviously owns a petrogenetic significance.

Pupin (1980) introduced a zircon typology diagram (Figure 5.27a) for granitic rocks that forms the basis of a genetic classification and divided into three major types: granites of crustal or mainly crustal origin (orogenic granites), granites of crustal with mantle origin, hybrid granites (orogenic granites) and granites of mantle or mainly mantle origin (anorogenic granites). This scheme provides a better visualization of the zircon typology grid where I-type granites are characterized by a predominance of zircon crystals with flat pyramids {101} whereas S-type granites mainly have zircon crystals with steep pyramids {211} (Pupin, 1980; Schermaier *et al*., 1992; Benisek and Finger, 1993; Sturm, 1999; Belousova *et al*., 2006; Köksal *et al*., 2008).

In this study, detrital zircon populations from two lithological sections belonging to Enagi (Agbonna ridge) and Bida (Dokko ridge) formations were analyzed for morphological characteristics in order to provide an overview of the variety of textural relations observed in zircon and their links to particular rock forming and modifying processes, hence to decipher the history and evolution of a rock.

The observed zircons belong to subpopulations with well-developed pyramid {101} and two prisms {100} - {110} that fall in the subtypes P1-P5 of zircon morphological types of Pupin (1980) classification. Internal morphological study allowed the identification of different types of zircon; flat, prismatic (short, long and acicular) and lamellar zircons. The prismatic zircons revealed an inner zone surrounded by a well-developed magmatic oscillatory zoning whereas lamellar zircons have very homogeneous crystals devoid of cores and showing generally a faint zoning with dominant oscillatory internal structures. Some zircons have cores, which could correspond to an earlier magmatic crystallization according to Pidgeon (1992). Some are also characterized by an external well-developed magmatic oscillatory zoning, which is interpreted as typical of magmatic zoning. Xenocrystic cores were observed especially among the fine sub-facies and this occurrence is a common feature of many igneous rocks (Figure 5.27b). Metamictization were also observed in some zircon and this characterizes generally very good preservation of zircon in exhumed lower crustal rocks according to Rudnick and Williams (1987), Hanchar and Rudnick (1995).

Some zircons that are surrounded by a weakly zoned outer rim are interpreted to have formed by recrystallization of the primary grown during the cooling of the granite according to Pidgeon *et al*. (1998). The observation of the two morphological types on the typology diagram, coupled with the external characteristics of zircon grains seems to indicate a supply probably from two main sources therefore, suggesting a possible mixing from two igneous source materials (Adepoju *et al*., 2019b). The internal structures revealed by SEM (BSE-CL) images are very similar and present typical magmatic patterns.

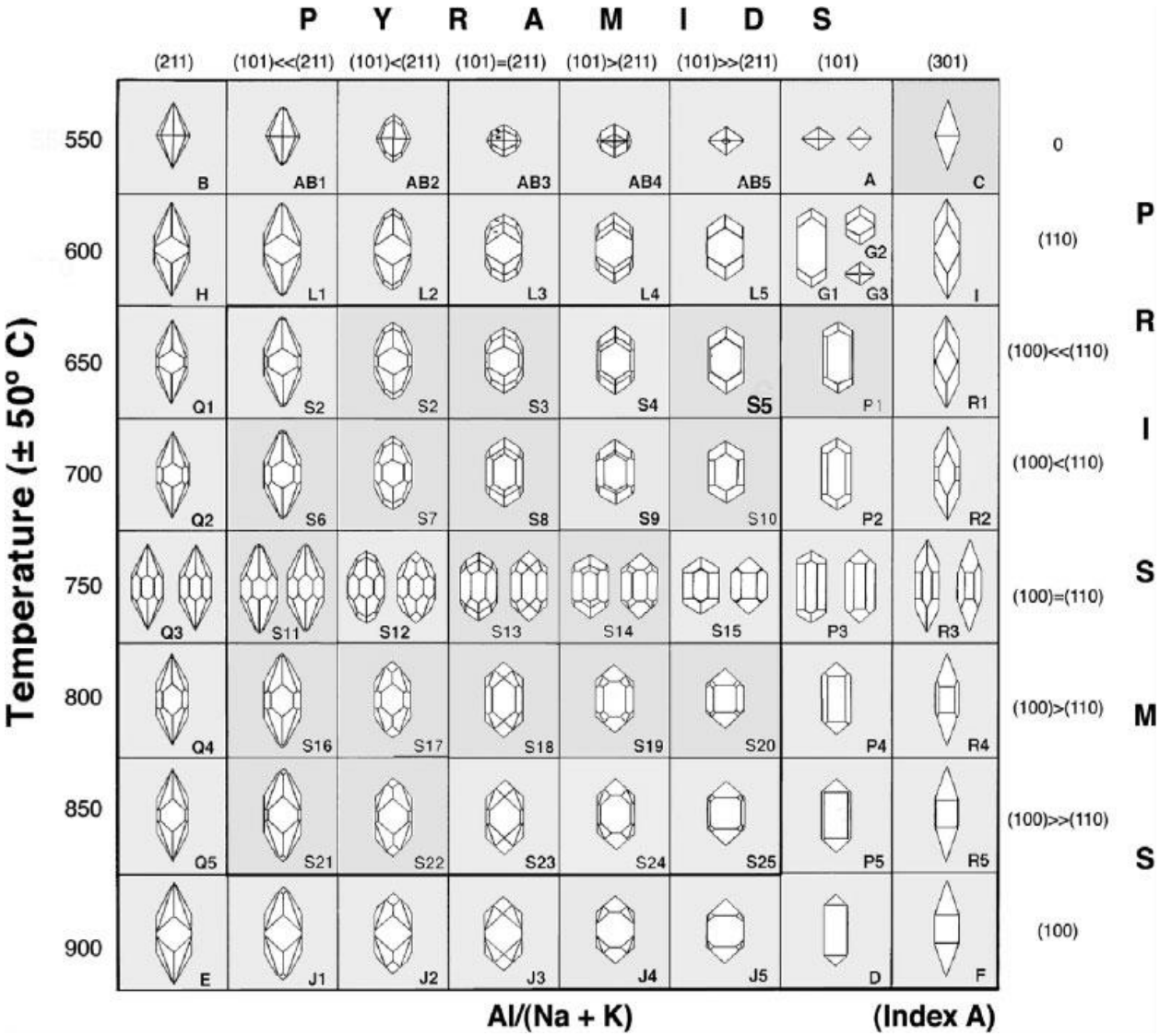


Figure 5.27a: Zircon typological classification and corresponding geothermometric scale proposed by Pupin (1980). Index A reflects the Al/alkali ratio, controlling the development of zircon pyramids, whereas temperature affects the development of different zircon prisms.

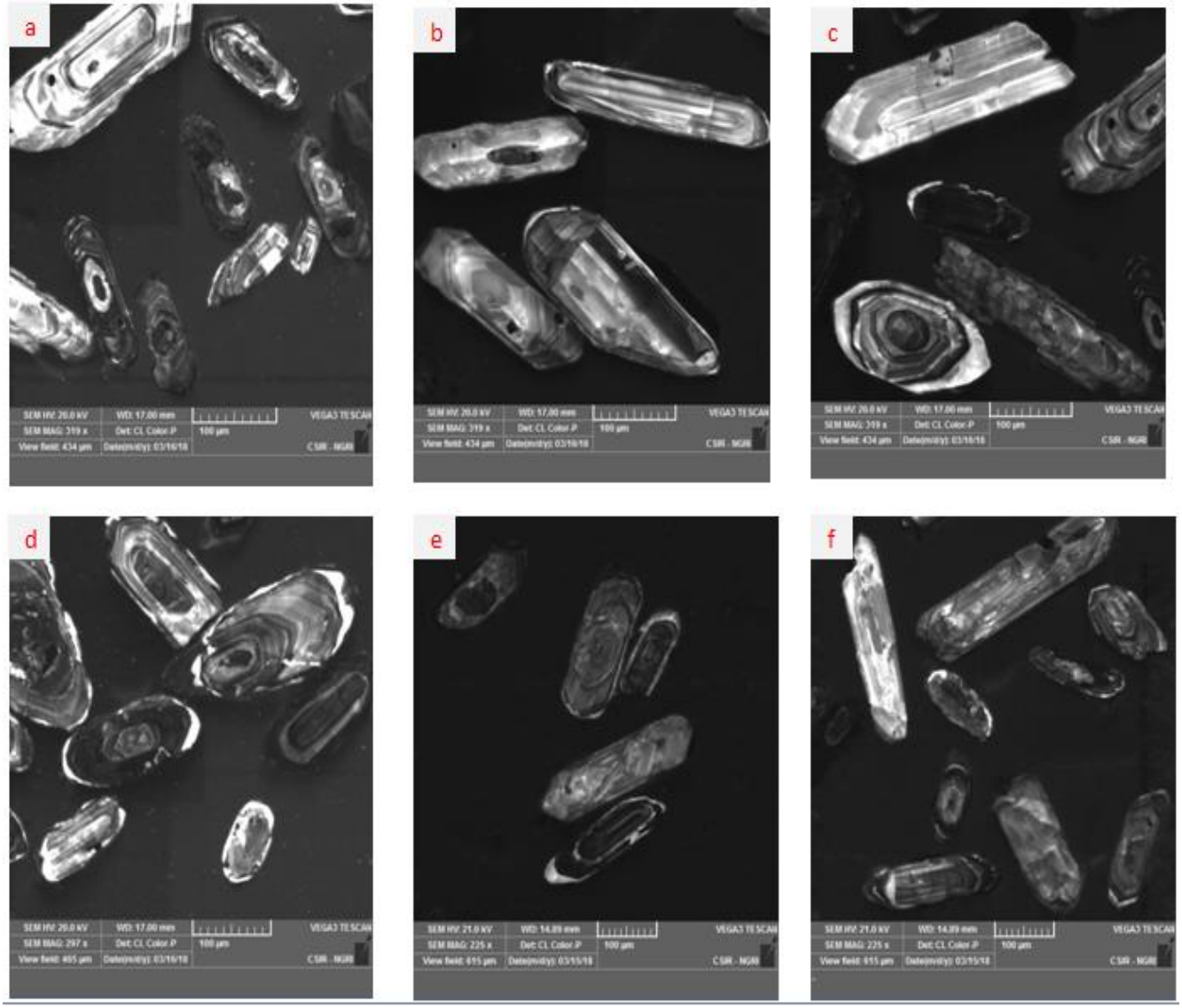


Figure 5.27b: CL images showing representative, typology and assemblage of subhedral and euhedral detrital, microsteps reflecting successive overgrowth zones in zircon minerals of the Northern Bida Basin sandstone.

CHAPTER SIX

CONCLUSIONS AND RECOMMENDATIONS

6.1 Conclusions

A number of Cretaceous (Campanian-Maastrichtian) sediment exposures made up of conglomerates, sandstones, siltstone and claystones are found throughout the northern part of Bida Basin. The present study of the provenance, tectono-sedimentary evolution, depositional and diagenetic history of the sediments within study area investigated the facies associations, textural and mineralogical composition, inorganic bulk elemental composition, zircon cathodololuminescence and scanning electron microscopy (SEM) with backscattered electron microscopy (BSEM) analysis have led to the following conclusions:

1. Textural analysis indicate a river deposited sediments with an overall decrease in grain size from the southeastern and southwestern towards the central and northern part of the study area which imply main southwestern with minor southeastern sediments source. Paleocurrent data also indicate a major flow towards northeastern and eastern directions with minor northwestern directions.

2. Sedimentological studies identified ten sub-facies, five facies associations, six architectural elements and four sandbody geometry that occurred in a predictable order within the individual fining and coarsening-upward cycles and interpreted as fluvial to shallow marine environments. The coarse (conglomerates and sandstones) sub-facies which are most frequent in the eastern and south-eastern part of the study area is interpreted as high energy braided system with low sinuosity channels and are typical of the Bida Formation. The lateral facies changes were recorded in the central to northern parts of the study area as the channel sandstones of higher energy, low sinuosity passes to braided river of less

energy but higher sinuosity (overbank fines of claystone, siltstone and silty-claystone facies).

3. Predominance of angular to sub-angular detrital grains in the south-western part suggest contemporary derivation from primary sources and less textural maturity while sub-angular to sub-rounded with minor rounded grains found in central and northern parts indicate a long sedimentary history and more textural maturity. Variations in quartz abundance among the detrital framework with monocrystalline/polycrystalline ratio and calculated HMI suggest sediment compositional and mineralogical maturity in the eastern and southwestern parts than central and northern parts of the study area.

4. Multivariate statistical methods of factor and principal component analysis methods identified the main underlying factors controlling major, trace and rare earth elements that influence the weathering, provenance and diagenetic processes which are prevalence in the environment.

5. Petrofacies analysis shows quartzarenite to sublitharenite while geochemical classification as confirmed the quartz rich for the studied sediments. Petrographic plots; Qt-F-Lt, Qm-F-Lt and Qt-F-L with geochemical data; Al_2O_3/TiO_2, SiO_2/Al_2O_3, K_2O/Al_2O_3, Zr, Nb, Th, La, Sc, Co, La/Th, La/Co, Th/Co, La/Sc, Th/Sc, Cr/Th, Th/Co Ba/Rb, Zr/Nb, Zr/Hf, Zr/Th and discriminant plots; $\log(K_2O/Na_2O)$ versus SiO_2, TiO_2 versus (Fe_2O_3+MgO), Al_2O_3/SiO_2 versus (Fe_2O_3+MgO), $SiO_2/20-(K_2O+Na_2O)-(TiO_2+Fe_2O_3+MgO)$, La/Y versus Sc/Cr, La-Th-Sc and Th-Sc-Zr/10 with values similar to the published values (UCC and PAAS) reveal a felsic source rocks in a tectonically stable passive continental margin within craton interior/continental block to recycled orogeny provenance.

6. High chemical index of alteration (CIA= 71.73-99.68), plagioclase index of alteration (PIA= 92.33-99.76), chemical index of weathering (CIW= 93.90-99.76), chemical proxy for alteration (CPA= 97.74-99.90) with low weathering index of Parker (WIP= 0.16-27.34) compared to UCC and PAAS values imply that the source area was affected by intensive chemical weathering and therefore indicate chemical maturity.

7. The main diagenetic stages identified: cementation, physical and chemical compaction, dissolution and replacement of minerals with grain-deformation and fracturing have affected the studied sandstones. Silica, iron oxide and clay are the main cementing materials and have occluded the pore spaces in varying proportions during compaction and cementation, although strong evidences of dissolution/alteration of feldspar and rock fragments have enhanced porosity.

6.2 Recommendations

In the light of this study, assessing subsurface samples in the northern Bida Basin is recommended so that further useful petrographic work would include study of a suite of more deeply-buried samples to investigate the stages of increased cement development noted in the current study and to document the expected variability of reservoir properties at advanced stages of burial.

Other data such as seismic and core samples are required to complement the surface data for determining the degree of confidence in the geologic model and interpretation of the sediments in Northern Bida Basin. It will also help better in understanding the sandstone porosity evolution and reservoir quality as a guide for future exploration and production of groundwater and hydrocarbon reservoirs in the Basin.

REFERENCES

Abimbola, A.F., 1997. Petrographic and paragenetic studies of the Agbaja Ironstone Formation, Nupe Basin, Nigeria. Journal of African Earth Sciences, 25, 169-181.

Abimbola, A.F., Badejoko, T.A., Elueze, A.A. and Akande, S.O., 1995.4. The Agbaja Ironstone Formation, Nupe Basin, Nigeria – A product of replacement of a kaolinite precursor. Global Journal of Pure and Applied Science, 5, 375-384.

Adeleye, D.R. and Dessauvagie, T.F.J., 1972. Stratigraphy of the Niger Embayment, near Bida, Nigeria: In: African Geology, Dessauvagie, T.F.J. and Whiteman, A.J., (ed.), University of Ibadan Press, Ibadan, p. 181–185.

Adeleye, D.R., 1972. Cretaceous Sediments from the Shores of Lake Kainji, Nigeria. Journal of Mining and Geology, 7, 5-12.

Adeleye, D.R., 1973. Origin of Ironstones, an example from the Middle Niger Basin, Nigeria. Journal of Sedimentary Petrology, 43(3), 709-727.

Adeleye, D.R., 1974. Sedimentology of the Fluvial Bida Sandstones (Cretaceous), Nigeria. Sedimentary Geology, 112, 1-24.

Adeleye, D.R., 1989. The Geology of the Middle Niger Basin: In: Geology of Nigeria, Kogbe, C.A., (ed.), Geology of Nigeria, 2nd edition, Elizabethan Publ. Co., Lagos, p. 283-287.

Adeniran, B.V., 1991. Maastrichtian tidal flat sequences from the northern Anambra Basin, Southern Nigeria. Nigerian Association Petroleum Explorationists Bulletin, 6, 56–65.

Adeniyi, J. O., 1984. Ground total magnetic intensity in parts of the Nupe Basin and the adjacent basement complex, Niger State, Nigeria. Nigerian Journal of Applied Sciences, 3, 67–78

Adepoju, S.A. Ojo, O.J. and Akande, S.O, 2018a. Lithofacies, Pebble Morphogenesis and Provenance of the Bida Formation, Northern Bida Sub-Basin, North-Central Nigeria, FUOYE Journal of Pure and Applied Sciences, FJPAS, vol. 3(2).

Adepoju, S.A. Ojo, O.J. and Akande, S.O, 2018b. Petrographic study of Bida Formation, Northern Bida Sub-Basin, Nigeria: Implications for Diagenetic History and Reservoir Quality, 36th NAPE Annual International Conference Book of Abstracts, p. 152.

Adepoju, S.A. Ojo, O.J., Akande, S.O. and Sreenivas, B., 2019a. Petrological Studies of the Cretaceous sedimentary rocks in the Northern Bida Basin: Implications for Provenance and Diagenesis. Accepted for presentation at the Young Earth Scientist

Network German Chapter, Rocking Earth's Future, Freie Universität Berlin, Germany, 9-13, September, 2015.4.

Adepoju, S.A. Ojo, O.J., Akande, S.O. and Sreenivas, B., 2019b. Provenance and Tectonic Settings of the Cretaceous Clastic Rocks in the Northern Bida Basin, North-Central Nigeria: Constrain from Geochemistry, Detrital Zircon Morphology and Typology. Accepted for presentation at the Goldschmidt Annual, International Conference on Geochemistry and related subjects, organized by the European Association of Geochemistry and the Geochemical Society, Barcelona, Spain, 18-23, August, 2015.4.

Agyingi, C.M., 1991. Geology of upper Cretaceous rocks in the eastern Bida Basin, Central Nigeria: Unpublished Ph.D Thesis, University of Ibadan, Nigeria, 501 pp.

Agyingi, C.M., 1993. Palynological evidence for a late Cretaceous age for Patti Formation, eastern Bida Basin, Nigeria. Journal of African Earth Sciences, 17, 513–523.

Akande, S.O. and Erdtmann, B.D., 1998. Burial Metamorphism (Thermal Maturation) in Cretaceous sediments of the southern Benue Trough and Anambra Basin, Nigeria: American Association of Petroleum Geologists Bulletin, 82, p. 1191-1205.

Akande, S.O. and Ojo, O.J., 2002. Organic Petrology and Rock-eval Studies on Source Rock Facies of the Campano–Maastrichtian Patti Formation, Southern Bida Basin, Nigeria. Nigerian Association Petroleum Explorationists, 16, 22-38.

Akande, S.O., Ojo, O.J., Erdtmann, B.D. and Hetenyi, M., 2004. Palaeoenvironments, Organic Petrology and Rock-eval Studies on Source Rock Facies of the Lower Maastrichtian Patti Formation, Southern Bida Basin, Nigeria. Journal of African Earth Sciences, 41, 394-405.

Akhtar, K. and Ahmad, A.H.M., 1991. Single cycle cratonic quartzarenites produced by tropical weathering: the Nimar Sandstone (Lower Cretaceous), Narmada Basin, India. Sedimentary Geology, 71, 23-32.

Alam, M., Alam, M. M., Curray, J. R., Chowdhury, M. L. R., and Gani, M. R., 2003, An overview of the sedimentary geology of the Bengal Basin in relation to the regional tectonic framework and basin-fill history: Sedimentary Geology, 155, 179-208.

Alvarez, N.O. and Roser, B.P., 2007. Geochemistry of black shales from the Lower Cretaceous Paja Formation, Eastern Cordillera, Colombia: source weathering, provenance and tectonic setting. Journal of South America Earth Sciences, 23 (4), 271–285.4.

Amireh, B.S., 1997. Sedimentology and paleogeography of the regressive–transgressive Kurnub Group (Early Cretaceous) of Jordan. Sedimentary Geology, 112, 69–88.

Armstrong-Altrin, J.S., 2009. Provenance of sands from Cazones, Acapulco, and Bahía Kinobeaches, México. Revista Mexicana de Ciencias Geológicas, 26, 764–782.

Armstrong-Altrin, J.S., Lee, Y.I., Verma, S.P. and Ramasamy, S., 2004. Geochemistry of sandstones from the upper Miocene Kudankulam Formation, southern India: Implications for provenance, weathering, and tectonic setting. Journal of Sedimentary Research, 74, 285-297.

Asiedu, D.K., Dampare, S.B., Sakyi, P.A., Banoeng-Yakubo, B., Osae, S., Nyarko, B.J.B. and Manu, J., 2004. Geochemistry of Paleoproterozoic metasedimentary rocks from the Birim diamontiferous field, southern Ghana: implications for provenance and crustal evolution at the Archean-Proterozoic boundary. Geochemical Journal, 38, 215–228.

Bandopadhyay, P.C. and Ghosh, B., 2014. Provenance analysis of the Oligocene turbidites (Andaman Flysch), South Andaman Island: a geochemical approach. Journal of Earth System Science, 124, 1019-1037.

Basu, A., 1975. Petrology of Holocene fluvial sand derived from plutonic source rocks: Implications to paleoclimate interpretation. Journal of Sedimentary Petrology, 46, 694-705.4.

Basu, A., 1984. Reading provenance from detrital quartz, *In* Zuffa, G.G., ed., Provenance of Arenites: Dordrecht, NATO-ASI, Reidel, 231-248.

Basu, A., Young, S.W. and Suttner, L. J., 1974. Re-evaluation of the use of undulatory extinction and polycrystallinity in detrital quartz for provenance interpretation. Journal of Sedimentary Petrology, 4, 873-882.

Belousova, E.A., Griffin, W.L. and Pearson, N.J., 1998. Trace element composition and cathodoluminescence properties of southern African kimberlitic zircons. Mineral Magazine, 62, 355-366

Benisek, A. and Finger, F., 1993. Factors controlling the development of prism faces in granite zircons: A microprobe study. Contributions to Mineralogy and Petrology, 114, 441-451.

Benkhelil, J., 1989. The origin and evolution of the Cretaceous Benue Trough, Nigeria. Journal of African Earth Sciences, 8, 51–282

Bhatia, M. R., 1983. Plate tectonics and geochemical composition of sandstones. The Journal of Geology, 91, 611-627.

Bhatia, M.R. and Crook, K.A.W., 1986. Trace element characteristics of graywackes and tectonic setting discrimination of sedimentary basins. Contributions to Mineralogy and Petrology 92, 181–193.

Bhatia, M.R. and Taylor, S.R., 1981. Trace-element geochemistry and sedimentary provinces: a study from the Tasman Geosyncline, Australia. Chemical Geology, 33, 115-124.

Bhatia, M.R., 1985. Rare earth element geochemistry of Australian Paleozoic graywackes and mudrocks: Provenance and tectonic control. Sedimentary Geology, 45, 97–113.

Bjorlykke, K., 1974. Geochemical and mineralogical influence of Ordovician island arcs on epicontinental clastic sedimentation: a study of Lower Palaeozoic sedimentation in the Oslo region, Norway. Sedimentology, 21(2), 251-272.

Blatt, H., Middleton, G. and Murray, R., 1980. Origin of Sedimentary Rocks. Prentice-Hall Inc., Englewood Cliffs, 782p.

Blott, S. J. and Pye, K., 2012. Particle size scales and classification of sediment types based on particle size distributions; Review and recommended procedures. Sedimentology, 1-25.

Blum, M.D. and Aslan, A., 2006, Signatures of climate vs. sea-level change within incised valley-fill successions: Quaternary examples from the Texas Gulf Coast. Sedimentary Geology, 190, 177–211.

Bock, B., McLennan, S.M. and Hanson, G.N., 1998. Geochemistry and provenance of the Middle Ordovician Austin Glen Member (Normanskill Formation) and the Taconian Orogeny in New England. Journal of Sedimentology, 45, 635–655.

Boynton, W.V., 1984. Cosmochemistry of the rare earth elements: meteorite studies. In: Henderson, P. (Ed.) Rare Earth Element Geochemistry. Elsevier Science, 63–114.

Braide, S. P., 1992a. Syntectonic Fluvial Sedimentation in the Central Bida Basin. Journal of Mining and Geology, 28, 55-64.

Braide, S. P., 1992b. Alluvial Fan Depositional Model in the Northern Bida Basin. Journal of Mining and Geology, 28, 65-73.

Cant, D. J. and Walker, R.G., 1978. Fluvial process and facies sequences in sandy braided South Saskatechewan River, Canada: Sedimentology, 25, 625-648.

Carozzi, A.V., 1993. Sedimentary petrography: Englewood Cliffs, New Jersey, PTR Prentice Hall, 263 p.

Chamley, H., 1989. Clay Sedimentology: Berlin (Springer-Verlag).Hardy and Tucker.

Chaodong, W., Changsong, L., Yanping, S. and Xue, F., 2004. Computation of Sandstone and heavy minerals implies the provenance of Kuqa Depression in Jurassic, Tarim basin, China – progress in Natural Science, 15(7), 633 – 640.

Cingolani, C.A., Manassero, M. and Abre, P., 2003. Composition, provenance, and tectonic setting of Ordovician siliciclastic rocks in the San Rafael block: Southern extension of the Precordillera crustal fragment, Argentina. Journal of South American Earth Sciences, 16(1), 91-105.

Collinson, J.D., 1970. Bedformsof the Tana River.Norway. Geografiska Annaler 52A, 31–56.

Collinson, J.D., 1996. Alluvial sediments. In: Reading, H.G. (ed.). Sedimentary Environments: Processes, Facies and Stratigraphy. London, Blackswell Scientific Publications. pp. 37-82.

Conceptian, R.A.B., Dimalanta, C.B., Yumul, G.P., Faustino-Eslava, D.V., Queano, K.L., Tamayo, R.A. and Imai, A., 2012. Petrography, geochemistry, and tectonics of a rifted fragment of Mainland Asia: evidence for the Lasala Formation, Mindoro Island, Philippines. International Journal of Earth Sciences, 101, 273-290.

Condie, K.C. and Wronkiewicz, D.J., 1990. A new look at the Archean-Proterozoic boundary: Sediments and the tectonic setting constraint. In: S.M. Naqvi (Editor), Precambrian Continental Crust and Its Economic Resources. Elsevier, Amsterdam, 61-84.

Condie, K.C., 1993. Chemical composition and evolution of the upper continental crust: contrasting results from surface samples and shales. Chemical Geology, 104, 1–37.

Condie, K.C., Boryta, M.D., Liu, J. and Quian, X., 1992. The origin of khondalites: geochemical evidence from the Archean to Early Proterozoic granulitic belt in the North China Craton. Precambrian Research, 59(3-4), 207-223.

Condie, K.C., Lee, D. and Farmer, L., 2001. Tectonic setting and provenance of the Neoproterozoic Uinta Mountain and Big Cootonwood groups, northern Utah: constraints from geochemistry, Nd isotopes, and detrital modes. Sedimentary Geology, 141-142, 443-464.

Corfu, F., Hanchar, J.M. and Kinny, P., 2003. Atlas of zircon textures. Reviews in Mineralogy and Geochemistry, 53, 468–500.

Cox, R. and Lowe, D.R., 1994. A conceptual review of regional-scale controls on the composition of clastic sediment and the co-evolution of continental blocks and their sedimentary cover. Journal of Sedimentary Research, 65, 1–12.

Cox, R., Lowe, D.R. and Cullers, R.L., 1994. The influence of sediment recycling and basement composition on evolution of mudrock chemistry in the southwestern United States. Geochimica et Cosmochimica Acta, 59 (14), 2919-2940.

Crook, K.A.W., 1974. Lithogenesis and geotectonics: the significance of compositional variation in flysch arenites (graywackes). In: Dott Jr., R.H., Shaver, R.H. (Eds.), Modern and Ancient Geosynclinal Sedimentation, SEPM Special Publication, 19, 304–310.

Cullers, R.L. and Graf, J., 1983. Rare earth elements in igneous rocks of the continental crust: intermediate and silicic rocks, or petrogenesis. Rare-Earth Geochemistry, Elsevier, Amsterdam, 275-312.

Cullers, R.L. and Podkovyrov, V.N., 2000. Geochemistry of the Mesoproterozoic Lakhanda shales in southeastern Yakutia, Russia: implications for mineralogical and provenance control, and recycling. Precambrian Research, 104, 77–93.

Cullers, R.L., 1994a. The chemical signature of source rocks in size fractions of Holocene stream sediment derived from metamorphic rocks in the wet mountains region, Colorado, USA. Chemical Geology, 113, 327-343.

Cullers, R.L., 1994b. The controls on the major and trace element evolution of shales, siltstones and sandstones of Ordovician to Tertiary age in the Wet Mountain region, Colorado, U.S.A. Chemical Geology, 123(1-4), 107-131.

Cullers, R.L., 2000. The geochemistry of shales, siltstones and sandstones of Pennsylvanian-Permianage, Colorado, U.S.A.: implications for provenance and metamorphic studies. Lithos, 51, 181–203.

Cullers, R.L., 2002. Implications of elemental concentrations for provenance, redox conditions, and metamorphic studies of shales and limestones near Pueblo, CO, USA. Chemical Geology, 191, 305-327.

Cullers, R.L., Barrett, T., Carlson, R. and Robinson, B., 1987. Rare-Earth element and mineralogic changes in Holocene soil and stream sediment: a case study in the wet mountains region, Colorado, USA. Chemical Geology, 63, 275–297.

Cullers, R.L., Basu, A. and Suttner, L.J., 1988. Geochemical signature of provenance in sand-size material in soils and stream sediments near the Tobacco Root batholith, Montana, USA. Chemical Geology, 70, 335–348.

Cullers, R.L., Chaudhuri, S., Arnold, B., Lee, M., Wolf, C.W., 1974. Rare earth distributions in clay minerals and in clay-sized fraction of the lower Permian Havensville and Eskridge shales of Kansas and Oklahoma. Geochim. Cosmochim. Acta 39, 1691–1703.

Dabard, M.P., Loi, A. and Peucat, J.J., 1996. Zircon typology combined with Sm-Nd whole-rock isotope analysis to study Brioverian sediments from the American Massif. Journal of Sedimentary Geology, 101, 243-260.

Dapples, E.C., 1972. Some concepts of Cementation and Lithification of Sandstones. Bull. American Association of Petroleum Geologist, 56, p. 3-24.

Datta, B., 2005, Provenance, tectonics and palaeoclimate of Proterozoic Chandarpur sandstones, Chattisgarh basin: a petrographic view: Journal of Earth System Science, 114, 227–244.

Deer, W.A., Howie, A. and Zussman, J., 1991. An Introduction to the Rock-forming Minerals. Longman, London, 528p.

DePaolo, D.J., 1988, Neodymium isotope geochemistry. Springer, Berlin, 187p.

Descourvieres, C., Douglas, G., Leyland, L., Hartog, N. and Prommer, H., 2011. Geochemical reconstruction of the provenance, weathering and deposition of detrital-dominated sediments in the Perth Basin: the Cretaceous Leederville Formation, south-west Australia. Sedimentary Geology, 236, 62–75.

Dewey, J.F. and Mange, M.A., 1999. Petrography of Ordovician and Silurian sediments in the western Irish Caledonides: tracers of a short-lived Ordovician continent-arc collision orogeny and the evolution of the Laurentian Appalachian–Caledonian margin. In: Mac Niocaill, C., Ryan, P.D. (Eds.), Continental Tectonics: Geological Society, London, Special Publications, 164, 55–107.

Dia, A., Dupre, B., Gariepy C. and Allbcre, C.J., 1990. Sm-Nd and trace-element characterization of shales from tie Abitibi Belt, Labrador Trough, and Appalachian Belt: Consequences for crustal evolution through time. Canadian Journal of Earth Sciences, 27, 758-765.

Dickinson, W.R. and Rich, E.I., 1972. Petrologic intervals and petrofacies in the Great Valley sequence, Sacramento Valley, California. Geological Society of America Bulletin, 83, 3007–3024.

Dickinson, W.R. and Suczek, C.A., 1979. Plate tectonics and sandstone compositions. American Association of Petroleum Geologists Bulletin, 63, 2164–2182.

Dickinson, W.R. and Valloni, R., 1980. Plate settings and provenance of sands in modern ocean basins. Geology, 8, 82– 85.

Dickinson, W.R., 1985. Interpreting provenance relations from detrital modes of sandstones. In: Zuffa, G.G. (Ed.), Provenance of Arenites. NATO-ASI Series, 148. Reidel Publishing Company, Dordrecht, 333–361.

Dickinson, W.R., Beard, L.S., Brakenridge, G.R., Evjavec, J.L., Ferguson, R.C., Inman, K.F., Knepp, R.A., Lindberg, F.A. and Ryberg, P.T., 1983. Provenance of North American Phanerozoic sandstones in relation to tectonic setting. Geological Society of America Bulletin, 94, 222–234.

Dill, H., 1985. Metallogenesis of early Paleozoic graptolite shales from the Graefenthal Horst (northern Bavaria-Federal Republic of Germany). Economic Geology, 81, 889-903.

Dill, H., Teschner, M. and Wehner H., 1988. Petrography, inorganic and organic geochemistry of Lower Permian Carbonaceous fan sequences ("Brandschiefer Series"), Federal Republic of Germany: constraints to their paleogeography and assessment of their source rock potential. Chemical Geology, 67, 307-324.

Dobkins, J.E. and Folk, R.L. (1970). Shape development on Tahiti-Nui. J. of Sed. Petr., 40, 1167-1203.

Dypvik, H., 1984. Geochemical compositions and depositional conditions of Upper Jurassic and Lower Cretaceous Yorkshire clays, England. Geological Magazine, 121(5), 489-504.

Eberth, D.A., 1995. Origin and significance of mud-filled incised valleys (Upper Cretaceous) in southern Alberta, Canada. Sedimentology, 43, 459–477.

El-Enen, M.M.A., Abu-Alam, T.S., Whitehouse, M.J., Ali, K.A. and Okrusch, M., 2015. PeT path and timing of crustal thickening during amalgamation of East and West Gondwana: a case study from the Hafafit Metamorphic Complex, Eastern Desert of Egypt. Lithos.

Eriksson, K.A., Taylor, S.R. and Korsch, R.J., 1992. Geochemistry of 1.8–1.67 Ga mudstones and siltstones from the Mount Isa inlier, Queensland, Australia: Provenance and tectonic implications. Geochimica et Cosmochimica Acta, 56, 899–905.4.

Ernst, W., 1970. Geochemical facies analysis: Methods in geochemistry and geophysics. Elsevier, Amsterdam, 152p.

Falconer, J.D., 1911. The geology and geography of Northern Nigeria. Macmillan, London, 135 p.

Faundez, V., Herve, F. and Lacassie, J.P., 2002. Provenance and depositional setting of pre-Late Jurassic turbidite complexes in Patagonia, Chile. New Zealand Journal of Geology and Geophysics, 45, 411-424.

Fedo, C.M., Eriksson, K.A. and Krogstad, E.J., 1995. Geochemistry of shales from the Archean (3.0 Ga) Buhwa Greenstone Belt, Zimbabwe: implications for provenance and source-area weathering. Geochimica et Cosmochimica Acta, 60, 1751–1763.

Fedo, C.M., Nesbitt, H.W. and Young, G.M., 1994. Unraveling the effects of potassium metasomatism in sedimentary rocks and paleosols, with implications for paleoweathering conditions and provenance. Geology, 23, 921–924.

Feng, R. and Kerrich, R., 1990. Geochemistry of fine grained clastic sediments in the Archaean Abitibi greenstone belt, Canada: implication for provenance and tectonic setting. Geochimica et Cosmochimica Acta, 54, 1061–1081.

Fielding, C.R. and Webb, J.A., 1995. Facies and cyclicity of the Late Permian Bainmedart coal measures in the northern Prince Charles Mountains, MacRobertson Land, Antarctica. Sedimentology, 43, 295–322.

Floyd, P.A. and Leveridge, B.E., 1987. Tectonic environment of the Devonian Gramscatho basin, south Cornwall: framework mode and geochemical evidence from turbiditic sandstones. Journal of the Geological Society, 144 (4), 531-542.

Floyd, P.A., Franke, W., Shail, R. and Dörr, W., 1990. Provenance and depositional environment of Rhenohercynian synorgenic greywacke from the Giessen nappe, Germany. Geologische Rundschau, 79, 611-625.

Floyd, P.A., Winchester, J.A. and Park, R.G., 1989. Geochemistry and tectonic setting of Lewisian clastic metasediments from the Early Proterozoic Loch Maree Group of Gairloch, NW Scotland. Precambrian Research, 45, 203–214.

Folk, L., 1980. Petrology of Sedimentary Rocks: Austin Texas, Hemphill, 182p.

Folk, R. L, 1974. Petrology of sedimentary rocks, Hemphil, Austin, TX, pp. 1-155.4.

Franzinelli, E. and Potter, P.E., 1983. Petrology, chemistry and texture of modern river sands, Amazon River system. Journal of Geology, 91, 23–35.4.

Frasl, G., 1963. Die mikroskopische Untersuchung der akzessorischen Zirkone als Routinearbeit des Kristallingeologen. Jahrbuch Geol. Bundensanst. ŽAustria. ŽWien. 106, 405–428.

Friedman, G. M., 1967. Dynamic processes and statistical parameters compared for size frequency distribution of beach and river sands. *Journal of sedimentary Petrology*, 37, 327-354.

Friend, P. F., Slater, M. J. and Williams, R. C., 1979. Vertical and lateral building of river sandstone bodies, Ebro Basin, Spain. Journal of Geological Society of London, 146, 39–45.

Friis, H. and Johannesen, F.B., 1974. Late Tertiary weathering of fluvial deposits at La°sby, Denmark. Bulletin of the Geological Society of Denmark, 23, 197–202.

Fyffe, L.R. and Pickerill, R.K., 1993. Geochemistry of Upper Cambrian-Lower Ordovician black shale along a northeastern Appalachian transect. Geol. Soc. Am. Bull. 105, 896–910.

Galán, E. and Ferrell, R.E., 2013. Genesis of Clay Minerals, In: Bergaya, F., Lagaly, G. (Eds.), Handbook of Clay Science (2nd Ed.), Part A: Fundamentals. 5, pp. 83-125.

Garver, J.I., Royce, P.R. and Smick, T.A., 1996. Chromium and Nickel in Shale of the Taconic Foreland; a Case Study for the Provenance of Fine-Grained Sediments with an Ultramafic Source. Journal of Sedimentary Research, 66, 100–106.

Gebhardt, H., 1998. Benthic foraminifera from the Maastrichtian Lower Mamu Formation near Leru (Southern Nigeria): paleoecology and paleogeographic significance. Journal of Foraminiferal Research, 28, 76–89.

Girty, G. H., Barber, R W. and Knaack, C., 1993. REE, Th, and Sc evidence for the depostional setting and source rock characteristics of the Quartz Hill Chert, Sierra Nevada, Canifonia, In: M. J. Johnsson and A. Basu, (eds.), Processes Controlling the Composition of Clastic Sediments, Geological Society of America Special Paper, 284, 109-120.

Girty, G.H., 1991. A note on the composition of plutonic clastic sand produced in different climatic belts. Journal of Sedimentary Petrology, 61, 428-433.

Glaister, R.P. and Nelson, H.W., 1974. Grain-size distributions, an aid in facies identification. Bull. Can. Pet. Geol., 22, 203-240.

Goldstein, S.L., O'Nions, R.K. and Hamilton, P.J., 1984. A Sm–Nd isotopic study of atmospheric dust particulates from major river systems. Earth and Planetary Science Letters, 70, 221–235.

Goro A.I., Salihu H.D., Jibrin B.W., Waziri N.M. and Idris-Nda A., 2014. Characterization of a Massive Sandstone Interval: Example from Doko Member of Bida Formation, Northern Bida Basin, Nigeria. Universal Journal of Geoscience 2(2): 53-61.

Gotze, J., 1998, Geochemistry and provenance of the Altendorf feldspathic sandstone in the Middle Bunter of the Thuringian basin (Germany). Chemical Geology, 150, 43-61.

Graham, S. A., Ingersoll, R. Y. and Dickinson, W. R., 1975. Common provenance for lithic grains in Carboniferous sandstones from Ouachita Mountains and Black Warrior basin. Journal of Sedimentary Petrology, 46, 620-632.

Grantham, J.H. and Velbel, M.A., 1988. The influence of climate and topography on rock fragments abundance in modern fluvial sands of the southern Blue Ridge Mountains, North Carolina. Journal of Sedimentary Petrology, 58, 219-227.

Gromet L. P., Dymek R. F., Haskin L. A., and Korotev R. L., 1984. The North American Shale Composite: Its compilation, major and trace element characteristics. Geochimica et Cosmochimica Acta, 48, 2469-2482.

Gu, XX., Liu, J.M., Zheng, M.H., Tang, J.X. and Qi, L., 2002. Provenance and tectonic setting of the Proterozoic turbidities in Hunan, South China: geochemical evidence. Journal Sediment Research, 72(3), 393–407.

Hallam, A., Grose, J.A. and Ruffell, A.H., 1991. Paleoclimatic significance of changes in clay mineralogy across the Jurassic- Cretaceous boundary in England and France. Palaeogeogr. Palaeoclimatol. Palaeoecol. 81, 173–187.

Hanchar, J.M. and Rudnick, R.L., 1994. Revealing hidden structures: the application of cathodoluminescence and backscattered electron imaging to dating zircons from lower crustal xenoliths. Lithos, 36, 289-303.

Hayashi, K., Fujisawa, H., Holland, H. and Ohmoto, H., 1997. Geochemistry of 1.9 Ga sedimentary rocks from northeastern Labrador, Canada. Geochimica et Cosmochimica Acta, 61(19), 4115-4137.

Heaman, L.M., Bowins, R. and Crocket, J., 1990. The chemical composition of igneous zircon suites: implications for geochemical tracer studies. Geochimica et Cosmochimica Acta, 54, 1597–1607.

Herron, M.M., 1988. Geochemical classifications of terrigenous sands and shales from core or log data. Journal of Sedimentary Petrology, 58, 820–825.4.

Holland, H.D., 1984. The Chemical Evolution of the Atmosphere and Oceans. Princeton University Press, Princeton, NJ, 582 p.

Hoppe, G., 1963. Die Verwendbarkeit morphologischer Erscheinungen an akzessorischen Zirkonen für petrogenetische Auswertungen. Abhandlungen der Deutschen Akademie der Wissenschaften Berlin 1, 1–131.

Hoskin, P.W.O. and Schaltegger, U., 2003. The composition of zircon and igneous and metamorphic petrogenesis. Reviews in Mineralogy and Geochemistry, 53, 27–62.

Idowu, J.O. and Enu, E.I., 1992. Petroleum Geochemistry of some Late Cretaceous Shales from the Lokoja Sandstone of the Middle Niger Basin, Nigeria. Journal African Earth Sciences, 14, 433–454.

Ingersoll, R.V. and Suczek, C.A., 1979. Petrology and provenance of Neogene sand from Nicobar and Bengal fans. DSDP sites 211 and 218. Journal of Sedimentary Petrology, 49, 1217–1228.

Ingersoll, R.V., 1978. Petrofacies and petrologic evolution of the Late Cretaceous fore-arc basin, northern and central California. Journal of Geology, 86, 335-352.

Ingersoll, R.V., Bulard, T.F., Ford, R.L., Grimn, J.P., Pickle, J.P. and Sares, S.W., 1984. The effect of grain size on detrital modes: A text of the Gazzi-Dickinson Point Counting method. Journal of Sedimentary Petrology, 54, 103–115.

Ingersoll, R.V., Graham, S.A. and Dickinson, W.R., 1994. Remnant ocean basins. In: Busby, C.J., Ingersoll, R.V. (Eds.), Tectonics of Sedimentary Basins. Blackwell, Oxford, 363–391.

Jacobson, A.D., Blum, J.D., Chamberlain, C.P., Craw, D. and Koons, P.O., 2003. Climatic and tectonic controls on chemical weathering in the New Zealand Southern Alps: Geochimica et Cosmochimica Acta, 67(1), 29–46

Jan du Chene, J., Adegoke, O. S., Adediran, S. A. and Petters, S. W., 1979. Palynology and Foraminifera of the Lokoja Sandstone (Maastrichtian), Bida Basin Nigeria: Revista Espanola de Micropaleontologia, 10(3), 379–393.

Jocelyn, J. and Pidgeon, R.T., 1974. Examples of twinning and parallel growth in zircons from some Precambrian granites and gneisses. Mineral Magazine, 39, 587-594

Johnsson, M.J., 1993. The system controlling the composition of clastic sediments. In: Johnsson, M.J., Basu, A. (Eds.), Processes Controlling the Composition of Clastic Sediments: Geological Society of America, Special Paper, 284, 1–19.

Johnsson, M.J., Stallard, R.F. and Lundberg, N., 1991. Controls on the composition of fluvial sands from a tropical weathering environment: sands of the Orinoco River drainage

basin, Venezuela and Colombia. Geological Society of America Bulletin, 103, 1622–1647.

Johnsson, M.J., Stallard, R.F., and Meade, R.H., 1988. First-cycle quartz arenites in the Orinoco River basin, Venezuela and Colombia. Journal of Geology, 96(3), 263-277.

Jones, B. and Manning, D.C., 1994. Comparison of geochemical indices used for the interpretation of paleo-redox conditions in Ancient mudstones. Chemical Geology, 111(1-4), 111-129.

Jones, M.P., 1953. Preliminary investigation of the occurrence of Columbite in the Afu Hills Younger Granite Complex, Geological Survey of Nigeria, Unpublished Report, No. 1114

Kalsbeek, F. and Frei, R., 2010. Geochemistry of Precambrian sedimentary rocks used to solve stratigraphical problems: an example from the Neoproterozoic Volta basin, Ghana. Precambrian Research, 176, 66–74.

Kennedy, W.Q., 1965. The influence of basement structure on the evolution of the coastal (Mesozoic and Tertiary) basins. In: Recent Basins around Africa, Proceedings of the Institute of Petroleum Geologists Society, London p. 35–47.

Kermani, S., Boutiba, M., Boutaleb, A. and Fagel, N., 2015. Distribution of heavy and clay minerals in coastal sediment of Jijel, East of Algeria: indicators of sediment sources and transport and deposition environments. Arabian Journal of Geosciences, 9, 35.

Kimberley, M.M., Grandstaff, D.F., 1985. Profiles of elemental concentrations in Pre-cambrian paleosols on basaltic and granitic parent materials. Precambrian Research, 32, 133–154.

King, L.C., 1950. Outline and distribution of Gondwanaland. Geological Magazine, 87, 353-355.4.

Kogbe, C.A., 1976. Paleographic history of Nigeria from Albian times: In Kogbe (ed.) Geology of Nigeria-Elizabeth publish Co. p. 237-252.

Kogbe, C.A., Ajakaiye, D.E. and Matheis, G., 1983. Confirmation of Rift Structure along the Mid-Niger Valley, Nigeria. Journal of African Earth Sciences, 1, 127–131.

Köksal, S., Göncüoglu, M., Toksoy-Köksal, F., Möller, A. and Kemnitz, H., 2008. Zircon typologies and internal structures as petrogenetic indicators in contrasting granitoids types from central Anatolia, Turkey. Mineral Petrology, 93,185–211.

Korsch, R.J., 1984. Sandstone compositions from the New England Orogen, Eastern Australia: implications for tectonic setting. Journal of Sedimentary Petrology, 54, 192-211.

Kroonenberg, S.B., 1994. Effects of Provenance, sorting and weathering on the geochemistry of fluvial sands from different tectonic and climatic environment. Proceedings of the 29th International Geological Congress, Part A, 69-81.

Krynine, P.D., 1945. The Tourmaline group in sediments. Journal of Geology, 54, 65-87.

Ladipo, K.O., Akande, S.O. and Mucke, A., 1994. Genesis of Ironstones from the Middle Niger Sedimentary Basin, Evidence from Ore Microscopic and Geochemical Studies. Journal of Mining and Geology, 30, 161-168.

Lang, J., Kogbe, C.A., Alidou, S., Alzouma, K., Dubois, D., Houesson, A. and Trichet, J., 1986, La Série Sidérolitique du Tertiaire Oust-african et le Concept du Continental Terminal. Bulletin de la Société Géologique de France, 4, 605-622.

Le-Bas, M.J., Le Maitre, R.W., Streckeisen, A. and Zanettin, B., 1986. A chemical classification of volcanic rocks based on the total alkali-silica diagram. J. Petrol. 27, 745–750.

Long, X., Yuan, C., Sun, M., Xiao, W., Wang, Y., Cai, K. and Jiang, Y., 2012. Geochemistry and Nd isotopic composition of the Early Paleozoic flysch sequence in the Chinese Altai, Central 42 Asia: Evidence for a northward-derived mafic source and insight into Nd model ages in accretionary orogen. Gondwana Research, 22, 554-565.

Lonnie, T.P., 1982. Mineralogic and chemical composition of marine and nonmarine transitional clay beds on south shore of Long Island, New York. Journal of Sedimentary Petrology, 52, 529-535.

Mack, G.H., 1984. Exceptions to the relationship between plate tectonics and sandstone composition. Journal of Sedimentary Petrology, 54, 212-220.

Mange, M.A. and Maurer, H.F.W., 1992. Heavy Minerals in Colour. Chapman and Hall, London, 147pp.

Maynard, J.B., Valloni, R. and Yu, H., 1982. Composition of modern deep-sea sands from arc-related basins. Geological Society of London, Special Publication, 10(1), 551–561.

McBride, E.F., 1963. A classification of common sandstones. Journal of Sedimentary Petrology, 33, 664–665.4.

McLennan, S.M. and Hemming, S., 1992. Sm/Nd elemental and isotopic systematics in sedimentary rocks. Geochimica et Cosmochimica Acta, 56, 887-898.

Mclennan, S.M. and Taylor, S.R., 1991. Sedimentary rocks and crustal evolution: tectonic setting and secular trends. Journal of Geology, 99, 1-21.

McLennan, S.M., 1989. Rare earth elements in sedimentary rocks; influence of provenance and sedimentary processes, In Lipin, B.R., McKay, G.A. (eds.), Geochemistry and Mineralogy of Rare Earth Elements. Reviews in Mineralogy, 21, 169-200.

McLennan, S.M., 1993. Weathering and global denudation. Journal of Geology, 101, 295–303.

McLennan, S.M., Hemming, S., McDaniel, D.K. and Hanson, G.N., 1993. Geochemical approaches to sedimentation, provenance, and tectonics. In: Johnsson, M.J., Basu, A. (Eds.), Processes Controlling the Composition of Clastic Sediments. Special Paper of Geological Society of America, 284, 21–40.

Mclennan, S.M., Nance, W.B. and Taylor, S.R., 1980. Rare earth element-Thorium correlation in sedimentary rocks, and the composition of the continental crust. Geochimica et Cosmochimica Acta, 44, 1833-1835.4.

McLennan, S.M., Taylor, S.R., Eriksson, K.A., 1983. Geochemistry of Archaean shales from the Pilbara Supergroup, Western Australia. Geochim. Cosmochim. Acta, 47, 1211–1222.

McLennan, S.M., Taylor, S.R., McCulloch, M.T. and Maynard, J.B., 1990. Geochemical and Nd-Sr isotopic composition of deep-sea turbidites: Crustal evolution and plate tectonic associations. Geochimica et Cosmochimica Acta, 54, 2015-2050.

Miall A.D., 1977. Fluvial Sedimentology. Canadian Society of Petroleum Geologists, Calgary, 111 pp.

Miall, A.D., 1985. Architectural-element analysis: a new method of facies analysis applied to fluvial deposits. Earth Science Reviews, 22, 261-308.

Miall, A.D., 1988. Architectural elements and bounding surfaces in fluvial deposits: anatomy of the Kagenta Formation (Lower Jurasssic), southwest Colorado. Sedimentary Geology, 55, 233-262.

Miall, A.D., 1988. Reservoir heterogeneities in fluvial sandstones: lessons from outcrop studies: American Association of Petroleum Geologists Bulletin, 72(6), 682-697.

Miall, A.D., 1992. Alluvial deposits. In R.G. Walker and N.P. James, eds., Facies models: response to sea level change. Geological Association of Canada, 119-142.

Miall, A.D., 1996. The Geology of Fluvial Deposits: Sedimentary Facies, Basin Analysis, and Petroleum Geology. Heidelberg, Springer Verlag Inc., 582 p.

Miller R.G. and O'Nions R.K., 1984. Source of Precambrian chemical and clastic sediments. Nature, 314, 325-325.4.

Milner, H.B., 1962. Sedimentary Petrography, 4th revised edition: vol. II. Principles and Applications. Allen and Unwin, London. 715 pp.

Moiola, R. J. & Weiser, D. 1968. Texture parameters: An evaluation. Journal of Sedimentary Petrology, 38, 45-53.

Morton, A.C. and Hallsworth, C.R. 1994. Identifying provenance specific features of detrital heavy mineral assemblages in sandstones. Sedimentary Geology, 90, 241–255.

Morton, A.C. and Hurst, A. 1994. Correlation of sandstones using heavy minerals: an example from the Statfjord Formation of the Snorre Field, northern North Sea. In: Dunay R.E. and Hailwood E.A. (Eds), Non-biostratigraphical methods of dating and correlation. Geological Society of London, Special Publication, 89, 3–22.

Morton, A.C., 1991. Geochemical studies of detrital heavy minerals and their application to provenance studies. In. Morton, A.C., Todd, S. P. and Haughton, P.D.W. (eds) Developments in Sedimentary Provenance Studies. Geological Society of London, Special Publication, 57, 31-44.

Morton, A.C., Davies, J.R. and Waters, R.A., 1992. Heavy minerals as a guide to turbidite provenance in the Lower Paleozoic southern Welsh basin: a pilot study. Geological Magazine, 129 (5), 573–580.

Mucke, A. 1994. Post-diagenetic ferruginization of sedimentary rocks sandstones, oolitic ironstones, kaolins and bauxites, including a comparative study of the bedding of red beds. In: WolfKH, Chiiingarian GV (eds) Development of sedimentology. Diagenesis 4, Elsevier Amsterdam. Pp. 361-423.

Mucke, A., Badejoko, T. A., Akande, S.O., 1999, Petrographic-Mechanical studies and origin of Agbaja Phanerozoic ironstone formation, Nupe Basin, Nigeria, a product of a ferruginised ooidal kaolin precursor not identical to the Minette type: Mineralium Deposita, 34, 284–295.

Murphy, J.B., 2000. Tectonic influence on sedimentation along the southern flank of the late Paleozoic Magdalen basin in the Canadian Appalachians: Geochemical and isotopic

constrains on the Horton Group in the St. Marys basin, Nova Scotia. Geological Society of America Bulletin, 112, 997–1011.

Nagarajan, R., Armstrong-Altrin, J.S., Nagendra, R., Madhavaraju, J. and Moutte, J., 2007. Petrography and geochemistry of terrigenous sedimentary rocks in the Neo-proterozoic Rabanpalli Formation, Bhima Basin, Southern India: implications for paleoweathering condition, provenance, and source rock composition. Journal Geological Society India, 70, 297–312.

Nath, B.N., Bau, M., Ramalingeswara Rao, B. and Rao, Ch.M., 1997. Trace and rare earth elemental variation in Arabian Sea sediments through a transect across the oxygen minimum zone: Geochimica et Cosmochimica Acta, 61(12), 2375-2388.

Nathan, S., 1976. Geochemistry of the Greenland Group (early Ordovician), New Zealand. N.Z.J. Geology and Geophysics, 19, 683-705.

Nesbitt, H.W. and Young, G., 1982. Early Proterozoic climates and plate motions inferred from major elements chemistry of lutites. Nature, 299, 715–717.

Nesbitt, H.W. and Young, G.M., 1984. Prediction of some weathering trends of plutonic and volcanic rocks based on thermodynamic and kinetic considerations. Geochimica et Cosmochimica Acta, 48, 1523-1534.

Nesbitt, H.W., Young, G.M., McLennan, S.M. and Keays, R.R., 1995. Effects of chemical weathering and sorting on the petrogenesis of siliciclastic sediments, with implications for provenance studies. Journal of Geology, 104(5), 525–542.

Nichols, G., 2009. Sedimentology and stratigraphy, Cambridge, Blackwell Science Ltd., 355p.

Nwajide, C.S. and Reijers, T.J.A., 1995. Sequence architecture in outcrops: examples from the Anambra Basin, Nigeria. Nigerian Association Petroleum Explorationists, 11, 23–33.

Obaje, N. G., Musa, M. K., Odoma, A. N., and Hamza, H. 2011. The Bida Basin in north-central Nigeria: Sedimentology and petroleum geology. Journal of Petroleum and Gas Exploration Research, 1(1), 001-013.

Obaje, N.G., 2009. Geology and Mineral Resources of Nigeria. Springer, Heidelberg, 221 p.

Obaje, N.G., Attah, D.O. and Opeloye, S.A., 2005. Geochemical evaluation of the hydrocarbon prospects of sedimentary basins in Northern Nigeria. Geochemical Journal, 40, 227-243.

Obaje, N.G., Balogun, D. O., Idris-Nda, A., Goro, I. A., Ibrahim, S. I., Musa, M. K., Dantata, S. H., Yusuf, I., Mamud-Dadi, N and Kolo, I. A., 2013. Preliminary Integrated Hydrocarbon Prospectivity Evaluation of the Bida Basin in North Central Nigeria. Petroleum Trust Development Journal, 3(2), 36-64.

Obaje, N.G., Wehner, G., Scheeder, G., Abubakar, M. B. and Jauro, A., 2004. Hydrocarbon Prospectivity of Nigeria's Inland Basins: From the Viewpoint of Organic Geochemistry and Organic Petrology. American Association of Petroleum Geologists Bulletin, 88(3), 325-353.

Ojo O.J., 2012. Depositional Environments and Petrographic Characteristics of Bida Formation around Share-Pategi, Northern Bida Basin, Nigeria. Journal of Geography and Geology, 4(1), 224-241.

Ojo, O.J. and Akande, S.O., 2003, Facies Relationships and Depositional Environments of the Upper Cretaceous Lokoja Formation in the Bida Basin, Nigeria. Journal of Mining and Geology, 39, 39-48.

Ojo, O.J. and Akande, S.O., 2004, Facies Architecture and Sequence Stratigraphy of the Upper Cretaceous Sediments in the Southern Bida Basin, Nigeria. 23rd Nigerian Association Petroleum Explorationists Annual International Conference Book of Abstracts, p. 23.

Ojo, O.J. and Akande, S.O., 2009a, Sedimentology and depositional environments of the Maastrichtian Patti Formation, southeastern Bida Basin, Nigeria. Cretaceous Research, 30, 1415-1424.

Ojo, O.J. and Akande, S.O., 2009b, Microflora Assemblage and Paleoenvironment of the Upper Cretaceous Patti Formation, Southern Bida Basin, Nigeria. Journal of Mining and Geology, 44, 71-81.

Ojo, S.B. and Ajakaiye, D.E., 1989. Preliminary interpretation of gravity measurements in the middle Nıger Basin area, Nigeria: In Kogbe, C.A. (Ed.), Geology of Nigeria, 2nd ed. Elizabethan Publishing Company, Lagos, p. 347–358.

Ojo, S.B., 1984. Middle Niger Basin revisited: magnetic constraints on gravity interpretations. Abstract, 20th Conference of the Nigeria Mining and Geosciences Society Book of Abstracts, Nsukka, p. 52–53.

Olaniyan, O. and Olobaniyi, S.B., 1995. Facies analysis of the Bida Sandstone Formation around Kajita, Nupe Basin, Nigeria. Journal of African Earth Sciences, 23, 253–255.

Olugbemiro, R. and Nwajide, C.S., 1997. Grain Size Distribution and Particle Morphogenesis as Signatures of Depositional Environment of Cretaceous (non- Ferruginous) Facies in the Bida Basin, Nigeria. Journal of Mining and Geology, 33, 89-101.

Osae, S., Asiedu, D.K., Banoeng-Yakubo, B., Koeberl, C. and Dampare, S.B., 2006. Provenance and tectonic setting of Late Proterozoic Buem sandstones of southeastern Ghana: evidence from geochemistry and detrital modes. Journal of African Earth Sciences 44, 85–96.

Petters, S.W., 1978. Middle Cretaceous paleoenvironments and biostratigraphy of the Benue Trough, Nigeria. Geological Society of America Bulletin, 89, 151–154.

Pettijohn, F.J., 1957. "Sedimentary Rocks" (2rd Ed), Harper and Bros, New York, 718p.

Pettijohn, F.J., 1975. "Sedimentary Rocks" (3rd Ed), Harper and Bros, New York, 628p.

Pettijohn, F.J., Potter, P.E. and Siever, R., 1972. Sand and Sandstone: New York, Springer, 618p.

Pidgeon, R.T., 1992. Recrystallization of oscillatory zoned zircon: some geochronological and petrological implications. Contribution of Mineral Petrology, 110, 463–472.

Pidgeon, R.T., Nemchin, A.A. and Hitchen, G.J., 1998. Internal structures of zircons from Archean granites from the Darling Range batholith: Implications for zircon stability and the interpretation of zircon U-Pb ages. Contribution of Mineral Petrology, 132, 288-299.

Poldervaart, A., 1955. Zircons in rocks 2: Igneous rocks. American Journal of Science, 254, 521–554.

Potter, P.E., 1978. Petrology and chemistry of modern big river sands. Journal of Geology, 86, 423-449.

Potter, P.E., Maynard, J.B. and Pryor, W.A., 1980. Sedimentology of Shale. Berlin, Germany: Springer-Verlag.

Price, J.R. and Velbel, M.A., 2003. Chemical weathering indices applied to weathering profiles developed on heterogeneous felsic metamorphic parent rocks. Chemical Geology, 202, 397–415.

Prothero, D.R. and Schwab, F., 2004. Sedimentary Geology: An Introduction to Sedimentary Rocks and Stratigraphy (2nd Edition), New York, W, H, Freeman and Co., 557 p.

Pupin, J.P., 1980. Zircon and granite petrology. Contributions to Mineralogy and Petrology, 73, 207–220.

Rahman, M.J.J. and Suzuki, S., 2007. Composition of Neogene shales from the Surma Group, Bengal Basin, Bangladesh: implications for provenance and tectonic setting. Austrian Journal of Earth Sciences, 100, 54-64.

Ramkumar, M., 1999. Lithostratigraphy, depositional history and constraints on sequence stratigraphy of the Kallan kurichchi Formation (Maastrichtian), Ariyalur Group, south India. Geolo{ki anali Balkanskoga poluostrva, 63, 19–42.

Ramos-Vázquez, M., Armstrong-Altrin, J. S., Rosales-Hoz, L., Machain-Castillo, M. L., and Carranza-Edwards, A., 2017. Geochemistry of deep-sea sediments in two cores retrieved at the mouth of the Coatzacoalcos river delta, Western Gulf of Mexico, Mexico. Arabian Journal of Geosciences, In press DOI: 10.1007/s12517-017-2934-z

Reyment, R.A. and Morner, N.A., 1977. Cretaceous transgressions and regressions exemplified by the South Atlantic. Paleontological Society of Japan, Special Papers, 21, 247-261.

Reyment, R.A., 1964. Aspects of the geology of Nigeria. Ibadan University Press, 133 pp.

Rhee, C.W., Ryand. W.H. and Chough, S.K., 1993. Contrasting development patterns of crevasse channel deposits in Cretaceous alluvial successions, Korea. Sedimentary Geolology, 85, 401-410.

Roaldset, E., 1973. Rare earth elements in Quaternary clays of Numedal area, Southern Norway. Lithos, 6, 349–372.

Roddaz, M., Viers, J., Brusset, S., Baby, P., Boucayrand, C. and Herail, G. 2005. Controls on weathering and provenance in the Amazonian foreland basin: Insights from major and trace element geochemistry of Neogene Amazonian sediments; Chemical Geological, 23, 31–64.

Rollinson, H., 1992. Using Geochemical Data: Evaluation, Presentation, Interpretation, Longman, 352p.

Ronov, A.B., Balashov, Y.A., Girin, Y.P., Bratishko, R.K.H. and Kazakov, G.A., 1974. Regularities of rare earth element distribution in the sedimentary shell and in the crust of the earth. Sedimentology, 21, 171–193.

Rosen, O.M., Abbyasov, A.A. and Tipper, J.C., 2004. MINLITH; an experience-based algorithm for estimating the likely mineralogical compositions of sedimentary rocks from bulk chemical analyses. Computers and Geosciences, 30(6), 647-661.

Roser, B.P. and Korsch, R.J., 1986. Determination of tectonic setting of sandstone-mudstone suites using SiO_2 content and K_2O/Na_2O ratio. Journal of Geology, 94, 635–650.

Roser, B.P. and Korsch, R.J., 1988. Provenance signatures of sandstone-mudstone suites determined using discrimination function analysis of major-element data. Chemical Geology, 67, 119–139.

Roy, P.D., Caballaeroa, M., Lozanoc, R. and Smykatz-Klossd, W., 2008. Geochemistry of late quaternary sediments from teccomulco lake, central Mexico: implications to chemical weathering and provenance. Chemie der Erde, 68, 383-393.

Rudnick, R. and Gao, S., 2003. Composition of the continental crust. Treatise on geochemistry 3, 1-64.

Rudnick, R.L. and Williams, I.S., 1987. Dating the lower crust by ion microprobe. Earth Planet Science Letter, 85, 145-161.

Ruffell, A. and Worden, R. 2000. Palaeoclimate analysis using spectral gamma-ray data from the Aptian (Cretaceous) of southern England and southern France. Palaeo Palaeo Palaeo 155: 265–283.

Ruiz, G.M.H., Seward, D. and Winkler, W., 2007. Evolution of the Amazon Basin in Ecuador with special reference to hinterland tectonics: data from zircon fission-track and heavy mineral analysis. In: M. Mange, D.K. Wright (Eds.), Heavy Minerals in Use, Developments in Sedimentology, 58, 907-934.

Russ, W., 1930. The Minna-Birnin Gwari Belt. Reports of the Geological Survey of Nigeria, 10-14.

Ruxton, B.P., 1970. Labile quartz-poor sediments from Young Mountain ranges in Northeast Papua: Journal of Sedimentary Petrology, 40, 1262–1270.

Schermaier, A., Haunschmid, B., Schubert, G. and Frasl, G., 1992. Diskriminierung von S-Typ und I-Typ Graniten auf der Basis zircon typologischer Untersuchungen. Frankfurter Geowissenschaftliche Arbeiten Serie A, 149–153.

Scholle, P.A., 1975.4. A Color Illustrated Guide to Constituents, Textures, Cements, and Porosities of Sandstones and Associated Rocks: Tulsa, Oklahoma, American Association of Petroleum Geologists, Memoir, 201.

Schwab, F.L., 1974. Framework mineralogy and chemical composition of continental margin-type sandstone, Geology, 3, 487-390.

Schwab, F.L., 1981. Evolution of the western continental margin. French-Italian Alps: sandstone mineralogy as an index of plate tectonic setting. Jour. Geol., 89, 349-368.

Schwab, F.L., 1986. Sedimentary "signatures" of foreland basin assemblages: real or counterfeit? In: Allen, P.A., and Homewood, P (Eds.) Foreland basins: Int. Assoc. Sediment. Sp. Publ., 8, 395-410.

Selvaraj, K., Lin, B.Z., Lou, J.Y., Xia, W.L., Huang, X.T. and Chen, C.T.A., 2015. Lacustrine sedimentological and geochemical records for the last 170 years of climate and environmental changes in 174 southeastern China. Boreas, 45, 165-179.

Shaw, T.J., Gieskes, J.M. and Jahnke, R.A., 1990. Early diagenesis in differing depositional environments: the response of transition metals in pore water. Geochimica et Cosmochimica Acta, 54, 1233–1245.

Singh, S.K., Sarin, M.M., France-Lanord, C., 2004. Chemical erosion in the eastern Himalaya: major ion composition of the Brahmaputra and δ13C of dissolved inorganic carbon. Geochimica et Cosmochimica Acta, 69, 3573–3588.

Spalletti, L.A., Queralt, I, Matheos, S.D., Colombo, F. and Maggi, J., 2008. Sedimentary petrology and geochemistry of siliclastic rocks from the upper Jurassic Tordillo Formation (Neuquen basin, western Argentina): Implications for provenance and tectonic setting. Journal of South America Earth Science. doi: 10.1016/j.james.

Srinivasan, M.S., 1989. Recent advances in Neogene planktonic foraminiferal biostratigraphy, chemostratigraphy and paleoceanography, Northern Indian Ocean. Journal of the Palaeontological Society of India, 34, 1–18.

Stratten, J. 1973. Notes on the application of shape parameters to differentiate between beach and river deposits in southern Africa. Trans Geolo. Soc. S. Africa, 76, 59-64.

Sturm, R., 1999. Longitudinal and cross section of zircon: a new method for theinvestigation of morphological evolutional trends. Schweiz. Mineral Petrograpic Mitt. 79, 309–315.

Sugitani, K., Horiuchi, Y., Adachi, M. and Sugisaki, R., 1996. Anomalously low Al_2O_3/TiO_2 values for Archean cherts from the Pilbara Block, Western Australia: Possible evidence for extensive chemical weathering on the early earth. Precambrian Research, 80(1-2), 49-75.

Suttner, L.J. and Dutta, P.K., 1985. Alluvial sandstone deposition and paleoclimate, I. Framework mineralogy. Journal of Sedimentary Petrology, 56, 329-344.

Suttner, L.J., Basu, A. and Mack, G.H., 1981. Climate and the origin of quartz arenites. Journal of Sedimentary Petrology, 5, 1235-1245.

Tattam, C.M. 1944. “A Review of Nigeria Stratigraphy”. Rep. Geol. Surv., Nigeria. 27-46.

Taylor, S.R. and McLennan, S.M., 1985. The Continental Crust: Its Composition and Evolution. Blackwell Scientific Publications, Oxford, 312p.

Taylor, S.R., Rudnick, R.L., McLennan, S.M., and Eriksson, K.A., 1985. Rare earth element patterns in Archean high-grade metasediments and their tectonic significance, Geochim. Cosmochim. Acta, 50, 2267-2275.4.

Udensi, E.E. and Osazuwa, I.B., 2004. Spectra Determination of Depths to Magnetic Rocks under the Nupe Basin, Nigeria. Nigerian Association Petroleum Explorationists Bulletin, 17, 22-37.

Valloni, R. and Maynard, J.B., 1981. Detrital modes of recent deep-sea sands and their relation to tectonic setting: a first approximation. Sedimentology, 28, 75-83.

Valloni, R., 1984. Reading provenance from modern marine sands. In: Zuffa, G.G. (Ed.), Provenance of Arenites, Reidel Publ., Dordrecht, 309– 332.

van de Kamp, P. C. and Helmhold, K.P., 1991. Compositions of sediments derived from granitic basement rocks in glacial to humid tropical climates [abs.]. Geological Society of America Abstracts with Programs, 23(5), 72.

Verma, S.P. and Armstrong-Altrin, J.S., 2015. Geochemical discrimination of siliciclastic sediments from active and passive margin settings. Sedimentary Geology, 332, 1-12.

Walker, R.G., 1979, Facies models: Geosciences Canada Reprint Series, 1, 211 p.

Weltje, G. J., Meijer, X. D. and de Boer, P. L., 1998. Stratigraphic inversion of siliciclastic basin fills: a note on the distinction between supply signals resulting from tectonic and climatic forcing: Basin Research, 10, 129–153.

Weltje, G.J. and Eynatten, H.V., 2004. Quantitative provenance analysis of sediments: review and outlook. Sedimentary Geology 171 (1–4), 1–11.

Weltje, G.J., 1994. Provenance and dispersal of sand-sized sediments: Geol. Ultraiectina, v. 121, p. 1–208.

Weltje, G.J., 2005. Ternary sandstone composition and provenance: an evaluation of the Dickinson model’. In: Buccianti, A., Mateu-Figueras, G., Pawlowsky-Glahn, V. (Eds.), Compositional data analysis: from theory to practice. Geological Society of London, Special Publications, 264, 611–627.

Weltje, G.J., Meijer, X.D. and de Boer, P.L., 1998. Stratigraphic inversion of siliciclastic basin fills: a note on the distinction between supply signals resulting from tectonic and climatic forcing. Basin Research, 10, 129–153.

Whiteman, A.J., 1982. Nigeria: It's Petroleum Geology: Resources and Potential, Graham and Trotman, London, 1-2, 394 p.

Wortmann, U.G., Herrle, J.O. and Weissert, H., 2004. Altered carbon cycling and coupled changes in early Cretaceous weathering patterns: evidence from integrated carbon isotope and sandstone records of the western Tethys. Earth and Planetary Science Letters, 220, 69–82.

Wright, J.B., Hastings, D. A., Jones, W.B. and Williams, H.R., 1985, Geology and Mineral Resources of West Africa, George Allen and Unwin, London, 187 p.

Wronkiewicz, D.J. and Condie, K.C., 1990. Geochemistry and provenance of sediments from the Pongola Supergroup, South Africa: Evidence for a 3.0-Ga-old continental Craton. Geochimica et Cosmochimica Acta, 53, 1537–1549.

Xie, Y. and Chi, Y., 2015. Geochemical investigation of dry- and wet-deposited dust during the same dust-storm event in Harbin, China: constraint on provenance and implications for formation of aeolian loess. Journal of Asian Earth Sciences, 120, 43-61.

Yamamoto, K., Sugisaki, R. and Arai, F., 1985. Chemical aspects of alteration of acidic tuffs and their application to siliceous deposits. Chemical Geology, 55, 61–75.

Yan, Y., Xia, B., Lin, G., Cui, X., Hu, X., Yan, P. and Zhang, F., 2007. Geochemistry of the sedimentary rocks from the Nanxiong Basin, South China and implications for provenance, palaeoenvironment and palaeoclimate at the K/T boundary. Sedimentary Geology, 197, 127–140.

Yerino, L.N. and Maynard, J.B., 1984. Petrography of modern marine sands from the Peru-Chile Trench and adjacent areas. Sedimentology, 31, 83–89.

APPENDICES

APPENDIX I

Table I: Samples selected for Pebble morphometric analysis

Lithofacies	Sub-facies Code after Miall (1985, 1988, 1992)	Locations	Sample Codes	Number of pebble and samples
Conglomerate	Clast Supported Conglomerate (Gcm)	Patti-Chin	PAT-1E	22
		Baganko	BAK-1C	23
	Matrix Supported Conglomerate (Gmm)	Patti-Chin	PAT-1D	28
		Baganko	BAK-1E	21
	Crudely bedded Conglomerate (Gh)	Baganko	BAK-1B	18
		Baganko	BAK-1G	16

Table II: Samples selected for grain Size Analysis

Lithofacies	Sub-facies Code after Miall (1985, 1988, 1992)	Sample Codes	Number of rock samples
Conglomerate	**Clast Supported Conglomerate (Gcm)**	BAR-1A, LAD-1B, PTG-1C, PTG-1E, SHG-IH, WAR-1E	6
	Matrix Supported Conglomerate (Gmm)	BAR-1B, DOK-1C, GBL-1E, GBU-1C, GB-2C, GB-2F, GDW-1B, LAD-1E, LAF-1E, PTG-1D, SHG-IC, SHG-IG, WUS-1D, WUS-1F, ZAM-1B	15
	Crudely bedded Conglomerate (Gh)	AGE-1D, BDA-1J, BGK-1G, DOK-1B, DOK-1E, DOK-1G, DOK-1J, DOK-1L, ENAG-1C, ENAG-1K, ENAG-1M, ENAG-1S, GBU-1D, GBU-2B, GBU-2E, GDW-1A, GDW-1C, JIM-1K, KAC-1C, KAC-1G, KAC-1X3, KJT-1C, KJT-1Q, KUT-1C, LEM-1B, LEM-1K, MAR-1G, MAR-1J, PAT-1F, PTG-1B, RAB-1C, RAB-1N, SHG-1J, SHG-IA, SHG-IK, SHG-IN, SHG-IQ, SHG-IT, SHG-IW, SHT-1B, SHT-1C, WAR-1F, WAR-1J, WUS-1G, ZAM-1A	45
Sandstone	**Crudely stratified Sandstone (Se)**	AGB-1B, AGB-1F, AGB-1L, AGE-1F, BAR-1E, BAR-1G, BAR-1L, BDA-1H, BDA-1N, BDA-1Q, BGK-1A, BGK-1F, DOK-1A, DOK-1D, DOK-1H, ENA-1J, ENA-1T, GBU-2D, JIM-1E, JIM-1H, JIM-1L, JIM-1R, JIM-1X, KAC-1E, KAC-1F, KAC-1J, KAC-1M, KAC-1P, KAC-1Z, KCH-1A, KJT-1A, KJT-1D, KJT-1E, KJT-1G, KJT-1H, KJT-1K, KJT1L, KJT-1N, KUT-2B, LAD-1A, LAD-1D, LAF-1C, LEM-1C, LEM-1E, LEM-1G, LEM-1M, MAR-1E, PAT-1A, PAT-1E, PTG-1A, RAB-1K, RAB-1M, RAT-1C, RAT-1F, RAT-1M, RUG-1B, RUG-1E, SHG-1B, SHG-1E, SHG-1R, SHG-1X, SHJ-1B, SHJ-1D, SHJ-1E, SHT-1A, TAN-1B, WUS-1C	67

Table II contd.: Samples selected for grain Size Analysis

Lithofacies	Sub-facies Code after Miall (1985, 1988, 1992).	Sample Codes	Number of samples (N)
	Planar cross-stratified sandstone (Sp)	AGB-1K, BAR-1D, BAR-1H, BAR-1M, BDA-1A, BDA-1C, BDA-1E, BDA-1G, BDA-1L, BDA-1P, BDA-1R, JIM-1S, JIM-1Y, KAC-1B, KAC-1D, KAC-1H, KCH-1E, KJT-1P, KUT-2H, LAF-1D, LEM-1R, MAR-1B, MAR-1D, MAR-1L, MGT-1A, PAT-1J, PAT-1N, RAB-1E, RAB-1G, RAT-1D, RAT-1K, TAN-1A, TAN-1G, TAN-1H	35
	Rippled cross-stratified sandstone (Sr)	AGB-1J, LAF-1B, MAN-1F, RAB-1P	4
	Horizontally stratified sandstone (Sh)	AGB-1A, AGB-1C, AGB-1G, AGB-1M, AGE-1E, BAR-1F, BAR-1K, BDA-1B, BDA-1F, BDA-1M, BDA-1S, BGK-1D, DOK-1K, DOK-1M, ENA-1A, ENA-1E, ENA-1H, ENA-1L, ENA-1N, ENA-1V, JIM-1A JIM-1C, JIM-1J, JIM-1Q, JIM-1V, KAC-1W, KCH-1B, KCH-1D, KCH-1G, KUT-2A, KUT-2E, KUT-2J, KUT-2K, LEM-1A, LEM-1H, LEM-1Q, MAN-1G, MAN-1H, MAR-1C, MAR-1F, MAR-1M, MGT-1B, MGT-1E, MGT-1F, PAT-1B, PAT-1G, PAT-1H, RAB-1F, RAB-1H, RAT-1E, RAT-1L, RUG-1F, SHJ-1A, SHG-1F, SHG-1L, SHG-1P, SHG-1V, SHJ-1C, SHT-1E, TAN-1C, TAN-1D, WAR-1C, WAR-1H, WUS-1A, WUS-1B, WUS-1E	66
	Massive sandstone (Sm)	AGE-1A, AGE-1C, AGE-1G, GBU-2A, KAC-1K, KAC-1N, KAC-1Q, LEM-1D, LEM-1F, LEM-1L, PAT-1D, RUG-1C, WAR-1G.	13
Mudstone	**Finely laminated mudstone (Fl)**	AGE-1B, AGE-1H, BAR-1J, BDA-1K, GBU-1B, JIM-1B, JIM-1D, JIM-1G, JIM-1M, JIM-1T, JIM-1W, KAC-1L, KAC-1V, KAC-1X, KAC-1Y, KCH-1C, KCH-1F, KJT-1F, KJT-1J, KUT-2C, LEM-1N, LEM-1T, MAN-1B, MAN-1J, MAR-1H, MAR-1K, PAT-1C, RAB-1J, RAB-1L, RAT-1G, TAN-1F, TAN-1J, WUS-1H	33
	Massive mudstone (Fm)	AGB-1E, DOK-1F, ENA-1B, ENA-1D, ENA-1Q, ENA-1R, GBU-1A, KAC-1R, KAN-1A, KUT-1B, MAN-1A, MAN-1C, PAT-1K, RUG-1A, RUG-1D, SHG-1M, WAR-1D	17

Table III: Samples selected for Petrographic (Thin Section) Analysis

Lithofacies	Sub-facies Code after Miall (1985, 1988, 1992)	Sample Codes	Number of rock samples
Conglomerate	**Crudely bedded Conglomerate (Gh)**	DOK-1G, ENG-1K, KJT-1Q, MAR-1G, PAT-1M	5
Sandstone	**Crudely stratified Sandstone (Se)**	AGB-1F, DOK-1N, JIM-1E, KAC-1E, KJT-1A, KUT-2B, KUT-2L, LEM-1E, PAT-1E, TAN-1C	10
	Planar cross-stratified sandstone (Sp)	BDA-1L, DOK-1V, ENG-1F, JIM-1S, KAC-1B, MAR-1B, MAR-1D, MAR-1L, MGT-1C, PAT-1J, PAT-1N, TAN-1A, TAN-1G	13
	Rippled cross-stratified sandstone (Sr)	AGB-1J, MAN-1F	2
	Horizontally stratified sandstone (Sh)	AGB-1C, BDA-1B, BDA-1F, BDA-1M, DOK-1K, DOK-1Y, DOK-Z2, ENG-1H, ENG-1V, JIM-1F, KCH-1D, KUT-2A, KUT-2G, KUT-2J, KUT-2K, LEM-1H, MAN-1H, MAR-1C, MGT-1H, RAB-1H, RAB-1P, RAT-1P, WAR-1H	23
	Massive sandstone (Sm)	AGE-1A, AGE-1G, AGE-1J, PAT -1L, RAT-1H	5
Mudstone	**Finely laminated mudstone (Fl)**	BDA-IK, JIM-1B, KAC-1V, KAC-1X, KAC-1Y, KCH-1F, MAN-1D, PAT-1C, PAT-1H, RAT-1J	10
	Massive mudstone (Fm)	AGB-1E, DOK-Z4, ENG-1P, KAC-1R, LEM-1P, PAT-1K, RAB-1D	7

Table IV: Samples selected for Heavy Mineral Analysis

Lithofacies	Sub-facies Code after Miall (1985, 1988, 1992).	Sample Codes	Number of rock samples
Conglomerate	**Matrix Supported Conglomerate (Gmm)**	DOK-1C	1
	Crudely bedded Conglomerate (Gh)	BDA-1J, DOK-1G, DOK-1S, LEM-1K, LEM-1B, RAB-1C	6
Sandstone	**Crudely stratified Sandstone (Se)**	BAR-1E, BAR-1L, BDA-1H, BDA-1Q, DOK-1A, DOK-1N, DOK-1P, JIM-1E, LEM-1C, LEM-1E, LEM-1G, LEM-1M	12
	Planar cross-stratified sandstone (Sp)	BDA-1C, BDA-1E, BDA-1P, BDA-1R, DOK-1R, DOK-1V, JIM-1Y, LEM-1R, PAT-1J, RAB-1E, TAN-1A	11
	Rippled cross-stratified sandstone (Sr)	AGB-1J, RAB-1P	2
	Horizontally stratified sandstone (Sh)	BDA-1B, BDA-1F, BDA-1M, BDA-1S, DOK-1T, JIM-1A, JIM-1Q, JIM-1V, KUT-2A, KUT-2E, KUT-2J, LEM-1A, LEM-1H, LEM-1Q, PAT-1B, PAT-1G	16
	Massive sandstone (Sm)	LEM-1D, LEM-1L, PAT-1D	3
Mudstone	**Finely laminated mudstone (Fl)**	BDA-1K, DOK-1D, DOK-1H, DOK-1Z, JIM-1D, JIM-1M, KUT-2C, LEM-1N	8
	Massive mudstone (Fm)	DOK-Z4, MAR-1N, PAT-1K	3

Table V: Samples selected for X-Ray Diffraction (XRD) Analysis

Lithofacies	Sub-facies Code after Miall (1985, 1988, 1992)	Sample Codes	Number of rock samples
Conglomerate	**Clast Supported Conglomerate (Gcm)**	PTG-1C	1
	Matrix Supported Conglomerate (Gmm)	GBU-1C	1
	Crudely bedded Conglomerate (Gh)	NDJ-1H, ZMB-1A, ZMB-1C	3
Sandstone	**Crudely stratified Sandstone (Se)**	AGB-1B, DOK-1D, LEM-1E, SHG-1B, SHG-1R	4
	Planar cross-stratified sandstone (Sp)	AGB-1K, DOK-1X, TAN-1A, PAT-1J	4
	Rippled cross-stratified sandstone (Sr)	No Sample	0
	Horizontally stratified sandstone (Sh)	AGB-1A, AGB-1C, DOK-1K, ENG-1L, ENG-1V, KUT-1A, KUT-1G, KUT-1M, NDJ-1C, PAT-1B, RAB-1P, SHG-1L, TAN-1D	13
	Massive sandstone (Sm)	AGB-1S, LAF-1E, LAF-1L, KUD-1A, RAB-1B	5
Mudstone	**Finely laminated mudstone (Fl)**	KUD-1C, LEM-1T	2
	Massive mudstone (Fm)	AGB-1E, ENG-1B	2

Table VI: Samples selected for X-Ray Fluorescence Analysis (Major Elements)

Lithofacies	Sub-facies Code after Miall (1985, 1988, 1992)	Sample Codes	Number of rock samples
Conglomerate	**Clast Supported Conglomerate (Gcm)**	GBL-1C, PTG-1E	2
	Matrix Supported Conglomerate (Gmm)	GBL-1E, PTG-1D	2
	Crudely bedded Conglomerate (Gh)	GBU-1D, PTG-1B, KJT-1C, KJT-1Q	4
Sandstone	**Crudely stratified Sandstone (Se)**	GBL-1D, PTG-1A, KJT-1A, BDA-1D, DOK-1D, AGB-1B, ENG-1J, KUT-2D	8
	Planar cross-stratified sandstone (Sp)	BDA-1A, BDA-1R, DOK-1X, AGB-1K	4
	Rippled cross-stratified sandstone (Sr)	No Sample	0
	Horizontally stratified sandstone (Sh)	BDA-1B, DOK-1K, AGB-1G, ENG-1E, ENG-1L, ENG-1N, ENG-1V, KUT-2A, KUT-2G, KUT-2K, RAB-1F, RAB-1H, RAB-1P	13
	Massive sandstone (Sm)	GBL-1A, KUD-1A	2
Mudstone	**Finely laminated mudstone (Fl)**	GBU-1B, KJT-1F, KJT-1J, BDA-1K, AGB-1D, KUD-1C	6
	Massive mudstone (Fm)	GBU-1A, DOK-1F, ENG-1B, KUD-1B, KUD-1F	5

Table VII: Samples selected for Inductive Coupled Plasma Mass Spectrometry (ICPMS) for trace and rare earth elements (TE and REE)

Lithofacies	Sub-facies Code after Miall (1985, 1988, 1992)	Sample Codes	Number of samples
Conglomerate	Clast Supported Conglomerate (Gcm)	GBL-1C, PTG-1E	2
	Matrix Supported Conglomerate (Gmm)	GBL-1E, PTG-1D	2
	Crudely bedded Conglomerate (Gh)	GBU-1D, PTG-1B, KJT-1C, PAT-1M, SHG-1K	5
Sandstone	Crudely stratified Sandstone (Se)	GBL-1D, PTG-1A, KJT-1A, BDA-1D, LEM-1C, LEM-1E, LEM-1G, JIM-1L, JIM-1R, JIM-1X, DOK-1D, AGB-1B, SHG-1B, SHG-1X, ENG-1J, KUT 2D	16
	Planar cross-stratified sandstone (Sp)	BDA-1A, BDA-1R, DOK-1X, BAR-1D, BAR-1H, PAT-1J, PAT-1N, AGB-1K, TAN-1A	9
	Rippled cross-stratified sandstone (Sr)	No Sample	0
	Horizontally stratified sandstone (Sh)	BDA-1B, LEM-1A, LEM-1H, DOK-1K, DOK-1T, BAR-1F, PAT-1B, PAT-1G, AGB-1G, SHG-1F, SHG-1P, ENG-1E, ENG-1H, ENG-1L, ENG-1N, ENG-1V, KUT-2A, KUT-2G, KUT-2K, RAB-1F, RAB-1H, RAB-1P, TAN-1C, TAN-1D	23
	Massive sandstone (Sm)	GBL-1A, KUD-1A, RAB-1E	3
Mudstone	Finely laminated mudstone (Fl)	GBU-1B, BDA-1K, JIM-1B, BAR-1J, AGB-1D, KUD-1C, RAB-1L	7
	Massive mudstone (Fm)	GBU-1A, LEM-1P, JIM-1N, DOK-1F, ENG-1B, KUD-1B, KUD-1F, KUT-2P, KUT-2Q, KUT-2R	10

Table VIII: Samples selected for diagenetic study using scanning electron microscope (SEM) and backscattered electron microscope (BSE)

Serial No	Location	Sample Codes
1	Agbonna ridge	AGB-1F
2	Dokko ridge	DOK-1N
3	Enagi ridge	ENG-1H
4	Patti-Chi ridge	PAT-1J
5	Rabba ridge	RAB-1P

Table IX: Samples selected for Zircon Typology using Cathodoluminescence (CL)

Serial No	Location	Sample Codes
1	**Agbonna Ridge 1 (AGB-1)**	AGB-1C
2		AGB-1G
3		AGB-1Q
4	**Doko Ridge (DOK-1)**	DOK-1F
5		DOK-1N
6		DOK-1Y

APPENDIX II – LITHOLOGICAL SECTIONS

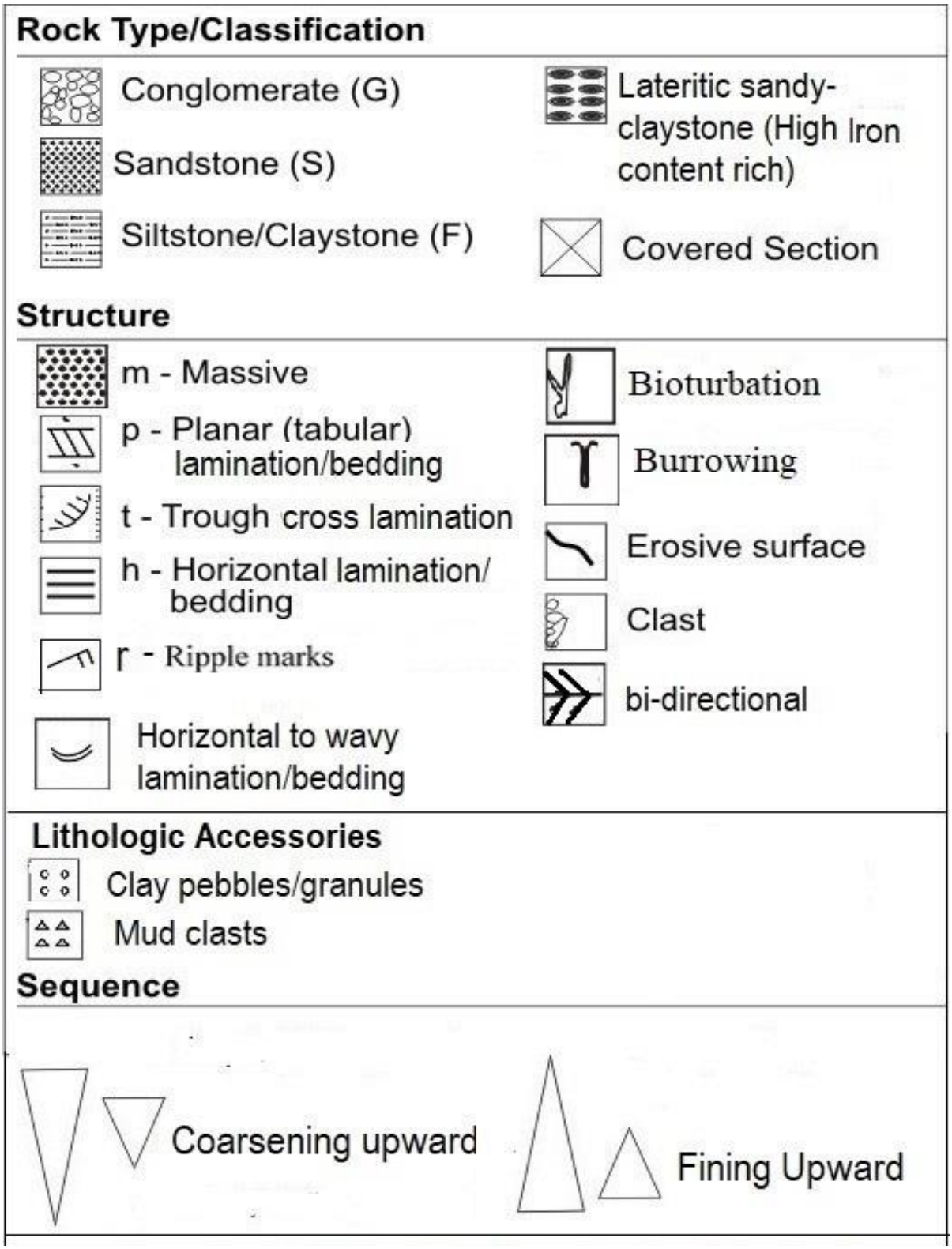


Figure I: Legend used in this study.

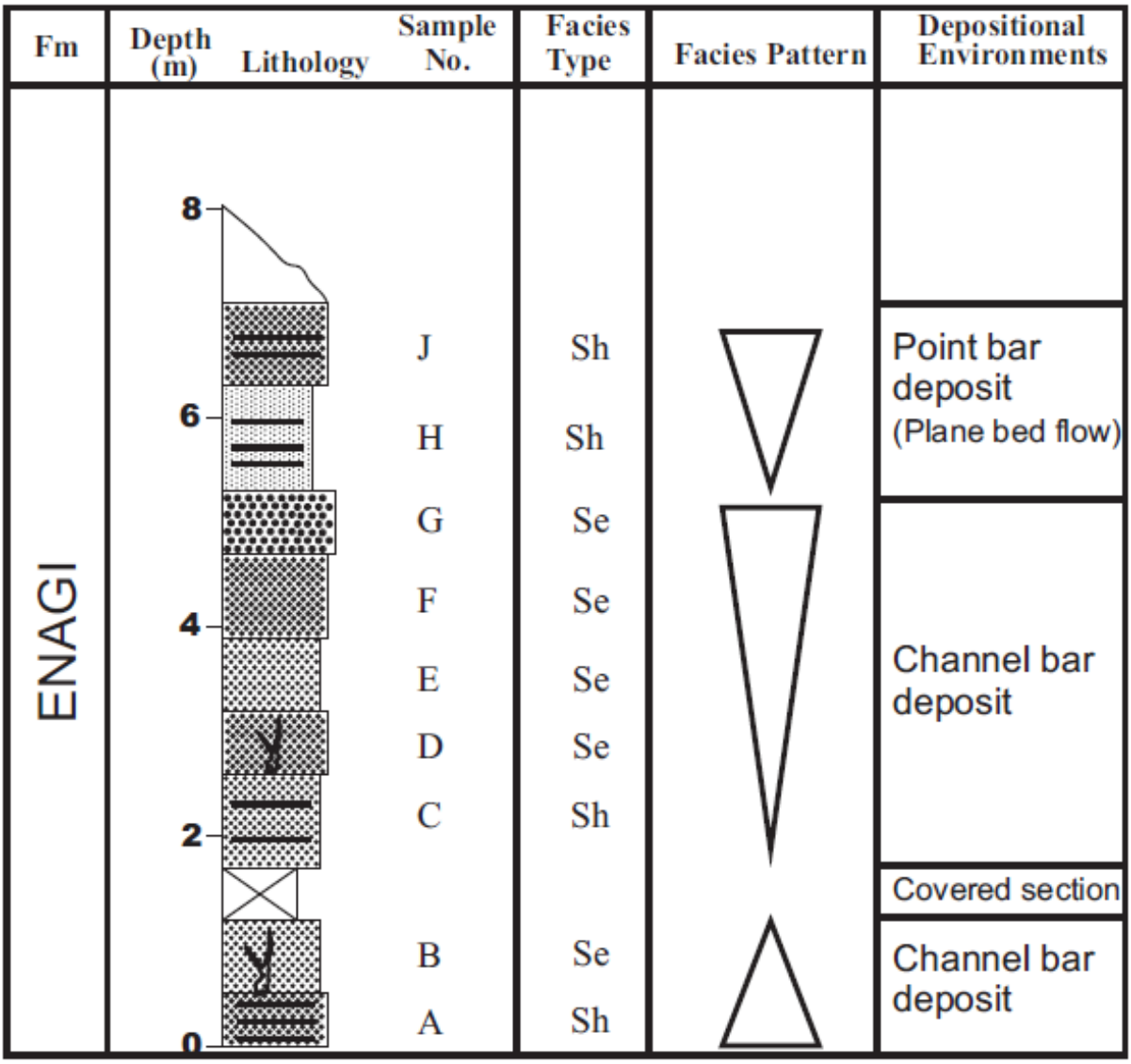


Figure II: Lithological section of Enagi Formation exposed at Share Junction (SHJ-1); Longitude: 004°56'04.6"E**; Latitude:** 08°49'27.5"N**.**

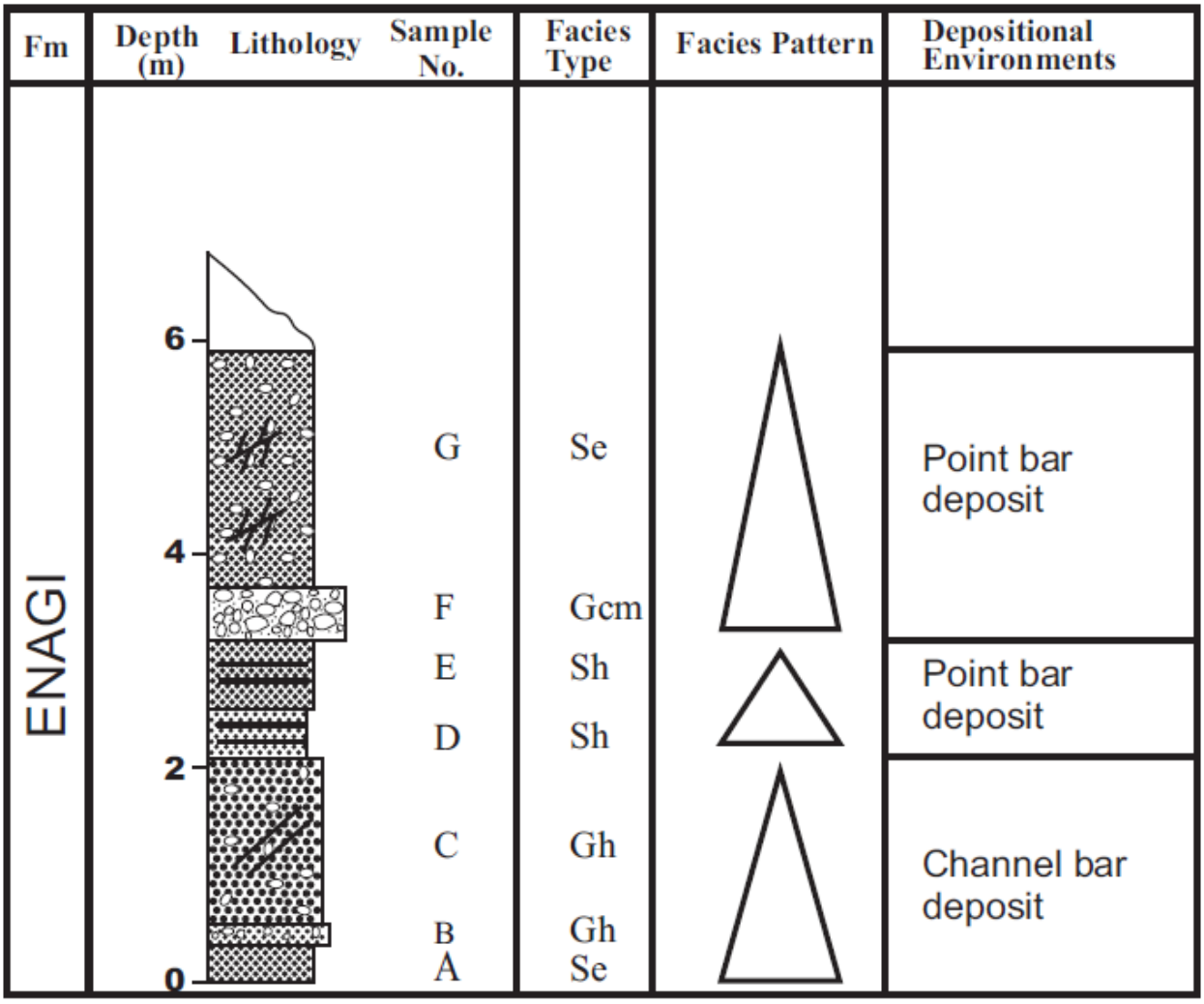


Figure III: Lithological section of Enagi Formation exposed at Share Township (SHT-1); SHJ-1 - Longitude: 004°58'16.1"E; **Latitude**: 08°49'05.7"N**.**

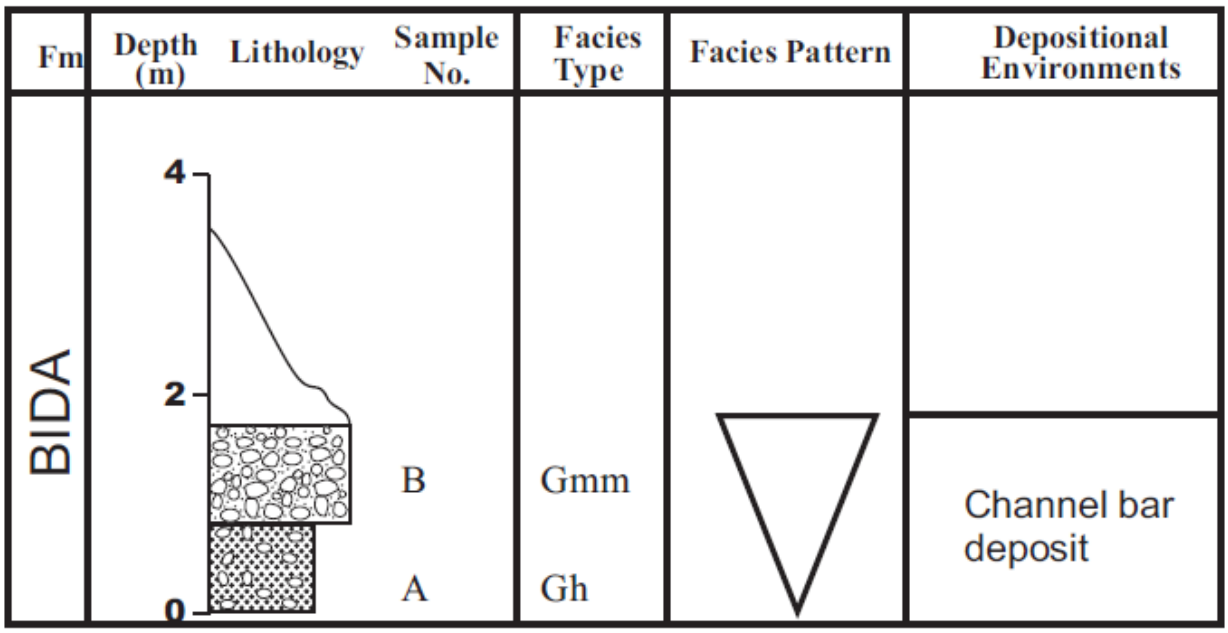


Figure IV: Lithological section of Enagi Formation exposed at Zambufu (ZMB-1); Longitude: 08°46'505"N; **Latitude**: 005°11'792"E**.**

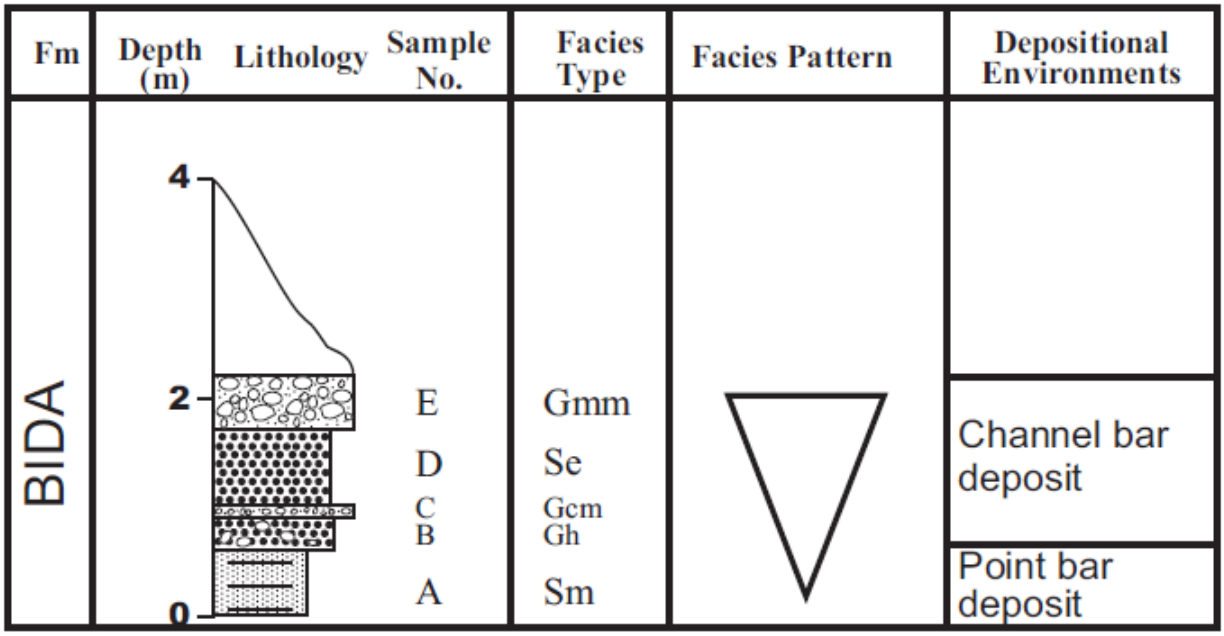


Figure V: Lithological section of Enagi Formation exposed at Gbale (GBL-1); Longitude: 08°45'23.7"N; **Latitude**: 005°11'16.7"E**.**

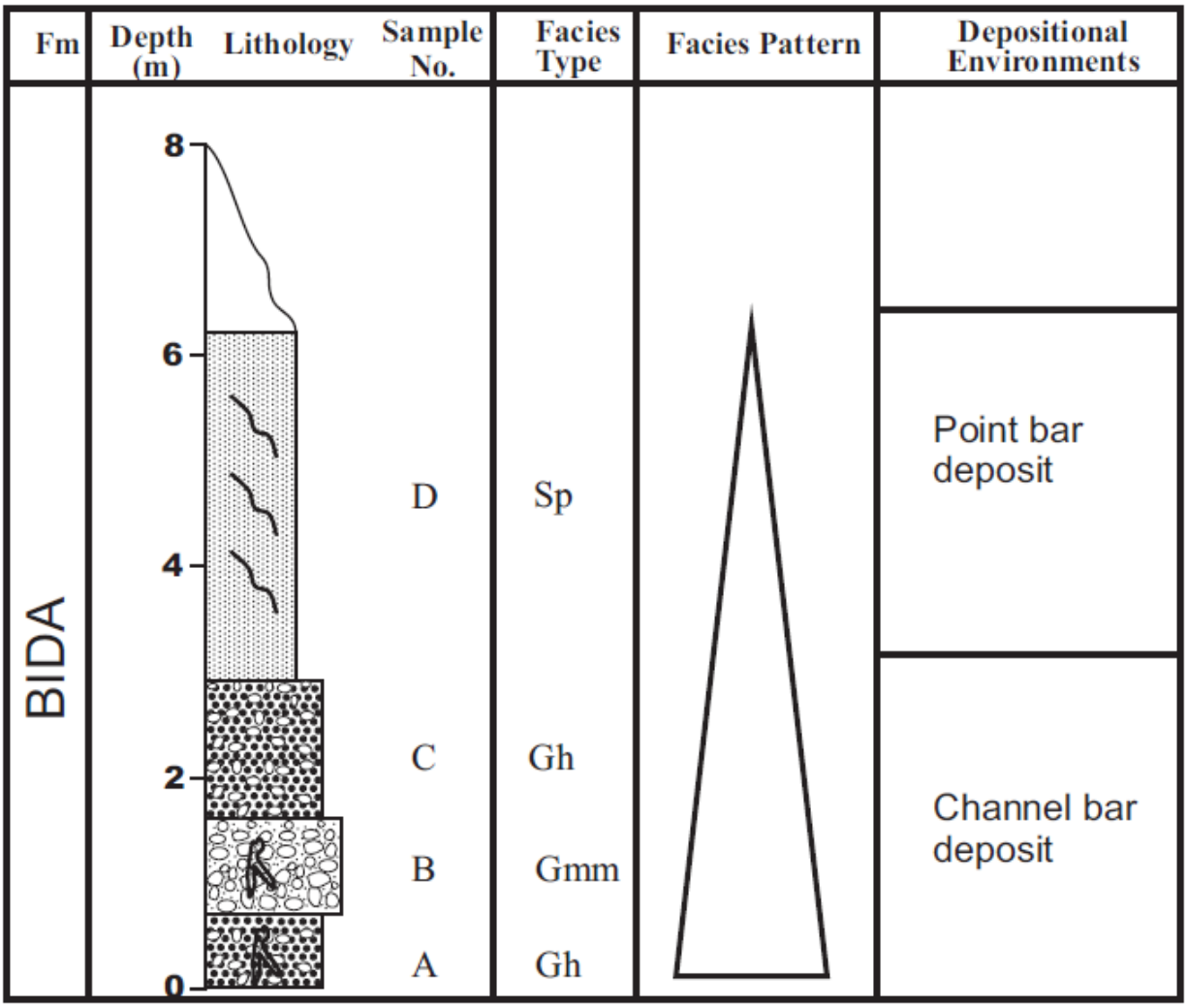


Figure VI: Lithological section of Enagi Formation exposed at Gbede-Woro (GDW-1); Longitude: 08°46'20.7"N; **Latitude**: 005°12'14.4"E**.**

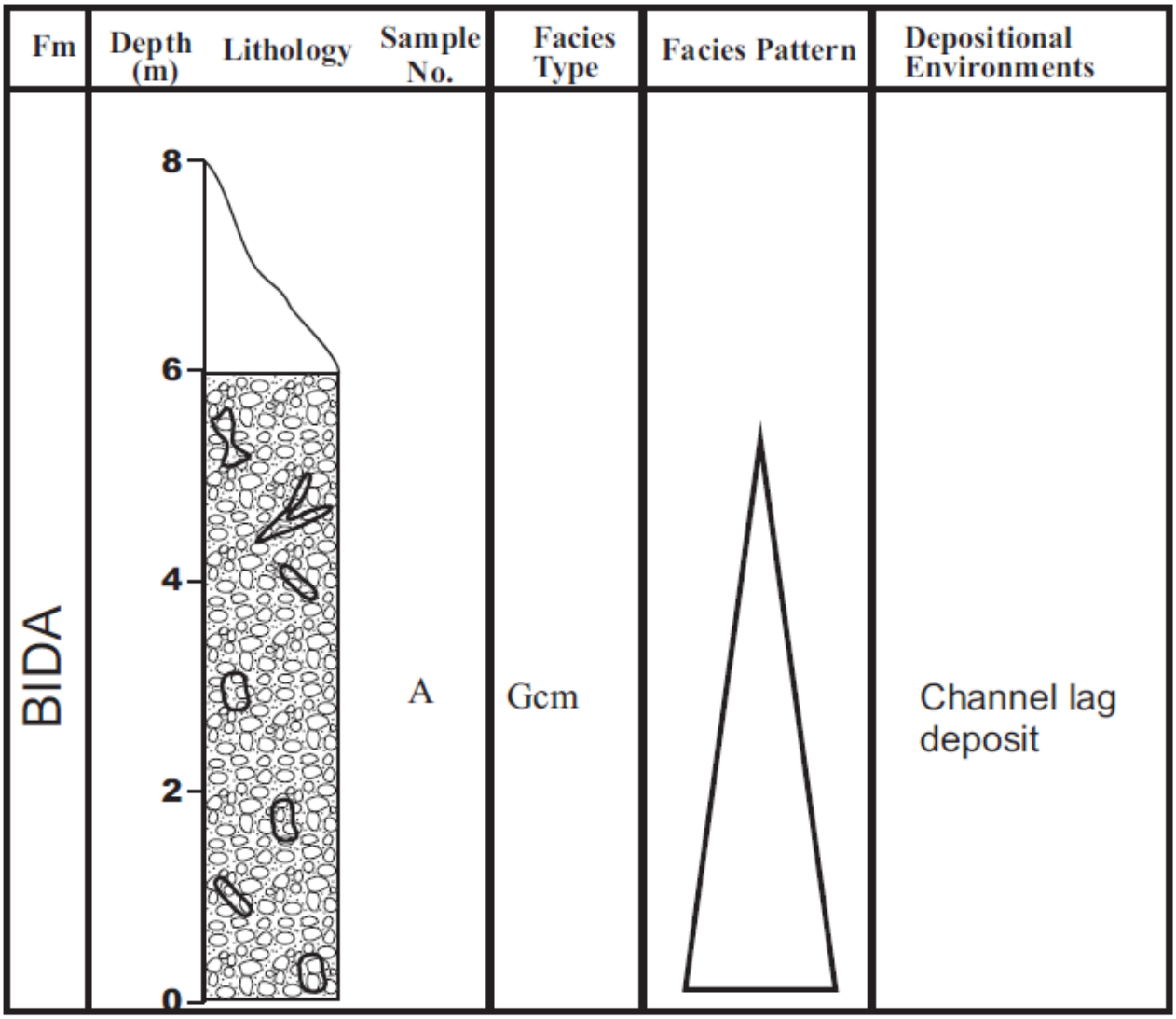


Figure VII: Lithological section of Enagi Formation exposed at Ndeji (NDJ-1); Longitude: 08°45'42.7"N; **Latitude**: 005°14'26.2"E**.**

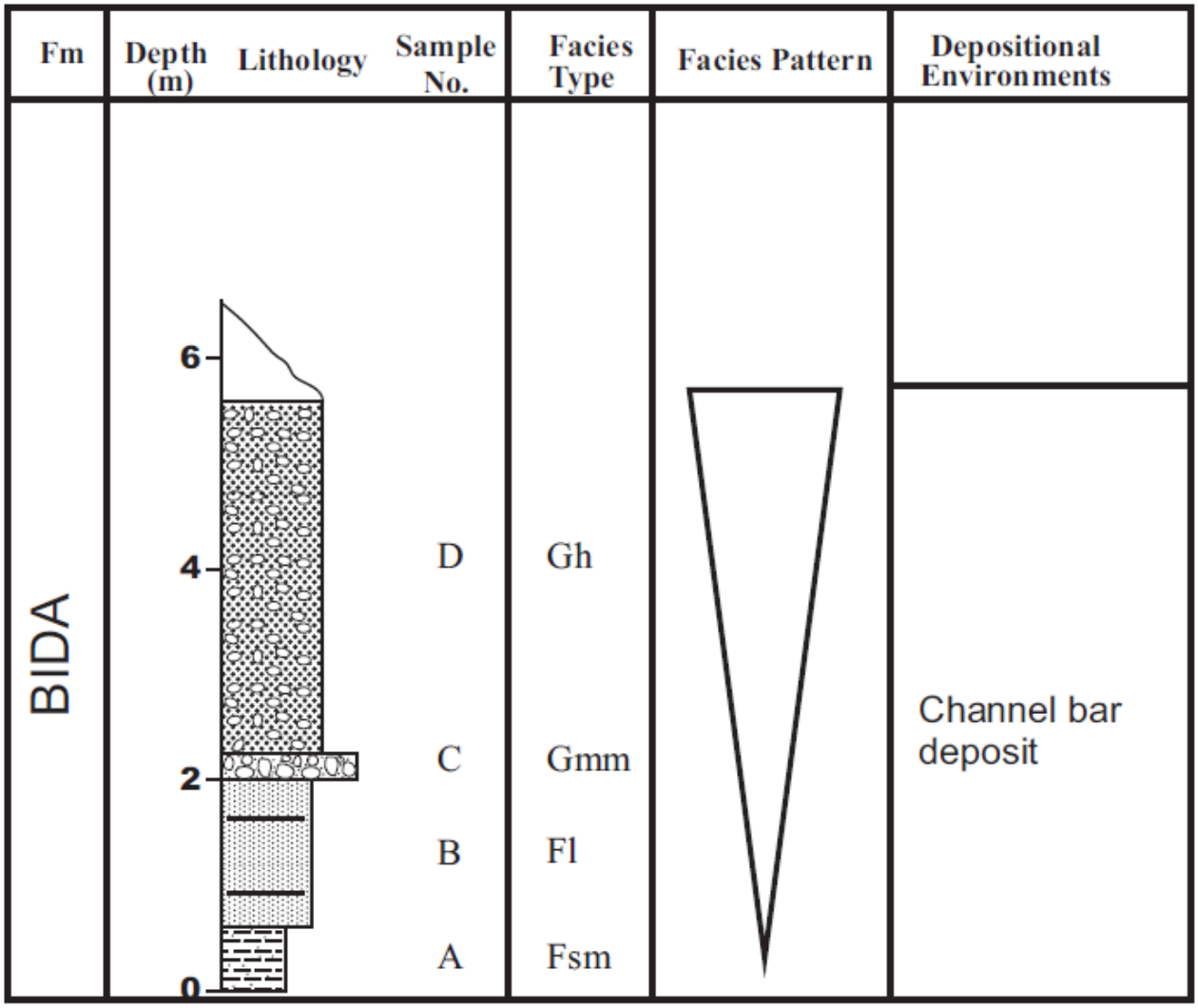


Figure VIII: Lithological section of Enagi Formation exposed at Gbugubu-1 (GBU-1); Longitude: 08°47'04.3"N; **Latitude**: 005°18'02.6"E**.**

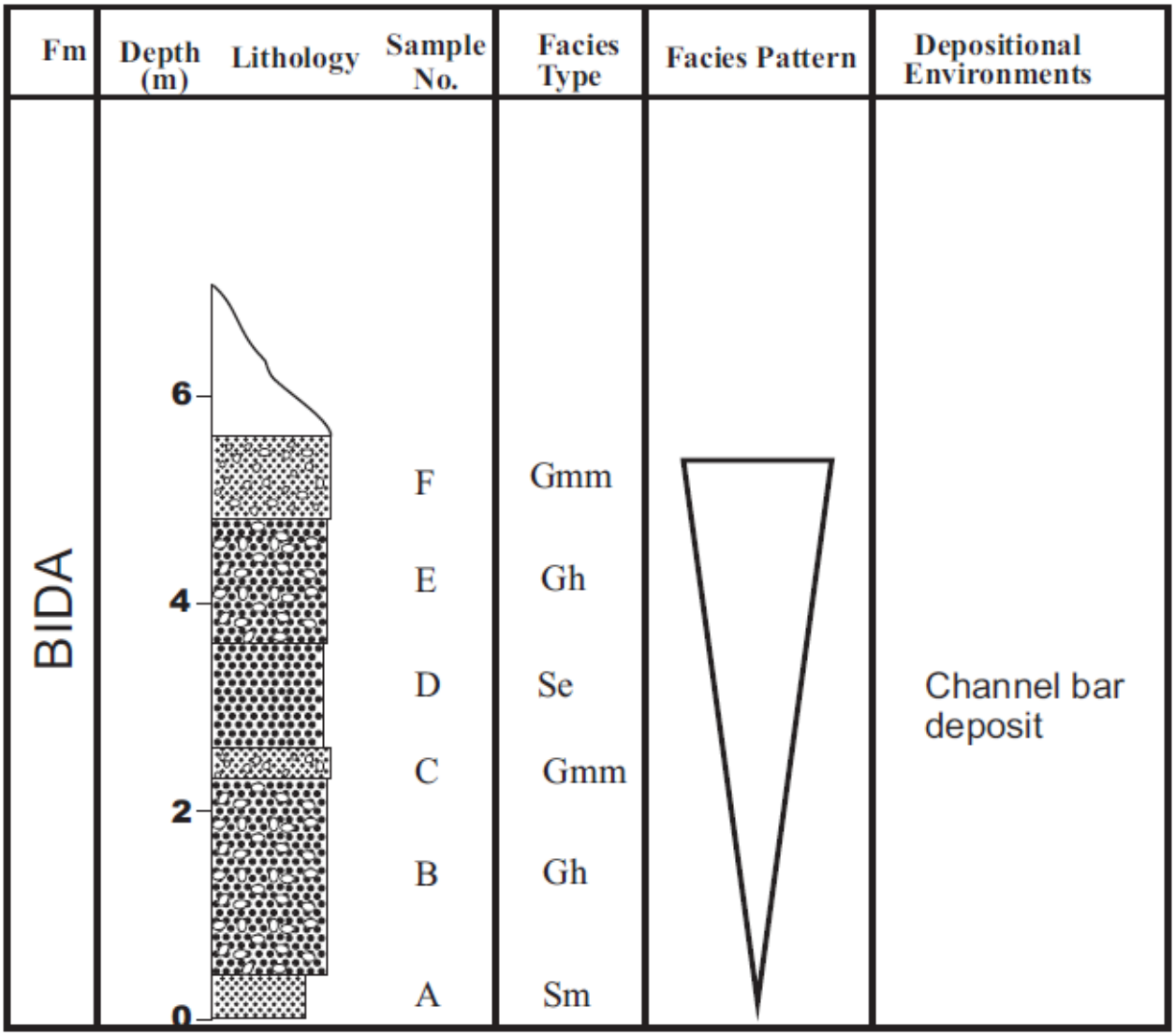


Figure IX: Lithological section of Enagi Formation exposed at Gbugbu-2 (GBU-2); Longitude: 08°47'05.3"N; **Latitude**: 005°17'55.3"E**.**

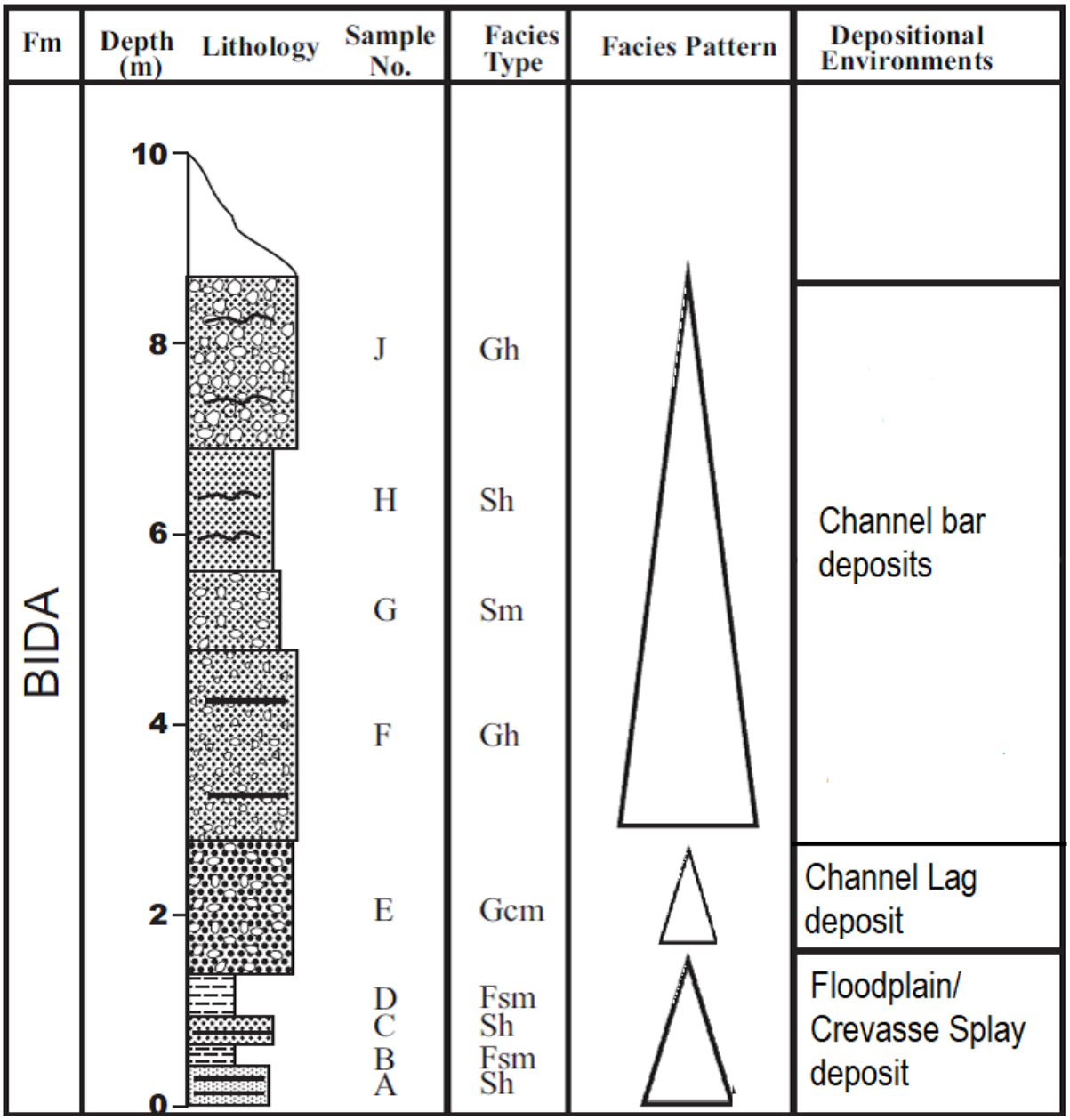


Figure X: Lithological section of Enagi Formation exposed at Wariku Ridge (WAR-1); Longitude: 08°47'46.3"N; **Latitude**: 005°18'41.6"E**.**

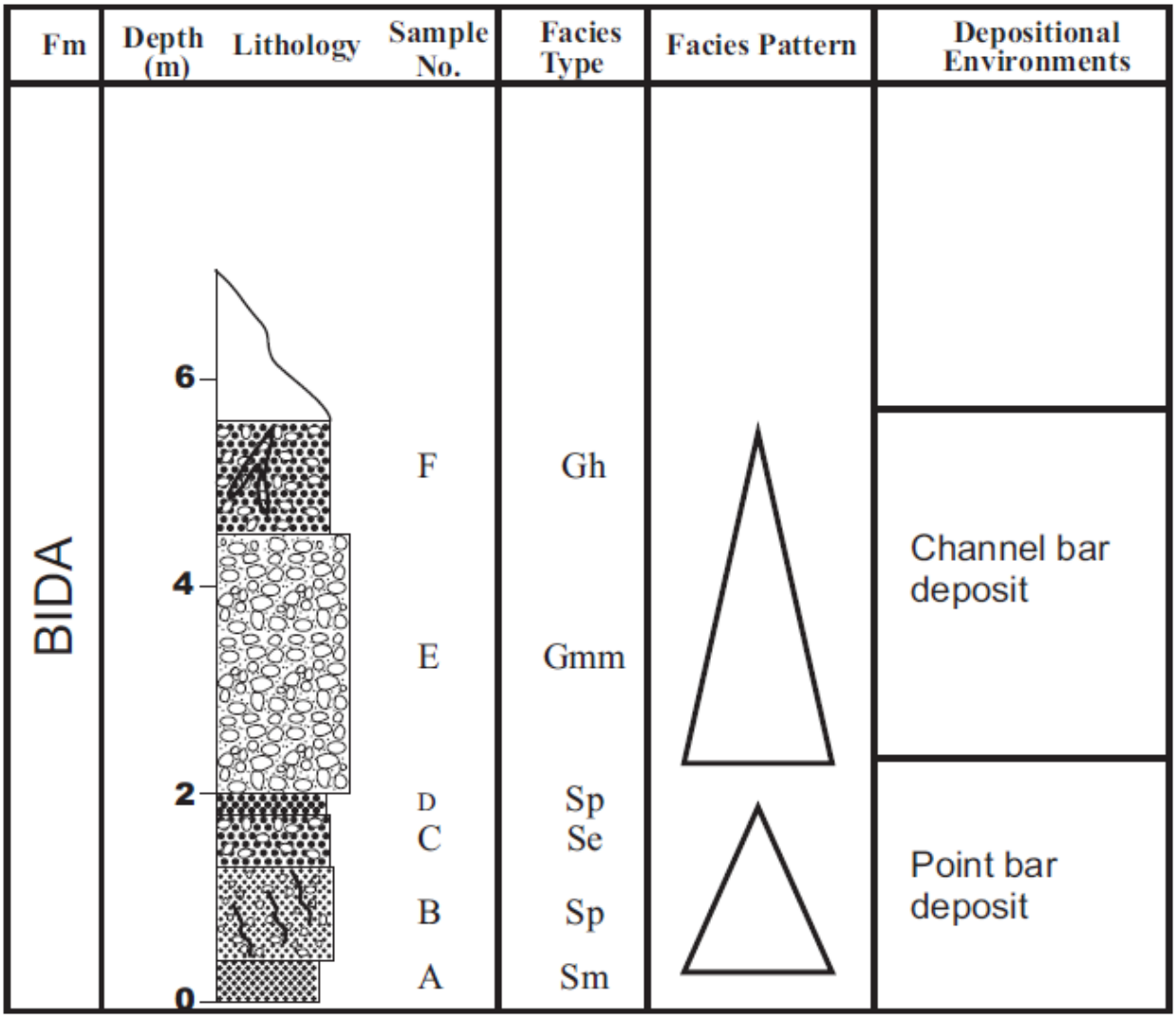


Figure XI: Lithological section of Bida Formation exposed at Lafiagi (LAF-1); Longitude: 08°50'44.0"N; **Latitude**: 005°25'03.0"E**.**

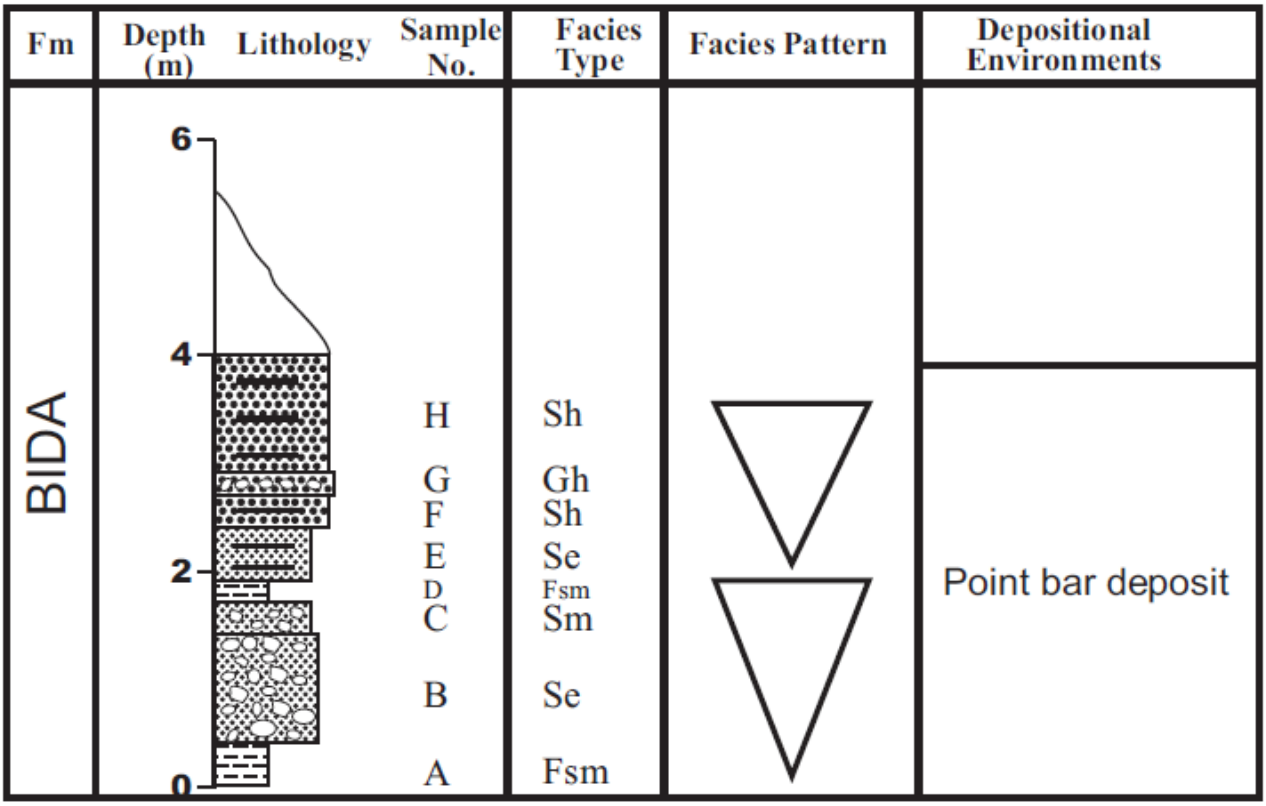


Figure XII: Lithological section of Bida Formation exposed at Rugga-Naggi (RUG-1); Longitude: 08°50'35.0"N; **Latitude**: 005°27'36.0"E**.**

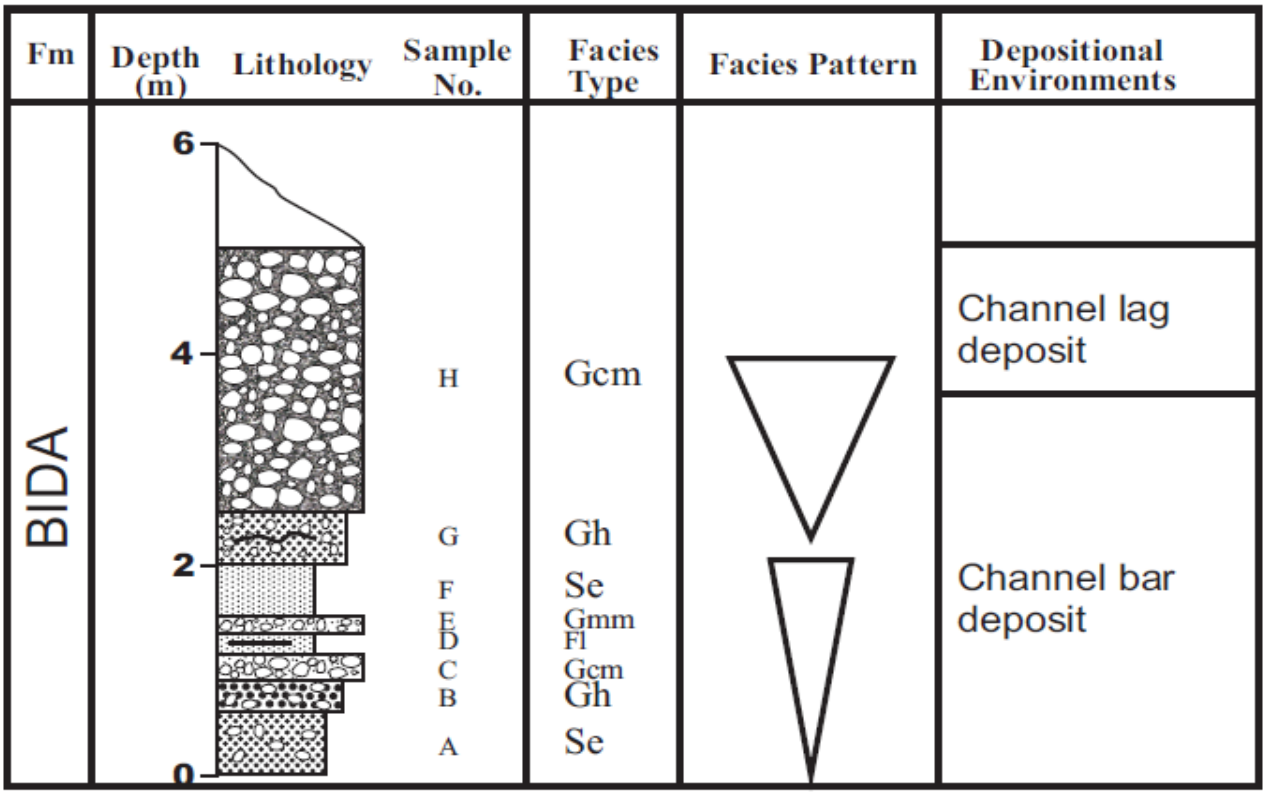


Figure XIII: Lithological section of Bida Formation exposed at Baganko (BGK-1); Longitude: 08°54'29.4"N; **Latitude**: 005°19'24.6"E**.**

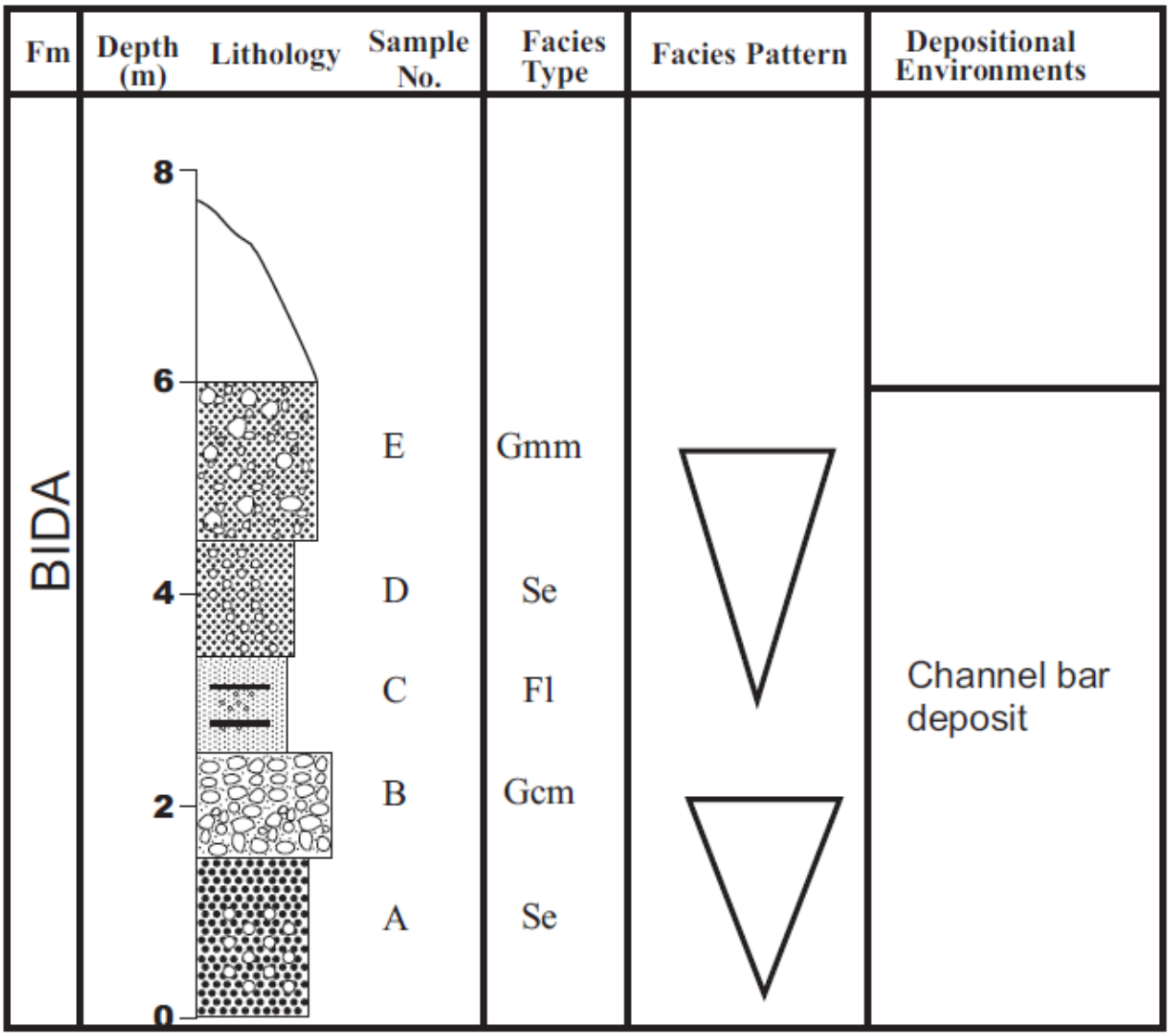


Figure XIV: Lithological section of Bida Formation exposed at Lade (LAD-1); Longitude: 08°45'47.3"N; **Latitude**: 005°35'37.9"E**.**

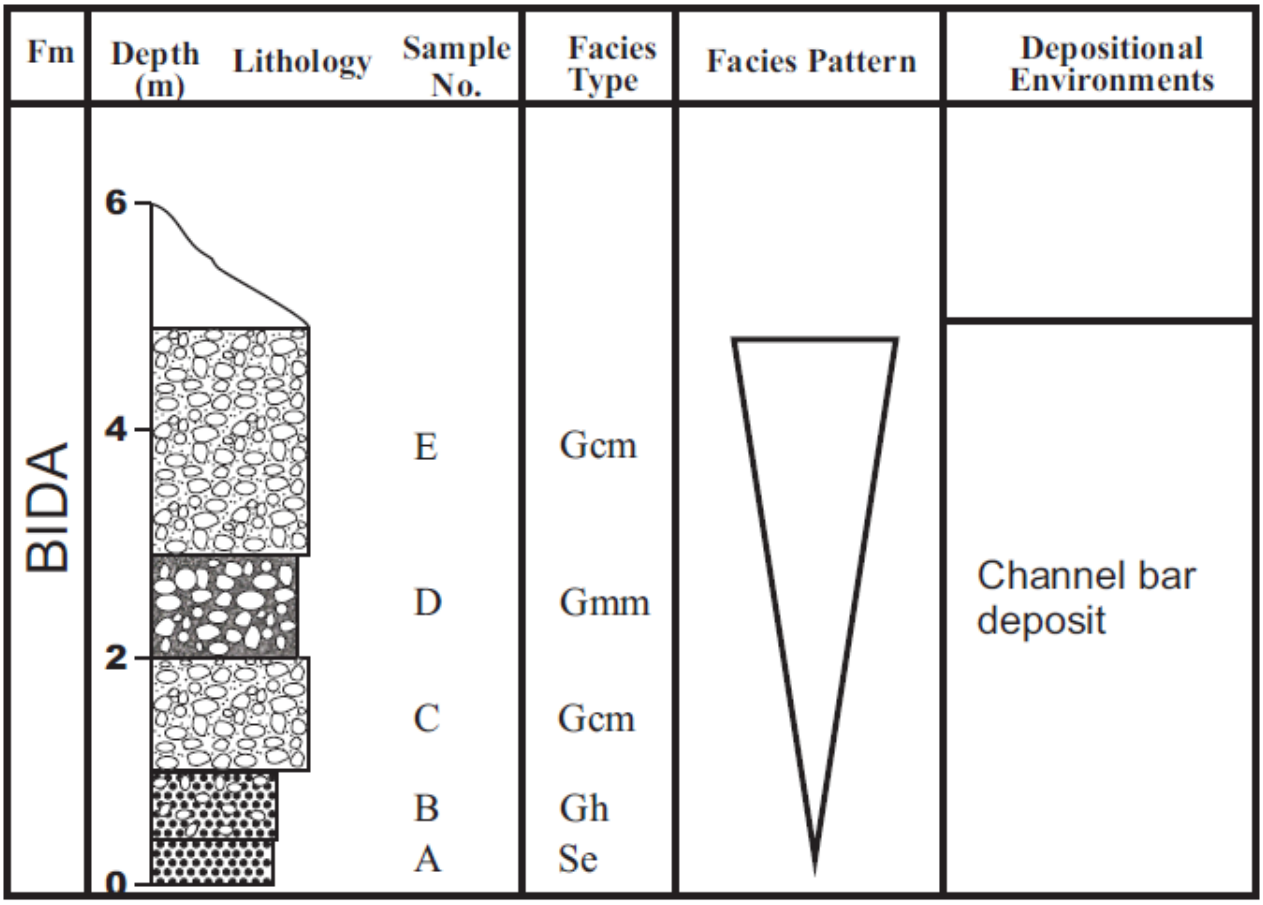


Figure XV: Lithological section of Bida Formation exposed at Patigi (PTG-1); Longitude: 08°42'53.5"N; **Latitude**: 005°46'55.7"E**.**

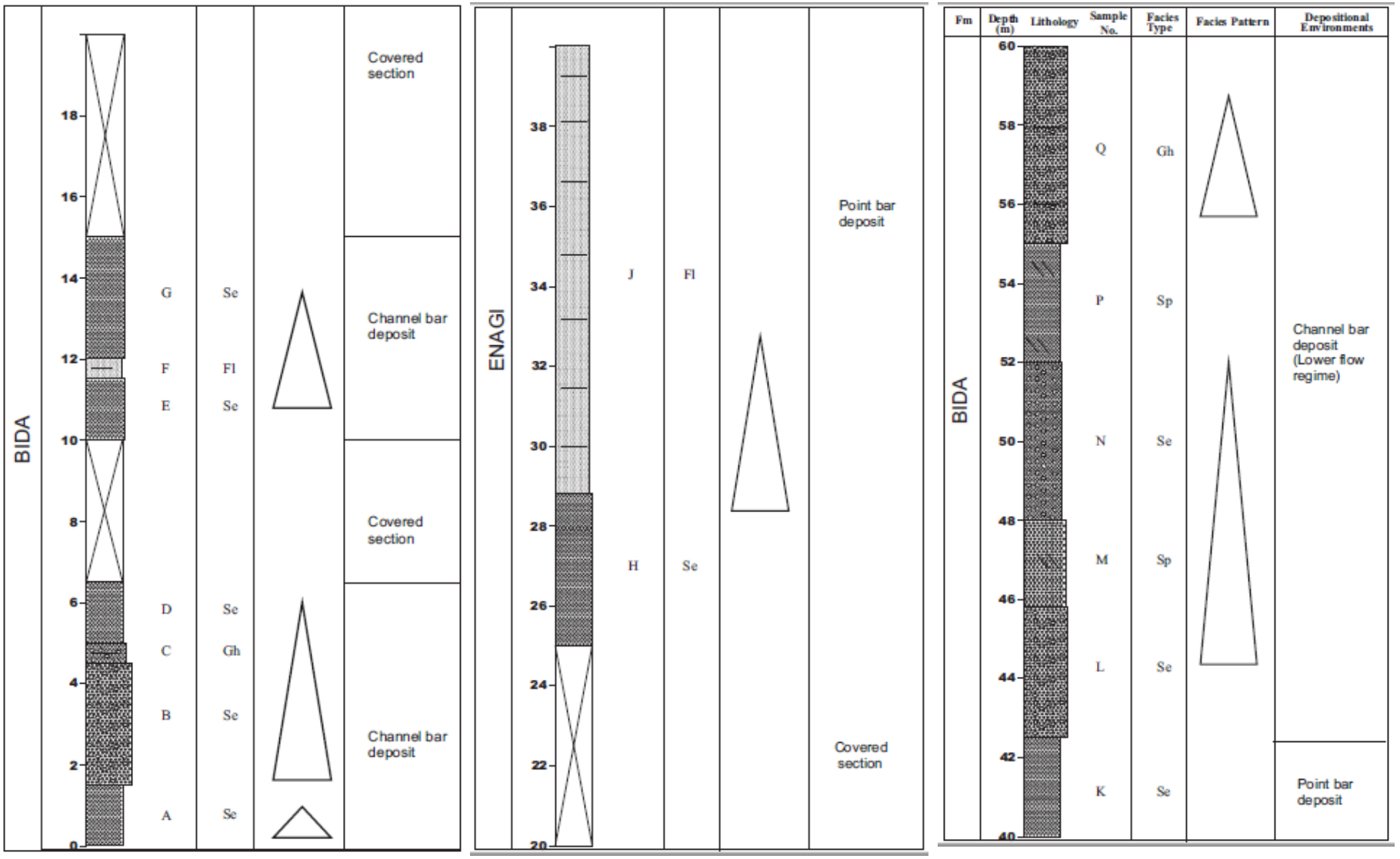


Figure XVI: Lithological section of Bida Formation exposed at Kajita (KJT-1); Longitude: 08°42'45.2"N; **Latitude**: 006°02'51.9"E**.**

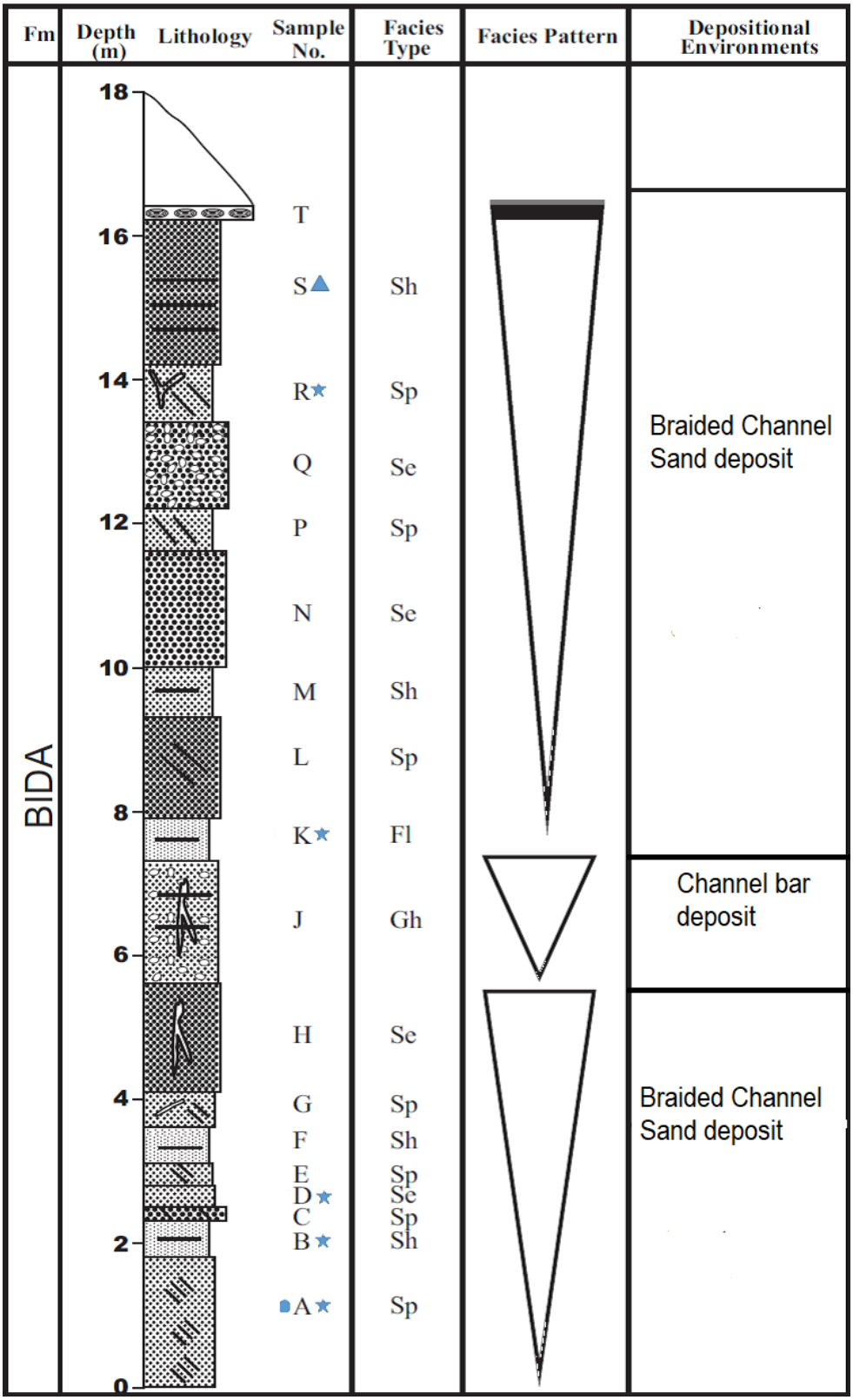


Figure XVII: Lithological section of Bida Formation exposed at Bida (BDA-1); Longitude: 005°59.98' E; **Latitude**: 09°05.98' N**.**

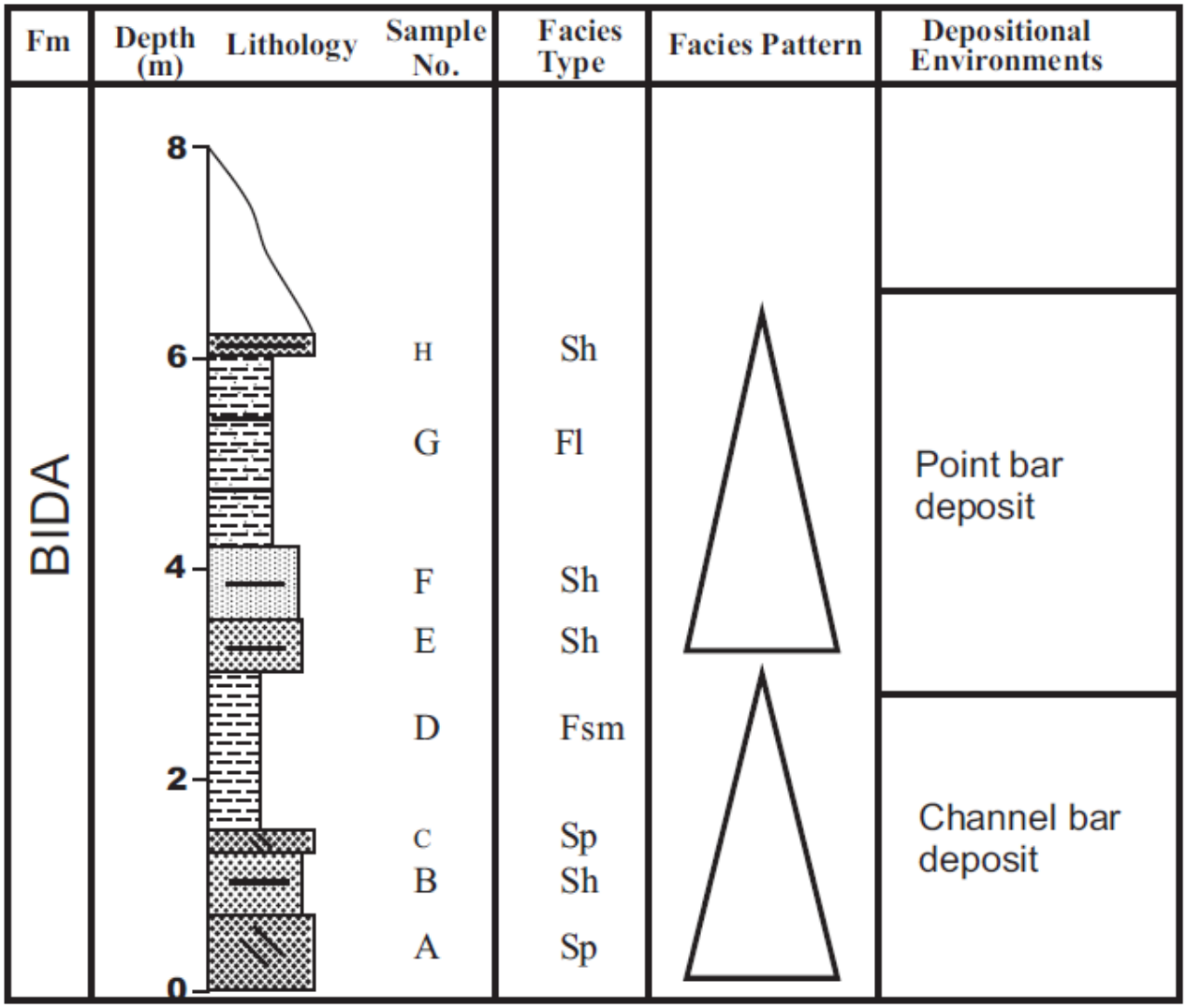


Figure XVIII: Lithological section of Bida Formation exposed at Mangotta (MGT-1); Longitude: 006°01.409'E**; Latitude:** 09°09.815'N**.**

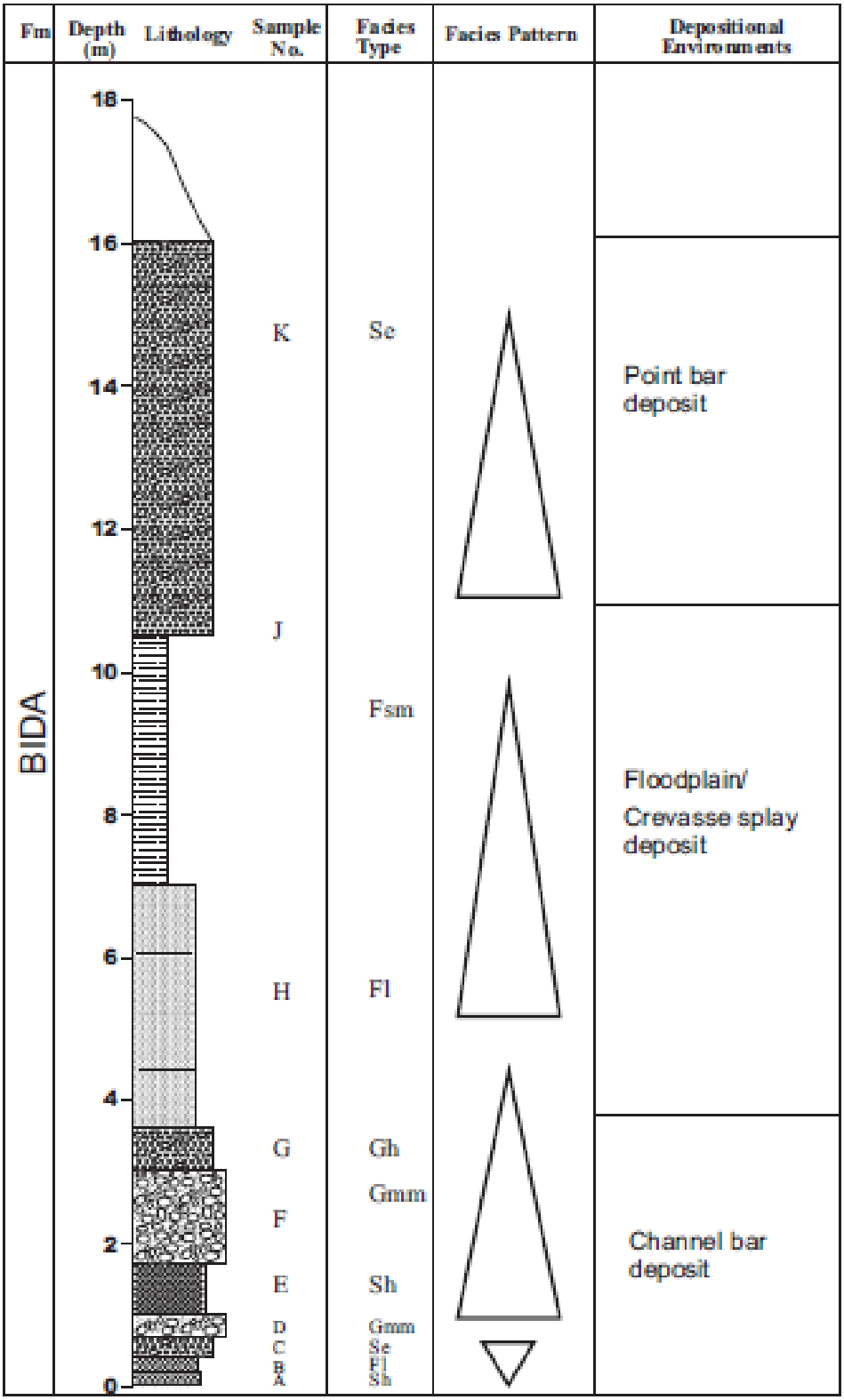


Figure XIX: Lithological section of Bida Formation exposed at Wushishi Section (WUS-1); Longitude: 006°03.846'E**; Latitude:** 09°43.621'N**.**

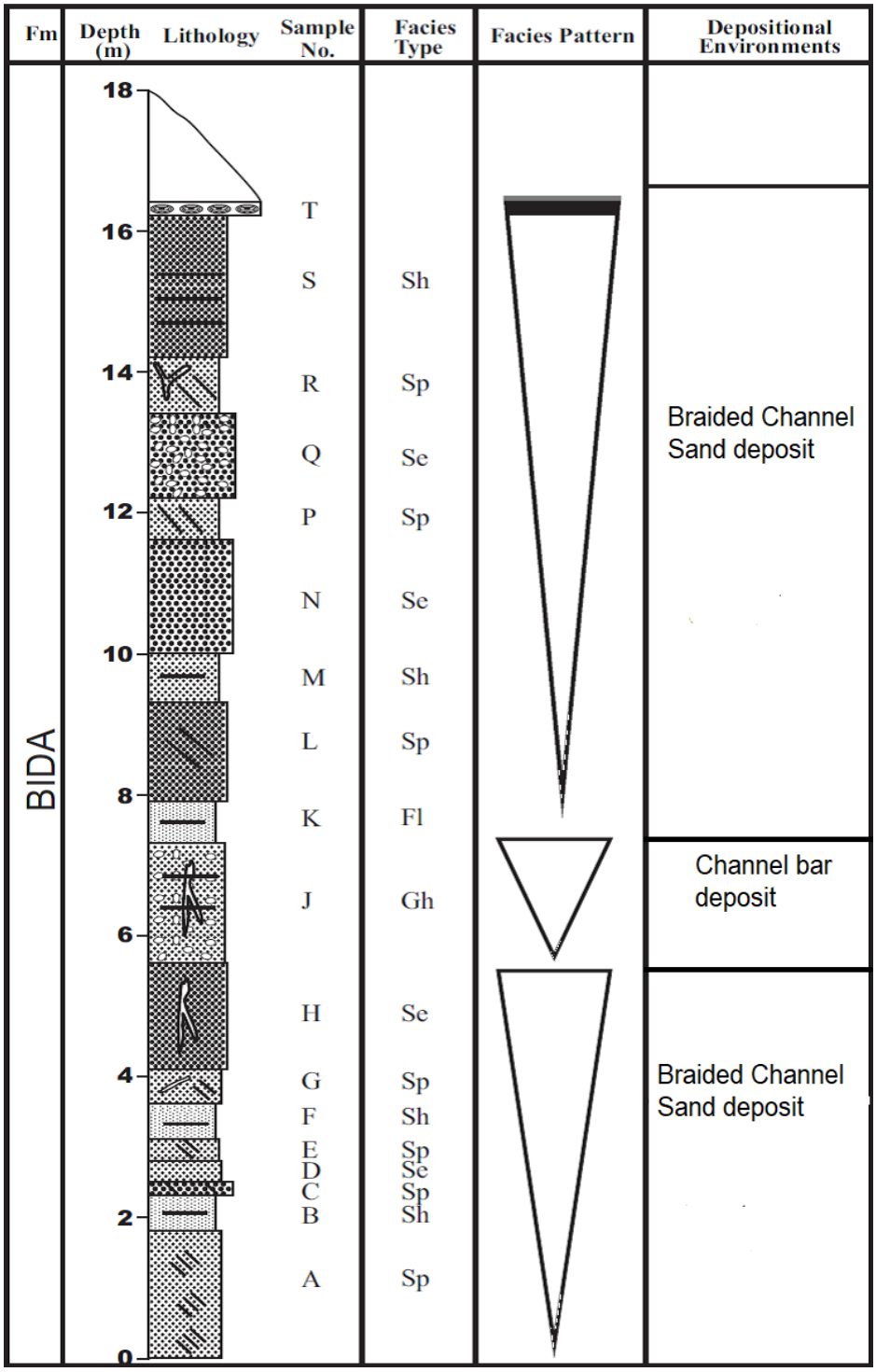


Figure XX: Lithological section of Bida Formation exposed at Lemu (LEM-1); Longitude: 005°12'14.4"E**; Latitude:** 08°46'20.7"N

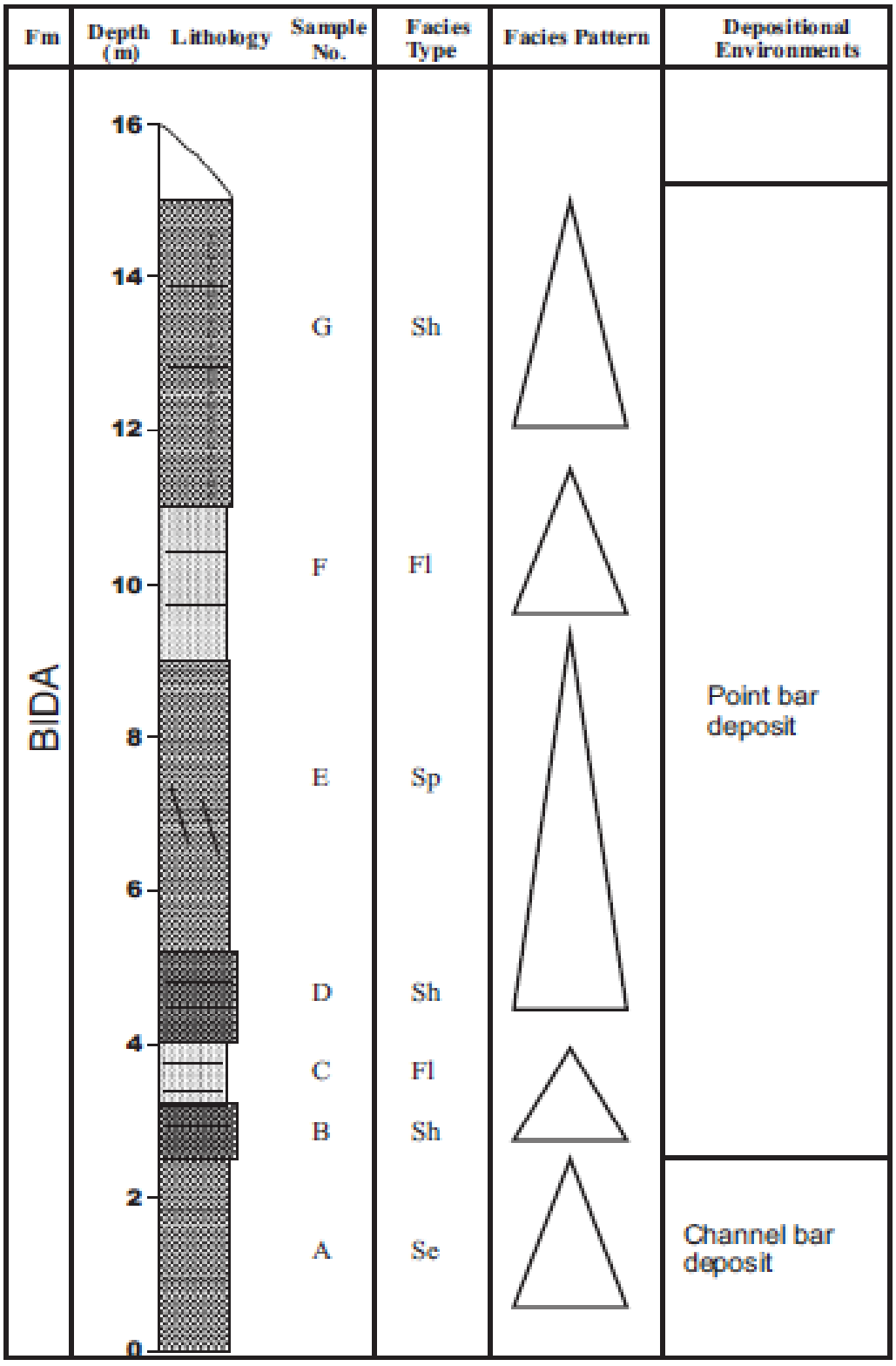


Figure XXI: Lithological section of Bida Formation exposed at Kuchi (KCH-1); Longitude: 005°59.289'E**; Latitude:** 09°01.554'N**.**

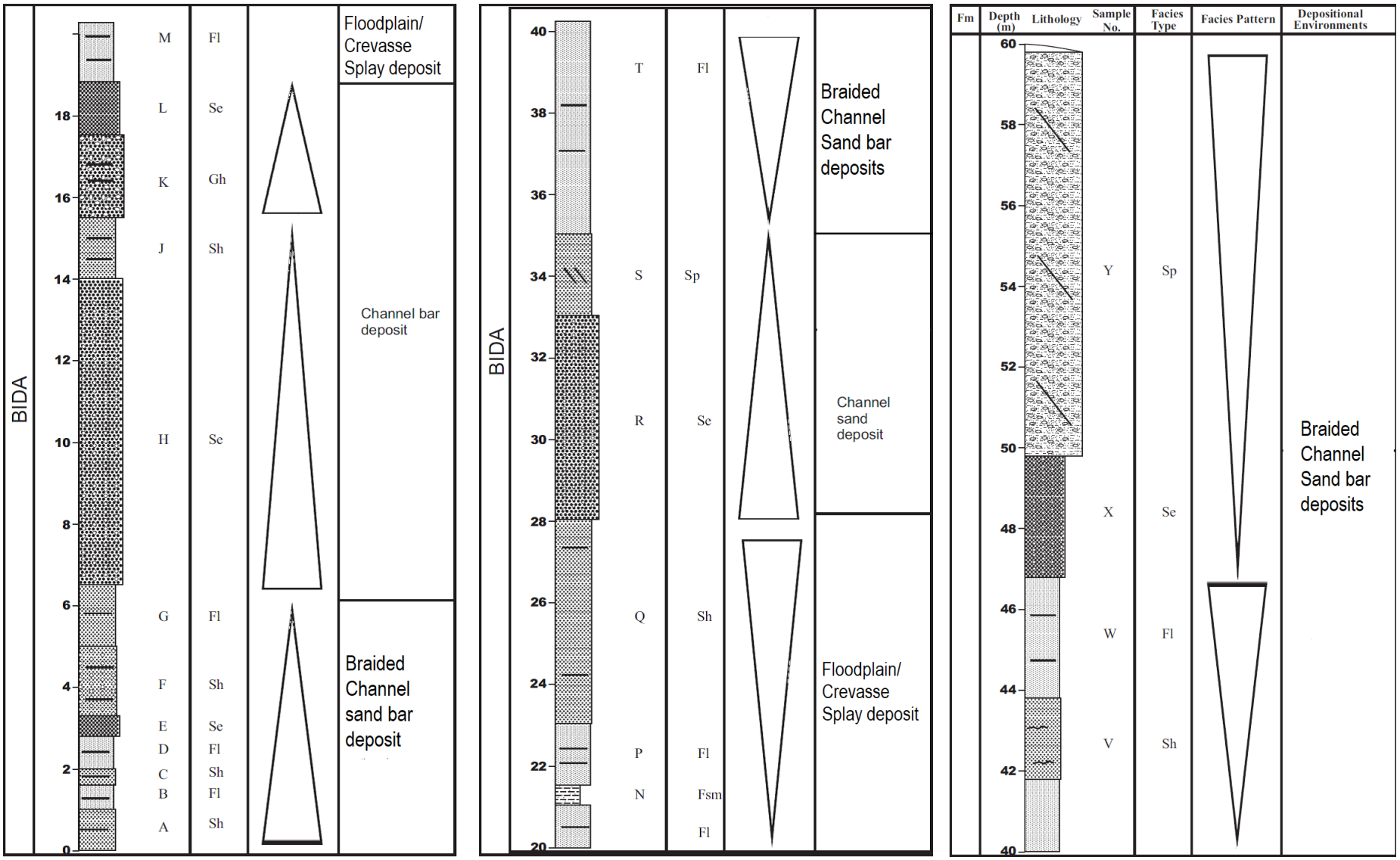


Figure XXII: Lithological section of Bida Formation exposed at Jimma (JIM-1); Longitude: 005°56.090'E**; Latitude:** 08°58.994'N**.**

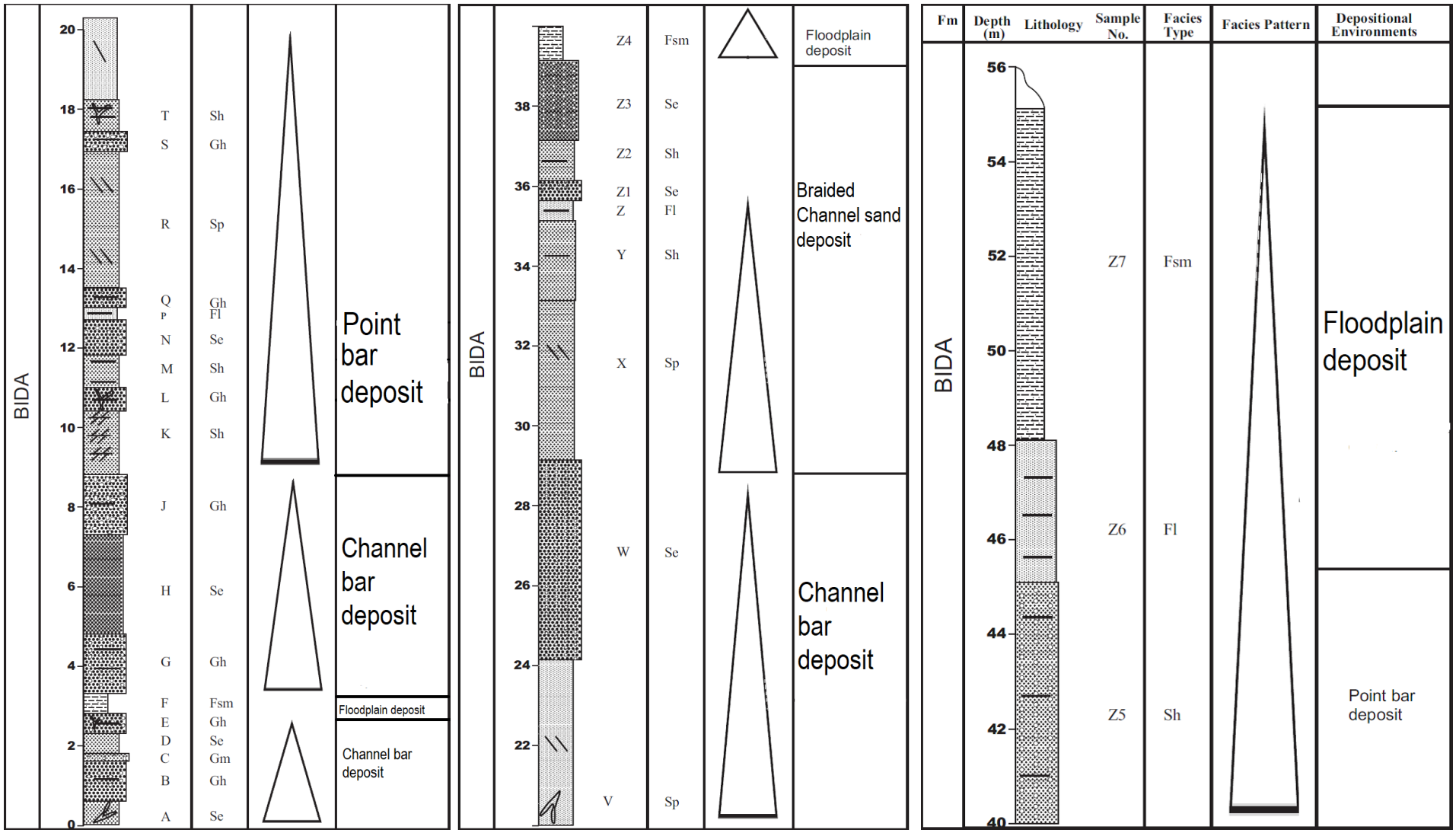


Figure XXIII: Lithological section of Bida Formation exposed at Dokko (DOK-1); Longitude: 005°37.545'E**; Latitude:** 08°56.744'N**.**

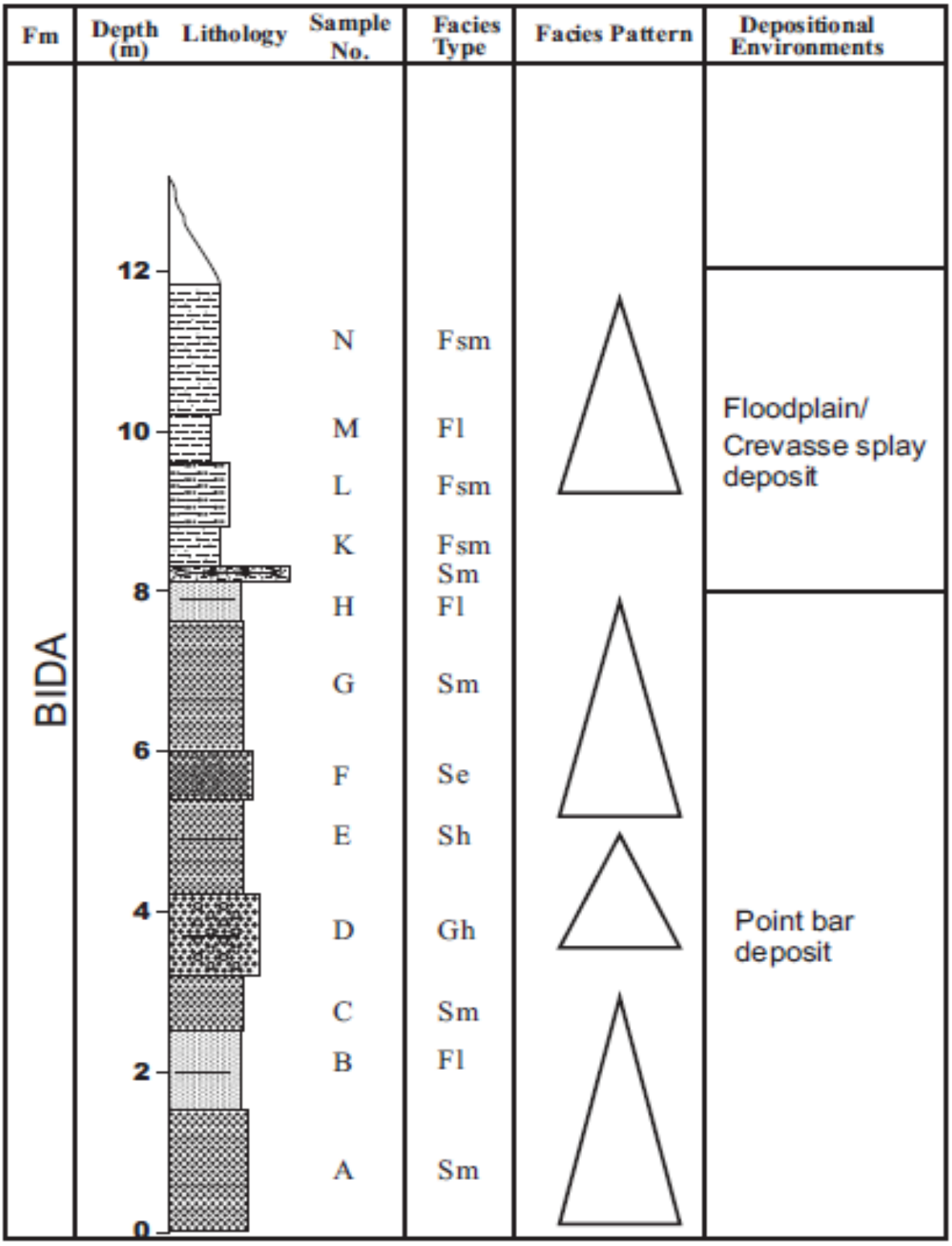


Figure XXIV: Lithological section of Bida Formation exposed at Agaei (AGE-1); Longitude: 006°19.119'E**; Latitude:** 09°02.197'N**.**

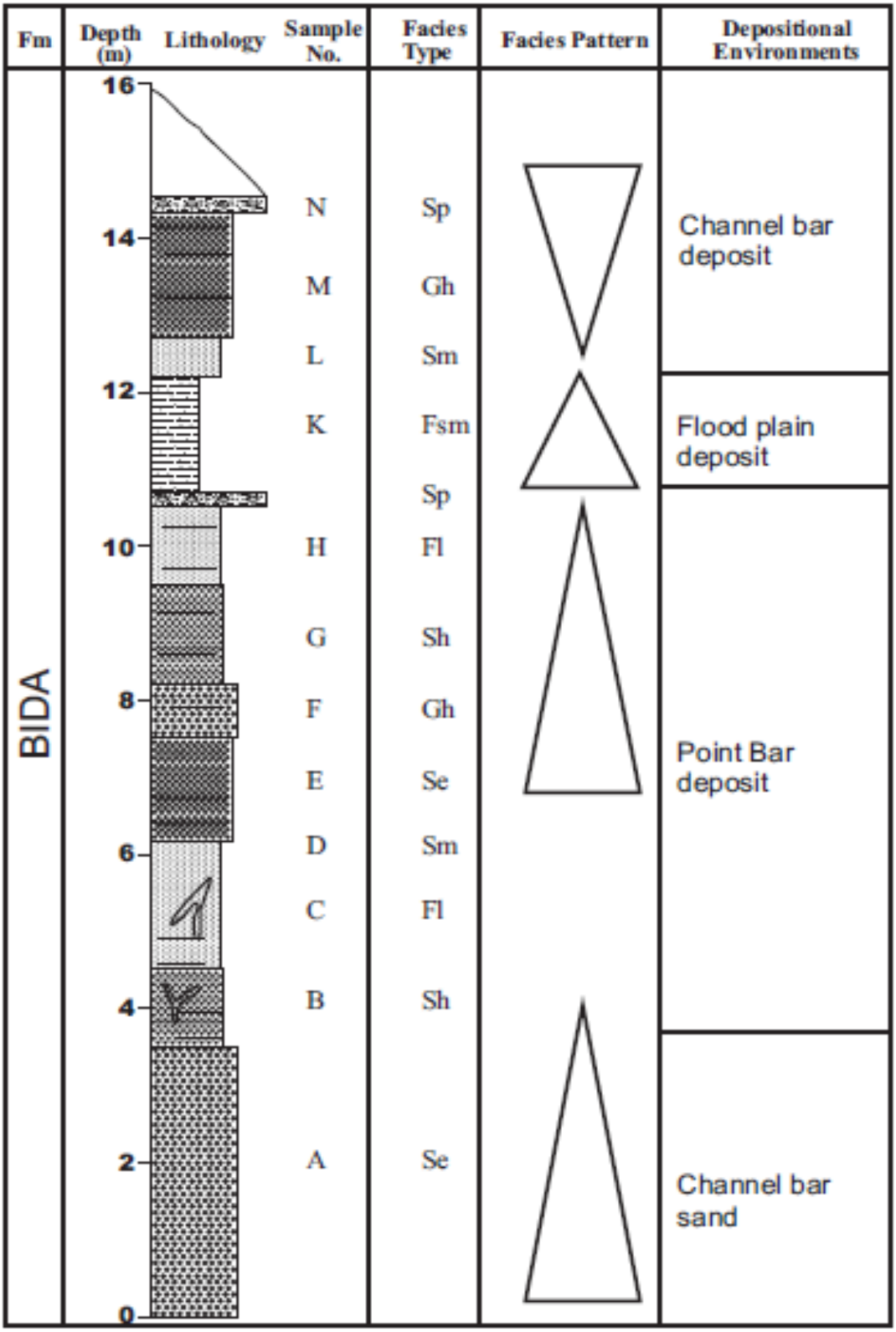


Figure XXV: Lithological section of Bida Formation exposed at Patti-Chin (PAT-1); Longitude: 09°04.449'N; **Latitude**: 006°14.018'E**.**

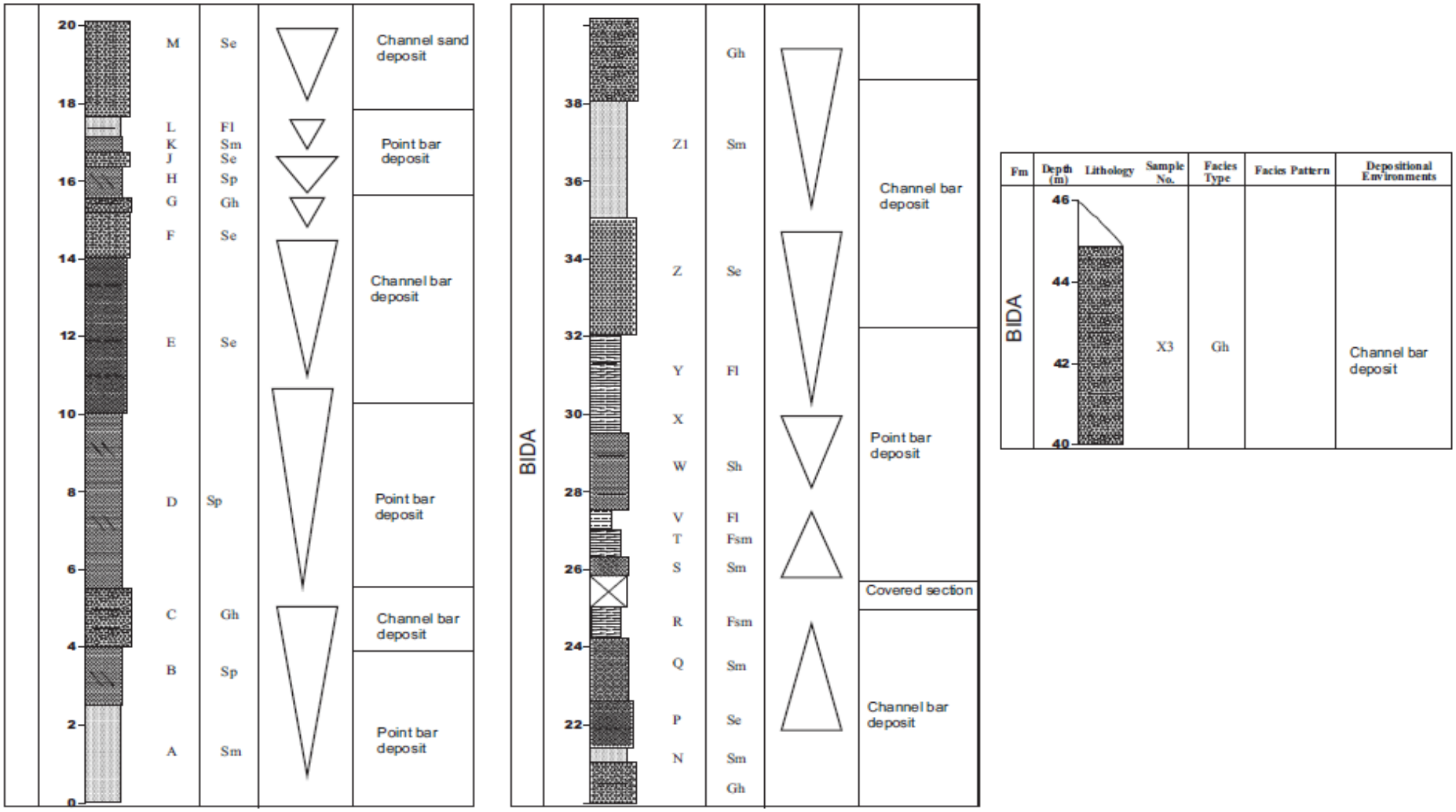


Figure XXVI: Lithological section of Bida Formation exposed at Katcha (KAC-1); Longitude: 006°18.910'E**; Latitude:** 08°45.127'N**.**

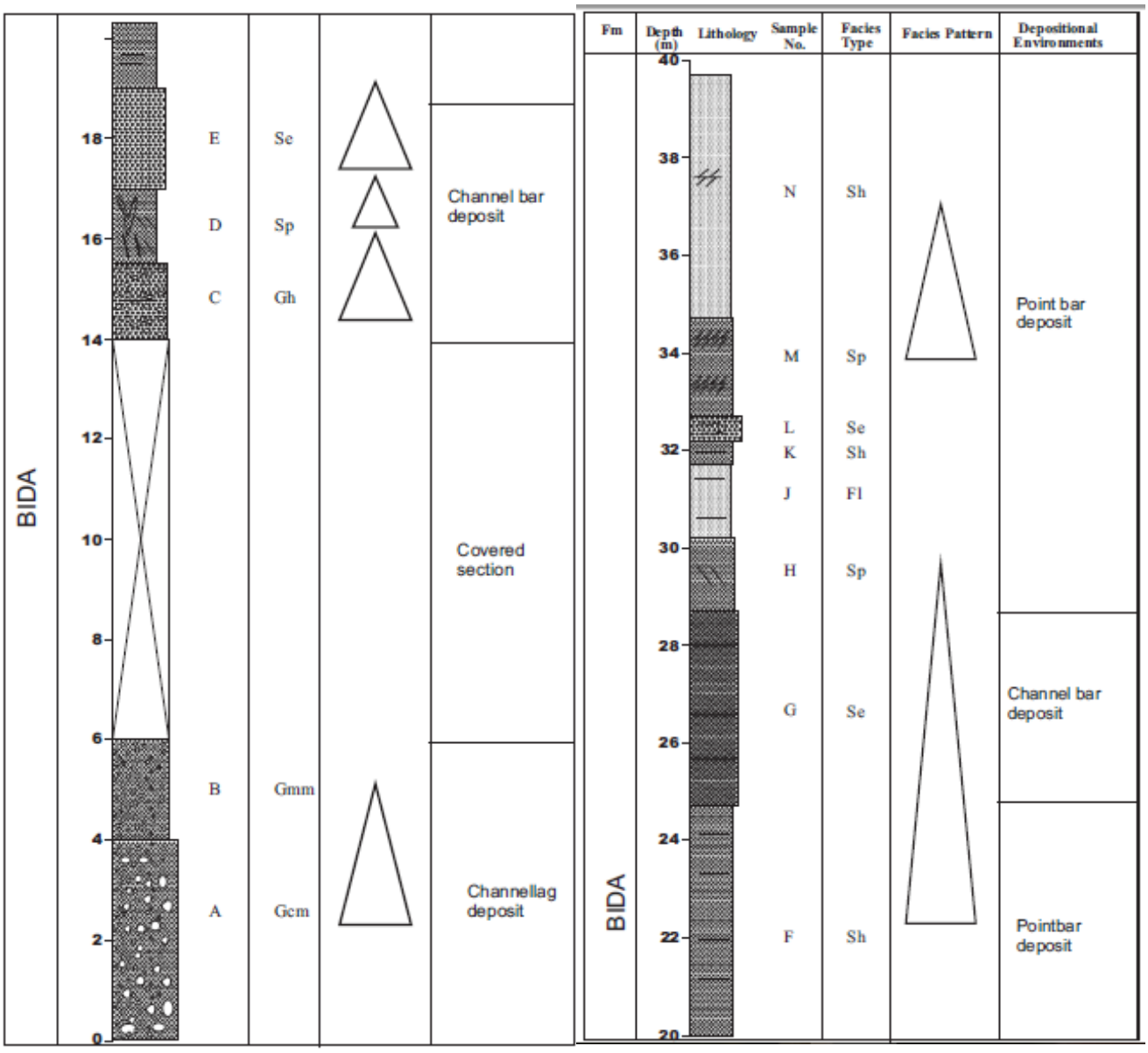


Figure XXVII: Lithological section of Bida Formation exposed at Baro (BAR-1); Longitude: 006°24.956'E**; Latitude:** 08°37.371'N**.**

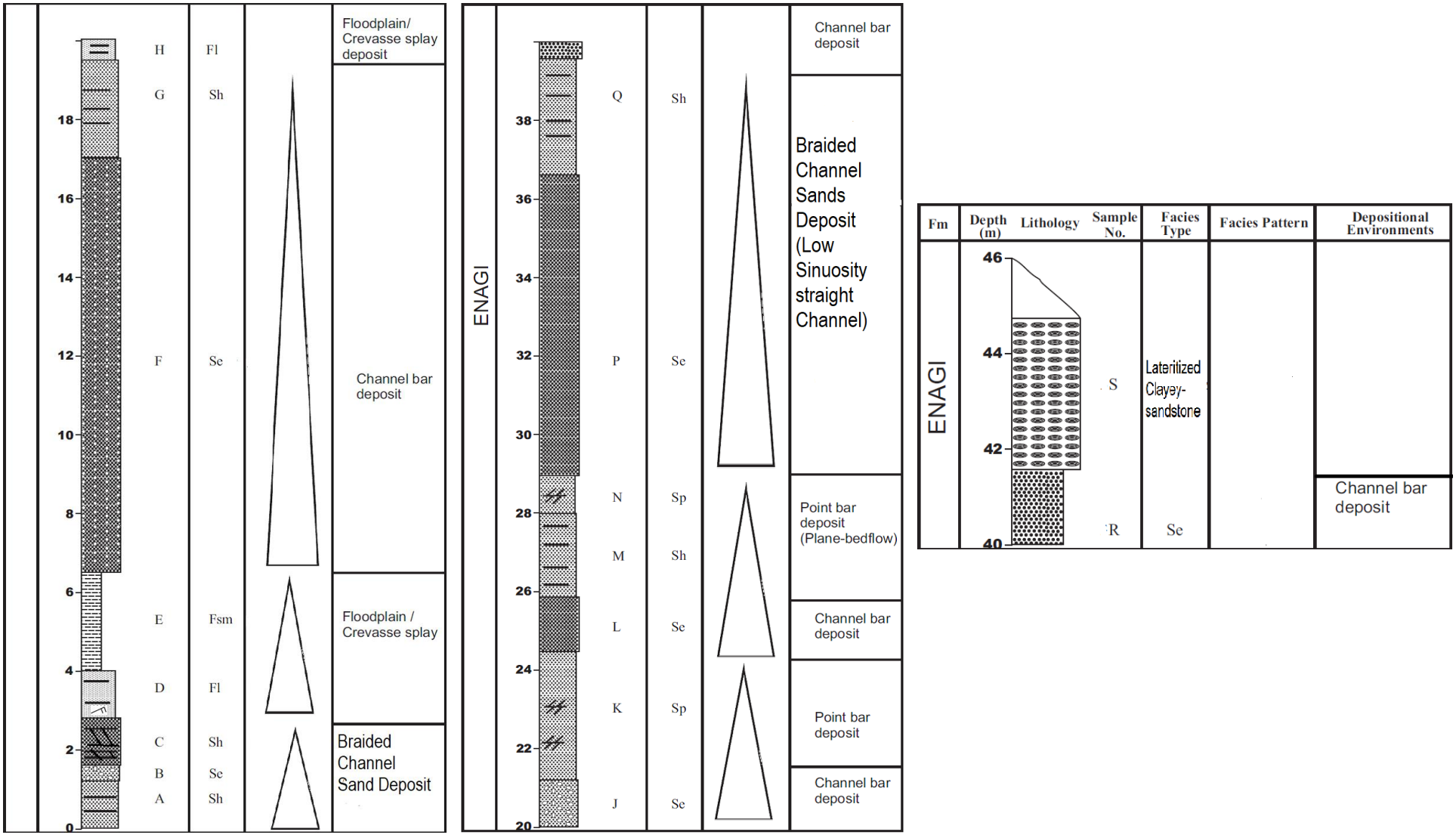


Figure XXVIII: Lithological section of Enagi Formation at exposed Agbonna Ridge (AGB-1); Longitude: 004°58'36.3"E; **Latitude**: 08°49'32.3"N**.**

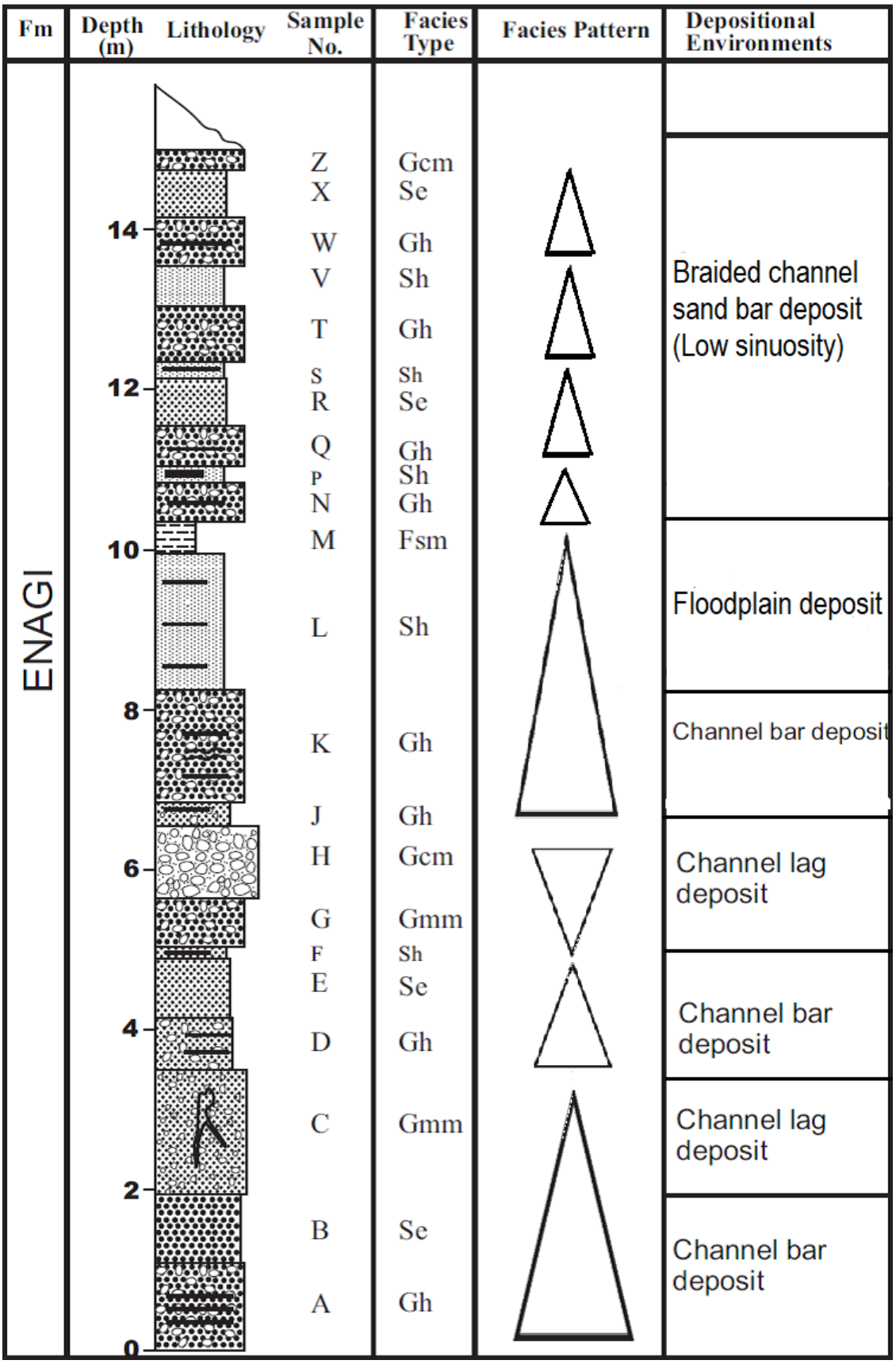


Figure XXIX: Lithological section of Enagi Formation exposed at Shonga (SHG-1); Longitude: 005°08'50.1"E; **Latitude**: 09°01'27.4"N.

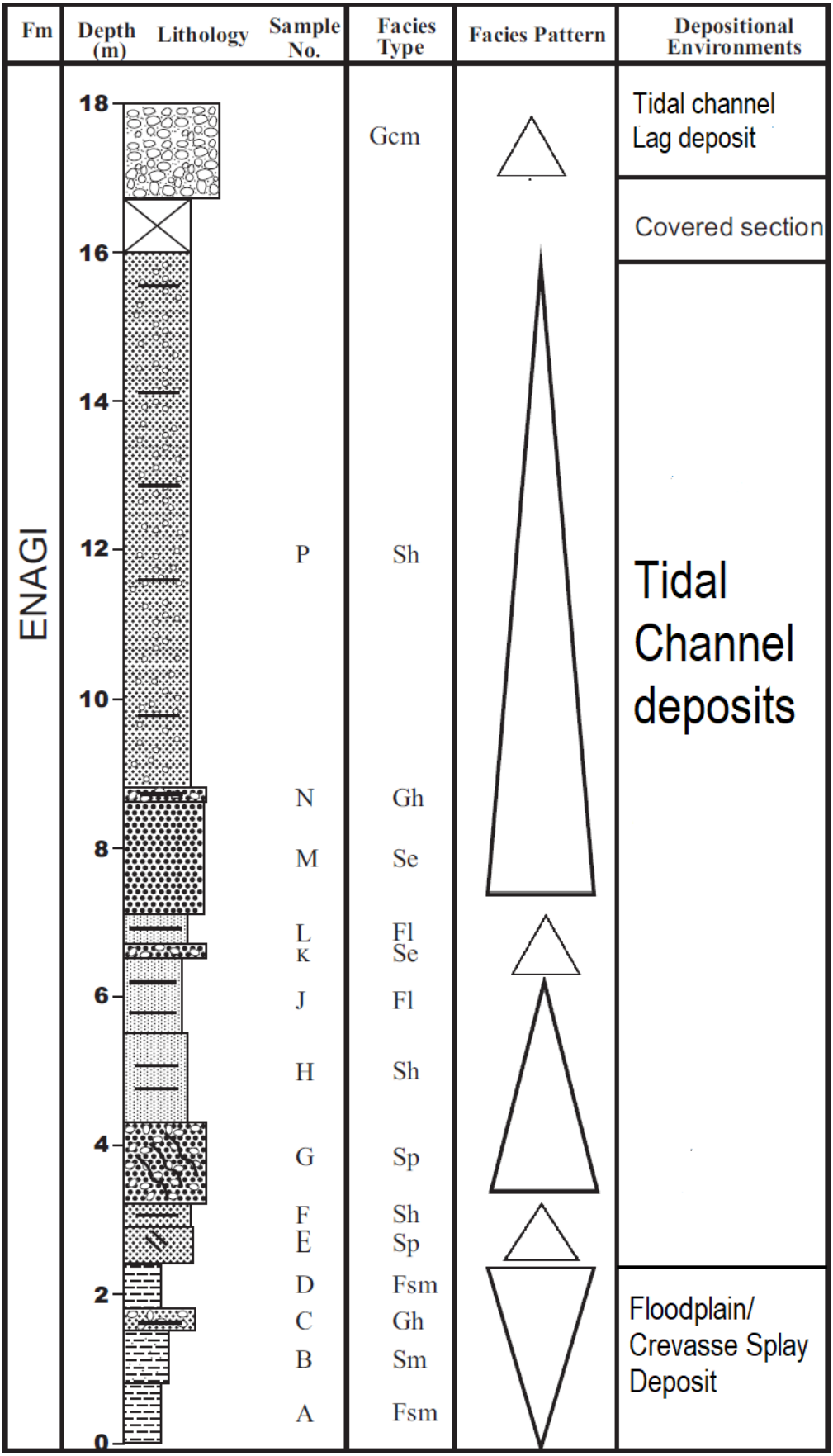


Figure XXX: Lithological section of Enagi Formation exposed at Rabba (RAB-1); Longitude: 005°01.691'E**; Latitude:** 09°12.538N**.**

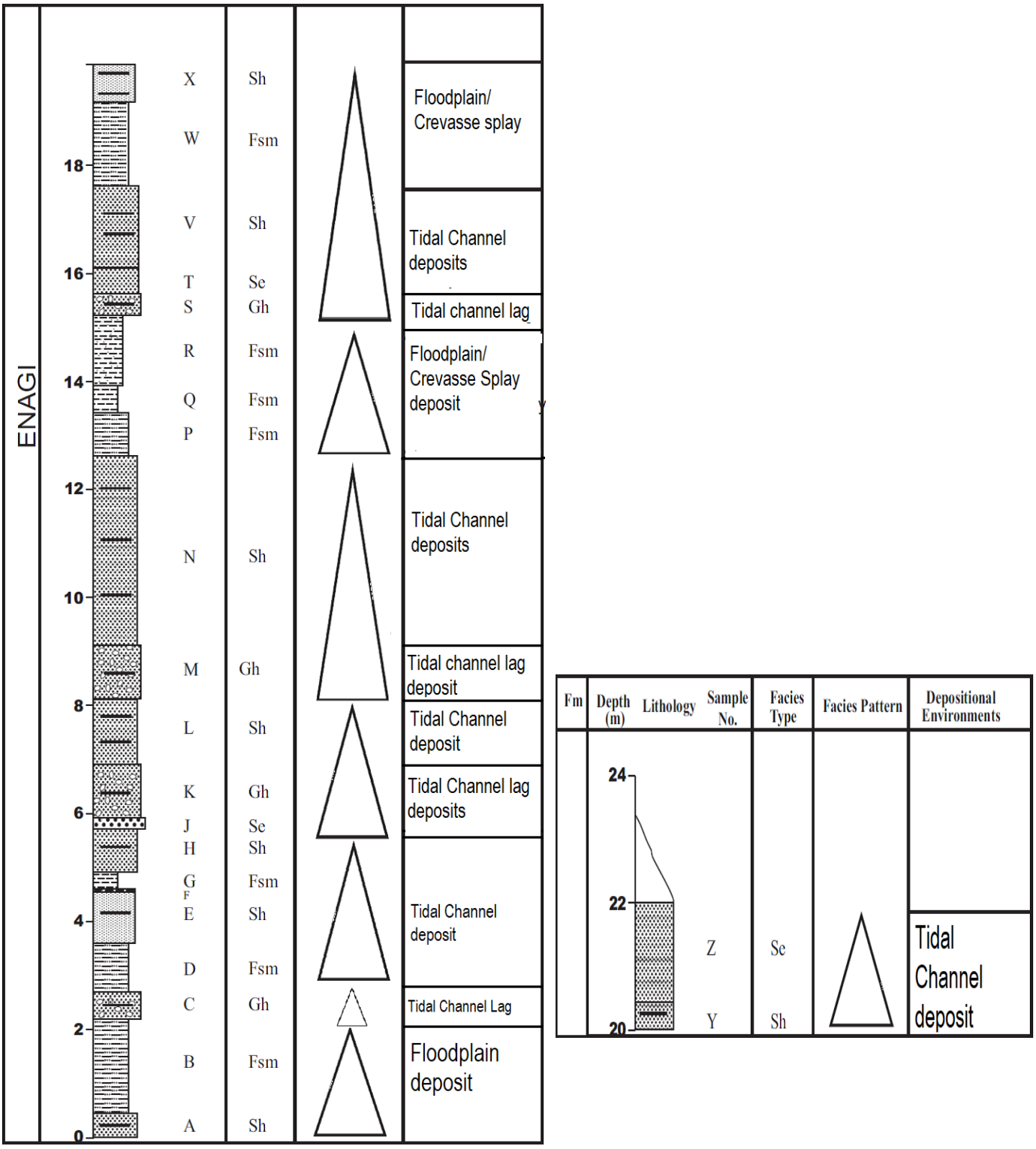


Figure XXXI: Lithological section of Enagi Formation exposed at Enagi (ENG-1); Longitude: 005°32.68' E; **Latitude**: 09°07.88' N.

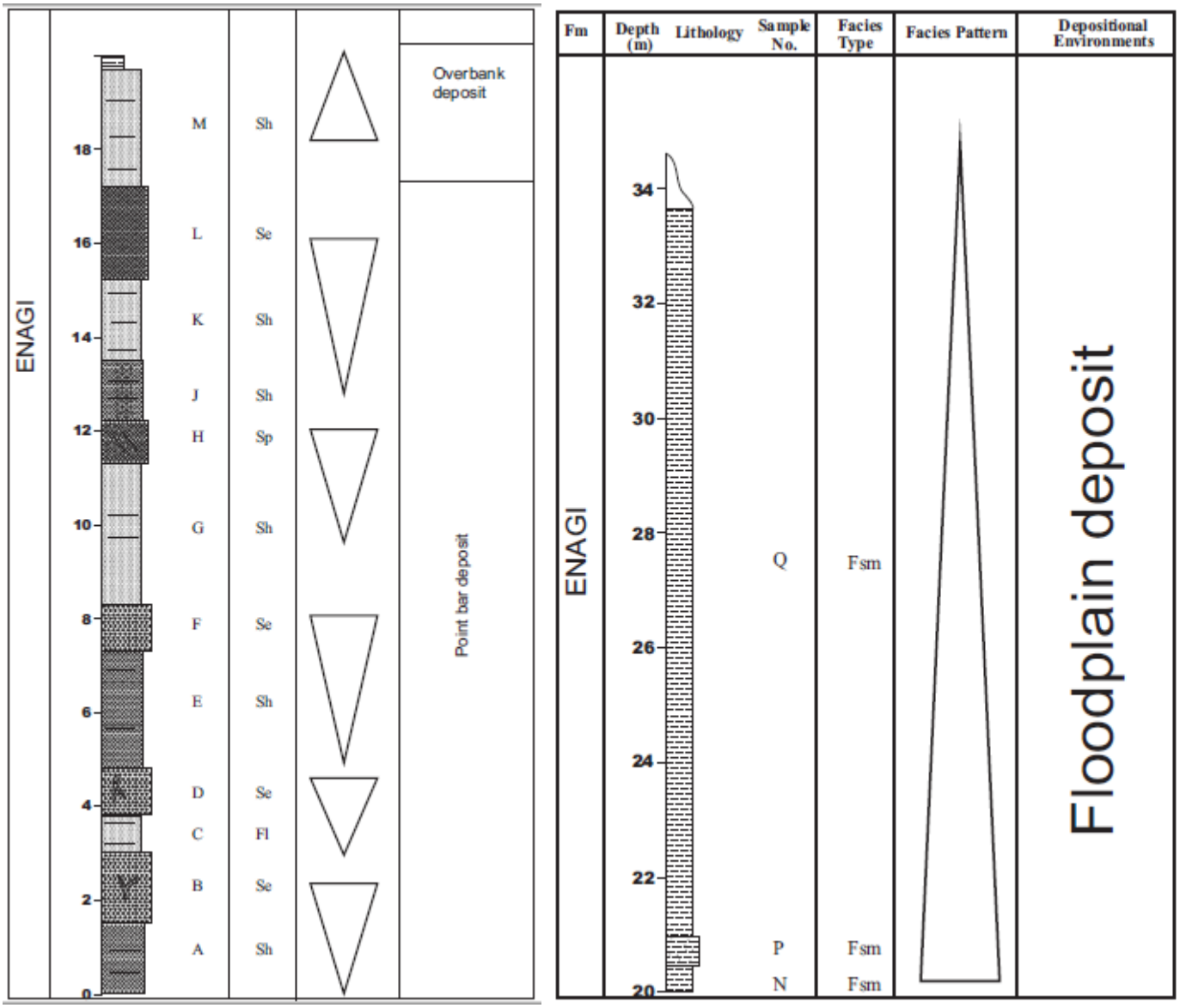


Figure XXXII: Lithological section of Enagi Formation exposed at Kutigi (KUT-1); Longitude: 005°35.43' E; **Latitude**: 09°12.03' N**.**

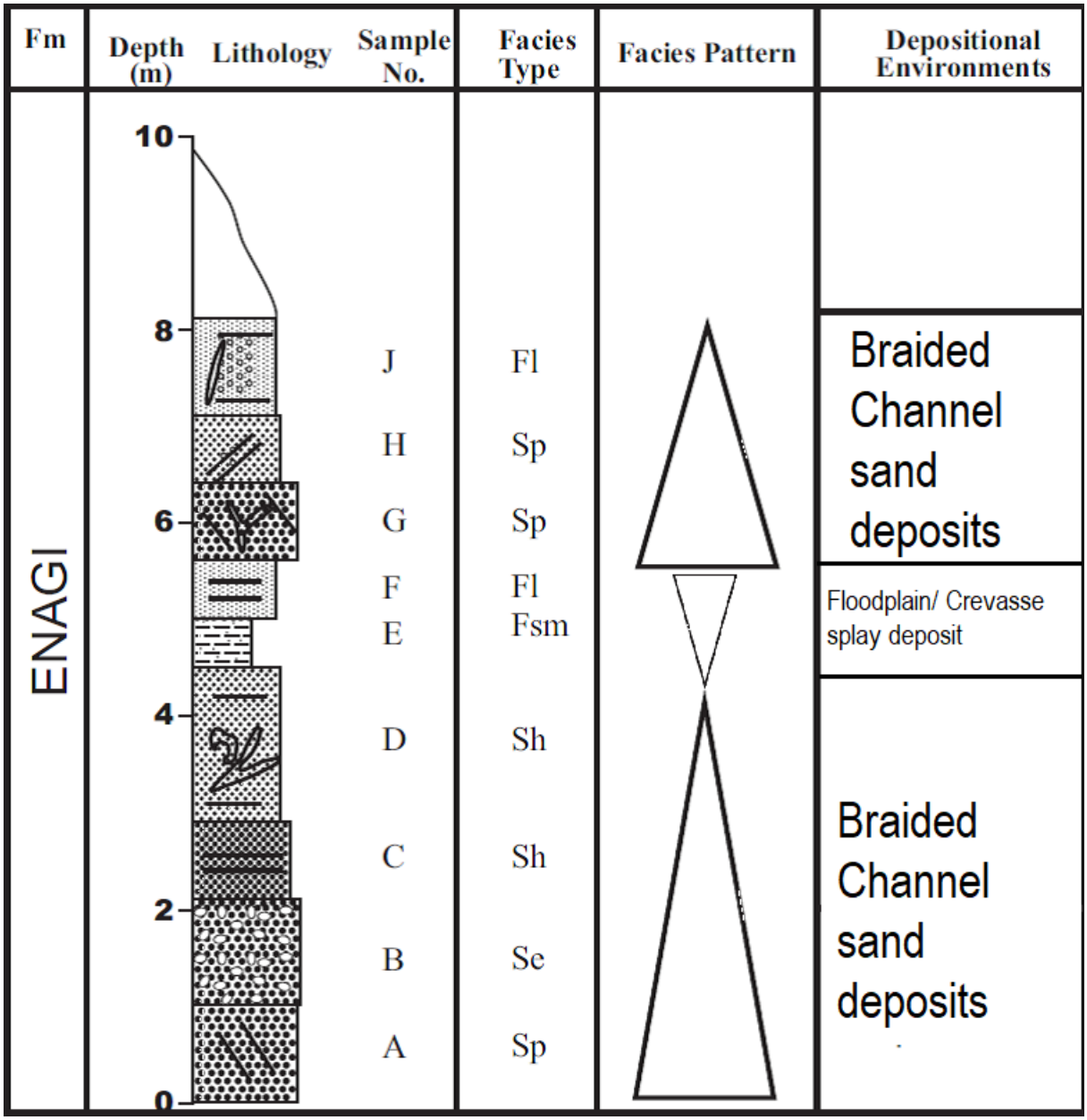


Figure XXXIII: Lithological section of Enagi Formation exposed at Tanagi (TAN-1); Longitude: 005°43.798' E; **Latitude**: 09°55.342' N**.**

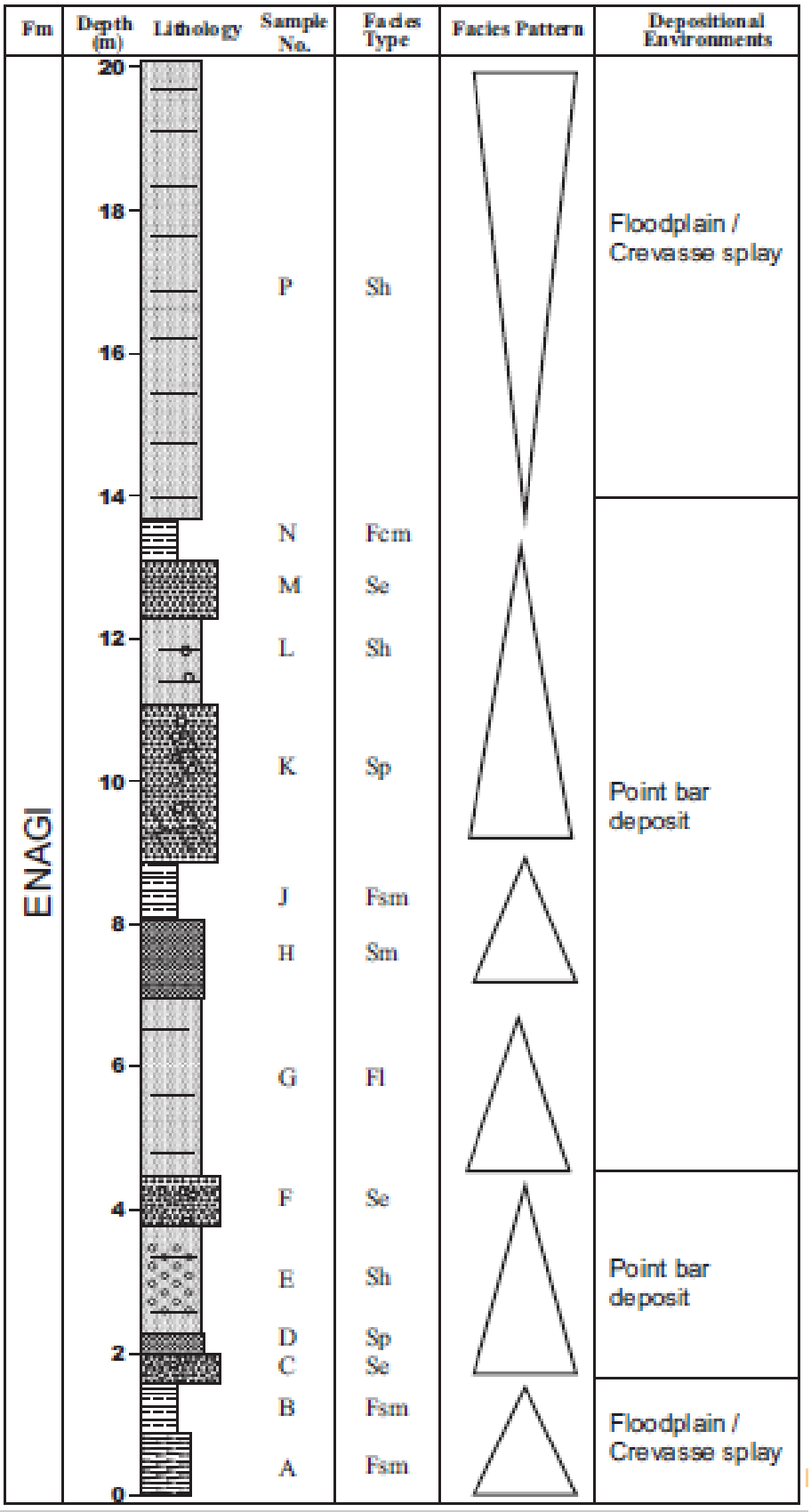


Figure XXXIV: Lithological section of Enagi Formation exposed at Rafingora-Tanagi (RAT-1); Longitude: 005°43.799' E; **Latitude**: 09°55.344' N**.**

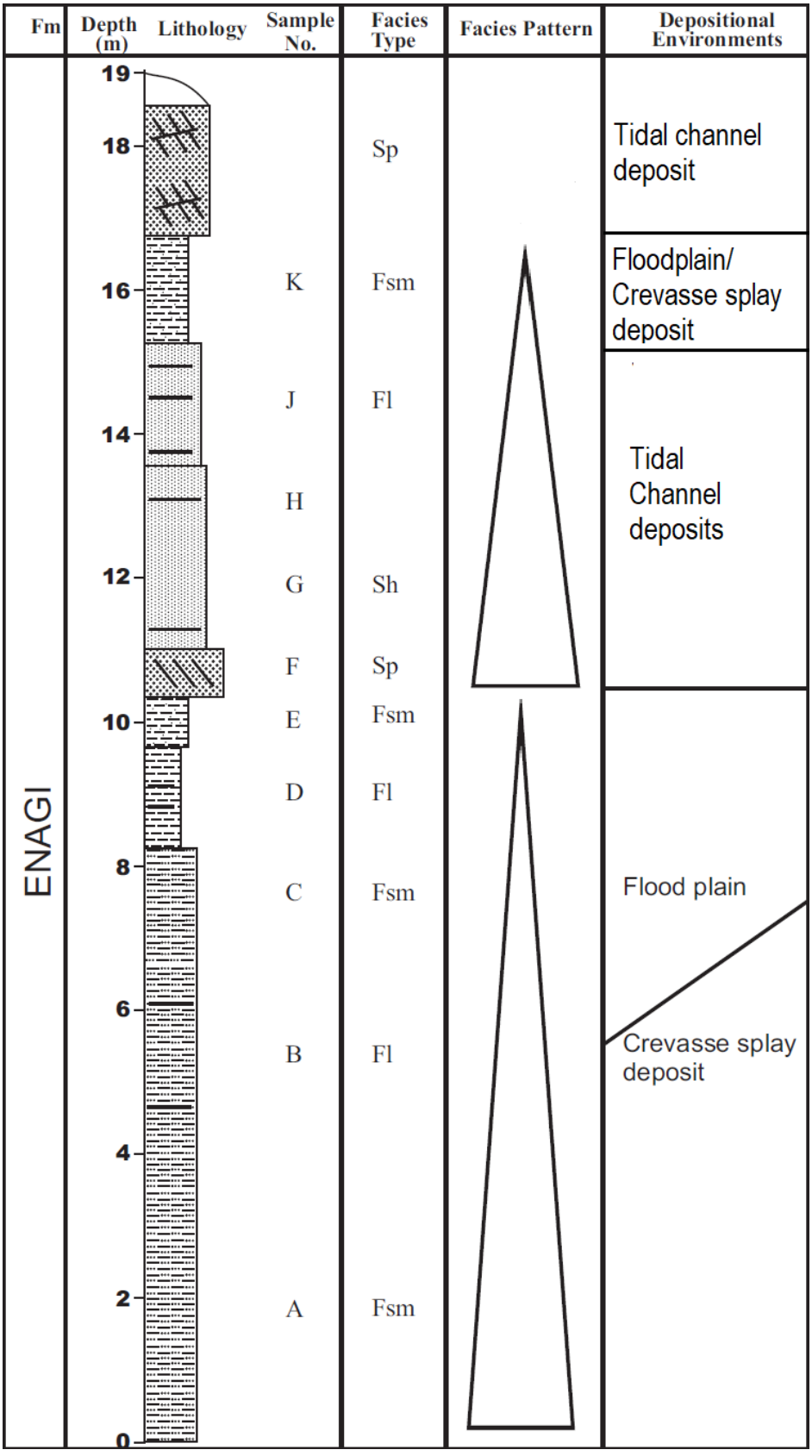


Figure XXXV: Lithological section of Enagi Formation exposed at Manigi (MAN-1); Longitude: 005°32.277' E; **Latitude**: 09°46.599' N**.**

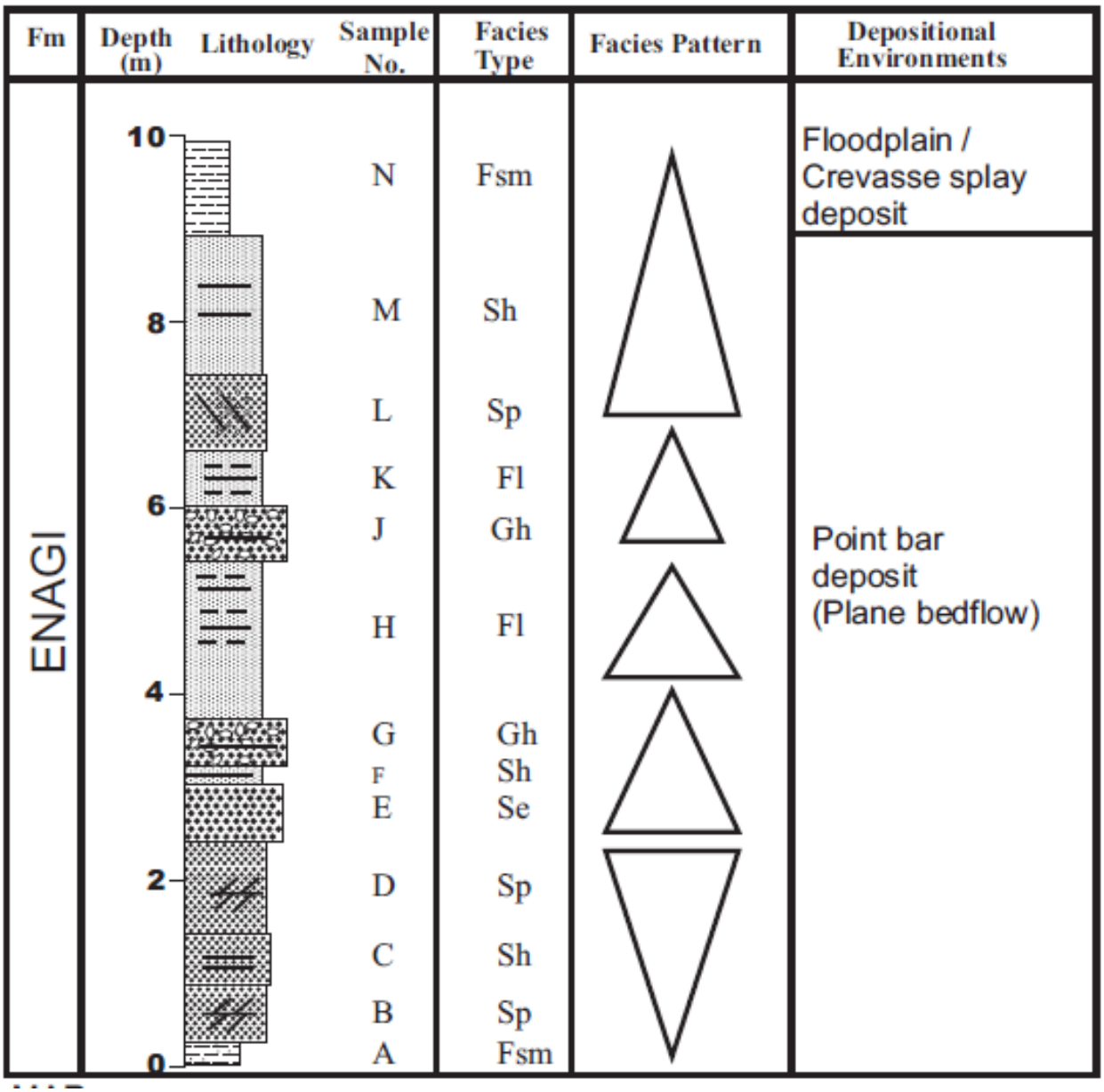


Figure XXXVI: Lithological section of Enagi Formation exposed at Maraba (MAR-1); Longitude: 005°08'50.1"E; **Latitude**: 09°01'27.4"N**.**

APPENDIX III – GRAIN SIZE ANALYSIS RESULT

Table Ia: Grain size distribution of clasts supported conglomerates (Gcm) sub-facies and interpretation after Folk and Ward (1957).

Sample No.	MEAN	S. DEVIATION	SKEWNESS	KURTOSIS	MEAN	S. DEVIATION	SKEWNESS	KURTOSIS
BAR-1A	-0.360	1.108	0.153	0.884	Very Coarse Sand	Poorly Sorted	Fine Skewed	Platykurtic
LAD-1B	-0.338	1.295	0.696	0.537	Very Coarse Sand	Poorly Sorted	Very Fine Skewed	Very Platykurtic
PTG-1C	-0.295	1.098	1.372	0.406	Very Coarse Sand	Poorly Sorted	Very Fine Skewed	Very Platykurtic
PTG-1E	0.039	1.439	0.062	0.495	Coarse Sand	Poorly Sorted	Symmetrical	Very Platykurtic
SHG-IH	-0.284	0.972	2.141	0.645	Very Coarse Sand	Moderately Sorted	Very Fine Skewed	Very Platykurtic
WAR 1E	0.021	1.436	0.163	0.756	Coarse Sand	Poorly Sorted	Fine Skewed	Platykurtic

Table Ib: Textural classification of clasts supported conglomerates (Gcm) sub-facies.

Sample No.	Gravel	Sand	Mud
BAR-1A	24.90	74.00	0.10
LAD-1B	43.20	55.00	0.80
PTG-1C	51.50	48.30	0.30
PTG-1E	11.60	88.10	0.40
SHG-IH	62.00	38.00	0.10
WAR 1E	24.40	74.00	0.60

Table IIa: Grain size distribution of matrix supported conglomerate (Gmm) sub-facies and interpretation after Folk and Ward (1957)

Sample No.	MEAN	S. DEVIATION	SKEWNESS	KURTOSIS	MEAN	S. DEVIATION	SKEWNESS	KURTOSIS
BAR-1B	-0.132	1.364	0.119	0.992	Very Coarse Sand	Poorly Sorted	Fine Skewed	Mesokurtic
DOK-1C	-0.822	1.183	0.739	0.636	Very Coarse Sand	Poorly Sorted	Very Fine Skewed	Very Platykurtic
GBL-1E	-0.068	1.576	0.464	0.580	Very Coarse Sand	Poorly Sorted	Very Fine Skewed	Very Platykurtic
GBU-1C	1.673	0.779	0.410	1.169	Medium Sand	Moderately Sorted	Very Fine Skewed	Leptokurtic
GBU-2C	-0.357	0.937	1.370	0.601	Very Coarse Sand	Moderately Sorted	Very Fine Skewed	Very Platykurtic
GBU-2F	-0.501	1.035	0.851	0.518	Very Coarse Sand	Poorly Sorted	Very Fine Skewed	Very Platykurtic
GDW-1B	-0.278	1.457	0.339	0.850	Very Coarse Sand	Poorly Sorted	Very Fine Skewed	Platykurtic
LAD-1E	-0.054	1.439	0.240	0.864	Very Coarse Sand	Poorly Sorted	Fine Skewed	Platykurtic
LAF-1E	-0.018	1.566	0.184	1.137	Very Coarse Sand	Poorly Sorted	Fine Skewed	Leptokurtic
PTG-1D	-0.372	1.091	0.167	0.703	Very Coarse Sand	Poorly Sorted	Fine Skewed	Platykurtic
SHG-IC	0.707	1.075	-0.441	1.189	Coarse Sand	Poorly Sorted	Very Coarse Skewed	Leptokurtic
SHG-IG	0.826	0.961	-0.256	1.318	Coarse Sand	Moderately Sorted	Coarse Skewed	Leptokurtic
WUS-1D	-0.259	1.196	0.042	0.945	Very Coarse Sand	Poorly Sorted	Symmetrical	Mesokurtic
WUS-1F	-0.315	1.198	0.709	0.445	Very Coarse Sand	Poorly Sorted	Very Fine Skewed	Very Platykurtic
ZAM-1B	0.782	1.651	-0.027	0.760	Coarse Sand	Poorly Sorted	Symmetrical	Platykurtic

Table IIb: Textural classification of matrix supported conglomerate (Gmm) sub-facies.

Sample No.	Gravel	Sand	Mud
BAR-1B	24.80	74.00	0.30
DOK-1C	51.50	48.30	0.20
GBL-1E	35.20	62.80	1.00
GBU-1C	30.30	69.40	0.30
GBU-2C	52.00	47.70	0.40
GBU-2F	45.30	53.30	0.50
GDW-1B	33.50	64.80	0.70
LAD-1E	25.00	73.30	0.80
LAF-1E	24.70	73.90	1.30
PTG-1D	42.60	57.10	0.30
SHG-IC	10.60	89.40	0.10
SHG-IG	25.20	73.70	0.10
WUS-1D	24.50	74.30	0.20
WUS-1F	43.30	55.30	0.40
ZAM-1B	18.20	81.40	0.40

Table IIIa: Grain size distribution of crudely bedded conglomerate (Gh) sub-facies and interpretation after Folk and Ward (1957).

Sample No.	MEAN	S. DEVIATION	SKEWNESS	KURTOSIS	MEAN	S. DEVIATION	SKEWNESS	KURTOSIS
AGE-1D	0.19	1.254	0.142	1.104	Coarse Sand	Poorly Sorted	Fine Skewed	Mesokurtic
BDA-1J	-0.156	1.206	0.047	1.238	Very Coarse Sand	Poorly Sorted	Symmetrical	Leptokurtic
BGK-1G	0.617	1.315	-0.095	0.435	Coarse Sand	Poorly Sorted	Symmetrical	Very Platykurtic
DOK-1B	-0.687	1.168	0.57	0.709	Very Coarse Sand	Poorly Sorted	Very Fine Skewed	Platykurtic
DOK-1E	-0.665	1.207	0.238	1.199	Very Coarse Sand	Poorly Sorted	Fine Skewed	Leptokurtic
DOK-1G	-0.622	1.036	0.337	0.735	Very Coarse Sand	Poorly Sorted	Very Fine Skewed	Platykurtic
DOK-1J	-0.211	1.382	0.151	0.990	Very Coarse Sand	Poorly Sorted	Fine Skewed	Mesokurtic
DOK-1L	-0.032	1.171	0.266	1.217	Very Coarse Sand	Poorly Sorted	Fine Skewed	Leptokurtic
ENG-1C	0.272	1.286	0.077	1.051	Coarse Sand	Poorly Sorted	Symmetrical	Mesokurtic
ENG-1K	0.522	1.295	0.065	1.039	Coarse Sand	Poorly Sorted	Symmetrical	Mesokurtic
ENG-1M	1.507	1.370	-0.201	1.443	Medium Sand	Poorly Sorted	Coarse Skewed	Leptokurtic
ENG-1S	-0.388	1.220	0.214	1.175	Very Coarse Sand	Poorly Sorted	Fine Skewed	Leptokurtic
GBU-1D	0.584	1.215	-0.119	1.039	Coarse Sand	Poorly Sorted	Coarse Skewed	Mesokurtic
GBU-2B	-0.1	1.349	0.101	0.648	Very Coarse Sand	Poorly Sorted	Fine Skewed	Very Platykurtic
GBU-2E	0.634	1.602	-0.229	0.972	Coarse Sand	Poorly Sorted	Coarse Skewed	Mesokurtic
GDW-1A	-0.395	1.187	0.195	1.137	Very Coarse Sand	Poorly Sorted	Fine Skewed	Leptokurtic
GDW-1C	-0.499	1.073	0.895	0.528	Very Coarse Sand	Poorly Sorted	Very Fine Skewed	Very Platykurtic
JIM-1K	-0.411	1.221	0.196	1.124	Very Coarse Sand	Poorly Sorted	Fine Skewed	Leptokurtic
KAC-1C	-0.106	1.153	0.209	0.822	Very Coarse Sand	Poorly Sorted	Fine Skewed	Platykurtic
KAC-1G	-0.009	1.088	-0.053	1.082	Very Coarse Sand	Poorly Sorted	Symmetrical	Mesokurtic
KAC-1X3	0.364	1.386	0.004	1.137	Coarse Sand	Poorly Sorted	Symmetrical	Leptokurtic
KJT-1C	0.536	1.386	-0.007	0.969	Coarse Sand	Poorly Sorted	Symmetrical	Mesokurtic
KJT-1Q	-0.37	1.161	0.177	0.773	Very Coarse Sand	Poorly Sorted	Fine Skewed	Platykurtic
KUT-1C	1.526	1.396	-0.545	1.276	Medium Sand	Poorly Sorted	Very Coarse Skewed	Leptokurtic
LEM-1B	0.76	1.787	-0.085	0.880	Coarse Sand	Poorly Sorted	Symmetrical	Platykurtic

LEM-1K	0.007	1.113	0.176	1.311	Coarse Sand	Poorly Sorted	Fine Skewed	Leptokurtic
MAR-1G	-0.077	1.182	0.549	0.445	Very Coarse Sand	Poorly Sorted	Very Fine Skewed	Very Platykurtic
MAR-1J	-0.612	1.434	0.501	1.122	Very Coarse Sand	Poorly Sorted	Very Fine Skewed	Leptokurtic
PAT-1F	-0.131	1.373	0.172	1.216	Very Coarse Sand	Poorly Sorted	Fine Skewed	Leptokurtic
PTG-1B	-0.159	1.431	0.199	0.545	Very Coarse Sand	Poorly Sorted	Fine Skewed	Very Platykurtic
RAB-1C	-0.823	0.762	1.217	0.498	Very Coarse Sand	Moderately Sorted	Very Fine Skewed	Very Platykurtic
RAB-1N	-0.675	0.704	2.742	0.763	Very Coarse Sand	Moderately Sorted	Very Fine Skewed	Platykurtic
SHG-1J	0.224	1.049	0.599	0.478	Coarse Sand	Poorly Sorted	Very Fine Skewed	Very Platykurtic
SHG-1A	1.350	0.659	-0.034	2.118	Medium Sand	Moderately Well Sorted	Symmetrical	Very Leptokurtic
SHG-1K	-0.361	1.121	0.213	0.930	Very Coarse Sand	Poorly Sorted	Fine Skewed	Mesokurtic
SHG-1N	1.888	1.307	-0.278	0.896	Medium Sand	Poorly Sorted	Coarse Skewed	Platykurtic
SHG-1Q	0.886	1.024	-0.117	1.680	Coarse Sand	Poorly Sorted	Coarse Skewed	Very Leptokurtic
SHG-1T	-0.431	1.251	0.339	0.628	Very Coarse Sand	Poorly Sorted	Very Fine Skewed	Very Platykurtic
SHG-1W	-0.402	1.23	0.327	1.433	Very Coarse Sand	Poorly Sorted	Very Fine Skewed	Leptokurtic
SHT-1B	0.254	1.401	-0.125	0.912	Coarse Sand	Poorly Sorted	Coarse Skewed	Mesokurtic
SHT-1C	0.696	0.674	-0.167	1.066	Coarse Sand	Moderately Well Sorted	Coarse Skewed	Mesokurtic
WAR-1F	0.362	1.389	0.11	0.935	Coarse Sand	Poorly Sorted	Fine Skewed	Mesokurtic
WAR-1J	0.884	1.029	0.254	1.317	Coarse Sand	Poorly Sorted	Fine Skewed	Leptokurtic
WUS-1G	-0.515	1.211	0.612	0.544	Very Coarse Sand	Poorly Sorted	Very Fine Skewed	Very Platykurtic
ZAM-1A	0.814	1.734	0.04	0.709	Coarse Sand	Poorly Sorted	Symmetrical	Platykurtic

Table IIIb: Textural classification of crudely bedded conglomerates (Gh) sub-facies.

Sample No.	Gravel	Sand	Mud
AGE-1D	14.60	84.10	0.30
BDA-1J	19.00	81.00	0.10
BGK-1G	38.30	60.60	1.20
DOK-1B	47.10	52.70	0.20
DOK-1E	42.00	58.00	0.10
DOK-1G	34.90	64.10	0.10
DOK-1J	28.60	71.40	0.00
DOK-1L	14.50	84.40	0.10
ENG-1C	14.00	84.70	0.30
ENG-1K	8.80	90.90	0.30
ENG-1M	7.50	92.00	0.50
ENG-1S	29.00	70.90	0.20
GBU-1D	9.60	90.40	0.10
GBU-2B	24.70	73.40	1.00
GBU-2E	18.60	80.10	1.30
GDW-1A	29.00	70.80	0.30
GDW-1C	47.90	51.60	0.50
JIM-1K	30.60	69.30	0.20
KAC-1C	20.20	79.60	0.20
KAC-1G	15.60	83.40	0.10
KAC-1X3	14.10	84.30	0.70
KJT-1C	13.50	84.80	0.70
KJT-1Q	28.20	71.50	0.30
KUT-1C	13.50	85.20	0.30
LEM-1B	18.50	80.70	0.80
LEM-1K	9.80	90.10	0.10
MAR-1G	31.60	68.20	0.30
MAR-1J	53.10	45.80	0.10
PAT-1F	21.90	77.90	0.20
PTG-1B	27.50	72.10	0.40
RAB-1C	55.60	43.30	0.10
RAB-1N	62.00	37.90	0.10
SHG-1J	44.30	54.60	0.10
SHG-1A	3.10	95.90	0.10
SHG-1K	29.80	70.10	0.10
SHG-1N	3.50	95.30	0.20
SHG-1Q	4.60	94.30	0.20
SHG-1T	29.70	70.30	0.10
SHG-1W	20.90	78.00	1.10
SHT-1B	4.20	94.60	0.30
SHT-1C	34.00	64.90	0.10
WAR-1F	15.60	82.80	0.60
WAR-1J	2.60	95.70	0.70
WUS-1G	41.50	58.20	0.30
ZAM-1A	19.10	80.40	0.60

Table IVa: Grain size distribution of crudely stratified sandstone (Se) sub-facies and interpretation after Folk and Ward (1957)

Sample No.	MEAN	S. DEVIATION	SKEWNESS	KURTOSIS	MEAN	S. DEVIATION	SKEWNESS	KURTOSIS
AGB-1B	1.176	0.928	-0.091	1.239	Medium Sand	Moderately Sorted	Symmetrical	Leptokurtic
AGB-1F	0.275	1.381	0.213	1.011	Coarse Sand	Poorly Sorted	Fine Skewed	Mesokurtic
AGB-1L	0.472	1.236	0.075	1.297	Coarse Sand	Poorly Sorted	Symmetrical	Leptokurtic
AGE-1F	0.198	1.147	0.219	1.120	Coarse Sand	Poorly Sorted	Fine Skewed	Leptokurtic
BAR-1E	-0.184	1.258	0.052	1.074	Very Coarse Sand	Poorly Sorted	Symmetrical	Mesokurtic
BAR-1G	0.619	1.286	0.025	1.007	Coarse Sand	Poorly Sorted	Symmetrical	Mesokurtic
BAR-1L	-0.027	1.102	0.023	1.056	Very Coarse Sand	Poorly Sorted	Symmetrical	Mesokurtic
BDA-1H	-0.241	0.947	0.251	1.384	Very Coarse Sand	Moderately Sorted	Fine Skewed	Leptokurtic
BDA-1N	-0.033	1.259	0.291	1.263	Very Coarse Sand	Poorly Sorted	Fine Skewed	Leptokurtic
BDA-1Q	-0.795	1.195	0.435	1.094	Very Coarse Sand	Poorly Sorted	Very Fine Skewed	Mesokurtic
BGK-1A	-0.285	1.219	0.593	0.538	Very Coarse Sand	Poorly Sorted	Very Fine Skewed	Very Platykurtic
BGK-1F	0.316	1.567	-0.172	0.658	Coarse Sand	Poorly Sorted	Coarse Skewed	Very Platykurtic
DOK-1A	0.033	1.519	0.200	0.950	Coarse Sand	Poorly Sorted	Fine Skewed	Mesokurtic
DOK-1D	0.199	1.377	0.863	0.500	Coarse Sand	Poorly Sorted	Very Fine Skewed	Very Platykurtic
DOK-1H	0.206	1.114	0.184	1.207	Coarse Sand	Poorly Sorted	Fine Skewed	Leptokurtic
ENG-1J	-0.156	1.417	0.228	0.948	Very Coarse Sand	Poorly Sorted	Fine Skewed	Mesokurtic
ENG-1T	-0.791	0.881	0.748	0.470	Very Coarse Sand	Moderately Sorted	Very Fine Skewed	Very Platykurtic
GBU-2D	-0.061	1.431	0.238	0.858	Very Coarse Sand	Poorly Sorted	Fine Skewed	Platykurtic
JIM-1E	0.595	1.323	0.025	1.044	Coarse Sand	Poorly Sorted	Symmetrical	Mesokurtic
JIM-1H	0.307	1.373	0.115	1.004	Coarse Sand	Poorly Sorted	Fine Skewed	Mesokurtic
JIM-1L	-0.652	0.924	0.088	1.309	Very Coarse Sand	Moderately Sorted	Symmetrical	Leptokurtic
JIM-1R	0.764	1.397	-0.337	1.069	Coarse Sand	Poorly Sorted	Very Coarse Skewed	Mesokurtic
JIM-1X	1.271	1.271	-0.209	0.980	Medium Sand	Poorly Sorted	Coarse Skewed	Mesokurtic

KAC-1E	0.111	1.671	0.144	0.595	Coarse Sand	Poorly Sorted	Fine Skewed	Very Platykurtic
KAC-1F	-0.314	1.097	0.155	0.860	Very Coarse Sand	Poorly Sorted	Fine Skewed	Platykurtic
KAC-1J	-0.085	1.011	0.060	1.092	Very Coarse Sand	Poorly Sorted	Symmetrical	Mesokurtic
KAC-1M	0.242	1.303	0.028	1.055	Coarse Sand	Poorly Sorted	Symmetrical	Mesokurtic
KAC-1P	0.589	1.397	-0.090	0.867	Coarse Sand	Poorly Sorted	Symmetrical	Platykurtic
KAC-1Z	0.151	1.462	0.017	0.918	Coarse Sand	Poorly Sorted	Symmetrical	Mesokurtic
KCH-1A	0.255	1.170	0.074	1.233	Coarse Sand	Poorly Sorted	Symmetrical	Leptokurtic
KJT-1A	0.539	1.367	-0.010	1.275	Coarse Sand	Poorly Sorted	Symmetrical	Leptokurtic
KJT-1D	0.160	1.278	-0.019	0.837	Coarse Sand	Poorly Sorted	Symmetrical	Platykurtic
KJT-1E	0.816	1.038	0.249	1.276	Coarse Sand	Poorly Sorted	Fine Skewed	Leptokurtic
KJT-1G	0.235	1.321	1.081	0.638	Coarse Sand	Poorly Sorted	Very Fine Skewed	Very Platykurtic
KJT-1H	0.215	0.831	-0.037	1.058	Coarse Sand	Moderately Sorted	Symmetrical	Mesokurtic
KJT-1K	0.203	1.278	0.171	0.387	Coarse Sand	Poorly Sorted	Fine Skewed	Very Platykurtic
KJT-1L	0.495	1.095	0.120	1.215	Coarse Sand	Poorly Sorted	Fine Skewed	Leptokurtic
KJT-1N	0.191	0.918	-0.081	1.130	Coarse Sand	Moderately Sorted	Symmetrical	Leptokurtic
KUT-2B	0.688	0.966	-0.230	0.966	Coarse Sand	Moderately Sorted	Coarse Skewed	Mesokurtic
LAD-1A	0.280	1.155	0.008	1.141	Coarse Sand	Poorly Sorted	Symmetrical	Leptokurtic
LAD-1D	-0.667	1.212	0.534	0.640	Very Coarse Sand	Poorly Sorted	Very Fine Skewed	Very Platykurtic
LAF-1C	0.414	1.445	-0.020	1.085	Coarse Sand	Poorly Sorted	Symmetrical	Mesokurtic
LEM-1C	0.029	1.248	0.116	1.075	Coarse Sand	Poorly Sorted	Fine Skewed	Mesokurtic
LEM-1E	0.324	1.070	-0.045	1.588	Coarse Sand	Poorly Sorted	Symmetrical	Very Leptokurtic
LEM-1G	0.673	1.411	-0.110	1.229	Coarse Sand	Poorly Sorted	Coarse Skewed	Leptokurtic
LEM-1M	0.485	1.264	0.113	1.197	Coarse Sand	Poorly Sorted	Fine Skewed	Leptokurtic
MAR-1E	0.942	1.488	-0.126	1.173	Coarse Sand	Poorly Sorted	Coarse Skewed	Leptokurtic
PAT-1A	0.319	1.635	0.082	0.835	Coarse Sand	Poorly Sorted	Symmetrical	Platykurtic
PAT-1E	0.404	1.273	0.056	1.059	Coarse Sand	Poorly Sorted	Symmetrical	Mesokurtic

PTG-1A	0.196	1.278	-0.028	0.832	Coarse Sand	Poorly Sorted	Symmetrical	Platykurtic
RAB-1K	-0.747	0.658	2.037	0.726	Very Coarse Sand	Moderately Well Sorted	Very Fine Skewed	Platykurtic
RAB-1M	-1.039	0.544	1.850	0.556	Very Fine Gravel	Moderately Well Sorted	Very Fine Skewed	Very Platykurtic
RAT-1C	-0.423	1.274	0.554	0.572	Very Coarse Sand	Poorly Sorted	Very Fine Skewed	Very Platykurtic
RAT-1F	-0.004	1.624	0.369	0.514	Very Coarse Sand	Poorly Sorted	Very Fine Skewed	Very Platykurtic
RAT-1M	0.551	1.075	0.083	1.064	Coarse Sand	Poorly Sorted	Symmetrical	Mesokurtic
RUG-1B	0.037	1.370	0.168	1.109	Coarse Sand	Poorly Sorted	Fine Skewed	Mesokurtic
RUG-1E	0.042	1.357	0.180	1.120	Coarse Sand	Poorly Sorted	Fine Skewed	Leptokurtic
SHG-1B	0.371	1.164	-0.438	0.912	Coarse Sand	Poorly Sorted	Very Coarse Skewed	Mesokurtic
SHG-1E	-0.131	1.332	0.527	0.533	Very Coarse Sand	Poorly Sorted	Very Fine Skewed	Very Platykurtic
SHG-1R	1.033	0.867	-0.286	1.625	Medium Sand	Moderately Sorted	Coarse Skewed	Very Leptokurtic
SHG-1X	-0.385	1.039	0.446	1.976	Very Coarse Sand	Poorly Sorted	Very Fine Skewed	Very Leptokurtic
SHJ-1B	0.892	0.953	-0.141	1.773	Coarse Sand	Moderately Sorted	Coarse Skewed	Very Leptokurtic
SHJ-1D	0.441	1.466	0.005	1.037	Coarse Sand	Poorly Sorted	Symmetrical	Mesokurtic
SHJ-1E	1.158	1.159	0.034	1.924	Medium Sand	Poorly Sorted	Symmetrical	Very Leptokurtic
SHT-1A	0.566	1.246	-0.269	1.511	Coarse Sand	Poorly Sorted	Coarse Skewed	Very Leptokurtic
TAN-1B	-0.062	1.029	0.140	1.083	Very Coarse Sand	Poorly Sorted	Fine Skewed	Mesokurtic
WUS-1C	-0.949	0.882	1.216	0.577	Very Coarse Sand	Moderately Sorted	Very Fine Skewed	Very Platykurtic

Table IVb: Textural classification of crudely stratified sandstone (Se) sub-facies

Sample No.	Gravel	Sand	Mud
AGB-1B	8.90	90.80	0.30
AGB-1F	2.40	95.80	0.80
AGB-1L	14.80	83.80	0.40
AGE-1F	8.10	91.10	0.80
BAR-1E	22.50	77.30	0.20
BAR-1G	8.60	91.00	0.40
BAR-1L	15.80	83.10	0.10
BDA-1H	14.90	83.90	0.20
BDA-1N	15.90	82.90	0.20
BDA-1Q	23.80	75.00	0.20
BGK-1A	14.00	84.50	0.50
BGK-1F	27.90	71.30	0.80
DOK-1A	27.10	72.30	0.60
DOK-1D	24.30	74.90	0.80
DOK-1H	7.50	92.20	0.30
ENG-1J	20.00	79.90	0.20
ENG-1T	17.50	82.40	0.10
GBU-2D	25.00	73.30	0.70
JIM-1E	9.50	89.80	0.70
JIM-1H	15.20	83.60	0.20
JIM-1L	20.20	79.70	0.10
JIM-1R	14.80	84.10	0.10
JIM-1X	5.20	93.70	0.10
KAC-1E	27.50	71.50	1.00
KAC-1F	24.20	74.50	0.30
KAC-1J	14.90	84.00	0.20
KAC-1M	15.30	83.40	0.30
KAC-1P	14.70	83.80	0.50
KAC-1Z	22.90	75.90	0.20
KCH-1A	10.70	88.90	0.40
KJT-1A	10.40	88.90	0.70
KJT-1D	19.40	80.30	0.30
KJT-1E	1.90	97.50	0.60
KJT-1G	18.20	80.30	1.50
KJT-1H	4.90	94.00	0.10
KJT-1K	21.20	78.40	0.50
KJT-1L	4.20	94.50	0.30
KJT-1N	5.70	93.20	0.10
KUT-2B	4.20	94.80	0.00
LAD-1A	10.80	88.90	0.30
LAD-1D	43.20	55.50	0.40
LAF-1C	14.40	84.00	0.60
LEM-1C	18.10	81.80	0.10

LEM-1E	8.60	91.00	0.40
LEM-1G	11.40	88.20	0.50
LEM-1M	7.50	92.00	0.50
MAR-1E	10.10	89.10	0.80
PAT-1A	23.90	74.60	0.50
PAT-1E	11.60	88.10	0.40
PTG-1A	18.80	80.90	0.30
RAB-1K	24.30	74.60	0.10
RAB-1M	21.40	78.50	0.10
RAT-1C	18.50	81.40	0.10
RAT-1F	14.40	84.20	0.40
RAT-1M	4.80	94.90	0.30
RUG-1B	19.60	80.00	0.40
RUG-1E	19.00	80.60	0.40
SHG-1B	15.00	83.80	0.20
SHG-1E	34.50	64.50	0.10
SHG-1R	3.90	95.10	0.10
SHG-1X	24.50	74.50	0.10
SHJ-1B	4.10	93.70	1.30
SHJ-1D	15.70	82.30	1.00
SHJ-1E	4.50	94.40	1.20
SHT-1A	9.60	89.40	1.00
TAN-1B	14.90	84.00	0.10
WUS-1C	25.20	73.50	0.30

Table Va: Grain size distribution of planar stratified sandstone (Sp) sub-facies and interpretation after Folk and Ward (1957).

Sample No.	MEAN	S. DEVIATION	SKEWNESS	KURTOSIS	MEAN	S. DEVIATION	SKEWNESS	KURTOSIS
AGB-1K	0.436	1.291	0.024	0.808	Coarse Sand	Poorly Sorted	Symmetrical	Platykurtic
BAR-1D	0.840	1.255	-0.157	1.051	Coarse Sand	Poorly Sorted	Coarse Skewed	Mesokurtic
BAR-1H	0.394	1.212	0.001	1.014	Coarse Sand	Poorly Sorted	Symmetrical	Mesokurtic
BAR-1M	0.784	0.941	0.050	1.019	Coarse Sand	Moderately Sorted	Symmetrical	Mesokurtic
BDA-1A	0.463	1.203	0.008	1.256	Coarse Sand	Poorly Sorted	Symmetrical	Leptokurtic
BDA-1C	-0.729	0.923	0.095	1.558	Very Coarse Sand	Moderately Sorted	Symmetrical	Very Leptokurtic
BDA-1E	0.488	1.456	-0.236	0.483	Coarse Sand	Poorly Sorted	Coarse Skewed	Very Platykurtic
BDA-1G	0.646	1.148	-0.240	1.089	Coarse Sand	Poorly Sorted	Coarse Skewed	Mesokurtic
BDA-1L	0.491	1.181	0.102	1.133	Coarse Sand	Poorly Sorted	Fine Skewed	Leptokurtic
BDA-1P	0.623	1.474	-0.149	1.052	Coarse Sand	Poorly Sorted	Coarse Skewed	Mesokurtic
BDA-1R	0.615	1.141	0.034	1.194	Coarse Sand	Poorly Sorted	Symmetrical	Leptokurtic
JIM-1S	-0.233	1.140	0.064	1.057	Very Coarse Sand	Poorly Sorted	Symmetrical	Mesokurtic
JIM-1Y	0.397	0.980	-0.039	1.149	Coarse Sand	Moderately Sorted	Symmetrical	Leptokurtic
KAC-1B	0.890	1.007	0.102	1.133	Coarse Sand	Poorly Sorted	Fine Skewed	Leptokurtic
KAC-1D	0.263	1.090	-0.024	1.160	Coarse Sand	Poorly Sorted	Symmetrical	Leptokurtic
KAC-1H	0.944	0.953	0.133	1.130	Coarse Sand	Moderately Sorted	Fine Skewed	Leptokurtic
KCH-1E	0.934	1.203	-0.052	0.985	Coarse Sand	Poorly Sorted	Symmetrical	Mesokurtic
KJT-1P	0.233	1.189	-0.059	1.189	Coarse Sand	Poorly Sorted	Symmetrical	Leptokurtic
KUT-2H	0.810	0.868	-0.096	0.942	Coarse Sand	Moderately Sorted	Symmetrical	Mesokurtic

LAF-1D	-0.444	1.342	1.018	0.475	Very Coarse Sand	Poorly Sorted	Very Fine Skewed	Very Platykurtic
LEM-1R	1.765	1.442	-0.389	1.601	Medium Sand	Poorly Sorted	Very Coarse Skewed	Very Leptokurtic
MAR-1B	1.295	1.347	-0.100	1.167	Medium Sand	Poorly Sorted	Symmetrical	Leptokurtic
MAR-1D	1.279	1.307	-0.203	1.241	Medium Sand	Poorly Sorted	Coarse Skewed	Leptokurtic
MAR-1L	0.248	1.245	0.473	0.422	Coarse Sand	Poorly Sorted	Very Fine Skewed	Very Platykurtic
MGT-1A	0.774	1.104	-0.076	1.033	Coarse Sand	Poorly Sorted	Symmetrical	Mesokurtic
PAT-1J	1.649	1.028	-0.092	1.12	Medium Sand	Poorly Sorted	Symmetrical	Leptokurtic
PAT-1N	0.665	1.243	-0.009	1.197	Coarse Sand	Poorly Sorted	Symmetrical	Leptokurtic
RAB-1E	-0.092	0.986	0.175	1.250	Very Coarse Sand	Moderately Sorted	Fine Skewed	Leptokurtic
RAB-1G	-0.642	1.098	0.327	0.903	Very Coarse Sand	Poorly Sorted	Very Fine Skewed	Mesokurtic
RAT-1D	1.498	1.650	-0.454	0.939	Medium Sand	Poorly Sorted	Very Coarse Skewed	Mesokurtic
RAT-1K	0.273	1.236	0.031	1.009	Coarse Sand	Poorly Sorted	Symmetrical	Mesokurtic
TAN-1A	0.187	0.917	0.098	1.203	Coarse Sand	Moderately Sorted	Symmetrical	Leptokurtic
TAN-1G	0.051	1.182	0.202	1.221	Coarse Sand	Poorly Sorted	Fine Skewed	Leptokurtic
TAN-1H	0.826	1.032	0.227	1.532	Coarse Sand	Poorly Sorted	Fine Skewed	Very Leptokurtic

Table Vb: Textural classification of planar stratified sandstone (Sp) sub-facies.

Sample No.	Gravel	Sand	Mud
AGB-1K	15.30	83.10	0.60
BAR-1D	7.90	91.80	0.30
BAR-1H	10.60	89.20	0.20
BAR-1M	1.60	98.30	0.10
BDA-1A	8.90	90.90	0.20
BDA-1C	30.50	69.50	0.10
BDA-1E	24.90	73.80	0.30
BDA-1G	11.70	88.20	0.20
BDA-1L	5.60	93.20	0.20
BDA-1P	14.70	83.70	0.60
BDA-1R	5.20	93.30	0.50
JIM-1S	22.40	77.60	0.10
JIM-1Y	5.40	93.20	0.40
KAC-1B	3.20	95.40	0.40
KAC-1D	10.70	89.30	0.10
KAC-1H	1.50	98.10	0.40
KCH-1E	4.00	94.70	0.30
KJT-1P	13.60	85.00	0.40
KUT-2H	1.90	98.10	0.00
LAF-1D	12.50	85.80	0.70
LEM-1R	10.20	89.20	0.60
MAR-1B	4.50	91.90	0.90
MAR-1D	7.30	92.00	0.70
MAR-1L	37.50	62.30	0.20
MGT-1A	4.30	94.60	0.10
PAT-1J	2.20	97.30	0.50
PAT-1N	8.40	91.40	0.20
RAB-1E	10.90	88.90	0.20
RAB-1G	39.20	60.70	0.10
RAT-1D	11.20	88.00	0.80
RAT-1K	15.20	83.60	0.20
TAN-1A	3.40	95.50	0.10
TAN-1G	13.80	85.00	0.20
TAN-1H	4.30	94.50	0.20

Table VIa: Grain size distribution of rippled stratified sandstone (Sr) sub-facies and interpretation after Folk and Ward (1957).

Sample No.	MEAN	S. DEVIATION	SKEWNESS	KURTOSIS	MEAN	S. DEVIATION	SKEWNESS	KURTOSIS
AGB-1J	-0.530	1.070	0.155	1.130	Very Coarse Sand	Poorly Sorted	Fine Skewed	Leptokurtic
LAF-1B	0.117	1.446	0.084	0.909	Coarse Sand	Poorly Sorted	Symmetrical	Mesokurtic
MAN-1F	1.574	0.955	-0.063	0.866	Medium Sand	Moderately Sorted	Symmetrical	Platykurtic
RAB-1P	0.312	1.438	-0.035	1.001	Coarse Sand	Poorly Sorted	Symmetrical	Mesokurtic

Table VIb: Textural classification of rippled stratified sandstone (Sr) sub-facies

Sample No.	Gravel	Sand	Mud
AGB-1J	32.40	67.40	0.20
LAF-1B	22.30	77.10	0.60
MAN-1F	0.10	99.70	0.20
RAB-1P	19.00	80.50	0.50

Table VIIa: Grain size distribution of horizontally stratified sandstone (Sh) sub-facies and interpretation after Folk and Ward (1957)

Sample No.	MEAN	S. DEVIATION	SKEWNESS	KURTOSIS	MEAN	S. DEVIATION	SKEWNESS	KURTOSIS
AGB-1A	0.246	1.155	0.067	1.193	Coarse Sand	Poorly Sorted	Symmetrical	Leptokurtic
AGB-1C	0.701	1.120	0.038	1.291	Coarse Sand	Poorly Sorted	Symmetrical	Leptokurtic
AGB-1G	0.686	1.365	-0.207	1.088	Coarse Sand	Poorly Sorted	Coarse Skewed	Mesokurtic
AGB-1M	-0.048	1.518	0.636	0.502	Very Coarse Sand	Poorly Sorted	Very Fine Skewed	Very Platykurtic
AGE-1E	0.488	1.029	0.169	1.511	Coarse Sand	Poorly Sorted	Fine Skewed	Very Leptokurtic
BAR-1F	0.597	1.176	0.014	1.032	Coarse Sand	Poorly Sorted	Symmetrical	Mesokurtic
BAR-1K	1.214	1.089	-0.123	1.034	Medium Sand	Poorly Sorted	Coarse Skewed	Mesokurtic
BDA-1B	0.262	1.438	0.252	0.854	Coarse Sand	Poorly Sorted	Fine Skewed	Platykurtic
BDA-1F	1.510	1.068	-0.188	1.944	Medium Sand	Poorly Sorted	Coarse Skewed	Very Leptokurtic
BDA-1M	0.982	1.049	0.082	1.118	Coarse Sand	Poorly Sorted	Symmetrical	Leptokurtic
BDA-1S	-0.170	1.317	0.167	0.536	Very Coarse Sand	Poorly Sorted	Fine Skewed	Very Platykurtic
BGK-1D	0.608	1.697	-0.057	0.454	Coarse Sand	Poorly Sorted	Symmetrical	Very Platykurtic
DOK-1K	0.708	1.167	0.034	1.122	Coarse Sand	Poorly Sorted	Symmetrical	Leptokurtic
DOK-1M	1.044	1.046	0.014	1.106	Medium Sand	Poorly Sorted	Symmetrical	Mesokurtic
ENG-1A	0.502	1.008	0.095	1.363	Coarse Sand	Poorly Sorted	Symmetrical	Leptokurtic
ENG-1E	0.744	1.367	-0.077	1.247	Coarse Sand	Poorly Sorted	Symmetrical	Leptokurtic
ENG-1H	0.775	1.860	-0.113	0.844	Coarse Sand	Poorly Sorted	Coarse Skewed	Platykurtic
ENG-1L	-0.267	1.395	0.350	0.715	Very Coarse Sand	Poorly Sorted	Very Fine Skewed	Platykurtic
ENG-1N	1.266	1.490	-0.219	1.355	Medium Sand	Poorly Sorted	Coarse Skewed	Leptokurtic
ENG-1V	-0.242	1.225	1.980	0.733	Very Coarse Sand	Poorly Sorted	Very Fine Skewed	Platykurtic
JIM-1A	0.588	1.359	0.04	0.976	Coarse Sand	Poorly Sorted	Symmetrical	Mesokurtic
JIM-1C	0.416	1.433	0.059	0.969	Coarse Sand	Poorly Sorted	Symmetrical	Mesokurtic
JIM-1J	0.539	1.875	0.020	0.773	Coarse Sand	Poorly Sorted	Symmetrical	Platykurtic

JIM-1Q	1.199	0.847	-0.110	1.111	Medium Sand	Moderately Sorted	Coarse Skewed	Leptokurtic
JIM-1V	1.234	0.881	-0.252	1.578	Medium Sand	Moderately Sorted	Coarse Skewed	Very Leptokurtic
KAC-1W	0.407	1.773	0.015	0.758	Coarse Sand	Poorly Sorted	Symmetrical	Platykurtic
KCH-1B	0.451	1.124	0.124	1.280	Coarse Sand	Poorly Sorted	Fine Skewed	Leptokurtic
KCH-1D	0.474	1.137	0.077	0.937	Coarse Sand	Poorly Sorted	Symmetrical	Mesokurtic
KCH-1G	0.728	1.248	0.108	1.012	Coarse Sand	Poorly Sorted	Fine Skewed	Mesokurtic
KUT-2A	0.152	1.014	0.019	0.964	Coarse Sand	Poorly Sorted	Symmetrical	Mesokurtic
KUT-2E	0.755	0.756	-0.101	1.081	Coarse Sand	Moderately Sorted	Coarse Skewed	Mesokurtic
KUT-2J	1.003	0.896	-0.097	1.181	Medium Sand	Moderately Sorted	Symmetrical	Leptokurtic
KUT-2K	1.185	0.858	-0.457	0.903	Medium Sand	Moderately Sorted	Very Coarse Skewed	Mesokurtic
LEM-1A	0.797	1.642	-0.061	1.013	Coarse Sand	Poorly Sorted	Symmetrical	Mesokurtic
LEM-1H	0.704	1.470	0.032	1.351	Coarse Sand	Poorly Sorted	Symmetrical	Leptokurtic
LEM-1Q	0.768	1.431	-0.365	1.132	Coarse Sand	Poorly Sorted	Very Coarse Skewed	Leptokurtic
MAN-1G	2.180	0.620	-0.288	0.933	Fine Sand	Moderately Well Sorted	Coarse Skewed	Mesokurtic
MAN-1H	1.386	1.296	-0.274	1.360	Medium Sand	Poorly Sorted	Coarse Skewed	Leptokurtic
MAR-1C	0.774	1.310	0.032	1.056	Coarse Sand	Poorly Sorted	Symmetrical	Mesokurtic
MAR-1F	1.500	1.230	-0.095	1.264	Medium Sand	Poorly Sorted	Symmetrical	Leptokurtic
MAR-1M	0.913	1.783	-0.184	0.810	Coarse Sand	Poorly Sorted	Coarse Skewed	Platykurtic
MGT-1B	0.601	1.802	-0.085	0.763	Coarse Sand	Poorly Sorted	Symmetrical	Platykurtic
MGT-1E	1.065	1.480	-0.190	1.047	Medium Sand	Poorly Sorted	Coarse Skewed	Mesokurtic
MGT-1F	0.778	1.859	-0.252	0.634	Coarse Sand	Poorly Sorted	Coarse Skewed	Very Platykurtic
PAT-1B	0.373	1.495	-0.040	0.870	Coarse Sand	Poorly Sorted	Symmetrical	Platykurtic
PAT-1G	0.400	1.396	-0.065	1.301	Coarse Sand	Poorly Sorted	Symmetrical	Leptokurtic
PAT-1H	-0.128	1.260	0.177	1.163	Very Coarse Sand	Poorly Sorted	Fine Skewed	Leptokurtic
RAB-1F	-0.754	0.636	1.917	0.707	Very Coarse Sand	Moderately Well Sorted	Very Fine Skewed	Platykurtic

RAB-1H	0.142	1.485	0.027	0.884	Coarse Sand	Poorly Sorted	Symmetrical	Platykurtic
RAT-1E	1.620	1.534	-0.531	1.197	Medium Sand	Poorly Sorted	Very Coarse Skewed	Leptokurtic
RAT-1L	1.870	1.115	-0.107	1.403	Medium Sand	Poorly Sorted	Coarse Skewed	Leptokurtic
RUG-1F	0.286	1.399	0.175	1.053	Coarse Sand	Poorly Sorted	Fine Skewed	Mesokurtic
SHG-1F	1.261	0.664	-0.195	1.733	Medium Sand	Moderately Well Sorted	Coarse Skewed	Very Leptokurtic
SHG-1L	1.976	0.739	0.206	0.997	Medium Sand	Moderately Sorted	Fine Skewed	Mesokurtic
SHG-1P	2.351	0.883	-0.241	0.897	Fine Sand	Moderately Sorted	Coarse Skewed	Platykurtic
SHG-1V	2.643	0.607	-0.19	1.031	Fine Sand	Moderately Well Sorted	Coarse Skewed	Mesokurtic
SHJ-1A	0.184	1.349	0.025	0.947	Coarse Sand	Poorly Sorted	Symmetrical	Mesokurtic
SHJ-1C	1.182	1.144	0.062	1.877	Medium Sand	Poorly Sorted	Symmetrical	Very Leptokurtic
SHT-1E	-0.500	1.377	0.640	0.761	Very Coarse Sand	Poorly Sorted	Very Fine Skewed	Platykurtic
TAN-1C	0.191	1.033	0.113	1.202	Coarse Sand	Poorly Sorted	Fine Skewed	Leptokurtic
TAN-1D	1.183	1.062	-0.226	1.379	Medium Sand	Poorly Sorted	Coarse Skewed	Leptokurtic
WAR-1C	0.196	1.386	0.006	0.716	Coarse Sand	Poorly Sorted	Symmetrical	Platykurtic
WAR-1H	-0.573	0.972	0.938	0.451	Very Coarse Sand	Moderately Sorted	Very Fine Skewed	Very Platykurtic
WUS-1A	0.771	1.007	-0.114	1.089	Coarse Sand	Poorly Sorted	Coarse Skewed	Mesokurtic
WUS-1B	-0.687	1.151	0.628	0.476	Very Coarse Sand	Poorly Sorted	Very Fine Skewed	Very Platykurtic
WUS-1E	-0.389	1.107	0.252	0.614	Very Coarse Sand	Poorly Sorted	Fine Skewed	Very Platykurtic

Table VIIb: Textural classification of horizontally stratified sandstone (Sh) sub-facies

Sample No.	Gravel	Sand	Mud
AGB-1A	9.30	90.40	0.30
AGB-1C	5.10	93.40	0.50
AGB-1G	14.80	83.40	0.80
AGB-1M	10.90	87.90	1.20
AGE-1E	2.20	97.40	0.40
BAR-1F	5.80	92.90	0.30
BAR-1K	3.20	95.70	0.10
BDA-1B	15.00	83.80	0.20
BDA-1F	5.00	93.60	0.40
BDA-1M	3.00	95.50	0.50
BDA-1S	29.10	70.80	0.10
BGK-1D	29.40	69.30	1.40
DOK-1K	4.70	93.90	0.40
DOK-1M	2.90	95.60	0.50
ENG-1A	4.20	94.60	0.20
ENG-1E	8.40	90.90	0.70
ENG-1H	19.60	79.30	1.10
ENG-1L	28.10	71.50	0.40
ENG-1N	9.90	89.40	0.70
ENG-1V	59.20	40.20	0.70
JIM-1A	10.70	88.90	0.40
JIM-1C	14.90	83.60	0.40
JIM-1J	25.30	72.50	1.30
JIM-1Q	2.00	97.90	0.10
JIM-1V	3.80	94.80	0.40
KAC-1W	25.80	72.60	0.60
KCH-1B	4.70	93.90	0.40
KCH-1D	5.30	93.50	0.20
KCH-1G	4.70	94.00	0.30
KUT-2A	12.70	87.30	0.00
KUT-2E	1.40	98.60	0.00
KUT-2J	2.60	97.40	0.00

KUT-2K	0.10	99.90	0.00
LEM-1A	14.50	84.10	0.50
LEM-1H	11.20	88.00	0.80
LEM-1Q	14.00	84.80	0.20
MAN-1G	0.60	99.30	0.10
MAN-1H	9.20	90.60	0.20
MAR-1C	7.40	92.20	0.40
MAR-1F	4.50	94.70	0.80
MAR-1M	19.20	80.00	0.80
MGT-1B	23.90	74.40	0.70
MGT-1E	11.40	88.30	0.30
MGT-1F	27.70	72.00	0.30
PAT-1B	19.20	80.40	0.40
PAT-1G	14.80	84.90	0.30
PAT-1H	20.00	79.70	0.30
RAB-1F	20.70	79.20	0.10
RAB-1H	24.20	74.60	0.20
RAT-1E	5.4.00	90.80	0.20
RAT-1L	4.00	94.50	0.50
RUG-1F	15.10	83.00	0.90
SHG-1F	2.90	97.10	0.10
SHG-1L	0.50	99.40	0.20
SHG-1P	1.00	98.60	0.40
SHG-1V	0.00	100.00	0.00
SHJ-1A	20.10	79.30	0.60
SHJ-1C	3.40	94.10	1.60
SHT-1E	14.00	84.60	1.40
TAN-1C	5.60	93.20	0.20
TAN-1D	4.20	94.30	0.50
WAR-1C	21.30	78.30	0.40
WAR-1H	49.20	50.60	0.30
WUS-1A	5.60	93.10	0.30
WUS-1B	45.50	53.40	0.10
WUS-1E	28.00	71.90	0.20

Table VIIIa: Grain size distribution of massive sandstone (Sm) sub-facies and interpretation after Folk and Ward (1957)

Sample No.	MEAN	S. DEVIATION	SKEWNESS	KURTOSIS	MEAN	S. DEVIATION	SKEWNESS	KURTOSIS
AGE-1A	0.664	1.030	0.184	1.431	Coarse Sand	Poorly Sorted	Fine Skewed	Leptokurtic
AGE-1C	0.437	1.267	0.088	1.051	Coarse Sand	Poorly Sorted	Symmetrical	Mesokurtic
AGE-1G	0.404	1.595	-0.101	0.923	Coarse Sand	Poorly Sorted	Coarse Skewed	Mesokurtic
GBU-2A	0.904	1.593	0.170	1.161	Coarse Sand	Poorly Sorted	Fine Skewed	Leptokurtic
KAC-1K	0.550	1.640	-0.040	0.931	Coarse Sand	Poorly Sorted	Symmetrical	Mesokurtic
KAC-1N	0.983	1.217	-0.186	1.101	Coarse Sand	Poorly Sorted	Coarse Skewed	Mesokurtic
KAC-1Q	0.843	1.183	-0.043	1.118	Coarse Sand	Poorly Sorted	Symmetrical	Leptokurtic
LEM-1D	-0.009	1.581	0.202	0.533	Very Coarse Sand	Poorly Sorted	Fine Skewed	Very Platykurtic
LEM-1F	0.505	1.583	-0.126	0.761	Coarse Sand	Poorly Sorted	Coarse Skewed	Platykurtic
LEM-1L	1.318	1.767	-0.455	0.859	Medium Sand	Poorly Sorted	Very Coarse Skewed	Platykurtic
PAT-1D	0.218	1.212	0.586	0.427	Coarse Sand	Poorly Sorted	Very Fine Skewed	Very Platykurtic
RUG-1C	0.334	1.624	0.202	1.026	Coarse Sand	Poorly Sorted	Fine Skewed	Mesokurtic
WAR-1G	-0.200	1.313	0.222	0.778	Very Coarse Sand	Poorly Sorted	Fine Skewed	Platykurtic

Table VIIIb: Textural classification of massive sandstone (Sm) sub-facies

Sample No.	Gravel	Sand	Mud
AGE-1A	2.60	95.90	0.50
AGE-1C	5.4.70	90.00	0.30
AGE-1G	20.40	75.4.20	0.40
GBU-2A	7.10	90.00	2.90
KAC-1K	17.90	81.50	0.60
KAC-1N	5.80	92.80	0.40
KAC-1Q	4.90	93.80	0.30
LEM-1D	29.80	69.80	0.40
LEM-1F	21.20	78.50	0.30
LEM-1L	14.00	84.10	0.90
PAT-1D	42.60	57.10	0.30
RUG-1C	17.80	81.30	0.90
WAR-1G	24.60	74.10	0.40

Table IXa: Grain size distribution of finely laminated mudstone (Fl) sub-facies and interpretation after Folk and Ward (1957)

Sample No.	MEAN	S. DEVIATION	SKEWNESS	KURTOSIS	MEAN	S. DEVIATION	SKEWNESS	KURTOSIS
AGB-1H	0.446	1.391	-0.143	0.94	Coarse Sand	Poorly Sorted	Coarse Skewed	Mesokurtic
AGE-1B	0.822	1.614	-0.135	1.054	Coarse Sand	Poorly Sorted	Coarse Skewed	Mesokurtic
AGE-1H	0.779	1.057	0.169	1.194	Coarse Sand	Poorly Sorted	Fine Skewed	Leptokurtic
BAR-1J	1.245	1.234	-0.094	0.953	Medium Sand	Poorly Sorted	Symmetrical	Mesokurtic
BDA-1K	0.919	1.005	-0.035	1.184	Coarse Sand	Poorly Sorted	Symmetrical	Leptokurtic
GBU-1B	0.303	1.332	-0.298	0.857	Coarse Sand	Poorly Sorted	Coarse Skewed	Platykurtic
JIM-1B	0.618	1.776	0.014	0.869	Coarse Sand	Poorly Sorted	Symmetrical	Platykurtic
JIM-1D	0.688	1.398	-0.040	0.96	Coarse Sand	Poorly Sorted	Symmetrical	Mesokurtic
JIM-1G	0.457	1.413	0.054	0.909	Coarse Sand	Poorly Sorted	Symmetrical	Mesokurtic
JIM-1M	1.106	0.782	-0.165	0.982	Medium Sand	Moderately Sorted	Coarse Skewed	Mesokurtic
JIM-1T	0.768	0.776	0.105	1.092	Coarse Sand	Moderately Sorted	Fine Skewed	Mesokurtic
JIM-1W	0.958	1.107	-0.219	1.121	Coarse Sand	Poorly Sorted	Coarse Skewed	Leptokurtic
KAC-1L	0.657	1.492	0.018	0.96	Coarse Sand	Poorly Sorted	Symmetrical	Mesokurtic
KAC-1V	0.689	1.221	-0.041	1.477	Coarse Sand	Poorly Sorted	Symmetrical	Leptokurtic
KAC-1X	0.964	1.593	-0.239	0.825	Coarse Sand	Poorly Sorted	Coarse Skewed	Platykurtic
KAC-1Y	0.755	1.866	-0.084	0.593	Coarse Sand	Poorly Sorted	Symmetrical	Very Platykurtic
KCH-1C	0.865	1.167	-0.149	1.065	Coarse Sand	Poorly Sorted	Coarse Skewed	Mesokurtic
KCH-1F	1.362	1.411	-0.178	1.201	Medium Sand	Poorly Sorted	Coarse Skewed	Leptokurtic
KJT-1F	0.042	1.043	-0.084	1.086	Coarse Sand	Poorly Sorted	Symmetrical	Mesokurtic

KJT-1J	0.277	1.123	0.002	1.202	Coarse Sand	Poorly Sorted	Symmetrical	Leptokurtic
KUT-2C	0.761	1.063	-0.220	0.98	Coarse Sand	Poorly Sorted	Coarse Skewed	Mesokurtic
LEM-1N	0.814	1.755	-0.247	0.704	Coarse Sand	Poorly Sorted	Coarse Skewed	Platykurtic
LEM-1T	1.110	1.77	-0.274	0.953	Medium Sand	Poorly Sorted	Coarse Skewed	Mesokurtic
MAN-1B	2.684	0.535	0.250	1.099	Fine Sand	Moderately Well Sorted	Fine Skewed	Mesokurtic
MAN-1J	2.183	0.991	-0.426	1.946	Fine Sand	Moderately Sorted	Very Coarse Skewed	Very Leptokurtic
MAR-1H	1.154	1.214	-0.190	1.292	Medium Sand	Poorly Sorted	Coarse Skewed	Leptokurtic
MAR-1K	1.887	1.126	-0.087	1.381	Medium Sand	Poorly Sorted	Symmetrical	Leptokurtic
PAT-1C	0.815	1.026	-0.002	1.102	Coarse Sand	Poorly Sorted	Symmetrical	Mesokurtic
RAB-1J	0.391	1.528	-0.098	0.872	Coarse Sand	Poorly Sorted	Symmetrical	Platykurtic
RAB-1L	0.522	1.621	-0.257	0.831	Coarse Sand	Poorly Sorted	Coarse Skewed	Platykurtic
RAT-1G	1.166	1.167	-0.072	1.106	Medium Sand	Poorly Sorted	Symmetrical	Mesokurtic
TAN-1F	1.193	1.761	-0.450	0.751	Medium Sand	Poorly Sorted	Very Coarse Skewed	Platykurtic
TAN-1J	0.843	1.202	-0.227	0.982	Coarse Sand	Poorly Sorted	Coarse Skewed	Mesokurtic
WUS-1H	1.060	1.818	-0.168	0.867	Medium Sand	Poorly Sorted	Coarse Skewed	Platykurtic

Table IXb: Textural classification of laminated, very-fine mudstone (Fl) sub-facies

Sample No.	Gravel	Sand	Mud
AGB-1H	15.80	82.80	0.40
AGE-1B	14.30	84.10	0.60
AGE-1H	3.10	95.50	0.40
BAR-1J	4.70	94.10	0.20
BDA-1K	4.40	94.30	0.30
GBU-1B	22.00	77.80	0.30
JIM-1B	20.30	78.70	1.10
JIM-1D	11.90	87.80	0.30
JIM-1G	14.30	84.40	0.30
JIM-1M	0.50	99.40	0.10
JIM-1T	1.40	98.40	0.20
JIM-1W	4.60	94.20	0.20
KAC-1L	13.40	85.00	0.70
KAC-1V	9.10	90.60	0.40
KAC-1X	14.90	84.70	0.40
KAC-1Y	24.40	74.80	0.80
KCH-1C	5.40	93.20	0.40
KCH-1F	9.00	90.20	0.80
KJT-1F	14.30	84.60	0.10
KJT-1J	9.80	89.90	0.30
KUT-2C	7.00	93.00	0.00
LEM-1N	22.70	75.80	0.50
LEM-1T	14.80	83.30	0.90
MAN-1B	0.00	99.50	0.50
MAN-1J	4.20	94.20	0.60
MAR-1H	8.10	91.40	0.50
MAR-1K	4.40	94.60	1.00
PAT-1C	4.50	94.10	0.40
RAB-1J	20.90	78.40	0.70
RAB-1L	23.30	74.90	0.80
RAT-1G	4.40	94.00	0.60
TAN-1F	17.40	82.20	0.40
TAN-1J	5.50	92.60	0.90
WUS-1H	15.50	81.70	1.80

Table Xa: Grain size distribution of very fine, massive mudstone (Fm) sub-facies and interpretation after Folk and Ward (1957)

Sample No.	MEAN	S. DEVIATION	SKEWNESS	KURTOSIS	MEAN	S. DEVIATION	SKEWNESS	KURTOSIS
AGB-1E	0.310	1.251	0.110	1.223	Coarse Sand	Poorly Sorted	Fine Skewed	Leptokurtic
DOK-1F	0.511	1.268	0.059	1.241	Coarse Sand	Poorly Sorted	Symmetrical	Leptokurtic
ENG-1B	1.012	1.432	-0.288	1.392	Medium Sand	Poorly Sorted	Coarse Skewed	Leptokurtic
ENG-1D	0.529	1.496	0.186	0.370	Coarse Sand	Poorly Sorted	Fine Skewed	Very Platykurtic
ENG-1Q	-0.413	1.426	0.260	1.173	Very Coarse Sand	Poorly Sorted	Fine Skewed	Leptokurtic
ENG-1R	-0.196	1.332	0.152	0.933	Very Coarse Sand	Poorly Sorted	Fine Skewed	Mesokurtic
GBU-1A	-0.037	1.379	0.409	0.860	Very Coarse Sand	Poorly Sorted	Very Fine Skewed	Platykurtic
KAC-1R	0.526	1.442	0.322	0.418	Coarse Sand	Poorly Sorted	Very Fine Skewed	Very Platykurtic
KAN-1A	2.904	0.981	-0.233	1.509	Fine Sand	Moderately Sorted	Coarse Skewed	Very Leptokurtic
KUT-1B	0.513	1.083	0.104	0.909	Coarse Sand	Poorly Sorted	Fine Skewed	Mesokurtic
MAN-1A	2.586	0.479	0.184	1.122	Fine Sand	Well Sorted	Fine Skewed	Leptokurtic
MAN-1C	0.126	1.719	0.337	0.661	Coarse Sand	Poorly Sorted	Very Fine Skewed	Very Platykurtic
PAT-1K	1.527	1.379	-0.351	1.274	Medium Sand	Poorly Sorted	Very Coarse Skewed	Leptokurtic
RUG-1A	-0.066	1.217	0.087	1.083	Very Coarse Sand	Poorly Sorted	Symmetrical	Mesokurtic
RUG-1D	-0.409	0.953	1.763	0.648	Very Coarse Sand	Moderately Sorted	Very Fine Skewed	Very Platykurtic
SHG-1M	2.475	0.685	-0.057	0.899	Fine Sand	Moderately Well Sorted	Symmetrical	Platykurtic
WAR-1D	1.012	1.460	-0.281	1.372	Medium Sand	Poorly Sorted	Coarse Skewed	Leptokurtic

Table Xb: Textural classification of very fine massive mudstone (Fm) sub-facies

Sample No.	Gravel	Sand	Mud
AGB-1E	10.40	85.4.10	0.50
DOK-1F	9.10	90.50	0.40
ENG-1B	10.80	88.40	0.80
ENG-1D	12.30	84.50	0.50
ENG-1Q	14.40	84.20	0.50
ENG-1R	14.50	82.70	0.10
GBU-1A	14.70	84.10	0.20
KAC-1R	14.70	83.70	0.60
KAN-1A	2.60	95.70	0.70
KUT-1B	3.90	94.80	0.30
MAN-1A	1.20	98.30	0.50
MAN-1C	15.10	83.80	0.20
PAT-1K	13.00	85.70	0.30
RUG-1A	19.00	80.50	0.50
RUG-1D	17.50	82.20	0.30
SHG-1M	0.30	99.60	0.10
WAR-1D	12.30	85.60	1.10

APPENDIX IV – RECALCULATED VALUES OF FRAMEWORK COMPOSITION

Table Ia: Recalculated framework composition (%) of crudely bedded conglomerate (Gh) sub-facies.

Sample Code	Quartz (Q)	Feldspar (F)	Rock/Lithic Fragment (R/L)	Total Quartz (Qt)	Feldspar (F)	Lithic Fragment (L)	Monocrystalline Quartz (Qm)	Feldspar (F)	Total Lithic Fragment (Lt)
	Q-F-R/L Plots After (McBride, 1963; Pettijohn, 1975; Folk, 1980)			Qt-F-L Plot After (Dickinson *et al*., 1983)			Qm-F-Lt Plot (After Dickinson , 1985)		
DOK-1G	97.50	0.00	2.50	97.50	0.00	2.50	97.47	0.00	2.53
ENG-1K	93.33	1.33	4.33	93.33	1.33	4.33	93.14	1.37	4.49
KJT-1Q	93.33	0.00	5.67	93.33	0.00	5.67	91.30	0.00	8.70
MAR-1G	89.74	2.56	7.69	89.74	2.56	7.69	89.56	2.61	7.83
PAT-1M	97.50	0.00	2.50	97.50	0.00	2.50	97.45	0.00	2.55

Table Ib: Mineralogical composition of crudely bedded conglomerate (Gh) sub-facies.

Sample Code	Qm	P	K	Q/(Q+F)	Qp/(F+R)	Qt/(F+R)	ln(Q/F)	ln(Q/L)	MMI
DOK-1G	97.17	0.00	2.83	1.00	0.40	39.00	0.00	3.66	39.00
ENG-1K	100.00	0.00	0.00	0.99	0.42	14.00	4.25	2.86	14.01
KJT-1Q	98.55	0.00	1.45	1.00	3.50	14.00	0.00	2.64	13.99
MAR-1G	100.00	0.00	0.00	0.97	0.18	8.75	3.56	2.46	8.76
PAT-1M	100.00	0.00	0.00	1.00	0.80	39.00	0.00	3.66	39.00

Table IIa: Recalculated framework composition (%) of crudely stratified sandstone (Se) sub-facies.

Sample Code	Quartz (Q)	Feldspar (F)	Rock/Lithic Fragment (R/L)	Total Quartz (Qt)	Feldspar (F)	Lithic Fragment (L)	Monocrystalline Quartz (Qm)	Feldspar (F)	Total Lithic Fragment (Lt)
	Q-F-R/L Plots After (McBride, 1963; Pettijohn, 1975; Folk, 1980)			Qt-F-L Plot After (Dickinson *et al*., 1983)			Qm-F-Lt Plot (After Dickinson , 1985)		
AGB-1F	97.40	0.00	2.60	97.40	0.00	2.60	97.38	0.00	2.62
DOK-1N	97.62	0.00	2.38	97.62	0.00	2.38	97.60	0.00	2.40
JIM-1E	92.11	3.95	3.95	92.11	3.95	3.95	91.72	4.14	4.14
KAC-1E	93.75	2.50	3.75	93.75	2.50	3.75	93.63	2.55	3.82
KJT-1A	94.44	1.39	4.17	94.44	1.39	4.17	94.33	1.42	4.25
KUT-2B	94.59	0.00	4.41	94.59	0.00	4.41	94.44	0.00	4.56
KUT-2L	97.47	0.00	2.53	97.47	0.00	2.53	97.42	0.00	2.58
LEM-1E	92.86	3.57	3.57	92.86	3.57	3.57	92.51	3.75	3.75
PAT-1E	94.24	1.19	3.57	94.24	1.19	3.57	94.15	1.21	3.64
TAN-1C	94.44	0.00	4.56	94.44	0.00	4.56	94.17	0.00	4.83

Table IIb: Mineralogical composition of crudely stratified sandstone (Se) sub-facies

Sample Code	Qm	P	K	Q/(Q+F)	Qp/(F+R)	Qt/(F+R)	ln(Q/F)	ln(Q/L)	MMI
AGB-1F	100.00	0.00	0.00	1.00	0.35	37.50	0.00	3.62	37.46
DOK-1N	100.00	0.00	0.00	1.00	0.40	41.00	0.00	3.71	41.02
JIM-1E	94.68	1.44	2.88	0.96	0.58	11.67	3.15	3.15	11.66
KAC-1E	97.35	0.00	2.65	0.97	0.30	14.00	3.62	3.22	14.00
KJT-1A	98.52	0.00	1.48	0.99	0.35	17.00	4.22	3.12	15.99
KUT-2B	100.00	0.00	0.00	1.00	0.53	17.50	0.00	2.86	17.48
KUT-2L	100.00	0.00	0.00	1.00	0.75	38.50	0.00	3.65	38.53
LEM-1E	95.11	1.30	2.59	0.96	0.65	13.00	3.26	3.26	13.01
PAT-1E	98.74	0.00	1.26	0.99	0.40	20.00	4.38	3.28	20.01
TAN-1C	100.00	0.00	0.00	1.00	0.85	17.00	0.00	2.83	15.99

Table IIIa: Recalculated framework composition (%) of planar cross-stratified sandstone (Sp) sub-facies

Sample Code	Quartz (Q)	Feldspar (F)	Rock/Lithic Fragment (R/L)	Total Quartz (Qt)	Feldspar (F)	Lithic Fragment (L)	Monocrystalline Quartz (Qm)	Feldspar (F)	Total Lithic Fragment (Lt)
	Q-F-R/L Plots After (McBride, 1963; Pettijohn, 1975; Folk, 1980)			Qt-F-L Plot After (Dickinson *et al*., 1983)			Qm-F-Lt Plot (After Dickinson , 1985)		
BDA-1L	97.33	0.00	2.67	97.33	0.00	2.67	94.58	0.00	2.72
DOK-1V	98.77	0.00	1.23	98.77	0.00	1.23	98.75	0.00	1.25
ENG-1F	98.59	0.00	1.41	98.59	0.00	1.41	98.58	0.00	1.42
JIM-1S	93.51	2.60	3.90	93.51	2.60	3.90	93.39	2.65	3.97
KAC-1B	97.62	0.00	2.38	97.62	0.00	2.38	97.60	0.00	2.40
MAR-1B	93.33	0.00	5.67	93.33	0.00	5.67	93.21	0.00	5.79
MAR-1D	93.75	3.75	2.50	93.75	3.75	2.50	93.45	3.93	2.62
MAR-1L	93.33	2.67	4.00	93.33	2.67	4.00	93.01	2.80	4.20
MGT-1C	97.50	1.25	1.25	97.50	1.25	1.25	97.43	1.29	1.29
PAT-1J	97.70	1.15	1.15	97.70	1.15	1.15	97.70	1.15	1.15
PAT-1N	98.84	0.00	1.16	98.84	0.00	1.16	98.83	0.00	1.17
TAN-1A	95.00	0.00	4.00	95.00	0.00	4.00	94.80	0.00	4.20
TAN-1G	84.42	0.00	14.58	84.42	0.00	14.58	81.25	0.00	18.75

Table IIIb: Mineralogical composition of planar cross-stratified sandstone (Sp) sub-facies

Sample Code	Qm	P	K	Q/(Q+F)	Qp/(F+R)	Qt/(F+R)	ln(Q/F)	ln(Q/L)	MMI
BDA-1L	100.00	0.00	0.00	1.00	0.75	35.50	0.00	3.60	35.45
DOK-1V	100.00	0.00	0.00	1.00	0.80	80.00	0.00	4.38	80.30
ENG-1F	100.00	0.00	0.00	1.00	0.70	70.00	0.00	4.25	69.92
JIM-1S	94.55	0.00	2.75	0.97	0.28	14.40	3.58	3.18	14.39
KAC-1B	100.00	0.00	0.00	1.00	0.40	41.00	0.00	3.71	41.02
MAR-1B	100.00	0.00	0.00	1.00	0.28	14.00	0.00	2.64	13.99
MAR-1D	94.96	1.35	2.69	0.96	0.74	14.00	3.22	3.62	14.00
MAR-1L	97.08	0.00	2.92	0.97	0.70	14.00	3.56	3.15	13.99
MGT-1C	98.70	0.00	1.30	0.99	1.15	39.00	4.36	4.36	39.00
PAT-1J	98.84	0.00	1.16	0.99	0.00	42.50	4.44	4.44	42.48
PAT-1N	100.00	0.00	0.00	1.00	0.80	84.00	0.00	4.44	84.21
TAN-1A	100.00	0.00	0.00	1.00	1.20	24.00	0.00	3.18	24.00
TAN-1G	100.00	0.00	0.00	1.00	1.08	4.42	0.00	1.69	4.42

Table IVa: Recalculated framework composition (%) of rippled cross-stratified sandstone (Sr) sub-facies.

Sample Code	Quartz (Q)	Feldspar (F)	Rock/Lithic Fragment (R/L)	Total Quartz (Qt)	Feldspar (F)	Lithic Fragment (L)	Monocrystalline Quartz (Qm)	Feldspar (F)	Total Lithic Fragment (Lt)
	Q-F-R/L Plots After (McBride, 1963; Pettijohn, 1975; Folk, 1980)			Qt-F-L Plot After (Dickinson *et al*., 1983)			Qm-F-Lt Plot (After Dickinson , 1985)		
AGB-1J	97.59	1.20	1.20	97.59	1.20	1.20	95.33	2.44	1.22
MAN-1F	97.65	1.18	1.18	97.65	1.18	1.18	97.60	1.20	1.20

Table IVb: Mineralogical composition of rippled cross-stratified sandstone (Sr) sub-facies

Sample Code	Qm	P	K	Q/(Q+F)	Qp/(F+R)	Qt/(F+R)	ln(Q/F)	ln(Q/L)	MMI
AGB-1J	97.52	0.00	2.48	0.98	0.73	27.00	3.70	4.39	40.66
MAN-1J	98.78	0.00	1.22	0.99	0.90	41.50	4.42	4.42	41.38

Table Va: Recalculated framework composition (%) of horizontally stratified sandstone (Sh) sub-facies.

Sample Code	Quartz (Q)	Feldspar (F)	Rock/Lithic Fragment (R/L)	Total Quartz (Qt)	Feldspar (F)	Lithic Fragment (L)	Monocrystalline Quartz (Qm)	Feldspar (F)	Total Lithic Fragment (Lt)
	Q-F-R/L Plots After (McBride, 1963; Pettijohn, 1975; Folk, 1980)			Qt-F-L Plot After (Dickinson *et al*., 1983)			Qm-F-Lt Plot (After Dickinson , 1985)		
AGB-1C	95.20	0.00	3.80	95.20	0.00	3.80	95.16	0.00	3.84
BDA-1B	94.52	0.00	2.78	94.52	0.00	2.78	97.19	0.00	2.81
BDA-1F	100.00	0.00	0.00	100.00	0.00	0.00	100.00	0.00	0.00
BDA-1M	97.40	0.00	2.60	97.40	0.00	2.60	97.38	0.00	2.62
DOK-1K	94.52	0.00	2.78	94.52	0.00	2.78	97.19	0.00	2.81
DOK-1Y	95.25	1.25	2.50	95.25	1.25	2.50	95.18	1.27	2.55
DOK-Z2	97.50	0.00	2.50	97.50	0.00	2.50	97.45	0.00	2.55
ENG-1H	95.39	0.00	3.61	95.39	0.00	3.61	95.28	0.00	3.72
ENG-1V	98.68	0.00	1.32	98.68	0.00	1.32	98.67	0.00	1.33
JIM-1F	84.29	0.00	14.71	84.29	0.00	14.71	83.92	0.00	15.08
KCH-1D	94.52	0.00	2.78	94.52	0.00	2.78	97.08	0.00	2.92
KUT-2A	98.72	0.00	1.28	98.72	0.00	1.28	98.66	0.00	1.34
KUT-2G	100.00	0.00	0.00	100.00	0.00	0.00	100.00	0.00	0.00
KUT-2J	100.00	0.00	0.00	100.00	0.00	0.00	100.00	0.00	0.00
KUT-2K	95.10	0.00	3.90	95.10	0.00	3.90	95.03	0.00	3.97
LEM-1H	94.00	2.50	2.50	94.00	2.50	2.50	94.90	2.55	2.55
MAN-1H	95.15	1.28	2.56	95.15	1.28	2.56	95.12	1.29	2.59
MAR-1C	95.25	1.25	2.50	95.25	1.25	2.50	95.18	1.27	2.55
MGT-1H	100.00	0.00	0.00	100.00	0.00	0.00	100.00	0.00	0.00
RAB-1H	95.10	0.00	3.90	95.10	0.00	3.90	94.91	0.00	4.09
RAB-1P	93.90	1.22	4.88	93.90	1.22	4.88	93.73	1.25	4.02
RAT-1P	97.73	0.00	2.27	97.73	0.00	2.27	97.73	0.00	2.27
WAR-1H	97.47	0.00	2.53	97.47	0.00	2.53	97.44	0.00	2.56

Table Vb: Mineralogical composition of horizontally stratified sandstone (Sh) sub-facies

Sample Code	Qm	P	K	Q/(Q+F)	Qp/(F+R)	Qt/(F+R)	ln(Q/F)	ln(Q/L)	MMI
AGB-1C	100.00	0.00	0.00	1.00	0.27	24.33	0.00	3.23	24.32
BDA-1B	100.00	0.00	0.00	1.00	0.35	34.00	0.00	3.56	34.97
BDA-1F	100.00	0.00	0.00	1.00	0.0	0.00	0.00	0.00	N.A
BDA-1M	100.00	0.00	0.00	1.00	0.35	37.50	0.00	3.62	37.46
DOK-1K	100.00	0.00	0.00	1.00	0.35	34.00	0.00	3.56	34.97
DOK-1Y	98.69	0.00	1.31	0.99	0.50	24.67	4.34	3.65	24.67
DOK-Z2	100.00	0.00	0.00	1.00	0.80	39.00	0.00	3.66	39.00
ENG-1H	100.00	0.00	0.00	1.00	0.13	25.67	0.00	3.28	25.70
ENG-1V	100.00	0.00	0.00	1.00	0.70	74.00	0.00	4.32	74.76
JIM-1F	100.00	0.00	0.00	1.00	0.58	4.80	0.00	1.76	4.80
KCH-1D	100.00	0.00	0.00	1.00	1.75	34.00	0.00	3.56	34.97
KUT-2A	100.00	0.00	0.00	1.00	3.10	77.00	0.00	4.34	77.13
KUT-2G	100.00	0.00	0.00	1.00	0.00	0.00	0.00	0.00	N.A
KUT-2J	100.00	0.00	0.00	1.00	0.00	0.00	0.00	0.00	N.A
KUT-2K	100.00	0.00	0.00	1.00	0.50	24.67	0.00	3.21	24.64
LEM-1H	97.39	0.00	2.61	0.97	0.38	19.00	3.64	3.64	19.00
MAN-1H	98.67	0.00	1.33	0.99	0.23	24.00	4.32	3.62	24.04
MAR-1C	98.69	0.00	1.31	0.99	0.50	24.67	4.34	3.65	24.67
MGT-1H	100.00	0.00	0.00	1.00	0.00	0.00	0.00	0.00	N.A
RAB-1H	100.00	0.00	0.00	1.00	1.23	24.67	0.00	3.21	24.64
RAB-1P	98.68	0.00	1.32	0.99	0.46	14.40	4.34	2.96	14.39
RAT-1P	100.00	0.00	0.00	1.00	0.00	43.00	0.00	3.76	43.05
WAR-1H	100.00	0.00	0.00	1.00	0.40	38.50	0.00	3.65	38.53

Table VIa: Recalculated framework composition (%) of massive sandstone (Sm) sub-facies.

Sample Code	Quartz (Q)	Feldspar (F)	Rock/Lithic Fragment (R/L)	Total Quartz (Qt)	Feldspar (F)	Lithic Fragment (L)	Monocrystalline Quartz (Qm)	Feldspar (F)	Total Lithic Fragment (Lt)
	Q-F-R/L Plots After (McBride, 1963; Pettijohn, 1975; Folk, 1980)			Qt-F-L Plot After (Dickinson *et al*., 1983)			Qm-F-Lt Plot (After Dickinson , 1985)		
AGE-1A	95.39	1.20	2.41	95.39	1.20	2.41	95.31	1.23	2.46
AGE-1G	97.62	2.38	0.00	97.62	2.38	0.00	97.53	2.47	0.00
AGE-1J	97.65	2.35	0.00	97.65	2.35	0.00	97.60	2.40	0.00
PAT-1L	95.59	1.14	2.27	95.59	1.14	2.27	95.44	1.19	2.38
RAT-1H	95.30	1.23	2.47	95.30	1.23	2.47	95.24	1.25	2.51

Table VIb: Mineralogical composition of massive sandstone (Sm) sub-facies

Sample Code	Qm	P	K	Q/(Q+F)	Qp/(F+R)	Qt/(F+R)	ln(Q/F)	ln(Q/L)	MMI
AGE-1A	98.74	0.00	1.26	0.98	0.53	26.67	4.38	3.69	25.70
AGE-1G	97.53	0.00	2.47	0.98	1.45	41.00	3.71	0.00	41.02
AGE-1J	97.60	1.20	1.20	0.99	0.85	41.50	3.73	0.00	41.55
PAT-1L	98.78	0.00	1.22	0.99	1.27	28.33	4.44	3.75	28.33
RAT-1H	98.71	0.00	1.29	0.99	0.40	26.00	4.36	3.66	25.03

Table VIIa: Recalculated framework composition (%) of laminated, very-fine sandstone and mudstone (Fl) sub-facies.

Sample Code	Quartz (Q)	Feldspar (F)	Rock/Lithic Fragment (R/L)	Total Quartz (Qt)	Feldspar (F)	Lithic Fragment (L)	Monocrystalline Quartz (Qm)	Feldspar (F)	Total Lithic Fragment (Lt)
	Q-F-R/L Plots After (McBride, 1963; Pettijohn, 1975; Folk, 1980)			Qt-F-L Plot After (Dickinson *et al*., 1983)			Qm-F-Lt Plot (After Dickinson , 1985)		
BDA-IK	95.30	0.00	3.70	95.30	0.00	3.70	95.26	0.00	3.74
JIM-1B	95.30	0.00	3.70	95.30	0.00	3.70	95.19	0.00	3.81
KAC-1V	90.67	2.67	5.67	90.67	2.67	5.67	90.49	2.72	5.79
KAC-1X	93.75	1.25	4.00	93.75	1.25	4.00	93.63	1.27	4.10
KAC-1Y	95.39	2.41	1.20	95.39	2.41	1.20	95.39	2.41	1.20
KCH-1F	94.89	0.00	4.11	94.89	0.00	4.11	94.85	0.00	4.15
MAN-1D	93.33	0.00	5.67	93.33	0.00	5.67	93.33	0.00	5.67
PAT-1C	93.18	2.27	4.55	93.18	2.27	4.55	93.18	2.27	4.55
PAT-1H	97.65	0.00	2.35	97.65	0.00	2.35	97.65	0.00	2.35
RAT-1J	94.81	1.30	3.90	94.81	1.30	3.90	94.76	1.31	3.93

Table VIIb: Mineralogical composition of laminated, very-fine sandstone and mudstone (Fl) sub-facies

Sample Code	Qm	P	K	Q/(Q+F)	Qp/(F+R)	Qt/(F+R)	ln(Q/F)	ln(Q/L)	MMI
BDA-IK	100.00	0.00	0.00	0.96	0.27	25.00	0.00	3.26	25.03
JIM-1B	100.00	0.00	0.00	0.96	0.77	25.00	0.00	3.26	25.03
KAC-1V	97.08	0.00	2.92	0.93	0.20	5.4.71	3.53	2.61	9.71
KAC-1X	98.66	0.00	1.34	0.95	0.30	14.00	4.32	2.93	14.00
KAC-1Y	97.56	0.00	2.44	0.99	0.00	25.67	3.69	4.38	25.70
KCH-1F	100.00	0.00	0.00	0.96	0.00	23.33	0.00	3.15	23.33
MAN-1D	100.00	0.00	0.00	0.93	0.00	14.00	0.00	2.64	13.99
PAT-1C	97.62	0.00	2.38	0.95	0.00	13.67	3.71	3.02	13.66
PAT-1H	100.00	0.00	0.00	0.98	0.00	41.50	0.00	3.73	41.55
RAT-1J	98.64	0.00	1.36	0.96	0.18	18.25	4.29	3.19	18.23

Table VIIIa: Recalculated framework composition (%) of very-fine, massive sandstone and mudstone (Fm) sub-facies.

Sample Code	Quartz (Q)	Feldspar (F)	Rock/Lithic Fragment (R/L)	Total Quartz (Qt)	Feldspar (F)	Lithic Fragment (L)	Monocrystalline Quartz (Qm)	Feldspar (F)	Total Lithic Fragment (Lt)
	Q-F-R/L Plots After (McBride, 1963; Pettijohn, 1975; Folk, 1980)			Qt-F-L Plot After (Dickinson *et al*., 1983)			Qm-F-Lt Plot (After Dickinson , 1985)		
AGB-1E	94.52	0.00	2.78	94.52	0.00	2.78	94.52	0.00	2.78
DOK-Z4	97.40	0.00	2.60	97.40	0.00	2.60	97.35	0.00	2.65
ENG-1P	95.59	0.00	3.41	95.59	0.00	3.41	95.56	0.00	3.44
KAC-1R	100.00	0.00	0.00	100.00	0.00	0.00	100.00	0.00	0.00
LEM-1P	94.51	0.00	4.49	94.51	0.00	4.49	94.51	0.00	4.49
PAT-1K	94.52	0.00	2.78	94.52	0.00	2.78	97.08	0.00	2.92
RAB-1D	91.89	1.35	5.76	91.89	1.35	5.76	91.81	1.36	5.82

Table VIIIb: Mineralogical composition of very-fine, massive sandstone and mudstone (Fm) sub-facies

Sample Code	Qm	P	K	Q/(Q+F)	Qp/(F+R)	Qt/(F+R)	ln(Q/F)	ln(Q/L)	MMI
AGB-1E	100.00	0.00	0.00	0.97	0.00	34.00	0.00	3.56	34.97
DOK-Z4	100.00	0.00	0.00	0.97	0.75	37.50	0.00	3.62	37.46
ENG-1P	100.00	0.00	0.00	0.97	0.27	28.33	0.00	3.34	28.33
KAC-1R	100.00	0.00	0.00	1.00	0.00	0.00	0.00	0.00	N.A.
LEM-1P	100.00	0.00	0.00	0.96	0.00	21.25	0.00	3.06	21.27
PAT-1K	100.00	0.00	0.00	0.97	1.75	34.00	0.00	3.56	34.97
RAB-1D	98.54	0.00	1.46	0.93	0.12	11.33	4.22	2.61	11.33

Table IX: The Standard mineralogical maturity index (MMI) values after Nwajide and Hoque (1985)

Standard Values	MMI Values	Interpretations
Q = ≥ 95% (F + RF) = 50%	≥ 19	Super-mature
Q = 95-90% (F + RF) = 5-10%	19 - 5.4.0	Mature
Q = 90-75% (F + RF) =10-25%	5.4.0-3.0	Sub-mature
Q = 75-50% (F + RF) = 25-50%	3.0 - 1.0	Immature
Q = < 50% (F + RF) > 50%	≤ 1	Extremely Immature

For the entire plot, below is the detail of the codes used for the compositional framework description;

A. Qt = Qm + Qp, where

Qt = total quart grains

Qm = monocrystalline quartz

Qp = polycrystalline quartz

B. Feldspar Grains (F = P + K), where

F = total feldspar grains

P = plagioclase feldspar grains

K = potassium feldspar grains

C. Lithic Fragments (Lt = Ls + Lv +Lm), where

Lt = total lithic fragments

Lv = volcanic lithic fragments

Ls = sedimentary lithic fragments

Lm = metamorphic lithic fragments

APPENDIX V- RESULTS OF HEAVY MINERAL COMPOSITIONS

Table I: Heavy mineral composition of matrix supported, massive conglomerate (Gmm) sub-facies.

Sample Code	Total Opaque	Total non-Opaque								Opaque/Non-opaque
		Zircon	Tourmaline	Rutile	Staurolite	Biotite	Muscovite	Sillimanite	Garnet	
DOK-1C	150	70	10	20	9	5	2	7	10	1.13

Table II: Heavy mineral composition of crudely bedded Conglomerate (Gh) sub-facies.

Sample Code	Total Opaque	Total Non-Opaque								Opaque/Non-opaque
		Zircon	Tourmaline	Rutile	Staurolite	Biotite	Muscovite	Sillimanite	Garnet	
BDA-1J	150	50	12	30	5	1	2	1	0	1.49
DOK-1G	260	60	20	90	25	1	2	3	5	1.26
DOK-1S	105	10	3	15	0	0	1	1	1	3.39
LEM-1K	70	1	25	20	12	1	3	0	3	1.08
LEM-1B	220	40	25	30	10	1	2	2	2	1.96
RAB-1C	270	100	60	80	10	0	5	10	15	0.96

Table III: Heavy mineral composition of crudely stratified Sandstone (Se) sub-facies.

Sample Code	Total Opaque	Total non-Opaque								Opaque/Non-opaque
		Zircon	Tourmaline	Rutile	Staurolite	Biotite	Muscovite	Sillimanite	Garnet	
BAR-1E	140	2	6	10	1	2	0	0	0	5.67
BAR-1L	220	30	30	90	8	2	3	0	6	1.30
BDA-1H	100	1	2	1	10	1	5	0	2	4.55
BDA-1Q	60	3	8	5	4	3	4	0	0	2.22
DOK-1A	260	25	30	40	5	2	3	1	4	2.36
DOK-1N	160	3	16	20	7	2	3	0	2	3.02
DOK-1P	190	16	20	15	0	8	0	6	2	2.84
JIM-1E	220	25	15	25	15	10	7	0	2	2.22
LEM-1C	200	40	35	50	10	2	5	2	2	1.37
LEM-1E	180	25	40	30	5	0	3	1	1	1.71
LEM-1G	185	25	20	23	3	2	2	2	5	2.26
LEM-1M	40	2	10	5	2	1	1	0	0	1.90

Table IV: Heavy mineral composition of planar cross-stratified sandstone (Sp) sub-facies.

Sample Code	Opaque	Non-Opaque								Opaque/Non-opaque
		Zircon	Tourmaline	Rutile	Staurolite	Biotite	Muscovite	Sillimanite	Garnet	
BDA-1C	120	6	7	10	12	2	3	0	1	2.93
BDA-1E	110	35	15	50	12	4	3	2	2	0.89
BDA-1P	130	4	6	5	3	2	3	1	0	4.42
BDA-1R	210	8	6	10	5	7	3	0	2	4.12
DOK-1R	650	80	35	40	20	15	10	5	1	3.16
DOK-1V	240	10	6	35	6	2	2	1	1	3.81
JIM-1Y	110	3	2	5	6	0	2	0	2	4.50
LEM-1R	160	7	30	15	3	2	2	1	3	2.54
PAT-1J	300	30	25	40	7	2	3	2	1	2.73
RAB-1E	310	7	5	35	5	2	2	4	2	4.00
TAN-1A	110	35	20	45	4	2	5	5	0	0.95

Table V: Heavy mineral composition of horizontally stratified sandstone (Sh) sub-facies.

Sample Code	Total Opaque	Non-Opaque								Opaque/Non-opaque
		Zircon	Tourmaline	Rutile	Staurolite	Biotite	Muscovite	Sillimanite	Garnet	
BDA-1B	270	11	13	15	5	1	4	0	1	4.40
BDA-1F	50	9	3	7	5	1	2	0	1	1.79
BDA-1M	60	3	7	6	8	2	5	0	0	1.94
BDA-1S	140	2	5	15	7	4	5	0	0	3.68
DOK-1T	600	65	50	55	20	10	5	2	4	2.84
JIM-1A	190	15	12	15	15	2	2	0	0	3.11
JIM-1Q	550	20	20	25	3	0	2	1	0	7.75
JIM-1V	250	25	15	40	10	0	5	10	1	2.36
KUT-2A	400	3	35	60	5	0	2	2	2	3.67
KUT-2E	800	2	15	15	5	0	2	0	0	2.05
KUT-2J	40	0	1	5	2	0	1	1	1	3.64
LEM1A	30	1	2	7	0	0	1	1	1	2.31
LEM-1H	140	15	13	25	7	1	2	2	1	2.12
LEM-1Q	100	10	25	30	5	1	2	2	2	1.30
PAT-1B	275	25	10	32	10	1	2	2	1	3.31
PAT-1G	90	0	1	1	2	0	1	0	0	18.00

Table VI: Heavy mineral composition of rippled stratified sandstone (Sr) sub-facies.

Sample Code	Total Opaque	Non-Opaque								Opaque/Non-opaque
		Zircon	Tourmaline	Rutile	Staurolite	Biotite	Muscovite	Sillimanite	Garnet	
AGB-1J	250	14.00	54.00	44.00	0.00	0.00	2.00	3.00	2.00	3.28
RAB-1P	110	10.00	14.00	40.00	0.00	0.00	0.00	2.00	3.00	4.57

Table VII: Heavy mineral composition of massive sandstone (Sm) sub-facies.

Sample Code	Total Opaque	Non-Opaque								Opaque/Non-opaque
		Zircon	Tourmaline	Rutile	Staurolite	Biotite	Muscovite	Sillimanite	Garnet	
LEM-1D	250	40	45	55	7	2	3	3	3	1.61
LEM-1L	300	85	100	120	3	2	2	5	2	0.95
PAT-1D	110	10	5	10	7	1	3	1	0	2.97

Table VIII: Heavy mineral composition of laminated mudstone (Fl) sub-facies.

Sample Code	Total Opaque	Non-Opaque								Opaque/Non-opaque
		Zircon	Tourmaline	Rutile	Staurolite	Biotite	Muscovite	Sillimanite	Garnet	
BDA-1K	100	2	3	3	2	2	0	1	0	7.69
DOK-1D	300	25	10	30	0	0	2	2	0	4.35
DOK-1H	50	1	7	8	2	10	0	2	0	1.67
DOK-1Z	220	10	5	20	0	2	1	1	2	4.37
JIM-1D	750	30	15	3	10	2	5	2	0	11.19
JIM-1M	500	35	20	65	7	2	2	2	0	3.76
KUT-2C	120	1	15	7	4	0	3	1	0	3.87
LEM-1N	500	55	65	110	10	2	5	7	3	1.95

Table IX: Heavy mineral composition of massive mudstone (Fm) sub-facies.

Sample Code	Total Opaque	Non-Opaque								Opaque/Non-opaque
		Zircon	Tourmaline	Rutile	Staurolite	Biotite	Muscovite	Sillimanite	Garnet	
DOK-Z4	360	60	85	40	15	2	5	4	2	1.69
MAR-1N	320	30	40	65	10	4	5	5	3	1.98
PAT-1K	300	20	20	30	5	2	2	2	3	3.57

For the entire heavy mineral description, below is the codes used;

Zr = Zircon

To = Tourmaline

Ru = Rutile

St = Staurolite

Bi = Biotite

Mu = Muscovite

Si = Sillimanite

Gr = Garnet

APPENDIX VI – RATIOS OF SOME MAJOR ELEMENTS VALUES AND GEOCHEMICAL LOGARITHM INDICATORS

Table Ia: Values of ratios of some major elements and geochemical logarithm indicators of Gcm, Gmm and Gh sub-facies in northern Bida Basin.

	Clast-supported, massive conglomerate (Gcm)		Matrix supported, massive conglomerate (Gmm)		Crudely bedded conglomerate (Gh)			
Sample	**GBL-1C**	**PTG-1E**	**GBL-1E**	**PTG-1D**	**GBU-1D**	**PTG-1B**	**KJT-1C**	**KJT-1Q**
SiO_2/Al_2O_3	9.49	8.06	8.77	9.76	19.48	17.49	11.95	8.91
Al_2O_3/SiO_2	0.11	0.12	0.11	0.10	0.05	0.06	0.08	0.11
Al_2O_3/TiO_2	34.6	25.68	50.33	14.08	24.83	18.44	5.37	25.28
TiO_2/Al_2O_3	0.03	0.04	0.02	0.07	0.04	0.05	0.16	0.04
Al_2O_3/Na_2O	445.00	70.5	74.5	704.00	77.50	498	43.16	95.27
Fe_2O_3/Al_2O_3	0.14	0.19	0.25	2.50	0.16	0.81	0.47	0.11
Fe_2O_3/K_2O	1.66	0.65	0.71	103.35	0.47	14.5	1.57	0.81
Fe_2O_3+MgO	1.30	2.17	2.70	17.62	0.78	4.07	3.50	1.06
CaO+Na_2O	0.03	0.30	0.33	0.03	0.07	0.02	0.36	0.14
K_2O/Al_2O_3	0.09	0.29	0.36	0.02	0.35	0.05	0.30	0.13
K_2O/Na_2O	38.50	20.79	27.00	17.00	25.83	25.00	13.02	12.88
Na_2O/K_2O	0.03	0.05	0.04	0.06	0.04	0.04	0.08	0.08
Na_2O+K_2O	0.79	3.05	3.36	0.18	1.67	0.27	2.33	1.40
Al_2O_3/(CaO+Na_2O)	295.67	32.9	27.45	234.67	65.43	249.00	20.13	71.49
Al_2O_3+K_2O+Na_2O	9.69	12.92	12.42	4.52	5.32	4.25	9.49	11.13
(Fe_2O_3+MgO)+(Na_2O+K_2O)	2.09	4.22	5.06	17.80	2.45	4.34	4.82	2.46
log(SiO_2/Al_2O_3)	0.98	0.91	0.94	0.99	1.29	1.24	1.08	0.95
log(Na_2O/K_2O)	-1.52	-1.30	-1.40	-1.22	-1.40	-1.40	-1.10	-1.10
log(K_2O/Na_2O)	1.59	1.32	1.43	1.23	1.43	1.41	1.11	1.11
log(Fe_2O_3/K_2O)	0.22	-0.19	-0.15	2.01	-0.33	1.19	0.20	-0.09

Table Ib: Values of ratios of some major elements and geochemical logarithm indicators of the Se and Sp sub-facies in the northern Bida Basin.

	Crudely stratified sandstone (Se) sub-facies								Planar cross-stratified sandstone (Sp) sub-facies			
Sample	**GBL-1D**	**PTG-1A**	**KJT-1A**	**BDA-1D**	**DOK-1D**	**AGB-1B**	**ENG-1J**	**KUT-2D**	**BDA-1A**	**BDA-1R**	**DOK-1X**	**AGB-1K**
SiO_2/Al_2O_3	10.89	14.99	8.82	12.24	4.53	11.29	19.18	18.85	7.53	10.79	9.51	5.14
Al_2O_3/SiO_2	0.09	0.06	0.11	0.08	0.18	0.09	0.05	0.05	0.13	0.09	0.11	0.16
Al_2O_3/TiO_2	13.5	29.05	15.20	25.50	14.46	24.04	28.54	20.96	50.00	20.39	31.01	13.09
TiO_2/Al_2O_3	0.07	0.03	0.06	0.04	0.06	0.04	0.04	0.05	0.02	0.05	0.03	0.08
Al_2O_3/Na_2O	783.00	138	113.77	428.65	838.24	191.17	71.77	482.00	562.50	541.00	577.56	520.8
Fe_2O_3/Al_2O_3	0.31	0.32	0.18	0.21	0.37	0.21	0.39	0.21	0.16	0.28	0.07	0.32
Fe_2O_3/K_2O	17.43	1.34	1.84	168.44	153.32	13.95	2.16	24.75	204.67	284.50	111.33	88.91
Fe_2O_3+MgO	2.47	1.80	1.81	1.51	4.25	1.69	1.83	1.04	1.85	2.29	0.68	4.22
CaO+Na_2O	0.03	0.05	0.17	0.03	0.04	0.09	0.08	0.02	0.03	0.03	0.03	0.07
K_2O/Al_2O_3	0.02	0.24	0.10	0.00	0.00	0.02	0.18	0.01	0.00	0.00	0.00	0.00
K_2O/Na_2O	14.00	32.75	11.06	0.53	2.00	2.93	12.82	4.00	0.45	0.53	0.38	1.88
Na_2O/K_2O	0.07	0.03	0.09	1.89	0.50	0.34	0.08	0.25	2.22	1.88	2.67	0.53
Na_2O+K_2O	0.15	1.35	1.04	0.03	0.05	0.16	0.91	0.05	0.03	0.02	0.02	0.07
$Al_2O_3/(CaO+Na_2O)$	261	110.4	59.30	7.31	407.14	90.09	60.73	241	11.28	8.14	354.42	183.38
$Fe_2O_3+K_2O+Na_2O$	7.98	5.87	10.82	220.82	14.30	8.00	4.65	4.87	415.67	300.56	5.4.26	13.09
$(Fe_2O_3+MgO)+(Na_2O+K_2O)$	2.62	3.15	2.84	1.54	4.30	1.85	2.75	1.09	1.88	2.32	0.70	4.30
$\log(SiO_2/Al_2O_3)$	1.04	1.20	0.95	1.09	0.74	1.05	1.28	1.28	0.88	1.03	0.98	0.79
$\log(Na_2O/K_2O)$	-1.15	-1.52	-1.05	0.28	-0.30	-0.47	-1.10	-0.60	0.35	0.27	0.43	-0.28
$\log(K_2O/Na_2O)$	1.15	1.52	1.04	-0.28	0.30	0.47	1.11	0.60	-0.35	-0.28	-0.42	0.27
$\log(Fe_2O_3/K_2O)$	1.24	0.13	0.26	2.23	2.19	1.14	0.33	1.41	2.31	2.46	2.05	1.95

Table Ic: Values of ratios of some major elements and geochemical logarithm indicators of horizontally stratified sandstone (Sh) sub-facies in the northern Bida Basin.

Sample	BDA-1B	DOK-1K	AGB-1G	ENG-1E	ENG-1L	ENG-1N	ENG-1V	KUT-2A	KUT-2G	KUT-2K	DOK-1T	DOK-1X	RAB-1F	RAB-1H	RAB-1P
SiO_2/Al_2O_3	10.58	8.16	4.58	12.56	8.93	12.10	14.22	21.91	15.75	15.75	5.33	5.4.51	15.16	12.69	8.87
Al_2O_3/SiO_2	0.09	0.12	0.18	0.08	0.11	0.08	0.07	0.05	0.06	0.06	0.16	0.11	0.06	0.08	0.11
Al_2O_3/TiO_2	25.58	34.77	10.40	28.66	23.61	14.29	8.07	11.22	14.29	10.49	55.36	31.01	48.47	23.76	35.15
TiO_2/Al_2O_3	0.04	0.03	0.10	0.03	0.04	0.07	0.12	0.09	0.07	0.10	0.02	0.03	0.02	0.04	0.03
Al_2O_3/Na_2O	464.11	697.67	177.18	94.15	118.93	129.56	189.81	415.00	535.00	535.00	789.00	577.56	71.18	71.52	146.26
Fe_2O_3/Al_2O_3	0.16	0.24	0.11	0.21	0.44	0.63	0.20	0.48	0.39	0.30	0.12	0.07	0.56	0.26	0.27
Fe_2O_3/K_2O	84.69	213.50	3.18	1.53	4.76	5.90	8.74	50.25	51.50	39.5	74.29	111.33	4.98	2.80	4.88
Fe_2O_3+MgO	1.38	2.58	1.63	1.51	4.23	4.54	1.22	2.03	2.09	1.62	1.58	0.68	3.19	1.91	2.75
CaO+Na_2O	0.03	0.03	0.09	0.11	0.13	0.08	0.08	0.04	0.03	0.05	0.03	0.03	0.14	0.35	0.23
K_2O/Al_2O_3	0.00	0.00	0.03	0.14	0.09	0.09	0.02	0.01	0.01	0.01	0.00	0.00	0.09	0.09	0.05
K_2O/Na_2O	0.89	0.80	5.01	12.92	10.98	11.91	4.31	4.00	4.00	4.00	1.24	0.38	5.68	5.68	7.95
Na_2O/K_2O	1.13	1.25	0.17	0.08	0.09	0.08	0.23	0.25	0.25	0.25	0.81	2.67	0.15	0.15	0.13
Na_2O+K_2O	0.03	0.03	0.58	1.04	0.96	0.71	0.17	0.05	0.05	0.05	0.04	0.02	0.61	0.75	0.59
$Al_2O_3/(CaO+Na_2O)$	8.41	337.58	159.85	67.32	74.91	91.36	79.92	103.75	178.33	107.00	495.78	354.42	40.75	19.80	42.9
$Fe_2O_3+K_2O+Na_2O$	322	10.49	14.29	8.18	10.47	7.84	5.24	4.20	4.40	4.40	13.45	5.4.26	5.23	7.76	10.24
$(Fe_2O_3+MgO)+(Na_2O+K_2O)$	1.42	2.60	2.22	2.55	4.19	4.25	1.39	2.08	2.14	1.67	1.62	0.70	3.80	2.67	3.34
$\log(SiO_2/Al_2O_3)$	1.02	0.91	0.75	1.10	0.95	1.08	1.18	1.34	1.22	1.22	0.80	0.98	1.21	1.10	0.95
$\log(Na_2O/K_2O)$	0.05	0.10	-0.77	-1.10	-1.05	-1.10	-0.64	-0.60	-0.60	-0.60	-0.09	0.43	-0.82	-0.82	-0.89
$\log(K_2O/Na_2O)$	-0.05	-0.10	0.78	1.11	1.04	1.08	0.63	0.60	0.60	0.60	0.09	-0.42	0.82	0.82	0.90
$\log(Fe_2O_3/K_2O)$	1.93	2.33	0.50	0.18	0.68	0.84	0.94	1.70	1.71	1.60	1.88	2.05	0.78	0.45	0.69

Table Id: Values of ratios of some major elements and geochemical logarithm indicators of the Sm, Fl and Fm sub-facies in the northern Bida Basin

	Massive sandstone (Sm) sub-facies		Laminated mudstone (Fl) sub-facies						Massive mudstone (Fm) sub-facies				
Sample	**GBL-1A**	**KUD-1A**	**GBU-1B**	**KJT-1F**	**KJT-1J**	**BDA-1K**	**AGB-1D**	**KUD-1C**	**GBU-1A**	**DOK-1F**	**ENG-1B**	**KUD-1B**	**KUD-1G**
SiO_2/Al_2O_3	5.25	10.49	13.69	10.18	12.24	13.61	4.08	11.79	4.65	4.16	5.4.28	7.42	11.06
Al_2O_3/SiO_2	0.16	0.10	0.07	0.10	0.08	0.07	0.25	0.08	0.18	0.19	0.11	0.13	0.09
Al_2O_3/TiO_2	44.74	4.93	22.71	24.46	35.48	1.29	14.07	7.46	41.75	55.22	15.43	7.48	4.87
TiO_2/Al_2O_3	0.02	0.17	0.04	0.04	0.03	0.77	0.07	0.13	0.02	0.02	0.06	0.13	0.21
Al_2O_3/Na_2O	109.82	795.00	105.00	48.82	105.76	301.10	278.55	746.00	334.00	738.9	42.15	1010	745.00
Fe_2O_3/Al_2O_3	0.25	0.32	0.18	0.55	0.21	0.50	0.21	0.12	0.22	0.13	0.20	0.75	0.63
Fe_2O_3/K_2O	1.02	32.13	0.71	2.54	1.90	263.75	15.05	17.80	2.14	75.44	1.44	84.00	78.83
Fe_2O_3+MgO	3.17	2.62	1.22	4.95	1.60	3.19	3.89	0.93	3.05	2.08	1.95	7.62	4.79
CaO+Na_2O	0.22	0.04	0.07	0.54	0.24	0.05	0.11	0.05	0.05	0.05	0.38	0.04	0.03
K_2O/Al_2O_3	0.24	0.01	0.25	0.22	0.11	0.00	0.01	0.01	0.10	0.00	0.14	0.01	0.01
K_2O/Na_2O	25.36	8.00	25.83	10.62	11.88	0.57	3.61	4.00	34.00	1.29	4.88	5.4.00	5.00
Na_2O/K_2O	0.04	0.13	0.04	0.09	0.08	1.75	0.28	0.20	0.03	0.78	0.17	0.11	0.17
Na_2O+K_2O	3.01	0.09	1.67	1.96	0.88	0.03	0.30	0.06	1.44	0.05	1.53	0.10	0.07
$Al_2O_3/(CaO+Na_2O)$	54.91	198.75	90.86	14.39	30.00	5.36	164.62	149.20	264.50	337.33	24.67	252.50	248.33
$Al_2O_3+K_2O+Na_2O$	14.09	8.04	8.03	10.21	8.14	140.51	18.69	7.52	14.80	14.57	10.93	10.20	7.52
$(Fe_2O_3+MgO)+(Na_2O+K_2O)$	5.18	2.71	2.89	5.92	2.48	3.22	4.19	0.99	4.49	2.13	3.49	7.72	4.86
$\log(SiO_2/Al_2O_3)$	0.80	1.02	1.14	1.01	1.09	1.13	0.61	1.07	0.75	0.71	0.97	0.87	1.04
$\log(Na_2O/K_2O)$	-1.40	-0.89	-1.40	-1.05	-1.10	0.24	-0.55	-0.70	-1.52	-0.11	-0.77	-0.96	-0.77
$\log(K_2O/Na_2O)$	1.42	0.90	1.43	1.03	1.07	-0.24	0.56	0.70	1.54	0.11	0.77	0.95	0.78
$\log(Fe_2O_3/K_2O)$	0.01	1.51	-0.15	0.40	0.28	2.42	1.21	1.25	0.33	1.88	0.16	1.92	1.90

Table Ie: Values of ratios of some major elements and geochemical logarithm indicators of Published Data using for comparison with this study

Sample	PAAS	UCC
SiO_2/Al_2O_3	3.32	4.32
Al_2O_3/SiO_2	0.30	0.23
Al_2O_3/TiO_2	18.9	24.06
TiO_2/Al_2O_3	0.05	0.04
Al_2O_3/Na_2O	14.75	4.71
Fe_2O_3/Al_2O_3	0.38	0.33
Fe_2O_3/K_2O	1.95	1.80
Fe_2O_3+MgO	9.42	7.52
$CaO+Na_2O$	2.5	5.86
K_2O/Al_2O_3	0.2	0.18
K_2O/Na_2O	3.08	0.86
Na_2O/K_2O	0.32	1.17
Na_2O+K_2O	4.9	5.07
$Al_2O_3/(CaO+Na_2O)$	7.56	2.24
$Fe_2O_3+K_2O+Na_2O$	12.12	11.11
$(Fe_2O_3+MgO)+(Na_2O+K_2O)$	14.32	13.59
$\log(SiO_2/Al_2O_3)$	0.52	0.64
$\log(Na_2O/K_2O)$	0.08	0.71
$\log(K_2O/Na_2O)$	0.49	-0.07
$\log(Fe_2O_3/K_2O)$	0.29	0.26

Table IIa: Trace elements ratios values of clast supported, massive conglomerate (Gcm) in the northern Bida Basin

Sample No	La/Sc	Th/Sc	Th/Co	La/Co	Ba/Sc	Ba/Co	La/Th	Zr/Sc	Th/Sc	Rb/Sr	Th/U	Ba/Rb	Zr/Hf	Zr/Nb	Zr/Th	U/Th	V/Cr	Ni/Co
GBL-1C	8.13	3.25	4.33	10.83	19.44	24.92	2.50	0.75	3.25	1.24	13.00	14.81	30.00	60.00	0.23	-1.33	0.61	2.75
PTG-1E	7.42	2.84	3.38	8.81	47.89	55.88	2.61	0.58	2.84	0.37	5.00	12.13	35.67	54.00	0.20	-0.90	1.25	1.94
Mean	7.78	3.05	3.86	9.82	33.67	41.40	2.56	0.67	3.05	0.81	9.50	13.47	33.34	57.50	0.22	-1.12	0.93	2.34
Min.	7.42	2.84	3.38	8.81	19.44	24.92	2.50	0.58	2.84	0.37	5.00	12.13	30.00	54.00	0.20	-1.33	0.61	1.94
Max.	8.13	3.25	4.33	10.83	47.89	55.88	2.61	0.75	3.25	1.24	13.00	14.81	35.67	60.00	0.23	-0.90	1.25	2.75

Table IIb: Trace elements ratios values of the matrix supported, massive conglomerate (Gmm) in northern Bida Basin.

Sample No	La/Sc	Th/Sc	Th/Co	La/Co	Ba/Sc	Ba/Co	La/Th	Zr/Sc	Th/Sc	Rb/Sr	Th/U	Ba/Rb	Zr/Hf	Zr/Nb	Zr/Th	U/Th	V/Cr	Ni/Co
GBL-1E	15.60	2.67	0.89	4.53	85.00	28.67	5.23	0.27	2.67	0.25	13.33	15.54	20.00	20.00	0.10	-1.03	0.51	1.13
PTG-1D	1.41	4.93	4.21	1.24	5.52	4.73	0.24	3.38	4.93	2.26	3.37	3.10	37.69	64.33	0.57	-0.63	2.00	1.76
Mean	9.01	4.30	3.05	3.39	45.26	14.50	3.24	1.83	4.30	1.26	8.35	9.82	28.85	42.67	0.34	-0.83	1.25	1.45
Min.	1.41	2.67	0.89	1.24	5.52	4.73	0.24	0.27	2.67	0.25	3.37	3.10	20.00	20.00	0.10	-1.03	0.51	1.13
Max.	15.60	4.93	4.21	4.53	85.00	28.67	5.23	3.38	4.93	2.26	13.33	15.54	37.69	64.33	0.57	-0.63	2.00	1.76

Table IIc: Trace elements ratios values of the crudely bedded conglomerate (Gh) sub-facies in northern Bida Basin.

Sample No	La/Sc	Th/Sc	Th/Co	La/Co	Ba/Sc	Ba/Co	La/Th	Zr/Sc	Th/Sc	Rb/Sr	Th/U	Ba/Rb	Zr/Hf	Zr/Nb	Zr/Th	U/Th	V/Cr	Ni/Co
GBU-1D	20.08	3.54	4.11	29.00	12.08	17.44	4.67	1.31	3.54	1.67	7.67	4.23	42.50	55.67	0.37	-0.93	0.36	3.22
PTG 1B	11.06	9.50	13.82	15.09	14.06	21.91	1.16	3.06	9.50	3.71	8.94	4.63	37.69	163.33	0.32	-3.37	2.09	2.45
KJT-1C	22.97	10.96	5.29	13.18	152.02	84.52	2.10	155.48	10.96	0.67	8.98	13.43	33.27	29.99	14.27	-11.15	0.07	1.74
PAT-1M	1.61	1.09	0.86	1.27	7.47	4.91	1.48	14.81	1.09	1.44	2.65	17.62	24.11	25.86	14.56	0.15	0.02	3.86
SHG-1K	7.07	1.73	1.45	4.92	14.56	14.45	4.10	54.96	1.73	0.60	4.05	10.54	29.49	24.85	31.82	-0.38	0.06	4.82
Mean	12.56	4.36	4.51	13.09	40.78	29.39	2.90	45.32	4.36	1.62	5.46	10.29	33.41	60.34	12.27	-3.14	0.52	3.22
Min.	1.61	1.09	0.86	1.27	7.47	4.91	1.16	1.31	1.09	0.60	2.65	4.63	24.11	24.85	0.32	-11.15	0.02	1.74
Max.	22.97	10.96	13.82	25.4.00	152.02	84.52	4.67	155.48	10.96	3.71	8.98	17.62	42.50	163.33	31.82	0.15	2.09	4.82

Table IId: Trace elements ratios values of the crudely stratified sandstone (Se) sub-facies in northern Bida Basin.

Sample No	La/Sc	Th/Sc	Th/Co	La/Co	Ba/Sc	Ba/Co	La/Th	Zr/Sc	Th/Sc	Rb/Sr	Th/U	Ba/Rb	Zr/Hf	Zr/Nb	Zr/Th	U/Th	V/Cr	Ni/Co
AGB-1B	5.62	1.87	2.00	7.06	13.49	14.39	3.54	34.00	1.87	0.18	8.79	10.76	31.45	15.44	18.69	-1.61	0.07	3.78
BDA-1D	4.14	2.71	1.91	3.63	8.36	4.91	1.90	100.01	2.71	0.40	8.49	13.53	33.76	42.12	35.94	-1.78	0.05	3.47
DOK-1D	4.39	3.46	4.40	5.85	4.64	8.80	1.27	159.45	3.46	0.33	5.70	11.96	34.16	52.66	45.06	-3.50	0.29	3.75
ENG-1J	8.73	2.32	1.94	7.30	58.73	49.14	3.76	60.50	2.32	1.24	4.76	5.58	34.45	34.11	25.04	-0.73	0.06	4.26
GBL-1D	4.69	4.90	8.35	9.71	10.14	14.59	1.16	1.31	4.90	0.63	17.75	14.47	31.67	125.67	0.27	-3.93	1.50	3.41
JIM-1L	7.13	1.63	1.84	8.05	5.07	5.85	4.37	22.15	1.63	0.23	4.34	11.30	31.19	14.72	13.58	-0.80	0.13	3.18
JIM-1R	3.99	1.69	1.24	2.91	8.77	5.40	2.35	51.81	1.69	0.25	4.86	17.63	32.57	21.54	30.60	-0.84	0.06	3.10
JIM-1X	4.75	2.03	1.99	4.67	9.79	5.4.63	2.34	112.67	2.03	0.22	4.42	25.12	34.52	37.87	54.62	-1.18	0.06	3.34
KJT-1A	7.09	3.38	2.98	5.24	90.09	79.27	2.09	155.63	3.38	0.67	4.26	14.23	33.27	39.74	45.28	-1.23	0.08	3.31
KUT-2D	3.36	2.57	2.40	3.13	3.93	3.67	1.31	2.50	2.57	1.18	3.91	4.23	38.89	43.75	0.97	-0.28	1.13	2.73
LEM-1C	12.56	3.45	5.21	22.61	20.31	35.56	3.64	93.67	3.45	0.23	7.87	17.36	33.17	37.81	27.14	-4.25	0.29	3.72
LEM-1E	4.42	2.44	1.55	3.46	52.55	33.49	2.23	88.72	2.44	2.73	2.89	7.47	32.75	42.64	35.42	0.07	0.01	3.85
LEM-1G	7.58	2.56	3.20	9.46	12.24	14.29	2.95	61.84	2.56	0.66	4.64	9.23	33.78	28.14	24.11	-2.16	0.17	3.16
PTG-1A	15.93	4.40	4.79	18.14	15.73	17.93	3.14	1.93	4.40	4.80	10.13	2.61	35.25	95.67	0.36	-1.90	1.31	2.43
SHG-1B	4.57	1.25	0.99	4.43	13.85	11.00	4.46	34.34	1.25	0.48	4.31	10.47	30.76	20.98	28.27	-0.48	0.05	4.06
SHG-1X	3.30	1.96	2.67	4.50	9.89	13.47	1.68	124.55	1.96	0.51	7.91	13.47	32.94	64.44	64.01	-2.22	0.10	3.93
Mean	5.77	2.73	3.15	7.63	21.29	20.57	2.64	69.32	2.73	0.92	5.88	12.09	33.47	44.08	28.46	-1.68	0.34	3.47
Min.	3.30	1.25	0.99	2.91	3.93	3.67	1.16	1.31	1.25	0.18	2.89	2.61	30.76	14.72	0.27	-4.25	0.01	2.43
Max.	15.93	4.40	8.35	22.61	90.09	79.27	4.46	159.45	4.40	4.80	17.75	25.12	38.89	125.67	64.01	0.07	1.50	4.26

Table IIe: Trace elements ratios values of the planar cross-stratified sandstone (sp) sub-facies in northern Bida Basin.

Sample No	La/Sc	Th/Sc	Th/Co	La/Co	Ba/Sc	Ba/Co	La/Th	Zr/Sc	Th/Sc	Rb/Sr	Th/U	Ba/Rb	Zr/Hf	Zr/Nb	Zr/Th	U/Th	V/Cr	Ni/Co
AGB-1K	7.62	1.99	2.55	9.76	14.12	18.09	3.83	92.45	1.99	0.03	4.25	37.08	33.35	25.16	45.47	-1.83	0.19	2.86
BAR-1D	10.29	3.21	4.04	12.92	65.15	83.08	3.20	87.51	3.21	2.29	4.97	9.44	24.23	44.33	24.54	-0.90	0.78	2.37
BAR-1H	4.17	1.04	2.79	11.12	4.52	19.27	3.99	18.83	1.04	1.67	3.02	8.13	21.06	19.35	18.04	-0.01	0.81	3.48
BDA-1A	4.69	1.78	1.74	4.57	8.96	8.78	3.20	50.35	1.78	0.28	7.16	14.78	31.65	25.11	28.30	-1.14	0.09	3.97
BDA-1R	2.96	2.44	2.76	3.36	4.05	4.59	1.22	53.90	2.44	0.39	9.54	9.99	32.15	24.21	22.13	-2.39	0.18	3.53
DOK-1X	9.38	2.59	2.71	9.83	12.14	12.72	3.62	84.35	2.59	0.11	5.48	29.70	32.12	38.09	32.60	-1.36	0.07	4.03
PAT-1J	2.10	1.08	1.27	2.47	9.36	11.02	1.94	43.46	1.08	1.63	1.37	87.89	254.58	64.22	40.24	7.73	0.01	0.17
PAT-1N	3.47	2.19	0.86	1.36	20.61	8.11	1.59	77.57	2.19	2.14	3.09	61.70	30.23	45.93	34.48	-0.13	0.07	2.06
TAN-1A	3.39	0.93	0.83	3.03	8.54	7.64	3.65	32.84	0.93	0.42	2.04	20.24	28.94	34.95	34.38	0.45	0.05	3.62
Mean	4.45	1.92	2.17	5.60	15.79	19.26	2.92	60.14	1.92	1.00	4.77	31.11	29.37	35.15	31.76	0.05	0.25	2.90
Min.	2.10	0.93	0.83	1.36	4.05	4.59	1.22	18.83	0.93	0.03	1.37	8.13	21.06	19.35	18.04	-2.39	0.01	0.17
Max.	10.29	3.21	4.04	12.92	65.15	83.08	3.99	92.45	3.21	2.29	9.54	87.89	33.35	64.22	45.47	7.73	0.81	4.03

Table IIf: Trace elements ratios values of the horizontally stratified sandstone (Sh) sub-facies in northern Bida Basin.

Sample No	La/Sc	Th/Sc	Th/Co	La/Co	Ba/Sc	Ba/Co	La/Th	Zr/Sc	Th/Sc	Rb/Sr	Th/U	Ba/Rb	Zr/Hf	Zr/Nb	Zr/Th	U/Th	V/Cr	Ni/Co
AGB-1G	4.90	2.04	4.41	10.59	14.68	31.78	2.40	92.77	2.04	0.31	5.18	10.88	32.54	28.66	44.55	-2.95	0.23	3.6
BAR-1F	8.35	2.76	4.91	14.86	11.51	20.49	3.03	45.22	2.76	0.80	4.63	11.56	27.74	24.33	15.77	-1.13	1.07	2.18
BDA-1B	7.95	2.73	2.46	7.18	10.18	5.4.19	2.91	71.56	2.73	0.39	7.53	15.30	31.90	28.74	25.23	-1.75	0.06	3.9
DOK-1K	5.14	1.92	1.35	4.31	11.44	8.04	3.20	41.72	1.92	0.22	4.43	14.98	31.23	22.10	21.75	-0.79	0.08	3.13
DOK-1T	7.79	2.47	2.09	5.59	9.91	8.39	3.16	54.01	2.47	0.19	7.90	14.14	30.96	23.95	22.30	-1.39	0.12	3.68
ENG-1E	11.45	3.82	3.29	9.85	83.06	71.46	3.00	67.37	3.82	1.13	7.34	8.16	32.00	24.57	17.62	-2.03	0.08	4.05
ENG-1H	7.69	1.96	3.46	13.56	20.41	35.00	3.92	59.95	1.96	1.13	4.93	7.15	33.38	28.36	30.52	-1.51	0.20	3.8
ENG-1L	3.84	2.02	3.15	4.98	44.46	69.21	1.90	57.14	2.02	1.16	4.94	8.77	33.11	28.56	28.23	-1.25	0.19	4.23
ENG-1N	8.99	3.55	2.16	4.48	34.48	21.62	2.53	105.06	3.55	1.06	4.18	8.64	32.98	39.35	29.88	-2.21	0.12	1.91
ENG-1V	10.95	4.58	7.41	17.70	15.66	25.93	2.39	200.92	4.58	0.52	4.99	13.61	33.92	49.98	43.85	-3.42	0.08	4.41
KUT-2A	9.35	3.75	3.75	9.35	9.10	9.10	2.49	2.75	3.75	0.59	5.58	14.00	42.31	35.67	0.73	-1.36	1.14	2.2
KUT-2G	3.29	2.58	3.44	4.39	2.92	3.89	1.27	2.46	2.58	0.79	5.60	5.36	35.88	59.00	0.95	-1.13	1.25	1.94
KUT-2K	5.35	3.48	5.67	12.17	4.09	7.83	1.83	2.26	3.48	0.52	9.20	7.83	32.50	104.00	0.65	-1.80	1.05	2.42
LEM-1A	8.29	3.08	3.18	8.58	38.17	39.48	2.69	104.74	3.08	0.97	4.73	9.17	32.79	34.51	34.03	-2.08	0.09	3.32
LEM-1H	5.11	2.00	0.49	1.51	51.19	12.64	3.05	37.01	2.00	2.45	2.05	14.74	27.40	22.25	18.49	1.04	0.04	2.90
PAT-1B	7.19	2.38	3.07	9.26	25.91	34.68	3.02	58.41	2.38	0.76	4.48	9.51	31.83	25.41	24.55	-1.34	0.12	4.07
PAT-1G	5.84	2.97	4.36	10.01	5.80	9.95	2.30	48.42	2.97	0.52	4.29	13.84	30.30	25.52	15.28	-2.28	0.19	3.08
RAB-1F	2.92	0.91	1.00	3.19	44.76	49.88	3.19	18.02	0.91	0.84	2.88	10.24	29.00	20.21	19.70	0.04	0.07	4.85
RAB-1H	4.34	1.19	1.23	4.49	55.00	57.88	3.65	44.81	1.19	0.64	3.27	10.60	31.19	20.92	38.48	-0.10	0.08	4.28
RAB-1P	3.55	1.15	1.17	3.60	47.59	48.22	3.08	32.98	1.15	0.75	4.97	9.74	34.30	14.92	28.57	-0.51	0.10	3.96
SHG-1F	7.54	1.73	2.02	8.80	13.15	14.35	4.37	39.03	1.73	0.39	7.40	13.18	32.87	20.44	22.59	-0.90	0.07	4.64
SHG-1P	4.04	1.98	2.32	4.74	9.24	10.83	2.04	99.78	1.98	0.55	7.71	11.44	32.74	28.63	50.36	-1.37	0.07	4.65
TAN-1C	4.11	2.79	3.15	4.77	44.94	50.76	1.83	73.71	2.79	0.87	4.88	9.74	33.39	35.30	25.45	-2.02	0.14	3.15
TAN-1D	4.27	1.34	1.90	5.05	54.72	77.53	3.18	43.64	1.34	1.10	1.85	7.88	30.71	21.91	32.54	0.89	0.08	4.18
Mean	5.55	2.47	3.02	7.83	27.85	30.46	2.77	58.66	2.47	0.78	4.66	11.02	32.42	32.22	24.88	-1.31	0.28	3.60
Min.	2.92	0.91	0.49	1.51	2.92	3.89	1.27	2.26	0.91	0.19	1.85	5.36	27.40	14.92	0.65	-3.42	0.04	1.91
Max.	11.45	4.58	7.41	17.70	83.06	77.53	4.1.2.7	200.92	4.58	2.45	5.4.20	15.30	42.31	104.00	50.36	1.04	1.25	4.64

Table IIg: Trace elements ratios values of the massive sandstone (Sm) sub-facies in northern Bida Basin.

Sample No	La/Sc	Th/Sc	Th/Co	La/Co	Ba/Sc	Ba/Co	La/Th	Zr/Sc	Th/Sc	Rb/Sr	Th/U	Ba/Rb	Zr/Hf	Zr/Nb	Zr/Th	U/Th	V/Cr	Ni/Co
GBL-1A	5.26	2.00	1.92	5.00	31.61	30.29	3.13	0.74	2.00	0.76	9.20	5.49	42.50	55.67	0.37	-1.03	1.48	1.54
KUD-1A	4.51	2.89	10.10	19.30	4.63	19.70	1.91	4.40	2.89	0.53	11.35	10.37	42.78	171.11	1.52	-2.48	1.33	3.10
RAB-1E	1.86	0.75	0.58	1.44	64.12	50.32	2.49	42.38	0.75	0.68	1.30	12.34	22.85	34.59	55.72	1.18	0.05	2.81
Mean	4.54	1.88	4.20	8.91	34.12	33.44	2.51	14.84	1.88	0.66	4.58	9.73	35.04	88.36	19.54	-0.78	0.95	2.48
Min.	1.86	0.75	0.58	1.44	4.63	19.70	1.91	0.74	0.75	0.53	1.30	5.49	22.85	34.59	0.37	-2.48	0.05	1.54
Max.	5.26	2.89	10.10	19.30	64.12	50.32	3.13	42.38	2.89	0.76	11.35	12.34	42.78	171.11	55.72	1.18	1.48	3.10

Table IIh: Trace elements ratios values of the laminated mudstone (Fl) sub-facies in northern Bida Basin.

Sample No	La/Sc	Th/Sc	Th/Co	La/Co	Ba/Sc	Ba/Co	La/Th	Zr/Sc	Th/Sc	Rb/Sr	Th/U	Ba/Rb	Zr/Hf	Zr/Nb	Zr/Th	U/Th	V/Cr	Ni/Co
GBU-1B	22.40	3.16	4.64	40.00	11.80	21.07	7.09	1.12	3.16	2.26	4.64	4.84	45.67	140.00	0.35	-1.23	1.03	1.71
BDA-1K	5.40	4.92	12.59	15.37	3.41	8.73	1.30	170.87	4.92	0.33	9.06	22.26	33.43	29.09	34.74	-15.22	0.27	2.42
JIM-1B	7.62	4.76	7.76	12.43	15.56	27.02	1.60	144.66	4.76	1.83	5.05	13.97	24.98	44.50	30.42	-3.03	0.06	3.59
BAR-1J	9.83	4.47	7.64	15.80	18.54	31.68	2.20	108.60	4.47	0.52	4.20	14.11	34.85	33.49	24.29	-0.75	2.02	21.54
AGB-1D	4.66	1.80	3.33	10.46	10.73	19.82	3.14	50.38	1.80	0.19	5.57	10.30	31.68	18.58	27.97	-3.23	0.19	3.19
KUD-1C	8.57	4.43	8.86	17.14	12.50	24.00	1.94	7.00	4.43	0.23	22.96	24.00	40.83	490.00	1.58	-1.80	0.93	2.57
RAB-1L	4.57	2.63	3.53	9.76	44.98	60.40	2.77	105.92	2.63	0.51	4.60	11.01	31.74	27.61	40.70	-1.72	0.13	3.46
Mean	9.68	3.74	7.05	17.57	15.93	27.67	2.86	84.22	3.74	0.84	8.58	14.50	34.03	111.90	22.86	-4.00	0.66	4.50
Min.	4.66	1.80	3.33	9.76	3.41	8.73	1.30	1.12	1.80	0.19	4.20	4.84	24.98	18.58	0.35	-15.22	0.06	1.71
Max.	22.40	4.92	12.59	40.00	44.98	60.40	7.09	170.87	4.92	2.26	22.96	24.00	45.67	490.00	40.70	-0.75	2.02	21.54

Table IIi: Trace elements ratios values of the massive mudstone (Fm) sub-facies in northern Bida Basin.

Sample No	La/Sc	Th/Sc	Th/Co	La/Co	Ba/Sc	Ba/Co	La/Th	Zr/Sc	Th/Sc	Rb/Sr	Th/U	Ba/Rb	Zr/Hf	Zr/Nb	Zr/Th	U/Th	V/Cr	Ni/Co
DOK-1F	5.66	1.92	1.79	5.18	11.46	10.63	3.46	40.03	1.92	0.15	5.03	22.00	32.38	25.52	20.80	-1.05	0.06	3.87
ENG-1B	8.63	3.64	3.33	7.89	79.69	72.84	2.37	100.13	3.64	0.95	7.87	8.95	34.15	27.36	27.49	-3.16	0.08	2.99
GBU-1A	2.36	2.12	4.83	5.50	8.73	24.00	1.11	1.09	2.12	3.45	17.50	4.17	30.00	180.00	0.51	-1.93	1.84	3.25
JIM-1N	7.18	2.60	4.70	14.73	5.70	14.69	2.76	114.54	2.60	0.47	4.59	13.07	34.85	43.74	44.04	-3.59	0.35	3.19
KUD-1B	4.29	2.51	4.54	12.35	3.10	8.94	1.71	3.86	2.51	0.68	7.41	4.43	44.00	157.50	1.54	-2.44	1.15	2.94
KUD-1F	4.33	4.58	14.71	18.29	5.04	20.71	1.16	7.67	4.58	0.73	17.74	9.06	38.33	204.44	1.67	-3.05	1.61	3.57
KUT-2P	4.79	3.06	9.80	18.53	2.23	7.13	1.89	2.02	3.06	0.45	9.25	8.23	40.42	484.00	0.66	-3.31	1.05	2.33
KUT-2Q	12.66	2.77	15.17	73.83	3.37	19.67	4.57	1.54	2.77	0.59	4.08	5.21	35.00	270.00	0.56	-1.32	1.36	2.67
KUT-2R	3.53	4.26	28.57	23.71	2.60	17.43	0.83	1.83	4.26	0.26	8.77	10.17	33.08	430.00	0.43	-4.39	2.15	3.29
LEM-1P	11.81	7.14	2.06	3.41	24.47	7.07	1.66	135.42	7.14	2.66	3.45	9.23	28.21	43.06	19.12	-1.16	0.10	1.94
Mean	5.82	3.46	9.62	18.64	14.84	20.31	2.15	40.91	3.46	1.04	8.87	9.65	34.24	185.76	11.68	-2.54	0.97	2.97
Min.	2.36	1.92	1.79	3.41	2.23	7.07	0.83	1.09	1.92	0.15	3.45	4.17	28.21	25.52	0.43	-4.3.9	0.06	1.94
Max.	12.66	7.14	28.57	73.83	79.69	72.84	4.57	135.42	7.14	3.45	17.74	22.00	44.00	484.00	44.04	-1.05	2.15	3.87

Table IIj: Trace Element ratios values of Composition (ppm) of Published Data using for comparison with this study

Sample No	La/Sc	Th/Sc	Th/Co	La/Co	Ba/Sc	Ba/Co	La/Th	Zr/Sc	Th/Sc	Rb/Sr	Th/U	Ba/Rb	Zr/Hf	Zr/Nb	Zr/Th	U/Th	V/Cr	Ni/Co
PAAS	2.39	0.91	0.63	1.66	40.63	28.26	2.62	13.13	0.91	0.80	4.71	3.25	42.00	11.05	14.38	-1.77	1.36	2.39
UCC	2.21	0.75	0.61	1.79	44.86	35.3	2.95	13.79	0.75	0.26	3.89	1.96	35.42	15.08	18.38	-0.80	1.05	2.72

APPENDIX VII

Selected Qualitative X-Ray Diffraction Peaks for the Studied Sediments

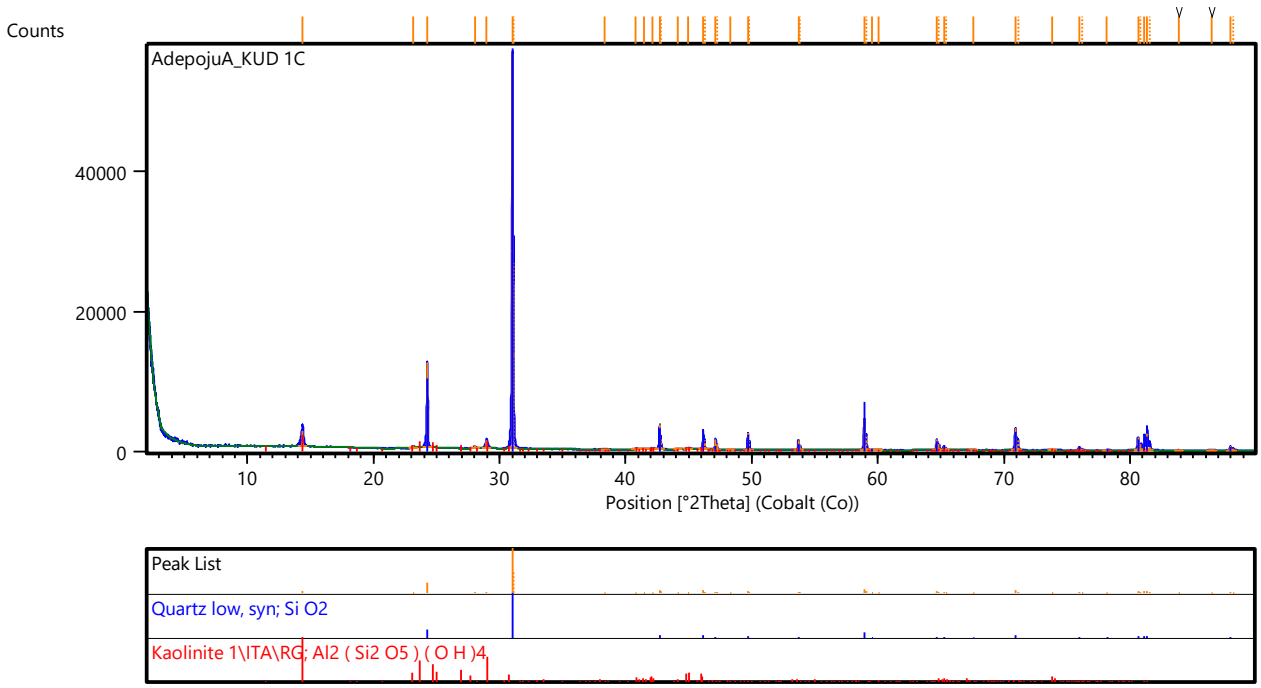


Figure I: X-Ray Diffractogram for sample KUD-1C.

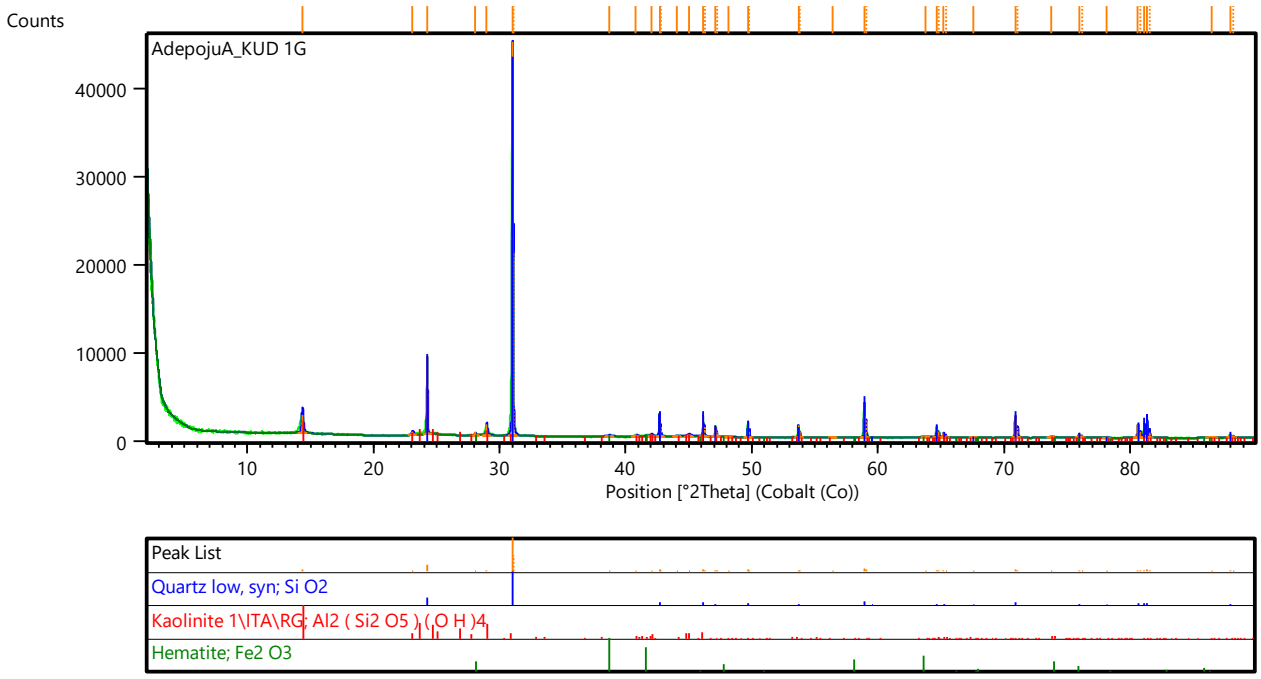


Figure II: X-Ray Diffractogram for sample KUD-1G.

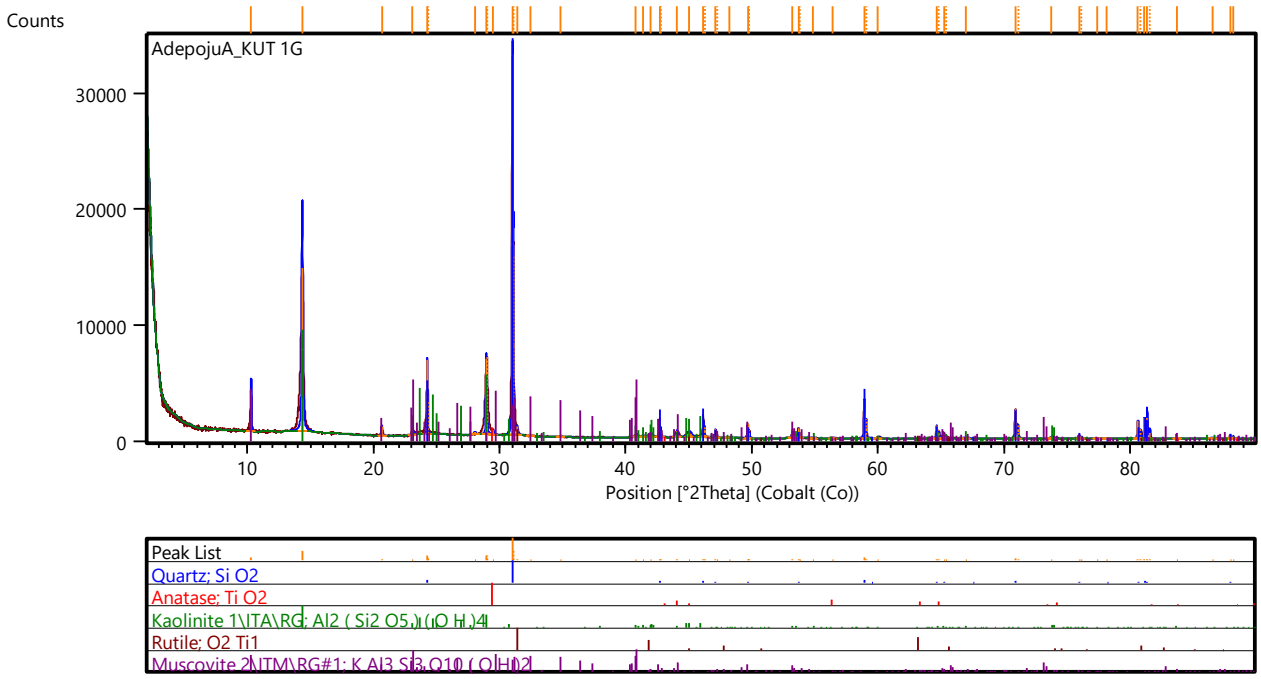


Figure III: X-Ray Diffractogram for sample KUT-1G.

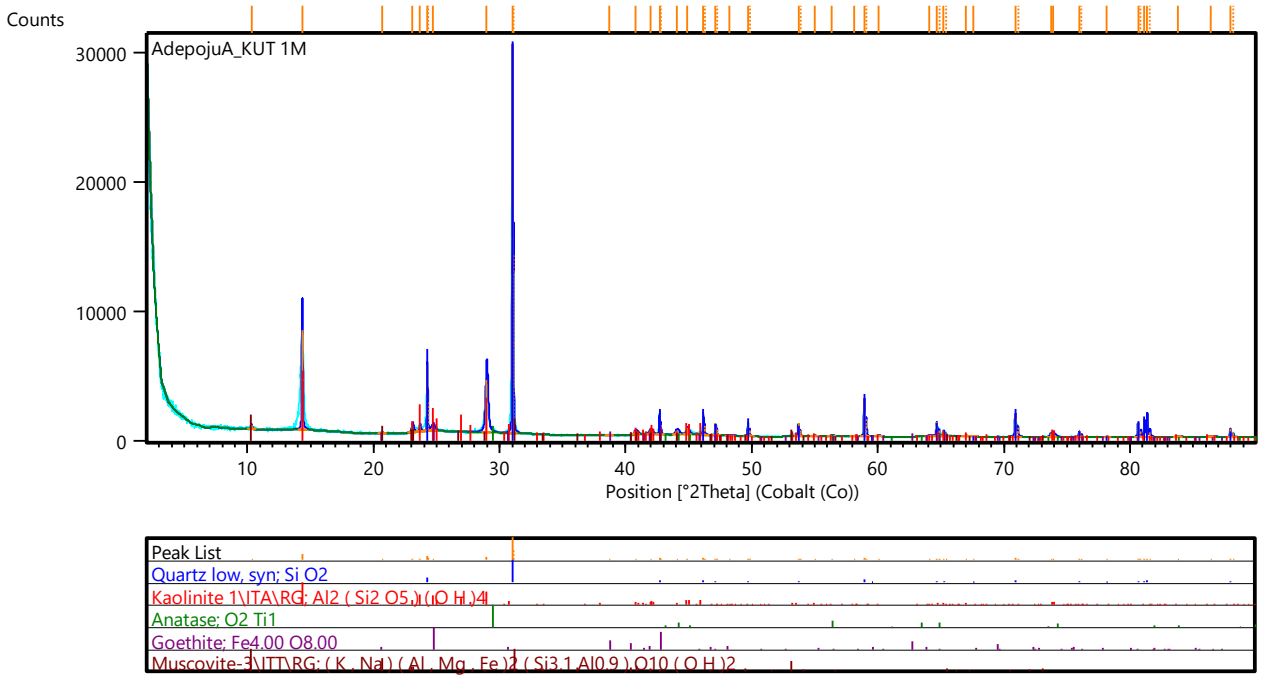


Figure IV: X-Ray Diffractogram for sample KUD-1M.

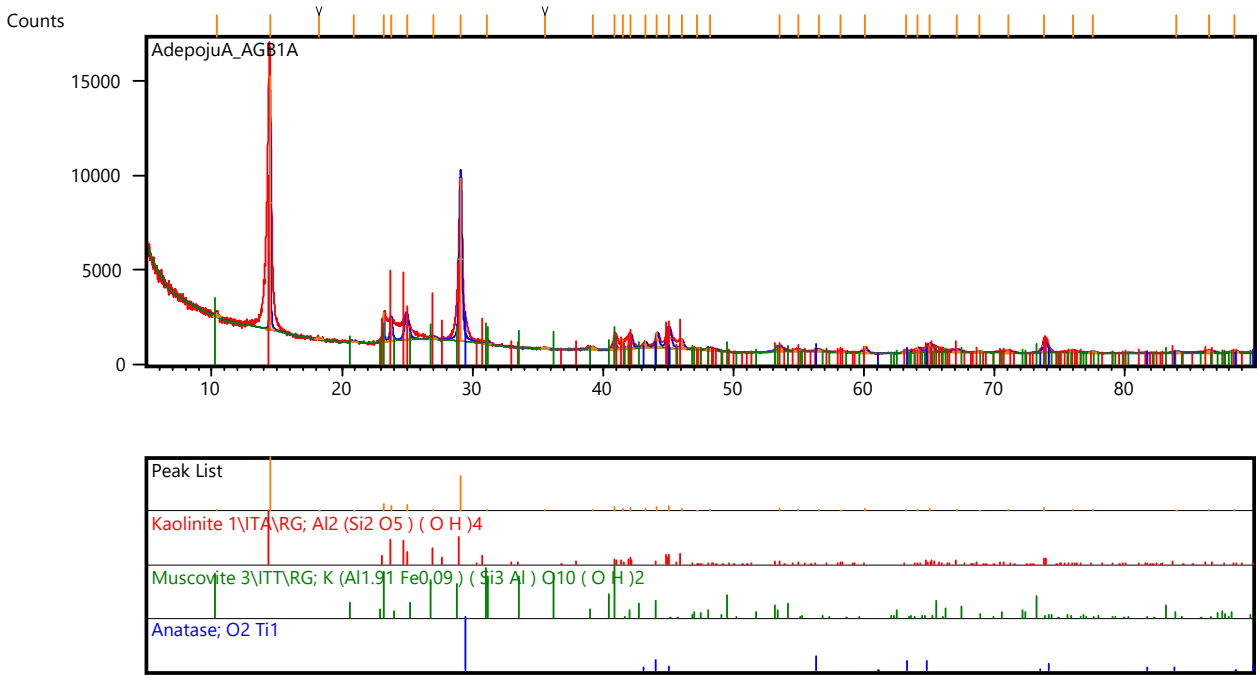


Figure V: X-Ray Diffractogram for sample AGB-1A.

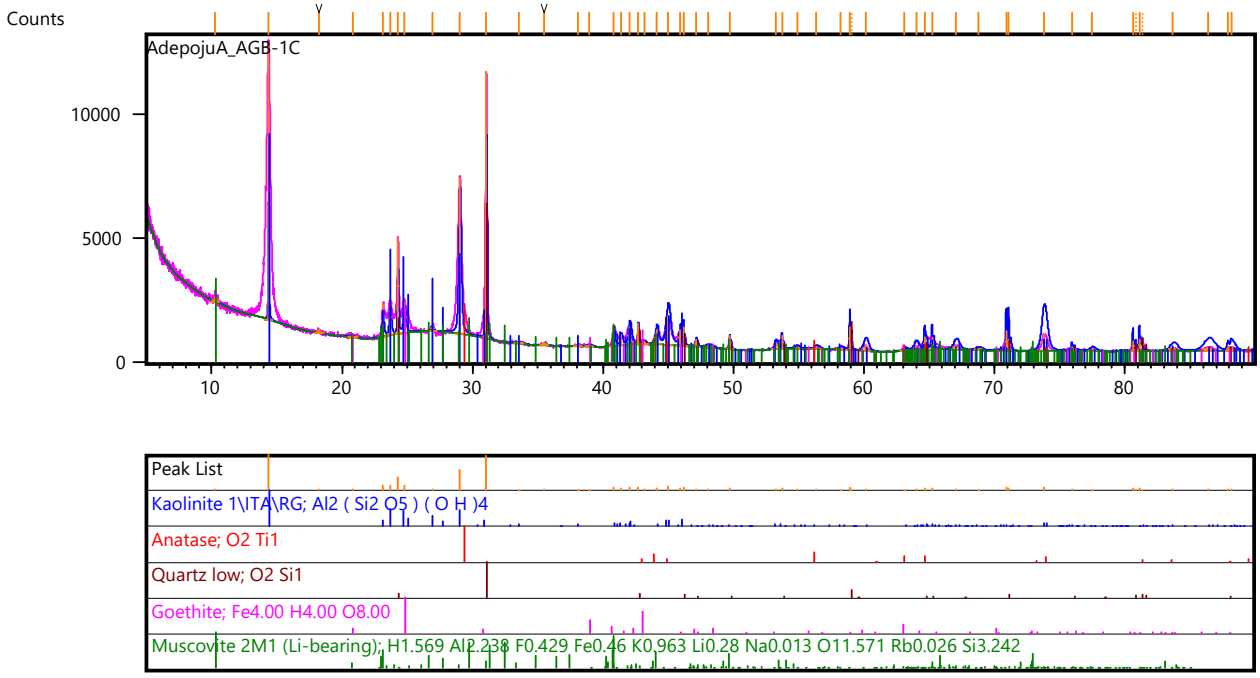


Figure VI: X-Ray Diffractogram for sample AGB-1C.

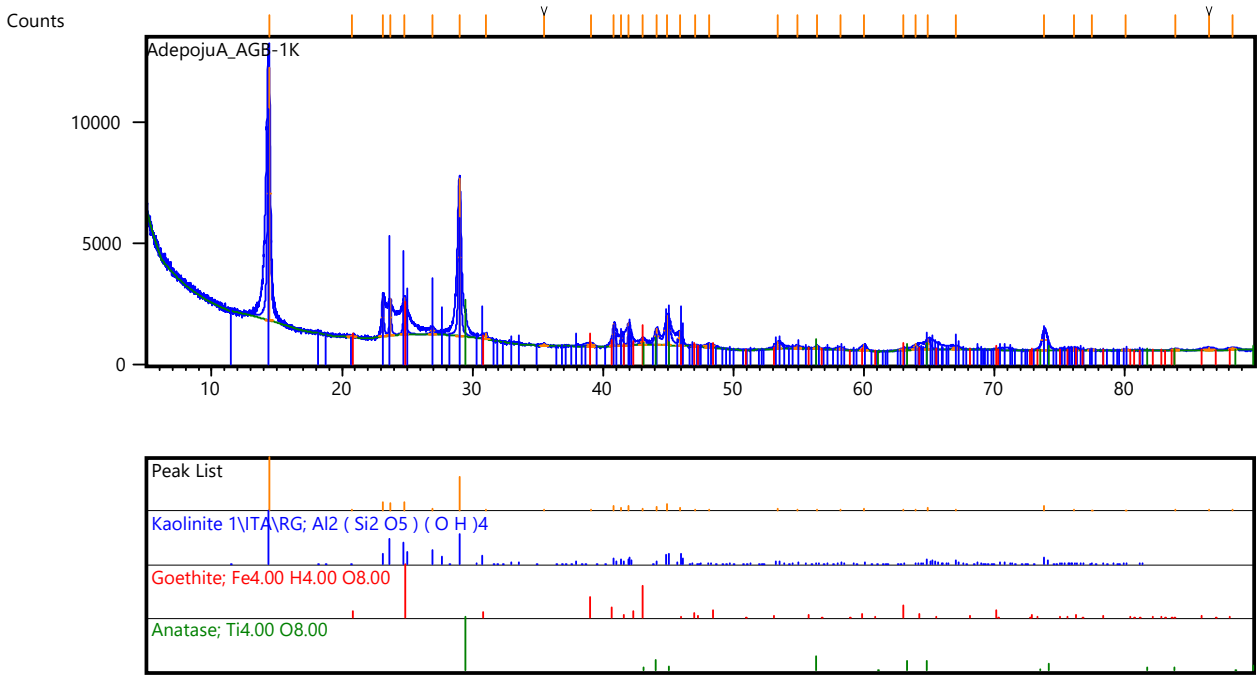


Figure VII: X-Ray Diffractogram for sample AGB-1K.

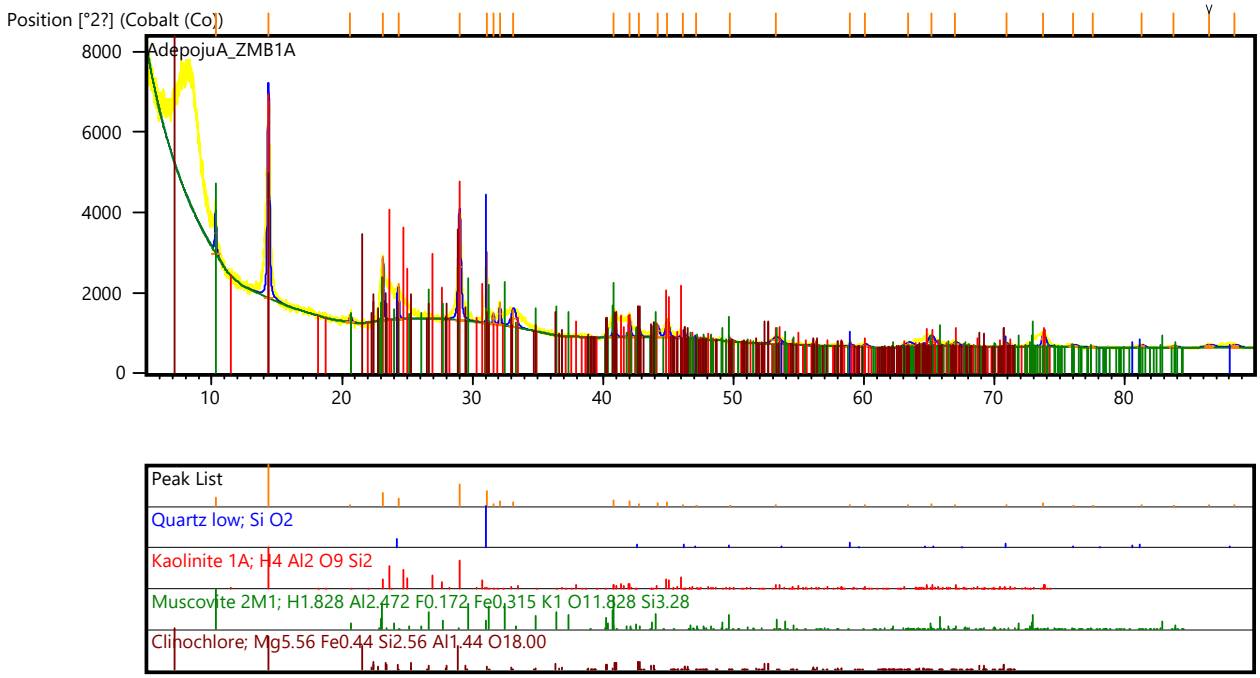


Figure VIII: X-Ray Diffractogram for sample ZMB-1A.

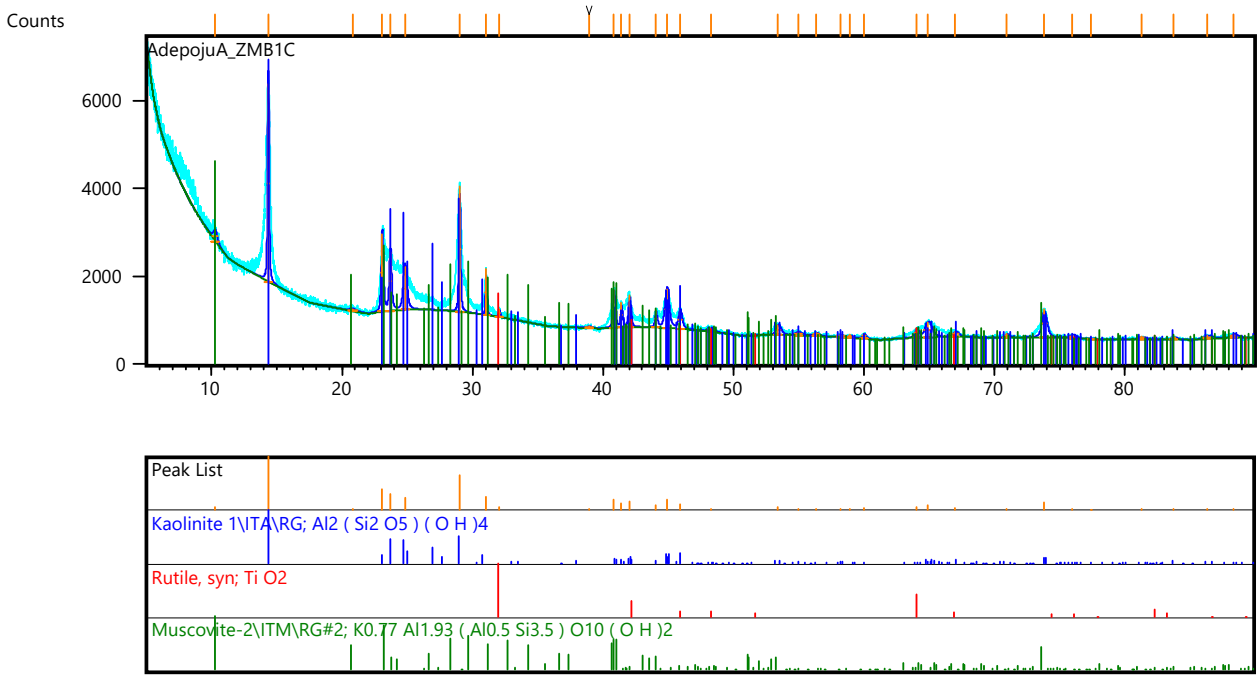


Figure IX: X-Ray Diffractogram for sample ZMB-1C.

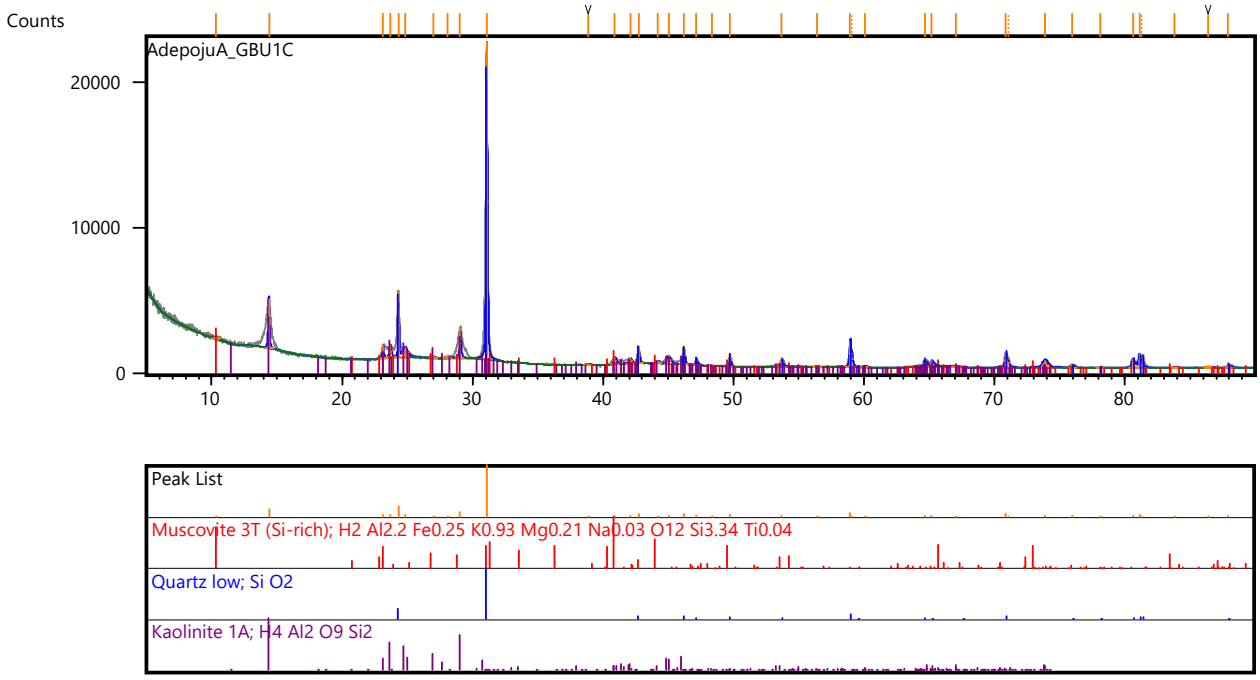


Figure X: X-Ray Diffractogram for sample GBU-1C.

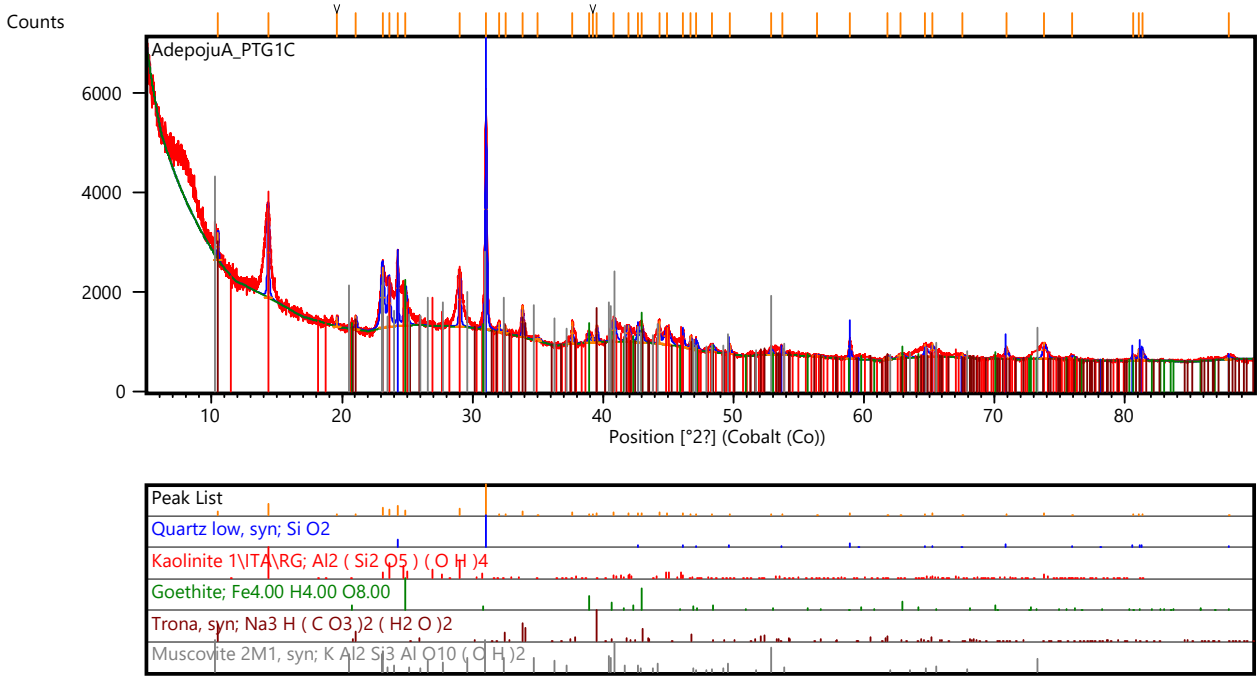


Figure XI: X-Ray Diffractogram for sample PTG-1C.

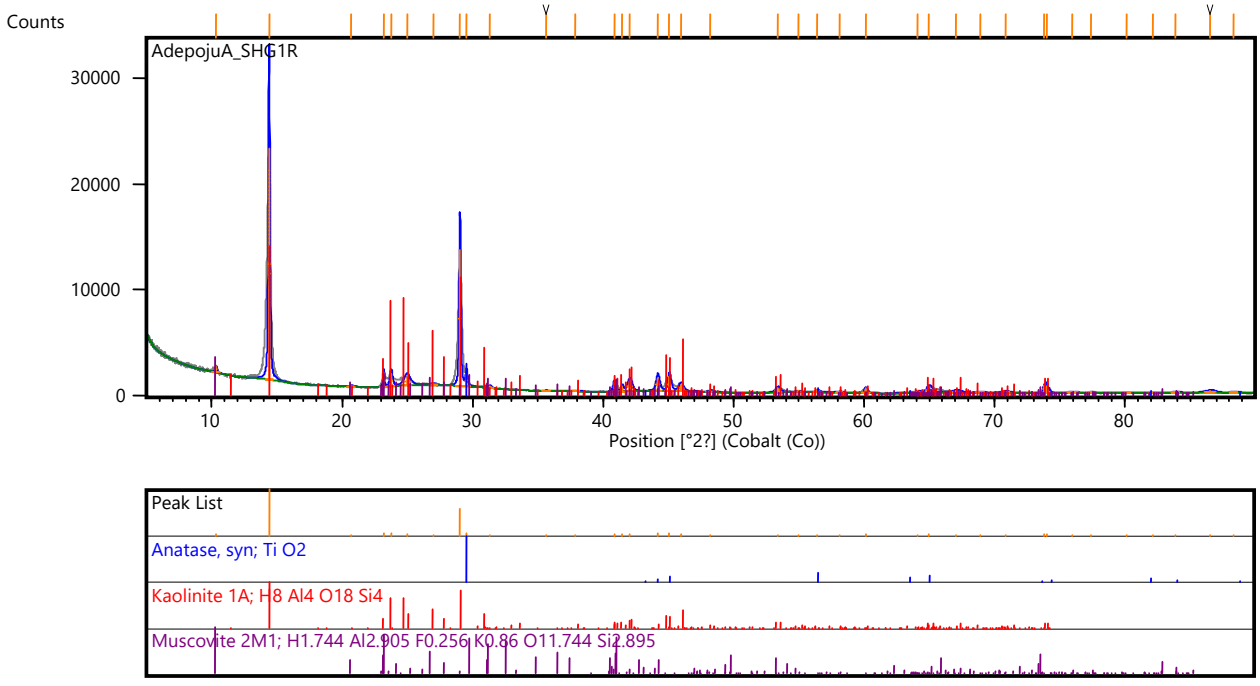


Figure XII: X-Ray Diffractogram for sample SHG-1R.